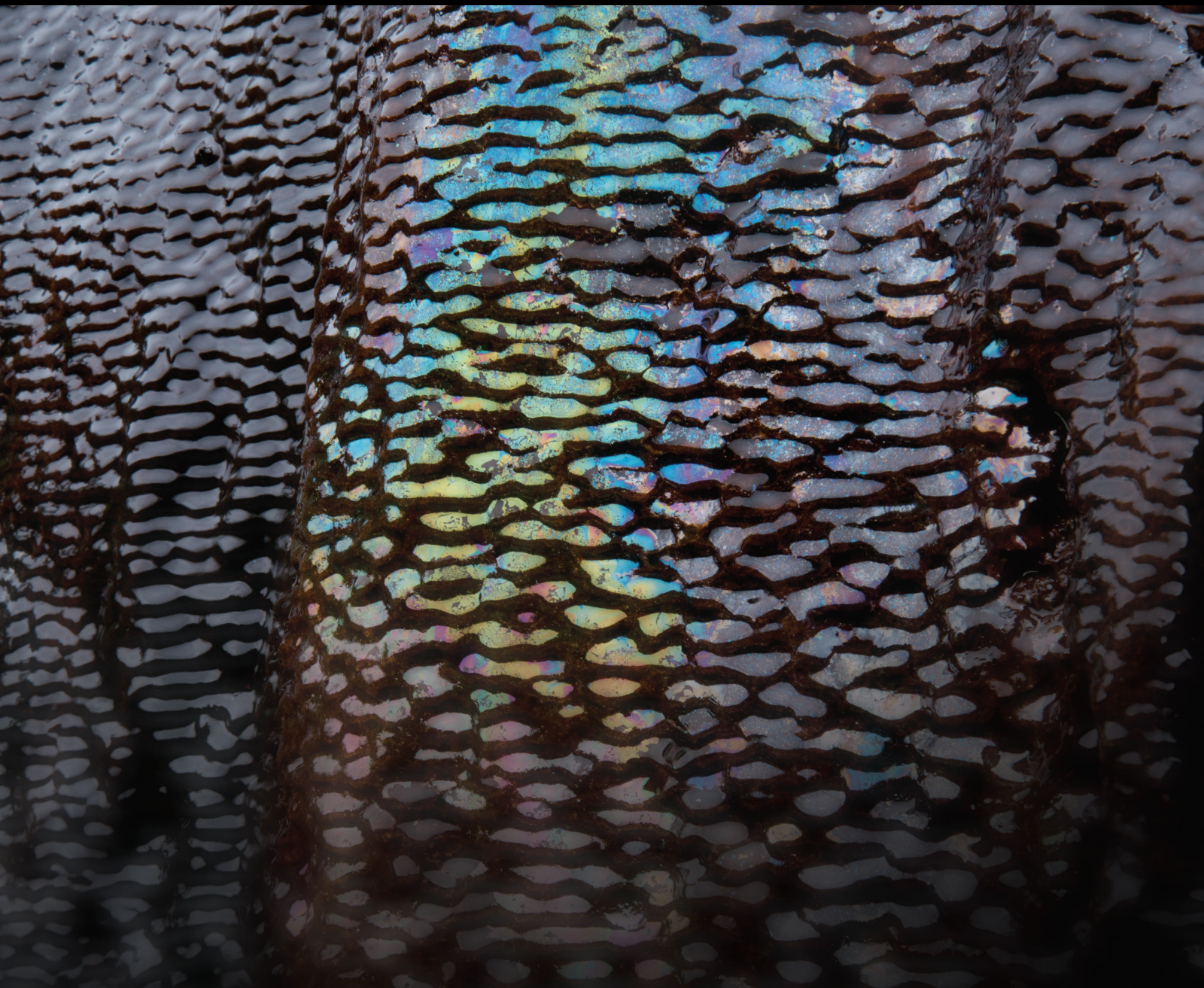


Behaviour and Composition of Fluids in Coal Mining

Lead Guest Editor: Tao Li

Guest Editors: Bo Li, Zhengyang Song, Binwei Xia, Wei Qiao, and Qiqing Wang





Behaviour and Composition of Fluids in Coal Mining

Geofluids

Behaviour and Composition of Fluids in Coal Mining

Lead Guest Editor: Tao Li

Guest Editors: Bo Li, Zhengyang Song, Binwei Xia,
Wei Qiao, and Qiqing Wang







Copyright © 2021 Hindawi Limited. All rights reserved.

This is a special issue published in "Geofluids." All articles are open access articles distributed under the Creative Commons Attribution License, which permits unrestricted use, distribution, and reproduction in any medium, provided the original work is properly cited.



























Chief Editor

































Umberta Tinivella, Italy

Associate Editors

Paolo Fulignati , Italy
Huazhou Li , Canada
Stefano Lo Russo , Italy
Julie K. Pearce , Australia

Academic Editors


Basim Abu-Jdayil , United Arab Emirates
Hasan Alsaedi , USA
Carmine Apollaro , Italy
Baojun Bai, USA
Marino Domenico Barberio , Italy
Andrea Brogi , Italy
Shengnan Nancy Chen , Canada
Tao Chen , Germany
Jianwei Cheng , China
Paola Cianfarra , Italy
Daniele Cinti , Italy
Timothy S. Collett , USA
Nicoló Colombani , Italy
Mercè Corbella , Spain
David Cruset, Spain
Jun Dong , China
Henrik Drake , Sweden
Farhad Ehya , Iran
Lionel Esteban , Australia
Zhiqiang Fan , China
Francesco Frondini, Italy
Ilaria Fuoco, Italy
Paola Gattinoni , Italy
Amin Gholami , Iran
Michela Giustiniani, Italy
Naser Golsanami, China
Fausto Grassa , Italy
Jianyong Han , China
Chris Harris , South Africa
Liang He , China
Sampath Hewage , Sri Lanka
Jian Hou, China
Guozhong Hu , China
Lanxiao Hu , China
Francesco Italiano , Italy
Azizollah Khormali , Iran
Hailing Kong, China

Karsten Kroeger, New Zealand
Cornelius Langenbruch, USA
Peter Leary , USA
Guangquan Li , China
Qingchao Li , China
Qibin Lin , China
Marcello Liotta , Italy
Shuyang Liu , China
Yong Liu, China
Yueliang Liu , China
Constantinos Loupasakis , Greece
Shouqing Lu, China
Tian-Shou Ma, China
Judit Mádl-Szonyi, Hungary
Paolo Madonna , Italy
Fabien Magri , Germany
Micòl Mastroicco , Italy
Agnes Mazot , New Zealand
Yuan Mei , Australia
Evgeniy M. Myshakin , USA
Muhammad Tayyab Naseer, Pakistan
Michele Paternoster , Italy
Mandadige S. A. Perera, Australia
Marco Petitta , Italy
Chao-Zhong Qin, China
Qingdong Qu, Australia
Reza Rezaee , Australia
Eliahu Rosenthal , Israel
Gernot Rother, USA
Edgar Santoyo , Mexico
Mohammad Sarmadivaleh, Australia
Venkatramanan Senapathi , India
Amin Shokrollahi, Australia
Rosa Sinisi , Italy
Zhao-Jie Song , China
Ondra Sracek , Czech Republic
Andri Stefansson , Iceland
Bailu Teng , China
Tivadar M. Tóth , Hungary
Orlando Vaselli , Italy
Benfeng Wang , China
Hetang Wang , China
Wensong Wang , China
Zhiyuan Wang , China
Ruud Weijermars , Saudi Arabia

Bisheng Wu , China
Da-yang Xuan , China
Yi Xue , China
HE YONGLIANG, China
Fan Yang , China
Zhenyuan Yin , China
Sohrab Zendeboudi, Canada
Zhixiong Zeng , Hong Kong
Yuanyuan Zha , China
Keni Zhang, China
Mingjie Zhang , China
Rongqing Zhang, China
Xianwei Zhang , China
Ye Zhang , USA
Zetian Zhang , China
Ling-Li Zhou , Ireland
Yingfang Zhou , United Kingdom
Daoyi Zhu , China
Quanle Zou, China
Martina Zucchi, Italy



Contents

Multisource Information Risk Evaluation Technology of Mine Water Inrush Based on VWM: A Case Study of Weng'an Coal Mine

Bo Li , Tao Li, Wenping Zhang, Zijie Liu, and Lei Yang





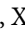



Research Article (12 pages), Article ID 8812144, Volume 2021 (2021)

A DOFS-Based Approach to Calculate the Height of Water-Flowing Fractured Zone in Overlying Strata under Mining

Chunde Piao , Jinjun Li, Dangliang Wang, and Wei Qiao 

Research Article (10 pages), Article ID 8860600, Volume 2021 (2021)

Gas Displacement Engineering Test by Combination of Low and Medium Pressure Injection with Liquid CO₂ in High Gas and Low Permeability Coal Seam

Hu Wen , Mingyang Liu , Gaoming Wei , Xiaowei Zhai , Shixing Fan , Xiaojiao Cheng , Hu Wang , and Jianchi Hao 

Research Article (13 pages), Article ID 8840602, Volume 2020 (2020)

Numerical Research of Fluid Flow and Solute Transport in Rough Fractures under Different Normal Stress

Min Wang , Qifeng Guo, Pengfei Shan , Meifeng Cai , Fenhua Ren , and Bing Dai



Research Article (17 pages), Article ID 8845216, Volume 2020 (2020)

Stability Analysis of a Slope considering Two Reinforcement Processes

Wei Chen , Dongbai Li, Ting Ma , Helin Fu, and Yanpeng Du



Research Article (13 pages), Article ID 8828747, Volume 2020 (2020)

Hydrogeochemical Evolution and Control Mechanism of Underground Multiaquifer System in Coal Mine Area

Qiding Ju , Yu Liu , Youbiao Hu, Yuquan Wang, Qimeng Liu, and Zitao Wang


Research Article (15 pages), Article ID 8820650, Volume 2020 (2020)

Hydromechanical Coupling Characteristics of the Fractured Sandstone under Cyclic Loading-Unloading

Tong Zhang , Yang Liu , Ke Yang, Ming Tang, Xiang Yu, and Fei Yu




Research Article (12 pages), Article ID 8811003, Volume 2020 (2020)

Study on Borehole Arrangement Methods for Gas Extraction by Hydraulic Slotting in Long-Distance Through-Coal Seam Tunnel

Cunfang Zhu and Shuang Cai 



Research Article (8 pages), Article ID 8834798, Volume 2020 (2020)

Design and Realization of the Intelligent Design System for Tunnel Blasting in Mine Based on Database

Zhengyu Wu , Dayou Luo , and Guan Chen 


Research Article (11 pages), Article ID 8878783, Volume 2020 (2020)

Height of Mining-Induced Fractured Zones in Overlying Strata and Permeability of Rock with Nonpenetrative Fractures

Yu Liu , Qimeng Liu , Wenping Li, and Youbiao Hu




Research Article (13 pages), Article ID 8829263, Volume 2020 (2020)

Cause Analysis and Prevention of Hole Collapse by Water Injection and Dust Removal in Qi Panjing Coal Mine

Hua Guo , Hai-Qiao Wang, Shi-Qiang Chen, and Zhi-Rong Wu


Research Article (8 pages), Article ID 8814015, Volume 2020 (2020)

A New Method for the Measurement of Gas Pressure in Water-Bearing Coal Seams and Its Application

Xiao Cui , Jiayong Zhang , Liwen Guo, and Xuemin Gong 



Research Article (11 pages), Article ID 8881063, Volume 2020 (2020)

Study on Statistical Damage Theory Model of Tailings in a Metal Ore under the Action of Moisture Absorption and Dehumidification Circulation

Bing Cao, Hua Wei, Mei-Qi Dou, Lin Hu, and Yao-hui Guo 

Research Article (7 pages), Article ID 8892904, Volume 2020 (2020)

Prediction and Analysis of Abnormal Gas Emission Law in Low-Gas Tunnel Based on K-Line Diagram

Haiyang Wang , Shulei Zhao, Jialiang Liu, Yanmin Zhou, Xiang Chen, Jie Wang, and Liang Cheng 



Research Article (11 pages), Article ID 8898394, Volume 2020 (2020)

Macroscopic and Mesoscopic Mechanical Properties of Mine Tailings with Different Dry Densities under Different Confining Pressures

Zhi-jun Zhang , Yao-hui Guo, Ya-kun Tian , Lin Hu, Xi-xian Wang, Huai-miao Zheng, and Ling-ling Wu 



Research Article (12 pages), Article ID 8832335, Volume 2020 (2020)

Rib Spalling 3D Model for Soft Coal Seam Faces with Large Mining Height in Protective Seam Mining: Theoretical and Numerical Analyses

Shuai Liu, Ke Yang , Tong Zhang , and Chunan Tang



Research Article (17 pages), Article ID 8828844, Volume 2020 (2020)

Experimental Study on MICP Aqueous Solution under the Action of Different Organic Substrates

Huai-miao Zheng, Ling-ling Wu , Kai-wen Tong, Lin Hu, Qing Yu, Gui-cheng He, and Zhi-jun Zhang 

Research Article (11 pages), Article ID 8843945, Volume 2020 (2020)

Experimental Study on the Mechanical Properties and Damage Evolution of Hollow Cylindrical Granite Specimens Subjected to Cyclic Coupled Static-Dynamic Loads

Yongming Xue, Bing Dai, Ying Chen , Lei Zhang, Guicheng He, and Zhijun Zhang 

Research Article (14 pages), Article ID 8881936, Volume 2020 (2020)


Contents

Overburden Damage Degree-Based Optimization of High-Intensity Mining Parameters and Engineering Practices in China's Western Mining Area

Xiang He, Cun Zhang , and Penghua Han

Research Article (21 pages), Article ID 8889663, Volume 2020 (2020)

Study on Fracturing and Diffusion Mechanism of Nonslab Fracturing Grouting

Hua Cheng, Xiangyang Liu , Jian Lin, Liangliang Zhang, Mingjing Li, and Chuanxin Rong


Research Article (9 pages), Article ID 8838135, Volume 2020 (2020)

Experimental and Numerical Study on Hydromechanical Coupled Deformation Behavior of Beishan Granite considering Permeability Evolution

Z. H. Wang , W. G. Ren, Y. L. Tan, and Heinz Konietzky


Research Article (14 pages), Article ID 8855439, Volume 2020 (2020)

Effective Methane Extraction Radius after High-Pressure Water Jet Slotting

Hu Ke , Xia Binwei, Liu Chengwei, and Lu Yiyu

Research Article (12 pages), Article ID 8820540, Volume 2020 (2020)

An Improved C-V Model and Application to the Coal Rock Mesocrack Images

Yulong Chen and Hongwei Zhang 

Research Article (11 pages), Article ID 8852209, Volume 2020 (2020)

Research Article

Multisource Information Risk Evaluation Technology of Mine Water Inrush Based on VWM: A Case Study of Weng'an Coal Mine

Bo Li^{1,2}, Tao Li³, Wenping Zhang², Zijie Liu², and Lei Yang⁴

¹Key Laboratory of Karst Georesources and Environment, Ministry of Education, Guizhou University, Guiyang 550025, China

²College of Resource and Environmental Engineering, Guizhou University, Guiyang 550025, China

³School of Mines and Civil Engineering, Liupanshui Normal University, Liupanshui 553004, China

⁴Guizhou Zhong Gui Environmental Technology Co. Ltd., Guiyang 550025, China

Correspondence should be addressed to Bo Li; libo1512@163.com

Received 29 May 2020; Revised 26 April 2021; Accepted 9 May 2021; Published 24 May 2021

Academic Editor: Giovanni Mongelli

Copyright © 2021 Bo Li et al. This is an open access article distributed under the Creative Commons Attribution License, which permits unrestricted use, distribution, and reproduction in any medium, provided the original work is properly cited.

The use of multisource information fusion technology to predict the risk of water inrush from coal floor is a research hotspot in recent years, but the current evaluation method is mainly based on a constant weight evaluation model. Using constant weights to reflect the control effect of changing factor state values on water inrush evaluation has obvious limitations, and it is unable to describe the control effect of the hydrogeological condition mutation on the water inrush from the floor. In order to solve the above problems, this manuscript introduces the idea of variable weight into the field of water inrush evaluation, expounds on the significance of variable weight theory for water inrush evaluation, analyzes the characteristics of mine water inrush variable weight evaluation, and, on this basis, further combines GIS-based multisource information fusion technology and typical engineering case to compare with the evaluation effect map, evaluation unit, and comprehensive evaluation values. The differences between the variable weight model (VWM) and the constant weight model (CWM) are analyzed, which proves that the evaluation process of the variable weight evaluation model is more reasonable and can effectively improve the evaluation accuracy.

1. Introduction

Mine water risk has always been one of the important factors restricting coal mining in China, and it is of great application value to carry out research on mine water inrush risk prediction technology [1–5]. In China, the forecast of coal floor water inrush has been studied for more than 40 years. In the early 1960s, according to a large number of mine water inrush data, the empirical formula of the water inrush coefficient method (WICM) for predicting water inrush was summarized, and it has been used until now [6–8]. However, there are many factors influencing water inrush disaster [9–12]. The WICM only considers the water pressure and aquiclude thickness. It does not fully reflect the nonlinear dynamic phenomenon controlled by multifactors. Based on the above reasons, from the beginning of the 20th century to the present, some scholars have adopted the geographic information systems (GIS) with linear or nonlinear integration technology and proposed the water inrush evaluation

method based on multisource information fusion technology. For example, Dai et al. analyzed the water inrush risk of the 11th coal seam in Hancheng mining area using GIS and analytic hierarchy process (AHP) [13]. Wu et al. proposed a karst water inrush water risk prediction method based on GIS and artificial neural network (ANN) coupling technology [14]. Hu et al. obtained the weights of the evaluation factors through AHP and the entropy weight method and further determined water inrush risk zonation by using GIS technology [15]. Similar studies also include Liu et al. [16], Chen et al. [17], and Ruan et al. [18]. This type of method can better solve the problem of water inrush prediction [19]. However, in the process of applying multisource information fusion technology to predict water inrush, the currently widely used evaluation model is the weighted average model: $M(x_1, x_2, \dots, x_m) = \sum_{i=1}^m w_i x_i$, where x_i is the state value of factors influencing water inrush and $w_i \in [0, 1]$ is the weight of the influencing factor and needs to satisfy $\sum_{i=1}^m w_i = 1$ [20, 21]. In this model, regardless of how the

state vector $X = (x_1, x_2, \dots, x_m)$ of each factor changes, the weight vector $W = (w_1, w_2, \dots, w_m)$ of the factor always remains unchanged. This method reflects the relative importance of individual factors in the overall evaluation system to a certain extent and has certain scientific nature and applicability. However, under certain weight vector levels, the water inrush evaluation result is not only related to each basic importance of influencing factors but also related to the magnitude of the factor state value and the combination relationship of the state value of each factor; that is, the state vector $X = (x_1, x_2, \dots, x_m)$ of the constant coping factor of the weight vector $W = (w_1, w_2, \dots, w_m)$ has a certain limitation. The CWM ignores the influence of the internal differences of the factor state value on the evaluation process and is unable to describe the control effect of the change of state value caused by the change of hydrogeological conditions. The more factors involved in the evaluation, the more average the weights, the greater the probability of making a wrong judgment.

In order to solve the above technical defect, this paper introduces the variable weight idea into the process of water inrush risk evaluation. The VWM can realize the change of factor weight value with the change of its state value, which can more accurately reflect the influence effect of water inrush by a sudden change of hydrogeological condition. The evaluation process is more consistent with the law of occurrence of water inrush and has a positive effect on improving the accuracy of water inrush evaluation. The method proposed in this paper can provide a reference for the risk evaluation of water inrush from the coal floor in areas with similar geological conditions in the world.

2. Overview of the Research Area

2.1. Physical Geography. Weng'an Coal Mine is located in Weng'an county in Guizhou province within the geographic coordinate of $107^{\circ}28'30'' \sim 107^{\circ}32'30''$ (east longitude) and $26^{\circ}57'57'' \sim 27^{\circ}03'15''$ (north latitude); the geography location is shown in Figure 1. The topography of the mining area is generally high in the south and low in the north. The eastern and western regions are the ridges with a north-south direction, while the central region is a valley, with a long strip of about 20 km length and 3-5 km width.

2.2. Meteorological and Hydrological. The climate type of the mining area belongs to the subtropical humid monsoon climate, and the rainy season is concentrated from April to September, with the annual rainfall reaching 1148.2 mm. The rainfall in the rainy season accounts for more than 70% of the total annual rainfall. The surface water system of the mining area belongs to the tributaries of Baishui river tributary, Yangtze river basin. And the Baishui river runs through the whole area, and it is the main river in the region. Along both sides of the Baishui river develops a seasonal stream with short flow, small water, and dry season.

2.3. Geological Conditions. According to the borehole data, the exposed strata from old to new are the Middle Permian System Maokou Formation (P_2m), Upper Permian System

Emeishan Basalt Formation ($P_3\beta$), the Upper Permian System Wujiaping Formation (P_3w), the Upper Permian System Changxing Formation (P_3c), the Lower Triassic System Yelang Formation (T_1y), and the Quaternary (Q). The mine is located on the wings of the Yangzi washing horse syncline of quasistation, and the oblique axis is distributed in the north-south direction. The dip angle of the two wings is $10-37^{\circ}$, which is basically symmetrical. Three faults are developed in the mining area, one fault is nearly northeastward and extends longer, and the other two faults are near east-west and small in scale. The coal-bearing strata are Permian Wujiaping Formation (P_3w). It is a set of gray, light gray thin-layered carbon mudstone and silty mudstone with argillaceous siltstone, containing four layers of coal; only Dth coal seam can be mined. It is the target coal seam for this evaluation (Figure 2).

2.4. Hydrogeological Conditions. According to the geological borehole data of the mining area, the lithology of Middle Permian Maokou Formation (P_2m) is gray to grayish thick layer and the massive micritic limestone powder, containing a small amount of irregular chert nodule, and its thickness is greater than 60 m. According to the results of a hydrogeological survey, the karst fissure of this aquifer is strongly developed and belongs to a water-rich confined aquifer. There is a wide distribution range between limestone and main coal seam of Maokou Formation, but the thickness of which is not uniform. As an aquiclude, basalt can generally function as a water barrier under natural conditions. However, under the coupling of mining stress and high-pressure water, water inrush is easy to form in the weak area of the aquiclude.

3. The Thematic Maps of the Factors

At present, there has been a lot of research in the field of water inrush control factors, such as Wu et al. [22], Li et al. [23], and Zeng [24]. Based on the previous research data, according to the hydrogeological conditions and the current geological exploration degree, ignoring the factors that have little effect on the water inrush process, the following six key control factors were selected as the control factors for the water inrush from the floor in Weng'an Coal Mine: (1) Equivalent thickness of effective aquiclude (ETEA): the effective aquiclude is equal to the total thickness of the aquiclude minus the depth of the failure zone of the mine, and the equivalent thickness is the thickness that converts the effective thickness of different lithologies into the same standard lithology. (2) Thickness of brittle rock under failure zone of the mine (TBRFZM): there are brittle rocks such as sandstone and limestone in the aquifuge, which have strong compressive capacity for preventing water inrush. Therefore, the total thickness of brittle rock after the failure zone is reduced as one of the evaluation indicators of water inrush. (3) Distribution of faults and folds (DFF): the rock mass integrity of the aquiclude in the fault and fold distribution is generally poor, and the fractures formed by these geological structures can easily become the passage of groundwater into the mine. (4) Rock quality designation of aquiclude (RQDA): the rock quality designation of aquiclude refers to the ratio of the core

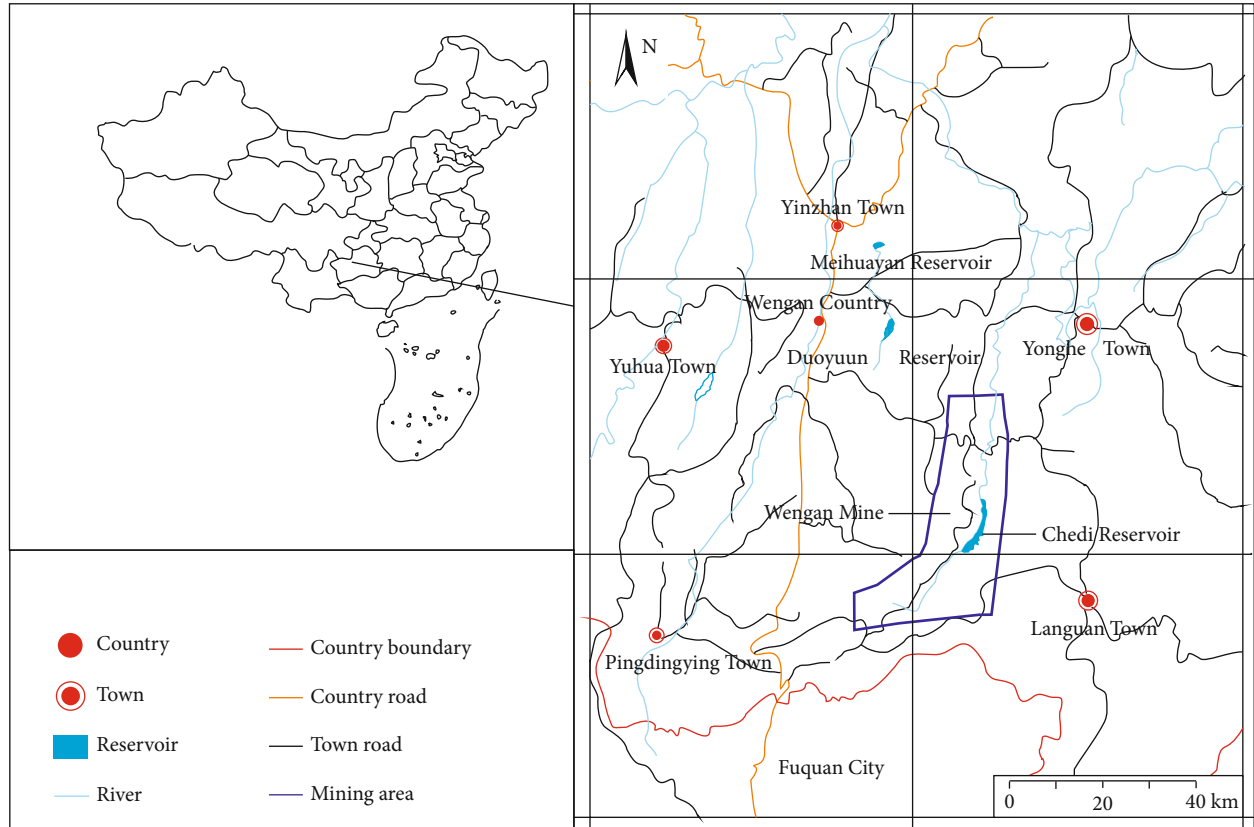


FIGURE 1: Geography location.

length obtained by drilling to the corresponding actual drilling footage, which can reflect the degree of fracture development of the aquiclude. (5) Water abundance of limestone aquifer (WALA): the water abundance of the aquifer is the water-bearing capacity of the aquifer, which determines the amount of water inrush. (6) Water pressure of limestone aquifer (WPLA): high water pressure is the driving factor for the groundwater suddenly flooded into the mine, and it is a prerequisite for the formation of water inrush. The data of various influencing factors of water inrush from the D coal floor of Weng'an Coal Mine were collected and organized, and the original data were processed and interpolated to generate thematic maps of various control factors and establish the factor database. For the method of data processing and interpolation calculation, please refer to Wu et al. [22, 25]. Because of the limited space, only the WPLA thematic map is taken as an example in the text, as shown in Figure 3; the other thematic maps (Figures S1–S5) are in Supplementary Materials.

The purpose of normalizing is to eliminate the influence of different dimensions on the evaluation results, so that it is statistically significant and comparable [19, 26]. The normalization formula used is as follows:

$$N_i = \eta + \frac{(u - \eta) \times (x_i - \min(x_i))}{\max(x_i) - \min(x_i)}. \quad (1)$$

N_i is the normalized value, $\min(x_i)$ is the minimum

state value, $\max(x_i)$ is the maximum state value, u is the upper limit of the normalized range, and η is the lower limit of the normalized range; in the normalization process, $u = 1$, $\eta = 0$.

Among the identified influencing factors, the WALA, RQDA, WPLA, and DFF are positively related to the water inrush risk, which means that the larger the quantified value of these factors, the more likely it is to produce a sudden change. The ETEA and DFF are negatively correlated. In this paper, the negative correlation data is normalized by $(1 - N_i)$.

4. Risk Evaluation of Water Inrush Based on VWM

4.1. Overview of Variable Weight Theory. The variable weight theory is a new comprehensive decision-making method first proposed in the book *Fuzzy Sets and Projectable Random Sets* in the 1980s. Subsequently, Li [27, 28], Liu [29], Li and Li [30], Cai and Li [31], and other mathematicians continued their research on this theory and gradually formed a relatively complete theory. The VWM can realize the weight changes with the change of the factor state value, so that the influence of each factor on the evaluation system under different combination states is better reflected by the change of the weight, which makes it a more scientific weight. The relevant content of the variable weight theory can be found in references, which will not be explained in the paper.


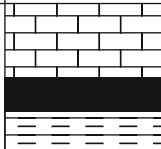
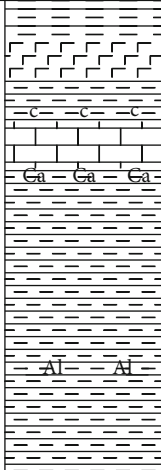
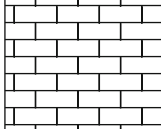
Stratigraphic	Aquifer	Lithology	Thickness (m)	Lithology characterization
	The Dth coal seam 			Limestone Coal seams Mudstone
	Aquifuge		This average is 29.61 m 15.02–38.13	Mudstone Basalt Limestone Carbonaceous mudstone Calcareous mudstone Aluminum mudstone
	Aquifer		>50 m	Limestone

FIGURE 2: Structural relationship between coal seam and aquifer.

4.2. Evaluation Steps

- (1) Determine the water inrush risk evaluation factors of the coal seam floor and produce thematic maps
- (2) Use the analytic hierarchy process (or other weight calculation methods) to determine the constant weight of each factor
- (3) Formulate the weight adjustment plan and construct the state variable weight vector formula according to the plan (formula (3)). It should be noted that researchers can construct the corresponding state variable weight vector according to the actual geological conditions of the coal mine
- (4) On the basis of determining the state variable weight vector formula, according to formula (2), establish the water inrush risk assessment model and use Matlab software to compile the solution program
- (5) According to industry specifications and the geological conditions of the research area, determine the variable weight interval thresholds of different factors. Through continuous debugging of the model, determine the optimal weight adjustment parameter values
- (6) On the basis of determining the model parameters, the variable weight of different evaluation units of each factor is calculated. According to the state value

and variable weight of the factors in different evaluation units, the comprehensive evaluation value of all evaluation units is obtained

- (7) Identify the accuracy of the water inrush risk assessment results

4.3. Evaluation Idea and Model. In the process of GIS-based floor water inrush risk evaluation, the evaluation area will be divided into many evaluation units, each evaluation unit contains all the control factors, and the status value of each control factor is different in different evaluation units. Especially when the status value of a factor in the evaluation unit is very high or very low, it often means that this factor has a stronger control effect on water inrush. In order to avoid the very high or very low state value of a factor in the evaluation unit being neutralized by other factors, the model can significantly increase the weight value of this type of factor. At the same time, the high state value will lead to a significant increase in risk, but the state value is very low and does not necessarily significantly reduce the risk; therefore, the weight of the high state value is increased by a larger amount in the model. It should be noted that the weight of each factor is a secondary adjustment based on its constant weight, so the adjusted weight value does not change the relative importance relationship between each factor. According to the ideas, a risk evaluation model for water inrush based on variable weight theory is constructed [22], as follows:

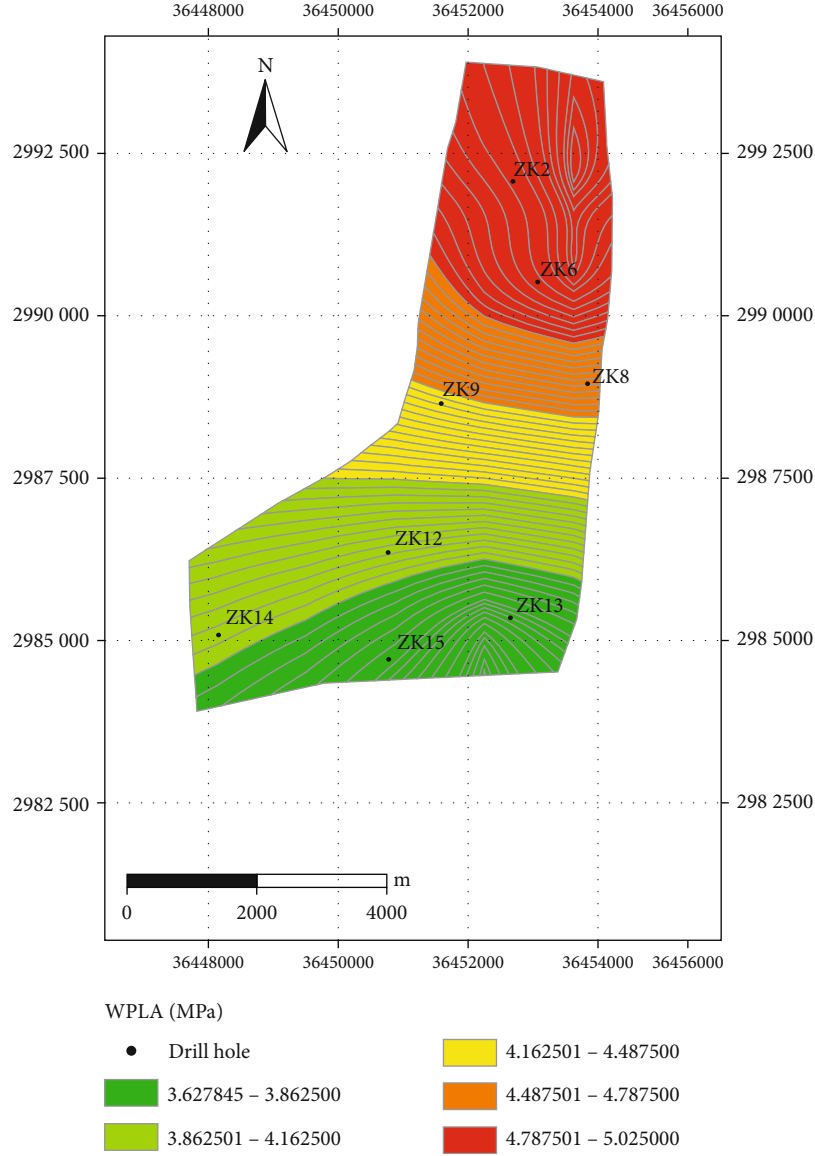


FIGURE 3: The thematic map of WPLA.

$$\begin{aligned}
 RI &= \sum_{i=1}^m w_i \cdot f_i(x, y) = \sum_{i=1}^m \frac{w_i^{(0)} V_i(X)}{\sum_{j=1}^m w_j^{(0)} V_j(X)} f_i(x, y) \\
 &= \frac{w_1^{(0)} V_1(X)}{\sum_{j=1}^m w_j^{(0)} V_j(X)} f_1(x, y) + \frac{w_2^{(0)} V_2(X)}{\sum_{j=1}^m w_j^{(0)} V_j(X)} f_2(x, y) \quad (2) \\
 &\quad + \dots + \frac{w_m^{(0)} V_m(X)}{\sum_{j=1}^m w_j^{(0)} V_j(X)} f_m(x, y),
 \end{aligned}$$

$$V_j(x) = \begin{cases} e^{a_1(b_{j1}-x)} + p - 1, & x \in [0, b_{j1}), \\ c, & x \in [b_{j1}, b_{j2}), \\ e^{a_2(x-b_{j2})} + p - 1, & x \in [b_{j2}, b_{j3}), \\ e^{a_3(x-b_{j3})} + e^{a_2(b_{j3}-b_{j2})} + p - 2, & x \in [b_{j3}, 1], \end{cases} \quad (3)$$

where RI is the risk index, w_i is the variable weight vector, $f_i(x, y)$ is the state value, x and y are the coordinates, $w^{(0)}$ is the constant weight vector, m is the number of factors, and $V(X)$ is the state variable weight vector, expressed as follows:

where a_1, a_2, a_3 , and p are adjustment weight parameters; in this evaluation, $a_1 = 1.46, a_2 = 0.9, a_3 = 0.819$, and $p = 1.635$. b_{j1}, b_{j2} , and b_{j3} are threshold values of the j th factor variable weight interval.

The different status values of the factors have different control effects on water inrush, and the variable weight

TABLE 1: Variable weight interval of main control factors.

Main controlling factors	Variable weight interval			
	$[0, b_{j1}]$	$[b_{j3}, 1]$	$[b_{j2}, b_{j3}]$	$[b_{j3}, 1]$
WPLA	$0 \leq x < 0.288$	$0.288 \leq x < 0.561$	$0.561 \leq x < 0.818$	$0.818 \leq x \leq 1$
ETEA	$0 \leq x < 0.196$	$0.196 \leq x < 0.537$	$0.537 \leq x < 0.728$	$0.728 \leq x \leq 1$
TBRFZM	$0 \leq x < 0.228$	$0.228 \leq x < 0.506$	$0.506 \leq x < 0.825$	$0.825 \leq x \leq 1$
WALA	$0 \leq x < 0.288$	$0.288 \leq x < 0.561$	$0.561 \leq x < 0.818$	$0.818 \leq x \leq 1$
DFE		$0 \leq x < 0.500$	$0.500 \leq x < 0.800$	$0.800 \leq x \leq 1$
RQDA	$0 \leq x < 0.183$	$0.183 \leq x < 0.567$	$0.567 \leq x < 0.800$	$0.800 \leq x \leq 1$

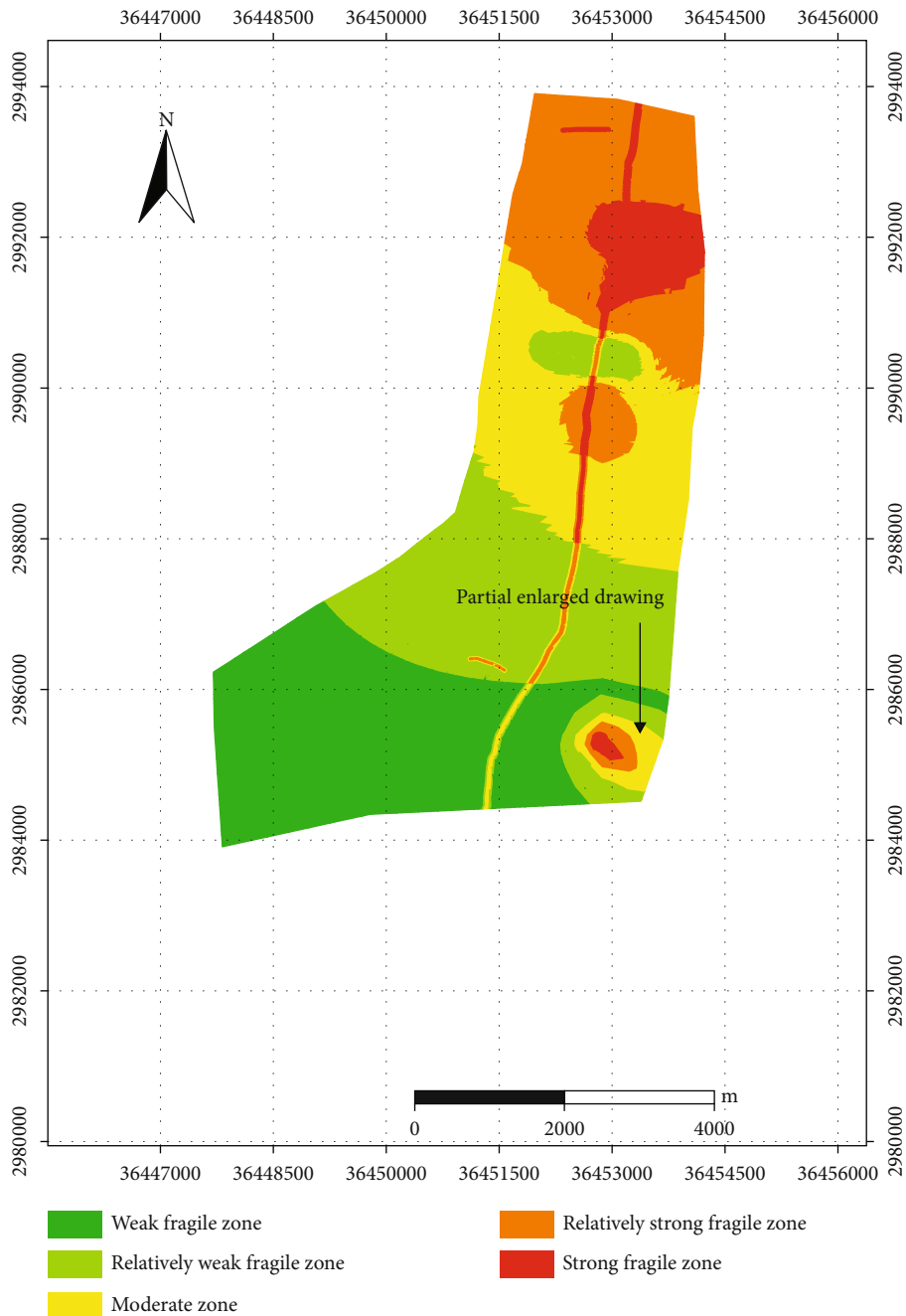


FIGURE 4: Risk partition map based on VWM.

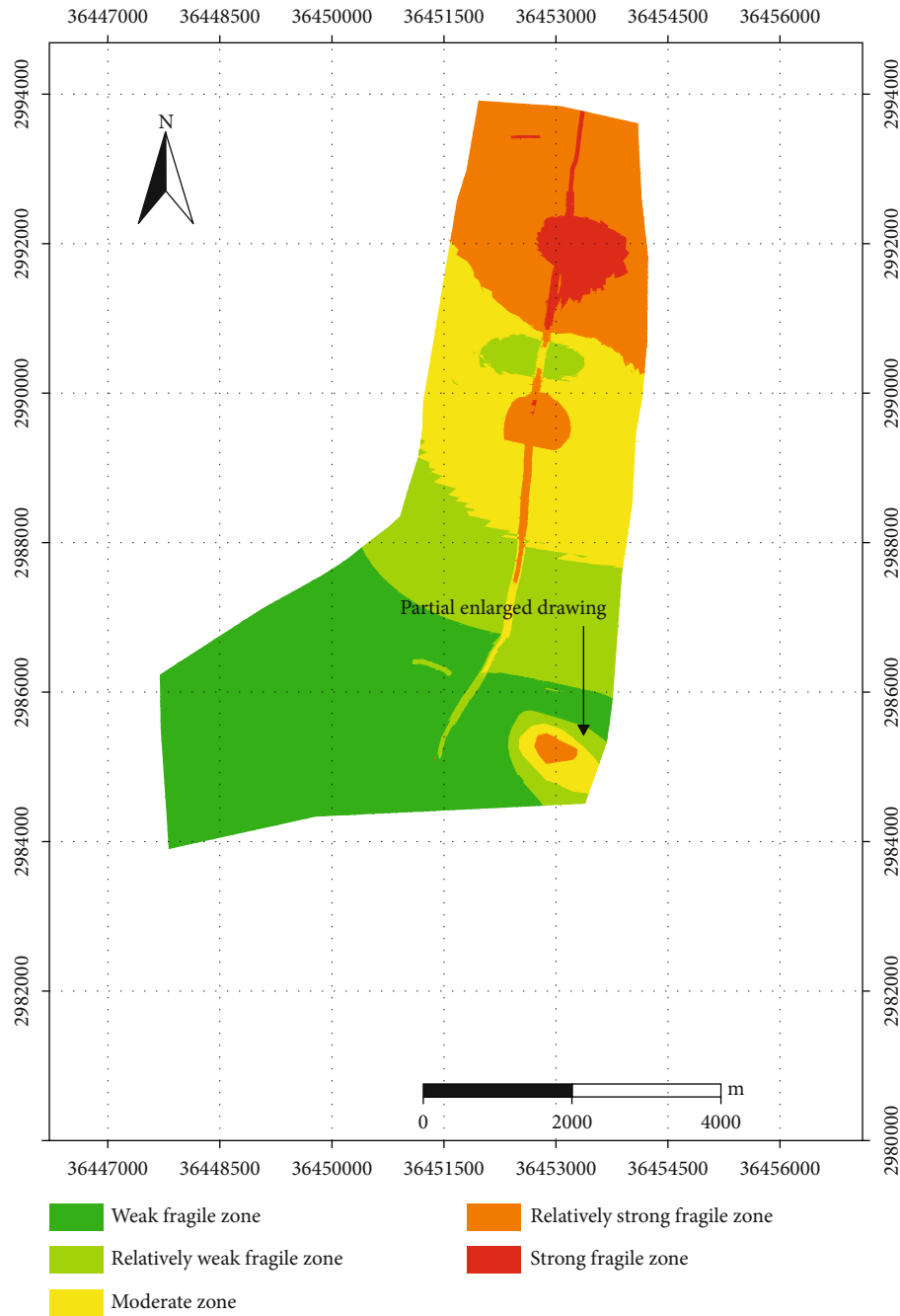


FIGURE 5: Risk partition map based on CWM.

interval threshold determines the degree of weight adjustment of different types of state values of each factor. In $[b_{j_3}, 1]$, the weight increases as the state value increases; in $[b_{j_2}, b_{j_3})$, the weight increases as the state value increases, but the magnitude of the increase is smaller than the $[b_{j_3}, 1]$ interval. In $[b_{j_1}, b_{j_2})$, the weight is neither increased nor decreased; at $[0, b_{j_1})$, the weight increases as the state value decreases. In this paper, according to the characteristics of the difference in the spatial distribution of the state values of the factors, the clustering analysis method is used to determine the variable weight interval of each main control factor, as shown in Table 1.

4.4. Water Inrush Risk Evaluation. Before multifactor fusion analysis, firstly, the composite superposition processing must be carried out. The information superposition function of GIS technology is used to superimpose the thematic maps of control factors, and the information storage layers of each relevant factor are combined into one information storage layer to form the superimposed units containing all relevant factor information. Then, the constant weight of each evaluation factor is determined according to the analytic hierarchy process. On this basis, Matlab software is used to calculate the coal floor water inrush variable weight vulnerability evaluation model (formula (2)), and the weight calculation program

TABLE 2: Comparison of typical unit evaluation results.

Controlling factors	Normalized value	Constant weight	Variable weight	Constant weight evaluation value	Variable weight evaluation value
WALA	0.196	0.1478	0.1121	0.0290	0.0220
RQD	0.483	0.0564	0.0565	0.0272	0.0273
WPLA	0.286	0.2956	0.2670	0.0845	0.0764
TBRFZM	0.325	0.1292	0.1290	0.0420	0.0419
DFE	1.000	0.1128	0.1763	0.1128	0.1763
ETEA	0.367	0.2582	0.2591	0.0948	0.0951
Total value		1	1	0.3903	0.4389

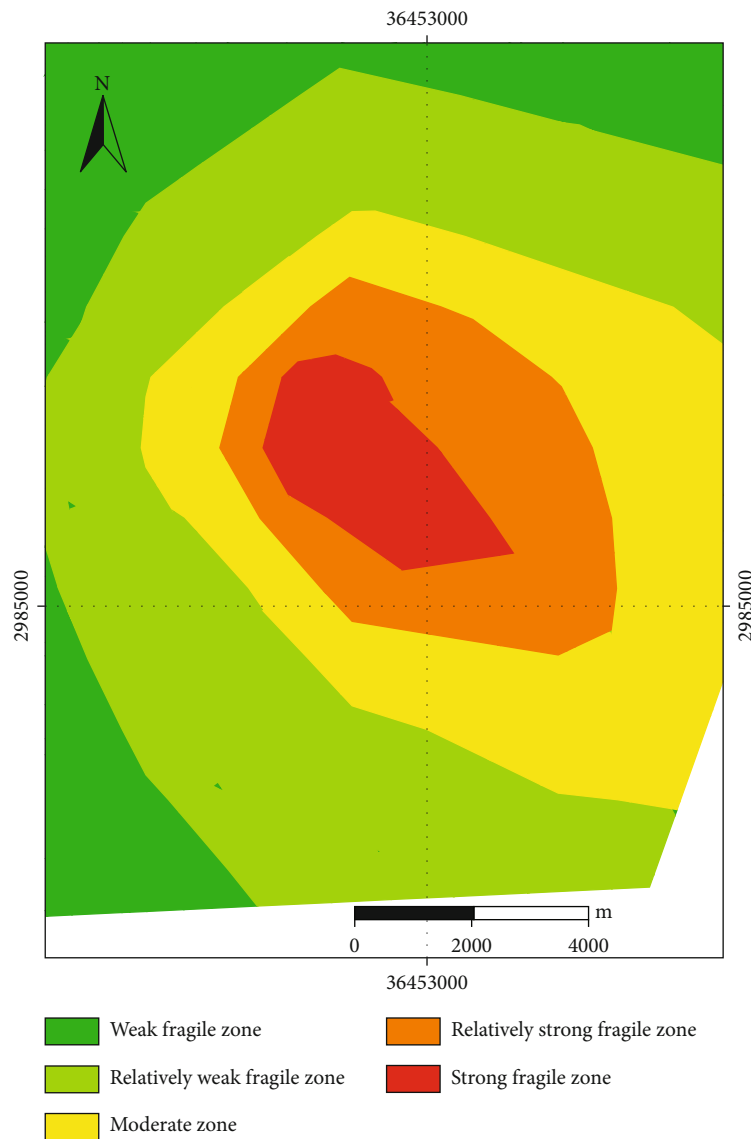


FIGURE 6: Partial enlarged map based on VWM.

can be obtained from Supplementary Materials. Finally, the water inrush vulnerability evaluation index of all superimposed units is obtained. Then, the natural break classification method in GIS software is used to classify, and finally, a floor

water risk evaluation partition map is formed (Figure 4). For comparative analysis, we also made a partition map based on constant weights (Figure 5). The weights were obtained using the AHP, which was proposed by Saaty [32]. This method

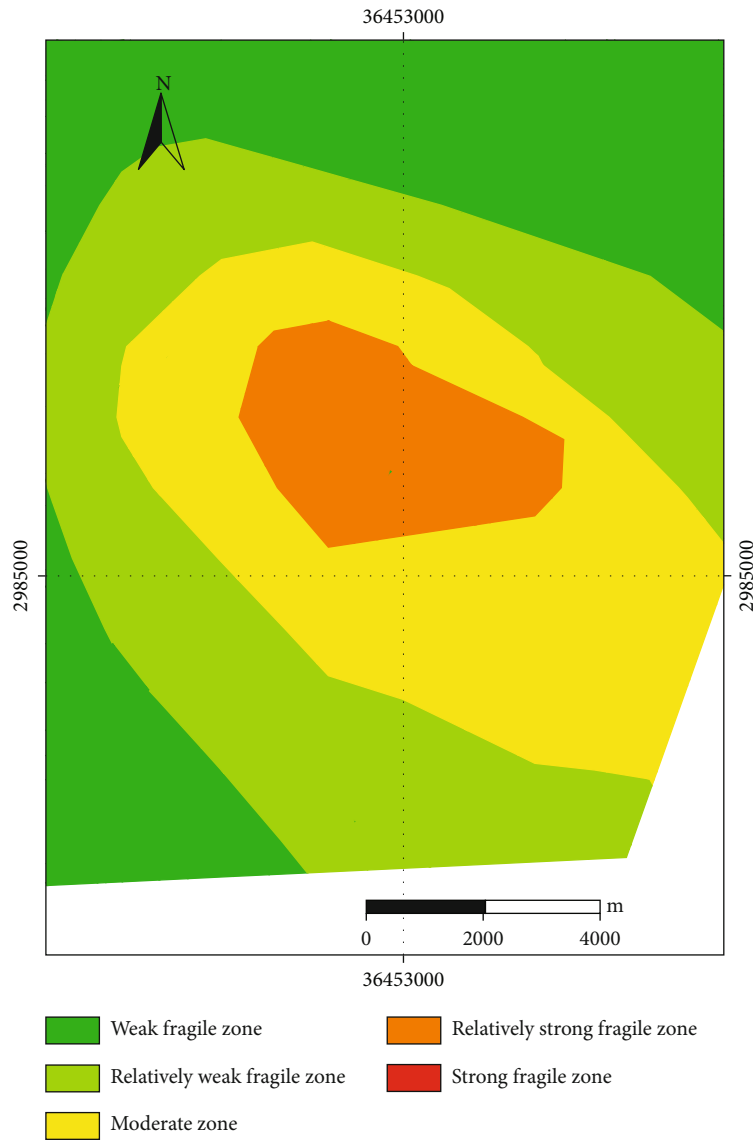


FIGURE 7: Partial enlarged map based on CWM.

obtains the factor weight by calculating the maximum eigenvalue of the judgment matrix and the eigenvectors. The constant weight calculation results are shown in Table 2.

5. Evaluation Effect Analysis

5.1. Comparison of Evaluation Maps. From the evaluation results (Figure 4), the fragile region areas are mainly distributed in the northern, central, and southeastern parts of the mining area. The main reason is that the WALA is rich and the WPLA is large in the northern mining area. The RQDA is poor, and the crack is very developed in the middle of the mining area. The ETEA is very thin in the southeastern mining area. The overall trend of the evaluation results of the two models is basically consistent, and the location of each fragile region is roughly the same, but the risk degree and scope of local have a difference; by the local amplification maps of Figures 6 and 7, it can be seen that the central position evaluation result of this region is the red fragile region under the

VWM. And under the CWM, the corresponding position evaluation result is the orange fragile area. The main reason for the difference is the uplift of limestone in the Maokou Formation in this area, and its aquiclude is very thin. The ETEA is much smaller than the surrounding area. The conventional CWM cannot reflect the sudden change of the ETEA in this area by adjusting the weight value. But in the process of variable weight evaluation, the weight of ETEA in this area is increased from the constant value of 0.2582 up to 0.326~0.336. Therefore, the control effect of ETEA on water inrush is effectively highlighted. Compared with the traditional CWM, the evaluation results are more in line with the law of mine floor water inrush evaluation, which can better describe the control effect of key influencing factors on water inrush, and the evaluation results are more accurate.

5.2. Comparison of Evaluation Results of the Typical Unit. A typical evaluation unit in the research area is selected, and a

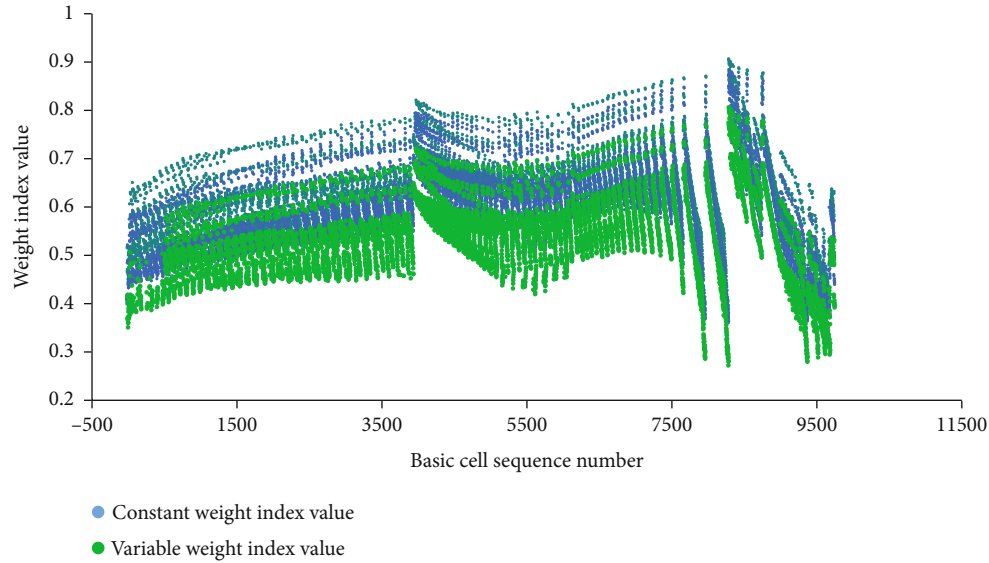


FIGURE 8: Comparison of the range of comprehensive evaluation values.

comprehensive evaluation value is calculated by using two methods of VWM and CWM (Table 2).

From Table 2, it can be clearly seen that the normalized value of the DFF of the evaluation unit is extremely large, and the value is 1, which means that there is a geological structure at the location, and it is easy to induce a water inrush disaster. Compared with other factors, the DFF plays a stronger control role in water inrush. However, in the evaluation process of the CWM, the risk of these two factors was neutralized by the other five factors, resulting in the risk comprehensive evaluation value being reduced to 0.3903. And by using the VWM for risk evaluation, according to the magnitude of the state value of control factors, VWM redistribute the weight of the control factors and increase the weight value of the DFF; the weight value increased from 0.1128 to 0.1763, so that the risk comprehensive evaluation value increased to 0.4389, which effectively prevents the key control factor of water inrush from being neutralized by other factors. Therefore, compared with the CWM, the evaluation process of the VWM is more in line with the actual geological conditions of the mining area, and the risk evaluation results are more accurate.

5.3. Comparison of the Range of Comprehensive Evaluation Values. For each evaluation superimposed unit in the study area, both two evaluation methods of the CWM and the VWM are used to calculate the risk index of water inrush. From the final calculation results, the risk index range of the CWM is 0.3456554~0.8890497 and the risk index range of VWM is 0.314419~0.925728. The risk index distribution ranges of all evaluation units are shown in Figure 8. It can be seen that the risk index range of the VWM is larger than the CWM, and the dispersion is better. For the GIS-based multisource information fusion risk evaluation method of coal seam floor water inrush, a larger value range and a better dispersion mean that it is easier to determine the critical thresholds of different risk zones.

6. Conclusion

The coal seam floor water inrush evaluation technology based on GIS combined with linear or nonlinear mathematical theory is the current research hotspot, and the CWM is currently widely used. In order to overcome the shortcomings of the traditional evaluation method, the variable weight theory is introduced into the field of risk evaluation of water inrush from coal floor and puts forward the variable weight evaluation idea of water inrush. The VWM can overcome the defect that the weight value of the traditional evaluation model remains unchanged and can consider the effect of state value change of the influencing factors on the water inrush, especially the state value mutation on the water inrush, which can effectively improve the evaluation accuracy of water inrush based on multisource information fusion technology. In addition, the CWM is greatly affected by human factors in the weight determination process. The VWM realizes the weight change based on the constant weight, which will also be affected by certain human factors, but the weight change is determined according to the objective difference of the factor state value, which can effectively reduce the influence of human factors.

Combined with the example of the water inrush evaluation project of the coal floor in Weng'an Coal Mine, the differences in evaluation effects between VWM and CWM are compared from three aspects: evaluation map, typical unit, and comprehensive evaluation values. It is demonstrated that the VWM can better reflect the control effect of mine hydrogeological condition mutations on water inrush; the evaluation process and evaluation results are more consistent with the formation mechanism of coal floor water inrush.

The current VWM still has defects such as the lack of a versatile method of parameter determination, the evaluation process will be disturbed by human factors, and the research on the change law of the weight value under the condition that the state values of different factors are combined with

each other is not deep. In the follow-up research work, it is necessary to continue to improve the variable weight evaluation theory of water inrush from coal floor, reduce the interference of human factors on the evaluation process, and explore a VWM that is more consistent with the evaluation characteristics of water inrush from coal floor.

Data Availability

All data included in this study are available upon request by contact with the corresponding author.

Conflicts of Interest

The authors declare that they have no conflicts of interest.

Acknowledgments

This research was financially supported by the National Natural Science Foundation (41702270), Guizhou Science and Technology Department Project (Qian Ke He Ji Chu [2019]1413, Qian Ke He Zhi Cheng [2020]4Y048, and Qian Ke He Zhi Cheng [2020]4Y007 and [2017]5788), and Department of Education of Guizhou Province ([2018]113).

Supplementary Materials

Figure S1: the thematic map of WALA. Figure S2: the thematic map of RQD. Figure S3: the thematic map of TBRBZU. Figure S4: the thematic map of ETEA. Figure S5: the thematic map of DFF. And factor weight calculation program. (*Supplementary Materials*)

References

- [1] C. F. Santos and Z. T. Bieniawski, "Floor design in underground coalmines," *Rock Mechanics and Rock Engineering*, vol. 22, no. 4, pp. 249–271, 1967.
- [2] S. K. Chaulya, "Water resource development study for a mining region," *Water Resources Management*, vol. 17, no. 4, pp. 297–316, 2003.
- [3] J. C. Murphy, G. M. Hornberger, and R. G. Liddle, "Concentration-discharge relationships in the coal mined region of the New River basin and Indian Fork sub-basin, Tennessee, USA," *Hydrological Processes*, vol. 28, no. 3, pp. 718–728, 2014.
- [4] K. F. Fan, W. P. Li, Q. Q. Wang et al., "Formation mechanism and prediction method of water inrush from separated layers within coal seam mining: a case study in the Shilawusu mining area, China," *Engineering Failure Analysis*, vol. 103, pp. 158–172, 2019.
- [5] B. Li, Q. Wu, X. Q. Duan, and M. Y. Chen, "Risk analysis model of water inrush through the seam floor based on set pair analysis," *Mine Water and the Environment*, vol. 37, no. 4, pp. 281–287, 2018.
- [6] Engineering Geological Handbook Editorial Board, *Engineering Geological Handbook*, China Architecture & Building Press, Beijing, 1992.
- [7] E. T. Guan, "Water outburst coefficient and mine water disaster prevention and control," *Coal Engineering*, vol. 47, no. 1, pp. 46–48, 2011.
- [8] L. M. Fan, L. Q. Ma, Y. H. Yu, S. K. Wang, and Y. J. Xu, "Water-conserving mining influencing factors identification and weight determination in northwest China," *International Journal of Coal Science & Technology*, vol. 6, no. 1, pp. 95–101, 2019.
- [9] V. F. Bense, E. H. van den Berg, and R. T. van Balen, "Deformation mechanisms and hydraulic properties of fault zones in unconsolidated sediments; the Roer Valley Rift System, The Netherlands," *Hydrogeology Journal*, vol. 11, no. 3, pp. 319–332, 2003.
- [10] C. Drover, E. Villaescusa, and I. Onederra, "Face destressing blast design for hard rock tunnelling at great depth," *Tunneling and Underground Space Technology*, vol. 80, pp. 257–268, 2018.
- [11] D. L. Hughson and A. Gutjahr, "Effect of conditioning randomly heterogeneous transmissivity on temporal hydraulic head measurements in transient two-dimensional aquifer flow," *Stochastic Hydrology and Hydraulics*, vol. 12, no. 3, pp. 155–170, 1998.
- [12] B. Li, Q. Wu, and Z. J. Liu, "Identification of mine water inrush source based on PCA-FDA: Xiandewang coal mine case," *Geofluids*, vol. 2020, 8 pages, 2020.
- [13] G. Dai, X. Xue, K. Xu, L. Dong, and C. Niu, "A GIS-based method of risk assessment on no. 11 coal-floor water inrush from Ordovician limestone in Hancheng mining area, China," *Arabian Journal of Geosciences*, vol. 11, no. 22, p. 714, 2018.
- [14] Q. Wu, H. Xu, and W. Pang, "GIS and ANN coupling model: an innovative approach to evaluate vulnerability of karst water inrush in coalmines of north China," *Environmental Geology*, vol. 54, no. 5, pp. 937–943, 2008.
- [15] Y. B. Hu, W. P. Li, Q. Q. Wang, S. L. Liu, and Z. K. Wang, "Evaluation of water inrush risk from coal seam floors with an AHP-EWM algorithm and GIS," *Environmental Earth Sciences*, vol. 78, no. 10, p. 290, 2019.
- [16] S. L. Liu, W. T. Liu, Z. Huo, and W. C. Song, "Early warning information evolution characteristics of water inrush from floor in underground coal mining," *Arabian Journal of Geosciences*, vol. 12, no. 2, p. 30, 2019.
- [17] L. W. Chen, X. Q. Feng, D. Q. Xu, W. Zeng, and Z. Y. Zheng, "Prediction of water inrush areas under an unconsolidated, confined aquifer: the application of multi-information superposition based on GIS and AHP in the Qidong coal mine, China," *Mine Water and the Environment*, vol. 37, no. 4, pp. 786–795, 2018.
- [18] Z. Ruan, C. P. Li, A. X. Wu, and Y. Wang, "A new risk assessment model for underground mine water inrush based on AHP and D–S evidence theory," *Mine Water and the Environment*, vol. 38, no. 3, pp. 488–496, 2019.
- [19] Z. K. Zhu, Z. M. Xu, Y. J. Sun, and X. L. Huang, "Research on the risk evaluation methods of water inrush from coal floor based on dimensionless multi-source information fusion technique," *Journal of Mining & Safety Engineering*, vol. 30, no. 6, pp. 911–916, 2013.
- [20] Q. Wu and M. Wang, "Characterization of water bursting and discharge into underground mines with multilayered groundwater flow systems in the North China coal basin," *Hydrogeology Journal*, vol. 14, no. 6, pp. 882–893, 2006.
- [21] H. Chen, H. Qi, R. Y. Long, and M. L. Zhang, "Research on 10-year tendency of China coal mine accidents and the characteristics of human factors," *Safety Science*, vol. 50, no. 4, pp. 745–750, 2012.

- [22] Q. Wu, B. Li, and Y. L. Chen, "Vulnerability assessment of groundwater inrush from underlying aquifers based on variable weight model and its application," *Water Resources Management*, vol. 30, no. 10, pp. 3331–3345, 2016.
- [23] B. Li, X. Q. Wang, Z. J. Liu, and T. Li, "Study on multi-field catastrophe evolution laws of water inrush from concealed karst cave in roadway excavation: a case of Jiyuan coal mine," *Geomatics, Natural Hazards and Risk*, vol. 12, no. 1, pp. 222–243, 2021.
- [24] Y. F. Zeng, *Research on Risk Evaluation Methods of Groundwater Bursting from Aquifers Underlying Coal Seams and Applications to Coalfields of North China*, Springer Nature, 2018.
- [25] Q. Wu, Y. Z. Liu, D. H. Liu, and W. F. Zhou, "Prediction of floor water inrush: the application of GIS-based AHP vulnerable index method to Donghuantuo Coal Mine, China," *Rock Mechanics and Rock Engineering*, vol. 44, no. 5, pp. 591–600, 2011.
- [26] D. Ma, H. B. Bai, X. X. Miao, H. Pu, B. Y. Jiang, and Z. Q. Chen, "Compaction and seepage properties of crushed limestone particle mixture: an experimental investigation for Ordovician karst collapse pillar groundwater inrush," *Environmental Earth Sciences*, vol. 75, no. 1, pp. 1–14, 2016.
- [27] H. X. Li, "Factor spaces and mathematical frame of knowledge representation (VII)-variable weights analysis," *Fuzzy Systems & Mathematics*, vol. 9, no. 3, pp. 1–9, 1995.
- [28] H. X. Li, "Factor spaces and mathematical frame of knowledge representation-feedback extension of a concept and coincidence of factors," *Journal of Systems Engineering*, vol. 11, no. 4, pp. 7–16, 1996.
- [29] W. Q. Liu, "Balanced function and its application for variable weight synthesizing," *Systems Engineering-Theory & Practice*, vol. 17, no. 4, pp. 58–64, 1997.
- [30] D. Q. Li and H. X. Li, "The properties and constructions of state variable weight vectors," *Journal of Beijing Normal University (Natural Science)*, vol. 38, no. 4, pp. 455–461, 2002.
- [31] Q. F. Cai and H. X. Li, "Balance degree and variable weight," *Systems Engineering-Theory & Practice*, vol. 21, no. 10, pp. 83–87, 2001.
- [32] T. L. Saaty, "A scaling method for priorities in hierarchical structures," *Journal of Mathematical Psychology*, vol. 15, no. 3, pp. 234–281, 1977.

Research Article

A DOFS-Based Approach to Calculate the Height of Water-Flowing Fractured Zone in Overlying Strata under Mining

Chunde Piao ^{1,2}, Jinjun Li,³ Dangliang Wang,¹ and Wei Qiao ¹

¹School of Resources and Geosciences, China University of Mining and Technology, Xuzhou 221116, China

²State Key Laboratory for Geomechanics and Deep Underground Engineering, China University of Mining and Technology, Xuzhou 221116, China

³Shenhua Geological & Exploration Company Ltd., China Energy Group, Beijing 102211, China

Correspondence should be addressed to Chunde Piao; piaocd@cumt.edu.cn

Received 20 August 2020; Revised 18 September 2020; Accepted 5 March 2021; Published 17 March 2021

Academic Editor: Yingfang Zhou

Copyright © 2021 Chunde Piao et al. This is an open access article distributed under the Creative Commons Attribution License, which permits unrestricted use, distribution, and reproduction in any medium, provided the original work is properly cited.

The distributed optical fiber sensing (DOFS) is a technique that can obtain full spatial and temporal information concerning the behavior of a large range of measurand fields along a fiber path and realize the distributed monitoring of the overburden section under mining. To calculate the height of water-flowing fractured zone caused by the exploitation of coal, this study employed distributed optical fiber sensors with OSI-C-S optical frequency domain reflectometry (OFDR) technology and designed a similar-material model test based on the engineering geological conditions of Daliuta Coal Mine. Through the test, deformation characteristics of overlying strata were studied, the linear relationship was summarized between the strain gradient and the shear stress measured by fiber sensors when the rock layer cracks, and a method was proposed of using the measured strain to measure the height of the water-flowing fractured zone in overlying strata. The test results show that there are several locations where the sign of the shear stress changes (positive to negative or vice versa) in the overlying strata during the initial stage of coal seam mining. As the working face advanced, the change locations gradually concentrated at the place where the rock cracks. By identifying the breakpoints of the rock and the locations where the sign of the shear stress measured by fiber sensors changes, this paper calculated the height of the water-flowing fractured zone in Daliuta Coal Mine. After comparing the height with the abscission layer position in the model test and the predicted height by the empirical formulas in the *specification*, it has been found that the three results are basically consistent, which in turn verifies the accuracy of this method.

1. Introduction

After the coal seam is mined, the overlying strata gradually move to the gob. According to the severity of deformation and failure of the rock mass, the overlying strata in the gob can be divided into three zones: caving zone, fracture zone, and bending zone. The caving zone and fracture zone are collectively called the water-flowing fractured zone [1]. The water-flowing fractured zone caused by the exploitation of coal can form a channel for water inrush in the mine and pose a threat to the safety of coal mining under a body of water. As the height of the water-flowing fractured zone is a key parameter, therefore accurate calculation of its height is very important for safe mining as well as environment conservation [2]. According to the mining thickness of coal seam

and the properties and distribution characteristics of overlying strata, many theoretical formulas for calculating the height of water-flowing fractured zones have been proposed [3–5]. However, because coal mines are widely distributed in China, and geological conditions, overburden structures, and mining techniques in different areas vary greatly, the existing proposed formulas are affected by regional parameters, hypothetical conditions, and applicability, therefore cannot be used universally. For example, for the numerical simulation method, it is difficult to select the rock mass parameters involved, the model is difficult to accurately match the actual project, and it needs to be verified with actual monitoring data [6]. The monitoring of rock mass deformation is an important means to master the deformation rules of overlying strata. Common field-testing

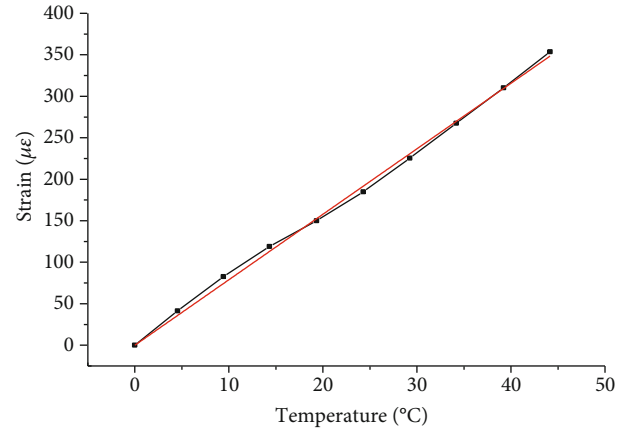
techniques for measuring the overburden deformation include loss observation of flush fluid, electromagnetic method, and borehole TV system. These testing techniques have their own advantages and disadvantages depending on the geological conditions and mining conditions. The loss observation of flush fluid is simple, but the test accuracy is greatly affected by human factors and the test time is relatively longer [7]. The electromagnetic method is affected by factors such as formation properties, structural distribution, and image interpretation and is mainly used to assist detection [8]. The borehole TV system can observe the geological conditions in the borehole by using photos or video images. The test method is simple, but the detection accuracy is undermined when the borehole contains water or the hole collapses [7, 9].

The distributed optical fiber sensing (DOFS) technology has many advantages such as distributed monitoring, long distance monitoring, good durability, strong anti-interference, and good performance of coordinating with the measured object. Though DOFS has been widely used in geotechnical engineering [10–12], the application research of this technology in the coal mining field is still in the exploration stage due to such features as the large depth of coal seams, complex multifield effects of rock and soil, and the sever deformation of mined overburden. In recent years, by analyzing the abnormal characteristics of measured values and the surge loss point of the optical fiber cable [13], the peak of the Brillouin frequency shift [14], and the layer of the fiber cable breakpoint [15], many research achievements have been made in measuring the height of the water-flowing fractured zone. But no specific criteria have been established. Through making a similar-material test model and using optical frequency domain reflectometry (OFDR) technology, this study analyzed the deformation and failure characteristics of overburden under mining conditions, studied the strain distribution rules, explored the strain changes and shear stress sign changes when the rock cracks, and proposed a method of using the measured strain to measure the height of the water-induced fractured zone in overlying strata. This paper has provided theoretical basis and technical support for the identification of rock cracks and safe mining of coal mines.

2. Theoretical Method to Measure the Height of the Water-Flowing Fractured Zone

2.1. OFDR Test Principle. Optical frequency domain reflectometry technology (OFDR) is a strain measurement technology based on variations of Rayleigh scattered light. It uses continuous wave frequency scanning technology to establish the linear dependence of frequency drifts of Rayleigh back-scattered light spectrum with the strain and temperature along the length of an optical fiber, thus realizing the distributed measurement of the measured structure and obtaining a high spatial resolution [16, 17].

When using OFDR to measure the tested structure, temperature changes affect the strain value. Therefore, the strain test of optical fiber was performed indoors under different



Equation	$y = a + b * x$		
Weight	No weighting		
Residual sum of squares	250.31135		
Pearson's r	0.9997		
Adj. R^2	0.99934		
		Value	Standard err
C	Intercept	0	--
	Slope	7.8913	0.06401

FIGURE 1: Linear relationship between strain and temperature (obtained by OFDR measurements).

temperature conditions. The test results are shown in Figure 1.

It can be seen from Figure 1 that when the structure was measured by using the OFDR, a strong linear relationship existed between the change in strain and temperature with the slope of $7.8913 \mu\epsilon/^\circ\text{C}$. That is, for each change of 1°C in temperature, the measured strain will change accordingly by $7.8913 \mu\epsilon$. According to the laboratory tests, a change of less than 10°C in rock mass temperature caused by aquifer leakage would result in a variation of $80 \mu\epsilon$ in strain [18], which was far smaller than the strain (greater than $600 \mu\epsilon$) generated during rock damage. Therefore, the temperature change induced by aquifer leakage when the cracks appeared in the rock layer had few impacts on the measured strain and could not affect the strain-based identification of open fractures.

2.2. Measure the Height of Water-Flowing Fractured Zone by Analyzing Strain Measured through Vertical Boreholes. In order to grasp the characteristics of deformation and failure of overlying strata under mining conditions, an optical fiber sensor was laid from the ground to the coal mining area. Figure 2 shows the distributed monitoring and deformation characteristics of overlying strata under coal mining.

There are two steps to determine the height of the water-flowing fracture zone based on the DOFS technology.

2.2.1. Rock Breakpoint Identification. It can be seen from Figure 2 that the coal seam mining caused the rock strata to move and deform towards the direction of the gob (worked-out area at the bottom) and two zones (water-flowing fractured zone and bending zone) were gradually

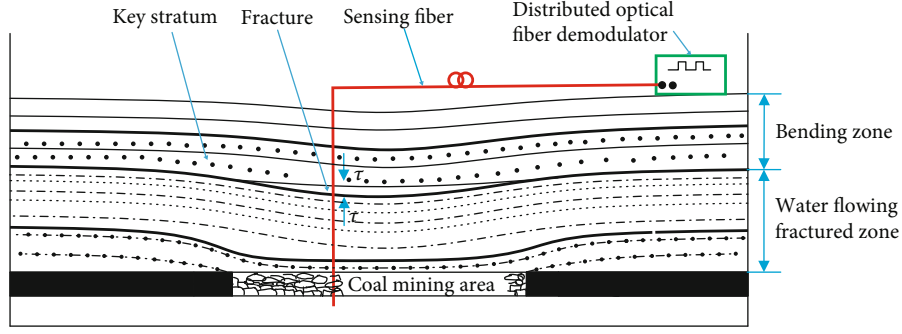


FIGURE 2: Distributed monitoring and deformation characteristics of overlying strata under coal mining.

generated in the overlying strata. The tensile strength of the rock was far weaker than its compressive strength. Most of the deformation was tensile deformation. When the stress of the rock caused by the mining of the coal seam is greater than its tensile strength, the rock will be damaged [13]. The identification of the breakpoint at this time can be calculated by formula (1).

$$[\sigma] \geq \sigma_t. \quad (1)$$

In the formula, $[\sigma]$ is the stress on the rock caused by coal seam mining, which is calculated by the formula $[\sigma] = E_{\text{rock}} \cdot \varepsilon$. Here, E_{rock} is the elastic modulus of the rock and ε is the strain on the rock. Before tension cracks appeared within the rock, the fiber sensor deformed along with the surrounding rock. Therefore, the strain monitored by the fiber sensor is considered as the degree of rock deformation. σ_t is the tensile strength of the rock.

2.2.2. Identification of Overburden Fracture Position. With the advance of the working face, the immediate roof and the basic roof were successively damaged, fractures and abscission layer occurred due to settlement differences between the main key stratum, inferior key stratum of the overlying rock layer or the hard rock, and the lower rock mass. When a fracture occurred in a key stratum or hard rock, the key stratum or the upper rock layer was settled, and the lower rock layer was further compressed.

In Figure 2, when fractures occurred in the rock, the upper and lower rock layers were relatively far away from each other, but shear deformation occurred between the fiber sensor and the rock. At this point, the direction of the shear stress on the fiber sensor at the lower part of the fractured rock was deviating from the mining area, while the direction of the shear stress on the fiber sensor at the upper part of the fractured rock was pointing to the mining area. The shear stress on the rock mass can be calculated by formula (2) [19].

$$\tau = \frac{E_{\text{fiber}} \cdot D}{4} \cdot \frac{d\varepsilon}{dx}. \quad (2)$$

In the formula, τ is the shear stress acting on the sensing optical fiber. The shear stress pointing to the mining area takes a negative value, and the shear stress deviating from the mining area takes a positive value.

E_{fiber} is the elastic modulus of the fiber sensor; D is the diameter of the fiber sensor; $d\varepsilon/dx$ is the strain gradient of fiber sensor along the vertical direction of overlying strata.

According to formula (2), the shear stress between the fiber sensor and the surrounding rock and soil mass is proportional to the strain gradient. The changes of the strain gradient directly reflect the magnitude of shear stress.

The overburden deformation started from the roof of the coal seam and gradually extended from the bottom to the top. By using formula (1) to identify rock breakpoints and using formula (2) to calculate the highest location where the shear stress changed from a positive value to a negative one, the study pinned down the height of the water-flowing fractured zone at the current mining stage.

3. Similar-Material Model Test of Coal Mining

3.1. Test Model Design. As one of the seven largest coal fields in the world, Shendong Coalfield is the largest coalfield with proven reserves in China. Daliuta Coal Mine in the Shendong Coalfield is located in the northernmost part of Shenmu county, 57 km away from the center of the county. By referring to the drilling data of J60 in Daliuta Coal Mine and using the working face of 2-2 coal seam as the background, the study made a test model with the length, height, and width at 300 cm, 105.9 cm, and 30 cm, respectively, based on the similarity theory.

According to field conditions of Daliuta Coal Mine, the following similarity parameters are selected: geometrical similarity ratio (taken as $C_l = 100$), time similarity ratio ($C_t = \sqrt{C_l} = 10$), bulk density similarity ratio ($C_\gamma = \gamma_M/\gamma_H = 1.5$), and stress similarity ratio ($C_R = R_M/R_H = C_l \cdot \gamma_M/\gamma_H = 150$). In the formula $C_R = R_M/R_H = C_l \cdot \gamma_M/\gamma_H$, R_M and R_H are the mechanical strength of the prototype and the model, respectively, and γ_M and γ_H are the bulk density of the prototype and the model, respectively. The mechanical parameters of the prototype and test model of Daliuta Coal Mine and the ratio of similar materials are shown in Table 1 [20].

The inclination angle of the strata in Daliuta Coal Mine is near horizontal. For the ease of laying, the model was treated as horizontal rock formations. Each rock stratum in the test model was developed based on the ratio for similar physical properties in Table 1. River sand was used as aggregate,

TABLE 1: Mechanical parameters of the prototype and the model and ratio of similar materials in Daliuta Coal Mine.

Rock layer name	Layer thickness/m	Prototype					Test model					Ratio of similar materials
		Layer thickness/m	Bulk density/kN/m ³	Compressive strength/MPa	Tensile strength/MPa	Elastic modulus/GPa	Layer thickness/cm	Bulk density/kN/m ³	Compressive strength/kPa	Tensile strength/kPa	Elastic modulus/MPa	
Unconsolidated layer	40	17	0.7	-	-	40	11.3	4.7	-	-	-	11:1:0
Sandy mudstone	6	24.1	17.2	1.84	1.58	6	16.1	114.9	12.3	10.6	10.6	8:6:4
Fine sandstone	5	28	36.5	1.81	3.08	5	18.7	243.8	12.1	20.6	20.6	3:5:5
Sandy mudstone	7	24.1	17.2	1.84	1.58	7	16.1	114.9	12.3	10.6	10.6	8:6:4
Mudstone	9	24.3	15.3	1.53	1.37	9	16.2	102	10.2	9.1	9.1	10:5:5
Fine sandstone	13.5	28	36.5	1.81	3.08	13.5	18.7	243.8	12.1	20.6	20.6	3:5:5
Sandy mudstone	6	24.1	17.2	1.84	1.58	6	16.1	114.9	12.3	10.6	10.6	8:6:4
2-2 coal	4.2	13	15	1.99	1.17	4.2	8.7	100.4	13.3	7.8	7.8	6:5:5
Sandy mudstone	6	24.1	17.2	1.84	1.58	6	16.1	114.9	12.3	10.6	10.6	8:6:4
2-3 coal	4.2	13	15	1.99	1.17	4.2	8.7	100.4	13.3	7.8	7.8	6:5:5
Sandy mudstone	5	24.1	17.2	1.84	1.58	5	16.1	114.9	12.3	10.6	10.6	8:6:4

calcium carbonate and gypsum were used as cement raw materials, and borax was used as retarder. After various materials were mixed evenly, the materials with similar physical properties were generated. In order to ensure the strength of the laying model, the generated materials were hammered and compacted layer by layer from the bottom to the top in the model test bed. The thickness of each layer of coal rock stratum was no more than 3 cm, and the surface of each layer was coated with coarse mica powder to separate the layers. The river sand used in the model was dried and screened to remove large particles and ensure particle uniformity and stability of test data. In the model test, wood strips with a length of 5 cm and a height of 4.2 cm were closely arranged to simulate coal seams to facilitate coal mining and ensure the same advance distance. According to the geometric similarity ratio, the actual advance distance and mining height simulated in this model test are 5 m and 4.2 m, respectively.

3.2. Overlying Stratum Monitoring Scheme for Coal Seam Mining. The test used OSI-C-S OFDR to measure the distribution of overburden strain during coal seam mining. Test equipment is shown in Figure 3.

Table 2 shows the test parameters of the OSI-C-S OFDR test equipment.

The test used the polyurethane sheath fiber sensor with a diameter of 2 mm to test the overburden strain. Figure 4 shows a physical view and a cross-sectional view of the polyurethane sheath fiber sensor.

The mechanical properties and sensing properties of the polyurethane sheath fiber sensor are shown in Table 3.

The outer layer of the polyurethane sheath fiber sensor is made of a smooth soft adhesive material. During the mining process, the monitoring positions may be staggered, affecting the accuracy of the measured data. Therefore, the fiber sensor in the test section was coated with colloid and sand and was dried to increase the roughness of the surface and to improve the coupling between the fiber sensor and the model rock mass. Figure 5 shows the pretreatment of the fiber sensor.

Figure 6 shows the similarity model made by similar materials of rock stratum in Daliuta Coal Mine in Table 1.

As can be seen from Figure 6, in order to ensure that the mining boundary does not affect the deformation of overlying strata of the coal seam, the open-off cut of 2-2 coal seam in the test was located at 75 cm from the left of the model, with the advance distance of the model being 125 cm and the advance distance of the simulated working face being 125 m. In order to detect the characteristics of overburden deformation of coal seam, line B and line C fiber sensors were embedded in the mining area of coal seam, and line A and line D fiber sensors were embedded in the pillar area of coal seam. The distances between lines A, B, C, and D and the left boundary of the model were 50 cm, 115 cm, 190 cm, and 250 cm, respectively. Considering the high-intensity mining of overlying strata in the coal seam, a section which was 115 cm to 170 cm away from the left boundary was selected as the study area, to test the method for measuring the height of the water-flowing fractured zone in the process of coal seam mining.



FIGURE 3: OSI-C-S OFDR test equipment.

Before the coal seam mining test, all fiber sensors were connected to the test instrument independently and the initial strain of overburden was tested. Each time when the working face advanced by 5 cm, the test model was left to stand still for 30 minutes. The data collection of each mining stage started only after the overburden deformation was stabilized during 30 minutes. This data collection procedure was adopted until the end of the test. The actual overburden strain equals to the overburden strain caused by coal seam mining minus the initial strain.

4. Test Result Analysis

After the working face passed the monitoring point of line B, the roof of the coal seam was taken as the starting reference point, and the deformation range from the starting reference point up to the ground was defined as the affected depth. The overburden strain distribution caused by each mining of the coal seam is shown in Figure 7.

As can be seen from Figure 7, the working face passed the monitoring section of line B fiber sensor. As the working face advanced by 5 cm, the strain value at the distance of 5 cm away from 2-2 coal seam roof was $1433 \mu\epsilon$. After comparing the strain value with the tensile strength of the rocks in Table 1 and combining the calculation of formula (1), it can be indicated that at this time, the rock layer 5 cm away from the roof has been damaged and the upper rock mass was in a stable state. With the advance of the working face, the strain value decreased gradually due to the stress release of the rock mass in the original disturbance area, but the strain between the key stratum of fine sandstone (9) and sandy mudstone (8) increased gradually. As the working face advanced to 40 cm, the strain gradually concentrated at 14.3 cm and 37.8 cm away from the roof of the coal seam, and its magnitude was $662 \mu\epsilon$ and $1836 \mu\epsilon$, respectively. After comparing the strain value with the tensile strength of the rocks in Table 1 and combining the calculation of formula (1), it can be indicated that the rock strata broke at this time. As the working face advanced to 55 cm, the strain value surged at the place 37.8 cm away from the roof of the coal seam, reaching $6065 \mu\epsilon$, after which the test signal weakened and the strain value could not be measured accurately.

TABLE 2: Test parameters of the OSI-C-S OFDR instrument.

Name	Test length	Number of test channels	Spatial resolution	Sampling rate	Strain test range	Strain test accuracy	Temperature range
Option	Up to 100 m	4	1 mm or 1 cm	4 hz as the fastest	$\pm 12000 \mu\epsilon$	$\pm 1.0 \mu\epsilon$	$-200^{\circ}\text{C}\sim 1200^{\circ}\text{C}$

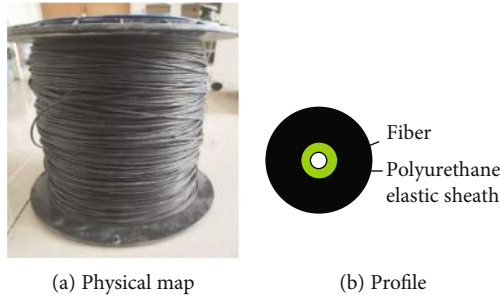


FIGURE 4: Polyurethane sheath fiber sensor.

TABLE 3: Mechanical properties and sensing performance of polyurethane sheath fiber sensor.

Parameter category	Fiber diameter/mm	Core diameter/mm	Maximum breaking force/N	Modulus of elasticity/GPa	Coefficient of strain/MHz/ $\mu\epsilon$	Temperature coefficient/MHz/ $^{\circ}\text{C}$	Strain measuring range/ $\mu\epsilon$
Value	2.0	0.9	220	0.2	0.04998	1.89	-10000~20000

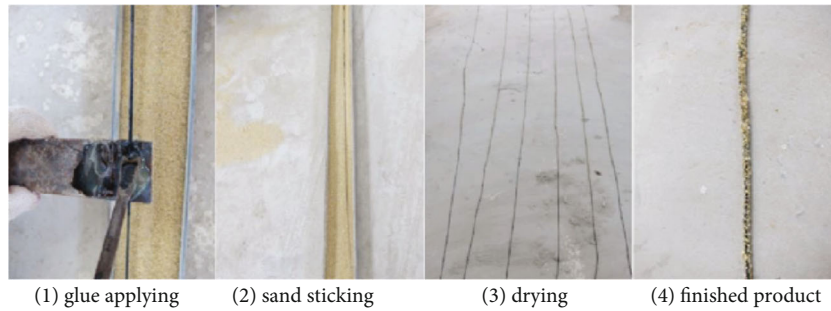


FIGURE 5: Pretreatment of fiber sensor.

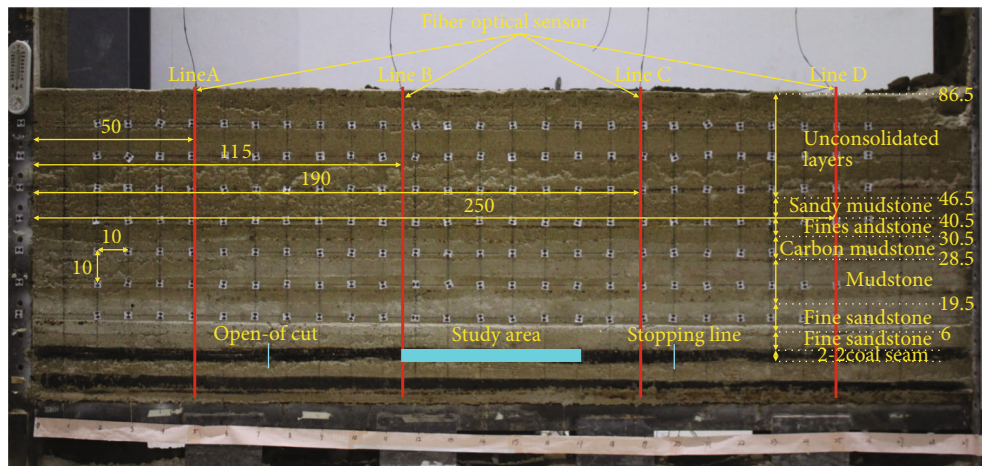


FIGURE 6: Rock distribution, fiber sensor arrangement, and research scope in model test (unit: cm).

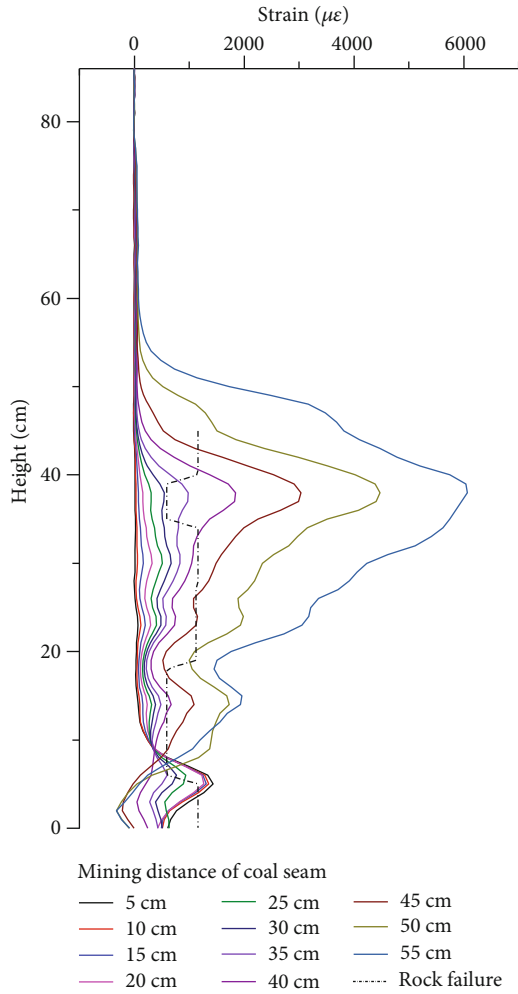


FIGURE 7: Mining-induced strain distribution measured by line B.

According to the overburden strain distribution in Figure 7, formula (2) was adopted to calculate the distributed shear stress of the fiber sensor after the working face passed the monitoring section of line B. The calculation result is shown in Figure 8. In order to facilitate the analysis of problems, this paper chose the distributed shear stress of the fiber sensor when the working face advanced to 5 cm, 30 cm, and 55 cm, respectively (as shown in Figure 8). It can be seen from Figure 2 that the distribution of tensile fractures in rock strata was related to the sign changes of shear stress during coal mining. Therefore, the mean value of the shear stress of the fiber sensor was obtained to form a solid line in Figure 8 by averaging the shear stress in the same direction (indicated by a dotted line). According to the position where the sign of the shear stress changed in the solid line in Figure 8, the overburden deformation caused by coal seam mining has the following characteristics: when the working face advanced to 5 cm, the sign of the shear stress changed for the first time at the position 5 cm away from the roof of the coal seam. When the working face advanced to 30 cm, the damaged rock mass moved towards the gob due to the pressure of the overlying strata, and the overlying rock strain gradually increased from the bottom to the top, and a num-

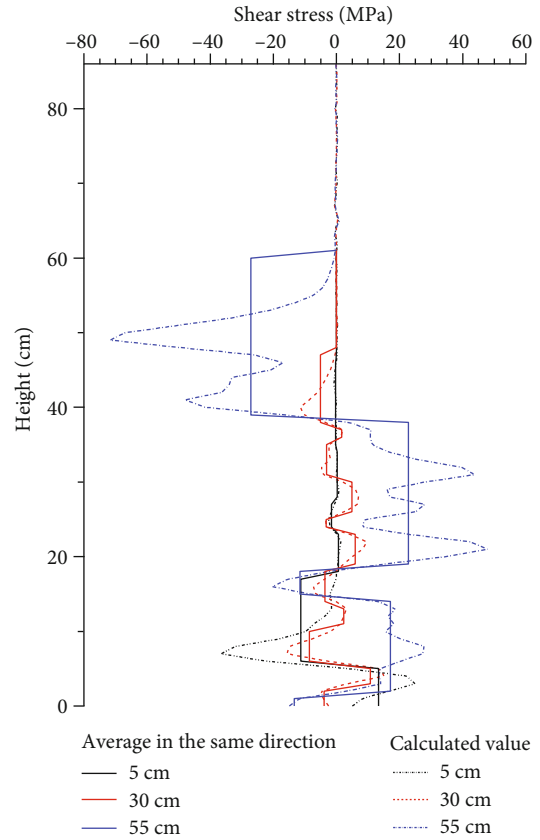


FIGURE 8: Mining-induced shear stress distribution measured by line B.

ber of sign change points of shear stress appeared. However, according to the rock breakpoint identification formula (1), the rock at the abovementioned positions where the sign of shear stress changed has not been broken. When the working face advanced to 55 cm, the degree of overburden disturbance intensified, and the change points of shear stress gradually concentrated at the positions 14.3 cm and 37.8 cm away from the roof of the coal seam. The magnitude of the shear stress exceeded the tensile strength of the rock. Therefore, in this test, it can be concluded that when the working face advanced to 55 cm, the height of the water-flowing fractured zone was 37.8 cm.

In order to grasp the characteristics of overlying stratum deformation and failure during coal seam mining, according to the monitoring requirements of photogrammetry system, noncoding points were set at 10 cm intervals along the horizontal and axial directions of the model, starting from the left boundary of the coal seam roof and model frame in the model test. In order to compare with the monitoring results of mining-induced overburden strain, representative images about overburden deformation after the working face passed through line B fiber sensor were selected, as shown in Figure 9. Figure 9(a) shows that when the working face advanced to 5 cm, the rock layer 5 cm away from the roof of the coal seam collapsed and moved towards the gob. Figure 9(b) shows that when the working face advanced to 40 cm, cracks appeared 14.3 cm and 37.8 cm away from the roof of the coal seam. Figure 9(c) shows that when the

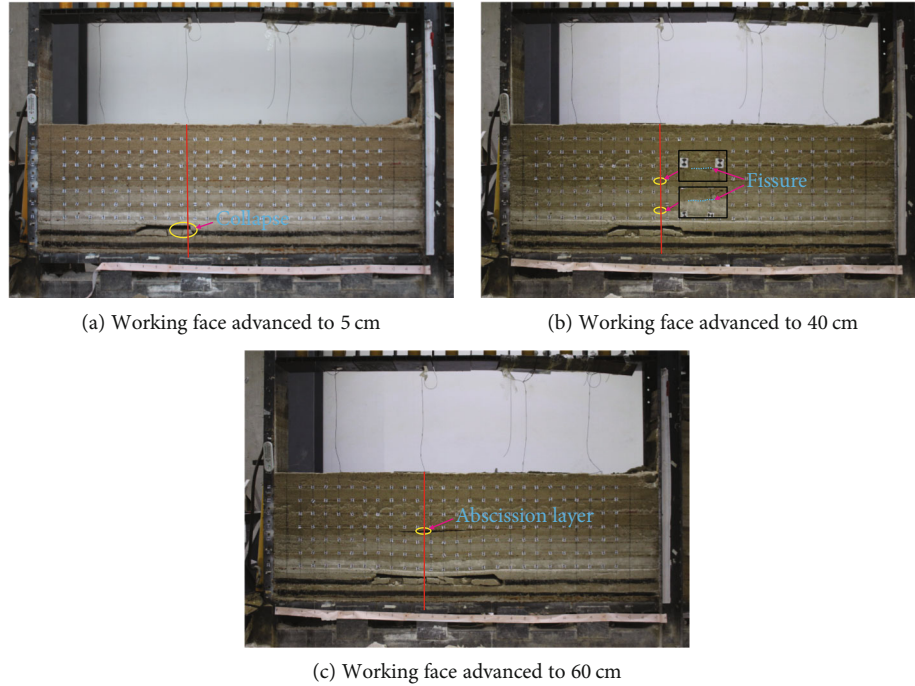


FIGURE 9: Overburden deformation and failure diagram after the working face passed line B fiber sensor.

working face advanced to 60 cm, the abscission layer was formed at 37.5 cm away from the roof of the coal seam, and the rock layers below the abscission layer were settled and compressed.

The height of the water-flowing fractured zone calculated by using the proposed strain-based method is basically the same with the deformation and failure results of the overlying strata in the model test.

The formula for calculating the height of the water-flowing fractured zone in *building, water, railway, and main shaft roadway pillar and coal mining specification (specification in short)* is shown in formula (3) [3].

$$H = \frac{100\sum M}{1.6\sum M + 3.6} \pm 5.6. \quad (3)$$

In the formula, $\sum M$ is the cumulative thickness. The cumulative mining thickness of the coal seam in this test was 4.2 cm.

According to formula (3), the predicted height of the water-flowing fractured zone is between 35.1 cm and 46.3 cm. This predicted height includes both the height of the water-flowing fractured zone calculated by the measured strain and the height of the abscission layer in the model test. It shows that the proposed method for calculating the height of water-flowing fractured zones in this paper is reliable.

5. Discussion

- (1) The method of using the measured strain to calculate the height of the water-flowing fractured zone shows

that as long as there was a crack between the upper and lower stratum layer, the sign of the shear stress changed. Due to the high resolution of the OFDR instrument, in the early stage of coal seam mining, even small strain differences in the overburden monitoring section can cause sign changes of the shear stress in many places. As the working face advanced, the crack that has appeared gradually closed, the shear stress gradually increased, and the sign changes concentrated at specific positions. Influenced by the fiber sensor's own strength, the overburden strain distribution curve was centered on the maximum deformation position of the rock mass, with the value gradually decreasing from that position to both the top layer and bottom layer. Therefore, when calculating the rock layer strength according to formula (1), a large fracture range appeared, which was not consistent with the results of the model test. The height of the water-flowing fractured zone can be accurately calculated only by combining the rock breakpoint identification formula (1) with the fracture position identification formula (2)

- (2) In the study of coupling between the fiber sensor and surrounding medium, Madjdabadi et al. [21] fixed the fiber sensor to the beam body with binder and analyzed the process of coordinated deformation and strain transfer between the two. Zhang et al. [22] developed a test device for testing the interaction between the fiber sensor and soil and proposed a coupling coefficient to quantitatively describe the coupling. In the aspect of mining-induced overburden

deformation measurement by DOFS technology, the coupling between the fiber sensor and rock mass is affected by the interaction between the two materials and rock mass structure, which needs further theoretical derivation and experimental verification to establish the shear-stress-based fracture identification criterion

- (3) Using single-point sensors such as resistance strain gauge or vibrating string stress meter to monitor mining-induced overburden deformation is prone to problems including leakage detection and electromagnetic interference [23]. By applying OFDR technique, the position where overburden fracture occurs is detected accurately. However, the strain measurement range of this technology is $\pm 12000 \mu\epsilon$. The initial deformation test in the overburden model test is relatively accurate. But when large deformation occurs, for example, an abscission layer forms, the test signal weakens until the fiber sensor breaks, and the signal cannot be tested. At present, Brillouin optical time domain reflectometry (BOTDR), Brillouin optical time domain analysis (BOTDA), Brillouin optical frequency domain analysis (BOFDA), and other testing instruments are widely used in the field of rock and soil deformation monitoring, and their strain measurement range is $\pm 15000 \mu\epsilon$ [24]. The Brillouin back-scattering signal of the BOTDR instrument is very weak, so it is easy to miss the signal when the rock breaks and an abscission layer forms in the model test. However, this instrument has the advantage of single-end measurement, and no circuit is needed, which is suitable for field test. According to stimulated Brillouin effect, BOTDA and BOFDA instruments receive strong signals and have a high spatial resolution, which are suitable for indoor model test. But this kind of equipment requires double-ended measurement to form a test loop, and the whole monitoring section cannot be measured when the rock mass deformation is too large and the fiber sensor breaks in the field application. Therefore, in the overburden monitoring during coal seam mining, it is important to select suitable test instruments and fiber sensors according to the measurement range and develop fiber sensors suitable for measuring large deformation

6. Conclusion

- (1) Based on the overburden strain distribution under the mining condition of coal seam, the study detected the deformation and failure state of rock mass. By combining the coordinated deformation characteristics between the fiber sensor and surrounding rock and soil mass, this paper summarized a linear relationship between the shear stress and strain gradient of the fiber sensor. By observing the position where the sign of the shear stress was changed from positive to negative, the study then detected the fracture posi-

tion and proposed a method to predict the height of the water-flowing fractured zone. In addition, according to the similarity model test by using similar materials of Daliuta Coal Mine, the height of the water-flowing fractured zone was calculated to be 37.8 cm based on measured strain. This result is in close agreement with the actual rock failure height in the model test and the predicted height by empirical formulas' result in the *specification*, which indicates that the calculated result of the proposed method meets the engineering practice. Besides, this method has the characteristics of distributed measurement, high sensitivity, and good stability and has a good application prospect in measuring the height of the water-flowing fractured zone in time in the process of coal mining

- (2) The OFDR measurement result shows that there was a strong linear relationship between strain and temperature. In general, if the change of temperature caused by water seepage from aquifer was small, the strain magnitude had little influence on the identification of rock fracture position. Due to the limitation of the deformation of the fiber sensor, the test signal was weakened when large deformation occurred, so it was difficult to measure the strain accurately. Therefore, it is necessary to develop a fiber sensor suitable for large deformation of overlying strata. The fracture position can be detected by the strain measured by the fiber sensor and the location where the sign of the shear stress changed, but the fracture identification based on shear stress value requires further study

Data Availability

The data used to support the findings of this study are available from the corresponding author upon request. I would like to declare on behalf of my co-authors that the work described was original research that has not been published previously and not under consideration for publication elsewhere, in whole or in part.

Conflicts of Interest

The authors declare that they have no conflicts of interest.

Acknowledgments

The work is funded by the Fundamental Research Funds for the Central Universities (2017XKQY057), and a project funded by the Priority Academic Program Development of Jiangsu Higher Education Institutions (2018).

References

- [1] T. Zhang, Q. Gan, Y. Zhao et al., "Investigations into mining-induced stress-fracture-seepage field coupling effect considering the response of key stratum and composite aquifer," *Rock*

- Mechanics and Rock Engineering*, vol. 52, no. 10, pp. 4017–4031, 2019.
- [2] D. Zhang, G. Fan, L. Ma, and X. Wang, “Aquifer protection during longwall mining of shallow coal seams: a case study in the Shendong coalfield of China,” *International Journal of Coal Geology*, vol. 86, no. 2-3, pp. 190–196, 2011.
- [3] SAWS, State Administration of Work Safety); SACMS (State Administration of Coal Mine Safety, NEA (National Energy Administration), and SRA (State Railway Administration), *Building, Water, Railway and Main Shaft Roadway Pillar and Coal Mining Specification*, China Coal Industry Publishing House, Beijing, 2017.
- [4] X. J. Hu, W. P. Li, D. T. Cao, and M. C. Liu, “Index of multiple factors and expected height of fully mechanized water flowing fractured zone,” *J Chin Coal Soc*, vol. 37, pp. 613–620, 2012.
- [5] V. Palchik, “Influence of physical characteristics of weak rock mass on height of caved zone over abandoned subsurface coal mines,” *Environmental Geology*, vol. 42, no. 1, pp. 92–101, 2002.
- [6] D. P. Adhikary and H. Guo, “Modelling of longwall mining-induced strata permeability change,” *Rock Mechanics and Rock Engineering*, vol. 48, no. 1, pp. 345–359, 2015.
- [7] H. Ding, “Law of overlying strata movement in large mining height working face of Bulianta coal mine,” *Safety in coal mines*, vol. 50, pp. 179–183, 2019.
- [8] D. Yang, W. Guo, and Y. Tan, “Application of magnetotelluric method to the detection of overburden failure height in shallow seam mining,” *Arabian Journal of Geosciences*, vol. 11, no. 13, 2018.
- [9] S. Liu, W. Li, and Q. Wang, “Height of the water-flowing fractured zone of the Jurassic coal seam in northwestern China,” *Mine Water and the Environment*, vol. 37, no. 2, pp. 312–321, 2018.
- [10] H. Sang, D. Zhang, Y. Gao et al., “Strain distribution based geometric models for characterizing the deformation of a sliding zone,” *Engineering Geology*, vol. 263, p. 105300, 2019.
- [11] H. F. Pei, J. Teng, J. H. Yin, and R. Chen, “A review of previous studies on the applications of optical fiber sensors in geotechnical health monitoring,” *Measurement*, vol. 58, pp. 207–214, 2014.
- [12] A. Klar, I. Dromy, and R. Linker, “Monitoring tunneling induced ground displacements using distributed fiber-optic sensing,” *Tunnelling and Underground Space Technology*, vol. 40, pp. 141–150, 2014.
- [13] D. Zhang, J. Wang, P. Zhang, and B. Shi, “Internal strain monitoring for coal mining similarity model based on distributed fiber optical sensing,” *Measurement*, vol. 97, pp. 234–241, 2017.
- [14] J. Chai, Z. W. Xue, R. Guo, D. D. Zhang, Q. Yuan, and Y. Li, “Experimental study of overlying mine strata collapse and its evolution by a distributed optical fiber system,” *J CHINA U MIN TECHNO*, vol. 47, pp. 1185–1192, 2018.
- [15] Y. Liu, W. Li, J. He, S. Liu, L. Cai, and G. Cheng, “Application of Brillouin optical time domain reflectometry to dynamic monitoring of overburden deformation and failure caused by underground mining,” *International Journal of Rock Mechanics and Mining Sciences*, vol. 106, pp. 133–143, 2018.
- [16] D. Tosi, E. Schena, C. Molardi, and S. Korganbayev, “Fiber optic sensors for sub-centimeter spatially resolved measurements: review and biomedical applications,” *Optical Fiber Technology*, vol. 43, pp. 6–19, 2018.
- [17] M. Froggatt and J. Moore, “High-spatial-resolution distributed strain measurement in optical fiber with Rayleigh scatter,” *Applied Optics*, vol. 37, no. 10, pp. 1735–1740, 1998.
- [18] H. Su, S. Tian, Y. Kang, W. Xie, and J. Chen, “Monitoring water seepage velocity in dikes using distributed optical fiber temperature sensors,” *Automation in Construction*, vol. 76, pp. 71–84, 2017.
- [19] C. C. Zhang, B. Shi, K. Gu et al., “Vertically distributed sensing of deformation using fiber optic sensing,” *Geophysical Research Letters*, vol. 45, no. 21, pp. 11,732–11,741, 2018.
- [20] H. M. Li, H. G. Li, G. J. Song, and K. L. Wang, “Physical and mechanical properties of the coal-bearing strata rock in Shendong coal field,” *Journal of China Coal Society*, vol. 41, no. 11, pp. 2661–2671, 2016.
- [21] B. Madjdabadi, B. Valley, M. B. Dusseault, and P. K. Kaiser, “Experimental evaluation of a distributed Brillouin sensing system for measuring extensional and shear deformation in rock,” *Measurement*, vol. 77, pp. 54–66, 2016.
- [22] C. C. Zhang, H.-H. Zhu, and B. Shi, “Role of the interface between distributed fibre optic strain sensor and soil in ground deformation measurement,” *Scientific Reports*, vol. 6, no. 1, 2016.
- [23] S. J. Chen, H. Zhou, W. J. Guo, H. L. Wang, and X. Z. Sun, “Study on long-term stress and deformation characteristics of strip pillar,” *Journal of Mining and Safety Engineering*, vol. 29, no. 3, pp. 376–380, 2012.
- [24] J. Shen, T. Li, H. Zhu, C. Yang, and K. Zhang, “Sensing properties of fused silica single-mode optical fibers based on PPP-BOTDA in high-temperature fields,” *Sensors*, vol. 19, no. 22, p. 5021, 2019.

Research Article

Gas Displacement Engineering Test by Combination of Low and Medium Pressure Injection with Liquid CO₂ in High Gas and Low Permeability Coal Seam

Hu Wen ^{1,2} Mingyang Liu ^{1,2} Gaoming Wei ^{1,2} Xiaowei Zhai ^{1,2} Shixing Fan ^{1,2}
Xiaojiao Cheng ^{1,2} Hu Wang ^{1,2} and Jianchi Hao ^{1,2}

¹College of Safety Science and Engineering, Xi'an University of Science and Technology, Xi'an 710054, China

²Shaanxi Key Laboratory of Prevention and Control of Coal Fire, Xi'an 710054, China

Correspondence should be addressed to Mingyang Liu; 17120089012@stu.xust.edu.cn and Shixing Fan; fanxing@xust.edu.cn

Received 27 August 2020; Revised 26 October 2020; Accepted 13 November 2020; Published 3 December 2020

Academic Editor: Bin-Wei Xia

Copyright © 2020 Hu Wen et al. This is an open access article distributed under the Creative Commons Attribution License, which permits unrestricted use, distribution, and reproduction in any medium, provided the original work is properly cited.

Mining high-gas coal seams in China has the characteristics mining of deep, high storage and low permeability, and low drainage efficiency, which seriously restrict the efficient prevention and control of mine gas disasters. Based on the characteristics of low viscosity and permeability, phase change pressurization, and strong adsorption potential energy of liquid CO₂, the technology system of liquid CO₂ displacement for high-gas and low-permeability coal seam was developed, and field industrial of low-pressure (0.5~2.5 MPa) and medium-pressure (2.5~15.0 MPa) combined injection test was carried out. In this test, the mode of injection followed by drainage was adopted, and the gas drainage effect was investigated for 30 days. The test results show that the effective influence radius of CO₂ in this test is 20 m, and the liquid seepage radius is 5 to 7 m. After the injection of liquid CO₂ into coal seam, the average gas drainage concentration and drainage purity of all drainage holes were increased by 3.2 and 3.4 times, respectively, and the gas promotion effect was significant. Taking the liquid CO₂ low-medium-pressure displacement gas test area as the calculation unit, from the comprehensive benefit analysis, compared with the original drainage mode, the liquid CO₂-combined pressure injection process can save 34.7% of the engineering cost and shorten the gas drainage standard time by 45.9%. Therefore, the application of this technology has important technical support and reference significance for the efficient management of gas in the same type of mine.

1. Introduction

“High storage and low permeability” is a common attribute of most of the coal seams in deep mines in China. That is, as the depth of coal seam mining increases, the gas content of the coal seam increases, and the permeability is low, which restrict the efficient extraction of coal seam gas and the effective prevention of mine gas [1]. Gas disaster can be said to be not only the most destructive disaster affecting mine safety production but also a serious threat to the safety of production workers one of the major disasters [2]. Excessive emissions of CH₄ cause incalculable damage to the environment, and the greenhouse effect of CH₄ is 25 times that of CO₂ [3]. From the perspective of energy utilization and environmental protection, gas is a kind of efficient and

clean energy; capturing and utilizing this gas are able to decrease greenhouse gas emissions [4]. Coalbed methane (CBM) is abundant in China. With the importance of environmental protection in China, enhanced coalbed methane (ECBM) recovery technology has become the focus of gas prevention and control.

ECBM recovery technology is one of the key technologies that must urgently be addressed in the process of coalbed methane development both within and outside of China. Based on the mechanism of CH₄ generation, storage, and migration, increasing coal seam CH₄ production mainly starts from two aspects: one is to promote the desorption of coalbed methane, so that the CH₄ adsorbed on the inner surface of the coal matrix pores can be changed from the adsorbed state to the free state as much as possible, and the

diffusion of CBM from the matrix and micropores to the cracks is expanded [5]. The second is to expand the gas migration channel, so that CBM seeps to the borehole along more fracture channels [6, 7]. To improve the efficiency of CBM disaster control and reuse in deep well mining, a variety of coal seam permeability enhancement and gas drainage promotion technologies have been developed, mainly including protective layer mining, hydraulic fracturing, hydraulic slotting, high-energy detonation wave blasting fracturing, shock wave fracturing, and liquid CO₂ blasting [8–10]. From the analysis of the engineering application effect, the above-mentioned technical processes can obviously improve the permeability of the coal seam and achieve the purpose of promoting gas drainage. However, due to the limitations of the technology, there are all kinds of technical defects and negative effects in the engineering application process. Therefore, it is very urgent to research and develop a new innovative technology for gas extraction in high-gas permeability and low-permeability coal seams.

Liquid CO₂ is a fluid with the properties of low viscosity, easy permeability, phase change enhancement, and high adsorption potential. The liquid CO₂ injection into a coal seam improves gas extraction by fracture enhancement and displacement replacement, with incomparable advantages in reservoir construction and CBM income elevation. On the one hand, coal has a higher adsorption capacity for CO₂. The adsorption of CO₂ by coal is about 2–10 times that of CH₄, and the injection of CO₂ reduces the partial pressure of CH₄ and promotes the desorption of CH₄ [11]. On the other hand, after the competitive adsorption of CO₂ and CH₄, CBM is replaced. Furthermore, liquid CO₂ injection into the coal seam will generate phase change pressurization, which will increase the mutual reverse seepage and diffusion rate of CO₂ and CH₄ in the coal seam, and then promote the CH₄ escape from the coal seam [12]. In terms of engineering applications, the United States, Canada, Poland, Japan, etc. have all carried out engineering tests of CO₂ injection, flue gas, air, nitrogen, etc. to ECBM recovery, and significant results have been achieved [13–19]. However, because the output phase of liquid CO₂ is unstable, the aging characteristics are complex and dynamic. Relatively few fundamental studies on ECBM recovery technologies using liquid CO₂ have been conducted, and related studies have mainly focused on the promotion of coal seam gas drainage by gaseous and supercritical CO₂ [20, 21].

Based on the special properties of liquid CO₂, this paper develops a liquid CO₂ cracking coal seam and gas displacement technology system suitable for high-gas and low-permeability coal seams. The research team carried out engineering tests at the 401102 working face of Mengcun Coal Mine of Binchang Mining Group, Shaanxi Coal Mining Group. The feasibility of the process technology was debugged on site, the key parameters of the field test were investigated, and the comprehensive benefits of the process technology were verified by subsequent gas drainage effects.

2. The Principle of Liquid CO₂ Enhance Permeability and Displace CBM

2.1. Effect of Liquid CO₂ on Permeability Enhancement. Coal is a porous medium; a large pore volume is ineffective despite

being interconnected in a porous medium. Microcapillary pores, which do not allow a fluid to pass through, and pores surrounded by microcapillary pores are considered an ineffective pore space for infiltration. Liquid CO₂ is used as a low-temperature fluid (with a low temperature of -19.5°C). The original temperature of the actual coal seam on-site is higher than 30°C. When liquid CO₂ is injected into the coal seam, convective and phase transformation heat transfers take place upon contact with the coal mass, causing an increase in temperature. A temperature gradient is generated inside the coal matrix scaffold, forming thermal stress. During the injection of liquid CO₂, heat exchange with the coal mass takes place when CO₂ infiltrates the pores and fractures, causing a cryogenic freezing damage effect [22], triggering a shrinkage of the coal matrix scaffold and damaging the structure of the pores and fractures of the coal mass. During the heat exchange between liquid CO₂ and coal, liquid CO₂ undergoes a phase transformation and an increase in both temperature and pressure as the coal matrix swells [23], inducing a compressive or tensile stress in the pore network inside the coal mass, which forces coal pores to restructure and cracks to extend and elongate. As a result, most of the ineffective pore space, which does not allow a fluid flow, becomes interconnected. Consequently, an ineffective pore space in the coal matrix transforms into an effective pore space, improving the effective porosity of the porous medium. The pore surface area of coal is expanded to a certain extent, improving the permeability [24] (as shown in Equation (1)) [25]. The gas migration channel can be broadened, allowing coal seam gas to flow toward the extraction borehole through more cracks, thus achieving an enhanced permeability by liquid CO₂ [26].

$$\mu_i = -\lambda_i \frac{dp}{dx} = -\lambda_i \text{grad}p, \quad (1)$$

where μ is the flow rate (m²·Pa⁻¹·s⁻¹), λ is the permeability coefficient, and dp/dx is the total pressure gradient in the direction of pressure reduction (Pa·m⁻¹).

2.2. Displacement Effect of Liquid CO₂. The process of gas displacement through the injection of liquid CO₂ into highly gassy coal seams is illustrated in Figure 1 [27]. Liquid CO₂ is injected into a borehole and diffused along the cracks of the coal seam around the borehole [28]. Under the effect of cryogenic damage from CO₂ and the thermal stress generated from the heat exchange between the CO₂ and the coal seam, a swelling of the coal matrix occurs [29]. The coal pores are restructured and the cracks elongate, increasing the effective porosity and permeability of the coal [30], causing an infiltration of liquid CO₂ into the coal. When infiltrated into a certain zone, liquid CO₂ absorbs heat from the coal and gradually transforms into a gaseous state. Gaseous CO₂ continues to infiltrate under pressure and a difference in concentration. Numerous studies have shown that 80%–90% of gas is in an adsorbed state under identical conditions [31] and that the adsorption capacity of CO₂ in a coal matrix is higher than that of CH₄, leading to competitive adsorption between them [32]. Subsequently, the partial pressure of CO₂ entering

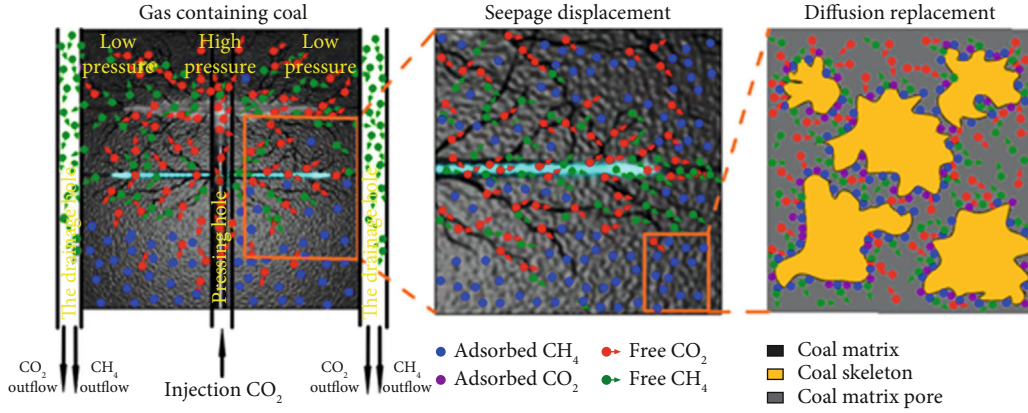


FIGURE 1: Schematic diagram of coal seam liquid CO₂ injection gas flow displacement.

the adsorption site of the coal matrix increases from the transport force, and with the transformation stress of liquid CO₂, thereby lowering the partial pressure of the CH₄, the adsorption-desorption equilibrium of the gas components inside the coal matrix is destroyed. The adsorption sites of CH₄ are occupied by CO₂ molecules with a higher adsorption capacity, leading to the desorption and displacement of CH₄ molecules [33, 34]. As the volume of the CO₂ injection increases, the CH₄ molecules are driven out of the coal mass through the competitive adsorption of CO₂, changing from an adsorbed state to a free state (as shown in Equation (2)). Simultaneously, as the migration channel of the gas is extended, a difference in concentration is formed by the components of the gas mixture at the two ends of the gas migration channel, displacing the CH₄ molecules into the corresponding migration channel [35], as shown in Equation (3). Eventually, the dual effects of pressure and a difference in concentration cause a large number of CH₄ molecules to seep and diffuse through the voids of the coal toward the extraction borehole [36].

$$\frac{\partial c_i}{\partial t} + \nabla(-D_i \nabla c_i) = -Q_i, \quad (2)$$

where i is the gas component (CO₂ or CH₄), c_i is the concentration of component i (kg·m⁻³), D_i is the diffusion coefficient of component i (m²·s⁻¹), and ∇ is the Hamiltonian operator.

$$c_i(p) = \frac{a_i b_i p_i}{1 + b_{\text{CO}_2} p_{\text{CO}_2} + b_{\text{CH}_4} p_{\text{CH}_4}} \rho_i p_e, \quad (3)$$

where $c_i(p)$ is the adsorption capacity of component i (kg·m⁻³), a_{CO_2} and a_{CH_4} are, respectively, the maximum adsorption capacity of CO₂ and CH₄ when they are adsorbed separately in the coal seam (kg·m⁻³), b_{CO_2} and b_{CH_4} are adsorption equilibrium constants of CO₂ and CH₄, respectively (MP⁻¹), and p_{CO_2} and p_{CH_4} are the adsorption partial pressure of CO₂ and CH₄, respectively (MPa).

3. Process System for Methane Displacement with Liquid CO₂ in High-Gas and Low-Permeability Coal Seam

This on-site test was selected at the mechatronics chamber of the 401102 working face in the 4# main coal seam of Mengcun Mining Co., Ltd. in the Binchang mining area, Shaanxi (as shown in Figure 2). The 4# coal seam belongs to low metamorphic bituminous coal, and internal fissures developed not well. The average coal thickness is 13.0 m, and the average inclination angle of the coal seam is 3°. Coal industry analysis and coal quality determination results are shown in Table 1.

The predicted value of absolute gas emission in the mine is 110.5 m³/min, while the predicted value of relative gas emission is 8.1 m³/t. The 4# coal seam is a typical coal seam with high gas, low permeability, and bursting liability. When gas extraction is carried out by dense drilling, problems such as high cost, long extraction time, and poor extraction effect exist. Mengcun Coal Mine has successively adopted hydraulic fracturing, hydraulic slicing, and other technologies, aiming to reduce the bursting liability of coal seam and improve the efficiency of gas extraction. Through the above technical effect analysis, it can reduce the impact of coal seam and improve the permeability of coal seam. However, due to the water-locking effect of the large-area pore and fracture network in the coal seam [37], the effect of gas extraction is reduced.

Therefore, based on technology comparison and comprehensive benefit analysis, the mine chose to develop liquid CO₂ displacement technology. The purpose is to improve the efficiency of coal seam gas extraction through the implementation of technical processes and reduce the cost of mine gas disaster management.

3.1. Test Process System. The process diagram of the liquid CO₂ pressure injection system is shown in Figure 3. It is mainly composed of a liquid CO₂ tanker, a cryogenic pressure pump, a data acquisition instrument (DAI), a pressure transmitter (PT), a pressure-resistant conveying pipeline, a stop valve, and a pressure relief valves and other components. The cryogenic pressure pump is mainly used for boosting

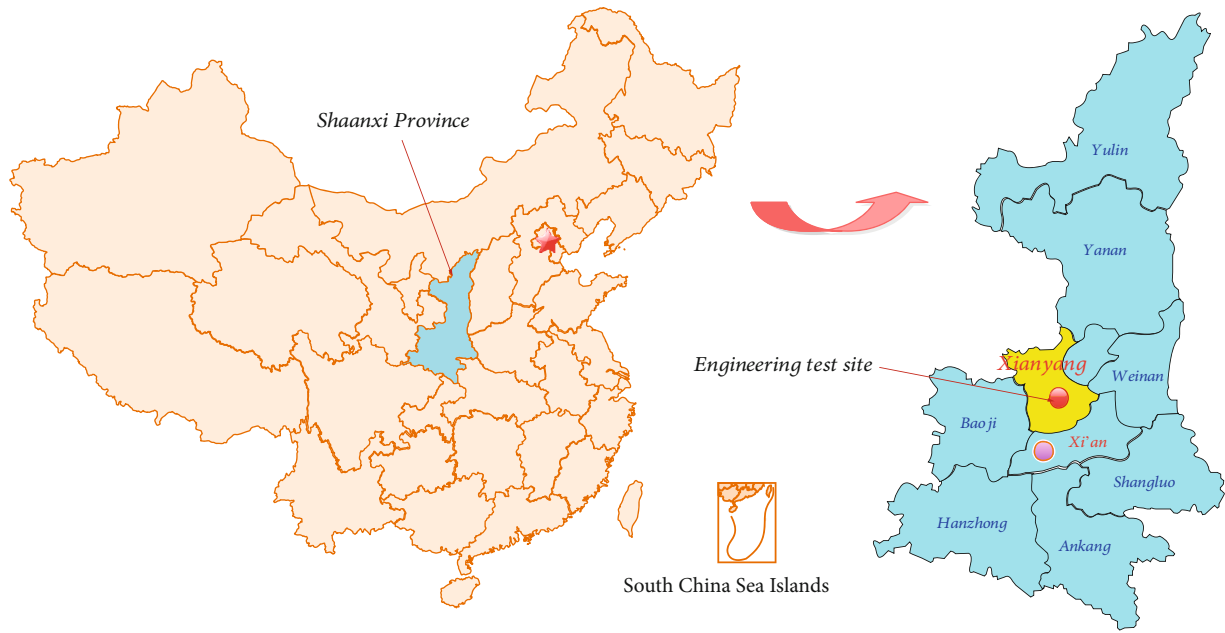


FIGURE 2: The location of the on-site test.

TABLE 1: Coal industry analysis and coal quality test results.

Coal sample	Industrial analysis (%)					Coal composition (%)			R_{max}^0 (%)
	M_{ad}	V_{ad}	A_{ad}	FC_{ad}	f_x	V_0	I_0	E_0	
Nonstick coal	3.73	35.53	6.92	51.21	2.46	54.36	43.55	20.8	0.63

M_{ad} is the moisture content of the coal; V_{ad} is the volatile matter of the coal; A_{ad} is the ash content of the coal; FC_{ad} is the fixed carbon of the coal; f_x is the hardness coefficient of the coal; V_0 is the vitrinite of the coal; I_0 is the inertia of the coal group; E_0 is the coal body's external group; R_{max}^0 is the coal body's maximum vitrinite reflectance.

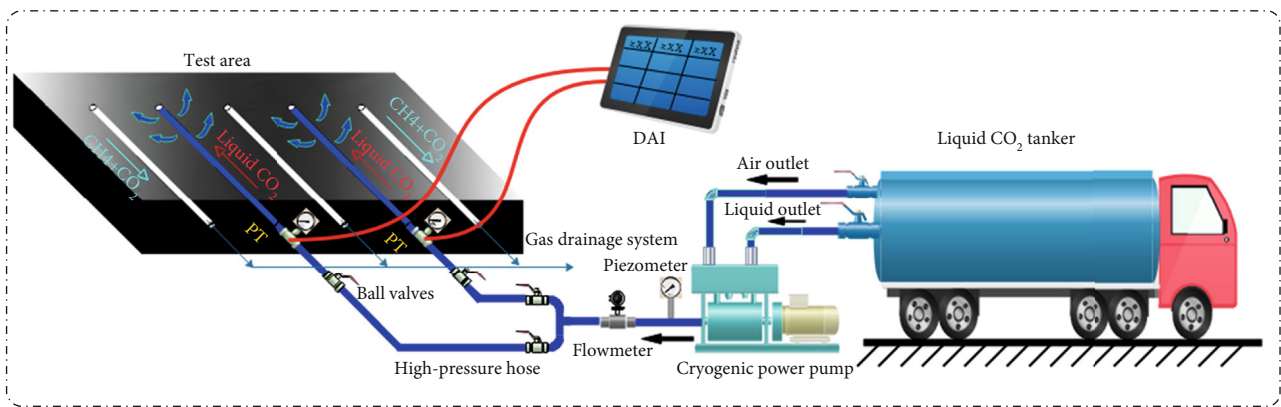
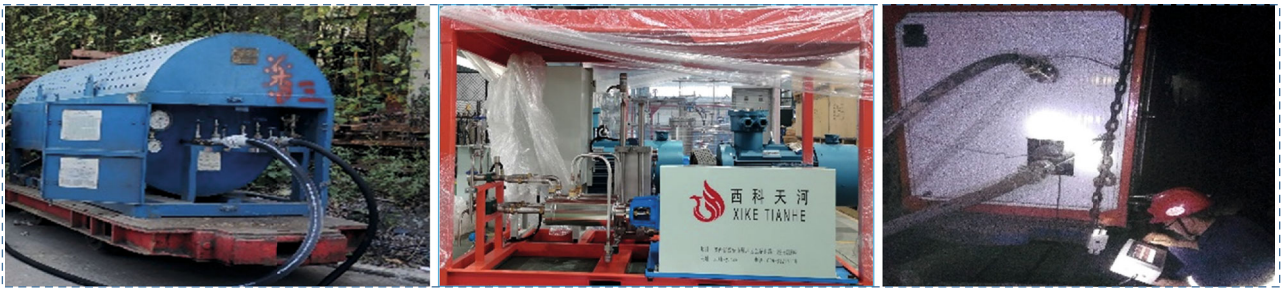


FIGURE 3: Process diagram of liquid CO₂ injection system.

liquid CO₂, with rated power of 22 KW, flow rate of 2000 L/h, and maximum working pressure of 15 MPa, which can supercharge and convey liquid CO₂. The data acquisition instrument can realize multiple sets of data acquisition and monitoring, mainly collecting pump outlet pressure, orifice pressure, etc. The monitoring medium of the tank vehicle differential pressure meter (vortex flowmeter) is liquid, which is mainly used to monitor the flow rate in the pressure injection process and count the accumulative pressure injection amount. The pressure transmitter has a range of 0–30 MPa and mainly monitors the variation of orifice pressure in the process of injection. The conveying pipeline is a high-pressure rubber hose with pressure resistance of 0–40 MPa, which has the characteristics of high-pressure and low-temperature resistance. Globe valve and relief valve are mainly used for backflow, relief, and blowout of pipeline at the end of pressure injection [8].

3.2. Drilling Layout of Working Face. The field test was carried out in the newly excavated 401102 electromechanical chamber. The coal seam in the test area is well distributed, and no gas drainage is carried out. A total of 15 in seam boreholes were constructed, 2 of which were boreholes for the injection of liquid CO₂ (1# and 2#), and 13 were observation boreholes (1#–13#). The drilling layout of the working face is shown in Figure 4, and the detailed parameters of the drilling design are shown in Table 2.

4. Industrial Test Results and Discussion

4.1. Dynamic Parameter Analysis of CH₄ Displacement by Liquid CO₂ in High-Gas and Low-Permeability Coal Seam. The liquid CO₂ low-pressure injection system adopts the direct injection of liquid CO₂ tanker, and the maximum pressure of liquid CO₂ tanker is 2.5 MPa. Low-temperature pressure pump is used to supercharge liquid CO₂ with a flow rate of 2000 L/h and a maximum working pressure of 15 MPa. The pressure transmitter and data acquisition instrument were used to monitor the pressure change of the orifice and check the stability of the system. Meanwhile, the CO₂ verification tube (20% range) was used to detect the influence radius of CO₂ seepage.

Low-pressure injection was mainly used to debug the reliability and stability of the injection system. The liquid CO₂ transformed into gaseous CO₂ to disturb the concentration gradient of gas in the steady state of the coal. The medium pressure injection was mainly based on the low-temperature freezing damage and instantaneous phase change of liquid CO₂, which in order to expand the CO₂ migration radius and increase the influence range of CO₂ displacement gas in the coal seam. When the liquid CO₂ was injected, the pressure gradient and the concentration gradient together drove the migration of CO₂ molecules and competed with the gas in the coal for adsorption and desorption, so as to achieve efficient gas extraction.

4.1.1. Pressure Change during Injection of Liquid CO₂ into Bedding Borehole

(1) Pressure Change of Liquid CO₂ Injection at Low Pressure of Coal Seam. The liquid CO₂ tank was used to conduct two

low-pressure injection on the 1# injection hole (1#-1_L, 1#-2_L) and 2# injection hole (2#-1_L, 2#-2_L), respectively. The injection parameters are shown in Table 3. The variation of orifice pressure during injection was observed, as shown in Figures 5(a) and 5(b). Using liquid CO₂ increases the permeability and displacement function, pushing the gas migration and desorption, and through the aperture of the gas extraction effect for 30 days observation. At the same time, in the original area, select raw gas drainage borehole as a comparison and mainly observed the gas concentration of extraction, extraction of pure gas amount, and comprehensive inspection of liquid CO₂ displacement test effect of CBM.

It can be seen from the pressure curves of injection processes in 1# and 2# injection holes. The maximum pressure of each hole during the second injection is greater than the maximum pressure of the first one, and the rate of pressure rise is higher than the first one. In the initial stage of pressure injection, liquid CO₂ had good permeability and fast permeability in the coal. During the second injection, the coal matrix expanded, and the pore pressure in the coal body increased [38, 39]. At this time, the permeability was relatively slow, and the pressure gradually increased and kept balance.

Figure 5(b) is an enlarged diagram of the downward trend of each pressure curve. According to the analysis, the pressure decline rate of the second injection is slower than that of the first injection. The pressure curve of 2#-1 declines faster and finally reaches 0 due to leakage of #9 observation hole around 2# injection hole. When liquid CO₂ is injected into coal seam, it changes from liquid to gaseous state. Gas molecules will adsorb on the surface of coal, resulting in the decrease of surface tension of coal and the expansion of coal matrix. At the same time, under the action of overburden stress, the increase of CO₂ adsorption pressure and effective stress both increase the internal expansion coefficient of coal [40]. In this case, CO₂ slowly permeates and diffuses under the action of internal pressure difference and concentration difference of coal seam, and competitive adsorption with CH₄ occurs in the coal matrix [41].

(2) Pressure Change of Liquid CO₂ Injection at Medium Pressure of Coal Seam. The stability of the system was verified by the test of the liquid CO₂ low-pressure injection system. The injection hole and observation hole were checked, and the leakage area was sealed. On the basis of the low-pressure injection system, the liquid CO₂ medium-pressure injection system adopts the low-temperature pressure pump to pressurize. The 1# injection hole (1#-1_M, 1#-2_M) and 2# injection hole (2#-1_M, 2#-2_M) are, respectively, pressurized. The maximum working pressure of the low-temperature pressure pump is 15 MPa, and the flow is 2000 L/h. The pressure transmitter and data acquisition instrument were used to monitor the pressure change of the orifice and check the stability of the system. Meanwhile, the CO₂ verification tube (20% range) was used to detect the influence radius of CO₂ seepage [42]. The injection parameters are shown in Table 4. The variation of orifice pressure during injection was observed (as shown in Figures 6(a) and 6(b)).

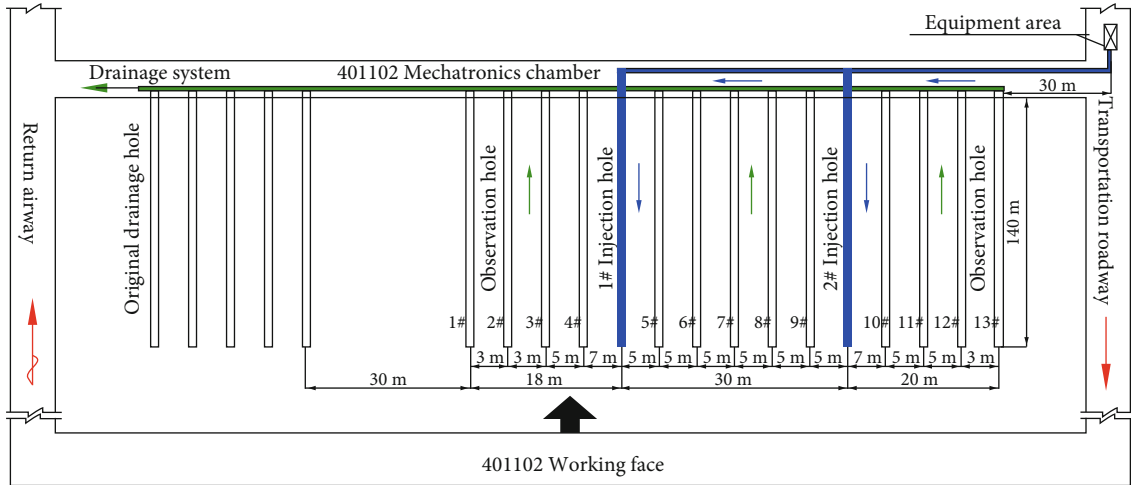


FIGURE 4: Schematic diagram of drilling layout of liquid CO₂ injection system.

TABLE 2: Drilling parameter design table.

Drilling name	Hole depth (m)	Azimuth (°)	Inclination (°)	Aperture (mm)	Sealing length (m)
Injection hole	140	90	0.5°–1°	113	40
Observation hole	140	90	0.5°–1°	113	12
Original drainage hole	140	90	0°–1°	113	12

TABLE 3: Table of low-pressure injection parameters.

Drilling name	Volume of injection (m ³)	Rate of flow (m ³ /min)	Pressure rise rate (MPa/min)	Maximum pressure (MPa)	Dwell time (min)	Depressurization rate (MPa/min)	Minimum pressure (MPa)
1#-1 _L	2.0	0.028	0.020	0.70	105	0.010	0.17
1#-2 _L	1.8	0.038	0.069	1.50	38	0.008	0.42
2#-1 _L	1.8	0.040	0.048	0.95	58	0.040	0
2#-2 _L	2.0	0.030	0.041	1.30	12	0.022	0.11

According to Figure 6(a), it can be seen that there are basically two stages in the pressure change curve during medium pressure injection. After the initial pressure rises to a certain value, the pressure will remain stable for a period of time and keep rising with the increase of pressure and flow. The reason why the pressure of 1#-1 drops to 0.48 MPa is that leakage phenomenon is observed around 1# inspection hole.

The variation trend of boost rate of medium pressure injection is similar to that of low-pressure injection. The maximum pressure at the second injection of each hole was greater than that at the first injection; meanwhile, pressure rise rate is higher than that of the first injection. Figure 6(b) is an enlarged diagram of the downward trend of each pressure curve. The second injection drop rate of medium pressure injection is slower than that of the first injection.

The pore pressure rises and slippage effect gradually decreases with the increase of injection pressure during medium pressure injection. The gas molecules adsorbed on the surface of the coal matrix increase, and the coal matrix expands further. In this case, CO₂ in coal seam under the action of internal pressure and the concentration difference

of slow diffusion compete with CH₄ in coal matrix inside. Low-pressure and medium-pressure injection tests have proved the stability of the system. At the same time, the sealing quality of the borehole is a key factor in the test. In order to maintain the pressure, sufficient liquid CO₂ raw materials should be ensured.

4.1.2. Effective Influence Radius of Liquid CO₂ Displacement.

According to 2# injection hole pressure and the temperature curve of 5 m and 7 m (as shown in Figure 7), the pressure and temperatures at 210 min were taken as a reference. The pressure and temperature values corresponding to distances of 5 m and 7 m are (4.06 MPa, -20.70°C) and (4.06 MPa, 13.90°C) respectively. CO₂ is liquid at 5 m away from the injection hole, while CO₂ is gaseous at 7 m away from the injection hole, so it can be judged that the seepage radius of liquid CO₂ is from 5 m to 7 m.

In the process of injecting liquid CO₂ into coal seam, the migration force generated in the process of phase transition to gaseous CO₂. The seepage of liquid CO₂ along the large-scale through fracture and the diffusion of gaseous CO₂ in

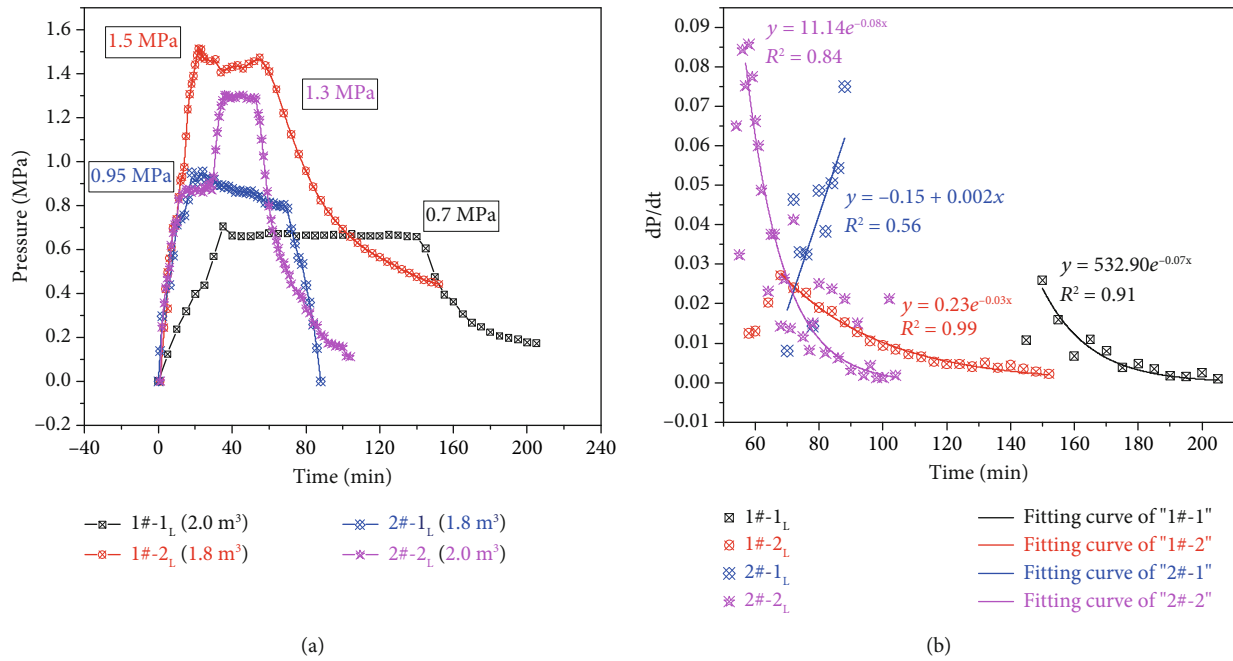


FIGURE 5: Variation of orifice pressure during low pressure injection.

TABLE 4: Table of medium pressure injection parameters.

Drilling name	Volume of injection (m ³)	Rate of flow (m ³ /min)	Pressure rise rate (MPa/min)	Maximum pressure (MPa)	Dwell (time/min)	Depressurization rate (MPa/min)	Minimum pressure (MPa)
1#-1 _M	2.0	0.018–0.025	0.048	3.16	25	0.038	0.48
1#-2 _M	2.0	0.020–0.025	0.090	3.28	15	0.005	2.73
2#-1 _M	2.0	0.015–0.020	0.040	5.30	30	0.027	1.34
2#-2 _M	2.0	0.015–0.025	0.067	5.90	25	0.010	3.50

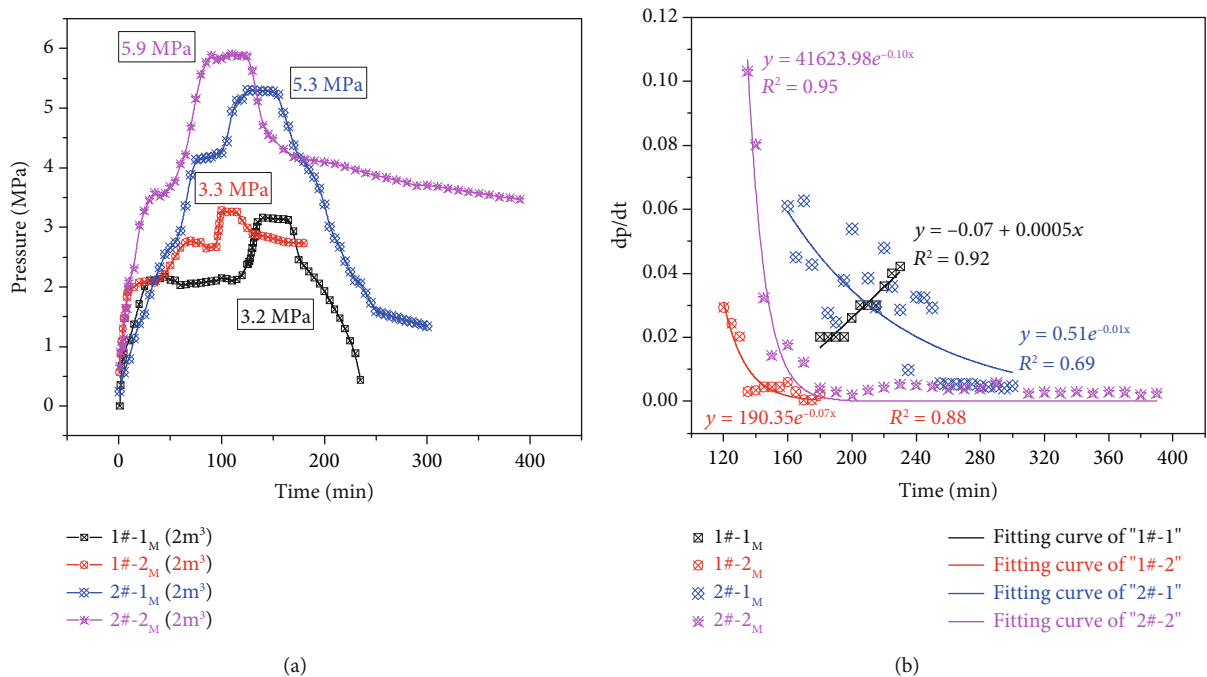


FIGURE 6: Variation of orifice pressure during medium pressure injection.

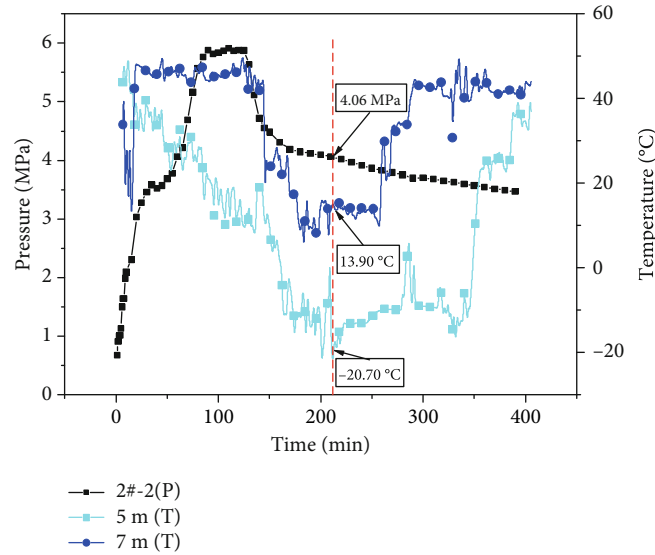


FIGURE 7: Temperature-pressure curve.

the open pore were promoted. This is a solid-liquid-gas coupling process, temperature, stress, concentration, and other multifield coupling results. Therefore, in order to determine the effective influence range of liquid CO_2 displacement in coal seam, the effective influence range of CO_2 in coal seam was determined by the concentration of CO_2 in coal seam. After a period of holding pressure, the CO_2 concentration of each observation hole on both sides of the injection hole was monitored by using industrial CO_2 calibration tube (with a maximum measurement range of 20.0%, where a measurement of 20% indicates that the CO_2 concentration exceeded the measurement range). The variation of CO_2 concentration in observation holes at different distances is shown in Figures 8. The CO_2 concentration at different distances after first medium pressure injection in 1# and 2# holes is shown in Figure 8(a), and after second injection in 1# and 2# holes is shown in Figure 8(b).

According to the data analysis of gas drainage, the maximum original CO_2 concentration in coal seam is 2.78%. As shown in Figure 8(a), when the low pressure is injected, the accumulated injection quantity of liquid CO_2 is 3.8m^3 in the 1# injection hole, and the concentration of CO_2 was 2.4% at 25 m from 1#, slightly lower than the maximum original CO_2 content of coal seam by 2.78%. The concentration of CO_2 was 1.64% at 25 m from no. 2 less than 2.78% of the maximum original CO_2 concentration in coal seam, when liquid CO_2 was injected 3.8m^3 cumulatively. It showed that the gas-phase migration range of liquid CO_2 might be 20–25 m, and the minimum is not less than 20 m. From Figure 8(b), it showed that the CO_2 concentration at the distance of 25 m from 1# injection hole is 1.6%, which is lower than 2.78% of the maximum original CO_2 concentration of coal seam. While the accumulated injection quantity of liquid CO_2 is 4.0m^3 in no. 2 injection hole, the CO_2 concentration is 1.2% at 25 m from 2# injection hole, which is lower than 2.78% of the maximum original CO_2 concentration in coal seam. It can be concluded that the gas-phase migration of liq-

uid CO_2 might be in the range of 20–25 m, and the minimum is not less than 20 m.

Therefore, the effective influence radius of liquid CO_2 displacement is basically the same between low-pressure injection and medium-pressure injection, the gas migration range is 20–25 m, and the minimum is not less than 20 m. The CO_2 diffusion is faster in the middle-pressure injection, but with the increase of the injection volume and pressure, it could spread further. Based on the observation of the distribution of CO_2 concentration after the injection holes of 1# and 2#, it is determined that the effective influence radius of gas displacement by liquid CO_2 is 20 m in bedding boring of 4# seam in Mengcun coal mine; this result is basically similar to the method and results used in previous field tests [43].

4.2. Analysis on Gas Displacement Effect of Coal Seam by Liquid CO_2 . After field test of gas displacement by liquid CO_2 injection in coal seam of 401102 mechatronics chamber, the effect of gas drainage was investigated for 30 days, and the gas drainage concentration and flow rate were observed. The gas drainage purity was calculated, while the 5#–9# observation hole was selected; the Y01–Y05 was selected as the contrast hole. The contrast hole are 30 m away from the test area in the same roadway; the effect of gas displacement by liquid CO_2 was investigated by comparing the average gas drainage concentration and the average gas drainage purity between the test area and the original gas drainage area. The relationship between the average gas drainage concentration and the average gas drainage purity is shown in Figures 9(a) and 9(b).

As shown in Figure 9(a), the maximum concentration of gas drainage from observation holes in the test area is 39.28%, the minimum is 9.39%, and the average is 17.73%, while the maximum, the minimum, and the average concentration of gas drainage from original holes are 11.64%, 1.46%, and 5.60%, respectively. The concentration of gas drainage in the test area is 3.2 times that of the original gas drainage. According to the concentration curve of gas drainage from

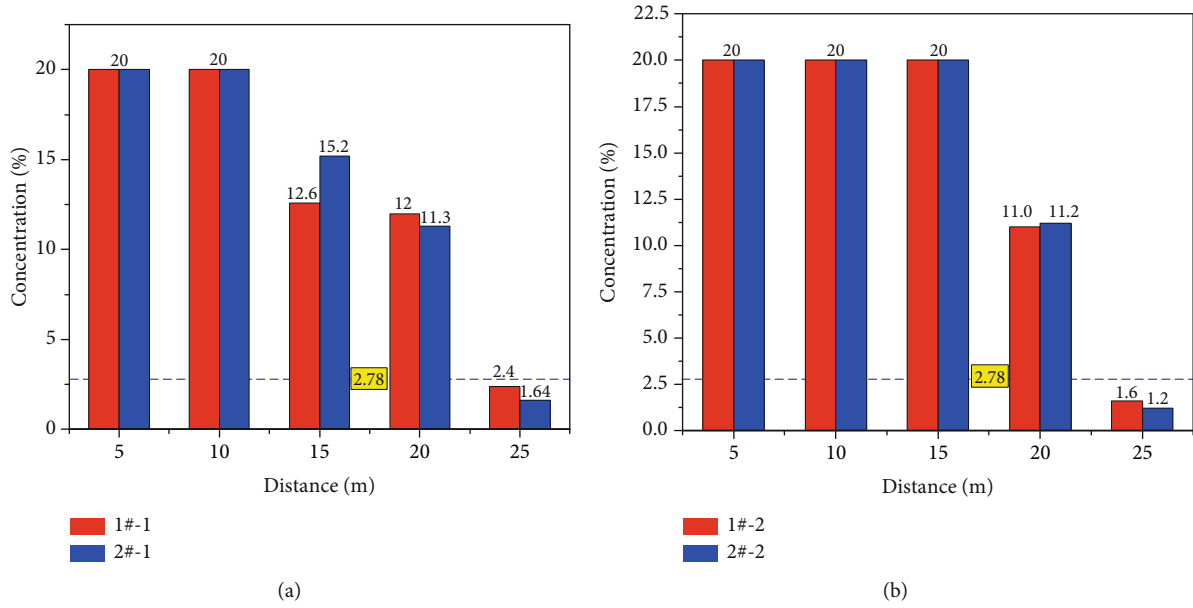


FIGURE 8: Concentration variation of observation hole.

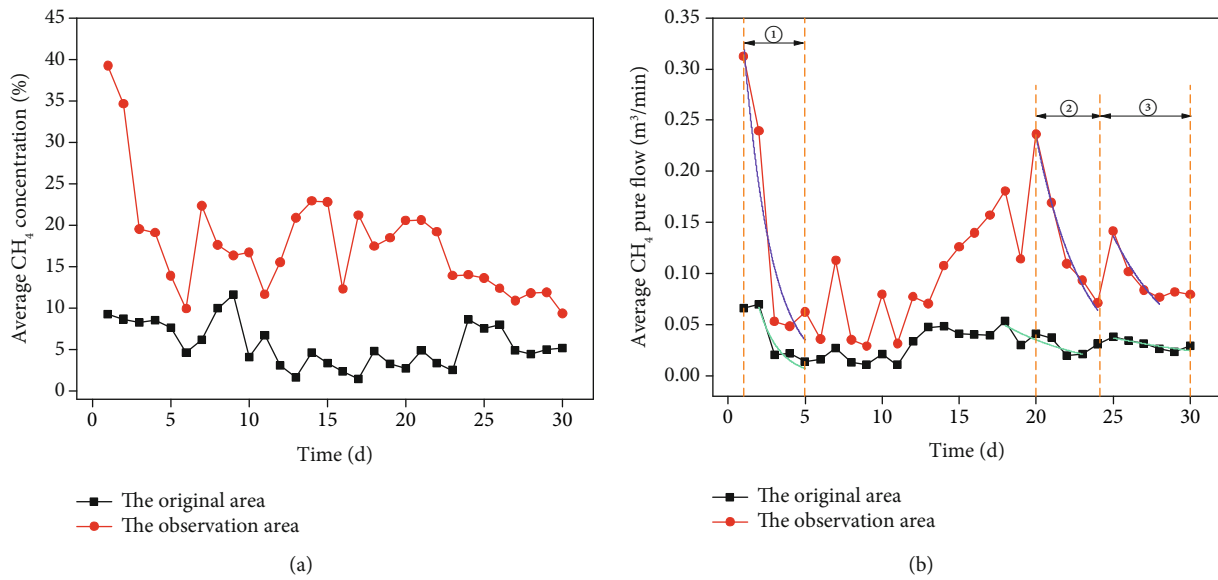


FIGURE 9: Correlation diagram between average gas drainage concentration and average gas drainage purity.

observation hole, it can be seen that in the early period of liquid CO₂ injection, the coal matrix was embrittled deformed by the low-temperature damage of liquid CO₂, and the pores of coal body developed twice. The fractures continued to expand and extend; the pore ratio of coal and the permeability of coal seam increases; meanwhile, there were more migration pathway. Under the action of concentration difference and pressure difference, the gas can be released advantageously, and the moving power and rate of gas in coal seam can be further improved. With the heat exchange between liquid CO₂ and coal, liquid CO₂ is gradually transformed into gas and diffused in coal; meanwhile, it competed with CH₄ in coal to adsorb and displaces the adsorbed CH₄ in coal. The

concentration of gas extraction decreases rapidly and fluctuates about 17% after 5 days.

It can be seen from Figure 9(b) that the change law of gas extraction purity is consistent with the change law of gas extraction concentration from observation hole and original gas extraction hole. The comparison curve of gas extraction purity can be divided into three stages, which correspond to the ①, ②, and ③ stages of the curve, and the 123 stages of the curve, respectively; a large amount of free CH₄ is transported along the original fracture of coal seam and the new fracture formed by pressure injection of liquid CO₂, and the attenuation coefficient of gas extraction purity is 0.5583, the attenuation coefficient of gas extraction purity is 0.7426 in

the original gas extraction area, and the gas in the experimental area is more favorable for gas drainage. ② and ③ stages of curves show that after 15 days of gas pumping, CO₂ gas is adsorbed in the coalbed matrix, which forms competitive adsorption with CH₄ and displaces the adsorbed CH₄, and the pure measuring range changes periodically. Among them, the attenuation coefficient of the pure gas extraction is 0.3229 and 0.2236, and the attenuation coefficient of the pure gas extraction is 0.1685 and 0.0830 in the original gas extraction area, the gas extraction purity is relatively low, and the gas attenuation coefficient is kept at a relatively low level, while the gas extraction purity remains at a relatively high level in the experimental area with the CO₂ percolation and diffusion, CO₂ adsorption in the coal matrix and displacement of CH₄. In the test area, the maximum value and the average value of gas extraction purity are 0.313 m³/min, 0.029 m³/min, 0.109 m³/min, 0.70 m³/min, 0.011 m³/min, and 0.032 m³/min, respectively. The purity of gas extraction in the test area is 3.4 times of that of the original gas extraction, and the active period of gas extraction is about 30. The results show that liquid CO₂ injected into coal seam increases the gas drainage flow, especially the displacement effect of gas is the most obvious. Based on the 30-day observation data, the gas drainage effect of CH₄ test in coal seam driven by liquid CO₂ is obviously improved, and the gas drainage efficiency will inevitably decline in the later period and timely observation of pressure injection effect [44, 45].

4.3. Comprehensive Benefit Analysis

4.3.1. Economic Benefit Analysis. By means of measuring the gas pressure and gas concentration of coal seam before and after the injection of liquid CO₂, it is shown that the gas pressure of coal seam in the field test area reduced by 12% after 30 days promoting of gas drainage. Ton coal with gas content decreased from 3.12 m³/t to 1.41 m³/t, which decreased the gas pressure and gas drainage time significantly. According to the gas displacement test using liquid CO₂ and the borehole layout for mine gas extraction, the economic costs of the project under two scenarios were compared. An observation area with a length of 70 m was applied as the basis of the calculation. In the original gas drainage area, there were 28 boreholes for methane extraction, distributed at intervals of 2.5 m, each of which was 140 m long. In the observation area used during the test, there were 15 boreholes of 140 m in length and with a liquid CO₂ consumption of 20 m³, with 2 of the boreholes used for the pressure injection. The construction cost of the boreholes was RMB 55 per meter. The costs of the liquid carbon dioxide displacement zone included the construction cost of the boreholes, cost of laboratory equipment, and the raw material cost of the liquid CO₂. A cost comparison is shown in Table 5. It was calculated that a reduction in the project cost of approximately RMB 139,700 can be achieved from the gas displacement test through the use of CO₂ within this calculation unit, cutting the project cost by 34.7%.

4.3.2. Time Analysis of Gas Extraction Standard. Because the gas emissions of the mine are mainly from the mining face of

the production layer, a predrainage rate of the gas of $\eta \geq 35\%$ was set based on the standard for coal mine gas extraction (where η is the volume of gas extracted/volume of gas reserve). Combined with the characteristics of the experiment area used in this study, a calculation unit of 80 m in length with a working face of 180 m in width was selected for comparison with the time required to meet the gas extraction standard.

For the volume of gas extracted, η represents the volume of gas extracted from a unit of coal mass within the target time period (m³).

For the volume of the gas reserve, the gas reserve from the coal mass is within the control area of the unit of the predrainage borehole (m³).

For the calculation of the gas reserve, a length of 80 m with a 180 m wide working face, an average coal seam thickness of 13 m, and an average original coal seam gas content of 3.12 m³/t were applied. Therefore,

$$Q_{\text{reserve}} = 80 \times 180 \times 13 \times 1.36 \times 3.12 = 584000 \text{ m}^3. \quad (4)$$

According to the observation data of the volume of pure gas extracted from a single borehole, the average gas emission from a single borehole in the original extraction project was 0.032 m³/min, whereas that from a single borehole in the experimental project of gas displacement using CO₂ was 0.109 m³/min. As a result, the corresponding predrainage times required to meet the standard are as follows:

$$T_1 = \frac{Q_{\text{reserve}} \times \eta}{Q_{\text{daily extraction}}} = \frac{58.4 \times 0.35}{(0.032 \times 24 \times 60 \times 24)} = 185 \text{ d}, \quad (5)$$

$$T_1 = \frac{Q_{\text{reserve}} \times \eta}{Q_{\text{daily extraction}}} = \frac{58.4 \times 0.35}{(0.109 \times 13 \times 60 \times 24)} = 100 \text{ d}. \quad (6)$$

From the above calculations, it was found within the calculation unit that the predrainage time required to meet the standard for the original extraction project was 185 days, whereas that for the gas displacement through the liquid CO₂ project was 100 days. The time required to meet the standard was decreased by 85 days, thus reducing the extraction time by 45.9%, and significantly improving the extraction efficiency. Within the calculation unit, the gas extraction time required to meet the standard was decreased by 85 days, cutting the drainage duration by 45.9% [42].

5. Conclusions

- (1) A liquid CO₂ pressure injection system was tested using a low-pressure injection system in high-gas and low-permeability coal seam. The results showed that the injection process system is stable. The dynamic parameters such as pressure and flow rate keep fluctuating characteristics in the process of liquid CO₂ injection. Among them, the pressure of liquid CO₂ injection at low pressure fluctuated between 0.7 MPa and 1.51 MPa, while that of liquid

TABLE 5: Comparison of economic benefits.

Name of project	Number of boreholes	Depth of borehole (m)	Construction cost (in RMB 10000)	Raw material cost (in RMB 10,000)	Project cost (in RMB 10,000)
Original gas extraction project	56	140	43.12	—	43.12
Project of gas displacement by liquid CO ₂	15	140	11.55	16.6	28.15

CO₂ injection at medium pressure ranged from 5.3 MPa to 5.9 MPa. When the single hole liquid CO₂ injection volume reaches 4–6 m³, the liquid seepage radius is 5 to 7 m, and the effective migration radius of CO₂ is 20 m in the process of liquid CO₂ displacement gas in the test area through the distribution law of CO₂ gas concentration in the coal seam

- (2) It was found from the inspection of the gas extraction field during the test process that the concentration of CH₄ extracted increased from 5.60% to 17.73% after the injection of liquid CO₂ into the coal seam, increasing the concentration of gas extracted by 3.2-fold. The pure flow of gas extracted increased from 0.032 m³/min to 0.109 m³/min, increasing the pure flow of gas extracted by 3.4-fold. The gas extraction efficiency improved significantly
- (3) The test results of gas displacement using liquid CO₂ in calculation unit showed that the project cost can be reduced by 34.7% and the time required to meet the extraction standard within the calculation unit can be shortened by 45.9%. The use of gas displacement technology by applying liquid CO₂ can not only reduce the project cost but also improve the extraction efficiency and shorten the time required to meet the extraction standard, ensuring a continuous mine production. A reduction in the efficiency of the gas extraction was not considered in the selection of the calculation unit. In an actual experiment, a second pressure injection into the original boreholes can be conducted when a reduction in the extraction efficiency occurs, ensuring that the concentration and pure flow of the gas extracted are maintained at highly efficient levels. The new technology and reference for mine gas extraction were put forward

Data Availability

The data are all available and have been explained in this article; readers can access the data supporting the conclusions of the study.

Conflicts of Interest

The authors declare that they have no conflicts of interest.

Acknowledgments

The project was supported by the National Natural Science Foundation of China (grant numbers 51974240 and 51904234), the Key R & D Program of Shaanxi Provincial (grant number 2017ZDCXL-GY-01-02-03), and the China Postdoctoral Science Foundation (grant number 2020M683678XB).

References

- [1] H. Wen, Z. Li, Z. Wang, L. Ma, Y. Guo, and X. Wang, “Experiment on the liquid CO₂ fracturing process for increasing permeability and the characteristics of crack propagation in coal seam,” *Journal of China Coal Society*, vol. 41, no. 11, pp. 2793–2799, 2016.
- [2] H. Lin, J. Li, M. Yan, S. Li, L. Qin, and Y. Zhang, “Damage caused by freeze-thaw treatment with liquid nitrogen on pore and fracture structures in a water-bearing coal mass,” *Energy Science & Engineering*, vol. 8, no. 5, pp. 1667–1680, 2020.
- [3] IPCC, “IPCC fourth assessment report: climate change,” *The Physical Science Basis*, vol. 2, pp. 580–595, 2007.
- [4] C. Ö. Karacan, F. A. Ruiz, M. Cotè, and S. Phipps, “Coal mine methane: a review of capture and utilization practices with benefits to mining safety and to greenhouse gas reduction,” *International Journal of Coal Geology*, vol. 86, no. 2–3, pp. 121–156, 2011.
- [5] H. Wen, Z. Li, J. Deng et al., “Influence on coal pore structure during liquid CO₂-ECBM process for CO₂ utilization,” *Journal of CO₂ Utilization*, vol. 21, pp. 543–552, 2017.
- [6] E. Ozdemir, *Chemistry of the adsorption of carbon dioxide by Argonnepremium coals and a model to simulate CO₂ sequestration in coal seams*, The dissertation of Doctor of Philosophy of University of Pittsburgh, 2004.
- [7] Y. Cai, D. Liu, Z. Pan, Y. Yao, J. Li, and Y. Qiu, “Pore structure and its impact on CH₄ adsorption capacity and flow capability of bituminous and subbituminous coals from Northeast China,” *Fuel*, vol. 103, pp. 258–268, 2013.
- [8] L. Ma, G. M. Wei, S. B. Wang, Z. B. Li, and X. M. Liu, “Experimental study of displacing and replacing methane in low permeability coal seam by liquid CO₂ injection,” *Journal of Chongqing University*, vol. 41, no. 6, pp. 76–83, 2018, (in Chinese).
- [9] F. Zhou, T. Xia, X. Wang, Y. Zhang, Y. Sun, and J. Liu, “Recent developments in coal mine methane extraction and utilization in China: a review,” *Journal of Natural Gas Science and Engineering*, vol. 31, pp. 437–458, 2016.
- [10] Y.-k. Du, R.-h. Wang, H.-j. Ni, M.-k. Li, W.-q. Song, and H.-f. Song, “Determination of rock-breaking performance of

- high-pressure supercritical carbon dioxide jet,” *Journal of Hydrodynamics*, vol. 24, no. 4, pp. 554–560, 2012.
- [11] H. Wen, S. X. Fan, L. Ma, J. Guo, G. M. Wei, and J. C. Hao, “A case study of methane drainage promotion by injecting liquid carbon dioxide into low permeability coal seam,” *Journal of Xi’an University of Science and Technology*, vol. 37, no. 4, pp. 530–537, 2018, (in Chinese).
- [12] H. Chen, Z. Wang, X. Chen, X. Chen, and L. Wang, “Increasing permeability of coal seams using the phase energy of liquid carbon dioxide,” *Journal of CO2 Utilization*, vol. 19, pp. 112–119, 2017.
- [13] W. Gunter, M. Mavor, and J. Robinson, “CO₂ storage and enhanced methane production: field testing at Fenn big Valley, Alberta and Canada with application,” in *7th International Conference on Greenhouse Gas Control Technologies 5*, pp. 413–421, Vancouver, Canada, September 2004.
- [14] F. V. Bergen and H. J. M. Pagnier, “Development of a field experiment of CO₂ storage in coal seams in the Upper Silesian Basin of Poland,” in *Greenhouse Gas Control Technologies - 6th International*, pp. 569–574, Elsevier Ltd., Oxford, 2003.
- [15] S. R. Reeves and A. Taillefert, *Reservoir modeling for the design of the recopol CO₂ sequestration project, Poland*, U.S. Department of Energy, 2002.
- [16] J. Q. Shi, S. Durucan, and M. Fujioka, “A reservoir simulation study of CO₂ injection and N₂ flooding at the Ishikari coalfield CO₂ storage pilot project, Japan,” *International Journal of Greenhouse Gas Control*, vol. 2, no. 1, pp. 47–57, 2008.
- [17] G. Wei, H. Wen, J. Deng et al., “Liquid CO₂ injection to enhance coalbed methane recovery: an experiment and in-situ application test,” *Fuel*, vol. 284, pp. 119043–119244, 2021.
- [18] H. Wen, H. Wang, S. Fan et al., “Improving coal seam permeability and displacing methane by injecting liquid CO₂: an experimental study,” *Fuel*, vol. 281, p. 118747, 2020.
- [19] X. Cheng, H. Wen, S. Fan et al., “Liquid CO₂ high-pressure fracturing of coal seams and gas extraction engineering tests using crossing holes: a case study of Panji Coal Mine No. 3, Huainan, China,” *International Journal of Energy Research*, pp. 1–16, 2020.
- [20] G. Cui, L. Zhang, C. Tan, S. Ren, Y. Zhuang, and C. Enechukwu, “Injection of supercritical CO₂ for geothermal exploitation from sandstone and carbonate reservoirs: CO₂-water-rock interactions and their effects,” *Journal of CO2 Utilization*, vol. 20, pp. 113–128, 2017.
- [21] A. S. Ranathunga, M. S. A. Perera, P. G. Ranjith, and H. Bui, “Super-critical CO₂ saturation-induced mechanical property alterations in low rank coal: an experimental study,” *The Journal of Supercritical Fluids*, vol. 109, pp. 134–140, 2016.
- [22] J. Xu, C. Zhai, S. Liu, L. Qin, and Y. Sun, “Feasibility investigation of cryogenic effect from liquid carbon dioxide multi cycle fracturing technology in coalbed methane recovery,” *Fuel*, vol. 206, pp. 371–380, 2017.
- [23] J.-S. Bae and S. K. Bhatia, “High-pressure adsorption of methane and carbon dioxide on coal,” *Energy & Fuels*, vol. 20, no. 6, pp. 2599–2607, 2006.
- [24] X. Sun, Z. Wang, B. Sun, and W. Wang, “Research on hydrate formation rules in the formations for liquid CO₂ fracturing,” *Fuel*, vol. 33, pp. 1390–1401, 2016.
- [25] Z. B. Li, *Thermal cracking and displacement for enhancing methane extraction by phase transition of liquid CO2 injection in coal seam*, Xi’an University of Science and Technology, Xi’an, 2017.
- [26] V. Vishal, “In-situ disposal of CO₂: liquid and supercritical CO₂ permeability in coal at multiple down-hole stress conditions,” *Journal of CO2 Utilization*, vol. 17, pp. 235–242, 2017.
- [27] H. Wen, X. Cheng, J. Chen et al., “Micro-pilot test for optimized pre-extraction boreholes and enhanced coalbed methane recovery by injection of liquid carbon dioxide in the Sangshuping coal mine,” *Process Safety and Environmental Protection*, vol. 136, pp. 39–48, 2020.
- [28] S. Ranathunga, M. S. A. Perera, P. G. Ranjith, X. G. Zhang, and B. Wu, “Super-critical carbon dioxide flow behaviour in low rank coal: a meso-scale experimental study,” *Journal of CO2 Utilization*, vol. 20, pp. 1–13, 2017.
- [29] B. Dutka, M. Kudasik, Z. Pokryszka, N. Skoczylas, J. Topolnicki, and M. Wierzbicki, “Balance of CO₂/CH₄ exchange sorption in a coal briquette,” *Fuel Processing Technology*, vol. 106, pp. 95–101, 2013.
- [30] B. Dutka, M. Kudasik, and J. Topolnicki, “Pore pressure changes accompanying exchange sorption of CO₂/CH₄ in a coal briquette,” *Fuel Processing Technology*, vol. 100, pp. 30–34, 2012.
- [31] Z. Wang, Y. Cheng, K. Zhang et al., “Characteristics of microscopic pore structure and fractal dimension of bituminous coal by cyclic gas adsorption/desorption: an experimental study,” *Fuel*, vol. 232, pp. 495–505, 2018.
- [32] R. Sakurovs, “Relationships between CO₂ sorption capacity by coals as measured at low and high pressure and their swelling,” *International Journal of Coal Geology*, vol. 90–91, pp. 156–161, 2012.
- [33] D. Zhou, Z. C. Feng, D. Zhao, Y. S. Zhao, and T. T. Cai, “Experimental study of meso-structural deformation of coal during methane adsorption-desorption cycles,” *Journal of Natural Gas Science and Engineering*, vol. 42, pp. 243–251, 2017.
- [34] X. Cui, R. M. Bustin, and G. Dipple, “Selective transport of CO₂, CH₄, and N₂ in coals: insights from modeling of experimental gas adsorption data,” *Fuel*, vol. 83, no. 3, pp. 293–303, 2004.
- [35] C. O. Karacan and G. D. Mitchell, “Behavior and effect of different coal microlithotypes during gas transport for carbon dioxide sequestration into coal seams,” *International Journal of Coal Geology*, vol. 53, no. 4, pp. 201–217, 2003.
- [36] V. Vishal, “Saturation time dependency of liquid and supercritical CO₂ permeability of bituminous coals: implications for carbon storage,” *Fuel*, vol. 192, pp. 201–207, 2017.
- [37] C. M. Xu, X. H. Wang, and F. Y. Guo, “Water locking mechanics characteristics and countermeasures of low permeability gas reservoir,” in *Proceedings of 2013 International Conference on Sport Material, Modelling and Simulation(ICSMMMS 2013)*, pp. 314–318, Information Engineering Research Institute, USA, 2013.
- [38] Z. Feng, D. Zhou, Y. Zhao, and T. Cai, “Study on microstructural changes of coal after methane adsorption,” *Journal of Natural Gas Science and Engineering*, vol. 30, no. 5, pp. 28–37, 2016.
- [39] G. Yin, B. Deng, M. Li et al., “Impact of injection pressure on CO₂-enhanced coalbed methane recovery considering mass transfer between coal fracture and matrix,” *Fuel*, vol. 196, pp. 288–297, 2017.
- [40] D. S. Hou, W. G. Liang, B. N. Zhang, and C. Li, “Seepage law of mixed gases in CO₂ displacement of coal seam CH₄,” *Journal of China Coal Society*, vol. 44, no. 11, pp. 3463–3471, 2019, (in Chinese).

- [41] Q. H. Niu, L. W. Qing, and X. Z. Zhou, "Experimental study of the influences of CO₂ injection on stress-strain and permeability of coal reservoir," *Coal Geology & Exploration*, vol. 46, no. 5, pp. 43–48, 2018.
- [42] C. Shen, B. Lin, C. Sun, Q. Zhang, and Q. Li, "Analysis of the stress-permeability coupling property in water jet slotting coal and its impact on methane drainage," *Journal of Petroleum Science and Engineering*, vol. 126, pp. 231–241, 2015.
- [43] H. Kumar, D. Elsworth, J. Liu, D. Pone, and J. P. Mathews, "Optimizing enhanced coalbed methane recovery for unhindered production and CO₂ injectivity," *International Journal of Greenhouse Gas Control*, vol. 11, pp. 86–97, 2012.
- [44] Z. F. Wang, X. M. Sun, T. K. Lu, and Y. B. Han, "Experiment research on strengthening gas drainage effect with fracturing technique by liquid CO₂ phase transition," *Journal of Henan Polytechnic University(Natural Science Edition)*, vol. 21, no. 1, pp. 1–5, 2015, (in Chinese).
- [45] X. G. Zhang, P. G. Ranjith, M. S. A. Perera, A. S. Ranathunga, and A. Haque, "Gas transportation and enhanced coalbed methane recovery processes in deep coal seams: a review," *Energy & Fuels*, vol. 30, no. 11, pp. 8832–8849, 2016.

Research Article

Numerical Research of Fluid Flow and Solute Transport in Rough Fractures under Different Normal Stress

Min Wang ¹, Qifeng Guo,^{1,2} Pengfei Shan ², Meifeng Cai ¹, Fenhua Ren ¹, and Bing Dai³

¹School of Civil and Resource Engineering, University of Science and Technology Beijing, Beijing 100083, China

²State Key Laboratory of Coal Resources in Western China, Xi'an University of Science and Technology, Xi'an 710054, China

³School of Resource Environment and Safety Engineering, University of South China, Hengyang 421001, China

Correspondence should be addressed to Fenhua Ren; renfh_2001@163.com

Received 19 August 2020; Revised 27 September 2020; Accepted 21 October 2020; Published 25 November 2020

Academic Editor: Qiqing Wang

Copyright © 2020 Min Wang et al. This is an open access article distributed under the Creative Commons Attribution License, which permits unrestricted use, distribution, and reproduction in any medium, provided the original work is properly cited.

The effects of roughness and normal stress on hydraulic properties of fractures are significant during the coupled shear flow test. Knowing the laws of fluid flow and solute transport in fractures is essential to ensure the nature and safety of geological projects. Although many experiments and numerical simulations of coupled shear flow test have been conducted, there is still a lack of research on using the full Navier-Stokes (N-S) equation to solve the real flow characteristics of fluid in three-dimensional rough fractures. The main purpose of this paper is to study the influence of roughness and normal stress on the fluid flow and solute transport through fractures under the constant normal stiffness boundary condition. Based on the corrected successive random addition (SRA) algorithm, fracture surfaces with different roughness expressed by the Hurst coefficient (H) were generated. By applying a shear displacement of 5 mm, the sheared fracture models with normal stresses of 1 MPa, 3 MPa, and 5 MPa were obtained, respectively. The hydraulic characteristics of three-dimensional fractures were analyzed by solving the full N-S equation. The particle tracking method was employed to obtain the breakthrough curves based on the calculated flow field. The numerical method was verified with experimental results. It has been found that, for the same normal stress, the smaller the fracture H value is (i.e., more tough the fracture is), the larger the mechanical aperture is. The ratio of hydraulic aperture to mechanical aperture (e_h/e_m) decreases with the increasing of normal stress. The smaller the H value, the effect of the normal stress on the ratio e_h/e_m is more significant. The variation of transmissivity of fractures with the flow rate exhibits similar manner with that of e_h/e_m . With the normal stress and H value increasing, the mean velocity of particles becomes higher and more particles move to the outlet boundary. The dispersive transport behavior becomes obvious when normal stress is larger.

1. Introduction

In some rock masses with low permeability, fractures are the main channels for fluid flow. The hydraulic characteristics of fractures are of great concern in some rock mechanics and geotechnical applications, such as nuclear waste disposal, geothermal energy mining, and deep mineral mining. The fluid flows through the fractures while the solutes or particles also move with the fluid by the convection and diffusion mechanisms. Understanding the laws of fluid flow and solute migration behavior in fractures is essential to ensure the safety of these geological engineering.

The fracture surface of the natural rock mass is generally rough [1], causing the rock fractures to be composed of void spaces and contact areas, rather than many studies assumed that fractures are composed of two relatively smooth parallel plates. Fluid bypasses the contact area and flows through the void space with tortuosity. The characteristics of void space geometry and the contact area distribution have significant effects on the hydraulic properties of a fracture [1]. It has been demonstrated that the fluid flow and transportation process in a single fracture are heavily influenced by the roughness of the fracture surface, and the mechanical aperture of a rock fracture is usually larger than its hydraulic

aperture [2]. Li et al. [3] implemented a series of coupled shear flow tests to analyze the influence of geometric features of fracture on rock mechanical behavior and proposed the empirical correlations to evaluate the effects of surface roughness and contact area on the behavior of fluid flow through rough fractures. Zou et al. [4] investigated the effects of wall surface roughness on fluid flow through fractures; the result indicated that the flow rate and the roughness of the fracture surface are the main reasons for the dynamic evolution of the vortex area in the flow field; when the flow rate is high, the fluid flow field is usually not only nonlinear but also constantly produces eddies in the boundary layer region of the rough fracture which will affect the solute transportation in fractured rock masses. Wang et al. [5] adopted 3D lattice Boltzmann method and combined wavelet analysis technique to investigate the impact of surface roughness on the nonlinear fluid flow 3D rock fractures. The result shows that the primary roughness mostly controls the pressure distribution and fracture flow paths at a large scale, whereas the secondary roughness determines the nonlinear properties of the fluid flow at a local scale.

For a single rock fracture, the roughness of the upper and the lower surfaces is the same under the initial conditions, and then, the deformation occurs with the normal stress and shear stress applied to the natural rock [6–8]. In order to study the effect of shear on fluid flow in fractures, some scholars have carried out a series of experimental and numerical simulation research on coupled shear flow. The laboratory research on the shear behavior of fractures is usually implemented under the condition of constant normal stress (CNL). However, for many field situations, the normal stress imposing on the fracture surface will change during the shearing process. The expansion of fractures is usually constrained by the closed environment which is represented by the constant normal stiffness (CNS) [9]. Therefore, it is necessary to study the shear characteristics of the fractures under the boundary condition of constant normal stiffness. Indraratna et al. [9] studied the effect of initial normal stress levels on shear behavior of joints under CNS conditions. The result revealed that the initial normal stress has significant effect on the shear dilation rate. Different initial normal stresses will lead to the variety of the distribution of voids and contact areas in the fractures under shear.

In rock mechanics and rock engineering practices, the fractures are usually simplified to two parallel plates in which the fluid flow follows the cubic law. However, the parallel models are inadequate to describe the hydraulic and transport properties of natural fractures with rough surfaces [10]. To further take into account the geometrical characteristics of fractures, the simplified forms of the full Navier-Stokes equations, such as the Reynolds equation [11–17] and the Stokes equations [18, 19], were used in the estimation of hydromechanical properties of rock fracture. The flow rate and Reynolds number in natural rock fracture are not always small, and the inertial effects usually increase with the complexity of void space geometry; therefore, the nonlinear term is not always negligible [4, 20–25]. Without considering the influence of inertia effects, the simplified form usually shows deviation from the actual situation. In order to accurately

describe the fluid flow in the fractures, numerical simulation by solving the full N-S equations should be adopted, especially for rough natural fracture.

Many coupled shear flow experiments have been carried out. These studies mainly focused on using the simplified N-S equation to describe the fluid flow in a two-dimensional fracture. And there is still a lack of research on using the full N-S equation to solve the real flow characteristics of fluid in three-dimensional fractures. It should be noted that most of published research considered only simplified fracture surface topography or specific boundary conditions (e.g., constant normal stress boundary). A comprehensive study of the impact of normal stress and roughness on fluid flow and particle transport under the constant normal stiffness boundary condition was rarely presented in existing publication. In this study, several 3D fracture surfaces with different roughness coefficients were obtained at first. The fracture used for numerical simulation was composed of two fracture surfaces with the same roughness and the initial aperture was zero. A series of shear tests under the constant normal stiffness with different normal stress were then employed. Finally, a number of numerical simulations by solving the full 3D Navier-Stokes equations were adopted to investigate the fluid flow behavior and solute transportation through fractures.

2. Geometry Model of 3D Rough Fractures

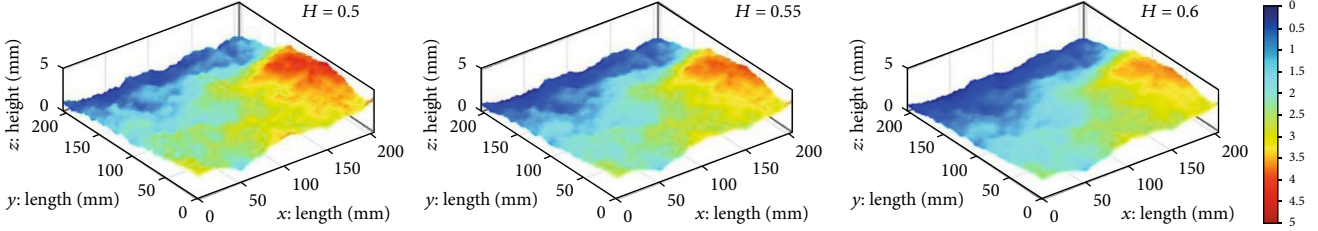
2.1. 3D Self-Affine Fracture Surface. The natural rough rock fracture surface typically follows a self-affine fractal distribution [26–28], and the topography of a fracture surface can be characterized by fractional Brownian motion (fBm) [29]. Several methods such as the Fourier transformation, the randomized Weierstrass-Mandelbrot function, and the successive-random addition (SRA) were widely used to model the fBm [30–33]. In this study, the efficient SRA algorithm, which is easy to understand and use, is adopted to generate rough fracture surface.

In fBm, the surface asperity height is defined as a random and single-valued function $z(x, y)$ of two independent spatial variables, x and y . The stationary increments, $z(x + h_x, y + h_y) - z(x, y)$, over the distance (lag) h displays a Gaussian distribution with zero mean and variance σ^2 [5, 34]. The statistical self-affinity of fBm can be expressed as follows:

$$\begin{aligned} \langle z(x + h_x, y + h_y) - z(x, y) \rangle &= 0, \\ \sigma(h)^2 &= h^{2H} \cdot \sigma(1)^2, \end{aligned} \quad (1)$$

where $\langle \cdot \rangle$ represents the mathematical expectation, and H is the roughness exponent or Hurst exponent varying from 0 to 1 and related to the 3D fractal dimension (D_f) by $D_f = 3 - H$.

Liu et al. developed a corrected SRA algorithm to generate the 3D self-affine fracture surfaces which overcomes the problems associated in the traditional SRA algorithms that provide stochastic fractal distributions of questionable scaling and correlation properties [30, 35]. In this study, a series of rock fracture surfaces, with $H = 0.5, 0.55,$ and 0.6 (the

FIGURE 1: Generated self-affine fracture surfaces with $H = 0.5, 0.55,$ and 0.6 .

corresponding joint roughness coefficient (JRC) was calculated using Equation (2) [36] and the values are 18.2940, 12.3983, and 6.5396, respectively, were generated by employing Liu's algorithm. These surfaces are both 204.8 mm in length and width. As shown in Figure 1, the fracture surface asperity becomes flatter with the increase of H .

$$\text{JRC} = 32.2 + 32.47 \log Z_2, \quad (2)$$

$$Z_2 = \left[\frac{1}{M(\Delta x)^2} \sum_{i=1}^M (z_{i+1} - z_i)^2 \right]^{1/2}, \quad (3)$$

where M is the number of intervals, Δx is the interval, and z_i is the height of surface.

2.2. Aperture Distribution of Fractures under Different Normal Stress. A lot of research revealed that the aperture which is defined as the distance between the two fracture surfaces has a significant influence on the hydromechanical characteristics of the rock fractures [37–41]. In this study, it is assumed that the two fracture surfaces are in contact with each other at the initial condition. The aperture between the surfaces was assigned zero. When shearing occurs, the fracture surfaces separated in the horizontal and vertical directions. Under a specific shear displacement, the aperture distribution can be calculated by the following formula [37]:

$$b(x, y) = \begin{cases} z(x + u_s, y) - z(x, y) + u_n, & \text{for } (z(x + u_s, y) - z(x, y) + u_n > 0), \\ 0, & \text{for } (z(x + u_s, y) - z(x, y) + u_n \leq 0). \end{cases} \quad (4)$$

In the above, $z(x, y)$ is the asperity height of the generated 3D self-affine fracture surfaces, u_s is the shear displacement, and u_n is the normal displacement or dilation caused by the shear displacement.

Research on the fracture shear behavior in the laboratory was usually carried out under constant normal stress boundary conditions, where the normal stress always remains constant and the rock joint dilates freely during shearing [9]. However, some researchers have pointed out that the joint dilation may be constrained by a restricted environment, which usually represents a constant normal stiffness condition (CNS) in engineering practice and the CNS boundary conditions are more applicable to many areas [9, 42–45]. In this study, the following analytical model of dilation and

TABLE 1: Related parameters for numerical simulation.

Parameters	Value
Hurst exponent	0.5; 0.55; 0.6
Shear displacement (mm)	5
σ_{n0} (MPa)	1; 3; 5
c_0	0.3
c_1	0.3
c_2	1.2

shear displacement under CNS conditions proposed by Indraratna et al. [9] was used to calculate the dilation caused by shear displacement.

$$\delta_v = \int_0^{\delta_h} (\dot{v}) d\delta_h, \quad (5)$$

where δ_h is the shear displacement and v^* is the dilation rate that change with the ratio of shear displacement to peak shear displacement ($\delta_h/\delta_{h\text{-peak}}$) for a fracture subjected to shear under CNS boundary condition.

The value of dilation rate can be calculated by the following equation.

$$\dot{v} = \begin{cases} 0, & \text{for } 0 < \left(\frac{\delta_h}{\delta_{h\text{-peak}}} \right) \leq c_0, \\ \dot{v}_{\text{peak}} \left(1 - \frac{1}{(c_0 - 1)^2} \left(\frac{\delta_h}{\delta_{h\text{-peak}}} - 1 \right)^2 \right), & \text{for } c_0 < \left(\frac{\delta_h}{\delta_{h\text{-peak}}} \right) \leq 1, \\ \dot{v}_{\text{peak}} \exp \left(- \left(c_1 \left(\frac{\delta_h}{\delta_{h\text{-peak}}} - 1 \right) \right)^{c_2} \right), & \text{for } \left(\frac{\delta_h}{\delta_{h\text{-peak}}} \right) > c_0. \end{cases} \quad (6)$$

Here, c_1 and c_2 are decay constants which can be calculated from experimental data. $\delta_{h\text{-peak}}$ is peak shear displacement. The value of c_0 at which the dilation rate is assumed to begin is about 0.3 for rough fracture [14, 46]. \dot{v}_{peak} is the peak dilation rate and can be obtained from the following equation.

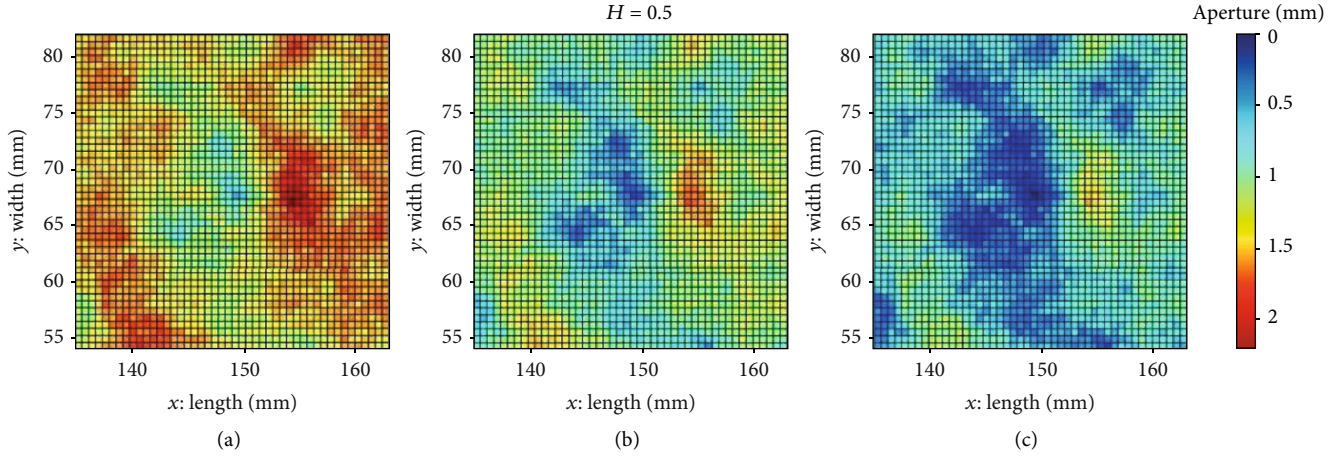


FIGURE 2: Aperture distribution with $H = 0.5$: (a) σ_{n0} is 1 MPa, (b) σ_{n0} is 3 MPa, and (c) σ_{n0} is 5 MPa.

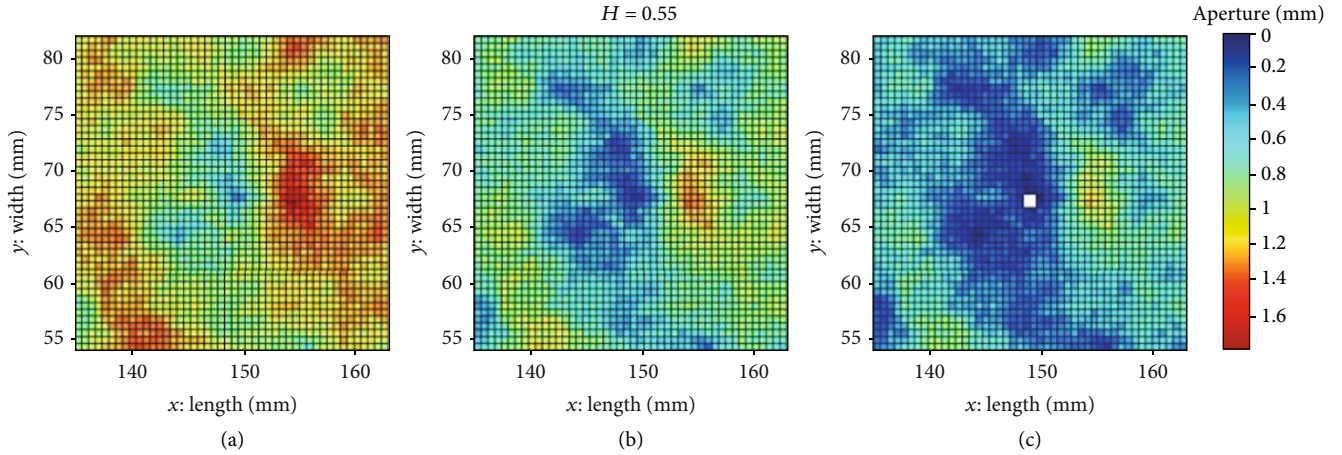


FIGURE 3: Aperture distribution with $H = 0.55$: (a) σ_{n0} is 1 MPa, (b) the σ_{n0} is 3 MPa, and (c) σ_{n0} is 5 MPa.

$$\begin{aligned}
 \dot{v}_{\text{peak}} &= \left(\frac{\tan \beta}{1 - (K_n (-\alpha \sec^2 \beta + \lambda))} \right), \\
 \alpha &= \frac{\delta_{h\text{-peak}} \times \text{JRC} \times \pi}{M \times \ln 10 \times \sigma_{n0} \times 180}, \\
 \beta &= \frac{1}{M} \times \text{JRC} \times \log_{10} \left(\frac{\text{JCS}}{\sigma_{n0}} \right), \\
 \lambda &= \frac{k_{ni} \times V_m^2}{(k_{ni} \times V_m + \sigma_{n0})^2}.
 \end{aligned} \tag{7}$$

In the above, JRC is the joint roughness coefficient, JCS is the compressive strength of the joint surface, M is the damage coefficient that is given a value of 1 or 2 under low normal stress or high normal stress, K_n is the CNS at an external boundary, σ_{n0} is the initial normal stress, k_{ni} is the initial joint normal stiffness at zero normal stress level, and V_m is the maximum closure of the joint. Related parameters which are used in numerical simulation are listed in Table 1.

Either the joint roughness coefficient or the normal stress can significantly affect the aperture distribution under the

shearing. Limited by the challenging computational capacity of solving the N-S equations for the 3D roughness fractures with high precision, only a square area with a side length of 27.6 mm on the surface which is in a certain range of $x = [135, 162.6]$ mm and $y = [54, 81.6]$ mm was cut out to form the 3D models. Fractures exhibit poor connectivity, and no obvious fluid flow can be observed with small shear displacement. Finally, 5 mm was selected as the shear displacement, with which some of the main flow channel formed and the contact area was more concentrated. Figures 2–4 show the aperture distribution of different roughness fractures with the shear displacement of 5 mm under different normal stress.

3. Fluid Flow and Solute Transport Simulation

3.1. Fluid Flow Simulation

3.1.1. Governing Equation. The governing equation for a single fluid flow in a fracture is Navier-Stokes equations, which are derived from Newton's second law and are strict statements of the momentum conservation. For the steady-state

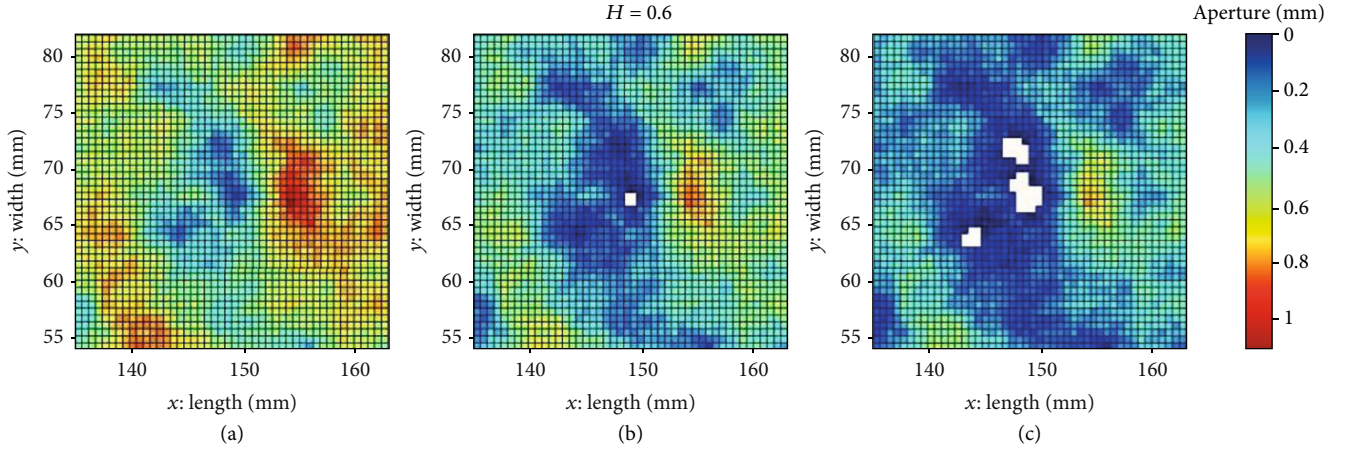


FIGURE 4: Aperture distribution with $H = 0.6$: (a) σ_{n0} is 1 MPa, (b) σ_{n0} is 3 MPa, and (c) σ_{n0} is 5 MPa.

and incompressible single Newtonian fluid, the Navier-Stokes equation can be expressed in a vector form as follows:

$$\begin{aligned} \nabla \cdot \mathbf{u} &= 0, \\ (\mathbf{u} \cdot \nabla) \mathbf{u} &= \nu \nabla^2 \mathbf{u} - \frac{1}{\rho} \nabla p + \mathbf{f}, \end{aligned} \quad (8)$$

where \mathbf{u} is the flow velocity which contains three velocity components in 3D rock fracture, ν is the kinematic viscosity of fluid defined as $\nu = \mu/\rho$, ρ is the fluid density, p is the pressure, and \mathbf{f} represents the body forces acting on the fluid.

The N-S equations are a set of nonlinear partial differential equations coupled with velocity and pressure fields [20]. The left of the N-S equations contains a nonlinear convection acceleration term, and the right has a viscous diffusion term, so the governing equation of viscous fluid is a nonlinear convection diffusion equation. It is difficult to use theoretical methods to obtain accurate solutions for complex three-dimensional flows, except for a few simple fluid flows which can obtain analytical solutions. In this study, the commercial FEM software of COMSOL Multiphysics was employed to simulate the fluid flow through the roughness fractures under the shearing. The density and viscosity of water at 10°C were taken as $\rho = 0.9997 \times 10^3 \text{ kg/m}^3$ and $\mu = 1.307 \times 10^{-3} \text{ Pa s}$.

3.1.2. Boundary Conditions. In this study, the y axis direction was selected as the main fluid flow direction. The two boundaries at $y = 0 \text{ mm}$ and $y = 27.6 \text{ mm}$ were set as the inlet boundary and outlet boundary. The combination of flow rate and pressure boundary conditions was used. Four laminar entrance inflow conditions with different constant flow rates were adopted at the inlet boundary to investigate the effect of inlet flow condition on the hydromechanical properties of rough fractures and the solute transport in fractures. At the same time, set the pressure at the outlet boundary to zero. The remaining upper, lower, and the two side boundaries were set to no flow and no slip, where the fluid velocity relative to the walls' velocity is zero. Such boundary conditions are consistent with many laboratories' experiment conditions [20].

3.2. Solute Transport Simulation. The particle tracking approach was adopted to simulate solute transport based on the flow result obtained from steady-state flow field. In this study, only advection process was considered, and the particles were driven by the fluid and transported along the fluid flow path. The random dispersion due to diffusion of the solute particles within the fluid in fractures and other retardation mechanisms such as sorption or decay were not taken into account [17]. The particle tracking method in the fluid was used to compute the motion of particles in a background fluid. The particle momentum comes from Newton's second law, which states that the net force on a particle is equal to its time rate of change of its linear momentum in an inertial reference frame. The particles in the fluid are driven by drag force and its momentum can be described as follows:

$$\begin{aligned} \frac{d}{dt} (m_p \mathbf{v}) &= \mathbf{F}_D, \\ \mathbf{F}_D &= \left(\frac{1}{\tau_p} \right) m_p (\mathbf{u} - \mathbf{v}). \end{aligned} \quad (9)$$

Here, m_p is the particle mass, τ_p is the particle velocity response time, \mathbf{v} is the velocity of the particle, \mathbf{u} is the fluid velocity, and \mathbf{F}_D is the drag force.

Once the flow velocity was calculated element by element by solving the N-S equation, all the particles travel following the streamlines. Particles were initially placed at one edge of a FEM element. They follow the velocity of each element. The travel time in each element was given by magnitude of the velocity of the element as follows [47]:

$$\Delta t_j^i = \frac{|\mathbf{x}_j^{i+1} - \mathbf{x}_j^i|}{|\mathbf{v}|}. \quad (10)$$

In the above, Δt_j^i is the travel time of particle j in tracking step i , $|\mathbf{x}_j^{i+1} - \mathbf{x}_j^i|$ is the travel distance of particle j inside the element corresponding to the tracking step i , and $|\mathbf{v}|$ is the

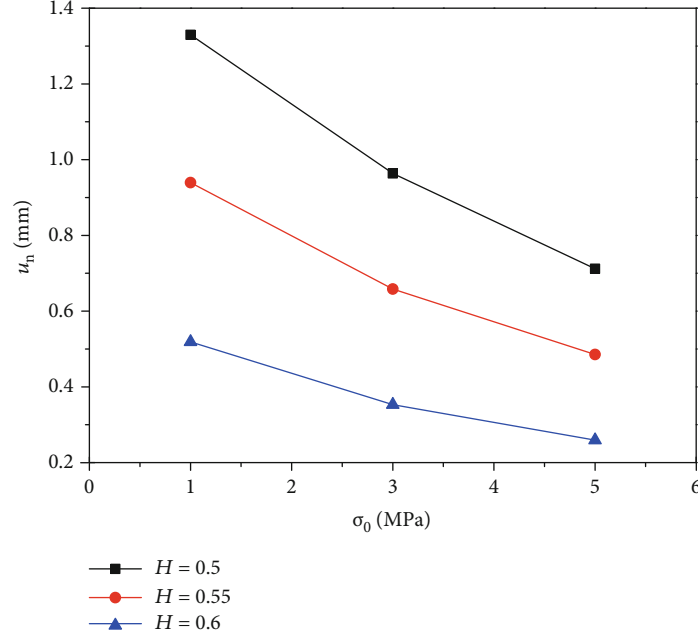


FIGURE 5: The normal displacement (u_n) varies with normal stress (σ_0).

magnitude of the velocity vector of the element corresponding to the tracking step i .

The total residence time for a particle j is the sum of the time of all the elements that the particle is passing through.

$$t_j = \sum_{i=1}^m \Delta t_j^i, \quad (11)$$

where t_j is the total travel time of particle j , and m is the number of tracking step for particle j .

The number of particles injected at each position along the entrance of the fracture is proportional to the velocity. This means that more particles will be attracted to places with higher flow velocity. From the particle tracking simulation, the breakthrough curve that represents the relationship between the percentage of particles collected at the outlet boundary and time can be obtained using the tracking time of each particle. The Peclet number can be defined in terms of the variance and mean travel time using the following equation [48].

$$Pe = 2 \left(\frac{\bar{t}}{\sigma_t} \right)^2, \quad (12)$$

where σ_t^2 and \bar{t} are the variance and mean travel time, respectively.

4. Result and Analysis

Three self-affine fracture surfaces were generated with $H = 0.5$, 0.55 , and 0.6 , respectively. The fracture models were composed of two fracture surfaces with the same roughness coefficient at the initial state. For fracture models with different H , a shear displacement equaling to 5 mm was used and

TABLE 2: Statistical parameters of local mechanical aperture.

σ_{n0} (MPa)	Mean aperture (mm)	Standard deviation (mm)
$H = 0.5$		
1	1.4092	0.202
3	1.0432	0.202
5	0.7917	0.202
$H = 0.55$		
1	1.0138	0.161
3	0.733	0.161
5	0.5600	0.161
$H = 0.6$		
1	0.5887	0.1283
3	0.423	0.1283
5	0.3297	0.1283

three normal stress that equal to 1 MPa, 3 MPa, and 5 MPa were loaded on the models with CNS boundary in the shear simulation. For each model, the normal displacement was calculated using the Equation (4). The final void distribution of each model was different due to the application of different normal stresses. Four flow rates that equal to 1.443×10^{-8} m³/s, 1.443×10^{-7} m³/s, 1.443×10^{-6} m³/s, and 1.443×10^{-5} m³/s were adopted at the inlet boundary. The corresponding Reynolds (Re) numbers are 0.4, 4, 40, and 400 which exist in ground flow in rock engineering, hydraulic engineering, and laboratory experiments [20].

4.1. Characteristics of Aperture Distribution. Distribution characteristics of aperture have an important influence on the simulation of fluid flow in fractures. The evolution of fracture aperture can be calculated with the values of asperity

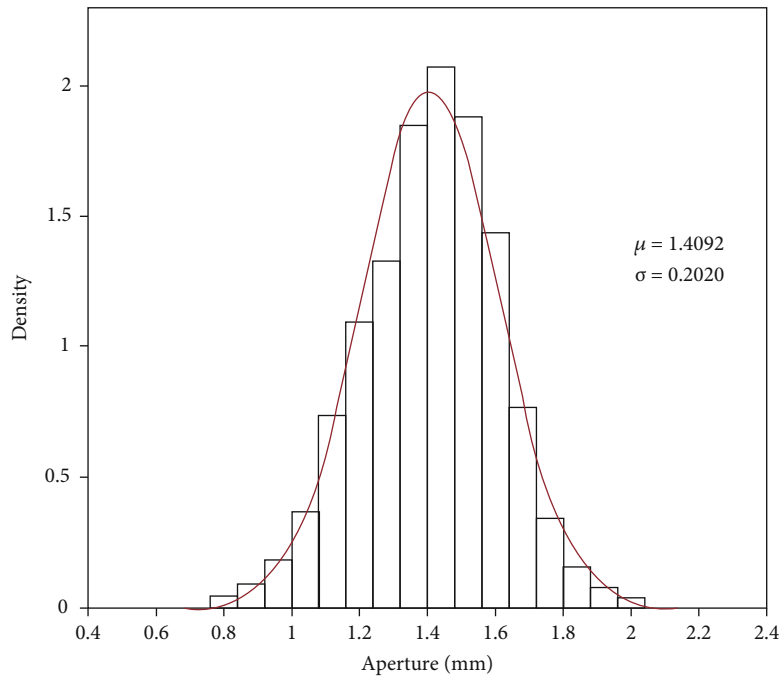


FIGURE 6: Aperture density distribution.

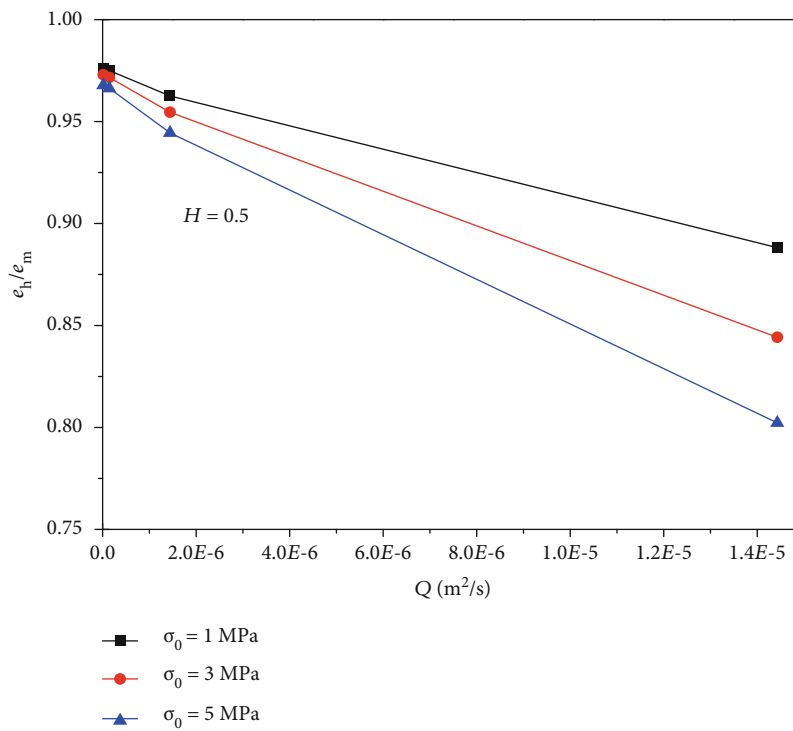


FIGURE 7: e_n/e_m varies with flow rate with $H = 0.5$.

height and the normal displacement during shear. Figure 5 shows the relationship of the variations of normal displacement and the normal stress for fractures with different roughness coefficients. Both roughness and normal stress can significantly affect the normal displacement. For all fracture models, the normal displacement (u_n) generally decreased as the normal stress (σ_0) increased. At the same

time, as the magnitude of H increased, the normal displacement (u_n) became smaller. In other words, the rougher the fracture surface was, the greater the normal displacement (u_n) could be obtained under the same normal stress during the shear. This can be attributed to the fact that the peak dilation rate decreases with an increasing normal stress but increases with the increasing JRC which represent the

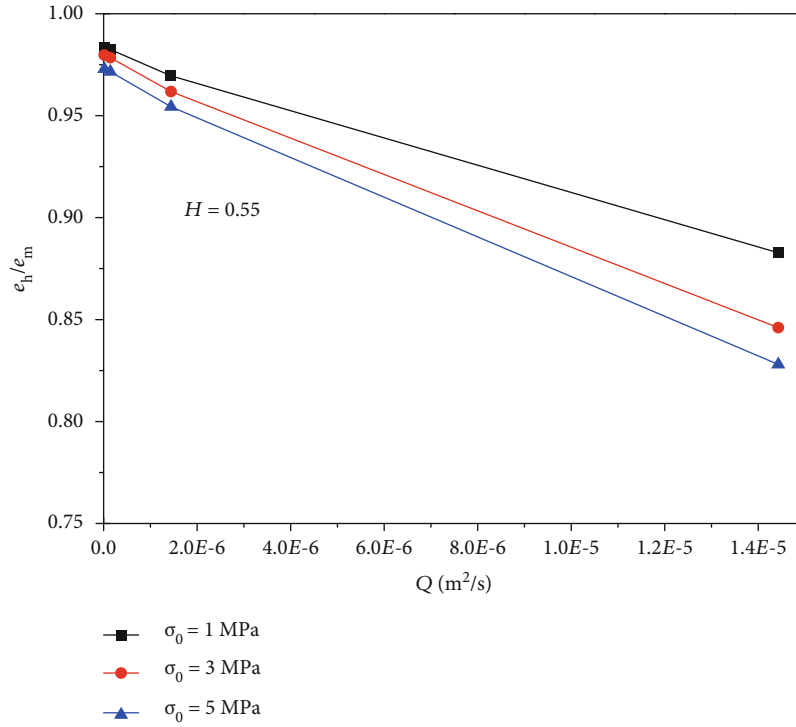


FIGURE 8: e_h/e_m varies with flow rate with $H = 0.55$.

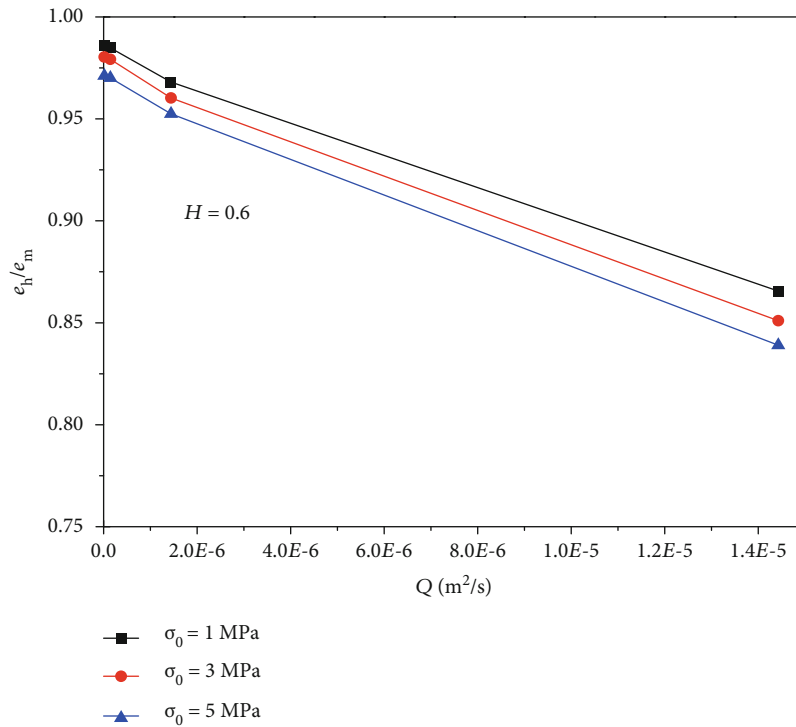


FIGURE 9: e_h/e_m varies with flow rate with $H = 0.6$.

roughness coefficient of surface. The larger the JRC value is, the rougher the surfaces are [9]. Many studies have shown that the aperture of fractures usually obeys a normal distribution [20, 49]. According to the obtained apertures, Gaussian

fitting was performed on the aperture of each fracture model. Some statistical parameters (the mean aperture and the standard deviation) of local mechanical aperture under different normal stress with different H are listed in Table 2. Figure 6

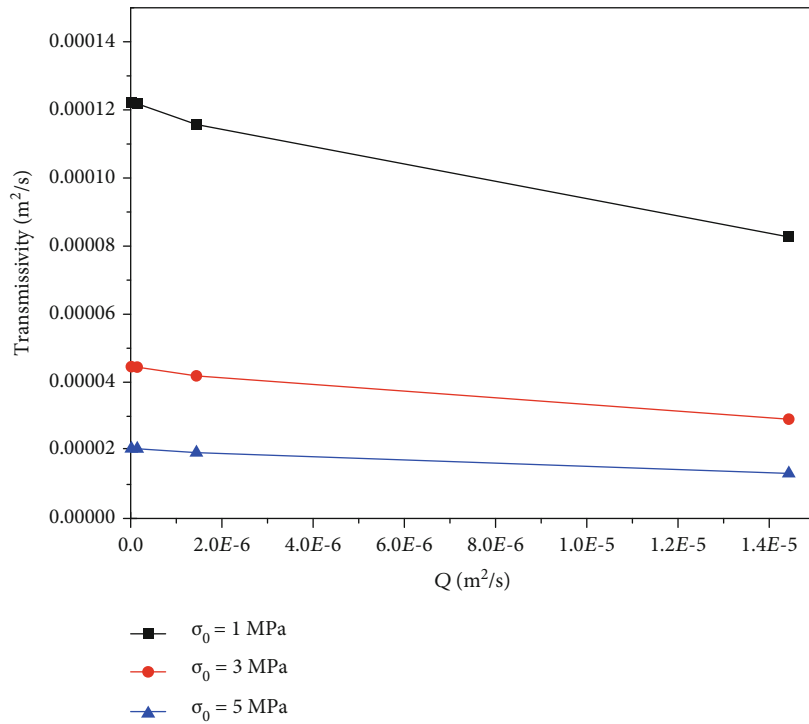


FIGURE 10: Transmissivity varies with flow rate with $H = 0.6$.

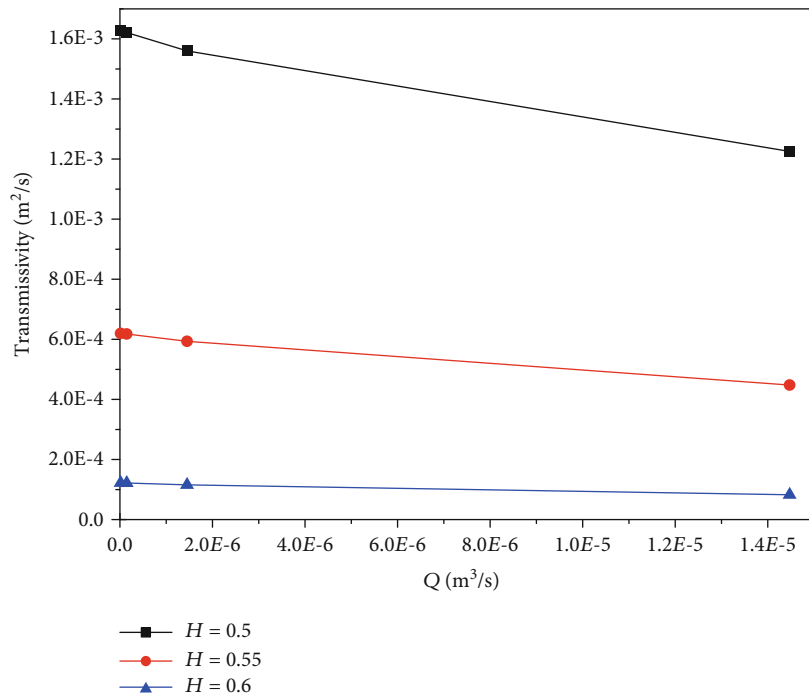


FIGURE 11: Transmissivity varies with flow rate with $\sigma_0 = 1$ MPa.

is the aperture density distribution of fracture under normal stress 1 MPa with H value equaling to 0.5. Both mean value and its standard deviation are decreased with the increment of normal stress and increased with the roughness.

Figures 2–4 show the spatial distribution of fracture aperture. The local apertures were discretely distributed in space,

but showed good connectivity. For a fracture with higher roughness at a lower normal stress, there was no contact area between opposite fracture surfaces. In contrast, some contact areas (small white squares representing zero aperture) were appeared gradually with lower roughness at a higher normal stress. Small aperture zones were shown around the

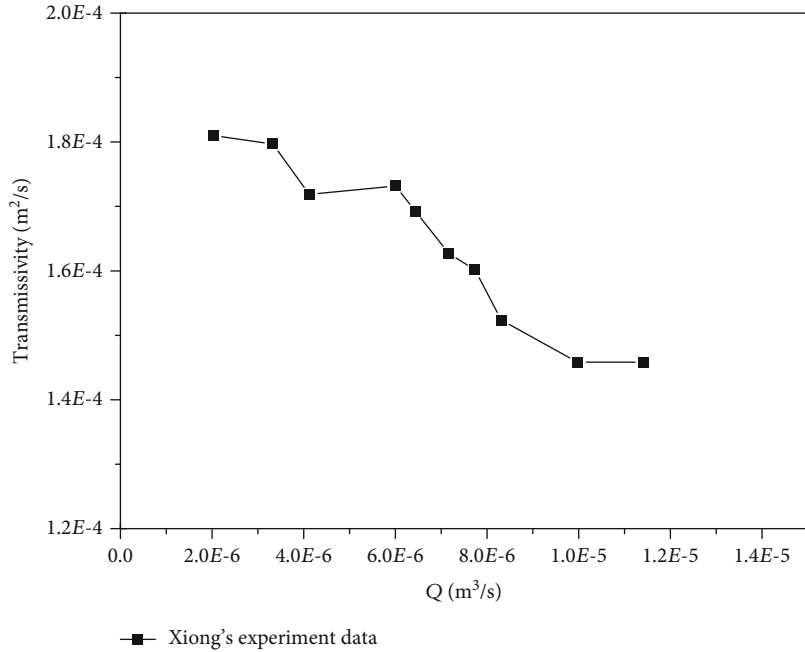


FIGURE 12: Transmissivity varies with flow rate with Xiong's experiment data [1].

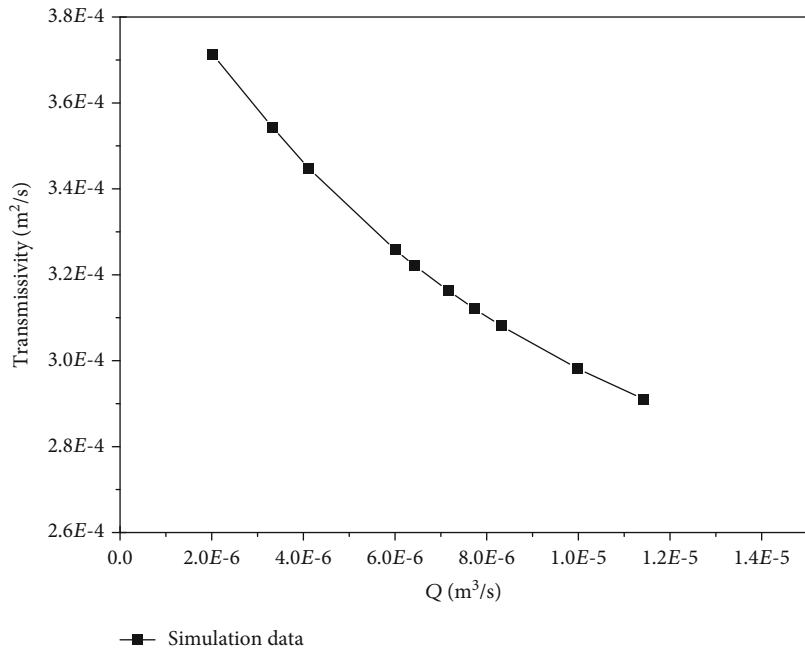
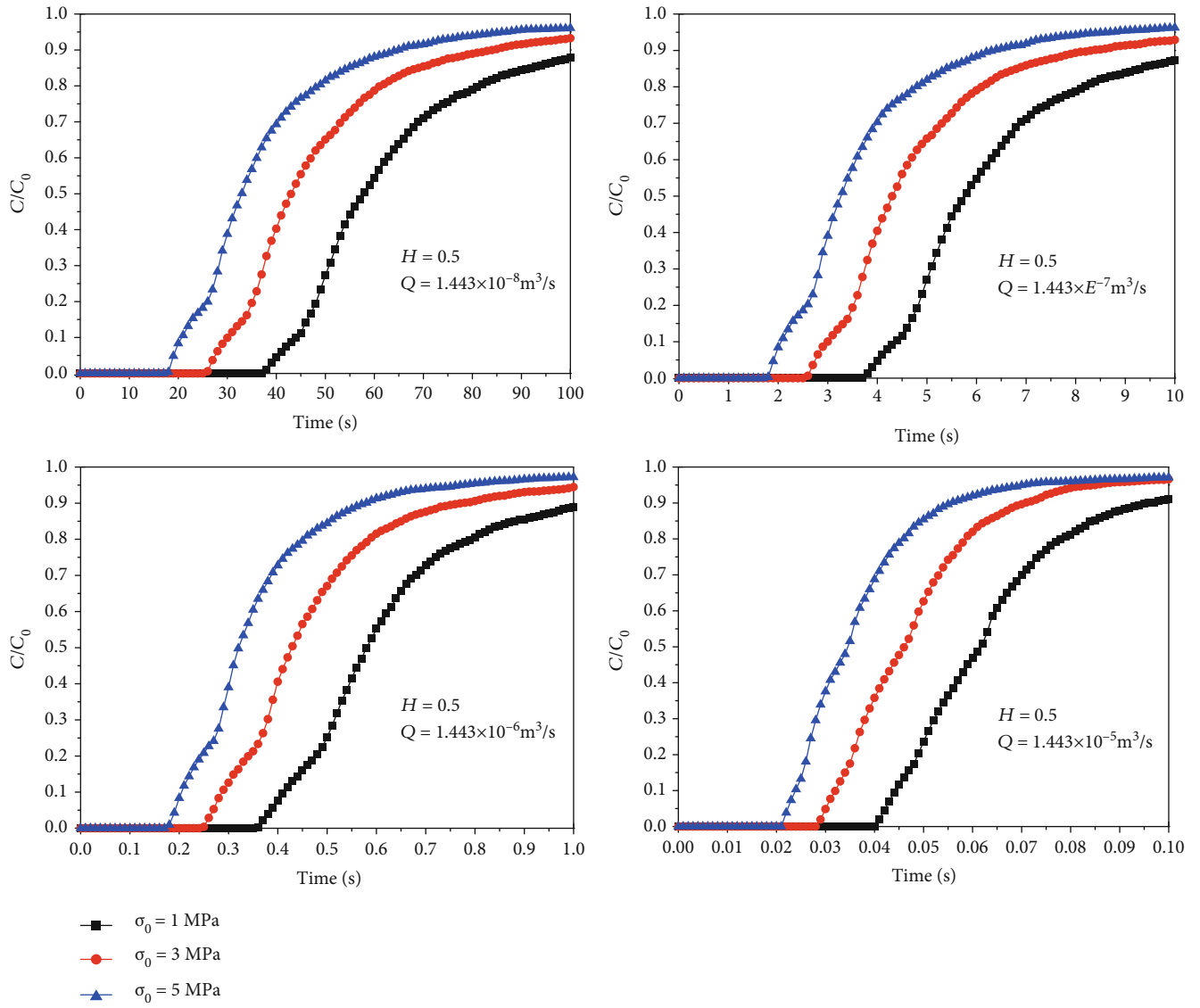


FIGURE 13: Transmissivity varies with flow rate with simulation data.

contacting area and fluid flow through the main channel with higher aperture.

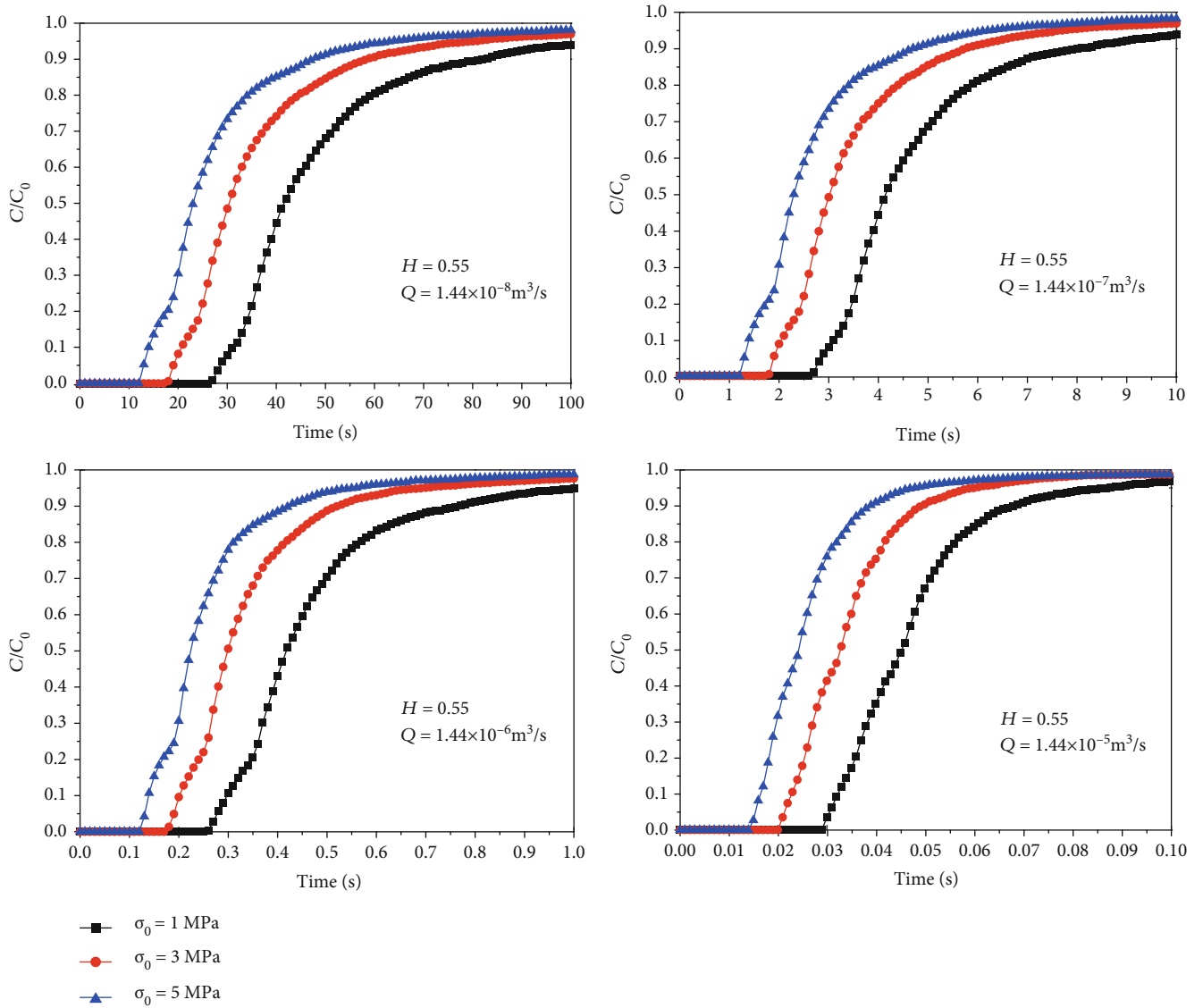
4.2. Hydraulic Characteristics of the Fracture. Generally, the calculated hydraulic aperture was lower than the mean mechanical aperture due to the existence of contact areas within the fractures and the tortuosity of streamlines. The complexity of the void geometry decreased as the shear displacement increased.

At the same time, more flow channels emerged accompanied with the decrease of contact ratio. When the shear displacement became larger, the void geometry became more like parallel plates model with large mechanical aperture. While choosing 5 mm as the shear displacement, the calculated ratio of hydraulic aperture to mechanical aperture is basically from 0.8 to 0.975 during the shear of both three fractures (Figures 7–9). As shown in



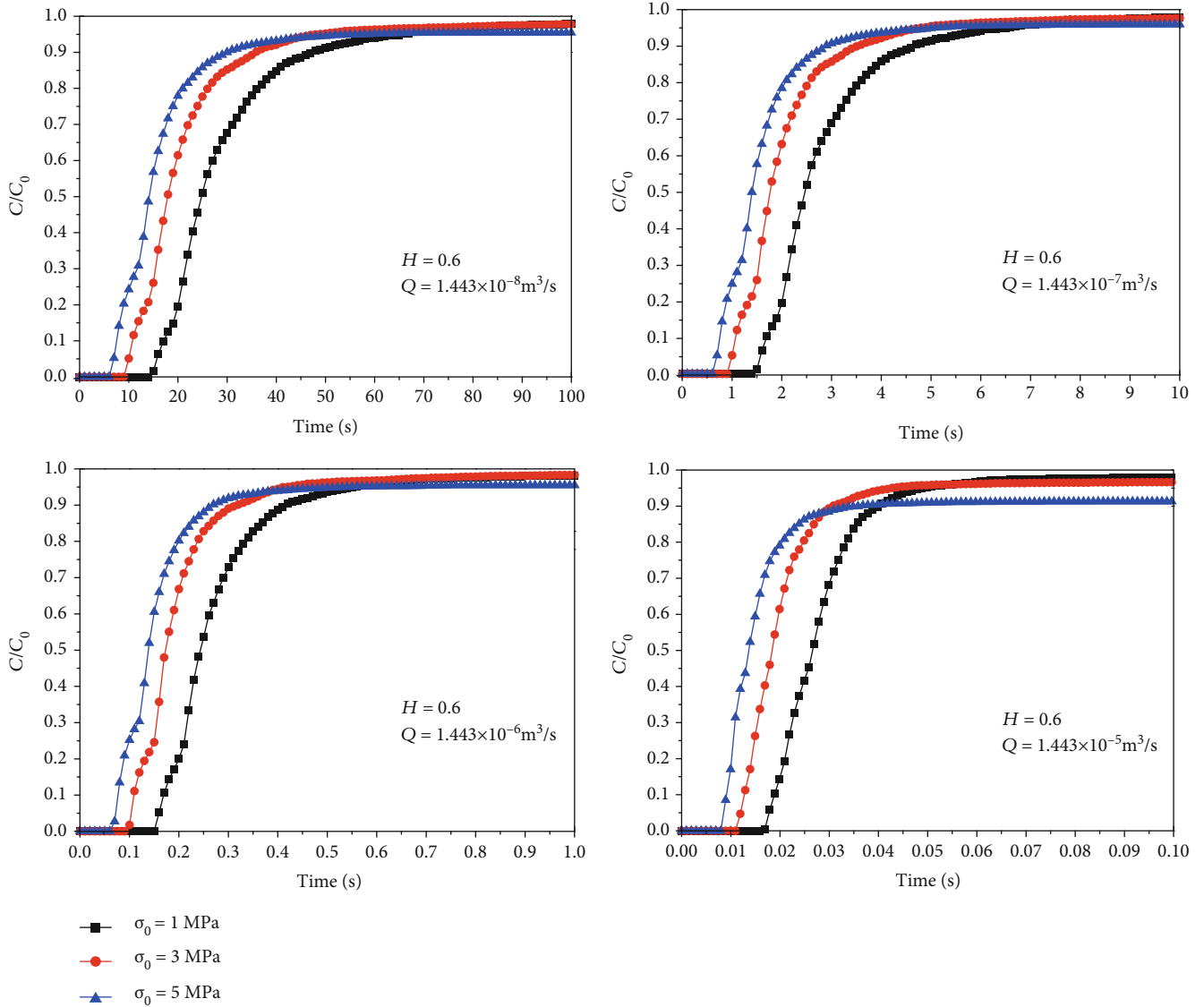
(a)

FIGURE 14: Continued.



(b)

FIGURE 14: Continued.



(c)

FIGURE 14: Breakthrough curves for different fracture models with different roughness coefficients: (a) $H = 0.5$, (b) $H = 0.55$, and (c) $H = 0.6$.

Figure 7, the rougher fracture with H equaling to 0.5 exhibits larger decrease comparing to other fractures with lower H value since the rougher fracture could produce more complex void geometries during the shearing. Lower normal stress produces larger shear dilation and results in larger local aperture. It can be seen from Figure 7 that the value of e_h/e_m decreases with the increment of σ_0 .

The variation of transmissivity of fractures with the flow rate exhibited similar manner with that of e_h/e_m , since the transmissivity is proportional to e_h^3 . Figure 10 elucidates the relationship of transmissivity and flow rates with $H = 0.6$ under different normal stress. It can be observed that the measured transmissivities under larger normal stress have smaller values and decrease with the flow rates, which indicates that transmissivity not only changes significantly with the increasing of flow rates but also affected by the

normal stress. Figure 11 shows the relationship of transmissivity and flow rates with $\sigma_0 = 1$ MPa.

Experiment data from Xiong et al. [1] were used to verify the proposed numerical method. Various flow rates from Xiong's experiment were imposed on the inlet boundary of fracture with H value 0.6. The normal stress was set as 1.5 MPa and the shear displacement adopted was 8 mm according to Xiong's experiments. Due to lack of original experimental data on the fracture geometry, the fracture was randomly generated with JRC 6.5. Figures 12 and 13 show the results from experiments and simulations, respectively. It could be seen that the simulation results show the same trend with the experimental data and the values of transmissivity are close. The difference between experimental and simulation values is very likely caused by the difference of fracture geometry in the simulations and the experiments.

TABLE 3: The mean and standard deviations of particle travel time.

H value	σ_0 (MPa)	Mean (s)	Standard deviation (s)
$Q = 1.443 \times 10^{-8} \text{ m}^3/\text{s}$			
0.5	1	55.9300	10.3600
	3	41.5710	8.87400
	5	31.4200	7.68000
0.55	1	40.6900	7.93000
	3	29.2800	6.39100
	5	22.0400	5.54000
0.6	1	24.1600	5.32900
	3	17.1700	4.31500
	5	13.2300	3.92100
$Q = 1.443 \times 10^{-7} \text{ m}^3/\text{s}$			
0.5	1	5.60400	1.05300
	3	4.14900	0.88120
	5	3.11600	0.74460
0.55	1	4.06900	0.79010
	3	2.91900	0.63700
	5	2.20000	0.55360
0.6	1	2.41100	0.52870
	3	1.68600	0.40910
	5	1.31900	0.39110
$Q = 1.443 \times 10^{-6} \text{ m}^3/\text{s}$			
0.5	1	0.55380	0.10366
	3	0.40990	0.08748
	5	0.30460	0.06889
0.55	1	0.40350	0.07723
	3	0.28810	0.06015
	5	0.21390	0.04990
0.6	1	0.23520	0.04545
	3	0.16750	0.03753
	5	0.12980	0.03602
$Q = 1.443 \times 10^{-5} \text{ m}^3/\text{s}$			
0.5	1	0.05757	0.01007
	3	0.04300	0.00843
	5	0.03228	0.00665
0.55	1	0.04227	0.00735
	3	0.03071	0.00593
	5	0.02264	0.00467
0.6	1	0.02536	0.00462
	3	0.01769	0.00352
	5	0.01316	0.00304

4.3. Solute Transport Simulation. In the previous section, flow velocity fields were calculated by using the N-S equation. Particles transported following different velocity trajectories with different numbers. The effects of flow velocity through the fractures on the particle movement characteristics were investigated in this section.

According to the simulation results of particle tracking, the breakthrough curves were obtained. As shown in

Figure 14, the breakthrough curves shift to the left without changing their shape when normal stress becomes larger. The mean velocity of particles becomes higher, and more particles move faster to the outlet boundary with larger normal stress. When $H = 0.6$, a long tail appears on the breakthrough curve and the number of particles finally reaching the outlet decreases with the increment of normal stress, which can be explained by the occurrence of contact areas. For the fracture with $H = 0.6$, the contact areas gradually appear with the increment of normal stress, which leads to the preferential flow field. Particles travel through the preferential flow. Such preferential transport behavior will result in earlier arrival of particles through the high-velocity zone in fracture, but heavy tailings of particles spread in the low-velocity zones around the contact areas [50]. The very low transmissivity region increases with the normal stress and more particles get trapped in this zone. With increasing roughness, the inclination of the breakthrough curves becomes larger. The preferential flow phenomenon becomes more obvious with larger H value and particles travel through the channels with higher velocity.

The mean and standard deviations of particle travel time were calculated using results obtained by solving the N-S equation at the identical percentage of particle collection at the outlet (Table 3). Using the statistical parameters of travel time, the Pelect numbers (Pe) for characterizing the dispersion of the transport can be obtained by Equation (12). The relationship between Pe and normal stress presents the similar evolution trend under different flow rates. Figure 15 shows that the Pe numbers decrease with increasing normal stress and H value. In other words, the dispersion (α) increases with increasing normal stress and H value, since Pelect number (Pe) has an inverse relationship with dispersion ($Pe = L/\alpha$, where L is the fracture length). One interpretation for this behavior may be that the preferential flow channels gradually appeared with the increasing normal stress and H value. The formation of preferential flow results in more discretization velocity field and finally causes the dispersive transport behavior of particles.

5. Conclusion

In this paper, several 3D self-affine fracture surfaces were generated at first by using the SRA method and then the effects of surface roughness and normal stress on fluid flow and solute transport in fractures were investigated through a series of coupled shear flow simulation. The fluid flow was simulated by solving the N-S equations, and the solute transport was simulated by the particle tracking method with the fluid velocity fields predicted by solving the N-S equations. The results revealed that the roughness and the normal stress may have significant influence on the fluid flow field and the residence time of particle, which is an important issue that needs to be considered in the safety assessment of radioactive waste repositories in fractured crystalline rocks.

Roughness may affect the tortuous degree of flow channel and make a sudden change of local mechanical aperture

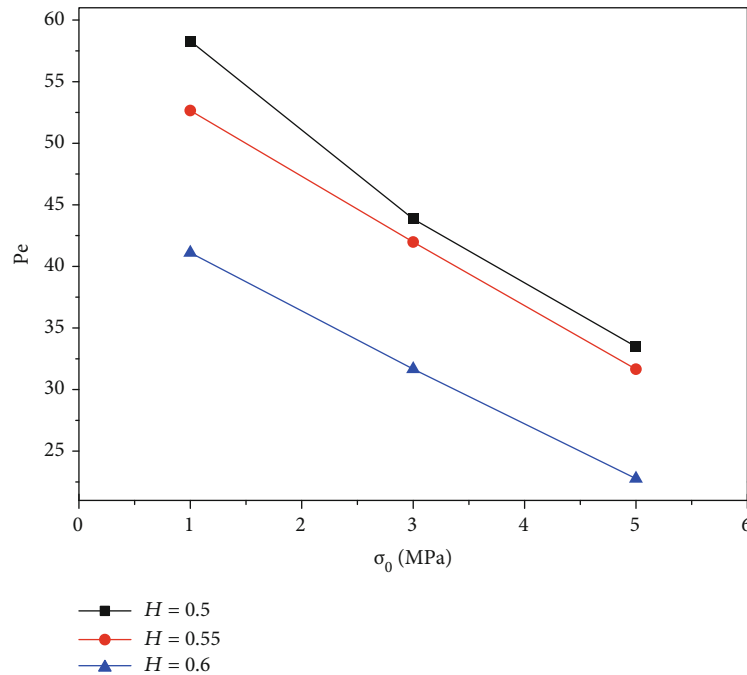


FIGURE 15: The Pe numbers when $Q = 1.443 \times 10^{-8} \text{ m}^3/\text{s}$.

which will make a profound impact on fluid flow and particle transport. The normal stress mainly affects the fracture aperture which can change the flow field in turn and finally affects the travel path and residence time of particles.

Data Availability

All the data used in the present study are available by contacting the corresponding author and/or the first author. Their email addresses are renfh_2001@163.com (Fenhua Ren) and b20170003@xs.ustb.edu.cn (Min Wang), respectively.

Conflicts of Interest

The authors declare that they have no conflicts of interest.

Acknowledgments

This study has been supported by the Key Laboratory of Western Mine Exploitation and Hazard Prevention, Ministry of Education (SKLCKRF1901) and the National Natural Science Foundation of China (51804163). These supports are gratefully acknowledged.

References

- [1] X. Xiong, B. Li, Y. Jiang, T. Koyama, and C. Zhang, "Experimental and numerical study of the geometrical and hydraulic characteristics of a single rock fracture during shear," *International Journal of Rock Mechanics and Mining Sciences*, vol. 48, no. 8, pp. 1292–1302, 2011.
- [2] Z. H. Zhao, B. Li, and Y. J. Jiang, "Effects of fracture surface roughness on macroscopic fluid flow and solute transport in fracture networks," *Rock Mechanics and Rock Engineering*, vol. 47, no. 6, pp. 2279–2286, 2014.
- [3] B. Li, Y. Jiang, T. Koyama, L. Jing, and Y. Tanabashi, "Experimental study of the hydro-mechanical behavior of rock joints using a parallel-plate model containing contact areas and artificial fractures," *International Journal of Rock Mechanics and Mining Sciences*, vol. 45, no. 3, pp. 362–375, 2008.
- [4] L. C. Zou, L. R. Jing, and V. Cvetkovic, "Roughness decomposition and nonlinear fluid flow in a single rock fracture," *International Journal of Rock Mechanics and Mining Sciences*, vol. 75, pp. 102–118, 2015.
- [5] M. Wang, Y. F. Chen, G. W. Ma, J. Q. Zhou, and C. B. Zhou, "Influence of surface roughness on nonlinear flow behaviors in 3D self-affine rough fractures: lattice Boltzmann simulations," *Advances in Water Resources*, vol. 96, pp. 373–388, 2016.
- [6] L. Z. Xie, C. Gao, L. Ren, and C. B. Li, "Numerical investigation of geometrical and hydraulic properties in a single rock fracture during shear displacement with the Navier–Stokes equations," *Environmental Earth Sciences*, vol. 73, no. 11, pp. 7061–7074, 2015.
- [7] X. Xi, X. Wu, Q. Guo, and M. Cai, "Experimental investigation and numerical simulation on the crack initiation and propagation of rock with pre-existing cracks," *IEEE Access*, vol. 8, pp. 129636–129644, 2020.
- [8] Y. Li, H. Zhou, L. Zhang, W. Zhu, S. Li, and J. Liu, "Experimental and numerical investigations on mechanical property and reinforcement effect of bolted jointed rock mass," *Construction and Building Materials*, vol. 126, pp. 843–856, 2016.
- [9] B. Indraratna, S. Thirukumaran, E. T. Brown, and S. P. Zhu, "Modelling the shear behaviour of rock joints with asperity

- damage under constant normal stiffness," *Rock Mechanics and Rock Engineering*, vol. 48, no. 1, pp. 179–195, 2015.
- [10] M. E. Thompson, "Numerical simulation of solute transport in rough fractures," *Journal of Geophysical Research: Solid Earth*, vol. 96, no. B3, pp. 4157–4166, 1991.
 - [11] R. Zimmerman, S. Kumar, and G. Bodvarsson, "Lubrication theory analysis of the permeability of rough-walled fractures," *International Journal of Rock Mechanics and Mining Sciences & Geomechanics Abstracts*, vol. 28, no. 4, pp. 325–331, 1991.
 - [12] T. Koyama, B. Li, Y. Jiang, and L. Jing, "Numerical modelling of fluid flow tests in a rock fracture with a special algorithm for contact areas," *Computers and Geotechnics*, vol. 36, no. 1–2, pp. 291–303, 2009.
 - [13] S. R. Brown, "Fluid flow through rock joints: the effect of surface roughness," *Journal of Geophysical Research: Solid Earth*, vol. 92, no. B2, pp. 1337–1347, 1987.
 - [14] N. Barton, S. Bandis, and K. Bakhtar, "Strength, deformation and conductivity coupling of rock joints," *International Journal of Rock Mechanics and Mining Sciences & Geomechanics Abstracts*, vol. 22, no. 3, pp. 121–140, 1985.
 - [15] T. Koyama and L. Jing, "Fluid flow and tracer transport simulations for rock fractures under normal loading and shear displacement," in *11th ISRM Congress*, International Society for Rock Mechanics and Rock Engineering, 2007.
 - [16] T. Koyama, B. Li, Y. Jiang, and L. Jing, "Coupled shear-flow tests for rock fractures with visualization of the fluid flow and their numerical simulations," *International Journal of Geotechnical Engineering*, vol. 2, no. 3, pp. 215–227, 2013.
 - [17] T. Koyama, I. Neretnieks, and L. Jing, "A numerical study on differences in using Navier–Stokes and Reynolds equations for modeling the fluid flow and particle transport in single rock fractures with shear," *International Journal of Rock Mechanics and Mining Sciences*, vol. 45, no. 7, pp. 1082–1101, 2008.
 - [18] S. R. Brown, H. W. Stockman, and S. J. Reeves, "Applicability of the Reynolds equation for modeling fluid flow between rough surfaces," *Geophysical Research Letters*, vol. 22, no. 18, pp. 2537–2540, 1995.
 - [19] V. V. Mourzenko, J.-F. Thovert, and P. M. Adler, "Permeability of a single fracture; validity of the Reynolds equation," *Journal de Physique II*, vol. 5, no. 3, pp. 465–482, 1995.
 - [20] L. C. Zou, L. R. Jing, and V. Cvetkovic, "Shear-enhanced nonlinear flow in rough-walled rock fractures," *International Journal of Rock Mechanics and Mining Sciences*, vol. 97, pp. 33–45, 2017.
 - [21] R. W. Zimmerman, A. Al-Yaarubi, C. C. Pain, and C. A. Grattoni, "Non-linear regimes of fluid flow in rock fractures," *International Journal of Rock Mechanics and Mining Sciences*, vol. 41, pp. 163–169, 2004.
 - [22] Q. Yin, L. X. He, H. W. Jing, and D. Zhu, "Quantitative estimates of nonlinear flow characteristics of deformable rough-walled rock fractures with various lithologies," *Processes*, vol. 6, no. 9, p. 149, 2018.
 - [23] R. C. Liu, B. Li, Y. J. Jiang, and L. Y. Yu, "A numerical approach for assessing effects of shear on equivalent permeability and nonlinear flow characteristics of 2-D fracture networks," *Advances in Water Resources*, vol. 111, pp. 289–300, 2018.
 - [24] R. Liu, B. Li, and Y. Jiang, "Critical hydraulic gradient for nonlinear flow through rock fracture networks: the roles of aperture, surface roughness, and number of intersections," *Advances in Water Resources*, vol. 88, pp. 53–65, 2016.
 - [25] Z. Zhang and J. Nemecek, "Fluid flow regimes and nonlinear flow characteristics in deformable rock fractures," *Journal of Hydrology*, vol. 477, pp. 139–151, 2013.
 - [26] N. Odling, "Natural fracture profiles, fractal dimension and joint roughness coefficients," *Rock Mechanics and Rock Engineering*, vol. 27, no. 3, pp. 135–153, 1994.
 - [27] E. Louis and F. Guinea, "The fractal nature of fracture," *EPL (Europhysics Letters)*, vol. 3, no. 8, pp. 871–877, 1987.
 - [28] B. B. Mandelbrot, "The fractal geometry of nature," *The College Mathematics Journal*, vol. 15, no. 2, p. 175, 1984.
 - [29] S. R. Brown and C. H. Scholz, "Broad bandwidth study of the topography of natural rock surfaces," *Journal of Geophysical Research*, vol. 90, no. B14, p. 12575, 1985.
 - [30] N. Huang, R. C. Liu, and Y. J. Jiang, "Numerical study of the geometrical and hydraulic characteristics of 3D self-affine rough fractures during shear," *Journal of Natural Gas Science and Engineering*, vol. 45, pp. 127–142, 2017.
 - [31] R. F. Voss, "Fractals in nature: from characterization to simulation," in *The Science of Fractal Images*, pp. 21–70, Springer, 1988.
 - [32] K. Develi and T. Babadagli, "Quantification of natural fracture surfaces using fractal geometry," *Mathematical Geology*, vol. 30, no. 8, pp. 971–998, 1998.
 - [33] D. Saupe, "Algorithms for random fractals," in *The Science of Fractal Images*, pp. 71–136, Springer, 1988.
 - [34] F. Molz, H. Liu, and J. Szulga, "Fractional Brownian motion and fractional Gaussian noise in subsurface hydrology: a review, presentation of fundamental properties, and extensions," *Water Resources Research*, vol. 33, no. 10, pp. 2273–2286, 1997.
 - [35] H.-H. Liu, G. S. Bodvarsson, S. Lu, and F. J. Molz, "A corrected and generalized successive random additions algorithm for simulating fractional Levy motions," *Mathematical Geology*, vol. 36, no. 3, pp. 361–378, 2004.
 - [36] R. Tse and D. Cruden, "Estimating joint roughness coefficients," *International Journal of Rock Mechanics and Mining Sciences & Geomechanics Abstracts*, vol. 16, no. 5, pp. 303–307, 1979.
 - [37] T. Esaki, S. Du, Y. Mitani, K. Ikusada, and L. Jing, "Development of a shear-flow test apparatus and determination of coupled properties for a single rock joint," *International Journal of Rock Mechanics and Mining Sciences*, vol. 36, no. 5, pp. 641–650, 1999.
 - [38] Z. Chen, S. Narayan, Z. Yang, and S. Rahman, "An experimental investigation of hydraulic behaviour of fractures and joints in granitic rock," *International Journal of Rock Mechanics and Mining Sciences*, vol. 37, no. 7, pp. 1061–1071, 2000.
 - [39] G. Rong, J. Yang, L. Cheng, and C. Zhou, "Laboratory investigation of nonlinear flow characteristics in rough fractures during shear process," *Journal of Hydrology*, vol. 541, pp. 1385–1394, 2016.
 - [40] T. Koyama, N. Fardin, L. Jing, and O. Stephansson, "Numerical simulation of shear-induced flow anisotropy and scale-dependent aperture and transmissivity evolution of rock fracture replicas," *International Journal of Rock Mechanics and Mining Sciences*, vol. 43, no. 1, pp. 89–106, 2006.
 - [41] K. Matsuki, Y. Kimura, K. Sakaguchi, A. Kizaki, and A. Giwelli, "Effect of shear displacement on the hydraulic conductivity of a fracture," *International Journal of Rock Mechanics and Mining Sciences*, vol. 47, no. 3, pp. 436–449, 2010.
 - [42] Y. Jiang, J. Xiao, Y. Tanabashi, and T. Mizokami, "Development of an automated servo-controlled direct shear apparatus

- applying a constant normal stiffness condition,” *International Journal of Rock Mechanics and Mining Sciences*, vol. 41, no. 2, pp. 275–286, 2004.
- [43] S. Saeb and B. Amadei, “Modelling joint response under constant or variable normal stiffness boundary conditions,” *International Journal of Rock Mechanics and Mining Sciences & Geomechanics Abstracts*, vol. 27, no. 3, pp. 213–217, 1990.
- [44] S. Saeb and B. Amadei, “Modelling rock joints under shear and normal loading,” *International Journal of Rock Mechanics and Mining Sciences & Geomechanics Abstracts*, vol. 29, no. 3, pp. 267–278, 1992.
- [45] Y. Li, H. Zhou, Z. Dong, W. Zhu, S. Li, and S. Wang, “Numerical investigations on stability evaluation of a jointed rock slope during excavation using an optimized DDARF method,” *Geomechanics and Engineering*, vol. 14, no. 3, pp. 271–281, 2018.
- [46] R. Olsson and N. Barton, “An improved model for hydromechanical coupling during shearing of rock joints,” *International Journal of Rock Mechanics and Mining Sciences*, vol. 38, no. 3, pp. 317–329, 2001.
- [47] V. Vilarrasa, T. Koyama, I. Neretnieks, and L. Jing, “Shear-induced flow channels in a single rock fracture and their effect on solute transport,” *Transport in Porous Media*, vol. 87, no. 2, pp. 503–523, 2010.
- [48] L. Moreno, Y. Tsang, C. Tsang, F. Hale, and I. Neretnieks, “Flow and tracer transport in a single fracture: a stochastic model and its relation to some field observations,” *Water Resources Research*, vol. 24, no. 12, pp. 2033–2048, 1988.
- [49] N. Huang, Y. J. Jiang, R. C. Liu, and Y. X. Xia, “Size effect on the permeability and shear induced flow anisotropy of fractal rock fractures,” *Fractals-Complex Geometry Patterns and Scaling in Nature and Society*, vol. 26, no. 2, 2018.
- [50] L. Zou, L. Jing, and V. Cvetkovic, “Modeling of solute transport in a 3D rough-walled fracture–matrix system,” *Transport in Porous Media*, vol. 116, no. 3, pp. 1005–1029, 2017.

Research Article

Stability Analysis of a Slope considering Two Reinforcement Processes

Wei Chen ¹, Dongbai Li,¹ Ting Ma ², Helin Fu,¹ and Yanpeng Du³

¹School of Civil Engineering, Central South University, Changsha 410075, China

²Sichuan College of Architectural Technology, Chengdu 610300, China

³Chongqing Communications Research and Design Institute Co., Ltd., Chongqing 400067, China

Correspondence should be addressed to Ting Ma; zmatinda@sina.com

Received 27 August 2020; Revised 21 September 2020; Accepted 9 October 2020; Published 5 November 2020

Academic Editor: Zhengyang Song

Copyright © 2020 Wei Chen et al. This is an open access article distributed under the Creative Commons Attribution License, which permits unrestricted use, distribution, and reproduction in any medium, provided the original work is properly cited.

The strength reduction method embedded in a distinct element code was used to analyse the stability of a slope in a coal mining area that had been reinforced twice, primarily with pile and retaining wall, followed by porous steel-tube bored grouting. For the primary reinforcement, the factor of safety was calculated, slip surface and failure mechanism were determined, and the damage phenomenon of primary reinforcement was analysed in detail. Failure time of slope without further strengthening was predicted by applying a new quantitative method based on monitoring displacement data. The slope instability at the primary reinforced stage was verified by these analyses. For the second reinforcement, the effect was evaluated by combining the new factor of safety and the final monitoring data, which validates the slope stability. Especially, variations of displacement and factor of safety due to water influence are analysed. Through this procedure, a systemic method for the slope safety evaluation and assurance is presented for engineering practice reference.

1. Introduction

The soil and rock material of slope is usually the porous unsaturated or saturated media [1], and the stability of the slope has a great relationship with the strength of the soil and rock material, the reinforcement measures, the influences of water, earthquake, and external load [2, 3]. Due to the disturbance caused during the process of infrastructure construction, rainfall in the monsoon season, the fragile geology, and the variation of topography, land sliding happens more often. In engineering practice, the landslides which are a potential threat to human life and transportation security are constantly monitored to ascertain that people could be safely evacuated and the damage to property could be minimized or eliminated. Therefore, slope stability is still an issue which needs to be analysed in detail. In the past decades, researchers developed plentiful methods for slope stability analysis. The authors recommend that the slope stability and safety assessment should include as many factors as possible.

Generally, the factor of safety (FOS) calculation is an appropriate and convenient way to evaluate slope stability. As a traditional and well-established method, the limit equilibrium method (LEM) is widely used by geotechnical engineers, not only for its simplicity in estimating FOS with a fewer input data but also for its ability to accommodate complex geometries and variable soil and water pressure conditions [4]. For example, Liu et al. [5] developed an efficient direct Monte Carlo simulation (MCS) method, called adaptive MCS, for slope system reliability analysis based on LEM; Wang et al. [6] proposed a 3D slope stability analysis method based on the Pan's maximum principle and under the framework of LEM. Despite all of its benefits, LEM has some pivotal deficiencies, such as neglecting the stress-strain relation of geomaterials and assuming numerous arbitrary slip surfaces for FOS calculation, which cannot represent a realistic failure mechanism. The limit analysis method (LAM), including upper and lower boundary approaches, has been used and improved by many researchers for slope stability analysis since Drucker

and Prager [7] applied plasticity limit theorems in soil mechanics. Chen [8] has systematically reviewed the theory. Zhao et al. [9] proposed a new parameter back analysis method by combining the 2D/3D upper bound LAM and reliability theory to accurately determine the shear strength parameters for a 3D slope with a single failure surface. Adopting finite elements and linear programming, Sloan [10, 11] and Kim et al. [12] conducted both lower bound and upper bound analyses. Although LAM is rigorous in the sense for statically admissible stress fields for lower bound analysis and kinematically admissible velocity fields for upper bound analysis, its application in complicated real problems is still limited and it is seldom used for routine designing. The strength reduction method (SRM) has been used in slope stability analysis as early as 1975 by Zienkiewicz et al. [13]. Afterwards, many researchers [14–18] have applied it. The major advantage of SRM is that the critical slip surface is determined by reducing selected strength parameters under the gravity load until failure occurs. Therefore, it is convenient to use SRM for slope stability analysis in engineering practice.

In addition, the failure time of slope (FTS) is another important quantitative method based on monitoring displacement data to analyse the slope stability. Considering complicated boundary conditions, doubtful triggering failure mechanisms, and the heterogeneity of the geomaterials, it is extraordinarily difficult to predict FTS by adopting the rheological theory and rock fracture mechanics. An empirical approach is diffusely preferred, which is derived from the accelerating creep stage and fundamentally using displacement or deformation rates for the failure indicators. Most of these empirical equations are based on power and exponential laws [19]. According to the measured slope displacements versus time before failure taking the form of the tertiary creep curve, Terzaghi [20] showed the presence of a connection between creep and landslides. Saito [21, 22] concluded a method for FTS prediction by laboratory measurements of the strain rate during secondary creep using load-controlled triaxial tests. Zavodni and Broadbent [23] introduced an equation to predict two stages of creep and the time of failure. Fukuzono [24] through an experimental study of small-scale slope models found the logarithm of acceleration displacement to be proportional to the logarithm of the velocity of surface displacement of the slope. Later, Fukuzono [24, 25] proposed an inverse velocity method to predict the time of failure. Based on the research of Fukuzono [24, 25] and through theoretical analysis on power law creep under different loading conditions, Voight [26] deduced the correlation of velocity, time at the prediction moment, and the time of failure. Rearranging the equation of Saito [21] and comparing it with Fukuzono's [24] inverse velocity method, Mufundirwa [27] invented a new method termed the SLO method for prediction of FTS.

In this paper, the authors analysed the stability of a slope that was reinforced twice, primarily with pile and retaining wall and secondly with porous steel-tube bored grouting. Using the geological data, the FOS in primary reinforced condition was calculated via the Universal Distinct Element Code (UDEC) equipped with the Shear Strength Reduction Method (SRM), which is capable of

automatically locating the critical failure surface. Subsequently, FTS was predicted with the SLO method of Mufundirwa [27]. After that, the second reinforcement effect was evaluated by combining the monitoring data and the numerical simulation results. In addition, variations of displacement and FOS due to water influence are analysed. Through this procedure, a systematic approach for the slope safety evaluation and assurance is presented for future engineering practice reference.

2. Engineering Background

The 55 m wide slope is located in a coal mining area, which is also near the mileage of K18+170 Beijing-Zhuhai Highway in the south of China. The slope, consisting of three steps, was primarily reinforced with pile and retaining wall. The first step was reinforced by piles and a 5 m high retaining wall (Figure 1). Covered with a protective frame, the second one was 10 m high. The third step of 10 m height had a protective frame and a row of piles on the top. The natural slope is located above these structures. The second and the third steps were backfilled with soil in order to lower the ramp rate from 1:0.75 to 1:1.

2.1. Engineering Geology. To determine the engineering geological characteristics and the slip surface, four exploration holes were drilled along the sliding direction of the slope. Detailed exploration results showed that the lithological layers of the slope from top to bottom consisted of the overlying Quaternary soil (I artificial fill soil, II Quaternary alluvium layer 0-4.8 m), highly weathered limestone (4.8-6.5 m), peat layer (6.5-10.0 m), moderately weathered limestone (10.0-13.75 m), carbonaceous shale (13.8-21.0 m), followed by thin and slightly weathered sandstone and alternating layers of carbonaceous shale (21.0-30.5 m).

On the basis of the geological mechanics analysis method, the engineers supposed the potential sliding surface to occur along the interface of the peat layer. An engineering geologic profile is shown in Figure 1.

2.2. Damage to Reinforced Structure. In October 2003, a curved crack of about 35 m was found behind the piles of the third step (Figure 2(a)). The crack after three years of its formation is shown in Figure 2(b). In addition to this crack, another 1.5 cm wide transverse crack appeared in the middle of the third protective frame, which grew to a width of 30 cm in January 2006 to such an extent that the protective surface of the mortar rubble loosened and water leaked through it.

2.3. Displacement of Slope. Being aware of the considerable change in appearance, the engineers deduced that the displacement rate of the slope was large. Due to the reason that this highway is a transportation artery in the south of China and a coal mining area is located behind the slope, in case of slope failure, there would have been a serious threat to human life and transportation security. A number of actions were taken to stabilize it, including safety monitoring, stability analysis, rereinforcement, and effect

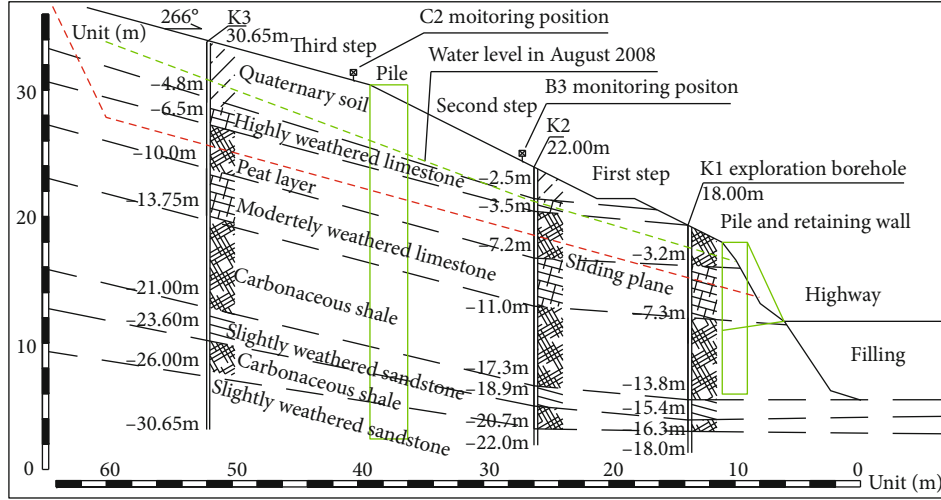


FIGURE 1: Engineering geologic profile.



FIGURE 2: (a) Crack behind the piles of the third step in 2003. (b) Crack behind the piles of the third step in 2006.

evaluation. The displacement versus time curves and displacement at depth as shown in Figure 3 were obtained through monitoring displacement at the surface and at depth. A tremendous increase in displacement occurred due to heavy rains during May 2006 to July 2006. Maximum surface displacement was noted to be about 80 mm, while the distinct displacement change at depth ranged from 6.5 m to 8.5 m along the peat layer. The potential slip surface is shown in Figure 1.

3. Stability Analysis Based on the Discrete Element Method with SRM

3.1. *Constitutive Models of Material and Contacts.* The Mohr-Coulomb failure criterion (equation (1)) is used to describe the failure of block materials. The constitutive model of contact is the Coulomb slip model with residual strength (equations (2) and (3), Figure 4) which is used to control the response of contact in the normal and shear direction [28].

$$\tau_b = C_b + \sigma_b \tan \varphi_b, \quad (1)$$

where τ_b is the shear strength, C_b is the cohesive strength, σ_b is the normal stress, and φ_b is the friction angle of the block.

$$\begin{cases} \sigma_n = -k_n u_n, \\ \text{if } \sigma_n < -T_1, \sigma_n = 0, \\ \text{if } u_n < u_c, \sigma_n = T_2, \end{cases} \quad (2)$$

$$\begin{cases} \tau_s = k_s u_s, \\ \tau_{\max} = C + \sigma_n \tan \varphi, \\ \text{if } |\tau_s| \geq \tau_{\max}, \tau_s = \text{sign}(\Delta u_s) \cdot (C_r + \sigma_n \tan \varphi_r), \end{cases} \quad (3)$$

where σ_n and τ_s are the normal stress and shear stress, respectively, k_n and k_s are the normal stiffness and shear stiffness, respectively, u_n and u_s are the normal displacement and shear displacement, respectively, u_c is the contact overlap tolerance, T_1 and T_2 are tensile strength and overlap tolerance strength, respectively, τ_{\max} is the shear strength of contact, C and C_r are the cohesive strength and residual cohesive strength, respectively, φ and φ_r are the friction angle and

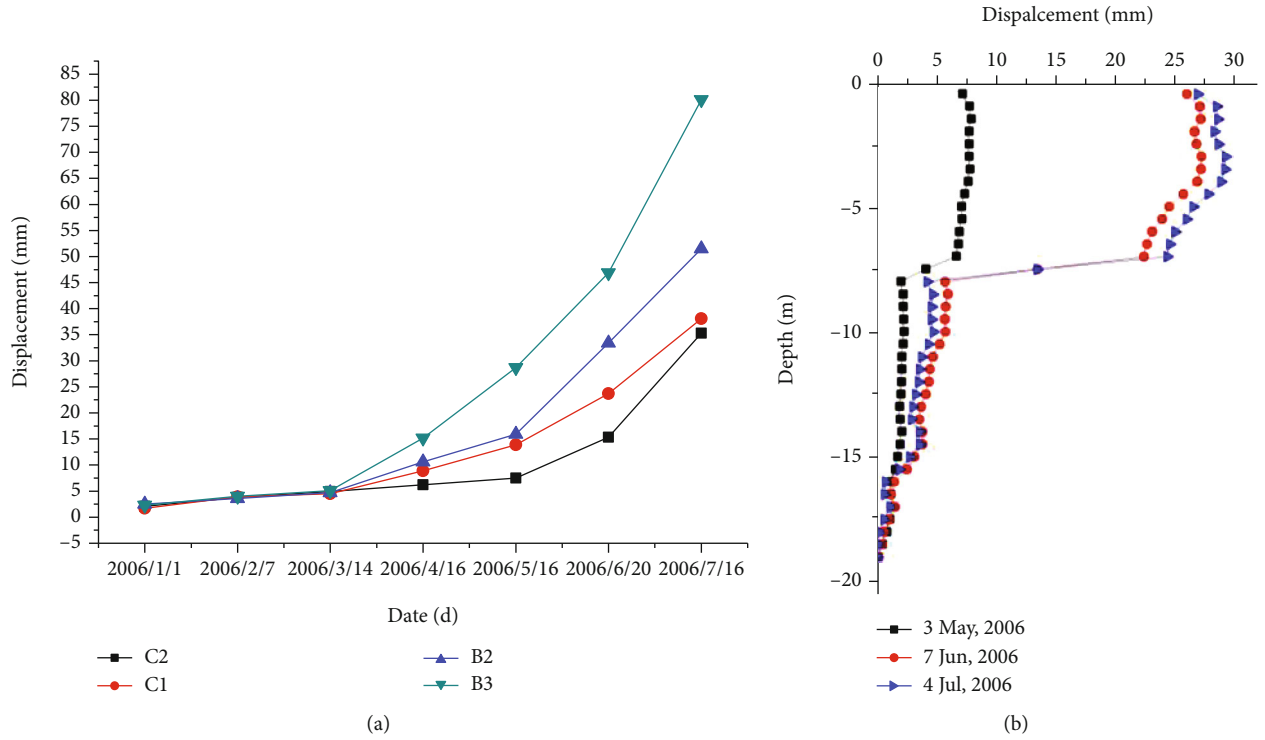


FIGURE 3: Monitoring data: (a) surface displacement; (b) displacement of slope at depth.

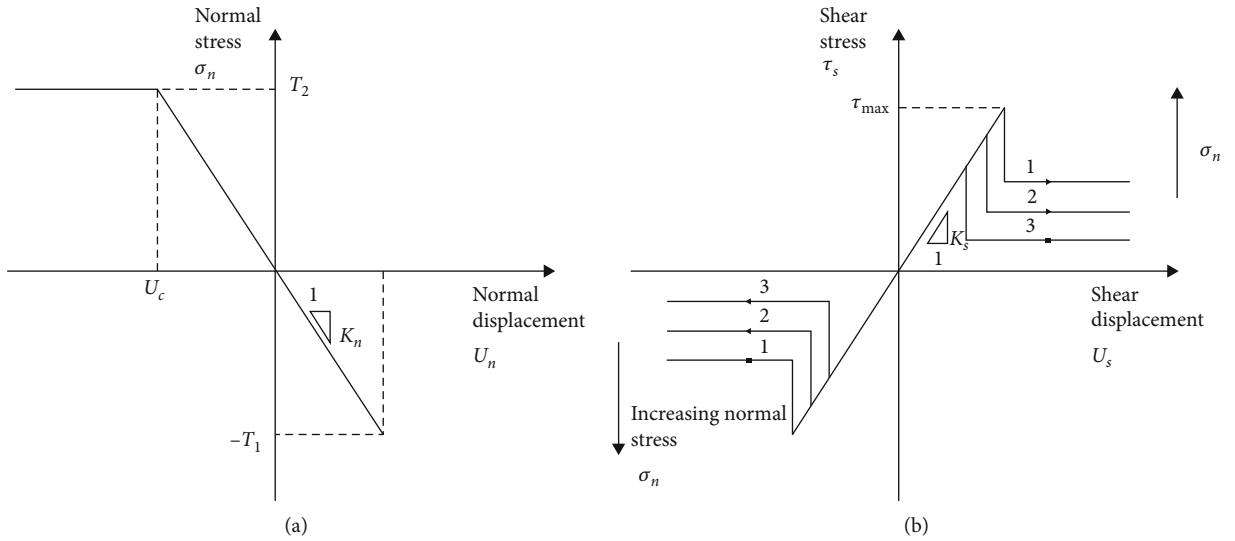


FIGURE 4: Coulomb slip with residual strength criteria: (a) in normal direction ; (b) in shear direction.

residual friction angle, respectively, and Δu_s is the incremental shear displacement.

3.2. Theory Background of SRM in UDEC. The UDEC is a two-dimensional numerical program based on the distinct element method for the discontinuum modelling [28]. In the strength reduction method, the selected strength properties are reduced until failure occurs and the FOS is calculated. The method is commonly applied with the Mohr-Coulomb

failure criterion. In this case, the FOS is defined according to the following equations:

$$c^{\text{trial}} = \frac{1}{F^{\text{trial}}} c, \quad (4)$$

$$\phi^{\text{trial}} = \arctan \left(\frac{1}{F^{\text{trial}}} \tan \phi \right),$$

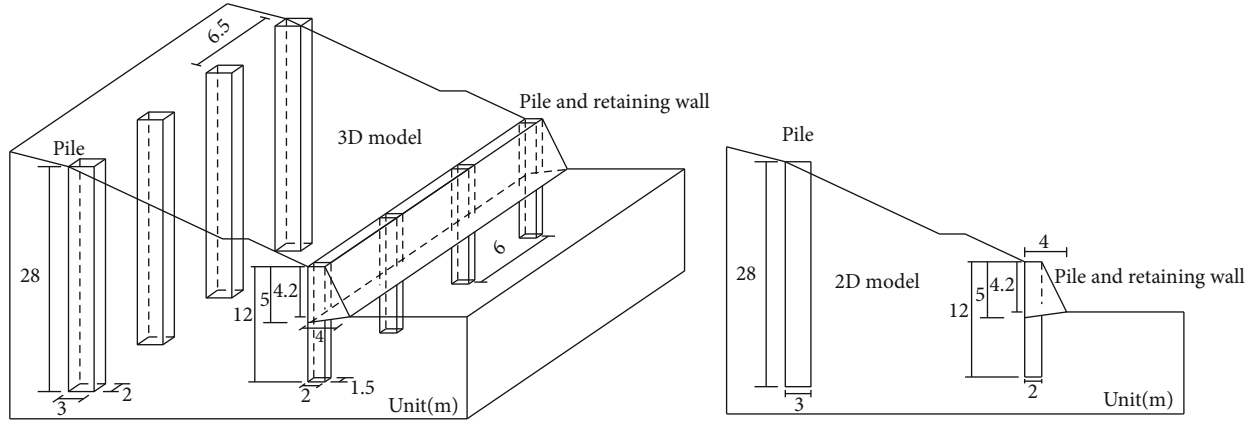


FIGURE 5: 3D and 2D calculation model.

where c^{trial} is the trial value of cohesion, F^{trial} is the trial value of the factor, c is the cohesion, ϕ^{trial} is the trial value of friction angle, and ϕ is the friction angle.

The original strength parameters of rock and soil (such as c and ϕ) are evaluated by tests during survey processes. When conducting the strength reduction method for the numerical model, the F^{trial} is chosen and the trial values of the strength parameters are obtained by equations (4 and 5). A series of simulations are conducted using the trial values of the factor F^{trial} to reduce the cohesion c and friction angle ϕ until slope failure occurs (note that if the slope is initially unstable, c and ϕ are increased until the limiting condition is found). One technique to find the strength values that correspond to the onset of failure is to monotonically reduce (or increase) the strength parameters in small increments until a failure state is found.

3.3. Basic Model. The lateral and vertical dimensions of the numerical model are $120\text{ m} \times 56\text{ m}$, respectively. The mesh consists of deformable triangle zones. The lower boundary is assumed to be fixed, while the vertical boundaries at the left- and right-hand sides are assumed to be on rollers to allow movement of soil/rock layers.

The pile and retaining wall are represented by a block with the corresponding material strength, and the cap rigidity of the pile is free. The slope that was reinforced by two rows of piles and retaining wall is a 3D problem, as shown in Figure 5. If the 3D simulation method is used, the numerical model will be huge and the calculation time will increase several times than that of the 2D simulation method. However, the UDEC is a 2D software which simulates the unit thickness of the slope. For this reason, some equivalent conversion for piles needs to be done.

As shown in Figure 5, the sliding force in 2D became one unit of the total sliding force in 3D. Because the distribution of the piles is discontinuous, the bending stiffness of the pile should also be equivalently transformed, which means that the elastic modulus and moment of inertia should be changed from 3D to 2D conditions. Donovan et al. [29] put forward a simple and convenient method to convert material parameters of the same distance distribution structure obey-

ing the equivalent conversion rule in the finite element analysis. Likewise, Zhang et al. [30] proposed the conversion method for pile, which is used in this paper.

The length of the pile (1) is 28 m in the upper part of the slope, and the length of the pile (2) is 12 m in the toe of the slope, respectively. The section of the pile (1) is $3.0\text{ m} \times 2.0\text{ m}$ with a 6.5 m distance between each of the two piles, and the section of the pile (2) is $2.0\text{ m} \times 1.5\text{ m}$ with a 6.0 m distance between the piles. As one part of the pile (2) was inserted into a continuous retaining wall, it was difficult to distinguish between them. So only the pile (1) and part of the pile (2) are converted, and the material parameters of the inserted part of the pile (2) are considered to be the same as that of the retaining wall for simplicity. Referring to the method of Zhang et al. [30], the width of the pile (1) and pile (2) are taken to be 3 m and 2 m, respectively, and the thickness of these two is taken as 1 m in the numerical model. The corresponding parameters of the pile were calculated as follows:

For pile (1)

$$E'_1 = \frac{E_0 I_1}{d_1 I'_1} = \frac{E_0 \times 2 \times 3^3/12}{6.5 \times 1 \times 3^3/12} = 0.308 E_0 = 0.924 \times 10^{10} \text{ pa.} \quad (5)$$

For the part of the pile (2) which was not inserted into the retaining wall

$$E'_2 = \frac{E_0 I_2}{d_2 I'_2} = \frac{E_0 \times 1.5 \times 2^3/12}{6 \times 1 \times 2^3/12} = 0.25 E_0 = 0.75 \times 10^{10} \text{ pa.} \quad (6)$$

Poisson's ratio of the pile is 0.2, so the bulk and shear modulus can be obtained using the following equations.

$$K = \frac{E}{3(1-2\nu)}, \quad (7)$$

$$G = \frac{E}{2(1+\nu)},$$

TABLE 1: Material parameters.

Layers	Density (kg/m ³)	Cohesion (kPa)	Friction angle (°)	Bulk modulus (MPa)	Shear modulus (MPa)
Quaternary soil	1900	18.5	14.7	2.0	1.1
Serious weathered limestone	2100	70	28	25	15
Peat layer	1950	4.7	10.9	1.5	0.7
Moderate weathered limestone	2200	200	30	867	550
Carbonaceous shale	2060	65	21.5	23.5	14.5
Slightly weathered sandstone	2250	800	35	1700	1150
Pile (1)	2500	920	38	5130	3850
Pile (2)	2500	920	38	4167	3125
Retaining wall	2400	820	36	18000	11600

Contacts	k_n (MPa/m)	k_s (MPa/m)	Friction angle (°)	C (kPa)
Between quaternary soil and serious weathered limestone	57.78	57.78	14.7	18.5
Between serious weathered limestone and peat layer	24.33	24.33	10.9	4.7
Between the peat layer and moderate weathered limestone	24.33	24.33	10.9	4.7
Between moderate weathered limestone and carbonaceous shale	214.17	214.17	21.5	65
Between carbonaceous shale and slightly weathered sandstone	214.17	214.17	21.5	65

where E'_1 is the equivalently transformed elastic modulus of the pile (1) in 2D condition, E_0 is the elastic modulus of the pile (1) and pile (2) in 3D condition, I_1 is the moment of inertia of the pile (1) in 3D condition, I'_1 is the moment of inertia of the pile (1) in 2D condition, d_1 is the horizontal distance between two piles (1), K is the bulk modulus, E is the elastic modulus, ν is the Poisson's ratio of the pile (1) and pile (2), and G is the shear modulus.

Table 1 summarizes the material parameters used in the analyses. The Mohr–Coulomb constitutive model was used for each layer. The soil/rock properties used in this study were originally obtained from geological exploration.

In order to get the joint parameters between different layers. The in situ shear tests should be carried out or the intact samples with joint should be taken from the slope and be tested on the laboratory. However, the above tests were not conducted due to the difficulty of in situ shear tests and taking the intact sample with a joint between layers during that time. From a conservative point of view, the friction angle and cohesion of the joint between two layers are assumed to be the same as that of the weaker layer, and the joint tensile strength is not considered. The joint normal and shear stiffnesses were calculated using the following formula [28] and are equal to one another.

$$k_n = k_s = 10 \max \left[\frac{(K + (4/3)G)}{\Delta z_{\min}} \right], \quad (8)$$

where z_{\min} is the smallest width of an adjoining zone in the normal direction.

3.4. The Simulation Results

3.4.1. FOS Calculation. In order to reduce the left boundary effects on the inclined soil and rock layers, we have added

the rectangle block on the left boundary. The rectangle block has several layers and the values of material parameters are the same with the inclined soil and rock layers. The failure state of velocity arrows identified using the SRM analysis shows that the minimum FOS is 1.06 (Figure 6). Obviously, the velocity at the outlines of the first layer and pile head is larger than that of the other layers. The slope surface movement is caused mainly by the first three layers because the modulus and strength parameters of these three highly weathered layers are small.

3.4.2. Displacement. Displacement in the lateral direction for the slope is depicted in Figure 7. It can be confirmed that there is large surface displacement in the second and third step, with maximum values of about 0.3 m and 0.35 m, respectively. The displacement is large in the cap of pile, in the upper part of the slope, which means that the bending stiffness of the pile was not adequate. Therefore, this phenomenon is logical in a way that the protective surface of mortar rubble loosens in these steps. Between the second step and the pile, there is a displacement difference which is shown behind the pile in Figure 7. This simulation result can explain why the crack behind the pile grew (shown in Figure 2).

3.4.3. Slip Surface. According to the maximum shear strain contours shown in Figure 8, the layer with a floating range of the shear strain from 0.04 to 0.1 represented by yellow and red is concluded to be the slip surface. It is the peat layer and is the weakest layer in the slope. This simulation result adheres to the deep displacement monitoring data shown in Figure 3. The failure mechanism of this slope is that the first two layers slid along the weakest peat layer whose strength was greatly influenced by water.

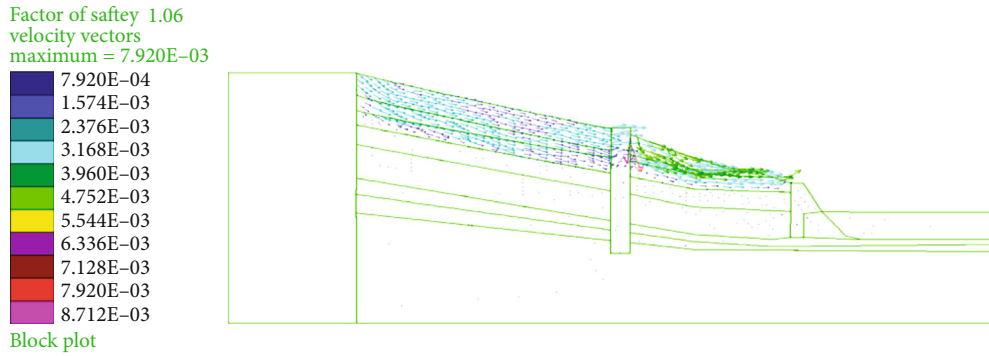


FIGURE 6: FOS and the failure state of velocity vectors.

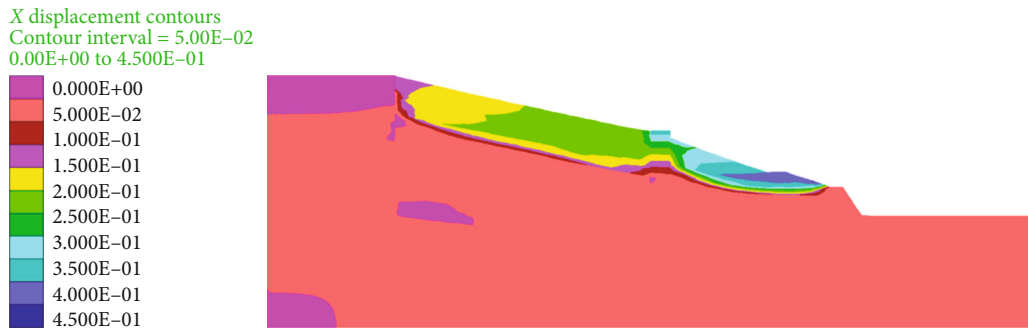


FIGURE 7: Lateral displacement contours.



FIGURE 8: Shear strain contours.

From the simulation results exhibiting small FOS and monitoring data confirming a large displacement rate, the authors deduce that this slope is not safe and the primary reinforcement process with pile and retaining wall has not reached the anticipant goal. Referring to Figures 7 and 8, it can be concluded that if the slope movement continues to increase, the pile will become unstable (bending stiffness does not satisfy the requirement) and the slope will fail.

4. Failure Time Prediction without the Second Reinforcement

In this section, the authors analyse the monitoring surface displacement data shown in Figure 3 and adopt the SLO

method to predict the failure time of slope (FTS) since the FOS is very small.

4.1. Theory and Background of Predicting Method. As early as 1950, Terzaghi [20] concluded that there are some connections between the creep of rock or soil mass and landsliding. After that, numerous researches have been carried out to find out the slope failure characteristics corresponding to the standard creep curve. Some researchers have verified that a slope will become unstable if the slope's sliding velocity accelerates or displacement versus time curve is similar to the tertiary creep curve. There are several laws describing the displacement versus time relationships during tertiary creep which can be used to forecast time of slope failure. These

TABLE 2: Time to failure prediction method.

Researcher	Equation	Comment
Saito [21]	$\dot{\varepsilon} = B/(T_f - t)^n$	$n = 1$, pure $n \neq 1$, generalized
Fukuzono [24]	$\dot{\varepsilon}^{-1} = [A(\alpha - 1)(T_f - t)]^{1/(\alpha-1)}$	$\alpha \in [1.5, 2.2]$ Inverse-velocity method
Voight [26]	$\dot{\varepsilon}^{-1} = [A(\alpha - 1)(T_f - t) + \dot{\varepsilon}_f^{1-\alpha}]^{1/(\alpha-1)}$	$\alpha \in [1.7, 2.2]$
Fukui and Okubo [31]	$\varepsilon = -B \log (T_f - t) + D$	
Mufundirwa [27]	$t(du/dt) = T_f(du/dt) - B$	SLO method

TABLE 3: Predicted results.

Monitoring sites	Sampling value $n = 1$	Sampling value $n = 2$
C1	$t(du/dt) = 208.3701du/dt - 9.3555$ $R = 0.9948$	$t(du/dt) = 212.1759du/dt - 8.1735$ $R = 0.9968$
C2	$t(du/dt) = 201.7514du/dt - 4.9768$ $R = 0.9995$	$t(du/dt) = 204.4508du/dt - 4.0417$ $R = 0.9997$
B2	$t(du/dt) = 200.1146du/dt - 9.2177$ $R = 0.9937$	$t(du/dt) = 206.4073du/dt - 9.2170$ $R = 0.9963$
B3	$t(du/dt) = 202.4147du/dt - 16.1495$ $R = 0.9923$	$t(du/dt) = 205.5890du/dt - 14.7284$ $R = 0.9915$

methods were proposed by Saito [21, 22], Fukuzono [24, 25], Voight [26], Fukui and Okubo [31], and Mufundirwa [27], as shown in Table 2.

In Table 2, where $\dot{\varepsilon}$ is the strain rate or velocity, ε is the strain or displacement, B , α , D , and n are constants, T_f is the failure time, t is the time, u is the displacement, and du/dt is the velocity.

The SLO method used in this paper for failure time prediction was proposed by Mufundirwa [27]. After substituting displacement u instead of strain ε and differentiating Fukui and Okubo's equation [31], equation (9) is deduced.

$$t \frac{du}{dt} = -\frac{B}{T_f - t}. \quad (9)$$

By rearranging equation (9), equation (10) is obtained.

$$t \frac{du}{dt} = T_f \frac{du}{dt} - B, \quad (10)$$

where T_f is the failure time evaluated as the slope of $t(du/dt)$ versus du/dt curve for equation (10); this new method is termed the SLO method.

Utilizing the monitoring data, the velocity is calculated using equation (11), which can filter the measured data in

order to smoothen the short-term deformation deviations that can be insignificant or may cause "false" results [32].

$$\left(\frac{du}{dt}\right)_i = \frac{u_i - u_{i-n}}{t_i - t_{i-n}}, \quad (i = n + 1, n + 2, \dots, m), \quad (11)$$

where $(du/dt)_i$ are the computed velocity points, u_i is the monitoring displacement, t_i is the corresponding time of monitoring displacement, t_m is the time at the instant of prediction, and u_m is the displacement at the instant of prediction. In this equation, the sampling value n is selected to yield a positive velocity only.

4.2. Predicting Results. Based on the monitoring surface displacement of four sites mentioned in Figure 3, the prediction procedure is displayed as follows. Choosing equation (10) to calculate all data which are smoothened using equation (11), the predicted results are shown in Table 3 (R is the correlation ratio).

The monitoring data in Figure 3 include the recorded surface displacement from 1st of January 2006 to 16th of July 2006, a total of 196 days. However, the predicted results in Table 3 indicate the slope failure time to range from 200 to 212 days, which means that if this tertiary-like slope movement continues (without any further strengthening), the landsliding will occur between 22nd of July 2006 to 1st of August 2006. It can be concluded that the T_f for sampling

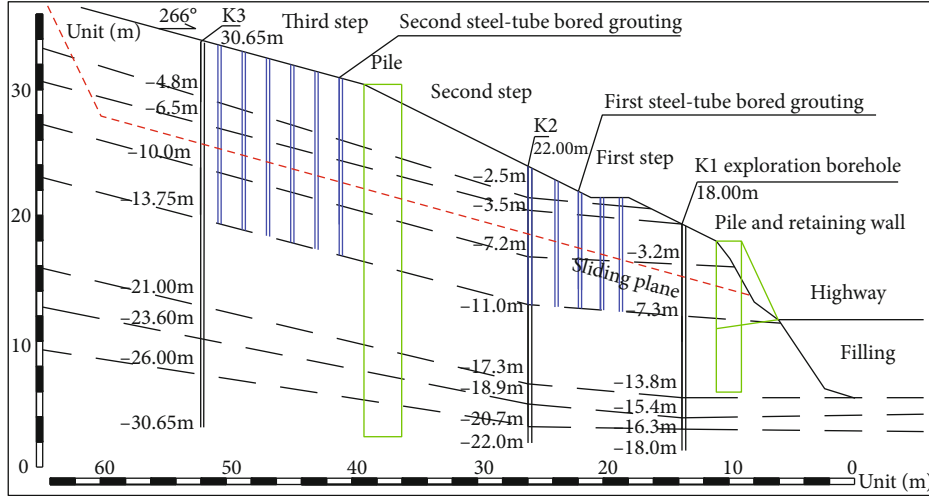


FIGURE 9: Grouting reinforcement scheme.

value $n = 2$ is bigger than that for $n = 1$. However, there is a difference of just a few days.

5. Second Reinforcement

5.1. Reinforcement Scheme. In order to mitigate the landsliding, the second reinforcement project was launched soon after the cracking in the primary reinforced structure and after a large displacement rate of the slope was discovered. The second reinforcement project included porous steel-tubes bored grouting, with the grouting area covering the first three weak layers from the top (Figure 9).

The diameter and separation distance of steel-tubes are 90 mm and 1.5 m, respectively. The diameter of the drilling hole for installing the steel-tube is 250 mm, and the end of the drilling hole is in the bottom of moderately weathered limestone. The cement pastes are injected into Ø22 mm PVC pipe, first flow through interspace between the steel-tube and drilling hole, then entering into the soil and rock mass voids, with the grouting pressure controlled less than 2.5 MPa. After hardening of the cement pastes, the steel-tube and the surrounding geomaterials bind so strongly together that a small pile is produced.

5.2. Effectiveness Evaluation

5.2.1. Final Monitoring Results. Figure 10(a) depicts the final monitoring surface displacements. Because the soil pore pressure increased and the strength of the saturated peat layer decreased during the monsoon rains from the end of April 2006 to the end of July 2007, the surface displacement rate monitored for four sites is at a relatively high value with an average of 0.18-0.41 mm/d. As a result of the effect of the first porous steel-tube bored grouting, the tertiary-like slope surface movement displacement rate decreased during September 2006 and March 2007. Due to the monsoon in April 2007, the surface displacement rate increased again with an average of 0.12-0.22 mm/d; that is why the second porous steel-tube bored grouting was conducted soon after October 2007. Then onwards, the slope displacement grew slowly

with an average rate of 0.02-0.03 mm/d. The displacement rate in 2007 was smaller than in 2006, which shows that the deformation of slope began to converge. While in the same year, the displacement rate in the rainy season was obviously bigger than in other seasons, which demonstrates that the water has a huge influence on slope stability.

Figure 10(b) displays the final displacement monitored at depth. It can be concluded that the slope's movement occurs mainly in the above three layers at a depth of 0 m to 8.5 m (Quaternary soil, highly weathered limestone, and peat layer) and that the slope is stable at depth (displacement rate close to zero).

5.2.2. Displacement Simulation considering the Water Influence. In consideration of the quick growing displacement during the monsoon rains, the influence of water has been analysed. There are two competing effects on the slope deformation related to the rise of the water level: first, the increase in pore pressure will generate a decrease in effective stress leading to shear strength degradation; second, water flowing in contacts and entering into the material pores will increase in density and cause settlement. In the numerical model, we proceed to simulate water can flow in contacts, pore pressure in block material, and density increases with water table rising.

The flow rate in contact is given by [28, 33]

$$q = -k_j a^3 \frac{\Delta p}{l}, \tag{12}$$

where k_j is the permeability factor in contact (whose theoretical value is $1/12\mu$), μ is the dynamic viscosity of the fluid, a is the contact hydraulic aperture, and l is the length assigned to the contact.

$$\Delta p = p_2 - p_1 + \rho_w g (y_2 - y_1), \tag{13}$$

where p_1 and p_2 are the pressure in domain 1 and domain 2, respectively, ρ_w is the fluid density, g is the acceleration of

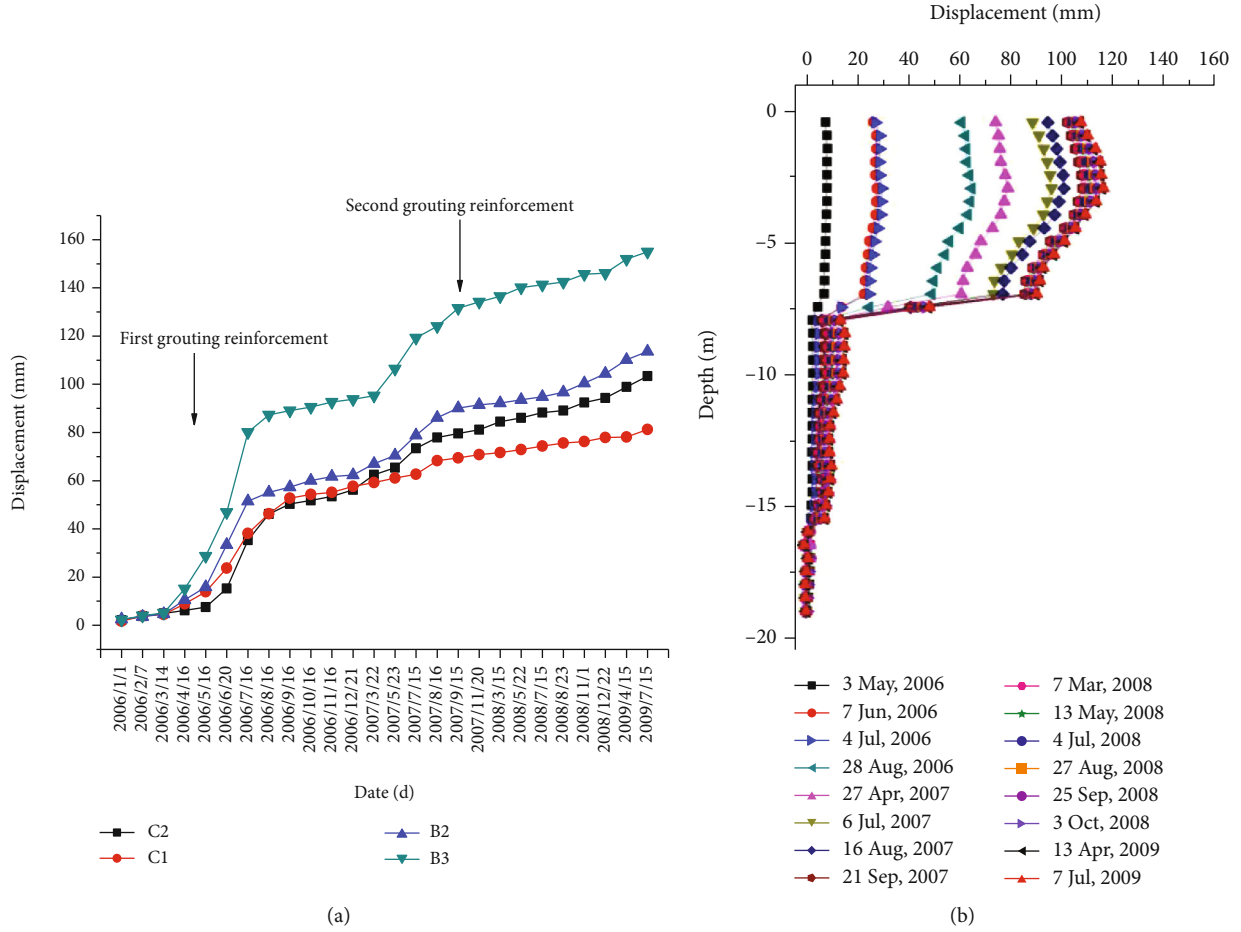


FIGURE 10: Final monitoring data: (a) surface displacement data; (b) deep displacement of the slope.

TABLE 4: Parameters of steel-tube and cement composite pile.

Composite pile	Density(kg/m ³)	Cohesion (kPa)	Friction angle (°)	Bulk modulus (MPa)	Shear modulus (MPa)
Original parameters	2500	810	34.5	16000	10890
Equivalent conversion parameters	2500	810	34.5	1570	1060

gravity, and y_1 and y_2 are the y -coordinates of the domain centers.

The contact hydraulic aperture is given by

$$a = a_0 + u_n, \quad (14)$$

where a_0 is the contact aperture at zero normal stress and u_n is the contact normal displacement.

For block material, shear strength is described as follows [34]

$$\tau_b = C_b + (\sigma_b - p_b) \tan \phi_b, \quad (15)$$

where p_b is the pore pressure in the block material.

After enforcing with grouting, the strength parameters of the first three layers increased. As a conservative analysis, only the steel-tube and cement composite piles (the diameter

is 250 mm) are added in the numerical model and the parameters of the first three layers are invariable. The original parameters and equivalent conversion parameters which consider the 2D to 3D effect of the steel-tube and cement composite piles (refer to equations (6), (8), and (9)) are listed in Table 4.

The friction angle and cohesion of the joint between the two layers are assumed to be the same as that of the weaker layer. The joint normal and shear stiffnesses were calculated using equation (8). The failure of the block materials is controlled by equation (15). In the following simulations, we assign $k_j = 1 \times 10^8 \text{ MPa}^{-1} \text{ sec}^{-1}$, $\rho_w = 1000 \text{ kg/m}^3$, and $a_0 = 5 \times 10^{-4} \text{ m}$ [28].

The displacement simulation results taking account into water table variation influence are illustrated in Figure 11. Figures 11(a) and 11(b) show different water tables in the slope reinforced with pile and retaining wall and then by

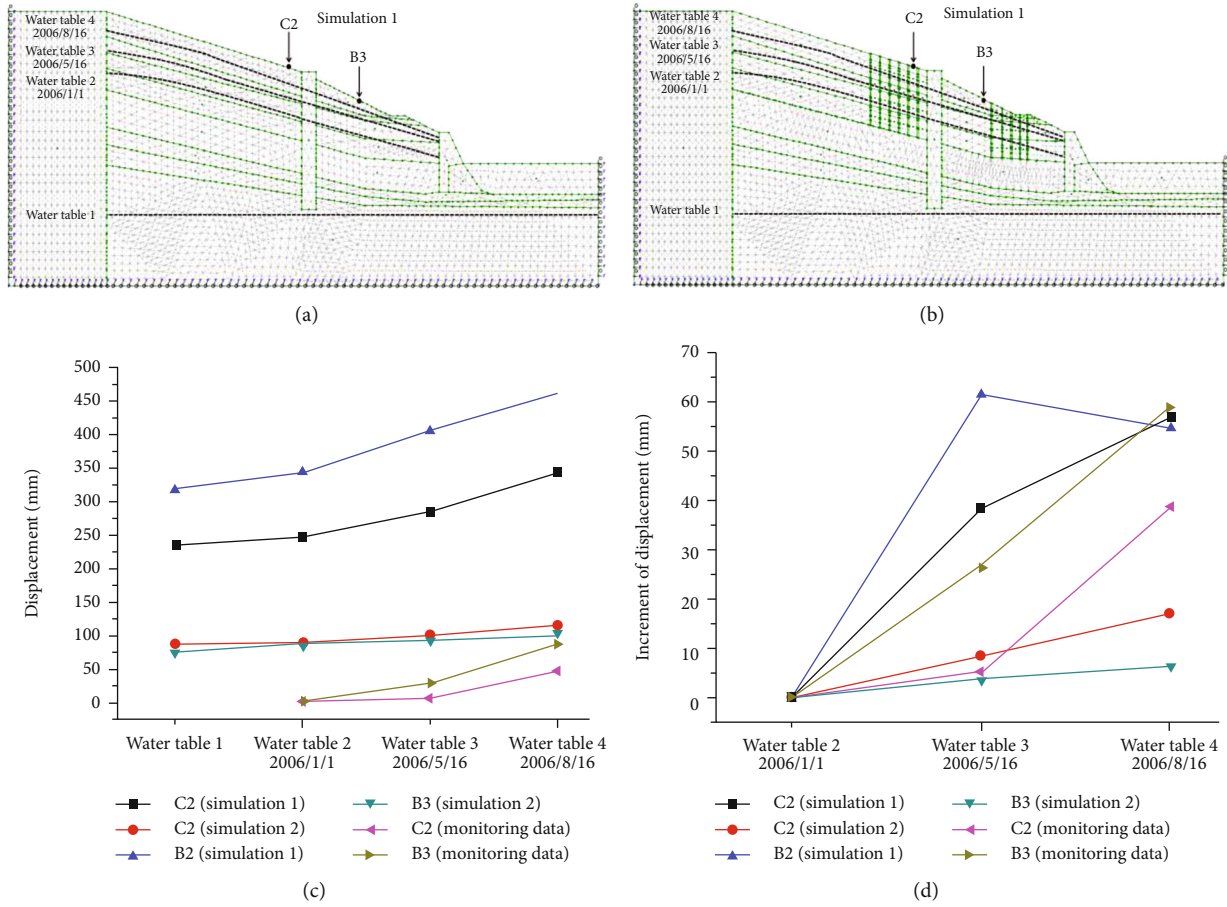


FIGURE 11: Displacement simulation results considering water level increase: (a) different water levels in the primary reinforcement condition; (b) different water levels in second reinforcement condition; (c) displacement versus water table curves; (d) increment curves of displacement.

porous steel-tube bored grouting. Water tables 1-4 represent the water level in 0 m, in the dry season (2006/1/1), in medium (2006/5/16), and high level (2006/8/16), respectively. Especially, the increase of water level from water tables 3 to 4 presents the whole effects of the monsoon rains. Figure 11(c) shows the displacement in two conditions corresponding to Figure 11(a) and 11(b). The exact displacement is bigger than the monitoring data because the deformation of slope began long before 2006, but the monitoring data initiate in 2006. That is why our simulated displacement is bigger than the monitoring displacement. In addition, the displacement in simulation 1 is obviously larger than in simulation 2. Assumed displacement in water table 2 (2006/1/1) as the initial displacement (0 mm), the increment is shown in Figure 11(d). It can be deduced that the maximum displacement increment occurs when the slope is in simulation 1 (primary reinforcement), the minimum occurs when the slope is in simulation 2 (all porous steel-tubes bored grouting have been finished), and the monitoring data is between the maximum and the minimum.

5.2.3. *New FOS Calculation.* According to the different water levels in Figure 11(b), the new FOS values are calculated (Figure 12). As shown in Figure 12, the FOS is decreased with the increase of water level. The FOS is 1.17 during the highest

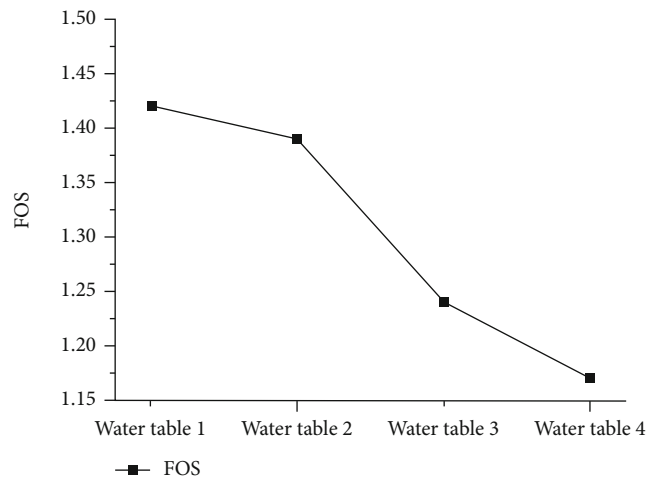


FIGURE 12: FOS versus different water levels.

water level, 1.39 during the dry season, and 1.42 without considering water influence, which is higher as compared to the FOS (1.06) grouting reinforced before. All the new FOS values are conservative calculation results, because only the steel-tube and cement composite piles are taken into account

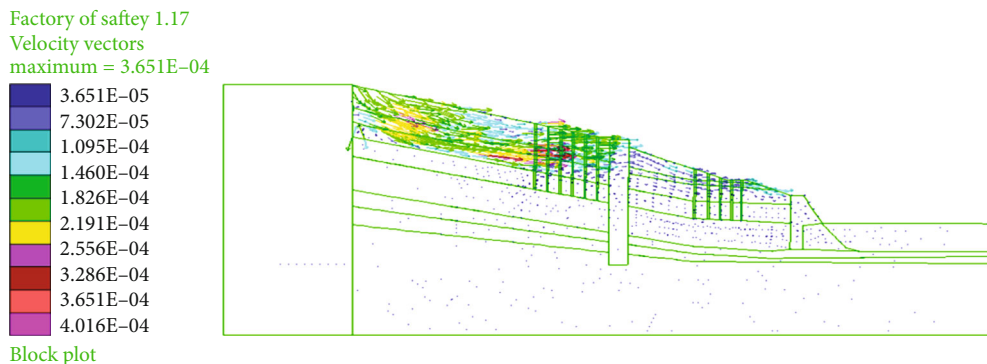


FIGURE 13: The minimum new FOS and the failure state of velocity vectors.

in the numerical model and the improvement for parameters of the first three layers by grouting is neglected.

The minimum new FOS and velocity vectors during the highest water level are shown in Figure 13.

Based on the comprehensive referencing, monitoring, and numerical simulation results, as shown in Figure 10, the increment speed of surface displacement and deep displacement of slope both became slow; as shown in Figure 12, all values of FOS for different water tables are bigger than 1.0. Therefore, the authors conclude that the slope became stable and safe after the second reinforcement project.

6. Conclusion

The stability of a slope was analysed at a primary (pile and retaining wall) and secondary (grouting) reinforcement stage. For the primary reinforced stage, the FOS is 1.06 calculated by the Shear Strength Reduction Method embedded in UDEC. In addition, the lateral displacement difference around the piles was chosen to explain the phenomenon that the crack emerged behind the piles of the third step. The shear strain contours demonstrate the sliding surface location which is the maximum shear strain area. In fact, it was the weakest layer of the slope. The failure mechanism of this slope is such that the first two layers slid along the weakest layer, i.e., the peat layer. Alongside, the failure time of slope was predicted applying the SLO method while using the monitoring data of the tertiary-like slope movement. The results show that without the second reinforcement scheme, the slope would have failed between 22nd July 2006 and 1st August 2006. The small FOS, failure time prediction results, monitoring data, and site damage phenomenon all show that the slope is unstable at this primary stage. For the second reinforced stage, the porous steel-tube bored grouting scheme was applied twice. When the parameters of the first three layers were increased by strengthening through grouting, the updated FOS increased to 1.42. Interpreting the final monitoring data and numerical simulations, two conclusions are deduced. One that the displacement rate in the rainy season was obviously higher than in other seasons and the water table has a great influence on the value of FOS. Secondly, the deformation of the slope began to converge and the slope is

considered stable keeping in view the new FOS and the supporting monitoring data.

The SRM is a good option for obtaining FOS for this kind of slopes whose failure mechanism is such that several upper layers slide along the weakest layer. The SLO method is an innovative way of quantitative analysis of monitoring displacement data for slope failure time prediction. The authors highly recommend the system method considering FOS, failure time prediction results, monitoring data, and the damage phenomenon to conduct slope stability analysis and reinforcement effect evaluation. Future research is expected to compare more engineering practices for further validating this system method.

Data Availability

The data used to support the findings of this study are available from the corresponding author upon request.

Conflicts of Interest

The authors declare that there is no conflict of interest regarding the publication of this paper.

Authors' Contributions

Wei Chen is responsible for the methodology, conceptualization, and writing of the original draft. Dongbai Li helped in data curation. Ting Ma contributed to the supervision and resources. Helin Fu contributed resources. Yanpeng Du wrote, reviewed, and edited the manuscript.

Acknowledgments

This work was supported by the Research Foundation of Education Bureau of Hunan Province (19K100).

References

- [1] W. Y. Chen, D. S. Jeng, W. Chen, G. X. Chen, and H. Y. Zhao, "Seismic-induced dynamic responses in a poro-elastic seabed: solutions of different formulations," *Soil Dynamics and Earthquake Engineering*, vol. 131, p. 106021, 2020.
- [2] H. W. Huang, S. C. Wen, J. Zhang, F. Y. Chen, J. R. Martin, and H. Wang, "Reliability analysis of slope stability under seismic

- condition during a given exposure time,” *Landslides*, vol. 15, no. 11, pp. 2303–2313, 2018.
- [3] G. P. Tang, J. S. Huang, D. C. Sheng, and S. W. Sloan, “Stability analysis of unsaturated soil slopes under random rainfall patterns,” *Engineering Geology*, vol. 245, pp. 322–332, 2018.
 - [4] K. Terzaghi and R. B. Peck, *Soil mechanics in engineering practice*, John Wiley and Sons, Inc., New York, 2nd edition edition, 1967.
 - [5] X. Liu, D. Q. Li, Z. J. Cao, and Y. Wang, “Adaptive Monte Carlo simulation method for system reliability analysis of slope stability based on limit equilibrium methods,” *Engineering Geology*, vol. 264, p. 105384, 2020.
 - [6] X. G. Wang, X. C. Lin, X. Li, P. Sun, and Y. Y. Ling, “3D slope stability analysis method based on Pan’s maximum principle,” *Landslides*, vol. 17, no. 5, pp. 1163–1176, 2020.
 - [7] D. C. Drucker and W. Prager, “Soil mechanics and plastic analysis or limit design,” *Quarterly of Applied Mathematics*, vol. 10, no. 2, pp. 157–165, 1952.
 - [8] W. F. Chen, *Limit Analysis and Soil Plasticity*, Elsevier Scientific Publishers, Amsterdam, New York, 1975.
 - [9] L. H. Zhao, S. Zuo, Y. L. Lin, L. Li, and Y. B. Zhang, “Reliability back analysis of shear strength parameters of landslide with three-dimensional upper bound limit analysis theory,” *Landslides*, vol. 13, no. 4, pp. 711–724, 2016.
 - [10] S. W. Sloan, “Lower bound limit analysis using finite elements and linear programming,” *International Journal for Numerical and Analytical Methods in Geomechanics*, vol. 12, no. 1, pp. 61–77, 1988.
 - [11] S. W. Sloan, “Upper bound limit analysis using finite elements and linear programming,” *International Journal for Numerical and Analytical Methods in Geomechanics*, vol. 13, no. 3, pp. 263–282, 1989.
 - [12] J. Kim, R. Salgado, and H. S. Yu, “Limit analysis of soil slopes subjected to pore-water pressures,” *Journal of Geotechnical and Geoenvironmental Engineering*, vol. 125, no. 1, pp. 49–58, 1999.
 - [13] O. C. Zienkiewicz, C. Humpheson, and R. W. Lewis, “Associated and nonassociated visco-plasticity and plasticity in soil mechanics,” *Geotechnique*, vol. 25, no. 4, pp. 671–689, 1975.
 - [14] I. B. Donald and S. K. Giam, “Application of the nodal displacement method to slope stability analysis,” in *Proceedings of the 5th Australia-New Zealand Conference on Geomechanics*, pp. 456–460, Sydney, Australia, 1988.
 - [15] K. Ugai and D. Leshchinsky, “Three-dimensional limit equilibrium and finite element analyses: a comparison of results,” *Soils and Foundations*, vol. 35, no. 4, pp. 1–7, 1995.
 - [16] E. M. Dawson, W. H. Roth, and A. Drescher, “Slope stability analysis by strength reduction,” *Geotechnique*, vol. 49, no. 6, pp. 835–840, 1999.
 - [17] R. E. Hammah, T. E. Yacoub, and J. H. Curran, “Investigating the performance of the shear strength reduction (SSR) method on the analysis of reinforced slopes,” in *Proceedings of the 59th Canadian Geotechnical and 7th Joint IAHC-CNC and CGS Groundwater Specialty Conferences—Sea to Sky Geotechnique*, Vancouver, Vancouver, 2006.
 - [18] Y. M. Cheng, T. Lansivaara, and W. B. Wei, “Two-dimensional slope stability analysis by limit equilibrium and strength reduction methods,” *Computers and Geotechnics*, vol. 34, no. 3, pp. 137–150, 2007.
 - [19] D. J. Varnes, “Time-deformation relations in creep to failure of Earth materials,” in *Proceedings 7th South East Asian Geotechnical Conference*, pp. 107–130, Hong Kong, 1983.
 - [20] K. Terzaghi, “Mechanism of landslides,” in *Application of geology to engineering practice (Berkey volume)*, pp. 83–123, Geological Society of America, New York, 1950.
 - [21] M. Saito, “Forecasting time of slope failure by tertiary creep,” in *Proceedings of 7th international conference on soil mechanics and foundation engineering*, pp. 677–683, Mexico, 1969.
 - [22] M. Saito, “Semi logarithmic representation for forecasting slope failure,” in *Proceedings 3rd international symposium on landslides*, pp. 321–324, New Dehli, 1980.
 - [23] Z. M. Zavodni and C. D. Broadbent, “Slope failure kinematics,” *Bulletin Canadian Institute of Mining*, vol. 73, no. 816, pp. 69–74, 1980.
 - [24] T. Fukuzono, “A new method for predicting the failure time of a slope,” in *Proceedings of 4th International Conference and Field Workshop on Landslides*, pp. 145–150, Tokyo, Japan, 1985.
 - [25] T. Fukuzono, “A simple method for predicting the failure time of slope using reciprocal of velocity,” *Technology Disaster Prevention Science Technology Agency Japan International Cooperation Agency*, vol. 13, no. 1989, pp. 111–128, 1989.
 - [26] B. Voight, “A method for prediction of volcanic eruptions,” *Nature*, vol. 332, no. 6160, pp. 125–130, 1988.
 - [27] A. Mufundirwa, Y. Fujii, and J. Kodama, “A new practical method for prediction of geomechanical failure-time,” *International Journal of Rock Mechanics and Mining Sciences*, vol. 47, no. 7, pp. 1079–1090, 2010.
 - [28] Itasca Consulting Group, Inc, *UDEC-Universal Distinct Element Code, Version 5*, ICG, Mineapolis, 2011.
 - [29] K. Donovan, W. G. Pariseau, and M. Cepak, “Finite element approach to cable bolting in steeply dipping VCR stopes,” in *Geomechanics Application in Underground Hardrock Mining*, pp. 65–90, Society of Mining Engineers, New York, 1984.
 - [30] X. P. Zhang, S. J. Wang, Y. M. Wang, and G. Y. Han, “Conversion of anti-sliding piles into 2-dimensional discrete element simulation,” *Chinese Journal of Geotechnical Engineering*, vol. 32, no. 2, pp. 271–278, 2010.
 - [31] K. Fukui and S. Okubo, “Life expectancy and tertiary creep for rock,” in *Proceedings of the fall meeting mining and materials processing institute of Japan*, pp. 91–94, Japan, 1997.
 - [32] N. D. Rose and O. Hungr, “Forecasting potential rock slope failure in open pit mines using the inverse-velocity method,” *International Journal of Rock Mechanics and Mining Sciences*, vol. 44, no. 2, pp. 308–320, 2007.
 - [33] P. A. Witherspoon, J. S. Wang, K. Iwai, and J. E. Gale, “Validity of cubic law for fluid flow in a deformable rock fracture,” *Water Resources Research*, vol. 16, no. 6, pp. 1016–1024, 1980.
 - [34] K. Terzaghi, “The shear resistance of saturated soils,” in *Proceedings for the 1st. International Conference on Soil Mechanics and Foundation Engineering*, pp. 54–56, Cambridge, MA, 1936.

Research Article

Hydrogeochemical Evolution and Control Mechanism of Underground Multiaquifer System in Coal Mine Area

Qiding Ju ^{1,2}, Yu Liu ¹, Youbiao Hu,² Yuquan Wang,³ Qimeng Liu,² and Zitao Wang²

¹State Key Laboratory of Mining Response and Disaster Prevention and Control in Deep Coal Mines, Anhui University of Science and Technology, Huainan 232001, China

²School of Earth and Environment, Anhui University of Science and Technology, Huainan 232001, China

³Wanbei Coal-electricity Group Company, Suzhou 234001, China

Correspondence should be addressed to Yu Liu; yliu@aust.edu.cn

Received 26 August 2020; Revised 29 September 2020; Accepted 16 October 2020; Published 2 November 2020

Academic Editor: Bo Li

Copyright © 2020 Qiding Ju et al. This is an open access article distributed under the Creative Commons Attribution License, which permits unrestricted use, distribution, and reproduction in any medium, provided the original work is properly cited.

Mining activities interfere into the natural groundwater chemical environment, which may lead to hydrogeochemical changes of aquifers and mine water inrush disasters. The study of hydrogeochemical evolution processes of underground aquifers is helpful to the prevention and control of mine water inrush. The results show that the study area is mainly impacted by four hydrogeochemical processes: dissolution, cation exchange, desulfurization and reduction, and pyrite oxidation. The Cenozoic aquifers are dominated by carbonate dissolution and desulfurization. The Permian aquifers are impacted mainly by cation exchange and sulfate dissolution, followed by pyrite oxidation. The Carboniferous aquifers are mainly impacted by dissolving sulfate, followed by pyrite oxidation and cation exchange. The hydrogeochemical evolution of the aquifers was controlled by mining activities and tectonic changes, and a certain regularity in space. For the Cenozoic aquifers, sulfate dissolution and cation exchange increase from west to east, and desulfurization weakens. For the Permian aquifers, cation exchange and sulfate dissolution are stronger near synclines and faults, pyrite oxidation is enhanced, and desulfurization decreases from the middle to the east of the mining area. For the Carboniferous aquifers, there is a higher dissolution of rock salt, pyrite oxidation, and cation exchange from west to east, and the desulfurization effect weakens.

1. Introduction

Human activities have led to different deterioration trends in the global groundwater environment; this trend is developing in a negative direction [1–3]. The mine water inrush and water contamination are two common groundwater problems in mining areas of China. After mining, the chemical environment of the groundwater becomes complex, forming a multiaquifer system with different hydrogeochemical characteristics. This leads to a complex groundwater flow field and chemical field. As the aquifer connects with the structure, different aquifers connect to form a water filling channel, which causes water inrush accidents and water pollution [4, 5]. This highlights the importance of studying water quality types and the hydrogeochemical evolution characteristics of underground aquifers, which can provide

the basis for the safe production of coal mines and the full utilization of water resources.

Variations in conventional ion levels in groundwater represent hydrogeochemical evolution processes. Hydrogeochemical analysis methods used to determine the evolution of groundwater chemical composition include: hydrogeochemical maps, multivariate statistical analysis, and GIS spatial analysis [6–8]. Huang et al. [9, 10] used a Piper diagram, Gibbs diagram, and Ion proportion coefficient diagram to analyse the chemical characteristics of groundwater. Multivariate statistical analyses were used to study the hydrogeochemical evolution process mainly include factor analysis, principal component analysis, and cluster analysis. Comprehensive consideration time and space indicators, Chen et al. [11] successfully revealed the chemical characteristics and spatiotemporal evolution mechanism of groundwater by

principal component analysis. Zhang et al. [12] studied the relationship between the hydrogeochemical characteristics of groundwater and the multilayer aquifer in a Karst subsided column mine, by combining a chemical analysis with a principal component analysis. Gomo et al. [13] used the traditional hydrochemical analysis method to describe the underground hydrogeochemical process of a submerged mine and analysed the groundwater chemical types and water quality evolution. Sunkari et al. [14] used factor analysis to transform original ion concentration data into a normal distribution, effectively explained the sourcing of groundwater ions. In recent years, based on GIS spatial interpolation analysis, some researchers studied the hydrochemical evolution process of underground aquifer, drew the hydrogeochemical action spatial map, and quantitatively described the hydrochemical spatial evolution process and control factors [15, 16]. In summary, hydrochemical analysis, factor analysis, and GIS spatial analysis can be combined to describe the hydrogeochemical evolution process and its controlling factors; this provides important information about the hydrogeological background.

The Hengyuan coal mine, operated by the Wanbei Coal Electricity Group, has complicated hydrogeological conditions. The mine is threatened by high-pressure limestone water and sandstone water from the coal seam roof and floor and poses potential safety hazards, such as the collapse of the karst column and water disasters in the loose layers. In this paper, factor analysis is used to name the main hydrogeochemical processes clearly and accurately, and then, it is combined with traditional hydrochemical methods. Finally, GIS spatial analysis reveals the hydrochemical evolution process of multiaquifer system. The study focused on identifying the hydrogeological and geochemical characteristics and control factors of water-filled aquifers. It provides a scientific basis for accurately identifying potential water inrush hazard sources and a basis for the rational protection and utilization of water resources. In addition, this method has a certain guiding significance for the concealed coalfields in North China.

2. Materials and Methods

2.1. Study Area and Hydrogeological Setting. The Hengyuan coal mine is located in Huaibei City in north of Anhui Province, China (Figure 1(a)). The geographical coordinates are $116^{\circ}36'04''$ - $116^{\circ}43'22''$ E and $33^{\circ}54'30''$ - $34^{\circ}0'59''$ N. The terrain in the mining area is flat, and the natural surface elevation is approximately 30 to 36 m, with a tendency to incline from the northwest to southeast. There is no bedrock outcrop; instead, the area is covered by an extremely thick Cenozoic loose layer. The climate in this area is mild, exhibiting a north temperate monsoon area marine continental climate. The annual average temperature is 16.8°C , the maximum temperature is 37°C (July 2019), and the minimum temperature is -7°C (January 2019). The average annual rainfall is 1067 mm, and the rainfall is mainly concentrated in July and August.

The strata in this area are rarely exposed and are mostly covered by Quaternary alluvial and proluvial plain materials

(Figure 1(b)). Drilling records show that the strata, from old to new, are Ordovician (O_{1+2}), Carboniferous (C_{2+3}), Permian (P), Tertiary (N), and Quaternary (Q). The coal-bearing strata in the Hengyuan coal mine include the lower Permian Shanxi Formation and Lower Shihezi Formation. There is no minable coal seam in upper Shihezi Formation, so it was not studied. The coal-bearing strata are 343.20 m thick and include eight coal seams (formations) and 2-17 coal seams. The total thickness of the coal seam is 5.52 m. The average total thickness of the mineable or partially mineable coal seam is 4.82 m, accounting for 87.3% of the total thickness of the coal seam. For all the seams, 4 and 6 coal seams are the main mineable coal seams, with an average total thickness of 4.48 m, accounting for 81.2% of the total thickness of the mineable coal seams.

The Cenozoic unconsolidated aquifer can be divided into three aquifers groups from top to bottom. The Cenozoic bottom aquifer forms a “skylight,” due to the lack of aquiclude in local areas, which directly cover the coal-bearing strata. They may also become the water supply source into the Permian aquifer. The main source of recharge is the regional interlayer runoff; the lithology of the Permian aquifer is composed of sandstone, mudstone, siltstone, and coal seam, with mostly mudstone and siltstone. The Permian aquifer is approximately 240 m thick, with a buried depth of approximately 500 m. From the top to the bottom of the mine, the location and degree of fractures development in the main mining coal seams are divided across the fifth aquifer, the sixth aquifer, the seventh aquifer, and the eighth aquifer.

According to water level observations, the water level in 12 Carboniferous aquifer observation holes had dropped to -146.14 m by the end of 2006. The Carboniferous aquifer is the water supply source for coal seam mining and is one of the hidden dangers, as water may fill the 6 coal seams. The lithology of the Ordovician limestone karst fissure aquifer is light grey thick layered limestone, with different regular grey and light grey white stripes, and local dolomite. It is pure and brittle with a microcrystalline structure and high angle fractures. Under normal conditions, no direct water fills the mine pit. However, it is possible that a water inrush could occur, with Ordovician limestone water directly entering the mine pit. This could occur when the shaft and roadway engineering encounter a water-conducting fault or water flowing subsided column.

2.2. Methods. A total of 74 water samples were collected between January and July 2018 in the Hengyuan Coal Mine area. The samples included 9 samples from the Cenozoic aquifers, 35 samples from the Permian aquifers, and 30 samples from the carboniferous aquifers (Figure 1).

Before sampling, each clean 550 mL polypropylene bottle and cap was rinsed with water 3-5 times [17-19]. Each water sample was collected in a bottle, leaving a 5-10 ml space at the top of the bottle. The temperature and pH were maintained at stable levels after the water samples were collected; a previously calibrated Hanna portable pH meter was used to measure all the parameters within five minutes. The water samples were put through a $0.45\ \mu\text{m}$ field filtering membrane, with each water sample divided into three bottles,

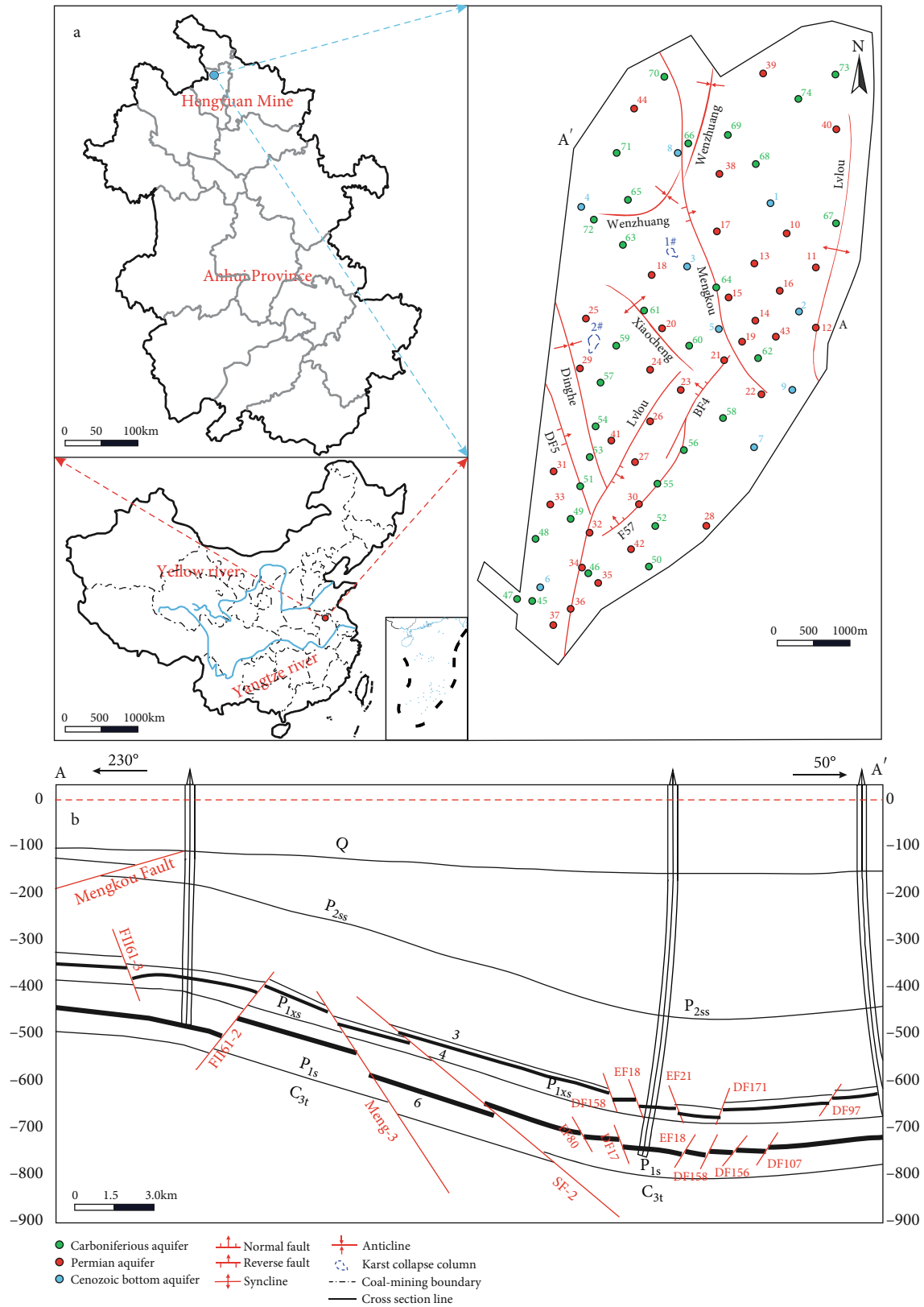


FIGURE 1: The map of the Hengyuan coal mine area, with the distribution of faults, folds, sampling sites, and cross section of the coal mine along line A-A'.

TABLE 1: Sample indexes-descriptive statistics.

Parameters	The Cenozoic aquifer				The Permian aquifer				The carboniferous aquifer			
	Min	Max	Mean	Skewness	Min	Max	Mean	Skewness	Min	Max	Mean	Skewness
K^+Na^+ (mg/L)	111	202.47	152.71	0.26	578.6	1550.27	1036.94	0.05	168.65	813.98	398.6	0.48
Ca^{2+} (mg/L)	79.55	124.73	99.89	0.24	1.13	63.15	25.59	0.63	2.42	447.56	202.17	0.09
Mg^{2+} (mg/L)	28.81	81.12	54.93	0.09	1.17	38.66	13.73	0.8	5.53	323.69	121.44	1.09
Cl^- (mg/L)	91.98	144.67	115.43	0.15	56.46	354.16	171.91	0.82	82.98	188.91	143.39	-0.37
SO_4^{2-} (mg/L)	207.06	417.26	283.62	1.01	833.2	2524.69	1668.09	0.45	1001.36	1770.6	1404.92	-0.16
HCO_3^- (mg/L)	279.83	541.86	419.79	-0.35	164.21	692.17	435.72	-0.14	129.91	340.89	240.28	0.29
TDS (mg/L)	899.23	1239.45	1058.24	0.22	2023.48	5005.01	3371.35	0.32	2020.85	3088.47	2534.47	0.02
PH	7.3	8.4	7.57	2.39	7.79	8.32	7.94	1.96	7.1	8.3	7.68	-0.6

two for anion analysis, and the other for standby experiment. The water samples were maintained at a low temperature to support the cation analysis. This prevented a chemical reaction [20, 21]. Eight general hydrogeochemical parameters were tested: K^+Na^+ , Ca^{2+} , Mg^{2+} , Cl^- , SO_4^{2-} , HCO_3^- , pH, and TDS. The samples for cation analysis were acidified with nitric acid to $pH \leq 2$. The tests were conducted within 24 hours after sampling at the Anhui University of Science and Technology, Quality Inspection Center. The Cl^- , SO_4^{2-} , and HCO_3^- tests were conducted using ion chromatography; and the K^+Na^+ , Ca^{2+} , and Mg^{2+} tests were conducted using inductively coupled plasma mass spectrometry. To review the reliability of test results, the anion and cation balance was calculated to confirm that any error was the standard limit of $\pm 5\%$ [22].

In this paper, the SPSS26.0 software was used to generate a descriptive statistical analysis of the data (Table 1). Then, the SPSS software was used to conduct a factor analysis on the hydrochemical data. The factor extraction method adopted a principal component analysis to reduce interference from redundant data, the main factor score equation is obtained by factor analysis, and the scores of different sampling points are obtained by substituting the variable values to equation. Finally, the contour map of the main factor score was drawn by using Surfer software. Thus, the hydrogeochemical characteristics and evolution process of each underground aquifer by spatial analysis of factor score.

3. Results and Discussion

3.1. Statistics Analysis. Table 1 shows the results of the hydrochemical statistical analysis for the samples from the Cenozoic aquifers, Permian aquifers, and carboniferous aquifers. The analysis shows that the pH value of all samples varies from 7.10 to 8.32, making the entire underground aquifer weakly alkaline. In the weakly alkaline environment, the CO_3^{2-} levels are less than 5% of the sum of HCO_3^- and CO_3^{2-} , making it unimportant to assess CO_3^{2-} levels.

The average salinity of the Cenozoic aquifers is 1058.24 mg/L. The cation concentrations in the water overall is highest for K^+Na^+ , followed in descending order by Ca^{2+} and Mg^{2+} . The anion concentrations are the highest for HCO_3^- , followed in descending order by SO_4^{2-} , and Cl^- . The mass concentration of K^+Na^+ is 1.5 times and 2.8 times

of the mass concentration of Ca^{2+} and Mg^{2+} , respectively. The mass concentration of HCO_3^- is 1.5 times and 3.6 times of SO_4^{2-} and Cl^- , respectively.

The average salinity of Permian aquifers is 3371.35 mg/L. The cation concentrations in the water overall are the same as Cenozoic aquifers, and the anion concentrations are the highest for SO_4^{2-} , followed in descending order by HCO_3^- , and Cl^- . The mass concentration of K^+Na^+ is 40.5 times and 75.5 times of the mass concentration of Ca^{2+} and Mg^{2+} , respectively. The mass concentration of SO_4^{2-} is 3.8 times and 9.7 times of HCO_3^- and Cl^- , respectively.

The average salinity of the carboniferous aquifers is 2534.47 mg/L. The cation concentrations in the water overall are the same as Cenozoic and Permian aquifers, and the anion concentrations are the same as Permian aquifers. This is consistent with the change of ion concentration in the coal measure sandstone aquifer. The mass concentration of K^+Na^+ is 1.9 and 3.3 times of the mass concentrations of Ca^{2+} and Mg^{2+} , respectively. The mass concentration of SO_4^{2-} is 5.8 and 9.8 times of HCO_3^- and Cl^- , respectively. The concentration skewness coefficient of each ionizer in the three aquifers is close to 0 and adheres to a normal stable distribution. This indicates that the distribution of ions in the aquifer is relatively stable and is less disturbed by hydrogeological conditions and other factors.

3.2. Analysis of Hydrochemical Components. The hydrochemical types and distribution of all aquifers in the study area are shown in Figure 2. The distribution of water sample drops in the Cenozoic aquifers is relatively concentrated, with alkaline metal ions Ca^{2+} and Mg^{2+} present at greater concentrations than alkali metal ions K^+Na^+ . The percentage of SO_4^{2-} exceeds 80%, and the percentage of HCO_3^- equivalent ranges from 40 to 60%. Therefore, the hydrochemical type of the quaternary aquifer is mainly the $SO_4 \cdot HCO_3 - Na \cdot Ca(Mg)$ type. The distribution of water samples in the Permian aquifers is also relatively concentrated. The percentages of Ca^{2+} and SO_4^{2-} equivalents both exceed 80%, and the percentage of Cl^- equivalent is within the range of 40-90%. This indicates that the hydrochemical type is the $SO_4 \cdot Cl - Ca$ type. The water samples in the Carboniferous aquifers are relatively dispersed, with hydrochemical types of $SO_4 \cdot Cl - Ca \cdot Mg$ or $SO_4 \cdot Cl - Na \cdot Ca(Mg)$. This overlaps with the sample drops of the Cenozoic aquifer and the Permian aquifers, indicating that the Carboniferous aquifers have

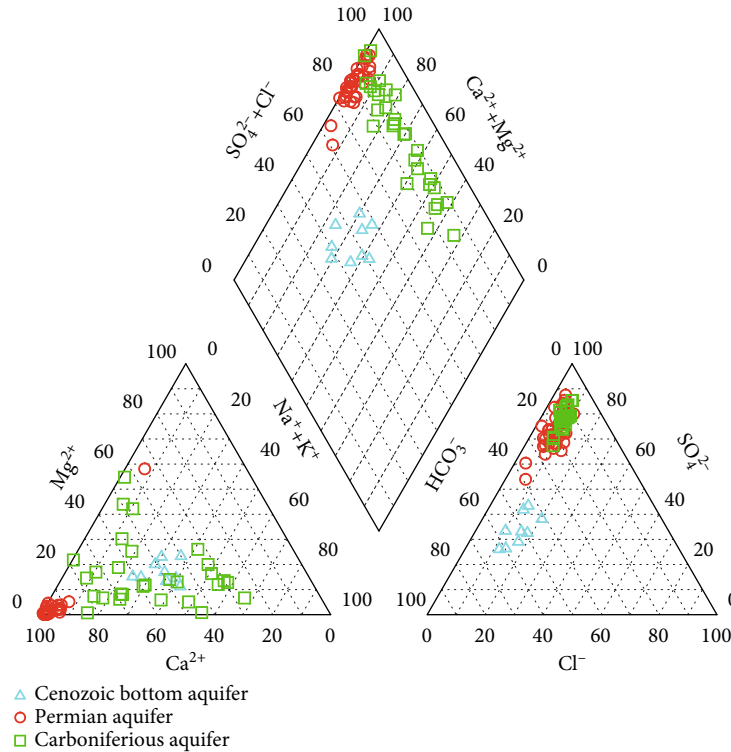


FIGURE 2: Piper diagram of groundwater samples from the Cenozoic, Permian, and Carboniferous aquifers.

similar hydrogeochemical characteristics and corresponding hydraulic relations.

The boxplot directly reflects the change of the ion levels in each aquifer [18]. Figures 3(a) and 3(d) show that the K^+Na^+ concentration in Permian aquifers is higher compared to the Carboniferous, due to the strong chloride dissolution effect in Permian aquifers. The levels in the Cenozoic aquifers are the lowest. Cl^- in the aquifer is the most stable ion in groundwater, leaving the Cl^- levels essentially unchanged. Figures 3(b) and 3(c) show that the Ca^{2+} and Mg^{2+} concentration in the Cenozoic and Carboniferous aquifers is significantly higher compared to the Permian aquifers. This is caused by the dissolution of carbonate and sulfate minerals. In Figures 3(e) and 3(f), the SO_4^{2-} concentration in the Cenozoic to Permian and Carboniferous aquifers gradually increased overall. In contrast, the HCO_3^- concentration in the water from the Permian to Carboniferous aquifers gradually decreased. This was caused by the enhanced sulfate dissolution and weakened desulfurization acid. Therefore, high HCO_3^- concentrations and low Mg^{2+} concentrations are characteristics of the three water-bearing strata. High K^+Na^+ , SO_4^{2-} , and HCO_3^- concentrations and low Ca^{2+} and Mg^{2+} concentrations are the characteristics of the Permian aquifers. However, the Carboniferous aquifers are characterized by high Ca^{2+} , Mg^{2+} , and SO_4^{2-} concentrations and low HCO_3^- concentrations. Because there are equivalent concentrations of the same ions in different aquifers, the simple comparison of changes in ion levels cannot reflect the main hydrogeochemical process and genesis.

3.3. Ion Source Analysis. There are differences in the ion combination ratio among groundwater components. As such, the source of groundwater chemical components can be determined using the ion proportion coefficient method [23]. The bubble diagram of the ion combination ratio of each aquifer is shown in Figure 4. The bubble size indicates the change in the TDS concentrations of the samples.

Cl^- is the most stable ion in groundwater, and the source of Na^+ can be characterized by analysing $\gamma(K^+ + Na^+)/\gamma(Cl^-)$ [24–27]. Figure 4(a) shows that $\gamma(K^+ + Na^+)/\gamma(Cl^-) > 1$ in all water samples from the three aquifers, and the Na^+ concentration increases with as the TDS value increases. This shows that in addition to the Na^+ produced by the dissolution of salt rock, cation exchange is also a source of Na^+ . The value of $\gamma(K^+ + Na^+)/\gamma(Cl^-)$ significantly exceeds 1 in the Permian aquifer, and the TDS value also exceeds the value in other aquifers. As such, cation exchange is stronger than in other aquifers, supporting the enrichment of Na^+ .

The source of Ca^{2+} and Mg^{2+} can be characterized by analysing $\gamma(Ca^{2+} + Mg^{2+})/[\gamma(SO_4^{2-}) + 0.5\gamma(HCO_3^-)]$ [28–30]. Figure 4(b) shows that only a small number of the Cenozoic aquifer water samples fall above the $y = x$ line, and the rest of the samples fall below that line. In particular, the values of $\gamma(Ca^{2+} + Mg^{2+})/[\gamma(SO_4^{2-}) + 0.5\gamma(HCO_3^-)]$ in the Permian aquifer is far less than 1. In addition, the TDS values in the Permian aquifer are significantly higher compared to other aquifers. It shows that cation exchange has occurred. Therefore, the dissolution of sulfate and carbonate is not the only source of Ca^{2+} and Mg^{2+} , further confirming that alternate cation adsorption is reasonable.

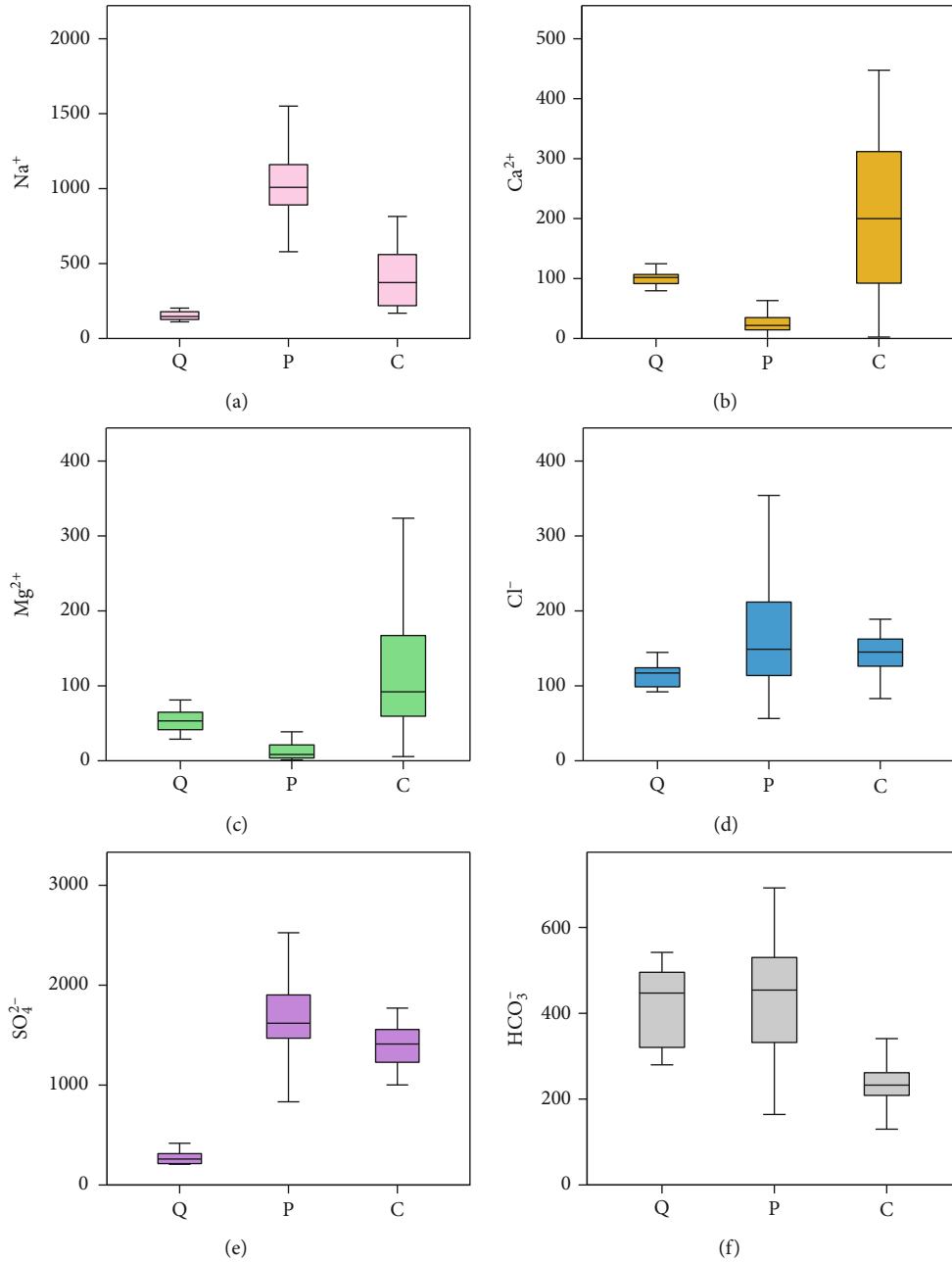


FIGURE 3: Ion box diagram.

When $\gamma(\text{Ca}^{2+} + \text{Mg}^{2+})/0.5\gamma(\text{HCO}_3^-) = 1$, it means that the Ca^{2+} , Mg^{2+} , and HCO_3^- in the groundwater are derived from carbonate dissolution [31]. The Cenozoic and Carboniferous aquifer samples fall above the $y = x$ line. The TDS values in the Carboniferous aquifer are significantly greater than in the Cenozoic aquifer. This indicates that Ca^{2+} , Mg^{2+} , and HCO_3^- are mainly derived from dissolution occurring in the Cenozoic and Carboniferous aquifer. A small number of the Permian aquifer samples are located above the line; however, the TDS values remain still higher compared to other aquifers. This indicates that the carbonate dissolution is not the only source of Ca^{2+} and Mg^{2+} and may also be caused by cation exchange in the Permian aquifer.

Most Permian aquifer samples align with the conditions of $\gamma(\text{Ca}^{2+} + \text{Mg}^{2+})/0.5\gamma(\text{HCO}_3^-) < 1$. This indicates that there are other sources of HCO_3^- , such as desulfurization.

Based on $\gamma(\text{Ca}^{2+} + \text{Mg}^{2+})/\gamma(\text{SO}_4^{2-}) = 1$, it appears that Ca^{2+} , Mg^{2+} , and SO_4^{2-} are mainly derived from the sulfate dissolution in Figure 4(d) [32]. The Ca^{2+} and Mg^{2+} concentrations are low in the Permian aquifer; however, the TDS values are higher compared to other aquifers. This is due to the cation exchange, which facilitates the enrichment of Na^+ . In the Permian and Carboniferous aquifers, the ratio of $\gamma(\text{Ca}^{2+} + \text{Mg}^{2+})/\gamma(\text{SO}_4^{2-})$ in some samples is less than 1, indicating that sulfate dissolution is not the only source of Ca^{2+} , Mg^{2+} , and SO_4^{2-} ; pyrite oxidation may be another source.

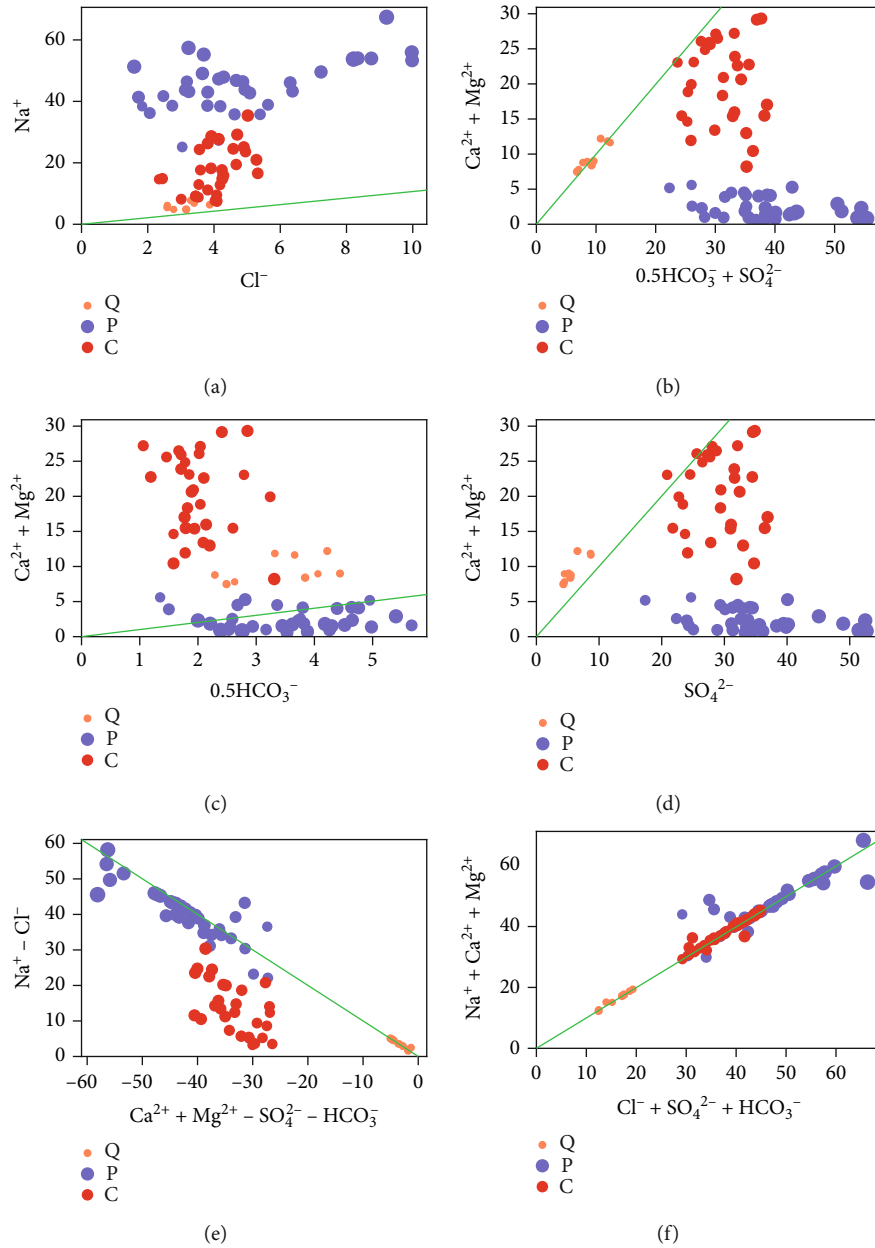


FIGURE 4: Bubble chart of ion combination of different aquifers.

The expression $\gamma(\text{Na}^+ - \text{Cl}^-)/\gamma(\text{Ca}^{2+} + \text{Mg}^{2+} - \text{SO}_4^{2-} - \text{HCO}_3^-)$ is used commonly to reveal the cation exchange rate [33]. Figure 4(e) shows that the Cenozoic and Permian aquifer samples are infinitely close to $y = -x$, and the TDS values are larger, confirming there is cation exchange. Part of the Permian aquifer is above $y = -x$, indicating there may be strong cation exchange. In Figure 4(f), each water sample is close to the $y = x$ line, which shows the mass concentration balance of the anions and cations.

The analytical results of each ion combination ratio show that Na^+ is mainly derived from salt rock dissolution and cation exchange. Ca^{2+} and Mg^{2+} are derived from sul-

fate or carbonate dissolution and cation exchange, as shown in Eq. (1). HCO_3^- and SO_4^{2-} are derived from sulfate and carbonate dissolution. Because the Permian aquifer in the study area is -350-800 m below ground surface, it is an overall reducing environment. This means that desulfurization is one of the important sources of HCO_3^- in the Permian aquifer, as shown in Eq. (2). Further, there are low sulfate levels and high pyrite levels in the Permian and Carboniferous aquifers. This indicates that the SO_4^{2-} may be derived from pyrite oxidation, as the deep aquifer is in an overall reducing environment. However, some areas are affected by coal mining activities. This leads to the area becoming a semiopen oxidizing environment,

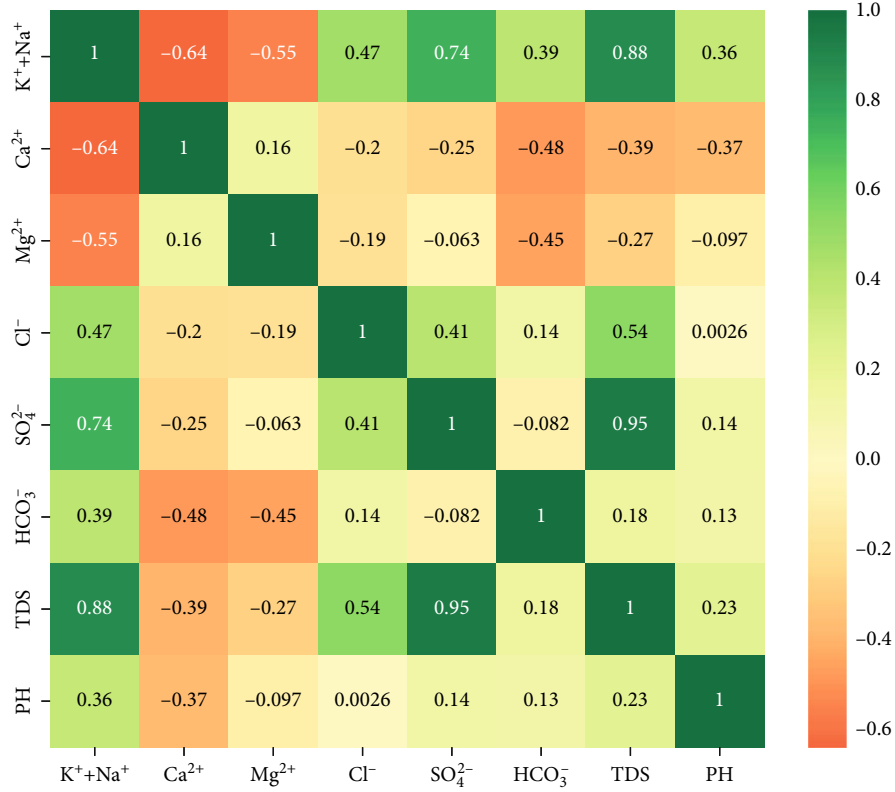
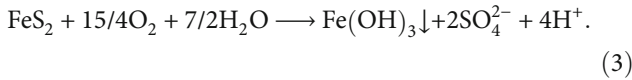
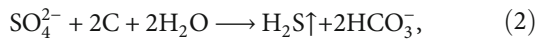
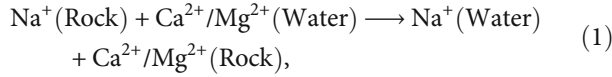


FIGURE 5: Heat map of the correlation coefficient for each parameter.

allowing CO₂ and O₂ to enter the aquifer and react with pyrite, as shown in Eq.(3).



3.4. Factor Analysis. Both the *R*-type factor analysis and principal component analysis provide approximations of the covariance matrix and dimension reduction interpretation of the data set, specifically for the positive index and standardization index automatically executed by the SPSS software [34]. The correlation between variables is determined using a correlation coefficient matrix, and the eigenvalues and eigenvectors of phase relation number matrix are generated. Principal components and factors are linearly independent, and the cumulative contribution rate, index standardization, and index standardization are used. The number of principal components and factors is determined without a loss of variables. The naming basis is the correlation coefficient of principal components, factors, and variables. The difference is that principal component analysis and factor analysis are separate from the initial factor load matrix. The principal component analysis generates the principal component coefficient matrix, principal component, and its value through the unit of the initial

factor load array vector or by dividing the corresponding eigenvalue root. The factor analysis generates the factor load matrix by rotating the initial factor load matrix and then obtaining the factor score and its value through regression. The *R*-type factor analysis has the advantage of clearly naming the main factors and enables a clear comprehensive evaluation of the causes [35–37]. The factor analysis method generally includes the following steps [38].

- (1) Firstly normalize the indicators, and then standardize the data to eliminate errors caused by large differences in values between variables
- (2) Use the SPSS software to obtain total variance explained and rotated component matrix. Total variance explained meets the contribution rate requirement, and the variables in the rotated component matrix are not lost, thereby comprehensively determining m principal factors
- (3) Calculate the factor load matrix B_m and classify the corresponding variable with the largest absolute value of the i th column of B_m into Z_i category, and then name Z_i for hydrogeochemical effects, which has high clarity
- (4) According to the factor score coefficient matrix obtained by the SPSS software, find the expression of the main factor score function: $S_{Z_i} = \omega_i X$

The correlation coefficient thermograph (Figure 5) directly describes the degree of correlation degree among

TABLE 2: Explanation of total variance.

Component	Extraction sums of squared loadings		
	Total	Variance percentage	Cumulative percentage
1	2.103	35.056	35.056
2	2.041	34.021	69.078

TABLE 3: Rotated component score matrix.

Parameters	Component	
	1	2
SO ₄ ²⁻	0.926	-0.068
Na ⁺	0.795	0.561
Cl ⁻	0.677	0.127
HCO ₃ ⁻	-0.068	0.893
Mg ²⁺	-0.116	-0.719
Ca ²⁺	-0.371	-0.625

the variables. The K⁺+Na⁺ value is positively correlated with Cl⁻, SO₄²⁻, and HCO₃⁻. This is due to the existence of rock salt dissolution. The K⁺+Na⁺ is negatively correlated with Ca²⁺ and Mg²⁺; and TDS is strongly positively correlated with K⁺ + Na⁺ and is negatively related to Ca²⁺ and Mg²⁺. This is caused by cation exchange. There is a weak negative correlation between SO₄²⁻ and HCO₃⁻, indicating that desulfurization has occurred in the aquifers.

The factor analysis method uses the principal component extraction method to generate the total variance explanation shown in Table 2. The cumulative variance contribution rate is 69.078%, and there is no variable loss. Then, two factors (Z1, Z2) are determined by the rotated component matrix in Table 3. The variance contribution rate of Z1 is 35.056%, which is characterized by a high positive loading of SO₄²⁻ and Na⁺, and a weak loading of HCO₃⁻, Ca²⁺, and Mg²⁺. This indicates the dissolution of sulfate minerals, pyrite oxidation, and cation exchange. The variance contribution rate of Z2 is 34.021%, in which Ca²⁺ and Mg²⁺ are strongly loaded. HCO₃⁻ is strongly positively loaded, and SO₄²⁻ is weakly loaded, indicating the dissolution and desulfurization of calcite and dolomite, respectively. Therefore, Z1 represents the dissolution of sulfate minerals, pyrite oxidation, and cation exchange, and Z2 represents the dissolution and desulfurization of calcite and dolomite. These are displayed using Figure 6.

Table 4 shows the factor score coefficients for the six ions of K⁺+Na⁺, Ca²⁺, Mg²⁺, Cl⁻, SO₄²⁻, and HCO₃⁻ in groundwater samples from the Hengyuan coal mine. These were used as the variables for analysis, yielding the following factor score functions:

$$S_{Z1} = 0.323x_1 - 0.081x_2 + 0.075x_3 + 0.342x_4 + 0.514x_5 - 0.208x_6, \quad (4)$$

$$S_{Z2} = 0.160x_1 - 0.278x_2 - 0.379x_3 - 0.059x_4 - 0.215x_5 + 0.511x_6. \quad (5)$$

Substituting the collected data from the 74 water samples into S_{Zi} (Eq. (4) and Eq. (5)) yields the dispersion point diagram illustrating the groundwater factors Z1-Z2 for the Hengyuan mine (Figure 7). The Cenozoic aquifers are mainly distributed in the second quadrant, indicating that calcite and dolomite experience significant dissolution with desulfidation. The Permian aquifers are mainly distributed in the first quadrant, with a partial distribution in the second quadrant. It indicates that the Permian aquifers experience the desulfidation and dissolution of calcite and dolomite and is accompanied by the dissolution of sulfate minerals, pyrite oxidation, and cation exchange. The Carboniferous aquifer samples are mainly located in the third and fourth quadrants, indicating they are mainly affected by sulfate mineral dissolution, pyrite oxidation, and cation exchange. The two Permian aquifer samples in the figure are in the range of Carboniferous aquifers, and a Carboniferous aquifer sample in the range of Permian aquifers. It indicates there may be a hydraulic connection between Permian and Carboniferous aquifers.

3.5. Hydrogeochemical Spatial Evolution Characteristics. The K⁺+Na⁺, Ca²⁺, Mg²⁺, Cl⁻, SO₄²⁻, and HCO₃⁻ values of 74 groundwater samples from the Hengyuan Coal Mine were substituted into the factor score function expression (Eq. (4), Eq. (5)). A Surfer Kriging interpolation was used to draw the load score contour map (Figures 8–10) of the principal factors Z1 and Z2. This was used to describe the water chemistry control factors of the multiaquifer system, as follows.

3.6. The Cenozoic Aquifer. Figure 8 shows that the S_{Z1} values are negative in the study area, with a uniform distribution. The S_{Z1} values range from -2.04 to -1.56. In contrast, the S_{Z2} values are positive, with a relatively uniform distribution, and the S_{Z2} values vary between 0.25 and 1. The S_{Z1} values gradually increase from west to east, and the S_{Z2} values gradually decrease. Due to the control of mining activities in the east, the Cenozoic aquifer is discharged, and the groundwater flow accelerates from west to east. This increases the dissolution and contact time of minerals and groundwater. At the same time, the aquifers are in a semioxidized environment during mining activities. In addition, the west area is controlled by structures such as the Wenzhuang syncline and the Mengkou fault, resulting in a relatively closed groundwater environment. From west to east, the sulfate dissolution and cation exchange are enhanced, while the desulfurization effect is weakened.

3.7. The Permian Aquifer. Figure 9 shows that S_{Z1} values are positive in most of the study area, with an uneven distribution. In the north, the S_{Z1} values vary from 0.2 to 2.0; in the south, they vary from 0.2 to 1.6; and in the east, they vary from -0.8 to 0.2. S_{Z2} values are positive and unevenly distributed in the study area, increasing gradually from the north and south sides to the middle. A high S_{Z1} value and a low S_{Z2} value appear near the Wenzhuang syncline. Under the action of syncline, this area is a closed

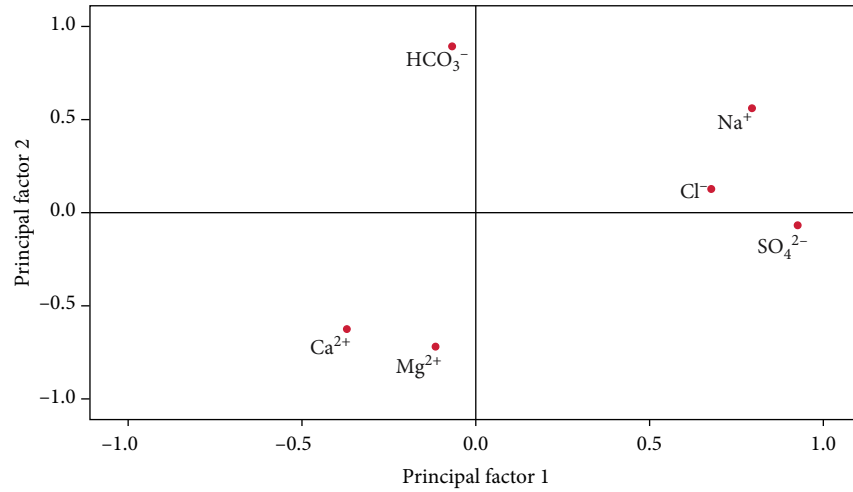


FIGURE 6: Load distribution of each parameter on the principal factor Z1–Z2.

TABLE 4: Principal factor score coefficients.

Parameters	Principal factor	
	1	2
Na ⁺	0.323	0.16
Ca ²⁺	-0.081	-0.278
Mg ²⁺	0.075	-0.379
Cl ⁻	0.342	-0.059
SO ₄ ²⁻	0.514	-0.215
HCO ₃ ⁻	-0.208	0.511

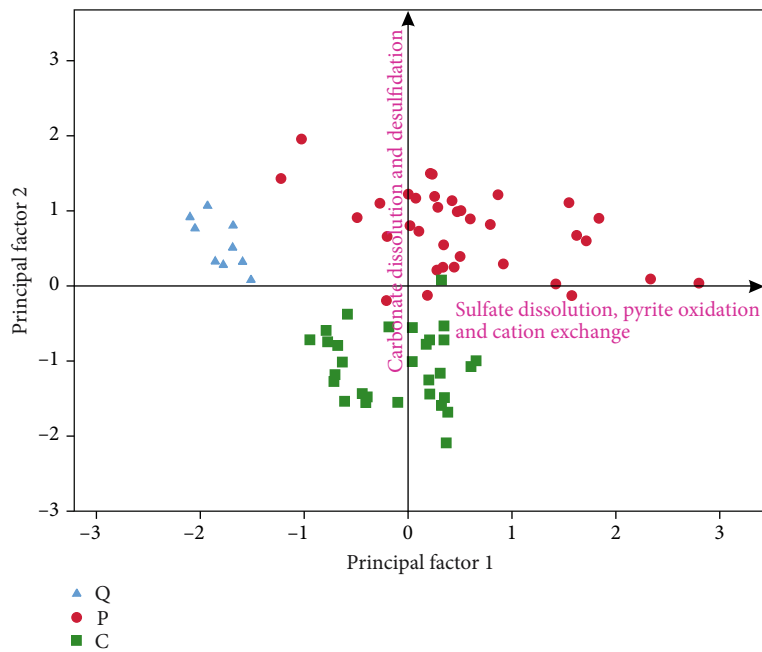


FIGURE 7: Scatter diagram with load scores from aquifer samples.

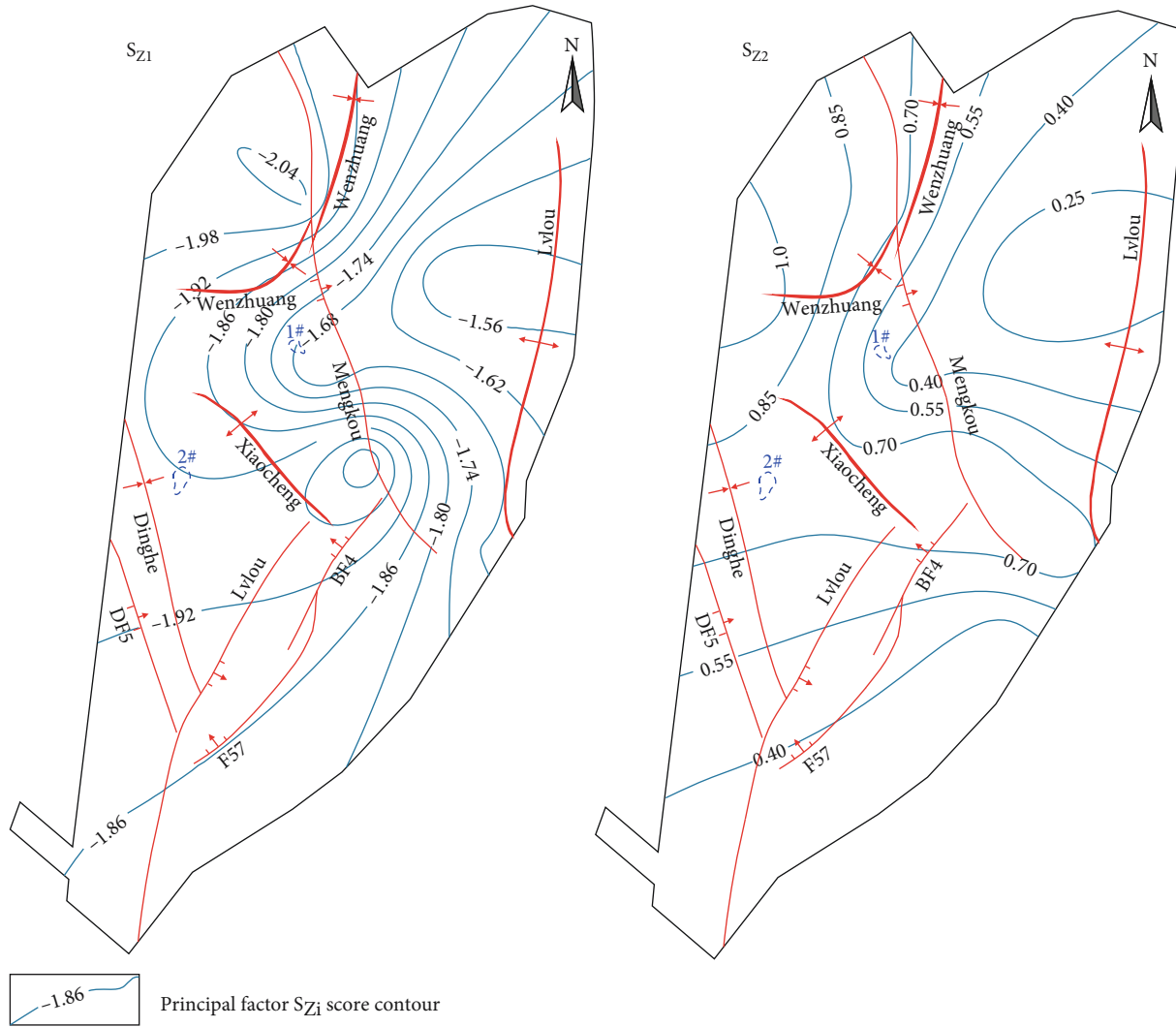


FIGURE 8: Contours of principal loading scores S_{Z1} , S_{Z2} for Cenozoic aquifer.

recharge area environment with a strong water yield. There is a long interaction time between groundwater and minerals, enhancing cation exchange and sulfate dissolution. In the area surrounded by the Lvlou fault, the BF4 fault, and the Xiaocheng anticline, the S_{Z1} value is high and the S_{Z2} value is low. The aquifers are well sealed, benefitting cation exchange and desulfurization. The S_{Z1} and S_{Z2} values are higher from the middle to east. Due to the long-term mining activities, the Permian aquifer has become a semioxidized environment in some areas. This benefits the carbonate and sulfate dissolution and the pyrite oxidation.

3.8. *The Carboniferous Aquifer.* Figure 10 shows that the S_{Z1} values in the study area are unevenly distributed; the values gradually decrease to the north between the Xiaocheng anticline and the Lulou anticline and gradually increase to the south of the Xiaocheng anticline. The S_{Z2} values are all negative. The values are low near the Mengkou fault; the highest value appears to the west of the Mengkou fault. The S_{Z2} values in the south are lower than other

areas overall and are higher at the Lvlou anticline in the east. The mining activities are mainly located in the north wing of the Xiaocheng anticline and the west wing of the Lvlou anticline. The groundwater circulation conditions at the axis of the anticline are good, enhancing the pyrite oxidation, the carbonate dissolution, sulfate dissolution, and cation exchange in the mining area. The groundwater flow near the Wenzhuang syncline is affected by the Mengkou fault, which leads to pyrite oxidation, carbonate and sulfate dissolution, and cation exchange. In contrast, the aquifers at the syncline are deeply buried, leading to increased desulfurization.

4. Conclusions

This study investigated the hydrogeochemical evolution characteristics of the complex underground multiaquifer system in Hengyuan Coal Mine in China. Traditional hydrochemical analysis methods and Q-factor analysis methods were used to analyse the collected water samples, leading to the following conclusions.

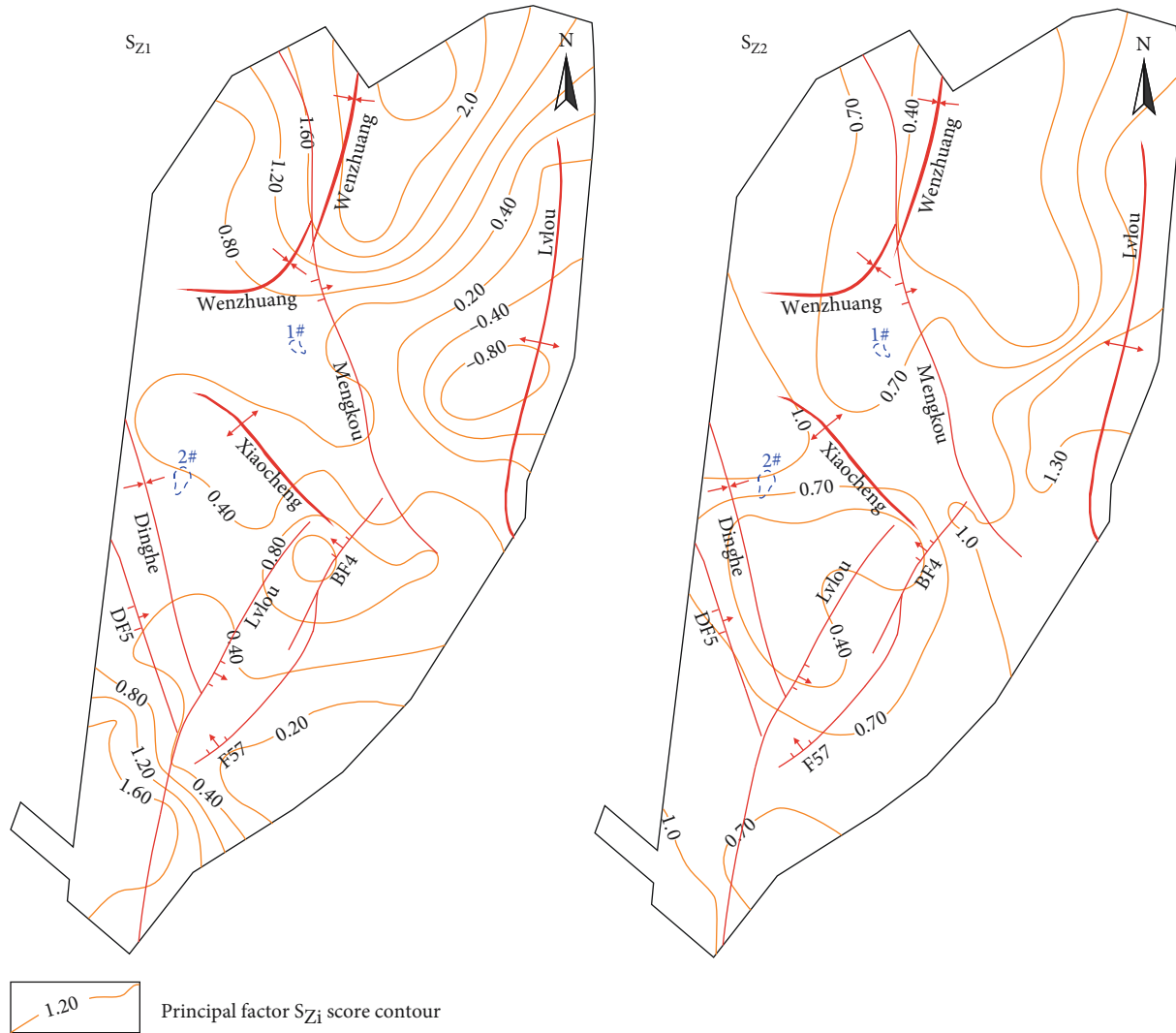


FIGURE 9: Contours of principal loading scores S_{Z1} , S_{Z2} for Permian aquifer.

- (1) The cation levels in the three aquifers were the highest for K^+Na^+ , followed in descending order by Ca^{2+} and Mg^{2+} . In the Permian and Carboniferous aquifers, SO_4^{2-} was present at the highest levels, followed by HCO_3^- and Cl^- . In the Cenozoic aquifers, HCO_3^- was the highest, followed by SO_4^{2-} and Cl^- . The overall TDS values of each aquifer were the highest for the coal, followed by the Taihui and Cenozoic. The TDS values successively decreased in the Permian, Carboniferous, and Cenozoic aquifers. The difference in ion skewness in different aquifers is due to the comprehensive reflection of different hydrogeochemical processes
- (2) The hydrogeological conditions and mining activities impact the hydrogeochemical processes of the Hengyuan coal mine. These processes mainly include carbonate and sulfate dissolution, cation exchange, desulfurization, and pyrite oxidation. Carbonate

dissolution and desulfurization are significant in the Cenozoic aquifer, and the cation exchange and pyrite oxidation in the Permian aquifers are the most significant. There is significant sulfate dissolution, cation exchange, and pyrite oxidation in the Carboniferous aquifers

- (3) The hydrogeochemical evolution process in underground aquifers is mainly controlled by mining activities, faults, and folds, and the hydrogeochemical evolution process of aquifers in the study area shows obvious zonation

Studying the chemical changes of groundwater can provide a geological basis for the accurate identification of potential water inrush sources and protection of water resources and has certain guiding significance for coal mine safety production. The chemical evolution of groundwater is a dynamic process, and water chemistry data should be collected regularly to find out the changes of groundwater in

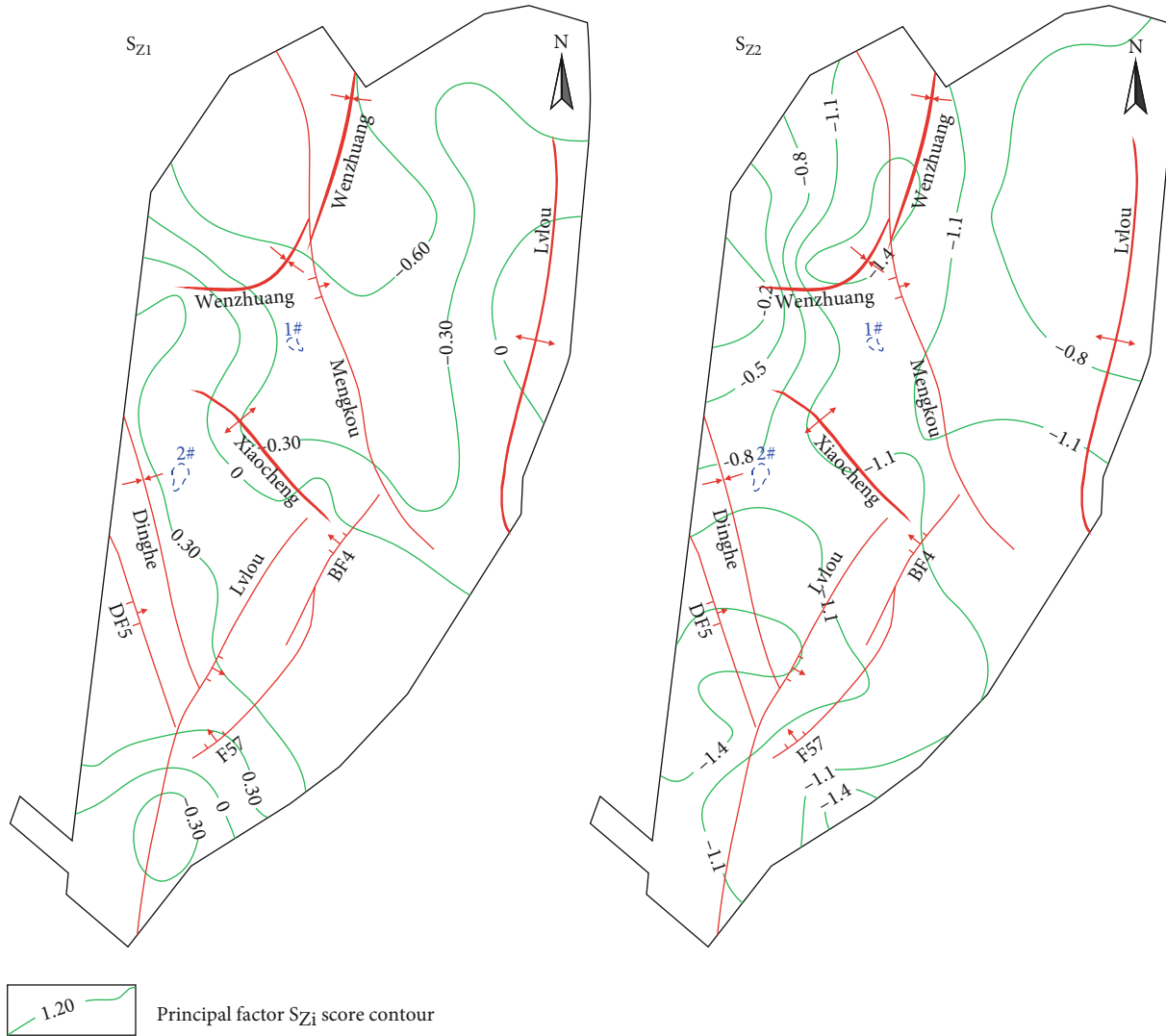


FIGURE 10: Contours of principal loading scores S_{Z1} , S_{Z2} for Carboniferous aquifer.

coal mine areas. In the future, we can study the evolution process of ground hydrology and geochemistry from the perspective of time and space.

Data Availability

The data used to support the findings of this study are available from the corresponding author upon request.

Conflicts of Interest

The authors declare that they have no conflicts of interest.

Acknowledgments

We gratefully acknowledge the support provided by the National Key Research and Development Program of China (NO.2017YFC0804101), the Natural Science Foundation of Anhui Province (NO.2008085QD191 and NO.1908085ME144), and the Independent Research fund

of The State Key Laboratory of Mining Response and Disaster Prevention and Control in Deep Coal Mines (Anhui University of Science and Technology) (NO.SKLMRDPC19ZZ06). The authors would also like to thank Dr. Huichan Chai, Dr. Shuhao Shen, and Dr. Yaoshan Bi for his valuable comments and suggestions for improvement of the manuscript.

References



- [1] Z. Li, B. Zhou, D. Teng, W. Yang, and D. Qiu, “Comprehensive evaluation method of groundwater environment in a mining area based on fuzzy set theory,” *Geosystem Engineering*, vol. 21, no. 2, pp. 103–112, 2017.
- [2] S. M. Gorelick and C. M. Zheng, “Global change and the groundwater management challenge,” *Water Resources Research*, vol. 51, no. 5, pp. 3031–3051, 2015.
- [3] D. A. Tran, M. Tsujimura, L. P. Vo, V. T. Nguyen, D. Kambuku, and T. D. Dang, “Hydrogeochemical characteristics of a multi-layered coastal aquifer system in the Mekong

- Delta, Vietnam,” *Environmental Geochemistry and Health*, vol. 42, no. 2, pp. 661–680, 2020.
- [4] H. Yin, H. Zhao, D. Xie, S. Sang, Y. Shi, and M. Tian, “Mechanism of mine water inrush from overlying porous aquifer in Quaternary: a case study in Xinhe Coal Mine of Shandong Province, China,” *Arabian Journal of Geosciences*, vol. 12, no. 5, 2019.
- [5] P. Li, J. Wu, R. Tian et al., “Geochemistry, hydraulic connectivity and quality appraisal of multilayered groundwater in the Hongdunzi Coal Mine Northwest China,” *Mine Water and the Environment*, vol. 37, no. 2, pp. 222–237, 2018.
- [6] Y. Xiao, J. Shao, Y. Cui, G. Zhang, and Q. Zhang, “Groundwater circulation and hydrogeochemical evolution in Nomhon of Qaidam Basin, northwest China,” *Journal of Earth System Science*, vol. 126, no. 2, 2017.
- [7] V. Cloutier, R. Lefebvre, R. Therrien, and M. M. Savard, “Multivariate statistical analysis of geochemical data as indicative of the hydrogeochemical evolution of groundwater in a sedimentary rock aquifer system,” *Journal of Hydrology*, vol. 353, no. 3–4, pp. 294–313, 2008.
- [8] C. Güler, M. A. Kurt, M. Alpaslan, and C. Akbulut, “Assessment of the impact of anthropogenic activities on the groundwater hydrology and chemistry in Tarsus coastal plain (Mersin, SE Turkey) using fuzzy clustering, multivariate statistics and GIS techniques,” *Journal of Hydrology*, vol. 414–415, pp. 435–451, 2012.
- [9] P. Huang and J. Chen, “Recharge sources and hydrogeochemical evolution of groundwater in the coal-mining district of Jiaozuo, China,” *Hydrogeology Journal*, vol. 20, no. 4, pp. 739–754, 2012.
- [10] W. G. Cao, H. F. Yang, C. L. Liu, Y. J. Li, and H. Bai, “Hydrogeochemical characteristics and evolution of the aquifer systems of Gonghe Basin, Northern China,” *Geoscience Frontiers*, vol. 9, no. 3, pp. 907–916, 2018.
- [11] L. Chen, W. Xie, X. Feng, N. Zhang, and X. Yin, “Formation of hydrochemical composition and spatio-temporal evolution mechanism under mining-induced disturbance in the Linhuan coal-mining district,” *Arabian Journal of Geosciences*, vol. 10, no. 3, 2017.
- [12] H. Zhang, G. Xu, X. Chen et al., “Groundwater hydrogeochemical processes and the connectivity of multilayer aquifers in a coal mine with karst collapse columns,” *Mine Water and the Environment*, vol. 39, no. 2, pp. 356–368, 2020.
- [13] M. Gomo and D. Vermeulen, “Hydrogeochemical characteristics of a flooded underground coal mine groundwater system,” *Journal of African Earth Sciences*, vol. 92, pp. 68–75, 2014.
- [14] E. D. Sunkari, M. Abu, M. S. Zango, and A. M. Lomoro Wani, “Hydrogeochemical characterization and assessment of groundwater quality in the Kwahu-Bombouaka Group of the Voltaian Supergroup, Ghana,” *Journal of African Earth Sciences*, vol. 169, p. 103899, 2020.
- [15] E. D. Sunkari and M. Abu, “Hydrochemistry with special reference to fluoride contamination in groundwater of the Bongo district Upper East Region, Ghana,” *Sustainable Water Resources Management*, vol. 5, no. 4, pp. 1803–1814, 2019.
- [16] E. D. Sunkari, M. S. Zango, and H. M. Korboe, “Comparative analysis of fluoride concentrations in groundwaters in northern and southern Ghana: implications for the contaminant sources,” *Earth Systems and Environment*, vol. 2, no. 1, pp. 103–117, 2018.
- [17] P. Huang, Z. Yang, X. Wang, and F. Ding, “Research on Piper-PCA-Bayes-LOOCV discrimination model of water inrush source in mines,” *Arabian Journal of Geosciences*, vol. 12, no. 11, 2019.
- [18] X. Guo, R. Zuo, J. Wang et al., “Hydrogeochemical evolution of interaction between surface water and groundwater affected by exploitation,” *Groundwater*, vol. 57, no. 3, pp. 430–442, 2018.
- [19] H. Zhang, H. Xing, D. Yao, L. Liu, D. Xue, and F. Guo, “The multiple logistic regression recognition model for mine water inrush source based on cluster analysis,” *Environmental Earth Sciences*, vol. 78, no. 20, 2019.
- [20] H. Zhang, G. Xu, X. Chen, J. Wei, S. Yu, and T. Yang, “Hydrogeochemical characteristics and groundwater inrush source identification for a multi-aquifer system in a coal mine,” *Acta Geologica Sinica-English Edition*, vol. 93, no. 6, pp. 1922–1932, 2019.
- [21] X. Zhang, X. Li, and X. Gao, “Hydrochemistry and coal mining activity induced karst water quality degradation in the Niangziguan karst water system China,” *Environmental Science and Pollution Research*, vol. 23, no. 7, pp. 6286–6299, 2016.
- [22] H. Zhang, G. Xu, X. Chen, and A. Mabaire, “Hydrogeochemical evolution of multilayer aquifers in a massive coalfield,” *Environmental Earth Sciences*, vol. 78, no. 24, 2019.
- [23] K. A. R. Kpegli, A. Alassane, R. Trabelsi et al., “Geochemical processes in Kandi Basin, Benin, West Africa: a combined hydrochemistry and stable isotopes approach,” *Quaternary International*, vol. 369, pp. 99–109, 2015.
- [24] P. Li, J. Wu, H. Qian et al., “Hydrogeochemical characterization of groundwater in and around a wastewater irrigated forest in the southeastern edge of the Tengger Desert, Northwest China,” *Exposure and Health*, vol. 8, no. 3, pp. 331–348, 2016.
- [25] M. Meybeck, “Global chemical weathering of surficial rocks estimated from river dissolved loads,” *American Journal of Science*, vol. 287, no. 5, pp. 401–428, 1987.
- [26] I. Farid, R. Trabelsi, K. Zouari, and R. Beji, “Geochemical and isotopic study of surface and groundwaters in Ain Bou Mourra basin, central Tunisia,” *Quaternary International*, vol. 303, pp. 210–227, 2013.
- [27] Z. Liang, J. Chen, T. Jiang et al., “Identification of the dominant hydrogeochemical processes and characterization of potential contaminants in groundwater in Qingyuan, China, by multivariate statistical analysis,” *RSC Advances*, vol. 8, no. 58, pp. 33243–33255, 2018.
- [28] P. Huang and S. Han, “Study of multi-aquifer groundwater interaction in a coal mining area in China using stable isotopes and major-ion chemical data,” *Environmental Earth Sciences*, vol. 76, no. 1, pp. 2–10, 2017.
- [29] P. Li, X. He, Y. Li, and G. Xiang, “Occurrence and health implication of fluoride in groundwater of loess aquifer in the Chinese loess plateau: a case study of Tongchuan, Northwest China,” *Exposure and Health*, vol. 11, no. 2, pp. 95–107, 2019.
- [30] J. Qian, Y. Tong, L. Ma, W. Zhao, R. Zhang, and X. He, “Hydro-chemical characteristics and groundwater source identification of a multiple aquifer system in a coal mine,” *Mine Water and the Environment*, vol. 37, no. 3, pp. 528–540, 2018.
- [31] L. W. Chen, D. Q. Xu, X. X. Yin, W. P. Xie, and W. Zeng, “Analysis on hydrochemistry and its control factors in the concealed coal mining area in North China: a case study of dominant inrush aquifers in Suxian mining area,” *Journal of China Coal Society*, vol. 4, no. 42, pp. 996–1004, 2017.

- [32] K. Schacht and B. Marschner, "Treated wastewater irrigation effects on soil hydraulic conductivity and aggregate stability of loamy soils in Israel," *Journal of Hydrology and Hydromechanics*, vol. 63, no. 1, pp. 47–54, 2015.
- [33] P. Li, J. Wu, and H. Qian, "Hydrochemical appraisal of groundwater quality for drinking and irrigation purposes and the major influencing factors: a case study in and around Hua County, China," *Arabian Journal of Geosciences*, vol. 9, no. 1, p. 15, 2016.
- [34] S. Jung and S. Seo, "A comparative study on factor recovery of principal component analysis and common factor analysis," *Korean Journal of Applied Statistics*, vol. 26, no. 6, pp. 933–942, 2013.
- [35] Z. Hoseinzade and A. R. Mokhtari, "A comparison study on detection of key geochemical variables and factors through three different types of factor analysis," *Journal of African Earth Sciences*, vol. 134, pp. 557–563, 2017.
- [36] J. H. Lee, J. H. Yoon, J. Y. Cheong, H. Jung, and S. G. Kim, "Hydrogeochemical evaluation of crystalline bedrock groundwater in a coastal area using principal component analysis," *Journal of Soil and Groundwater Environment*, vol. 22, no. 3, pp. 10–17, 2017.
- [37] A. Dinno, "Implementing Horn's parallel analysis for principal component analysis and factor analysis," *The Stata Journal: Promoting communications on statistics and Stata*, vol. 9, no. 2, pp. 291–298, 2018.
- [38] R. Aparecida Mendonça Marques, R. Bruno Dutra Pereira, R. Santana Peruchi, L. Cardoso Brandão, J. Roberto Ferreira, and J. Paulo Davim, "Multivariate GR&R through factor analysis," *Measurement*, vol. 151, article 107107, 2020.

Research Article

Hydromechanical Coupling Characteristics of the Fractured Sandstone under Cyclic Loading-Unloading

Tong Zhang ^{1,2,3} Yang Liu ^{1,2} Ke Yang^{1,2,3} Ming Tang^{1,2} Xiang Yu^{1,2} and Fei Yu^{1,2}

¹State Key Laboratory of Mining Response and Disaster Prevention and Control in Deep Coal Mines, Anhui University of Science & Technology, Huainan, Anhui 232001, China

²School of Mining and Safety Engineering, Anhui University of Science & Technology, Anhui 232001, China

³Institute of Energy, Hefei Comprehensive National Science Center, Anhui, Hefei 230031, China

Correspondence should be addressed to Yang Liu; 447253123@qq.com

Received 27 August 2020; Revised 15 September 2020; Accepted 24 September 2020; Published 31 October 2020

Academic Editor: Zhengyang Song

Copyright © 2020 Tong Zhang et al. This is an open access article distributed under the Creative Commons Attribution License, which permits unrestricted use, distribution, and reproduction in any medium, provided the original work is properly cited.

The mechanical and hydraulic properties of rock mass play a crucial role in underground engineering. To study the effect of hydraulic pressure, confining pressure, and axial cyclic loading-unloading on variation of the deformation and permeability in fractured rock mass, the coupling triaxial experiment of sandstone was conducted. The concept of permeability recovery rate (PRR) and permeability enhancement reduction rate (PERR) was proposed to characterize the change in permeability. The results show that the permeability of fractured sandstone quadratically varies with the change of hydraulic pressure and confining stress. In detail, the permeability decreases with the decrease of hydraulic pressure and increases with the decrease of confining stress, respectively. Compared with the single-fracture permeability, the double-fracture permeability is more sensitive to the change of hydraulic pressure. Furthermore, the permeability of fractured sandstone is more dependent on the hydraulic pressure than the confining stress. With the performance of axial cyclic loading-unloading, the permeability spirals down, and both the axial and radial residual strains quadratically evolve. Following the first axial cyclic loading-unloading, an obvious deformation memory phenomenon characterized by a parallelogram shape in axial stress-strain curves was observed for the sandstone. The cumulative PRR of 85%-95% was maintained in double-fracture sandstone. On the contrary, a fluctuation of cumulative PRR characterized by “V shape” was observed for single-fracture sandstone. The enhancement effect of axial cyclic loading on the permeability was characterized by the decrease of PERR for double-fracture sandstone and increase of PERR with a greater gradient for single-fracture sandstone.

1. Introduction

Understanding the mechanical and hydraulic properties of rock mass is critical for the safety of underground engineering, such as deep tunnel engineering [1], geothermal extraction [2–5], radioactive waste treatment [6–8], CO₂ geological storage [9–11], deep coal mining [12, 13], and underground reservoir [14]. The fluid flow mainly occurred in the strata comprised of plenty of natural and human activity-induced fractures and was easily influenced by the variable high stress [15]. To meet the widespread utilization of energy resources, underground mining has exploited into the deeper crust [16]. Therefore, recent research in geo-mechanical and hydromechanical mecha-

nism of fractured rock mass extensively studied in the deep underground activity.

The hydraulic conductivity as a vital index for fractured rock mass with the hydromechanical coupling effect has been extensively investigated using theoretical analysis, field and laboratory measurements, and numerical simulation [17]. In fractured rock mass, the deformation in the rock matrix and fracture caused by the effect of hydromechanical coupling also significantly affect the seepage and diffusion of fluid. Due to the high strength of the rock matrix, the deformation of fracture is more sensitive than that of rock matrix for stress-dependent deformities [18]. The equivalent continuum and discrete element algorithms have been employed in the characterization of the response of fractured rock mass to

changes in stress and hydraulic pressure [19–21]. Considerable efforts have been focused on the flow behaviors, including Darcy and non-Darcy flow, of fractured rock mass with the effect of hydromechanical coupling [22–25]. Furthermore, the study on the variation of permeability in deformable rough-walled fractures subjected to the change of fracture geometric is also performed [26, 27].

The rock mass, consist of matrix and fractures, is often subjected to mining stresses (cyclic or dynamic loads) in deep coal mining. It is important to study the effect of cyclic mining stresses on rock stratum, which would be beneficial to predict dynamic hazards in coal mines. Hence, the mechanical and seepage properties of different rocks under complicated stress conditions, especially under cyclic loading and unloading, have received extensive attention [28, 29]. For constant-amplitude cyclic loading-unloading, Chen et al. [30] investigated the deformation modulus of sandstone under different cyclic loading and found that the tangent modulus and Poisson ratio show a shape of asymmetric “X,” and the mean of unloading modulus is larger than the loading modulus under the sine wave cycle load. Fuenkajorn and Phueakphum [31] experimentally studied the deformation parameters and uniaxial compressive strength of salt rock under the effect of cycle loading and unloading. Liu and He [32, 33] researched the residual axial and volumetric strain characteristics with variable confining stress and frequency and described the degradation process of sandstone with damage variable under cycle loading-unloading. Liu et al. [34] experimentally investigated the permeability variation of fractured sandstone under confining stress cyclic loading. For cycle loading-unloading at different stress levels or tiered cyclic loading-unloading, Liu et al. [35] carried out the different stress level cyclic loading experiments to realize the damage evolution of salt rock and established a formula to describe the evolution of damage. Zhao et al. [36] studied the deformation and permeability of sandstone with cycle loading and unloading of different unloading rates. With the increase of cycle times, the shape of permeability curves is ∞ type. The relationship between the variation of axial strain, unloading rate, and loading stress can be described with a power function. Jiang et al. [37] experimentally studied the evolution of permeability, acoustic emission, and energy dissipation of gas-containing coal under tiered cyclic loading, described the relative process by defining permeability recovery rate, damping ratio, acoustic emission energy rate and ring count rate, and developing a coal damage variable equation. Duan et al. [38] carried out the hydromechanical experiments to analyze the inherent relationship between the residual strain, permeability, acoustic emission, and energy dissipation of gas-bearing coal under the confining stress cyclic unloading-loading. The existing studies are mainly focused on intact rock samples, while there are rare reports on the evolution of deformation and permeability of fractured rocks under cyclic loading-unloading.

In this study, the hydromechanical experiment of fractured sandstone comprised of single-fracture and double-fracture is carried out. The deformation and permeability of fractured sandstone subjected to the change of hydraulic pressure, confining stress, and axial cycle loading-unloading

are investigated and quantitatively analyzed based on the permeability recovery rate (PRR) and permeability enhancement reduction rate (PERR).

2. Experimental Methods

2.1. Experiment Principle. During the experiment process, we assume that (1) the permeable water is an incompressible fluid; (2) the steady seepage under constant pressure is regarded as continuous seepage; and (3) for low permeability fractured sandstone, the seepage obeys Darcy’s law during experiment process. The permeability formula is expressed as follows:

$$k = \frac{\mu LV}{A \Delta P \Delta t}, \quad (1)$$

where k is the permeability (m^2); V is the inflow volume of the seepage fluid during the time Δt (m^3); μ is the dynamic viscosity of water, $\mu = 1 \times 10^{-3} \text{ Pa}\cdot\text{s}$ ($T = 20^\circ\text{C}$); L is the length of the rock sample (m); A is the cross-sectional area of the rock sample (m^2); ΔP is the hydraulic pressure difference (Pa); and Δt is the increment of time (s).

2.2. Sample Preparation. The experimental samples were prepared with a dimension of $50 \text{ mm} \times 100 \text{ mm}$ (diameter \times length). The physical property of density and porosity is 2350 kg/m^3 and 7.78% , respectively. The fractured rock mass with a single fracture of 100 degree inclined angle relative to the horizontal plane and two mutually perpendicular fracture of 100 degree inclined angle and 90 degree inclined angle relative to the horizontal plane were obtained through the Brazilian splitting test, as shown in Figure 1. The specific mechanical property of the intact sandstone under different confining stress is shown in Table 1.

The hydromechanical tests were carried out by triaxial hydromechanical coupling experimental system, as shown in Figure 2. The triaxial hydromechanical coupling experimental system includes a triaxial cell and a fluid injection pump. The scope of confining stress, axial stress, and hydraulic pressure are $0\text{--}60 \text{ MPa}$, $0\text{--}600 \text{ MPa}$, and $0\text{--}30 \text{ MPa}$, respectively. The specific experimental process is presented in Figure 3.

2.3. Testing Scheme. To investigate the evolution of deformation and fluid conductivity subjected to the change of hydraulic pressure, confining stress, and cycle loading-unloading, the fractured sandstones were loaded into the triaxial chamber subjected to a complicated triaxial loading path, which consists of three parts. In the first part, the axial and confining pressure were initially loaded to the hydrostatic pressure of 36 MPa with a rate of 0.1 MPa/s , and the water pressure was reduced from 4.3 to 0.4 MPa with a gradient of 0.86 MPa . In the second part, the axial and confining pressure decreased from 36 to 18.5 MPa with a gradient of 2.5 MPa , while maintaining the hydraulic pressure of 0.4 MPa . Finally, the axial cyclic loading-unloading stress was set to an increment of 21.6 MPa at each cycle. The specific loading path is shown in Figure 4.

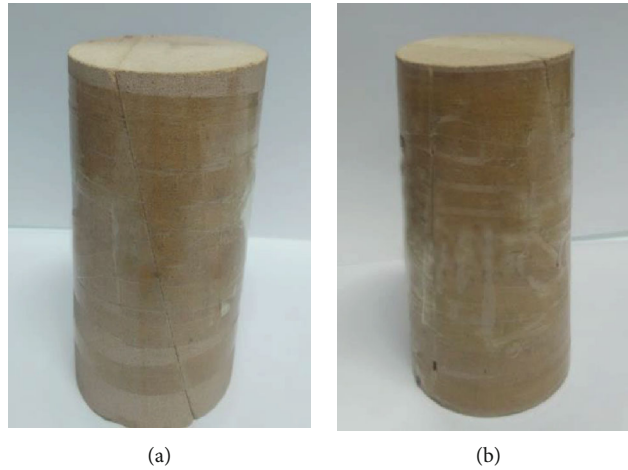


FIGURE 1: Fractured samples: (a) single-fracture; (b) double-fracture.

TABLE 1: Mechanical property of the sandstone.

Sample no.	Confining pressure (MPa)	Peak strength (MPa)	Poisson's ratio	Elastic modulus (GPa)	Cohesion (MPa)	Friction angle (°)
1	5	109.42	0.23	6.35		
2	15	170.67	0.19	9.01	14.76	48.93
3	25	225.69	0.18	13.37		

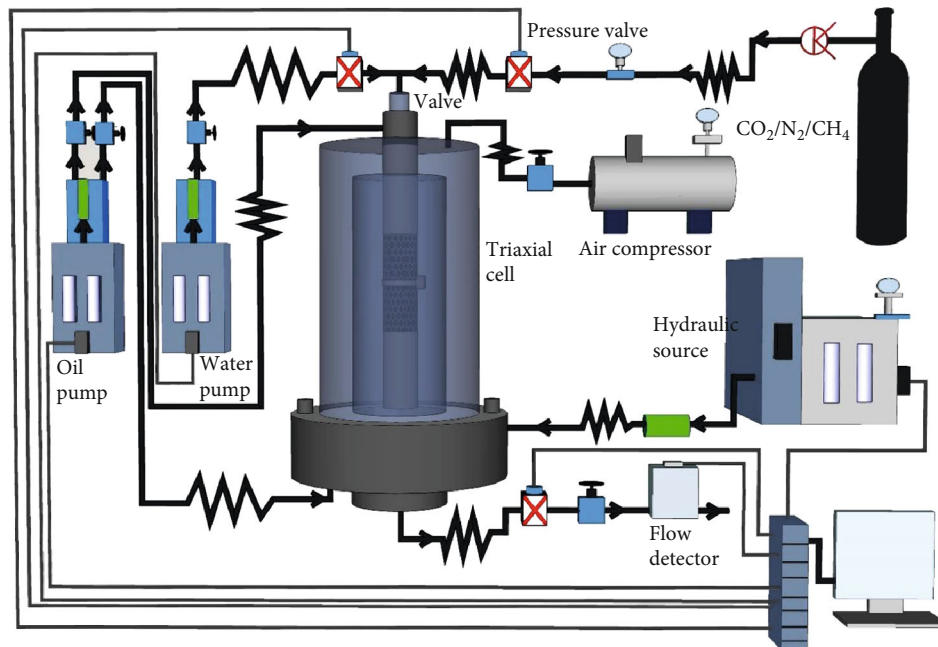


FIGURE 2: Triaxial hydromechanical coupling experimental system.

3. Experimental Results and Discussion

3.1. *Effect of Hydraulic Pressure and Confining Stress.* The deformations in the experiment procedure of 1st and 2nd are small, which are not the focus of this study. Therefore, the deformations of 1st and 2nd parts in this research are not analyzed in detail in Section 3.1.

3.1.1. *Relationship between Permeability and Hydraulic Pressure.* The relationship between permeability and hydraulic pressure is shown in Figure 5. The permeability of double-fracture sandstone is almost three times that of single-fracture sandstone under the initial stress condition. With the decrease of hydraulic pressure, the permeability of both single- and double-fracture sample gradually decreased as a

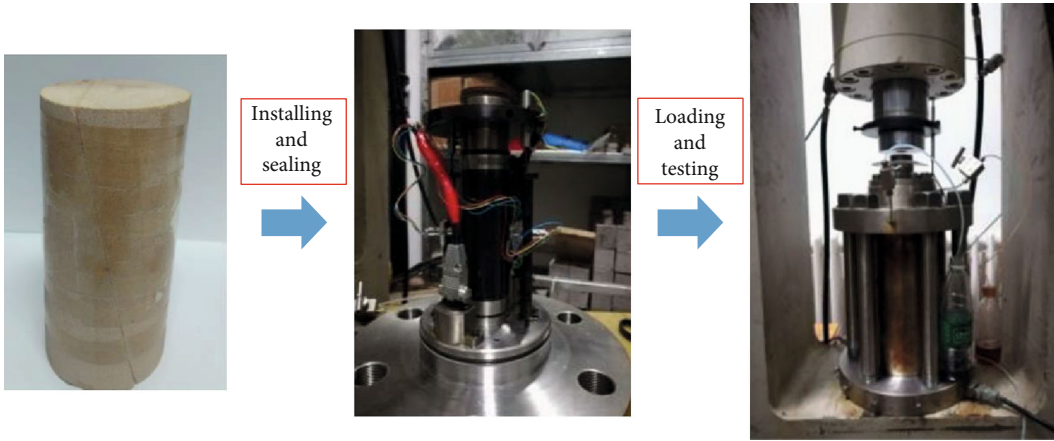


FIGURE 3: Triaxial hydromechanical coupling experiment process.

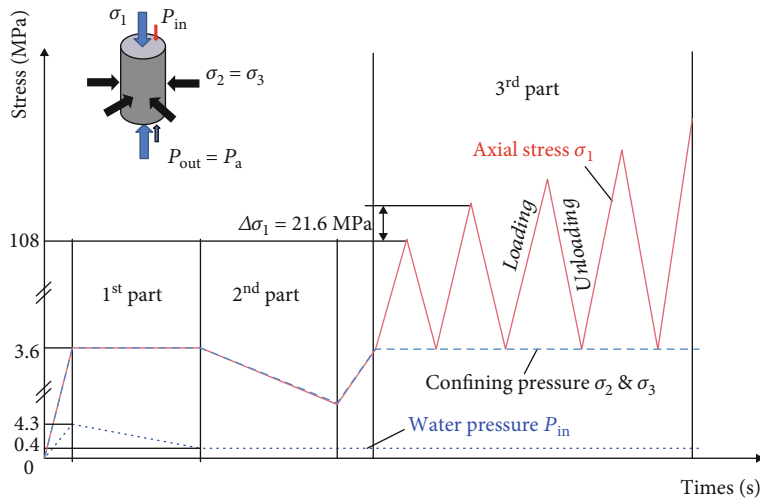


FIGURE 4: The triaxial loading path for testing.

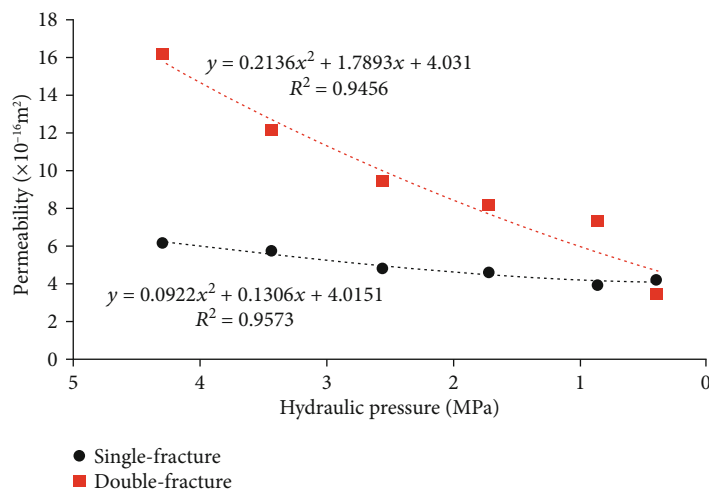


FIGURE 5: Permeability evolution of fractured sandstones under different hydraulic pressures.

quadratic function. Compared with the single-fracture sandstone, the double-fracture sandstone is more sensitive to the change of the hydraulic pressure. This illustrates that seepage

channels of the fractured sandstone are narrowed as the decrease of the hydraulic pressure, resulting in the decrease of the permeability. Furthermore, the decrease of double-

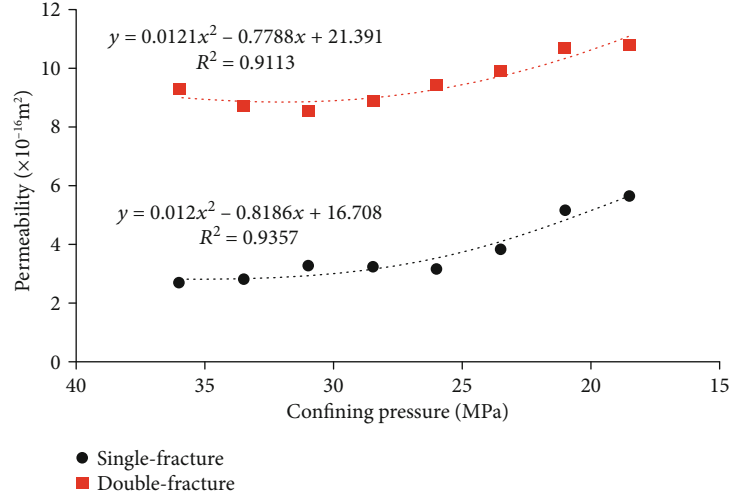


FIGURE 6: Permeability evolution of fractured sandstones under different confining stresses.

fracture sandstone is larger than single-fracture sandstone, due to more fractures exiting in the double-fracture sandstone.

3.1.2. Relationship between Permeability and Confining Stress. Figure 6 depicts the change of permeability of fractured sandstone subjected to the variation of confining stress at a constant hydraulic pressure. With the decrease of confining stress, the permeability of both single- and double-fracture sandstones increases slowly as a quadratic function. And the permeability of double-fracture sandstone in each stage is 2.7 times that of single-fracture sandstone. It is indicating that the effect of confining stress for fractured sandstone is relatively limited.

3.2. Effect of Axial Cyclic Loading-Unloading

3.2.1. Evolution Characteristics of the Deformation and Permeability. Figure 7 shows the relationship of the axial strain, axial stress, and permeability of the fractured sandstones in the process of axial cyclic loading and unloading. For single-fracture sandstone, with axial cyclic loading-unloading, both axial and radial strains gradually increase, and the correlative permeability spiralled down quickly in the compaction stage and slowly in the elastic and plastic stage. However, for double-fracture sandstone, the permeability slightly changes with axial cyclic loading and unloading. Furthermore, the axial stress-strain curves of both single- and double-fracture sandstones approximately present a parallelogram shape after the first cycle, showing obvious deformation memory characteristics.

The deformation and permeability characteristics of each cycle stage are presented in Figures 8 and 9. In the first cycle, the loading and unloading curves of both single-fracture sandstone and double-fracture sandstone did not form a closed loop, and a large amount of residual deformation was observed, resulting in nonlinear properties of rock materials and damages of artificial fractures [36]. The corresponding permeability decreased dramatically and did not completely recover with axial loading and unloading. For

single-fracture sandstone, the crossing of permeability curves at the loading state and unloading state was observed at the second cycle, while it was not found in the double-fracture sandstone. This phenomenon indicates that fractures were majorly compressed in the second cycle. Consequently, the flow channels were narrowed, and permeability reduced step-wise. In the third cycle, the permeability curves of both single-fracture sandstone and double-fracture sandstone gradually decreased with the loading and unloading, indicating that the fractures and secondary cracks also compressed during the third cycle. After the third cycle, the reexpansion of existing fractures and the generation of secondary cracks dominated the loading and unloading process. The compressed flow channels were expanded under the action of hydraulic pressure. As a result, the corresponding permeability of single- and double-fracture sandstones gradually increased. Finally, the axial stress-strain and permeability-axial strain curves of both single- and double-fracture sandstone have similar trend at the fifth loading.

3.2.2. Relationship between Axial Residual Strain and Axial Cycle Stress. To quantitatively analyze the irrecoverable deformation of fractured sandstone subjected to the axial cyclic loading-unloading, the cumulative residual strain, comprised axial, and radial residual strains are defined. And the cumulative residual strain ε_{pi}^j is expressed as [38]:

$$\varepsilon_{pi}^j = \varepsilon_i^j - \varepsilon_1^j, \quad (2)$$

where the superscripts j are 1 and 3 represent the axial and radial directions, respectively; ε_i^j is the strain at the i th cycle when the axial stress is 36 MPa, %; and ε_1^j is the strain for the initial axial stress of 36 MPa, %.

Figure 10 reflects the relationship between the cumulative residual strain and the cycle loading increment of the axial stress. Along the axial and radial direction, the cumulative residual strains increase in form of quadratic function as the increase in the loading increment of the axial stress. For cumulative axial residual strain and radial residual strain of

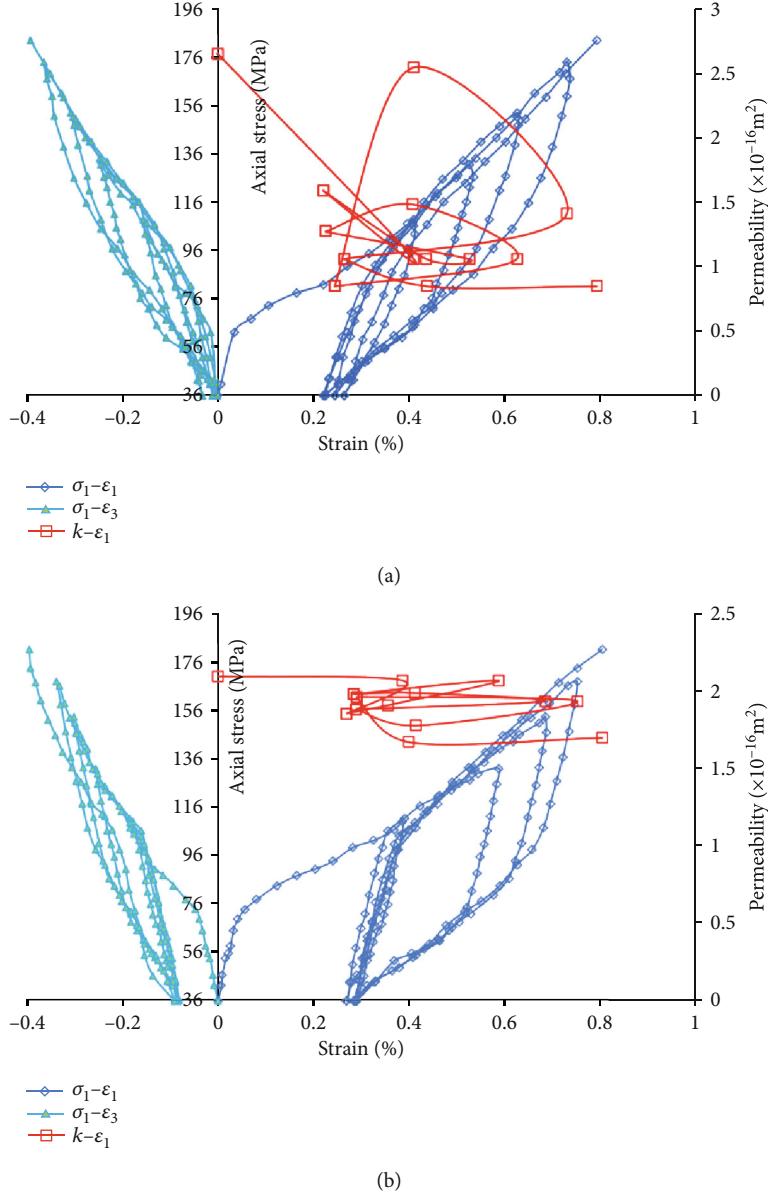


FIGURE 7: Stress-strain and permeability-axial strain curves for fractured sandstones under axial cyclic loading-unloading: (a) single-fracture sandstone; (b) double-fracture sandstone.

double-fracture sandstone, the increment of residual strain increases remarkably in the first cycle and then increases slowly. Conversely, when the increment of axial stress is small, the cumulative radial residual strain of single-fracture is small with a slight increase gradient. The radial residual strain increases sharply after the second cycle. Generally, the change of residual strains can be divided into two stages: the sharp increase stage and slow increase stage.

3.2.3. Evolution of Permeability Recovery Rates (PRR) and Permeability Enhancement Reduction Rates (PERR). To quantitatively characterize the permeability change of fractured rock caused by the axial cyclic loading-unloading and cyclic loading enhancement at $\sigma_1=108$ MPa, the concept of PRR and PERR was proposed, respectively. The PRR is defined as the ratio of the permeability in every cycle after

unloading to the permeability at time of initial loading (cumulative PRR) or at the last cycle after unloading (relative PRR). Similarly, the PERR is defined as the ratio of the permeability in every cyclic loading at 108 MPa to the permeability at initial loading at 108 MPa (cumulative PERR) or at the last cyclic loading at 108 MPa (relative PERR). And the formulas for calculating the cumulative PRR (CPRR) and cumulative PERR (CPERR) λ_c^j and relative PRR (RPRR) and relative PERR (RPERR) λ_r^j are as follows:

$$\lambda_c^j = \frac{k_i}{k_1} \times 100\%, \quad (3)$$

$$\lambda_r^j = \frac{k_{i+1}}{k_i} \times 100\%, \quad (4)$$

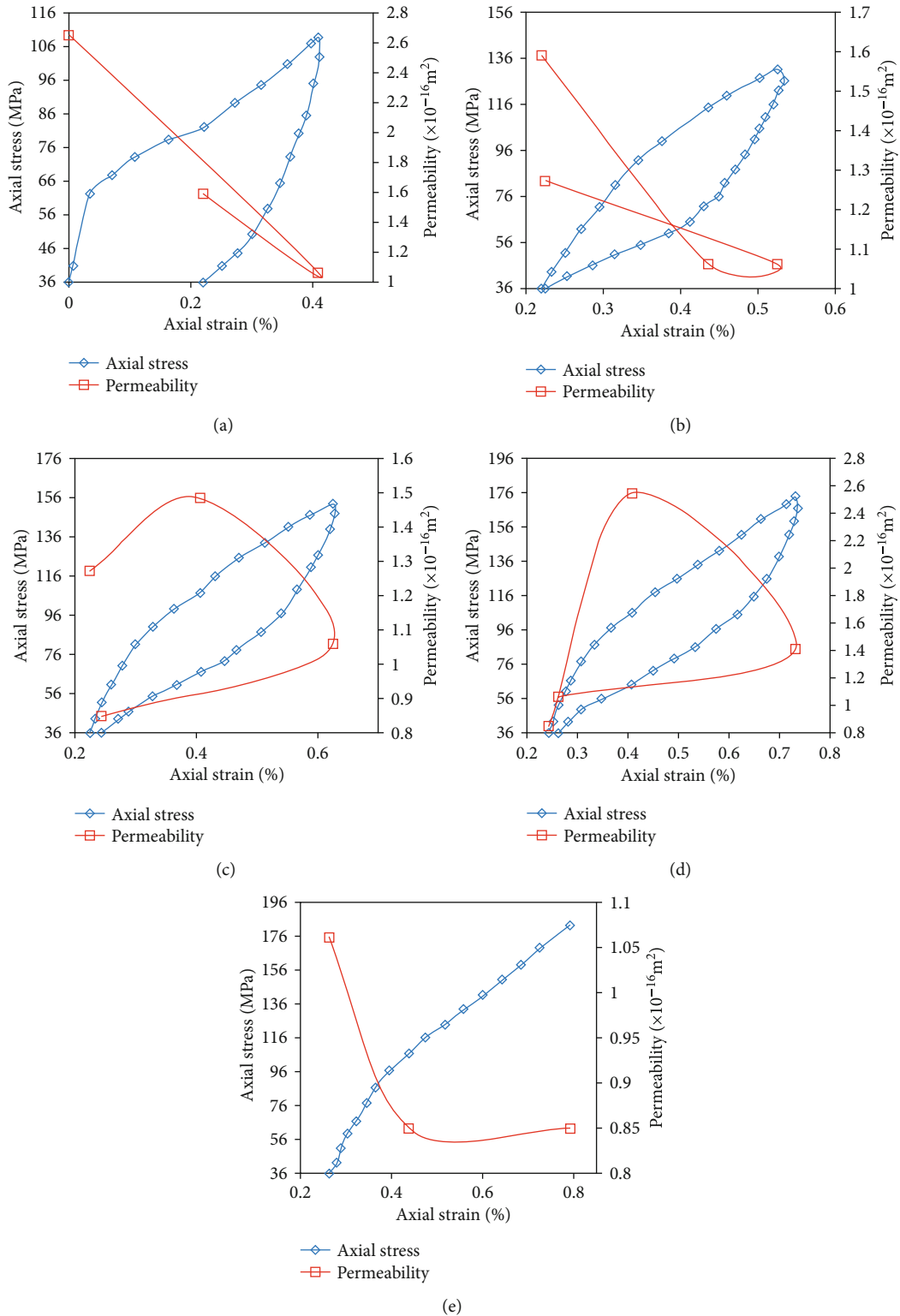


FIGURE 8: Stress-strain and permeability-strain curves for single-fracture sandstone at different cycles: (a) the first cycle; (b) the second cycle; (c) the third cycle; (d) the fourth cycle; (e) the fifth loading.

where the superscripts $j = 36$ and 108 indicate the PPR and PERR, respectively, and k_i is the permeability at the i th cyclic loading-unloading and loading when the axial stress is 36 MPa and 108 MPa, respectively, m^2 . k_1 is the correspond-

ing permeability when the initial axial stress is 36 MPa and 108 MPa for the first time, respectively, m^2 .

Figure 11 shows the relationship between PRR and axial cyclic loading and unloading. During the cyclic loading-

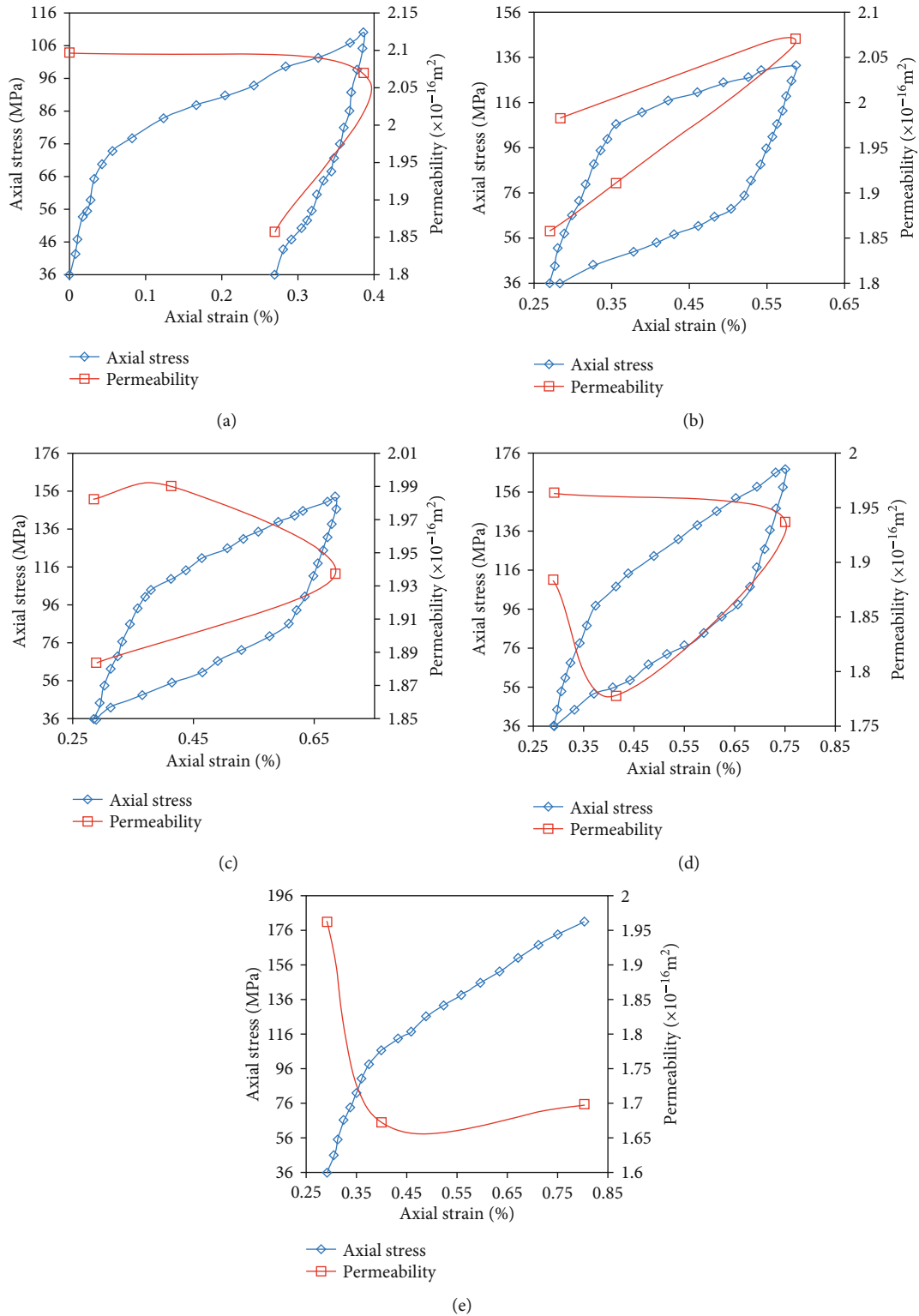


FIGURE 9: Stress-strain and permeability-strain curves for double-fracture sandstone at different cycles: (a) the first cycle; (b) the second cycle; (c) the third cycle; (d) the fourth cycle; (e) the fifth loading.

unloading process, the CPRR of single-fracture sandstone gradually decreased. This change mainly caused by the continuous increment of load stress. With the continuously increasing of axial stress, the seepage channels, consisting of

mainly compressed pores and fractures, were gradually narrowed. And the CPRR of double-fracture sandstone was stabilized at 85%-95%, while the RPRR of both single- and double-fracture sandstones shows a certain fluctuation. This

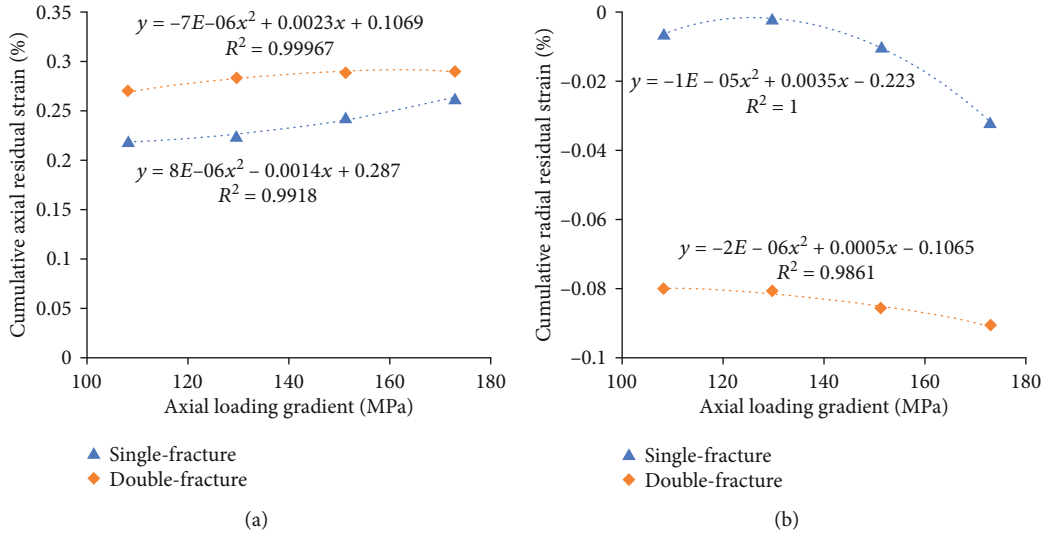


FIGURE 10: The residual strain at different cycle loading gradients: (a) cumulative axial residual strain; (b) cumulative radial residual strain.

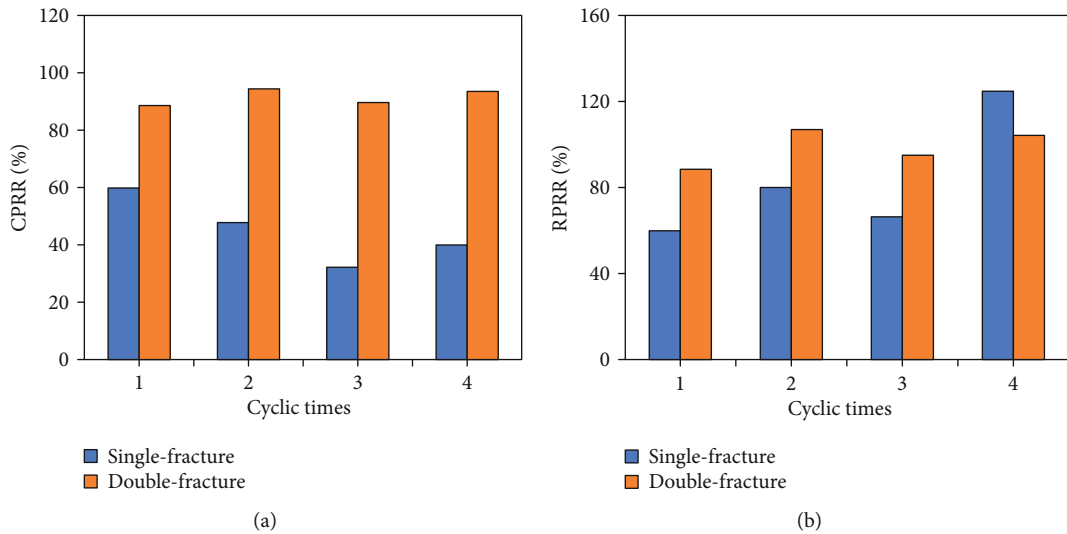


FIGURE 11: The permeability recovery at different cycles: (a) cumulative permeability recovery rate; (b) relative permeability recovery rate.

indicates that the stress sensitivity of permeability of double-fracture sandstone is lower than that of single-fracture sandstone, because it has more seepage channels.

Figure 12 presents the relationship between PERR and axial cyclic loading at the axial stress of 108 MPa. As the axial cyclic loading, the CPERR and RPERR of double-fracture sandstone decreased synchronously, presenting the enhancement effect of cyclic loading. The sandstone pore-fracture system was further compressed with increased cycle times, and then, the flow channels were narrowed. In contrast, the CPERR of single-fracture sandstone increased gradually with the first three axial loadings in the elastic stage, and the increasing degree was greater (about 2.4 times), which is attributed to the dislocation of artificial fracture surface. With axial cyclic loading time increase, the dislocated spaces increase, combining with fracture swelling and developing, the flow channels increase, and the permeability increases dramatically. Mine water inrush is one of the main disasters that

restrict the safe and efficient production of coal mines. Combining Figure 12, when mining above or below the deep confined aquifer, especially the effect of repeated mining, even if the aquifuge is not failure, the displacement of roof and floor should be controlled reasonably to prevent the dislocation of vertical fractures, the increase of permeability of rock stratum, and water inrush disaster.

4. Conclusions

Based on the hydromechanical experiments of triaxial loading, the change of the axial and radial strain and permeability subjected to the effect of the hydraulic pressure, confining stress, and cyclic loading-unloading was observed. And cumulative residual strain, PRR, and PERR were proposed to quantitatively analyze these changes. The main conclusions are as follows:

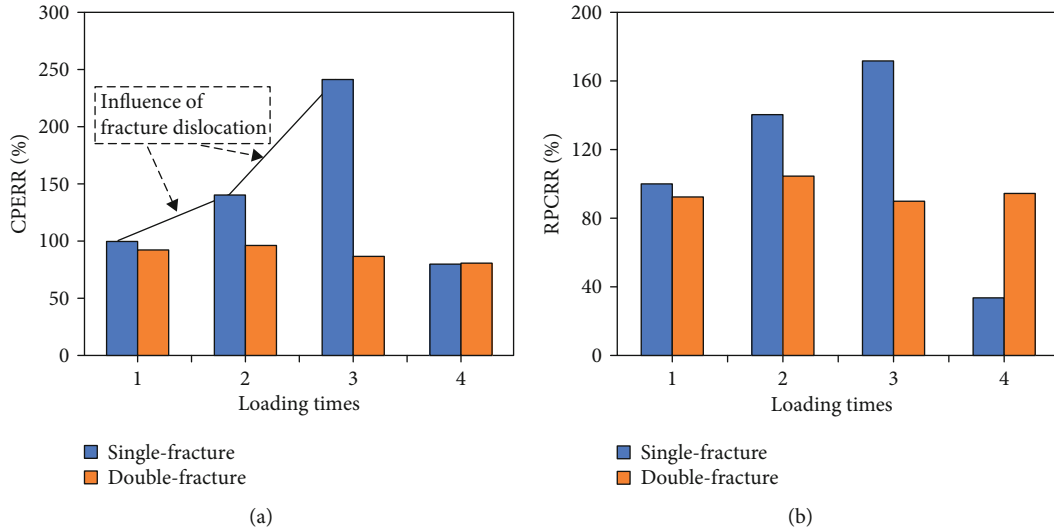


FIGURE 12: The permeability enhancement reduction at different loading stages (at 108 MPa): (a) cumulative permeability enhancement reduction rate; (b) relative permeability enhancement reduction rate.

- (1) The relative permeability of both single- and double-fracture sandstone varies as a quadratic function of hydraulic and confining stress. The permeability of fractured sandstone is positively related to the hydraulic pressure, and double-fracture sandstone is more sensitive to the hydraulic pressure than the single-fracture sandstone. The permeability of fractured sandstone is negatively related to the confining stress. However, the effect of confining stress on the strain is more obvious than the permeability
- (2) As the advance of axial cyclic loading-unloading, the axial and radial strains of fractured sandstone increase, and the permeability of single-fracture sandstone spirals down. However, for double-fracture sandstone, the permeability slightly changes with more seepage channels. Furthermore, the axial stress-strain curves approximately present a parallelogram shape after the first cycle, showing obvious deformation memory characteristics. The CPRR of single-fracture sandstone decreases first and then increases. The CPRR of double-fracture sandstone maintains 85%-95% with a fluctuated RPRR
- (3) With axial cycle enhancement loading, the PERR of double-fracture sandstone decreases gradually; in contrast, the PERR of single-fracture sandstone dramatically increases. For the single-fracture sandstone, the dislocation of fracture surface was presented and developed with the increase of the axial loading time, resulting in the increase of the seepage channels characterized by the increase of the permeability

Nomenclature

PRR:	Permeability recovery rate
PERR:	Permeability enhancement reduction rate
k :	Permeability
V :	Inflow volume

μ :	Dynamic viscosity
L :	Height of the rock sample
A :	Cross-sectional area of the rock sample
ΔP :	Hydraulic pressure difference
Δt :	Increment of time
ε_{pi}^j :	Cumulative residual strain
CPRR:	Cumulative permeability recovery rate
RPRR:	Relative permeability recovery rate
CPERR:	Cumulative permeability enhancement reduction rate
RPERR:	Relative permeability enhancement reduction rate.

Data Availability

The data used to support the findings of this study are included within the article.

Conflicts of Interest

The author declares no conflict of interest regarding the publication of this manuscript

Authors' Contributions

The manuscript was written through contributions of all authors. All authors have given approval to the final version of the modified manuscript.

Acknowledgments

This paper was supported by the National Youth Science Foundation (nos.51904011), the Anhui Provincial Natural Science Foundation (nos.1908085QE183), the Anhui University Scientific Research Foundation (no.QN2018108), and the National Key Research and Development Program of China (nos. 2016YFC0801401 and 2016YFC0600708).

References

- [1] X. Li, W. Cao, Z. Zhou, and Y. Zou, "Influence of stress path on excavation unloading response," *Tunnelling and Underground Space Technology*, vol. 42, pp. 237–246, 2014.
- [2] T. Babadagli, X. Ren, and K. Develi, "Effects of fractal surface roughness and lithology on single and multiphase flow in a single fracture: an experimental investigation," *International Journal of Multiphase Flow*, vol. 68, pp. 40–58, 2015.
- [3] K. K. Singh, D. N. Singh, and P. G. Ranjith, "Laboratory simulation of flow through single fractured granite," *Rock Mechanics and Rock Engineering*, vol. 48, no. 3, pp. 987–1000, 2015.
- [4] J. Schmittbuhl, A. Steyer, L. Jouniaux, and R. Toussaint, "Fracture morphology and viscous transport," *International Journal of Rock Mechanics and Mining Sciences*, vol. 45, no. 3, pp. 422–430, 2008.
- [5] J.-Q. Zhou, S.-H. Hu, S. Fang, Y.-F. Chen, and C.-B. Zhou, "Nonlinear flow behavior at low Reynolds numbers through rough-walled fractures subjected to normal compressive loading," *International Journal of Rock Mechanics and Mining Sciences*, vol. 80, pp. 202–218, 2015.
- [6] R. Hu, Y. Chen, and C. Zhou, "Modeling of coupled deformation, water flow and gas transport in soil slopes subjected to rain infiltration," *Science China-Technological Sciences*, vol. 54, no. 10, pp. 2561–2575, 2011.
- [7] A. Nowamooz, G. Radilla, and M. Fourar, "Non-Darcian two-phase flow in a transparent replica of a rough-walled rock fracture," *Water Resources Research*, vol. 45, no. 7, 2009.
- [8] Y. Chen, S. Hu, K. Wei, R. Hu, C. Zhou, and L. Jing, "Experimental characterization and micromechanical modeling of damage-induced permeability variation in Beishan granite," *International Journal of Rock Mechanics and Mining Sciences*, vol. 71, pp. 64–76, 2014.
- [9] G. Radilla, A. Nowamooz, and M. Fourar, "Modeling non-Darcian single- and two-phase flow in transparent replicas of rough-walled rock fractures," *Transport in Porous Media*, vol. 98, no. 2, pp. 401–426, 2013.
- [10] C. Noiriél, P. Gouze, and B. Made, "3D analysis of geometry and flow changes in a limestone fracture during dissolution," *Journal of Hydrology*, vol. 486, pp. 211–223, 2013.
- [11] L. J. Pyrak-Nolte and D. D. Nolte, "Approaching a universal scaling relationship between fracture stiffness and fluid flow," *Nature Communications*, vol. 7, no. 1, 2016.
- [12] D. Song, E. Wang, and J. Liu, "Relationship between EMR and dissipated energy of coal rock mass during cyclic loading process," *Safety Science*, vol. 50, no. 4, pp. 751–760, 2012.
- [13] D. Kong, Z. Cheng, and S. Zheng, "Study on the failure mechanism and stability control measures in a large-cutting-height coal mining face with a deep-buried seam," *Bulletin of Engineering Geology and the Environment*, vol. 78, no. 8, pp. 6143–6157, 2019.
- [14] D. Gu, "Theory framework and technological system of coal mine underground reservoir," *Journal of China Coal Society*, vol. 40, no. 2, pp. 239–246, 2015.
- [15] S. Linfang, F. Xiating, P. Pengzhi, and Z. Hui, "Experimental research on mechano-hydro-chemical coupling of granite with single fracture," *Chinese Journal of Rock Mechanics and Engineering*, vol. 29, no. 7, pp. 1379–1388, 2010.
- [16] H. Xie, Y. Ju, F. Gao, M. Gao, and R. Zhang, "Groundbreaking theoretical and technical conceptualization of fluidized mining of deep underground solid mineral resources," *Tunnelling and Underground Space Technology*, vol. 67, pp. 68–70, 2017.
- [17] Z. Zhang and J. Nemcik, "Fluid flow regimes and nonlinear flow characteristics in deformable rock fractures," *Journal of Hydrology*, vol. 477, pp. 139–151, 2013.
- [18] J. Rutqvist and O. Stephansson, "The role of hydromechanical coupling in fractured rock engineering," *Hydrogeology Journal*, vol. 11, no. 1, pp. 7–40, 2003.
- [19] J. Rutqvist, C. Leung, A. Hoch, Y. Wang, and Z. Wang, "Linked multicontinuum and crack tensor approach for modeling of coupled geomechanics, fluid flow and transport in fractured rock," *Journal of Rock Mechanics & Geotechnical Engineering*, vol. 5, no. 1, article S1674775513000073, pp. 18–31, 2013.
- [20] S. Zhang, D. Zhang, Z. Wang, and M. Chen, "Influence of stress and water pressure on the permeability of fissured sandstone under hydromechanical coupling," *Mine Water and the Environment*, vol. 37, no. 4, pp. 774–785, 2018.
- [21] Z. Song, H. Konietzky, and M. Herbst, "Three-dimensional particle model based numerical simulation on multi-level compressive cyclic loading of concrete," *Construction and Building Materials*, vol. 225, pp. 661–677, 2019.
- [22] J. C. S. Long, J. S. Remer, C. R. Wilson, and P. A. Witherspoon, "Porous media equivalents for networks of discontinuous fractures," *Water Resources Research*, vol. 18, no. 3, pp. 645–658, 1982.
- [23] D. J. Brush and N. R. Thomson, "Fluid flow in synthetic rough-walled fractures: Navier-Stokes, Stokes, and local cubic law simulations," *Water Resources Research*, vol. 39, no. 4, 2003.
- [24] J. Qian, H. Zhan, S. Luo, and W. Zhao, "Experimental evidence of scale-dependent hydraulic conductivity for fully developed turbulent flow in a single fracture," *Journal of Hydrology*, vol. 339, no. 3–4, pp. 206–215, 2007.
- [25] L. Zou, L. Jing, and V. Cvetkovic, "Roughness decomposition and nonlinear fluid flow in a single rock fracture," *International Journal of Rock Mechanics and Mining Sciences*, vol. 75, pp. 102–118, 2015.
- [26] Y. Chen, J. Zhou, S. Hu, R. Hu, and C. Zhou, "Evaluation of Forchheimer equation coefficients for non-Darcy flow in deformable rough-walled fractures," *Journal of Hydrology*, vol. 529, pp. 993–1006, 2015.
- [27] Y. Chen, W. Liang, H. Lian, J. Yang, and V. P. Nguyen, "Experimental study on the effect of fracture geometric characteristics on the permeability in deformable rough-walled fractures," *International Journal of Rock Mechanics and Mining Sciences*, vol. 98, pp. 121–140, 2017.
- [28] Z. Song, T. Frühwirt, and H. Konietzky, "Characteristics of dissipated energy of concrete subjected to cyclic loading," *Construction and Building Materials*, vol. 168, pp. 47–60, 2018.
- [29] Z. Song, T. Frühwirt, and H. Konietzky, "Inhomogeneous mechanical behaviour of concrete subjected to monotonic and cyclic loading," *International Journal Of Fatigue*, vol. 132, article 105383, 2020.
- [30] Y. Chen, S. Wang, and E. Wang, "Strength and elastic properties of sandstone under different testing conditions," *Journal of Central South University of Technology*, vol. 14, no. 2, pp. 210–215, 2007.
- [31] K. Fuenkajorn and D. Phueakphum, "Effects of cyclic loading on mechanical properties of Maha Sarakham salt," *Engineering Geology*, vol. 112, no. 1–4, pp. 43–52, 2010.
- [32] E. Liu and S. He, "Effects of cyclic dynamic loading on the mechanical properties of intact rock samples under confining

- pressure conditions,” *Engineering Geology*, vol. 125, pp. 81–91, 2012.
- [33] E. Liu, R. Huang, and S. He, “Effects of frequency on the dynamic properties of intact rock samples subjected to cyclic loading under confining pressure conditions,” *Rock Mechanics and Rock Engineering*, vol. 45, no. 1, pp. 89–102, 2012.
- [34] College of Civil Engineering, Chongqing University, Chongqing 400045, China, J. Liu, Key Laboratory of New Technology for Construction of Cities in Mountain Area (Chongqing University), Ministry of Education, Chongqing 400030, China et al., “Experimental and theoretical analysis of permeability characteristics of sandstone under loading and unloading,” *Journal of Engineering Science and Technology Review*, vol. 9, no. 5, pp. 36–43, 2016.
- [35] J. Liu, H. Xie, Z. Hou, C. Yang, and L. Chen, “Damage evolution of rock salt under cyclic loading in uniaxial tests,” *Acta Geotechnica*, vol. 9, no. 1, pp. 153–160, 2014.
- [36] H. Zhao, D. Zhang, G. Bian, and W. Li, “Deformation and permeability of sandstone at different cycling loading-unloading rates,” *Chinese Journal of Engineering*, vol. 39, no. 1, p. 140, 2017.
- [37] C. Jiang, M. Duan, G. Yin et al., “Experimental study on seepage properties, AE characteristics and energy dissipation of coal under tiered cyclic loading,” *Engineering Geology*, vol. 221, pp. 114–123, 2017.
- [38] M. Duan, C. Jiang, Q. Gan, M. Li, K. Peng, and W. Zhang, “Experimental investigation on the permeability, acoustic emission and energy dissipation of coal under tiered cyclic unloading,” *Journal Of Natural Gas Science And Engineering*, vol. 73, article 103054, 2020.

Research Article

Study on Borehole Arrangement Methods for Gas Extraction by Hydraulic Slotting in Long-Distance Through-Coal Seam Tunnel

Cunfang Zhu¹ and Shuang Cai² 

¹Qinghai Local Railway Construction Investment Co. Ltd., Xining 810001, China

²China Merchants Chongqing Communication Research & Design Institute Co., Ltd., Chongqing 400067, China

Correspondence should be addressed to Shuang Cai; caishuang@cmhk.com

Received 19 August 2020; Revised 17 September 2020; Accepted 28 September 2020; Published 28 October 2020

Academic Editor: Bin-Wei Xia

Copyright © 2020 Cunfang Zhu and Shuang Cai. This is an open access article distributed under the Creative Commons Attribution License, which permits unrestricted use, distribution, and reproduction in any medium, provided the original work is properly cited.

How to quickly eliminate outburst in long-distance through-coal seam tunnels is one of the major challenges faced by the tunnel industry in mountainous areas. Compared with coal mine rock crosscut coal uncovering, the work surrounding the rock of through-coal seam tunnels has a high degree of breakage, large cross-section of coal uncovering, and tight time and space. In this paper, a method of networked slotting in long-distance through-coal seam tunnels for rapid pressure relief and outburst elimination is proposed. Based on this method, the corresponding mathematical governing equations and numerical simulation models have been established. The optimal borehole arrangement spacing and the slot arrangement spacing obtained by numerical optimization are 2.85 m and 3.1 m, respectively. Field gas production data of through-coal seam tunnels show that compared with the traditional dense-borehole gas extraction, the method of networked slotting in long-distance through-coal seam tunnels for rapid pressure relief and outburst elimination can shorten the extraction time by about 66%, the net quantity of peak extraction is increased by 3.55 times, and the total quantity of gas extraction when reaching the outburst prevention index is increased by 1.26 times, which verifies the feasibility of this method and the reliability of numerical simulation results. This study could be used as a valuable example for other coal deposits being mined under similar geological conditions.

1. Introduction

With the rapid development of the national economies of the world, high-speed tunnels and railways have formed a comprehensive transportation system for modern cities to communicate and connect with each other. However, in some countries with complex terrain, mountainous areas rich in various lithologies will be encountered in the process of tunnel construction, which makes tunnel construction particularly difficult. As a representative of typical mountainous countries, China's mountainous area accounts for two-thirds of the country's total area. Especially in the face of the country's vigorous development of the central and western regions, China will usher in a new upsurge in the construction of large-scale projects of transport infrastructures such as high-speed railways and expressways. In addition to the complexity of mountainous terrain, there are many strata with developed coal measures in western China, which make gas tunnels an

unavoidable challenge in the construction of transport infrastructures. According to incomplete statistics, in the recent 20 years, more than 70 gas tunnels have been built in China, penetrating more than 300 coal seams [1]. The critical technical problems brought by unfavorable geological conditions of coal measure strata in mountainous areas are one of the challenges that we need to solve urgently.

Due to the complexity of the geological structures of coal measure strata, weak and broken rock mass, and high gas pressure, large deformation or even instability and collapse of surrounding rocks and various gas disasters are likely to occur. In the process of tunnel coal seam uncovering, the instable failure of coal rock mass in the original high geostress field and high gas pressure field induces coal and gas outburst accidents, which is a kind of disaster with the highest intensity and the greatest danger. Gas tunnel construction in China started fairly late, and there is no complete set of technical systems of tunnel coal uncovering and outburst prevention formed.

The research on tunnel gas disaster mainly focuses on risk assessment, construction safety management, and monitoring of surrounding rock deformation, while the research on outburst prevention technology is little. As a result, the technology of coal uncovering and outburst prevention measures in through-coal seam tunnels lags far behind the development of on-site production practice [2, 3].

The existing design and construction of through-coal seam tunnels are mainly based on the relevant theories and experiences of coal mine underground rock crosscut coal uncovering or coal roadway driving. Through-coal seam tunnels and underground coal mine roadway driving have some similarities in excavation and construction, but there are also obvious differences, especially the characteristics of large tunnel section and tight time and space for implementing outburst prevention measures, which make the difficulty and risk of coal uncovering much higher than that of coal mine rock crosscut coal uncovering. Therefore, it is unscientific to directly use the outburst prevention technology of coal mine rock crosscut coal uncovering to guide the construction of gas tunnels, and it is badly in need of research on the outburst prevention technology regarding the characteristics of gas tunnels. Li et al. [4], Jiang et al. [5], Wang and Li. [6], etc. have carried out researches on tunnel coal uncovering technologies from the aspects of exploration, prediction, and prevention and control and have achieved fruitful results. However, due to the extremely low gas permeability coefficient (as low as 0.01 mD) of most coal seams in Southwest China, the effect of conventional permeability-enhancing technologies is poor, and it takes a long time to eliminate outburst and reach the standard. Cheng et al. [7–9], Lu et al. [10], Feng and Kang [11] Wang et al. [12], etc. have studied preextraction coal seam permeability enhancement after coal mine underground hydraulic slotting, and practices have shown that this technology can quickly and extensively enhance the coal seam permeability and the preextraction effect, laying a foundation for quickly eliminating the danger of gas outburst [13, 14].

By analyzing the characteristics of gas disaster prevention in long-distance through-coal seam tunnels, this paper puts forward the method of networked slotting in long-distance through-coal seam tunnels for rapid pressure relief and outburst elimination, carries out theoretical and numerical analysis on the arrangement parameters of boreholes and hydraulic slots for long-distance through-coal seam tunnels, and verifies the reliability of this method through field tests of a gas tunnel in Qinghai, China, thus providing technical support for the technical system of rapid coal uncovering and outburst elimination in long-distance through-coal seam tunnels.

2. Analysis on Technical Challenges of Outburst Elimination in Through-Coal Seam Tunnels

Long-distance excavation of tunnels along the coal seam strike and through-coal seams actually has something in common with coal mine roadway driving, but also has its particularity. To sum up, the main differences are the following:

- (1) The buried depth of gas tunnels is generally not more than 300 m, and the surrounding rocks have high degree of breakage affected due to weathering. Compared with the buried depth up to nearly one kilometer of coal mines, gas tunnels are more affected by excavation disturbance, and the possibility of instability of tunnel-surrounding rocks is higher
- (2) Before mining, coal mines generally have detailed geological survey data, but the geological survey of gas tunnels is affected by many factors, which leads to a low degree of geological survey. Therefore, the formulated outburst prevention measures may not meet the needs of actual geological conditions
- (3) The cross-section of through-coal seam tunnels is larger than that of coal mine roadway driving. The cross-section of coal mine roadways is small, generally not more than 20 m², while the cross-section of gas tunnels is large. At present, the excavation section of double-line highway tunnels has exceeded 110 m², and the excavation section of double-line railway tunnels is even close to 150 m²
- (4) For through-coal seam tunnels, outburst prevention is difficult and the time is tight, which is because the advanced mining deployment of coal mines leaves plenty of time and space for the implementation of outburst prevention measures, while a gas tunnel has only a single working face, making it impossible to implement outburst prevention measures ahead of time
- (5) The cross-section excavation of tunnels causes frequent disturbance to the coal seam, while coal mine roadways generally adopt the method of full cross-section uncovering of coal seam at one time. In order to reduce the energy released during uncovering of coal and reduce the outburst danger, large-section tunnels often adopt the method of multiple-section partitioned coal uncovering, which is disturbed frequently by external forces and has more complex dynamic response characteristics
- (6) Through-coal seam tunnels have higher requirement for roadway support. The service life of roadways in a coal mining area will be abandoned after coal mining, and large deformation of roadway is allowed, while the service period of tunnels is long, generally ranging from several decades to one hundred years, and large deformation or large amount of gas emission is not allowed during the service period
- (7) Compared with the available circulating space in coal mines, gas tunnels' single-roadway ventilation with a length of up to one kilometer makes it more difficult to exhaust smoke and dilute gas

In summary, when excavating and uncovering coal in gas tunnels, it is necessary to consider the similarities and differences between long-distance through-coal seam tunnels and coal mine roadway driving according to specific engineering

conditions, take targeted outburst prevention measures with low damage to surrounding rocks on the premise of accurately predicting outburst dangers, and make timely adjustment according to the characteristics of dynamic behaviors to ensure safe and rapid uncovering of coal seams. This requires that the preextraction of gas in gas tunnels before mining needs the characteristics of less disturbance to the surrounding rocks of roadways, short gas emission period, high efficiency, etc.

According to the method of networked slotting in long-distance through-coal seam tunnels for rapid pressure relief and outburst elimination proposed in this paper, it is necessary to use as few boreholes and slots as possible to achieve the highest extraction efficiency, so as to meet the requirements of outburst prevention in gas roadways or tunnels. In this paper, through numerical analysis and field test verification on key parameters of borehole arrangement spacing and hydraulic slot arrangement spacing for preextraction of gas tunnels, it is intended to obtain the optimal borehole arrangement spacing and slotting that meets the gas preextraction index.

3. Mathematical Model Equations

3.1. Coal Mass Deformation Equation. Assuming that thermal expansion/contraction and matrix expansion/contraction are isotropic, the constitutive relation of a nonisothermal deformed coal seam can be written as (compression negative) [15, 16]

$$\varepsilon_{ij} = \frac{1}{2G}\sigma_{ij} - \left(\frac{1}{6G} - \frac{1}{9k}\right)\sigma_{kk}\delta_{ij} + \frac{\alpha}{3K}p_m\delta_{ij} + \frac{\beta}{3K}p_f\delta_{ij} + \frac{\alpha_T}{3}T\delta_{ij} + \frac{\varepsilon_s}{3}\delta_{ij}, \quad (1)$$

where σ_{ij} and δ_{ij} , respectively, represent total stress tensor and total strain tensor. $G = D/2(1 + \nu)$, $D = [1/E + 1/aK_n]^{-1}$, $K = D/3(1 - 2\nu)$, $\alpha = 1 - K/K_s$, and $\beta = 1 - K/a \cdot K_n$, and K is the bulk modulus of coal, K_s is the bulk modulus of the coal matrix, K_n is the normal stiffness of a single fissure, E is Young's modulus of coal, G is the shear modulus, ν is Poisson's ratio, α and β are coefficients of consolidation, δ_{ij} is the Kronecker symbol, and p is pore pressure. In the following tables, f and m represent matrix and fracture parameters, respectively; T is the coal reservoir temperature; and α_T is the thermal expansion coefficient of the coal matrix. Based on Equation (1), the volumetric strain ε_v is

$$\varepsilon_v = -\frac{1}{K}(\bar{\sigma} - \alpha p_m - \beta p_f) + \alpha_T T + \varepsilon_s, \quad (2)$$

where $\varepsilon_v = \varepsilon_{11} + \varepsilon_{22} + \varepsilon_{33}$ is the volumetric strain of coal mass; $\bar{\sigma} = -\sigma_{kk}/3$ is mean compressive stress. The volumetric strain ε_s generated by adsorption satisfies Langmuir-type curves, which can be calculated by Langmuir-type equations:

$$\varepsilon_s = \varepsilon_L \frac{p_m}{p_m + p_L}, \quad (3)$$

where ε_L is the Langmuir volumetric strain constant, representing the maximum volumetric strain caused by adsorption, and p_L is the Langmuir pressure constant.

The stress balance equation and geometric equation of coal containing gas can be expressed as

$$\sigma_{ij,j} + f_i = 0, \quad (4)$$

$$\varepsilon_{ij} = \frac{1}{2}(u_{i,j} + u_{j,i}), \quad (5)$$

where f_i is the body force component and u_i is the deformation displacement in the i direction. Combining Equations (1)–(5) and sorting them out, the Navier-type coal mass deformation equation can be obtained:

$$Gu_{i,jj} + \frac{G}{1-2\nu}u_{j,ii} - \beta_m p_{m,i} - \beta_f p_{f,i} - K\alpha_T T_{,i} - K\varepsilon_L \frac{p_L}{p_m + p_L} p_{m,i} + f_i = 0. \quad (6)$$

3.2. Coal Seam Gas Flow Equation. The gas flow in coal seams follows the mass balance equation:

$$\frac{\partial m}{\partial t} + \nabla \cdot (\rho_g \mathbf{q}) = Q_s, \quad (7)$$

where m is the gas mass per unit volume of coal, ρ_g is the gas density in coal mass, \mathbf{q} is the velocity vector of Darcy's law, and Q_s is the source item or sink item of gas. Assuming that gas adsorption only occurs in the coal matrix, the gas occurrence mass per unit volume of coal matrix m_m and the gas occurrence mass in fissures m_k can be expressed as

$$m_m = \phi_m \rho_{gm} + \rho_n \rho_c \frac{V_L p_m}{p_m + p_L}, \quad (8)$$

$$m_f = \phi_f \rho_{gf}, \quad (9)$$

where ρ_{gm} and ρ_{gf} , respectively, represent the gas density in coal matrix and coal mass fissures; ϕ_m and ϕ_f , respectively, represent the coal matrix porosity and coal fissure porosity; ρ_n is the gas density under the standard condition; and ρ_c is the density of coal. According to the equation of the state of ideal gas, the relationship between gas density and pressure can be expressed as

$$\rho_g = \frac{M_g}{RT} p, \quad (10)$$

where M_g is the molar mass of gas and R is the universal gas constant.

The mass exchange rate of gas between matrix and fissures is determined by the difference of gas content, which is directly proportional to gas pressure [17]:

$$Q_s = \frac{\rho_{gm} k_m \Psi}{\mu} (p_m - p_f), \quad (11)$$

where $\psi = 4(1/a_x^2 + 1/a_y^2)$ is the shape factor of coal and a_x and a_y are the lengths of the coal matrix.

Because the gaseous mass of gas is very small, ignoring the influence of gravity on the flow and diffusion process of gas in the coal seam and assuming that methane migration in coal seams is laminar, the velocity vector of gas can be obtained according to Darcy's law as follows:

$$\mathbf{q}_g = -\frac{k}{\mu} \nabla p. \quad (12)$$

Substituting Equations (8)–(11) into Equation (7) and sorting it out, the governing equation of coal matrix gas pressure changing with time can be obtained. The governing equation of gas migration in a dual-porosity media model is

$$\begin{aligned} \frac{\partial m_m}{\partial t} + \nabla \left(-\frac{k_m}{\mu} \rho_{gm} \nabla p_m \right) &= -\frac{\rho_m k_m \psi}{\mu} (p_m - p_f), \\ \phi_f \frac{\partial \rho_{fg}}{\partial t} + \rho_{gf} \frac{\partial \phi_f}{\partial t} + \nabla \left(-\frac{k_f}{\mu} \rho_{gf} \nabla p_f \right) &= \frac{\rho_m k_m \psi}{\mu} (p_m - p_f). \end{aligned} \quad (13)$$

The porosity change in the coal matrix can be expressed by the following equation [18]:

$$\phi_m = \frac{1}{1+S} [(1+S_0)\phi_{m0} + \alpha(S-S_0)], \quad (14)$$

where

$$\begin{aligned} S &= \varepsilon_v + \frac{p_m}{K_s} - \varepsilon_s - \alpha_T T, \\ S_0 &= \varepsilon_{v0} - \frac{p_{m0}}{K_s} - \varepsilon_L \frac{p_{m0}}{p_{m0} + P_L} - \alpha_T T_0. \end{aligned} \quad (15)$$

The permeability and porosity of the coal matrix meet the following relationship [19]:

$$\frac{k}{k_0} = \left(\frac{\phi}{\phi_0} \right)^3. \quad (16)$$

Bring Equation (14) into Equation (16), and coal matrix permeability

$$k_m = k_{m0} \left(\frac{1}{1+S} \left[(1+S_0) + \frac{\alpha}{\phi_{m0}} (S-S_0) \right] \right)^3. \quad (17)$$

Considering the anisotropy of the permeability of coal mass fissures, for a 2D model, the porosity and permeability in coal mass fissures can be calculated by the following equations [20]:

$$\frac{\phi_f}{\phi_{f0}} = 1 + 2(1-R_m)(\Delta\varepsilon_v - \alpha_T \Delta T - \Delta\varepsilon_s),$$

$$\frac{k_{fi}}{k_{f0}} = \left[1 + \frac{2(1-R_m)}{\phi_{f0}} \left(\Delta\varepsilon_j - \frac{1}{3} \alpha_T \Delta T - \frac{1}{3} \Delta\varepsilon_s \right) \right]^3, \quad i \neq j. \quad (18)$$

3.3. Heat Conduction Equation. Assuming that the constitutive equation of heat conduction satisfies Fourier's law, ignoring the interchangeability of thermal energy and mechanical energy, and considering that the temperature field in a binary medium is unitary, the heat transfer equation in the coal seam of a dual porosity model can be expressed as [21, 22]

$$\begin{aligned} (pC)_M \frac{\partial T}{\partial t} + TK_g \alpha_g (\nabla \mathbf{q}_{gm} + \nabla \mathbf{q}_{gf}) + TK \alpha_T \frac{\partial \varepsilon_v}{\partial t} \\ = \lambda_m \nabla^2 T - \rho_{gm} \mathbf{q}_{gm} C_g \nabla T - \rho_{gf} \mathbf{q}_{gf} C_g \nabla T, \end{aligned} \quad (19)$$

where $\lambda_M = (\phi_m + \phi_f)\lambda_g + (1 - \phi_m - \phi_f)\lambda_s$ and λ_g and λ_s are the thermal conductivity coefficients of solid and fluid components, respectively. $(pC)_M = \phi_m(\rho_{gm} C_g) + \phi_f(\rho_{gf} C_g) + (1 - \phi_m - \phi_f)(\rho_c C_s)$ is the heat capacity of porous media containing fluid; C_g and C_s are the specific heat capacities of a fluid and solid under constant volume, respectively; K_g is the volume modulus of pore gas; and $\alpha_g = 1/T$ is the thermal expansion coefficient of gas.

4. Project Overview and Calculation Model

A highway tunnel in Qinghai is 6024 m long with a buried depth of 116–452 m. The surrounding rock of the tunnel is an interbedding of strongly-moderately weathered macker, coal seams, and sandstone, and the rock mass has an argillaceous texture and thin-lamellar structure, which is fairly broken. The main mineral is argillaceous mineral. Due to the influence of stratum engineering geological conditions, the joints and fissures in this section are developed, the rock mass is broken, and the stability of the surrounding rock is poor, showing a cataclastic texture. According to the detection result, the left and right tunnels of this tunnel have more than 1,400 m or even longer sections passing through the coal seam gas area. The average thickness of the coal seam is 1.98 m, and the measured gas content and pressure are 11.5 m³/t and 1.2 MPa, respectively, which has an extremely high risk of coal and gas outburst. In order to improve the tunneling efficiency and quickly eliminate the danger of coal and gas outburst in the exposed coal seam, the water jet slotting technology was used to achieve permeability enhancement and gas extraction from the coal seam efficiently [23–25]. To optimize the slot arrangement in boreholes, a numerical model was established (as shown in Figure 1) to study the gas distribution in the coal seam and along the monitoring line under different slot arrangement modes. An unstructured triangular mesh domain in the numerical model is created. All the results obtained in this study are independent of mesh size and time

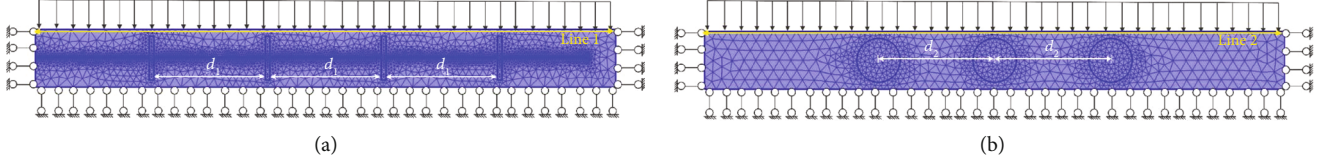


FIGURE 1: Schematic diagram of numerical simulation and corresponding boundary conditions.

TABLE 1: Main parameters for numerical simulation.

Model parameter	Parameter value
Model size (m)	20×1.98
Simulated buried depth (m)	200 m
Young's modulus of coal E (MPa)	1900
Young's modulus of coal matrix E_s (MPa)	8469
Poisson's ratio of coal ν	0.23
Apparent density of coal ρ_c (kg/m ³)	1400
CH ₄ Langmuir volume constant V_L (m ³ /t)	17.1
CH ₄ Langmuir pressure constant P_L (MPa)	1.729
CH ₄ dynamic viscosity μ (Pa·s)	1.84×10^{-5}
Borehole temperature (k)	293.15
Initial coal mass fissure permeability k_{f0} (m ²)	5.9×10^{-17}
Initial coal matrix permeability k_{m0} (m ³)	1×10^{-18}
Initial matrix porosity ϕ_m	0.07
Initial coal seam temperature T (K)	303
Maximum adsorption deformation of coal ϵ_L	0.025
Coefficient of thermal expansion of coal matrix α_T (K ⁻¹)	2.4×10^{-5}
Specific heat capacity of coal C_s (J/kg·K)	1.25×10^3
Specific heat capacity of gas C_g (J/kg·K)	1.625×10^3
Coefficient of heat conduction λ_s (J/kg·K)	0.2

step. Considering the construction efficiency onsite, the designed extraction period was 15 days. The slot length of the slotted borehole was 1.5 m and the width was 0.165 m, the slot spacing in the same along-seam borehole was d_1 (Figure 1(a)), and the slot spacing in the same plane of different along-seam boreholes was d_2 (Figure 1(b)). Parameters of the simulated coal seam are shown in Table 1.

4.1. Reasonable Slot Spacing in the Same Along-Seam Borehole d_1 . Figure 2 is a nephogram of gas distribution in coal matrix under different slot spacing d_1 after 15-day extraction. It can be seen from Figure 2 that, under the influence of negative pressure of extraction from the slotted borehole, the closer to the slotted borehole, the faster the gas pressure in the coal seam decreased. With the decrease of the number of slots in the borehole along the seam, the high gas pressure areas in the coal seam gradually increased. So, there is an optimal slot spacing arrangement. In China, the coal seam gas pressure below 0.74 MPa is taken as an index to judge whether the preextraction effect reaches the standard or not. Therefore, the optimal slot spacing d_1 was

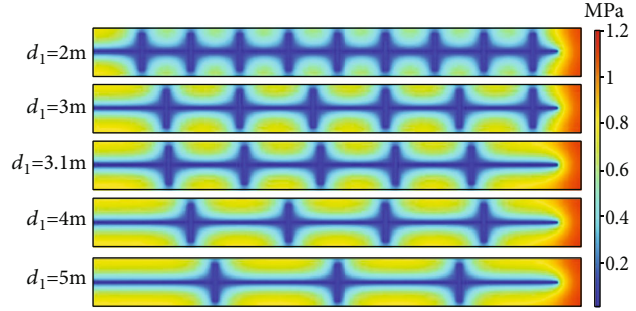


FIGURE 2: Gas pressure distribution in coal matrix under different slot spacing d_1 after 15-day extraction.

determined by detecting the gas pressure on the boundary monitoring line of the model under different slot spacing d_1 .

It can be seen from Figure 3 that, when the slot spacing was 2 m, the maximum coal matrix gas pressure between slots was 0.57 MPa, which was far lower than the index of 0.74 MPa, but the number of slots was too much, and it required cutting 9 slots within the 19 m long borehole along the seam, greatly increasing the construction cost. When the slot spacing was 4 m or 5 m, the maximum coal matrix gas pressure between slots exceeded 0.74 MPa, which was easy to bring the risk of outburst to later coal uncovering. In the end, through simulation, it was found that, when the slot spacing was 3.1 m, the gas pressure between slots was just less than the index value. Therefore, it was suggested that, in this study, the slot spacing in the same along-seam borehole in the coal seam should be designed to be 3.1 m, so as to optimize gas extraction of the coal seam within the extraction area before tunneling.

4.2. Reasonable Slot Spacing between Different Along-Seam Borehole d_2 . Figure 4 is a nephogram of gas distribution in the coal matrix under different slot spacing d_2 after 15-day extraction. Under the joint extraction of multiple slots, the gas pressure in the coal seam decreased, especially in the area between slots. With the increase of slot spacing between different along-seam boreholes, the residual gas pressure of the coal seam between slots gradually increased and gradually exceeded the index value from less than 0.74 MPa, which indicates that there is also an optimal slot spacing arrangement between different along-seam boreholes. By extracting the gas pressure of coal matrix on the monitoring line 2 (Figure 5), it was found that, when the slot spacing d_2 was 2.5 m, the maximum gas pressure in the coal seam between slots was 0.55 MPa, which reached the preextraction index. However, this arrangement is too dense, which will increase the construction amount. When the slot spacing d_2 was

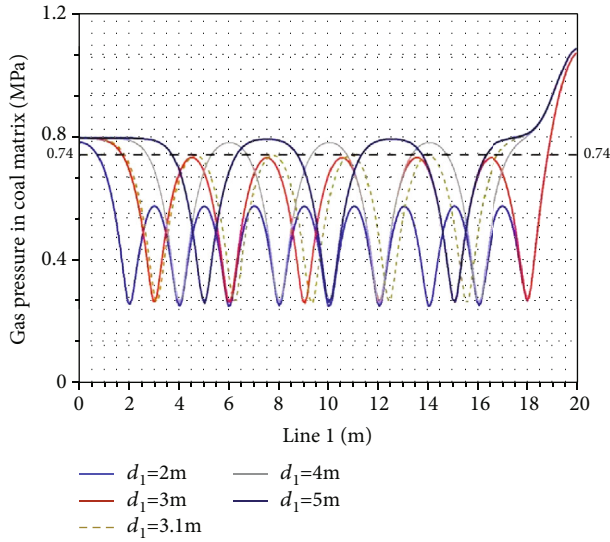


FIGURE 3: Distribution trend of gas pressure in coal matrix on monitoring line under different slot spacing d_1 .

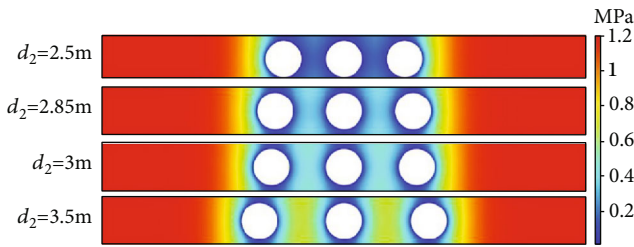


FIGURE 4: Gas pressure distribution in coal matrix under different slot spacing d_2 after 15-day extraction.

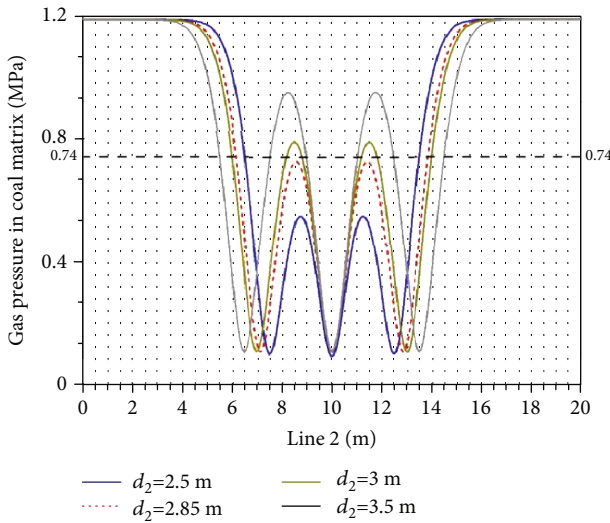


FIGURE 5: Distribution trend of gas pressure in coal matrix on monitoring line under different slot spacing d_2 .

2.85 m, the residual gas pressure between slots was 0.72 MPa, just reaching the preextraction index. However, when the slot spacing d_2 exceeded 2.85 m, reaching 3 m or 3.5 m, the residual gas pressure between slots reached 0.79 MPa and 0.95 MPa, respectively, which exceeded the preextraction index value of 0.74 MPa, and the gas extraction effect failed to reach the standard. In conclusion, it will be more reasonable to arrange the slot spacing d_2 between different along-seam boreholes in this coal seam as 2.85 m.

5. Analysis and Discussion of Application Results

In order to verify the correctness of the numerical analysis results, hydraulic slotting extraction was carried out at the optimized 2.85 m along-seam borehole spacing and 3.1 m slot spacing for the 60 m pretunneled through-coal seam tunnel. For another section of tunnel with the same length, a single-borehole extraction method was used as a blank controller for analysis, and the borehole spacing of this method was 2 m. A schematic diagram of the borehole design of the two methods is shown in Figure 6.

In order to compare the gas extraction effects of the two methods, we carried out statistical analysis on the field gas extraction, as shown in Figures 7 and 8, which are, respectively, the variations of gas extraction concentration, the net quantity of gas extraction, and the cumulative quantity of gas extraction quantity over time. It can be seen from the statistical data of gas extraction that it took 44 days to meet the outburst prevention requirements with the single-borehole extraction method, while it took only 15 days with the method of extraction after hydraulic slotting, which shortens the extraction period by 2/3 and greatly improves the efficiency. Figure 7 shows that the gas extraction concentration reached the peak concentration of 65% on the 43rd day by the single-borehole extraction method, while the gas concentration rose rapidly after hydraulic slotting, reaching the peak concentration of 61% only on the 8th day. In Figure 7, the net quantity of gas extraction of single-borehole extraction kept a relatively gentle trend during the first 35 days, all of which were below $0.2 \text{ m}^3/\text{min}$, and after the 35th day, the net quantity of extraction slowly increased to the peak value of $0.31 \text{ m}^3/\text{min}$. On the other hand, in the case with hydraulic slotting extraction method, it reached $0.4 \text{ m}^3/\text{min}$ on the 2nd day and quickly increased to the peak value on the 6th day, about $1.1 \text{ m}^3/\text{min}$, which was 3.55 times of the peak value of the net quantity of extraction with the single-borehole extraction method. According to the total quantity of extraction shown in Figure 8, the total quantity of gas extracted with the single-borehole extraction method was $10,011 \text{ m}^3$ after the gas pressure was lower than 0.74 MPa, while it reached this value on the 11th day with the method of extraction after hydraulic slotting, and after the gas pressure reached the standard, the total quantity of extraction reached $12,585.6 \text{ m}^3$, which was about 1.26 times that of the unslotted extraction method. The data in Figures 7 and 8 show that, compared with the traditional single-borehole extraction method, the long-distance through-coal seam tunnel adopting the method of hydraulic

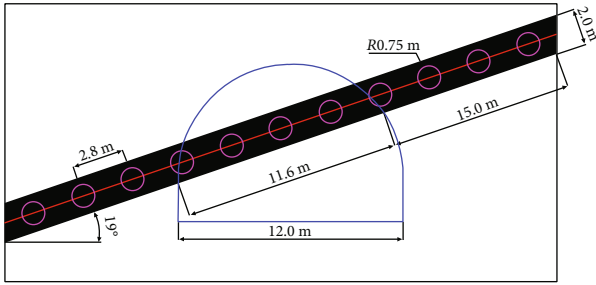


FIGURE 6: Schematic diagram of borehole arrangement for single-borehole extraction and hydraulic slotting extraction.

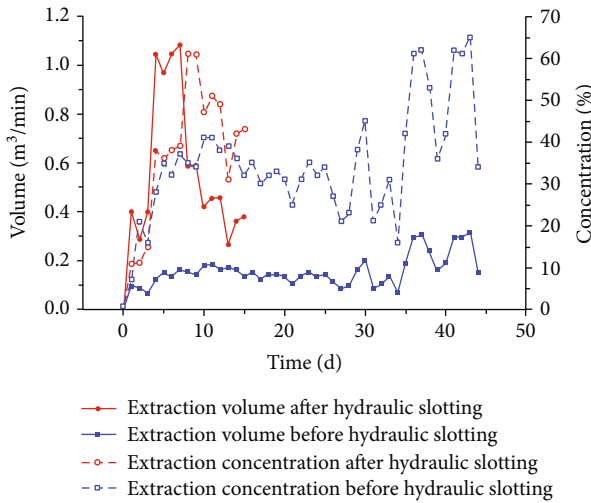


FIGURE 7: Gas extraction vs. time.

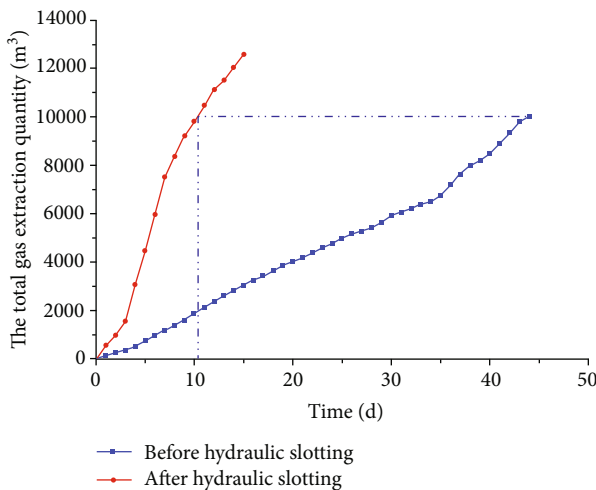


FIGURE 8: Total quantity of gas extraction vs. time.

slotting for quick pressure relief and gas extraction can quickly shorten the construction period, save the workload, and achieve the extraction outburst prevention index.

The residual gas quantity and residual gas pressure obtained with the two extraction methods are shown in Table 2. Both of the cases can meet the outburst prevention

TABLE 2: Outburst prevention index after extraction.

S/N	Extraction method	Residual gas content (m ³ /t)	Residual gas pressure (MPa)
1	Single-borehole extraction	7.2	0.71
2	Hydraulic slotting extraction	6.5	0.68

index, but the method of hydraulic slotting for quick pressure relief, because of the larger pressure relief area and higher extraction efficiency, can make the residual gas quantity and residual gas pressure even lower.

6. Conclusions

- (1) The differences between long-distance through-coal seam tunnels and underground coal mine roadway driving are analyzed. Compared with coal mine roadway driving, the work of long-distance through-coal seam tunnels generally has the characteristics of high degree of surrounding rock breakage, low degree of geological exploration, large cross-section of coal uncovering, tight time and space for implementing outburst prevention measures, strict control of surrounding rock deformation, etc. According to the outburst prevention characteristics needed for long-distance through-coal seam tunnels, this paper puts forward the method of networked slotting in long-distance through-coal seam tunnels for rapid pressure relief and outburst elimination
- (2) The mathematical governing equation and gas extraction numerical model of the method of networked slotting in long-distance through-coal seam tunnels for rapid pressure relief and outburst elimination has been established. The extraction simulation optimization analysis has been carried out on the arrangement of borehole spacing and slot spacing arrangement in this method, and the results that have been obtained are the following: the optimal borehole arrangement spacing is 2.85 m and the optimal slot arrangement spacing is 3.1 m
- (3) The efficiency of gas extraction of the method of networked slotting in long-distance through-coal seam tunnels for rapid pressure relief and outburst elimination and the method of dense-borehole gas extraction have been compared and analyzed, and the reliability of the method of networked slotting in long-distance through-coal seam tunnels for rapid pressure relief and outburst eliminations has been verified. The field experimental data of two kinds of gas extraction methods in the through-coal seam tunnel show that compared with the single-borehole extraction method, the method of networked slotting in long-distance through-coal seam tunnels for rapid pressure relief and outburst elimination can shorten

the extraction period by about 66%, increase the net quantity of peak extraction by 3.55 times, and increase the total quantity of gas extraction by 1.26 times when the outburst prevention index is reached. Due to the larger pressure relief area and higher extraction efficiency, the residual content and residual pressure of gas with this method are even lower. The experimental results has verified the correctness of the numerical analysis results as well as the reliability of this method

Data Availability

The numerical simulation data used to support the findings of this study are available from the corresponding author upon request.

Conflicts of Interest

The authors declare that they have no conflicts of interest.

Acknowledgments

This paper is jointly funded by the Qinghai Transportation Science and Technology Project (No. 2020-01).

References

- [1] D. Li, Y. Lu, Y. Rong et al., "Rapid uncovering seam technologies for large cross-section gas tunnel excavated through coal seams using directional hydraulic fracturing," *Rock and Soil Mechanics*, vol. 40, no. 1, pp. 363–370, 2019.
- [2] B. Li, Q. Wu, and Z. Liu, "Identification of mine water inrush source based on PCA-FDA: Xiandewang coal mine case," *Geofluids*, vol. 2020, Article ID 2584094, 8 pages, 2020.
- [3] D. Li, Y. Rong, S. Zhang, D. Zhou, and C. Guo, "Novel technology of large cross-section gas tunnel uncovering coal seam in Southwest China," *Chinese Journal of Underground Space and Engineering*, vol. 40, no. 1, pp. 363–370, 2019.
- [4] X. H. Li, T. L. Li, Y. L. Gu, and Y. Y. Lu, *Construction Technology of Uncovering Coal in Gas Tunnel*, Chongqing University Press, Chongqing, 2005.
- [5] D. Y. Jiang, C. Liu, G. Y. Zhang, and J. L. Zheng, "Technologies of whole cutting through coal seam and preventing collapse in highway tunnels," *Rock and Soil Mechanics*, vol. 26, no. 6, pp. 906–909, 2005.
- [6] G. B. Wang and Y. N. Li, "Application of comprehensive survey technique to gas tunnel of highway," *Rock and Soil Mechanics*, vol. 32, no. 4, pp. 1273–1277, 2011.
- [7] L. Cheng, Z. Ge, J. Chen, H. Ding, L. Zou, and K. Li, "A sequential approach for integrated coal and gas mining of closely-spaced outburst coal seams: results from a case study including mine safety improvements and greenhouse gas reductions," *Energies*, vol. 11, no. 11, p. 3023, 2018.
- [8] L. Cheng, Z. Ge, B. Xia et al., "Research on hydraulic technology for seam permeability enhancement in underground coal mines in China," *Energies*, vol. 11, no. 2, p. 427, 2018.
- [9] C. Liang, L. Yi-yu, G. Zhao-long, D. Hong, and Z. Ding-yun, "Initiation pressure calculation model and judgment criterion for hydraulic fracturing of inclined coal seam," *Rock and Soil Mechanics*, vol. 36, no. 2, pp. 444–450, 2015.
- [10] Y. Y. Lu, Y. Z. Jia, J. R. Tang, and S. Chen-peng, "Mechanism of hydro fracture propagation control by no uniform pore pressure field," *Journal of Northeastern University (Natural Science)*, vol. 37, no. 7, pp. 1028–1033, 2016.
- [11] Y. J. Feng and H. P. Kang, "Hydraulic fracturing initiation and propagation," *Chinese Journal of Rock Mechanics and Engineering*, vol. 32, no. 2, pp. 3169–3179, 2013.
- [12] W. Yaofeng, H. Xueqiu, W. Enyuan, and L. Zeng-yan, "Research progress and development tendency of the hydraulic technology for increasing the permeability of coal seams," *Journal of China Coal Society*, vol. 39, no. 10, pp. 1945–1955, 2014.
- [13] J. Wang, Z. Wan, Y. Wang et al., "Effect of stress and moisture content on permeability of gas-saturated raw coal," *Geofluids*, vol. 2020, Article ID 8837758, 13 pages, 2020.
- [14] J. Zhang, L. Si, J. Chen, M. Kizil, C. Wang, and Z. Chen, "Stimulation techniques of coalbed methane reservoirs," *Geofluids*, vol. 2020, Article ID 5152646, 23 pages, 2020.
- [15] J. Liu, Z. Chen, D. Elsworth, H. Qu, and D. Chen, "Interactions of multiple processes during CBM extraction: a critical review," *International Journal of Coal Geology*, vol. 87, no. 3–4, pp. 175–189, 2011.
- [16] Y. Wu, J. Liu, D. Elsworth, Z. Chen, L. Connell, and Z. Pan, "Dual poroelastic response of a coal seam to CO₂ injection," *International Journal of Greenhouse Gas Control*, vol. 4, no. 4, pp. 668–678, 2010.
- [17] K. T. Lim and K. Aziz, "Matrix-fracture transfer shape factors for dual-porosity simulators," *Journal of Petroleum Science and Engineering*, vol. 13, no. 3–4, pp. 169–178, 1995.
- [18] H. Zhang, J. Liu, and D. Elsworth, "How sorption-induced matrix deformation affects gas flow in coal seams: a new FE model," *International Journal of Rock Mechanics and Mining Sciences*, vol. 45, no. 8, pp. 1226–1236, 2008.
- [19] X. Cui and R. M. Bustin, "Volumetric strain associated with methane desorption and its impact on coalbed gas production from deep coal seams," *AAPG Bulletin*, vol. 89, no. 9, pp. 1181–1202, 2005.
- [20] J. Liu, Z. Chen, D. Elsworth, X. Miao, and X. Mao, "Linking gas-sorption induced changes in coal permeability to directional strains through a modulus reduction ratio," *International Journal of Coal Geology*, vol. 83, no. 1, pp. 21–30, 2010.
- [21] Y. Zhou, R. K. N. D. Rajapakse, and J. Graham, "A coupled thermoporoelastic model with thermo-osmosis and thermal-filtration," *International Journal of Solids and Structures*, vol. 35, no. 34–35, pp. 4659–4683, 1998.
- [22] W. C. Zhu, C. H. Wei, J. Liu, H. Y. Qu, and D. Elsworth, "A model of coal-gas interaction under variable temperatures," *International Journal of Coal Geology*, vol. 86, no. 2–3, pp. 213–221, 2011.
- [23] Y. Liu, J. Zhang, T. Zhang, and H. Zhang, "Optimal nozzle structure for an abrasive gas jet for rock breakage," *Geofluids*, vol. 2018, Article ID 9457178, 14 pages, 2018.
- [24] D. Su, D. Zheng, and L. Zhao, "Experimental study and numerical simulation of dynamic stress-strain of directional blasting with water jet assistance," *Shock and Vibration*, vol. 2019, Article ID 1659175, 15 pages, 2019.
- [25] D. Su, Y. Kang, D. Li, X. Wang, and F. Yan, "Analysis and numerical simulation on the reduction effect of stress waves caused by water jet slotting near blasting source," *Shock and Vibration*, vol. 2016, Article ID 5640947, 18 pages, 2016.

Research Article

Design and Realization of the Intelligent Design System for Tunnel Blasting in Mine Based on Database

Zhengyu Wu ¹, Dayou Luo ², and Guan Chen ³

¹School of Engineering, Fujian Jiangxia University, 2 Xiyuangong Road, Fuzhou 350108, China

²Engineering, Francis College of Engineering, University of Massachusetts Lowell, Lowell, MA 01854, USA

³State Key Laboratory of Water Resources and Hydropower Engineering Science, Institute of Engineering Risk and Disaster Prevention, Wuhan University, 299 Bayi Road, Wuhan 430072, China

Correspondence should be addressed to Dayou Luo; dayou_luo@uml.edu

Received 26 August 2020; Revised 8 October 2020; Accepted 14 October 2020; Published 27 October 2020

Academic Editor: Bin-Wei Xia

Copyright © 2020 Zhengyu Wu et al. This is an open access article distributed under the Creative Commons Attribution License, which permits unrestricted use, distribution, and reproduction in any medium, provided the original work is properly cited.

With the improvement of informatization and standardization of mine development, it is an inevitable trend to apply computer technology to the intelligent design of tunnel blasting excavation. Seeking to the problems existing in the intelligent design system of blasting excavation, a new intelligent design system of blasting excavation is constructed from the perspective of database technology. The new intelligent design system adopts the design of central database system and subuser rights to meet the data synchronization and sharing among different users. At the same time, the new system also extracts blasting design parameters and actual engineering data and designs a more reasonable and comprehensive database structure, database logic, and data word table. Based on the T-S fuzzy neural network model, the intelligent search rules of excavation blasting data are also constructed in the new system. Finally, based on Oracle and VB.NET as the new system development platform, MFC, and ADO as the new system development technology, the new intelligent design system for tunnel blasting and excavation was completed. The implementation of the new system addresses the needs of blasting data information storage and search and lays a foundation for the informatization and standardization of tunnel excavation blasting.

1. Introduction

1.1. Research Status of the Intelligent Blasting Design System.

Tunnel excavation is the most basic part of mining. The drilling and blasting method have the advantages of flexibility, convenience, and speed, which make the drilling and blasting method widely used in tunnel design and construction [1–3]. At present, the parameter design and data management are usually compiled manually, which leads to a series of problems in actual engineering, such as nonstandard blasting design, complex, and fragmentary blasting parameters. Therefore, how to change the backward situation of manual design calculation, drawing, and manual compilation and management of blasting data has become an urgent problem in the field of blasting and tunnel engineering [4–6]. With the continuous development of information technology and computer hardware, the concept of digital mines continues to deepen and improve. It has become an inevitable trend

to use computer technology to collect and summarize blasting parameters and to intelligently design and manage blasting and construction information [7, 8]. In recent years, many experts and scholars have developed a series of blasting parameter management systems and blasting and tunneling design software. For example, Li developed a deep hole blasting design system for water conservancy and hydropower projects based on the Access and Visual Basic platform [9], Yang et al. based on rules and typical case reasoning mechanisms, while using production rules and maximum matching reasoning strategies to achieve coal mine tunnel blasting intelligent design software [10], Zhang et al. combined software engineering and artificial intelligence to develop an intelligent system for tunnel blasting design [11], Mamurekli developed a set of open-pit mining intelligent design software based on the expert knowledge base and black box theory [12], and Chung and Preece developed a database system based on the SQL language platform [13]. However, the

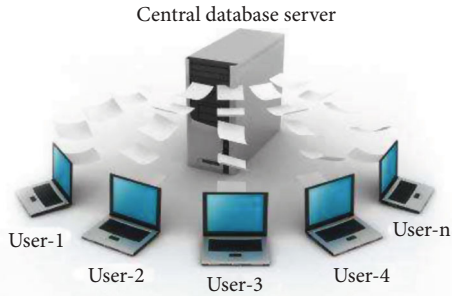


FIGURE 1: Central database system model.

current mainstream intelligent design and data management systems for tunnel blasting still have problems such as insufficient development depth, incomplete data synchronization, and chaotic logic flow [14]. In tunneling and blasting, whether it is parameter management or intelligent design software development, the key issue is the completeness and accuracy of the data [15, 16]. Therefore, to fundamentally solve the existing problems in the current tunnel blasting design system is only by solving the data problem. This paper takes database technology as the key and combines it with neural network technology and computer programming technology to develop a new intelligent tunnel blasting design system, which realizes the use of computer methods instead of manual management of tunnel blasting data and further promotes informationization and standardization of tunnel blasting.

1.2. Problems in Existing Blasting Intelligent Design System

1.2.1. Data Cannot Be Synchronized and Shared. Due to the development purpose and development platform, most of the current mining and blasting database systems are only attached to the software alone and cannot complete the real-time sharing and interaction of data between users. This leads to two problems when users use the database system: one is that data must be updated manually or imported manually, which greatly reduces the efficiency of work and the accuracy of data; the other is that users are using existing data for data. In management and intelligent design, there are obvious differences in the results of queries or calculations.

1.2.2. Selection of Blasting Data Is No Comprehensive and Data Flow Is Chaotic. The key to the blasting intelligent design system is data. The incomplete data content and the confusion of the data logic will prevent users from entering and querying the corresponding blasting data accurately and efficiently. At the same time, this problem also makes the subsequent development of the database suffer from design and function incompleteness.

1.2.3. Insufficient Use of the Database. At present, in the mainstream blasting design system, the development of the database is usually only used as a module of the system or as a data management tool and only realizes the functions of data storage calling and management. The functions are relatively simple, especially the search function, which is usu-

ally based on the database development software. Corresponding to the search mode, there is no intelligent search matching the characteristics of the tunneling blasting parameters.

2. Key Issues of Building an Intelligent Design System for Mine Tunnel Blasting Based on Database Technology

The design of tunnel blasting is based on engineering empirical data. In this design process, there are many inherent connections between parameters that have not been understood. Therefore, finding the relationship between blasting design parameters and blasting results based on tunneling blasting data and through some mathematical methods has become an important method to analyze and solve problems in tunneling blasting. Data is the basis for analyzing blasting problems, so the development of intelligent design system is based on database.

Given the existing problems in the development and implementation of the current blasting and tunneling database system, the paper studied the core issues of the construction of the mine tunneling blasting database system from the perspective of database technology, which is mainly reflected in the following three aspects:

2.1. Database System Structure and User Permissions

2.1.1. Database Architecture. The construction of the database system is related to the basic operating form and structure of the database system and determines how all users process blasting data. To solve the problem of data sharing and synchronization among users, the new intelligent design system adopts a central database structure system, and the system model is shown in Figure 1. The new system adopts a unified central database server when designing the database. The operation interface is only used as a front platform to reflect users' data operations. Data between users only interact through the central data server to complete data synchronization and sharing.

Figure 2 shows the basic workflow of a central database system model. The overall framework of the system is divided into four levels: instance, database, database server, and interface. The running process of the central database system: after data, commands are issued by multiple users to the operation interface layer, the unified database system server layer responds, then the syntax analysis, compilation, and execution are performed in the memory area of the instance layer, then the modified data is written into the data file, the modification information of the database layer is written into the log file, and finally, the execution result of the data command is returned to the operation interface layer to complete the user's management of blasting data and the application of the database system.

2.1.2. User Permission. In the database operation of the new system, three different types of user attributes are designed, and the corresponding permissions for different user attributes are set accordingly. Its purpose is to facilitate the

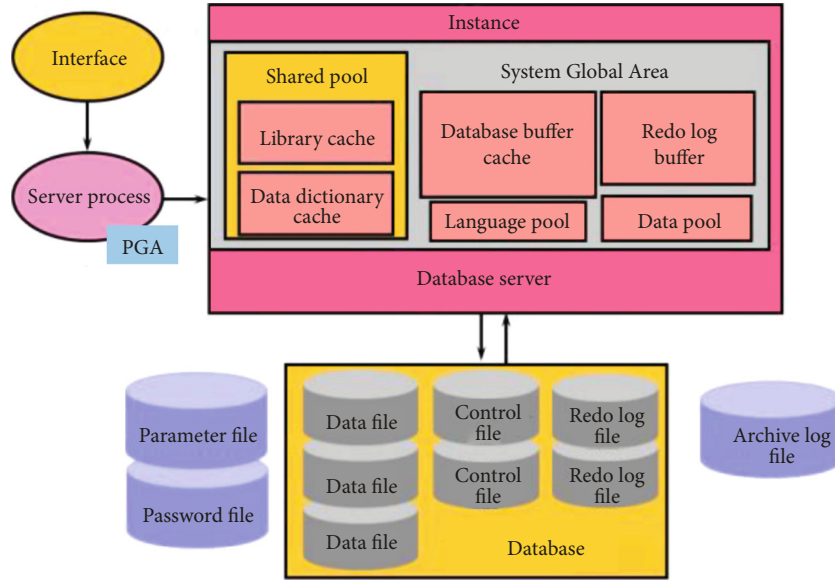


FIGURE 2: Basic architecture of the database system operation.

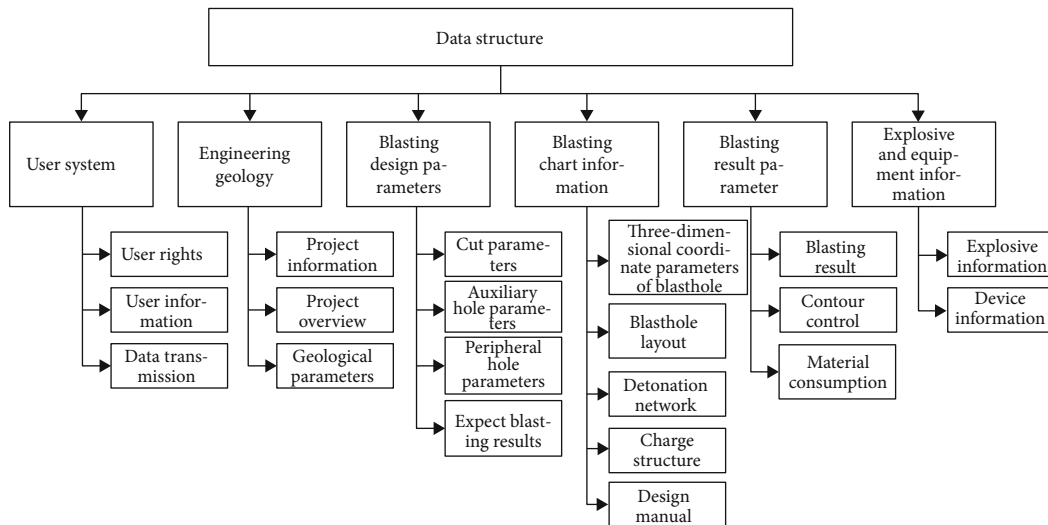


FIGURE 3: Date structure of intelligent design system for mine tunnel blasting based on database.

TABLE 1: User permission design.

User attributes	Operation authority and content		
	Self-data	Not self-data	Database system
Common user	Modify	Access	Non
Advanced user	Modify	Modify	Non
System administrator	Modify	Modify	Modify

management of the excavation blasting data by different users, ensure the security of data between different users, and further realize the sharing and synchronization of data. The specific design scheme is shown in Table 1.

2.2. Database System Design. Database system design is the core part of the new intelligent design system for tunnel

blasting, which ensures the reasonable and efficient operation of the new system. The database implementation process includes three parts: date content and structure (requirement analysis), data flow and logic (logical design), and data table design (physical design).

2.2.1. Date Content and Date Structure. The data content refers to all the data involved in the process of tunnel blasting which should be included in the database, and the data structure refers to the structure system of these data stored in the database.

(1) Data Content. According to references [17–20], in blasting design content and actual blasting experience, the data of tunnel blasting excavation should include three parts: engineering-geological parameters, blasting design

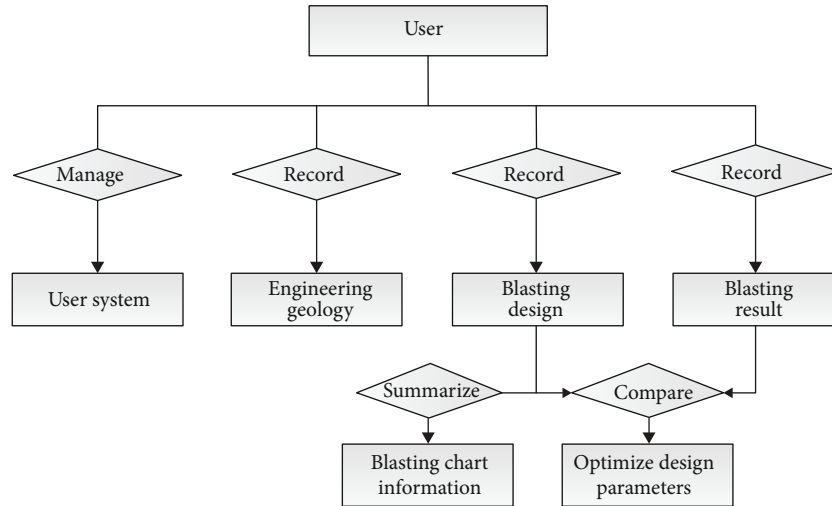


FIGURE 4: Global E-R diagram of the intelligent design system for mine tunnel blasting based on database.

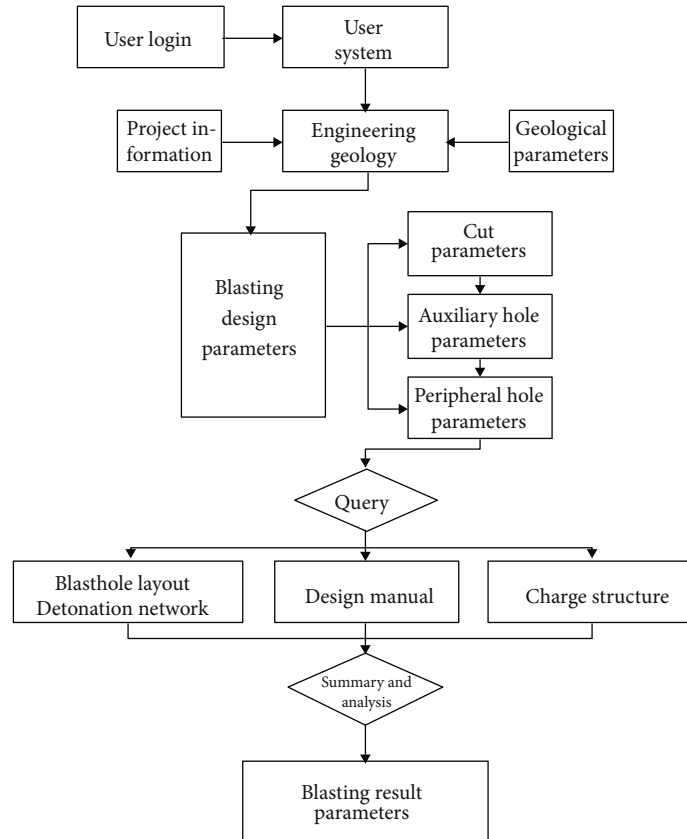


FIGURE 5: Data logic of intelligent design system for mine tunnel blasting based on database.

parameters, and blasting result parameters. Among them, the suitable engineering-geological parameters include the size of the design roadway section, surrounding rock type, rock f value, rock integrity, and groundwater. The suitable blasting design parameters include cutting mode and parameters, peripheral hole parameters, single-shot charge quantity, design cycle footage, and blasting hole layout parameters.

The suitable blasting result parameters include the actual cycle footage, explosive unit consumption, explosive consumption, and over-under excavation values. Overall, a total of 96 data contents were designed into the new system.

(2) *Date Structure*. To facilitate user operation and make the tunnel blasting data better management and query, three

TABLE 2: Design parameters of the peripheral hole.

Field name	Field data type	Length	Additional attributes	Remarks
Blasting section number	Text	30	Required	Index
Number of upper holes	Numeral	8	Required	Non
Depth of upper holes	Numeral	8	Required	Non
The angle of upper holes	Numeral	8	Required	Non
Distance between upper holes and contour	Numeral	8	Required	Non
Number of side holes	Numeral	8	Required	Non
Depth of side holes	Numeral	8	Required	Non
The angle of side holes	Numeral	8	Required	Non
Distance between side holes and contour	Numeral	8	Required	Non
Number of bottom holes	Numeral	8	Required	Non
Depth of bottom holes	Numeral	8	Required	Non
The angle of bottom holes	Numeral	8	Required	Non
Distance between bottom hole and contour	Numeral	8	Required	Non
Hole diameter	Numeral	8	Required	Non
Charge method	Text	30	Required	Non
Charge	Numeral	8	Required	Non
Forward view of the blasthole layout	Annex	-	Storage path	File
Side view of the blasthole layout	Annex	-	Storage path	File
Design time	Time	42	Required	Non

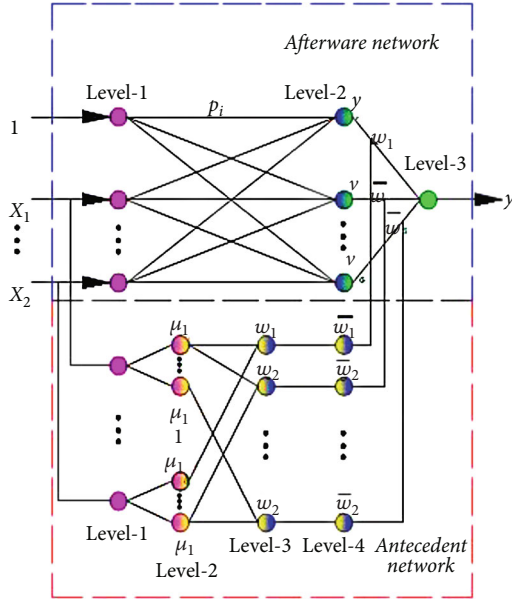


FIGURE 6: Fuzzy neural network structure based on T-S model.

parts of data content are extended to six types of data. The structure is illustrated in Figure 3. These six types of data are data structures, including user system module, engineering geology module, blasting design parameter module, blasting chart information module, blasting result parameter module, explosives, and equipment information module. The user system module manages user rights, user information, user data sharing, and synchronization. The engineering geol-

ogy module manages the specific information about the project and the geological conditions of the blasting area. The blasting design parameter module and the blasting chart information module are the core content of data, which manage blasting design parameters and design drawings. The blasting result parameter module manages the actual postblast data of each blasting scheme. The explosive and equipment information module manage the explosive and equipment information during blasting.

2.2.2. *Data Logic and Flow.* To simplify the database design and improve the utilization rate of the database word table, the database adopts the relational model in the logic design. When designing a relational database, it is necessary to establish a logical model for it. The logical model can be represented by a graph (E-R diagram) composed of entities and relationships. Due to space limitations, only the global E-R diagram of the system is shown, as shown in Figure 4. At the same time, according to the data correlation in the tunnel blasting design, the data flow diagram in the database is given, as shown in Figure 5.

2.2.3. *Data Table Design.* The design content of each corresponding data table is determined by the data content and data flow direction of tunnel blasting, including system user table, engineering item table, geological data table, cutting parameter table, and peripheral hole design table. The total number of data tables is 38 sheets. The design of each data sheet includes the following factors: field name, field data type, length, additional attributes, and remarks. Due to space limitations, only the datasheet of peripheral hole parameters

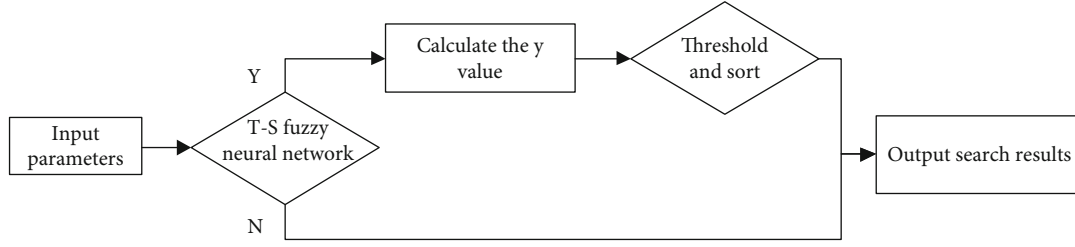


FIGURE 7: Data search flow chart of the database.

TABLE 3: Fuzzy digital index of joint fissure.

Criteria for the classification	<1/m	1-3/m	3-5/m	5-7/m	>7/m
Fuzzy index	0.1	0.3	0.5	0.7	0.9

is taken as an example. The specific content is shown in Table 2.

2.3. Data Intelligent Search. There are two main search behaviors in the new system. One is to search for existing user names or project names to obtain corresponding blasting data. The other is to search for design conditions or expected design results to obtain corresponding or similar blasting design data. The former adopts a common search model and can be realized by using the search function of the database itself. The latter is an intelligent search model, which can be realized only by designing a matching intelligent search algorithm. Considering that there is a certain “fuzziness” in blasting parameters during the intelligent search, and the membership weights between search parameters need to be calculated, the intelligent search model is researched and designed based on the T-S fuzzy neural network model to realize the intelligent search behavior of the new system.

Steps of intelligent search: first, collect the existing blasting design parameters through field tests and reference records. The parameters include geological condition parameters, blasting design parameters, and blasting result parameters. Secondly, the collected data is entered into the database, and part of the data is fuzzy and normalized to unify the data calculation standard. Subsequently, using T-S artificial neural network technology to analyze the influence of geological conditions and blasting design parameters on the blasting results determines the relationship between geological conditions, blasting design parameters, and blasting results, that is, determines the weight relationship between each parameter. Finally, by judging the weight relationship of the input search, the result of the intelligent search is determined.

2.3.1. T-S Fuzzy Neural Network Calculation Rules. The “T-S fuzzy model” has the characteristics of automatically updating and continuously correcting the membership function

of fuzzy subsets [21]. The neural network structure of this model is shown in Figure 6.

The T-S fuzzy model is usually defined in the form of the following “if-then” rule. When the rule is R^i , its fuzzy inference logic is as follows:

$$R^i: \text{if } x_1 \text{ is } A_1^i, x_2 \text{ is } A_2^i, \dots, x_k \text{ is } A_k^i, \text{ then } y_i = p_0^i + p_1^i x_1 + \dots + p_k^i x_k.$$

A_j^i is the sample set of all parameters of the fuzzy system, $p_j^i (j = 1, 2, 3, \dots, k)$ is the parameter of the fuzzy system, and y_i is the calculation output of the fuzzy rule. The above inference rules indicate that the determined output y_i is a linear combination of samples corresponding to the fuzzy input x_i .

Suppose that for the $x = [x_1, x_2, x_3, \dots, x_k]$ corresponding to the input parameter, the membership degree of each input variable x_i is first calculated by fuzzy rules:

$$\mu_{A_j^i} = \exp\left(\frac{-(x_j - c_j^i)^2}{b_j^i}\right) \quad j = 1, 2, \dots, k; i = 1, 2, \dots, n. \quad (1)$$

c_j^i and b_j^i represent the center and width of the input function; c_j^i is determined by input parameters, and b_j^i is determined by all input parameters. c_j^i and b_j^i need to normalize all samples and parameters before calculation; k is the input dimension, and n is the number of fuzzy subsets. Then, the fuzzy calculation of each membership degree is performed by the method of continuous multiplication by the fuzzy operator:

$$\omega^i = \mu_{A_j^1}(x_1) \times \mu_{A_j^2}(x_2) \times \dots \times \mu_{A_j^k}(x_k) \quad i = 1, 2, \dots, n. \quad (2)$$

Obtain the model output value y based on the fuzzy calculation result:

$$\begin{aligned} y &= \sum_{i=1}^n \omega^i (p_0^i + p_1^i x_1 + \dots + p_k^i x_k) / \sum_{i=1}^n \omega^i \\ &= \sum_{i=1}^n \bar{\omega}^i (p_0^i + p_1^i x_1 + \dots + p_k^i x_k). \end{aligned} \quad (3)$$

After the T-S fuzzy neural network completes the calculation, it sorts in descending order according to the magnitude of the value, sets a threshold Y , and makes the following reasoning:



FIGURE 8: The startup interface of the intelligent design system for mine tunnel blasting based on database.

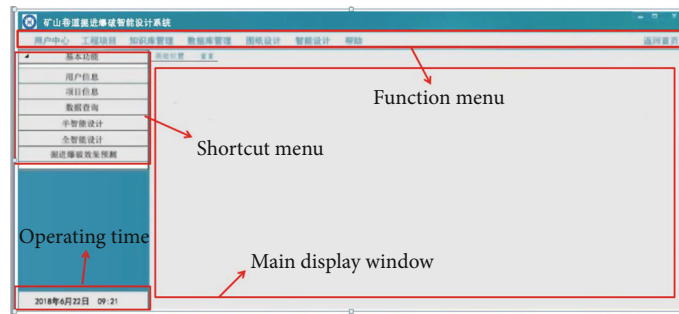


FIGURE 9: The operation interface of the intelligent design system for mine tunnel blasting based on database.

If: $y \geq Y$, then output “Data sample number corresponding to y value.”

2.3.2. *The Process of Data Intelligent Search.* The process of intelligent search is shown in Figure 7, which contains two processes:

(1) *Determine the Search Parameters of the Input Fuzzy Neural Network.* Considering the user’s usage habits and blasting site, the intelligent search selects two types of parameter input modes, one is based on geological conditions, and the other is based on blasting parameters. Geological condition search data = {hydrological conditions, joints and cracks, roadway section area, roadway height, width, surrounding rock strength f value, rock mass stability}. Blasting parameter search data = {cutting method, the total number of blastholes, charging method, explosive unit consumption, maximum single-shot charge, cycle footage}. Among them, some fuzzy indexes (joint cracks) and text indexes (hydrological conditions) need to be fuzzified mathematically. Due to space limitations, only the treatment values of {joint cracks} are shown in Table 3.

(2) *Fitting of Blasting Parameters Based on T-S Model Fuzzy Neural Network.* Based on the blasting data and input conditions, the T-S fuzzy neural network will perform corresponding self-learning and calculate the corresponding weights. The purpose of self-learning is to analyze the relationship between existing blasting data, and the purpose of

weight calculation is to obtain the specific weight of decision data under input conditions. At this time, the input parameter in the new system is the fitting coefficient of the neural network = {error calculation, coefficient correction, parameter correction} (generally it has been designed in advance). Finally, the system will output the search results according to the data output rules and complete the intelligent search at the same time.

3. Realization of Intelligent Design System for Mine Tunnel Blasting and Driving Based on Database

3.1. *System Development.* The new system chose Oracle as the database development platform [22], VB.NET as the system software development platform [23], MFC, and ADO as the development technology [24] and finally realized the mine tunnel intelligent blasting design system. Figure 8 shows the startup interface of the new system. Figure 9 shows the operation interface of the new system.

3.2. *Data Collection.* Data collection adopts two methods: engineering site and document extraction, of which the engineering site is the main one. Figure 10 shows a site parameter collection; Figure 10(a) is the collection of blasting design parameters, and Figure 10(b) is the collection of blasting result parameters.

To ensure the richness and source reliability of tunneling and blasting data, the new system has collected 594



(a) Collection of blasting design parameters

(b) Collection of blasting result parameters

FIGURE 10: Collection of engineering site parameters.

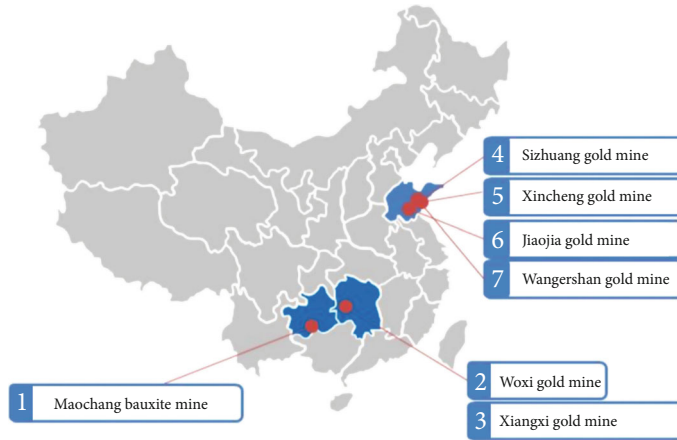


FIGURE 11: Data source and data distribution of tunnel blasting in the new system.

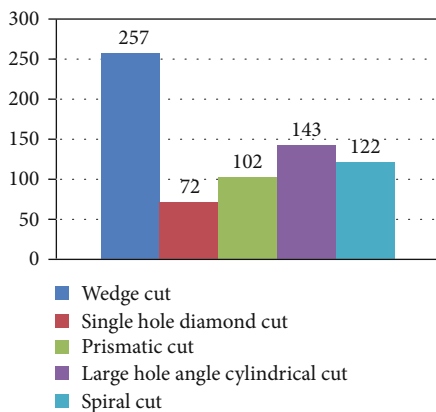


FIGURE 12: Number of cases under various cutting schemes.

tunneling blasting cases from 7 mines (mining areas) and 43 different roadways through field tests and case collection schemes for different cutting plans. For cases, Figure 11 shows the distribution of data sources in the

new system, and Figure 12 shows the number of cases under various cutting schemes.

4. Application of Intelligent Design System for Mine Tunnel Blasting Based on Database

Briefly show the practical application of intelligent systems.

Take the needs of an actual project as an example. Table 4 is the search parameter of the application example, which adopts the intelligent search method, and the default values are used for other values without specific values. The search interface is shown in Figure 13, and Figure 14 shows the corresponding output results.

It can be found from Figure 15 that through data search, 6 search results that meet the relevance calculation requirements are selected from the existing database files. Among them, the search results of No. 1 and No. 2 have a single parameter of 100% relevance. Figure 14 shows a schematic diagram of the specific blasting parameters and blasthole layout scheme numbered 1 in the search results. It can be found from the figure that the search results meet the search requirements.

TABLE 4: Input parameters.

Input parameters	Tunnel height/m	Tunnel width/m	Surrounding rock f value	Cycle footage/m	Relativity/%
Value	3.5	4.8	12-14	>1.6	80

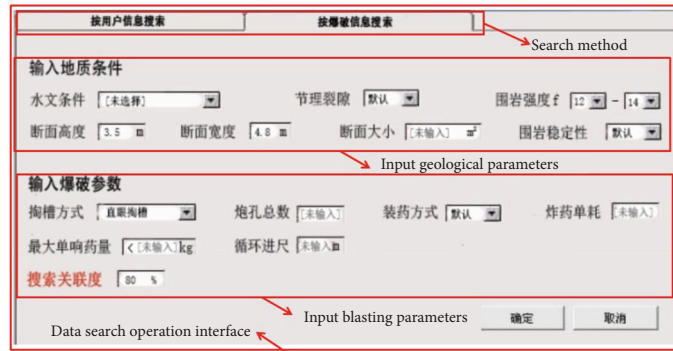


FIGURE 13: The search interface using intelligent search.

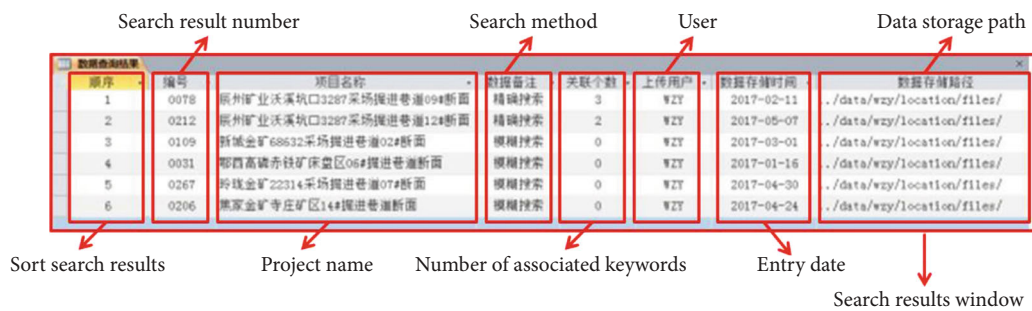


FIGURE 14: The output of the fuzzy search.

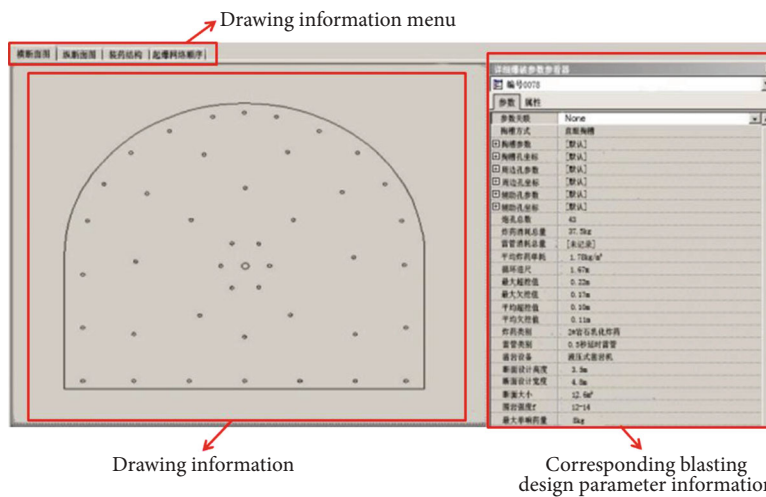


FIGURE 15: Blasting parameter table and blasting hole layout.

5. Conclusion

Aiming at the problems of the intelligent design system for blasting, starting from the key technology of the database, the research and development of the intelligent design system for tunnel blasting are carried out. This paper expounds the core problems in the development of an intelligent tunnel blasting design system based on database technology and proposes specific solutions:

- (1) The database of the new system adopts a central database system. At the same time, to ensure the synchronization and sharing of data, different user rights are designed
- (2) According to the characteristics of blasting design and parameters, select appropriate blasting design parameters and related data. Combining relational database theory, the database structure, and data table structure suitable for roadway blasting design are obtained, and each database table is created
- (3) Use the T-S fuzzy neural network model to determine the intelligent data search rules of the database

Finally, using Oracle as the database development platform, VB.NET as the system front-end and search rule development platform, and MFC and ADO as the development technology, the tunnel blasting intelligent design system was realized. Through this system, users can conduct unified management, search, and design of data in the tunnel blasting design process.

Data Availability

All data generated or analyzed during this study are included in this article.

Conflicts of Interest

The authors declare that they have no conflicts of interest.

Acknowledgments

This work was supported by the Foundation of Education Department of Fujian Province (Science and Technology) (JAT190459) and Natural fund project of Fujian Province Science and Technology Department (2020J0212307).

References

- [1] G. Chen, Q. Li, D. Li, Z. Y. Wu, and Y. Liu, "Main frequency band of blast vibration signal based on wavelet packet transform," *Applied Mathematical Modelling*, vol. 74, pp. 569–585, 2019.
- [2] Q. Li, G. Chen, D. Luo, H. P. Ma, and Y. Liu, "An experimental study of a novel liquid carbon dioxide rock-breaking technology," *International Journal of Rock Mechanics and Mining Sciences*, vol. 128, article 104244, 2020.
- [3] B. Dai and Y. Chen, "A novel approach for predicting the height of the water-flow fracture zone in undersea safety mining," *Remote Sensing*, vol. 12, no. 3, p. 358, 2020.
- [4] X. Q. Fang, T. F. Zhang, B. L. Li, and R. J. Yuan, "Elastic-slip interface effect on dynamic stress around twin tunnels in soil medium subjected to blast waves," *Computers and Geotechnics*, vol. 119, article 103301, 2020.
- [5] B. L. Li, X. Q. Fang, T. F. Zhang, and S. P. Yang, "Elastic-slip interface effect on dynamic response of underwater convey tunnel in saturated poroelastic soil subjected to plane waves," *Tunnelling and Underground Space Technology*, vol. 103, article 103468, 2020.
- [6] T. J. White and R. A. Fahn Field, "Computer and blasting," *Transactions of the Institution of Mining and Metallurgy, Section A: Mining Technology*, vol. 102, no. 4, pp. 19–24, 1993.
- [7] R. Steck, "Changing supplier after fifteen years of CAD history," *Kunststoffe International*, vol. 99, no. 7, pp. 20–27, 2009.
- [8] Z. Y. Wu, Q. Y. Li, D. G. Kong, G. Chen, and D. Luo, "The ANP-Fuzzy-TOPSIS model for the optimization of the scheme of large-section blasting," *Arabian Journal of Geosciences*, vol. 13, no. 2, pp. 1–9, 2020.
- [9] L. Ning, *Development and application research of deep hole step blasting design system for water conservancy and hydropower engineering*, Xi'an University of Technology, 2011.
- [10] R. S. Yang, X. M. Ma, Q. Li, and Z. R. Zhang, "Intelligent design system of tunneling blasting in coal mine and its application," *Journal of Coal*, vol. 38, no. 7, pp. 1131–1136, 2013.
- [11] J. C. Zhang, Q. H. Xiao, and Z. R. Xia, "Composition and structure of intelligent system for tunnel blasting design," *Explosion and Shock*, vol. 27, no. 5, p. 455, 2007.
- [12] D. Mamurekli, "A user-driven computer model for open pit blast design," *Journal of Mines Metals and Fuels*, vol. 50, no. 1, 2002.
- [13] S. H. Chung and D. S. Preece, "Benefits of using DMC-blast in open pit and underground mining," in *Proceedings of the Annual Conference on Explosives and Blasting Technique*, pp. 59–66, Nashville, Tennessee USA, 2002.
- [14] H. Jang and E. Topal, "A review of soft computing technology applications in several mining problems," *Applied Soft Computing*, vol. 22, pp. 638–651, 2014.
- [15] A. R. Misra, "IT application in blasting technology," *Journal of Mines, Metals and Fuels*, vol. 57, no. 8, pp. 214–218, 2009.
- [16] Q. Y. Li, D. Y. Luo, W. H. Wang, Z. Y. Wu, and D. H. Sun, "A case study on one shot raise driving using multi-spherical charges in an open pit mine," in *Rock Dynamics and Applications 3*, pp. 629–634, CRC Press, 2018.
- [17] G. L. Yang, L. L. Jiang, and R. S. Yang, "Research on double wedge-shaped deep hole blasting research," *Chinese Journal of Mining*, vol. 42, no. 5, pp. 754–760, 2013.
- [18] D. N. Lin and S. R. Chen, "Theoretical and experimental analysis of efficiency sensitive factors of straight hole cutting," *Journal of Coal*, vol. 30, no. 1, pp. 40–45, 2003.
- [19] X. Wang, *Manual of blasting*, Metallurgical Industry Press, 2005.
- [20] Q. Y. Li, D. Y. Luo, G. W. Feng, H. Ma, X. Wei, and G. Chen, "Dynamic characteristics of liquid CO₂ phase change fracturing, using experimental technique," *Geotechnical and Geological Engineering*, vol. 37, no. 4, pp. 3387–3398, 2019.
- [21] Z. Q. Sun and H. B. Xu, "Fuzzy neural network based on T-S model," *Journal of Tsinghua University*, vol. 37, no. 3, pp. 76–80, 1997.

- [22] C. Gonghe, *Database Foundation and Oracle application course*, Higher Education Press, 2003.
- [23] B. X. Wang, "Research on database access technology based on ADO.NET," *Computer Application and Software*, vol. 1, no. 2, pp. 95–99, 2004.
- [24] F. Xu, G. Z. Ma, and L. X. Liu, "Research and implementation of database access technology based on ADO," *Computer Engineering and Design*, vol. 15, no. 1, pp. 107–203, 2004.

Research Article

Height of Mining-Induced Fractured Zones in Overlying Strata and Permeability of Rock with Nonpenetrative Fractures

Yu Liu ¹, Qimeng Liu ², Wenping Li,³ and Youbiao Hu²

¹State Key Laboratory of Mining Response and Disaster Prevention and Control in Deep Coal Mines, Anhui University of Science and Technology, Huainan 232001, China

²School of Earth and Environment, Anhui University of Science and Technology, Huainan 232001, China

³School of Resources and Geosciences, China University of Mining and Technology, Xuzhou 221116, China

Correspondence should be addressed to Qimeng Liu; qmliu@aust.edu.cn

Received 26 August 2020; Revised 23 September 2020; Accepted 29 September 2020; Published 26 October 2020

Academic Editor: Zhengyang Song

Copyright © 2020 Yu Liu et al. This is an open access article distributed under the Creative Commons Attribution License, which permits unrestricted use, distribution, and reproduction in any medium, provided the original work is properly cited.

Exploitation of shallow thick coal seams that are overlain by phreatic aquifers may cause loss of the water resource and destruction of the surface ecological environment. In order to explain the phenomenon that the actual leakage of phreatic water is greater than the predicted value, field investigation and analogue simulation were carried out, and the nonpenetrative fractured zone (NFZ) was proposed based on the original three zone theory. Further, a “vertical four-zone model” was established and the overlying strata was divided into a caved zone (CZ), through-going fractured zone (TFZ), NFZ, and continuous zone (COZ) from the bottom to the top. The characteristics of fractured rock within NFZ and the determination method of its height were studied. The results showed that the height of NFZ ranged from 11.55 to 21.20 m, which was approximately 0.17 times the combined height of the TFZ and the CZ. To reveal the mechanism of phreatic water leakage, the permeability of rock within NFZ was studied for their premining and postmining using an in situ water injection test and laboratory test. The results showed that the permeability of the rock in NFZ was increased by 7.52 to 48.37 times due to mining, and the magnitude of the increase was nonlinear from top to bottom. The increase of permeability of tested specimens was also related to the lithology. The results of the study are helpful to the prediction of the potential loss of phreatic water and the determination of the mining thickness.

1. Introduction

Study on mining induced fractures in overlying strata, and their influence on rock mass permeability is very important for underground engineering such as coal, oil, and metal mining and tunnel excavation [1–3]. Coal, accounting for approximately 94% of China’s proven fossil energy reserves, is the most important energy source and the main industrial raw material to support China’s development [4]. The deformation and failure of overlying strata during coal mining often lead to ground subsidence and water resources leakage, thereby threatening production safety and damaging even destroying ground construction and the ecogeological environment [5–7].

Many theories including “pressure arch,” “cantilever beam,” “articulated rock mass,” “preformed fracture,” “voussoir beam,” “transferring rock beam,” and “key stratum” have

been put forward to explain the mining pressure and movement of overlying strata [8–11]. These theories have played an important role in understanding the overburden movement. In addition, the obvious zonation of the movement and failure of overlying strata due to longwall mining has been long recognized [12–14]. The “vertical three zone” model consisting of caved zone, fractured zone, and continuous zone of the strata movement and the distribution of mining induced fractures has been established [15, 16]. The fractured zone, also referred to as the vertical through-going fractured zone, and the caved zone are components of the fractured water-conducting fractured zone, which is the main pathway from the overlying aquifer into the gob [17–19]. However, the zonation is site specific. Other terms such as separation zone, loose alluvium zone, or downward fracture zone have been applied to different practical problems [3, 20–22].

The height of fractured zone in overlying strata is mainly influenced by rock mechanics parameters, lithology combination, stress, mining space size, and geological structure [23–25]. Methods for estimating the height mainly include material simulation, numerical simulation, and field measurement [26–28]. The results of field measurements are more representative of the actual situations; however, more effort is needed [29]. The failure heights of overlying strata have been observed and measured in hundreds of mining faces in different mining areas of eastern China. The empirical formula for calculating the heights of CZ and TFZ applicable to different mining conditions has been developed and included in the regulatory specifications and widely used [30]. However, there are few researches and studies in the mining areas of northwest China where thick coal seams are buried.

The study on permeability variation of fractured rock during coal mining was mainly based on numerical simulations and field tests [31]. Adhikary and Guo [29] carried out packer tests in an Australian coal mine to evaluate the permeability change of mining strata, and the results showed that the permeability of the surrounding rock was increased by more than 50 times, while the permeability of the roof rock over the goaf was increased by more than 1,000 times. Meng et al. [32] proposed a three-dimensional coupling model between stress and permeability and pointed out three stages of the permeability of coal seam roof during coal mining: decrease, increase, and gradual recovery. However, only few experimental works have been performed on the permeability of fractured rock after mining [33, 34].

The loss of sand layer water has a serious impact on coal mine production and longevity and the ecological environment in the arid and semiarid areas in NW China. The traditional three zone model takes the strata above the water conducting fractured zone as a whole, without considering its permeability change. However, the reduction of the water-resisting property of the rock in nonpenetrative fractured zone (NFZ) is the main reason for the loss of water resources. Using Stope #101 of Jinjitan Coal Mine as the case study, we designed and drilled nine boreholes from the ground surface down to the underground workings and established a “vertical four-zone model” with nonpenetrative fracture zone (NFZ) being proposed. The height of each zone was determined using hydrogeological borehole investigations and analogue simulation. Three types of rock, argillaceous sandstone, fine-grained sandstone, and siltstone within the NFZ, were studied for their premining and post-mining water-resistant capacities using in situ water injection tests and laboratory permeability test. The results are of significance for designing the mining thickness of coal seams and determining the risk to loss of phreatic water resources, which are important theoretical bases for green mining.

2. Mining and Geological Conditions

Jinjitan Coal Mine is located in the northern part of Shaanxi province and to the south of the Mu Us desert at longitudes $109^{\circ}42'32'' \sim 109^{\circ}51'44''$ and latitudes $38^{\circ}28'15'' \sim 38^{\circ}35'59''$, encompassing an area of approximately 98.52 km^2 (Figure 1). Figure 2 shows the lithology overlying coal seam

2-2. Aquifers that overlie the coal seam include the sandstone confined aquifers of Yan'an and Zhiluo formations and the Quaternary phreatic aquifer of Sara Wusu formation. The water abundance of the confined aquifers is weak with the unit water inflow (q) ranging from 0.001 to $0.02 \text{ L}/(\text{s}\cdot\text{m})$, while the water abundance of the phreatic aquifer is moderate with q ranging from 0.124 to $0.287 \text{ L}/(\text{s}\cdot\text{m})$. In addition, the phreatic water is the most important water source for local residents and the ecosystem [35]. Because of lack of the N2 laterite, the fine-grained sandstone and argillaceous sandstone become the only relative aquiclude to prevent the leakage of phreatic water. The valuable phreatic water resources can suffer a serious leakage crisis during mining if the permeability of bedrock is increased.

The fully mechanized Stope #101 has elevations between +991.7 and +1010.4 m, whereas the corresponding surface elevations are between +1229.8 and +1263.7 m, respectively. The panel has a designed advance length of 4,548 m and a designed net face length of 300 m (Figure 1). Although the coalbed average thickness is 9.4 m, however, the mining thickness is only 5.5 m in order to avoid a large volume of phreatic water leakage and an ecological deterioration. The direct roof of coal seam 2-2 consists of dark gray argillaceous sandstone with a thickness of 3.03 m. The integrity of overlying strata is good with an average thickness of approximately 10 m. The roof is mainly composed of mudstone, argillaceous sandstone, siltstone, fine-grained sandstone, and medium-grained sandstone. The argillaceous sandstone, siltstone, and fine-grained sandstone are the main strata, accounting for 27.91%, 31.81%, and 29.52% of the total bedrock thickness, respectively.

3. Methodology

3.1. Hydrogeological Borehole Investigation. Hydrogeological borehole investigation is one of the most commonly used methods to study the development characteristics of fractures in overlying strata. It can also be used to evaluate the rock permeability with simple hydrogeological observation. In this study, nine boreholes were drilled at 2 months after mining when the gob had been stabilized. Figure 3 shows locations of the boreholes. Borehole JE5 was drilled in the nonmining area 150 m south of #2 return airway tunnel on Stope #101 to obtain the background data as a reference for other drilling data. Two profiles, A-A' and B-B', were arranged along the sloping direction of the working face. There were three boreholes (JE2, JE3, and JE4) on the A-A' profile and three holes (JE6, JE7, and JE8) on the B-B' profile. In addition, profile C-C' was arranged along the advance direction on which there were four boreholes (JE1, JE3, JE8, and JE9). The buried depth of the coal seam in borehole JE1 through JE9 ranges from 258.58 to 267.28 m. Specifically, the buried depth of the coal seam is 262.70 m at JE1, 262.47 m at JE2, 260.55 m at JE3, 261.28 m at JE4, 263.20 m at JE5, 267.28 m at JE6, 262.10 m at JE7, 266.20 m at JE8, and 258.58 m at JE9. The hydrogeological investigations performed in these boreholes included drill-hole core analysis (DCA), drilling fluid loss measurement (DFLM), video camera observation (VCO), and field packer test (FPT).

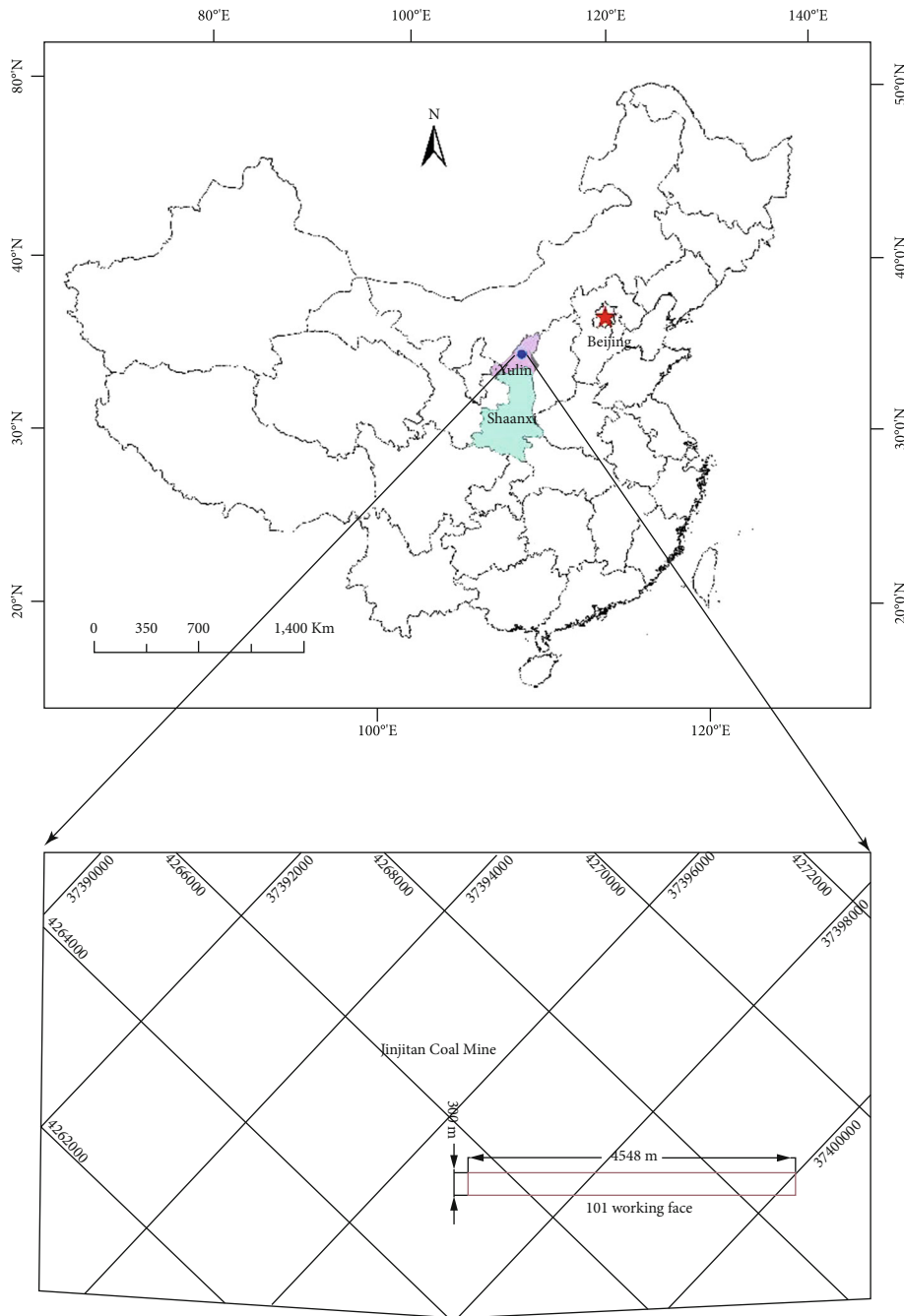


FIGURE 1: Location of Stope #101 and Jinjitan Coal Mine.

(i) Rock quality designation (RQD) can reflect the degree of rock integrity with higher values indicating better integrity. The appearance and density of fresh vertical or oblique fractures of the extracted cores were also visually observed. The RQD values of the normal rocks in the Jurassic Yan'an and Zhiluo formations of study area are generally greater than 60%. There are obvious differences of the rock permeability at different positions in overlying strata because of the differences in fracture shape, density, and width. The DCA method is particularly applicable

to determining the height of TFZ and CZ but not to determining the height of NFZ

(ii) The DFLM was conducted according to Standard MT/T865-2000. Drilling fluid consumption per unit time and the fluid depth were monitored dynamically. Where drilling fluid consumption started fluctuating and slowly increased with drilling depth and the fluid depth started to slightly decline or fluctuate, the position is regarded as the top interface of the NFZ. Where the fluid depth began to decline rapidly

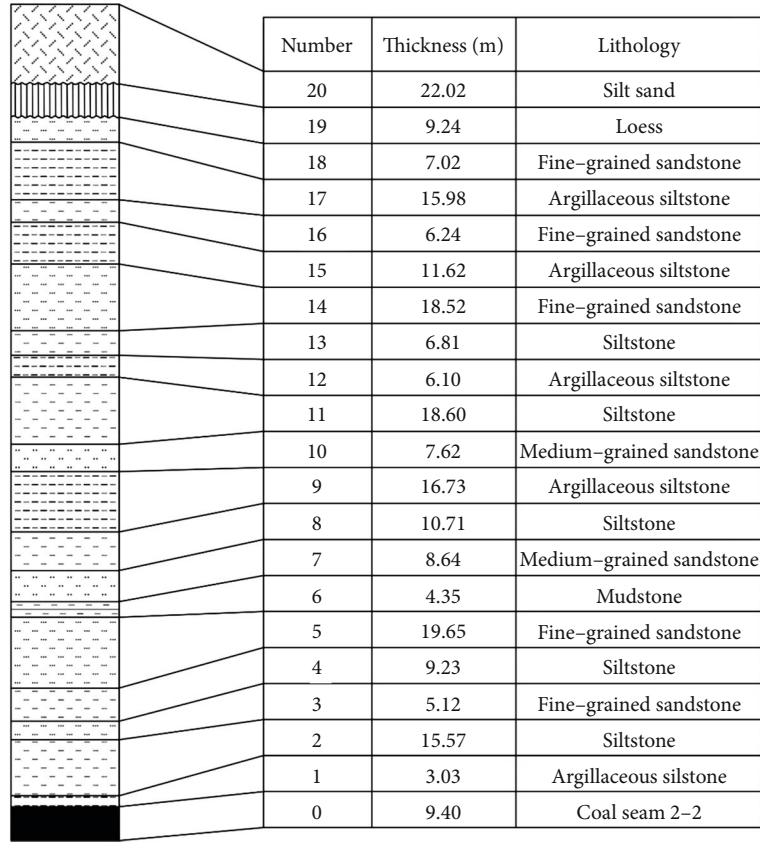


FIGURE 2: Typical geological log profile of No. 101 panel overlying strata.

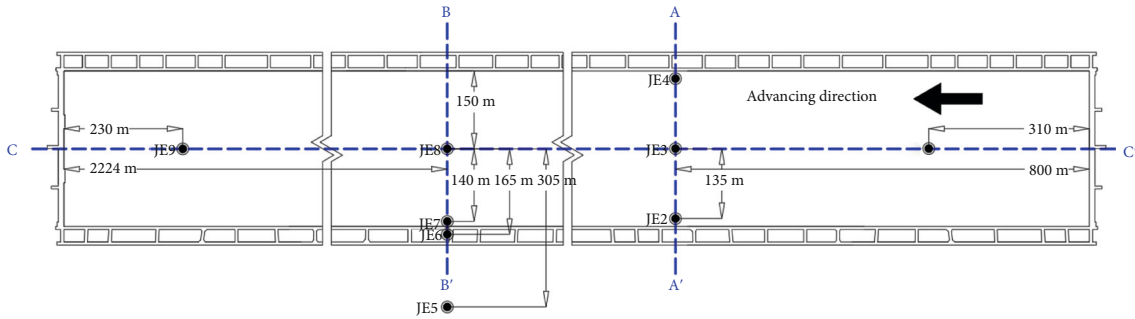


FIGURE 3: Boreholes layout at No. 101 working face.

and the fluid loss rate began to increase significantly with depth, the position is regarded as the top interface y of the TFZ

- (iii) WDY-HW-60 video camera was used to visualize fractures in the borehole walls. It must be noted that the observations are possible only when the water in the borehole is clear and still. As a result, the image of the CZ cannot be obtained. Based on the images, the development characteristics of fractures in the inner walls of the borehole were analyzed, and the top boundary of TFZ and NFZ could be confirmed
- (iv) The FPT was conducted by injecting water into the boreholes at 5 m intervals. The injection

sequence was from bottom to top. Five pressures (0.3 MPa~0.6 MPa~1.0 MPa~0.6 MPa~0.3 MPa) were applied to each interval. Based on the amount of water injected, the rock permeability could be calculated. The position where the permeability increased by at least one order of magnitude and was above the TFZ was considered the top boundary of NFZ

3.2. Similar Material Physical Model. Similar material physical models have been used to study fracture development of overburden [9]. In this study, the dimensions of the physical model were 2,000 mm long by 220 mm wide by 1,300 mm high. These dimensions were designed to simulate mining

panel #101 at a ratio of 1:200. The kinematic and kinetic similarities to the actual mine system were also considered. The similarity constants for geometric time, bulk density, Poisson's ratio, stress, and intensity are listed in Table 1. The model was fully consolidated after 15 days of its construction. Then, the material representing the coal seam in the model was mined to simulate the mining processes. The movement and failure of overlying strata in the physical model were observed and measured to obtain the patterns of formation and height of the induced fractures. The type of materials and their quantities for building the physical model were based on test results of the mechanical parameters. Analogous materials of rocks in this experiment were admixtures of sand, gypsum, calcium carbonate, mica, and water with sand as the aggregate materials; gypsum and calcium carbonate as the bonding materials; and mica fragments as the layered materials. The model consisted of 22 layers. The simulated extraction parameters included 5.5 m coal seam, 320 m advancing length, and two 40 m coal pillars reserved on both sides of the model.

3.3. Laboratory Permeability Test. Permeability tests of the rock with different lithology were designed and carried out to investigate the permeability change in the NFZ in response to longwall mining. Nine core samples were taken from the NFZ in the boreholes and were cut into cylinders with 50 mm in diameter and 100 mm in length according to the suggestion by International Society for Rock Mechanics. The average dry densities of the fine-grained sandstones, siltstone, and argillaceous sandstone specimens are 2,395.21, 2,406.30, and 2,385.63 kg/m³, respectively. The compressive strengths of the specimens were generally less than 20 MPa. According to the results of X-ray diffraction, the minerals in the sandstone material are feldspar, quartz, smectite, illite, calcite, and volcanic rock fragments. Table 2 lists the tested specimens and conditions. Because of low permeability of the test specimens, the transient flow method was adopted for permeability measurements.

The experiments for the sandstone specimens were carried out on a France-made TAW-1000 rock servo-controlled rock mechanics experimental system. Distilled water was chosen as the pore fluid. The test ambient temperature was kept at around 25 degrees to eliminate the effect of temperature on the experimental results.

4. Height of Fracture Zones in Overlying Strata

With the advance of panel, the overlying strata undergo a series of mechanical processes, such as movement, deformation, and fracture. According to the deformation and fracture characteristics of the overlying strata and its hydraulic conductivity, the overlying strata could be divided into several regions [12, 36]. For the purpose of evaluating leakage of phreatic water caused by mining of shallow thick coal seams, the results of field testing and similar material physical modeling suggest that the postmining overlying strata can be divided from bottom to top into four zones: caved zone (CZ), through-going fractured zone (TFZ), nonpenetrative fractured zone (NFZ), and continuous zone (COZ). The rock

stratum in the COZ has continuity and integrity and is the least affected by mining. The COZ may not exist under some conditions such as when the coal seam are shallow or the mining thickness is large. In addition, the height of COZ is mainly determined by the elevation difference between the top boundary of NFZ and the Surface. This article will discuss the three zones other than the COZ.

4.1. Formation and Height of the CZ. The CZ results from caving of the immediate roof strata into the mined-out area following coal extraction. The strata in the CZ lose not only the continuity of the formation but also the stratified bedding. The rock blocks in this zone are of different sizes and cluttered. The voids and thus connectivity are typically greater at the lower section of the zone. Because of the presence of collapsed rocks, one or more of the followings may occur when drilling into the CZ:

- (i) There are frequently dropped drills
- (ii) The drilling speed is unstable, and there are phenomena of being jammed and aggravated vibration of the drilling tools
- (iii) The drilling process has obvious air suction phenomenon with audible whirring sound

The above indicators help determine the position of the top boundary of the CZ. The elevation difference between the top boundary and the coal seam floor is the height of the CZ. The observed phenomenon may not be the same for all boreholes. For example, in borehole JE2, the drill tool was stuck at a depth of 240.10 m with strong vibration, and at 241.22 m, there was a suction phenomenon, whereas in borehole JE9, a suction phenomenon was observed at 238.00 m and the drill dropped with 45 cm distance at a depth of 247.72 m. Therefore, the depths of 240.10 m and 238.00 m were considered the top boundaries of the CZ in boreholes JE2 and JE9, respectively. Table 3 presents the top boundary of the CZ at each borehole and the pertinent lines of evidence.

Figure 4 shows the drill-core photographs of borehole JE1. Figure 4(a) shows that the value of RQD is zero below 238.00 m. In comparison, the RQD value at the same position in the background borehole JE5 is approximately 80%. As a result, the depth of 238.00 m was considered the top boundary of the CZ in borehole JE1. The heights of the CZ in boreholes JE1, JE2, JE3, JE4, JE7, JE8, and JE9 were identified as 24.70, 23.47, 23.27, 23.08, 22.95, 24.50, and 23.78 m, respectively. In addition, the CZ was not observed in the JE6, which is 15 m away from the mining area.

The height of the CZ in Stope #101, as determined by the anomalies in the drilling process, ranges from 19.18 to 23.16 m with an average of 21.83 m. However, the height determined by RQD ranges from 22.27 to 24.70 m with an average of 23.54 m. As shown in Table 3, except for borehole JE3, the results determined by RQD are slightly larger than those determined from the drilling observations. In most cases, the RQD method has a higher resolution in determining the top boundary of the CZ. The larger value of the two methods was selected.

TABLE 1: Similarity condition of similar material simulation model to actual mine system.

Model size (mm ³)	Geometric	Time	Bulk density	Poisson ratio	Stress	Strength
2,000 × 220 × 1,300	1:200	1:14.14	1:1.5	1:1	1:300	1:300

TABLE 2: Tested sandstone specimens in this research.

Specimen	Length (mm)	Diameter (mm)	Mass (g)	Dry density (kg/m ³)	Clay content (%)	Position of the NFZ
F1	99.26	49.57	458.88	2395.51	28.3	Upper
F2	100.05	49.57	462.88	2397.31	31.2	Middle
F3	99.63	49.33	455.63	2392.82	29.6	Lower
S1	97.92	49.48	453.04	2406.11	32.5	Upper
S2	99.96	49.58	464.61	2407.46	34.9	Middle
S3	98.73	49.59	458.67	2405.32	32.7	Lower
A2	100.82	49.58	464.77	2387.75	44.9	Lower
A4	99.89	49.4	456.66	2385.21	40.1	Middle
A5	100.79	49.58	463.89	2383.94	39.0	Upper

TABLE 3: Top boundary depths and heights of the CZ in boreholes.

Holes	Special phenomena in the drilling process			DCA			Results (m)
	Basis for determination	Top boundary depths the CZ (m)	Heights of the CZ (m)	Basis for determination	Top boundary depths the CZ (m)	Heights of the CZ (m)	
JE1	At the depth of 240.00 m, drill dropped with 25 cm distance; at 241.40 m, suction phenomenon	240.00	22.70	Below 238.00 m, extremely broken core, RQD = 0	238.00	24.70	24.70
JE2	Drill tool was stuck at a depth 240.10 m with strong vibration; at 241.40 m, suction phenomenon	240.10	22.37	Below 239.00 m, broken core, RQD = 8.0%	239.00	23.47	23.47
JE3	During 237.00~238.00 m, drill dropped with 60 cm distance	237.00	23.55	Below 238.28 m, fragmental core, RQD = 8.4%	238.28	22.27	23.55
JE4	At 238.12 m, drill dropped with 30 cm distance; at 238.56 m, suction phenomenon	238.12	23.16	Below 237.20 m, fragmental core, RQD = 0	237.20	23.08	23.08
JE5	None	—	0	Integrity core, RQD = 66 ~ 85%	—	0	0
JE6	None	—	0	Integrity core, RQD = 63 ~ 75%	—	0	0
JE7	At 240.80 m, drill dropped with 15 cm distance; at 243.15 m, suction phenomenon	240.80	21.30	Below 239.15 m, broken core, RQD = 7.3%	239.15	22.95	22.95
JE8	At 247.02 m, drill dropped with 35 cm distance; at 239.00 m, suction phenomenon	247.02	19.18	Below 241.70 m, broken core, RQD = 10%	241.70	24.50	24.50
JE9	At 238.00 m, suction phenomenon; at 247.72 m, drill dropped with 15 cm distance, and drill tool was stuck	238.00	20.58	During 234.80~238.00 m, disorder bedding, RQD = 5.8%	234.80	23.78	23.78



FIGURE 4: Drill-core photographs of JE1 borehole: (a) RQD is zero of CZ; (b) first fresh vertical fracture and smaller RQD of TFZ; (c) initial high angle fracture and larger RQD of NFZ.

Therefore, determination of the height of the CZ is based on multiple lines of evidence. The final height of the CZ ranges from 22.95 to 24.70 m with an average of 23.72 m.

Figure 5 shows the magnitude and spatial distribution of the overburden failure zones in the analog model. The size of the grid is $10\text{ cm} \times 10\text{ cm}$, corresponding to the actual $20\text{ m} \times 20\text{ m}$. The immediate roof strata began to collapse after the simulated excavation advanced 40 m. When the working face advanced 120 m, the height of the CZ reached the maximum value of 23.89 m. Further mining did not increase the height. The maximum value and field measurements are very comparable, which verifies the validity and accuracy of the approach to determining the height of the CZ.

According to the above results and analyses, the height of the CZ is relatively stable at around 24 m, whether it is along the advancing or sloping direction. This average height is approximately 4.36 times of the mining thickness. In addition, the fact that no CZ was observed in borehole JE6 proves that the CZ develops only in the area above the working face.

4.2. Formation and Height of the TFZ. The TFZ is located above the CZ, where the rock retains the stratified bedding. The mining-induced fractures are well interconnected and provide the pathways for groundwater entering the gob. In many cases, the strata breakage gradually reduces upwards, resulting in the decrease of fracture network development thus the permeability in the upper section of the TFZ.

The presence of fresh vertical fractures in the rock strata and significantly lower RQD values than the background one at borehole JE5 are two indicators in determining the position of the top boundary of the TFZ. Figure 4(b) shows that the first fresh vertical fracture was identified at the depth of 162.15 m in borehole JE1 and the RQD value decreased significantly at the same location. More fractures were found with the increase of depth.

The method of determining the position of the TFZ based on the characteristics of fluid loss rate and fluid surface depth during drilling is used and considered to be accurate [32]. The measurement results of the background borehole JE5 show that the average rate of fluid loss was 0.054 L/s in loess and 0.069 L/s in bedrock. As shown in Figure 6, the loss rate did not increase with the depth during the drilling of borehole JE5, and the mud circulation was normal. The top boundary of the TFZ was determined by comparing the variation characteristics of the rock (loess) permeability in other boreholes with those at borehole JE5. For example, in borehole JE8, the rate of fluid loss did not increase until the

TFZ was encountered at a depth of 155.20 m where the fluid loss was increased to 1.23 L/s and the depth of fluid surface decreased gradually. As showed in Figure 7(c), the borehole video camera image shows vertical penetrating fractures at the depth of 156.90 m in borehole JE3, and no penetrating fracture was noted in the shallower positions.

Although the degree of fracture development of the overlying strata can be observed intuitively and the relative quantitative evaluation can be carried out from core logs, however, the following two defects should be taken into account:

- (i) Due to the impact of the drill pipe, the rocks tend to be broken in the process of the core being raised, leading to an overestimate of the height
- (ii) Due to the small range of drilling, there might be no obvious longitudinal fractures in the core even if the TFZ is encountered, resulting in an underestimate of the height

With the video camera images, the fractures in the hole-walls can be visualized. The overestimate error could be reduced to a great extent by comprehensive analysis of DCA and BVCO results. DFLM reflects the development of both macrofractures and microfractures in the borehole. The underestimate error could be reduced by comprehensive analysis of DCA and DFLM results. Such analyses lead to the following procedures in determining the top boundary of the TFZ:

Firstly, the results of the DCA were compared with the results of the BVCO, and the larger value (h_{th}^1) was selected.

Secondly, the results of DCA and DFLM were compared to choose a smaller value (h_{th}^2).

Finally, the arithmetic mean (h_{th}) of the above two results was taken as the top boundary of TFZ, as calculated in the following equations:

$$\begin{cases} h_{th} = \frac{h_{th}^1 + h_{th}^2}{2}, \\ h_{th}^1 = \max(h_{th}^d + h_{th}^b), \\ h_{th}^2 = \min(h_{th}^d + h_{th}^f). \end{cases} \quad (1)$$

The estimated positions of the top boundary and the height of the TFZ are presented in Table 4.

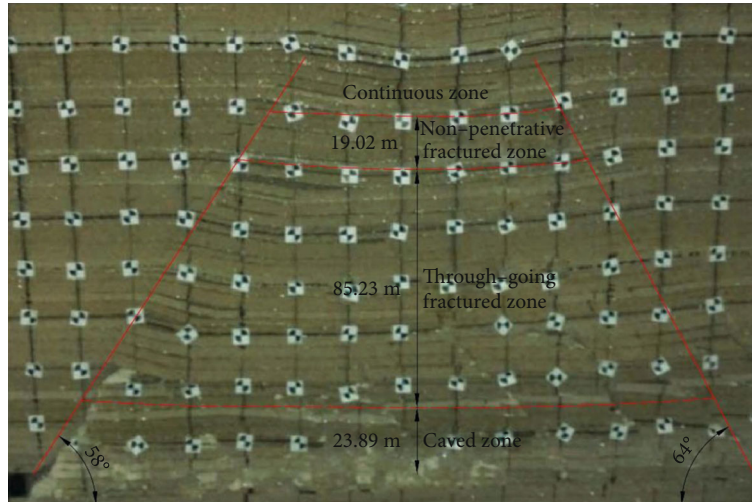


FIGURE 5: The characteristics of overburden failure on the model.

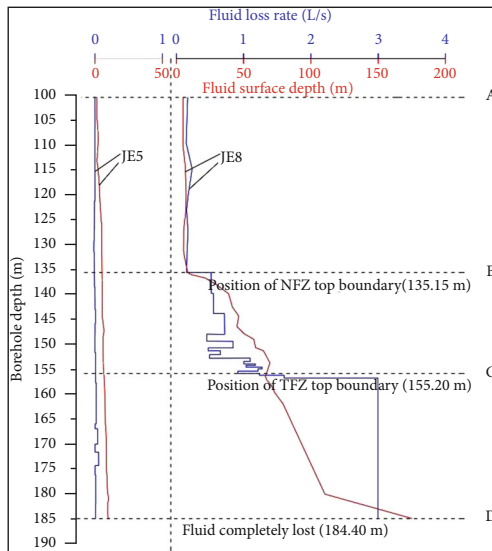


FIGURE 6: The change of drilling fluid loss rate and fluid surface depth in JE8 borehole.

The results of the physical simulation showed that the height of the TFZ reached its maximum value of 85.23 m when the mining advanced 300 m. Unlike the CZ, the height of the TFZ varies with the spatial position. Figure 8 shows cross-sectional views of the induced height of the TFZ above Stope #101. The TFZ is arch-shaped along the sloping direction of the panel (Figure 8(a)), whereas the height gradually increases in the advance direction (Figure 8(b)). The height at the end of the mining panel is 1.22 times of the height at the beginning of the mining panel.

4.3. Formation and Height of the NFZ. The NFZ is located above the TFZ and deflects upward without apparent open fractures. Mining-induced fractures are present but small and isolated. Rock permeability tends to get smaller from bottom to top of the NFZ. The changes of rock permeability of TFZ are of great significance to design the mining height

and to prevent leakage of overlying phreatic sand aquifer. If the sand phreatic water overlies directly the NFZ or the NFZ is missing, the leakage can be significant.

Because the fractures are not fully penetrated and their lengths are small, there are no significant changes in the RQD values. For the same reasons, the video camera images failed to identify the position of the top boundary of the NFZ in the boreholes. The techniques used to determine the top boundary of the NFZ included DCA, VCO, DFLM, and packer testing.

Based on the DCA and VCO, in particular, where high angle fractures start to emerge (Figures 4(c) and 7(b)), the top boundaries of the NFZ were estimated in boreholes JE1, JE3, JE4, JE7, and JE9. Figure 6 shows the fluid loss rate and fluid surface depth in boreholes JE5 and JE8. The fluid loss rate fluctuated in the B-C segment between 135.15 m and 155.20 m. However, there is no dramatic increase, and the fluid surface depth slowly fell. Packer testing was conducted in all boreholes with the exception of boreholes JE5 and JE6 where no NFZ was developed.

The results of the top boundary and height of the NFZ are presented in Table 5. The results of DCA are similar to those of VCO, and the results of DFLM are similar to those from FPT. It appears that the estimated heights from DFLM and FPT are smaller than those from DCA and VCO. The reason is the results of DCA and VCO were based on field observations, while the results of DFLM and FPT were based on the hydrogeological properties of the rock. It is more accurate to determine the top boundary of the NFZ from the changes of hydrogeological properties. The minimum value of the results from the four methods was used as the conservative estimate of the top boundary of NFZ. The results of analogue simulation show that there are independent small fractures in the range of 19.02 m above TFZ.

The estimated height of the NFZ ranges from 11.55 to 21.20 m (Table 5). The height of the NFZ is approximately 0.17 times the combined height of the TFZ and the CZ, and this ratio is also confirmed by the analogue simulation results.

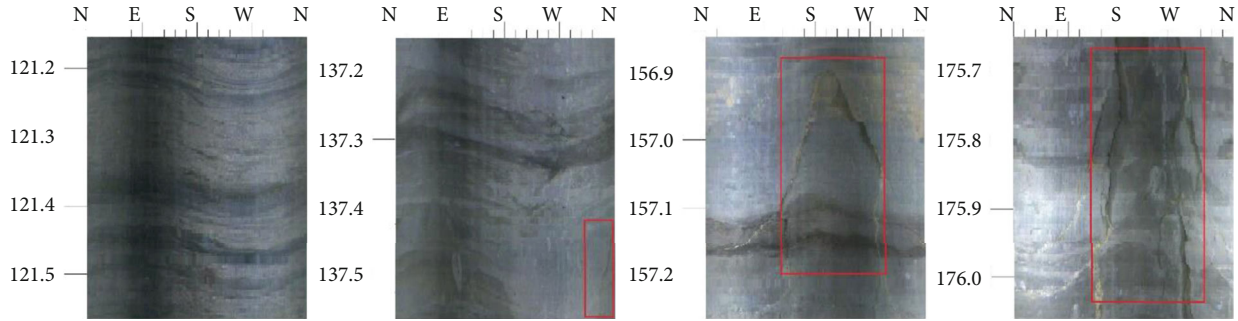


FIGURE 7: Video camera images of JE3 borehole: (a) no fracture; (b) initial high angle no-through fracture; (c) first fresh penetrative vertical fracture; and (d) TFZ.

TABLE 4: Top boundary depths and heights of the TFZ in boreholes.

Boreholes	Top boundary depths of the TFZ (m)				Heights of the TFZ (m)			
	DCA	DFLM	VCO	Final results	DCA	DFLM	VCO	Final results
JE1	162.15	161.7	162.15	161.93	75.85	76.3	75.85	76.07
JE2	199.43	199.47	199.55	199.51	39.57	39.53	39.45	39.49
JE3	155.98	155.55	156.9	156.23	81.02	81.45	80.1	80.77
JE4	191.47	195.28	196.78	194.13	46.73	42.92	41.42	44.07
JE5	0	0	0	0	0	0	0	0
JE6	0	0	0	0	0	0	0	0
JE7	172.2	172.1	172.2	172.15	46.95	47.05	46.95	47
JE8	155	155.2	155.3	155.15	86.7	86.5	86.4	86.55
JE9	145.83	145.58	145.63	141.71	88.97	89.22	89.17	93.09

5. Permeability of Rock within Nonpenetrating Fracture

The results of FPT in the background borehole JE5 show that the estimated permeability values of the argillaceous sandstone, siltstone, and fine-grained sandstone are 7.9×10^{-6} cm/s, 6.7×10^{-6} cm/s, and 5.5×10^{-6} cm/s, respectively. According to the standard for permeability classification of rock mass, the premining rocks are not conducive to water flow.

The transient-pulse permeability tests were used determine the permeability of postmining rock core samples collected in the boreholes. It took approximately one hour to reach a balance of the upstream pressure and downstream pressure, but after 0.1 h permeating, an obvious change trend occurred. If a transient pulse test lasts too long, the creep deformation of specimen under high compression stress occurs, which could cause a larger error of transient pulse tests. As a result, a proper test time ranging from 10 to 20 min was selected to short the total test time of a compression test.

Figure 9 shows the permeability test results. In this figure, P0 represents the position not affected by mining; P1, P2, and P3 represent the upper, middle, and lower sections of NFZ, respectively. Figure 9(a) shows that the permeability of the argillaceous sandstone was significantly increased after mining. The degree of change is closely correlated with the

locations of the argillaceous sandstone. The permeability coefficients of the upper, middle, and lower sections of the argillaceous sandstone of NFZ increased from 5.52×10^{-6} cm/s to 4.2×10^{-5} cm/s, 1.11×10^{-4} cm/s, and 1.88×10^{-4} cm/s, an increase of 7.53, 20.04, and 34.13 times, respectively. The mining operations caused increases in permeability of rocks within the NFZ by 7.52 to 48.37 times. The magnitude of the increase in permeability decreases from bottom to top (Figure 9). Figures 9(b) and 9(c) show the degree of change in the permeability of siltstones and fine-grained sandstones. Similar to argillaceous sandstones, the permeability changes were closely correlated with their locations. The permeability coefficient of the siltstone in the upper, middle and lower parts of the NFZ increased to 6.33×10^{-5} cm/s, 1.32×10^{-4} cm/s, and 2.82×10^{-4} cm/s from the original 6.73×10^{-6} cm/s, increasing by 9.40, 19.58, and 41.93 times, respectively. The permeability coefficient of the fine-grained sandstone located in the upper, middle, and lower parts of the NFZ increased from 7.92×10^{-6} cm/s in a natural state to 8.69×10^{-5} cm/s, 1.67×10^{-4} cm/s, and 3.83×10^{-4} cm/s, respectively, increasing by 10.97, 21.05, and 48.37 times. Affected by mining, the rock permeability was changed significantly, and the maximum increase of the permeability coefficient could reach two orders of magnitude. Under the influence of mining, the permeability of fine-grained sandstone is the largest, followed by siltstone, and argillaceous sandstone is the smallest.

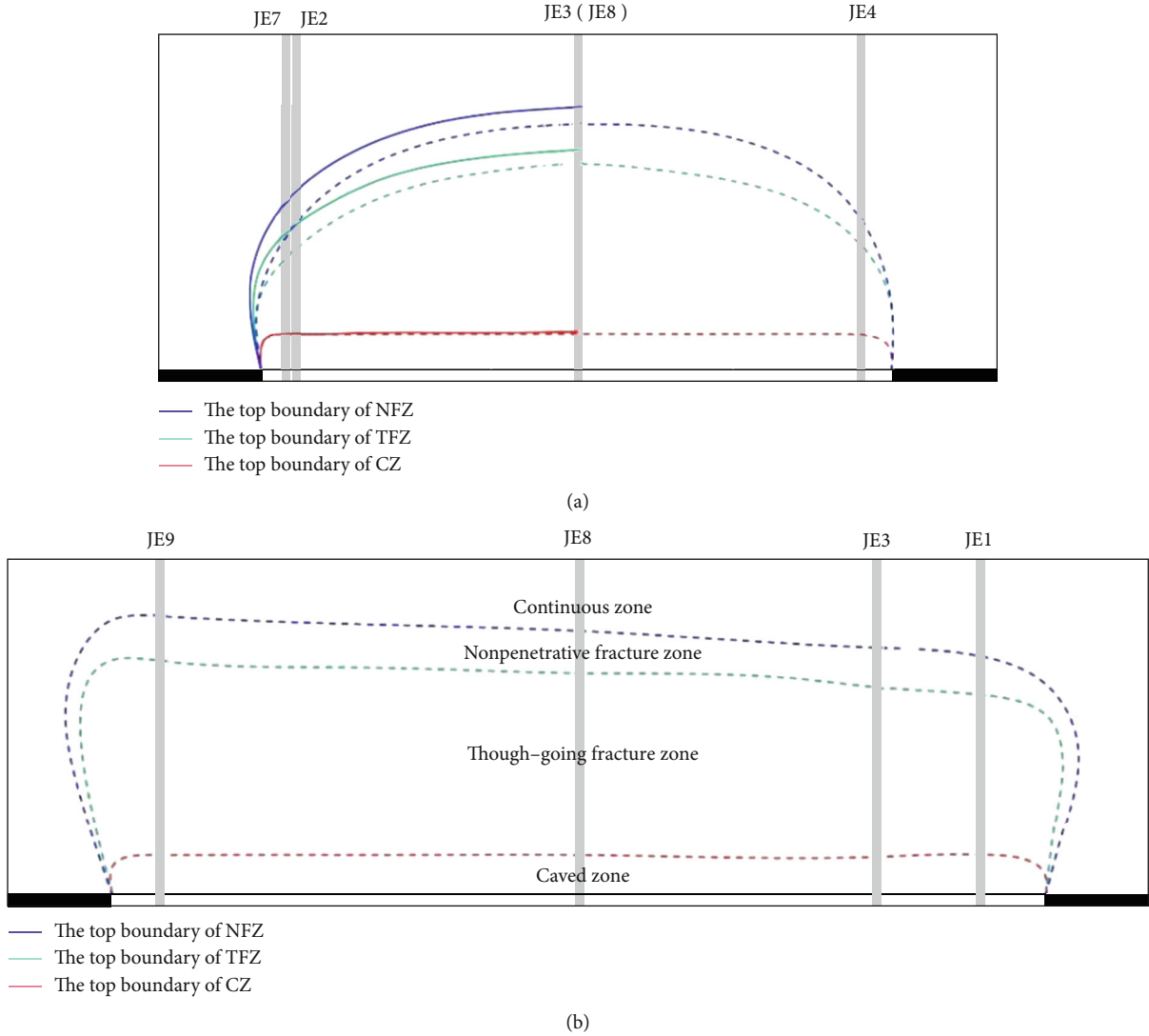


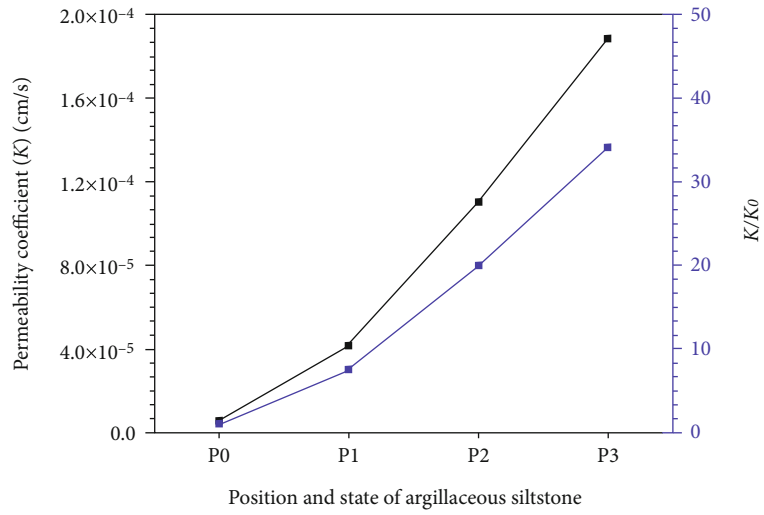
FIGURE 8: Profiles of top boundaries of CZ, TFZ, and NFZ.

TABLE 5: Top boundary depths and heights of the NFZ in boreholes.

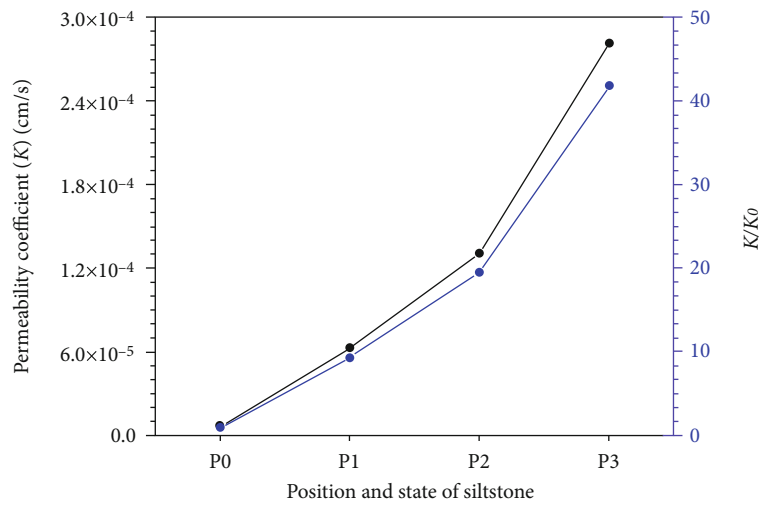
Boreholes	Top boundary depths of the NFZ (m)					Heights of the NFZ (m)				
	DCA	DFLM	VCO	FPT	Results	DCA	DFLM	VCO	FPT	Results
JE1	143.93	143.73	143.79	143.7	143.7	18.00	18.20	18.14	18.23	18.23
JE2	—	187.99	—	187.96	187.96	—	11.52	—	11.55	11.55
JE3	137.43	137.41	137.45	137.42	137.41	18.80	18.82	18.78	18.81	18.82
JE4	182.04	182.1	182.04	182.31	182.04	12.09	12.03	12.09	11.82	12.09
JE5	—	—	—	—	—	0	0	0	0	0
JE6	—	—	—	—	—	0	0	0	0	0
JE7	167.8	167.73	167.75	167.73	167.73	14.35	14.42	14.40	14.42	14.42
JE8	—	135.15	—	135.11	135.11	—	20.00	—	20.04	20.04
JE9	—	120.51	120.68	120.61	120.51	—	21.20	21.03	21.10	21.20

The increasing extent of rock permeability is related not only to the lithology of the rock but also to the location in the NFZ (the distance from the coal seam). The estimated rock permeability coefficient of the lower part of the NFZ is an order of magnitude larger than that of

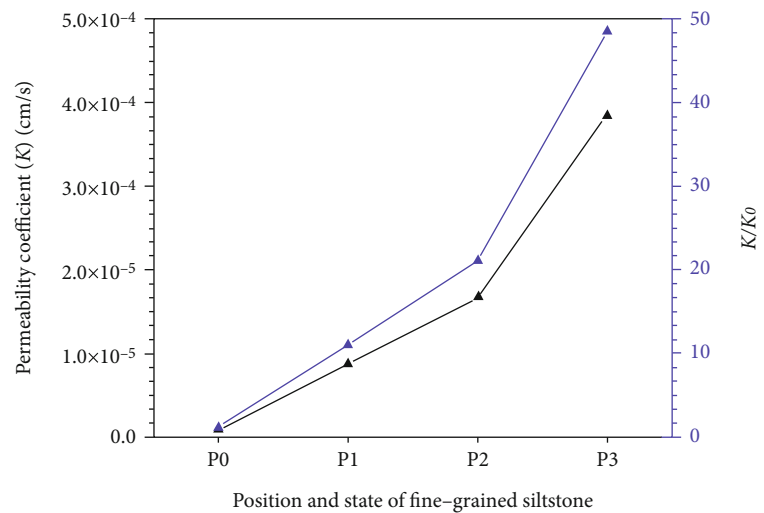
the upper part. The permeability coefficients of rock in the upper, middle, and lower parts of the NFZ are approximately 10 times, 20 times, and 40 times, respectively, higher than those estimated for their premining rock samples.



(a)



(b)



(c)

FIGURE 9: Permeability increase curves of rock with nonpenetrative fracture affected by coal mining: (a) argillaceous sandstone; (b) siltstone; (c) fine-grained sandstone.

6. Conclusions

According to the characteristics of fracture distribution and its potential effect on the leakage of sand phreatic water, the overlying strata was divided into four zones: CZ, TFZ, NFZ, and COZ, from the bottom to the top. The developmental height of CZ is relatively stable, which is roughly 4.36 times of the thickness of the mining coal seam. Along the advancing direction of the working face, the height of TFZ gradually increases to the maximum value of 93.09 m, approximately 16.93 times of the mining thickness. In the advancing direction, the vertical profile of TFZ was arch-shaped. The height of the NFZ ranges from 11.55 to 21.20 m, which is approximately 0.17 times of the combined height of CZ and TFZ. Affected by coal mining, the permeability of the rock in NFZ was increased by 7.52 to 48.37 times, and the magnitude of the increase is nonlinear from top to bottom. The results of the study are helpful to predict the potential loss of phreatic water and determine the mining thickness. It can provide the basis for water preserved mining in the arid and semiarid mining areas in western China.

Data Availability

The data used to support the findings of this study are included within the article.

Conflicts of Interest

The authors declare no conflict of interest.

Authors' Contributions

Yu Liu, Qimeng Liu, and Wenping Li designed and wrote the paper, Yu Liu and Qimeng Liu performed the experiments, and Youbiao Hu supervised the paper writing.

Acknowledgments

This work was supported by the Natural Science Foundation of Anhui Province (2008085QD191 and 1908085ME144), the National Key Research and Development Program of China (2017YFC0804101), and the Independent Research fund of the State Key Laboratory of Mining Response and Disaster Prevention and Control in Deep Coal Mines (Anhui University of Science and Technology) (No. SKLMRDPC19ZZ06). The authors are grateful to Prof. Wei and Dr. Xu for their assistance.

References

- [1] P. Ameli, J. E. Elkhoury, J. P. Morris, and R. L. Detwiler, "Fracture permeability alteration due to chemical and mechanical processes: a coupled high-resolution model," *Rock Mechanics and Rock Engineering*, vol. 47, no. 5, pp. 1563–1573, 2014.
- [2] S.-Y. Hamm, M. S. Kim, J.-Y. Cheong, J.-Y. Kim, M. Son, and T.-W. Kim, "Relationship between hydraulic conductivity and fracture properties estimated from packer tests and borehole data in a fractured granite," *Engineering Geology*, vol. 92, no. 1-2, pp. 73–87, 2007.
- [3] Q.-x. Huang and W.-z. Zhang, "Research on downward crack closing of clay aquiclude in shallow coal seam safety mining," *Journal of Coal Science and Engineering*, vol. 17, no. 3, pp. 349–354, 2011.
- [4] China's National Bureau of Statistics, *China National Bureau of Statistics Statistical yearbook of china*, China Statistics Press, Beijing, 2019.
- [5] Z. Bian, X. Miao, S. Lei, S.-e. Chen, W. Wang, and S. Struthers, "The challenges of reusing mining and mineral-processing wastes," *Science*, vol. 337, no. 6095, pp. 702–703, 2012.
- [6] J. Wei, F. Wu, H. Yin et al., "Formation and height of the interconnected fractures zone after extraction of thick coal seams with weak overburden in western China," *Mine Water and the Environment*, vol. 36, no. 1, pp. 59–66, 2017.
- [7] Z. H. Li, M. X. Ma, and Y. S. Bao, "Development and application of fluid-solid coupling similar materials in discharge test of old goaf water," *Geofluids*, vol. 2020, Article ID 8834885, 2020.
- [8] B. A. Poulsen, "Coal pillar load calculation by pressure arch theory and near field extraction ratio," *International Journal of Rock Mechanics and Mining Sciences*, vol. 47, no. 7, pp. 1158–1165, 2010.
- [9] X. X. Miao, X. Cui, J. Wang, and J. Xu, "The height of fractured water-conducting zone in undermined rock strata," *Engineering Geology*, vol. 120, no. 1-4, pp. 32–39, 2011.
- [10] G. Wang, M. Wu, R. Wang, H. Xu, and X. Song, "Height of the mining-induced fractured zone above a coal face," *Engineering Geology*, vol. 216, pp. 140–152, 2017.
- [11] G. R. Feng, J. Zheng, Y. F. Ren, C. M. Zhong, and L. X. Kang, "Mechanical model and analysis on movement of rock strata between coal seams in pillar upward mining of left-over coal," *Applied Mechanics and Materials*, vol. 58-60, pp. 393–398, 2011.
- [12] T. Q. Liu, *Coal Mine Surface Movement, Overburden Failure and its Application*, China Coal Industry Publishing House, Beijing, 1981.
- [13] L. Holla, "Ground movement due to longwall mining in high relief areas in new south wales, Australia," *International Journal of Rock Mechanics and Mining Sciences*, vol. 34, no. 5, pp. 775–787, 1997.
- [14] V. Palchik, "Formation of fractured zones in overburden due to longwall mining," *Environmental Geology*, vol. 44, no. 1, pp. 28–38, 2003.
- [15] S. Peng, *Surface Subsidence Engineering*, SME, New York, 1992.
- [16] W. Q. Zhang, Z. Y. Wang, X. X. Zhu, W. Li, B. Gao, and H. Yu, "A risk assessment of a water-sand inrush during coal mining under a loose aquifer based on a factor analysis and the fisher model," *Journal of Hydrologic Engineering*, vol. 25, no. 8, article 4020033, 2020.
- [17] D. Zhang, G. Fan, Y. Liu, and L. Ma, "Field trials of aquifer protection in longwall mining of shallow coal seams in China," *International Journal of Rock Mechanics and Mining Sciences*, vol. 47, no. 6, pp. 908–914, 2010.
- [18] W. H. Sui, Y. Hang, L. Ma et al., "Interactions of overburden failure zones due to multiple-seam mining using longwall caving," *Bulletin of Engineering Geology and the Environment*, vol. 74, no. 3, pp. 1019–1035, 2015.
- [19] F. Wang, S. Tu, C. Zhang, Y. Zhang, and Q. Bai, "Evolution mechanism of water-flowing zones and control technology for longwall mining in shallow coal seams beneath gully topography," *Environmental Earth Sciences*, vol. 75, no. 19, article 1039, 2016.
- [20] H. Zha, W. Q. Liu, and Q. H. Liu, "Physical simulation of the water-conducting fracture zone of weak roofs in shallow seam

- mining based on a self-designed hydromechanical coupling experiment system,” *Geofluids*, vol. 2020, Article ID 2586349, 2020.
- [21] G. W. Fan and D. S. Zhang, “Mechanisms of aquifer protection in underground coal mining,” *Mine Water and the Environment*, vol. 34, no. 1, pp. 95–104, 2015.
- [22] W. Winters and R. Capo, “Ground water flow parameterization of an appalachian coal mine complex,” *Ground Water*, vol. 42, no. 5, pp. 700–710, 2004.
- [23] J. Wang and H. Park, “Coal mining above a confined aquifer,” *International Journal of Rock Mechanics and Mining Sciences*, vol. 40, no. 4, pp. 537–551, 2003.
- [24] J. Zhang, “Investigations of water intrushes from aquifers under coal seams,” *International Journal of Rock Mechanics and Mining Sciences*, vol. 42, no. 3, pp. 350–360, 2005.
- [25] Y. Xu, L. Ma, and Y. Yu, “Water preservation and conservation above coal mines using an innovative approach: a case study,” *Energies*, vol. 13, no. 11, p. 2818, 2020.
- [26] J. Blachowski and S. Ellefmo, “Numerical modelling of rock mass deformation in sublevel caving mining system,” *Acta Geodynamica et Geomaterialia*, vol. 9, no. 9, pp. 379–388, 2012.
- [27] Y. Wang, X. Li, and B. Zhang, “Numerical modeling of variable fluid injection-rate modes on fracturing network evolution in naturally fractured formations,” *Energies*, vol. 9, no. 6, p. 414, 2016.
- [28] L. Ma, Z. Jin, J. Liang, H. Sun, D. Zhang, and P. Li, “Simulation of water resource loss in short-distance coal seams disturbed by repeated mining,” *Environmental Earth Sciences*, vol. 74, no. 7, pp. 5653–5662, 2015.
- [29] D. Adhikary and H. Guo, “Modelling of longwall mining-induced strata permeability change,” *Rock Mechanics and Rock Engineering*, vol. 48, no. 1, pp. 345–359, 2015.
- [30] State Administration for Safety Management and Control of China, *Specification for building, water body, railroad and main mine lane coal pillar with pressure mining*, China Coal Industry Publishing House, Beijing, 2017.
- [31] S. Liu, S. Dai, W. Li, B. Han, B. He, and J. Luo, “A new monitoring method for overlying strata failure height in Neogene laterite caused by underground coal mining,” *Engineering Failure Analysis*, vol. 117, article 104796, 2020.
- [32] Z. Meng, X. Shi, and G. Li, “Deformation, failure and permeability of coal-bearing strata during longwall mining,” *Engineering Geology*, vol. 208, pp. 69–80, 2016.
- [33] M. Li, J. Zhang, W. Zhang, A. Li, and W. Yin, “Experimental investigation of water-inrush risk based on permeability evolution in coal mine and backfill prevention discussion,” *Geofluids*, vol. 2019, pp. 1–9, 2019.
- [34] W. P. Li, Q. Q. Wang, and X. Q. Li, “Reconstruction of aquifuge: the engineering geological study of N₂ laterite located in key aquifuge concerning coal mining with water protection in Northwest China,” *Journal of Coal Science and Engineering*, vol. 42, no. 1, pp. 88–97, 2017, (In Chinese).
- [35] S. L. Liu, W. P. Li, W. Qiao, X. Q. Li, Q. Q. Wang, and J. H. He, “Zoning for mining-induced environmental engineering geological patterns: a case study in the Yushenfu mining area, northern Shaanxi, China,” *Journal of Hydrology*, vol. 579, article 124020, 2019.
- [36] Y. Chen, S. Zhu, and S. Xiao, “Discussion on controlling factors of hydrogeochemistry and hydraulic connections of groundwater in different mining districts,” *Natural Hazards*, vol. 99, no. 2, pp. 689–704, 2019.

Research Article

Cause Analysis and Prevention of Hole Collapse by Water Injection and Dust Removal in Qi Panjing Coal Mine

Hua Guo ^{1,2}, Hai-Qiao Wang,¹ Shi-Qiang Chen,^{3,4} and Zhi-Rong Wu¹

¹School of Resource, Environment and Safety Engineering, Hunan University of Science and Technology, Xiangtan, 411201 Hunan, China

²School of Civil and Environmental Engineering, Hunan University of Science and Engineering, Yongzhou, 425199 Hunan, China

³Hunan Provincial Engineering Techniques Research Centre of Mine Ventilation & Dedusting Equipment, Hunan University of Science and Technology, 411201 Hunan, China

⁴Work Safety Key Lab on Prevention and Control of Gas and Roof Disasters for Southern Coal Mines, Hunan University of Science and Technology, Xiangtan, 411201 Hunan, China

Correspondence should be addressed to Hua Guo; 160101050001@mail.hnust.edu.cn

Received 25 July 2020; Revised 2 September 2020; Accepted 14 September 2020; Published 20 October 2020

Academic Editor: Bin-Wei Xia

Copyright © 2020 Hua Guo et al. This is an open access article distributed under the Creative Commons Attribution License, which permits unrestricted use, distribution, and reproduction in any medium, provided the original work is properly cited.

To solve the “special coal seam” with complex coal seam structure, fault phenomenon, and many gangue layers and complex gangue lithology in Qi Panjing coal mine, the problems such as hole collapse and blockage of coal seam water injection dust removal drilling are caused. From the aspects of drilling layout, drilling technology, and gangue material consolidation, a complete set of key technologies for prevention and control of water injection and dust removal in “special coal seam,” have been formed. Seven boreholes have been drilled in I020902 return air roadway of Qi Panjing coal mine, and field comparative test has been carried out. The results show that: after adopting the complete set of key technologies of drilling prevention and control, the drilling depth is 85-100 m, the average depth is 98 m, and the drilling depth of coal seam water injection can reach 170-185 m; the footage per cycle is greatly improved, with the minimum increase of 30.86%, the maximum increase of 46.38%, and the average increase of 36.77%, to save drilling time and bring good economic benefits, and there is no collapse in the borehole hole, to ensure the safety of production. It has a good reference, and practical guiding significance for other coal mining faces, especially for “special coal seam” working face.

1. Introduction

A lot of dust is produced in the process of mine production, which affects the health of workers, accelerates the wear of machines, pollutes the working environment, and increases the probability of accidents [1]. To reduce the harm caused by dust, scholars at home and abroad have carried out a lot of research work. The dust control of fully mechanized caving face (FMCF) can be divided into dry type and wet type [2, 3]. The effect of wet dust removal in FMCF is more obvious, and the cost is lower. In all kinds of methods of wet dust removal, coal seam water injection dust removal effect is remarkable, high efficiency, and is a method to prevent and control dust from the root. To achieve the ideal effect, the drilling depth is the key. To ensure that the water

injection drilling reaches the design depth, it is necessary to prevent the borehole collapse.

In 2015, Li [4] proposed for the first time the measure of using the inner casing of drill pipe in soft coal seam to solve the hole collapse phenomenon in drilling, compared with the conventional drilling method, and applied to the engineering practice, the effect is remarkable. In 2018, Chen [5] introduced the principle and technology of large-diameter borehole permeability enhancement and applied it to coal seams with complex geological conditions and soft coal quality, laying a good foundation for improving borehole collapse. In 2012, Zhai [6] put forward a new theory that solidified holes are arranged around the construction boreholes, and grouting is carried out in the solidified holes. The slurry flows through the cracks and flows to the construction boreholes

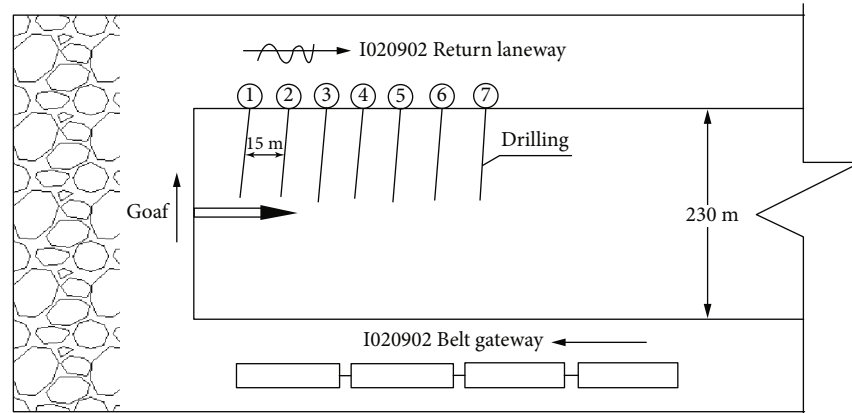


FIGURE 1: Arrangement of drilling for water injection and dedusting in FMCF.

and solidifies, and finally, the construction boreholes are drilled. Also, the stress field and displacement changes around the borehole after the soft coal seam and the solidification with high-strength materials are modelled and analysed. In 1998, Hahn [7] analysed the causes of borehole collapse and put forward a new theory of casing while drilling and setting liner during drilling. The liner and drilling are carried out at the same time to ensure the integrity of drilling, thus establishing a systematic prevention and control system for borehole collapse. Although the above prevention measures have achieved some results, the prevention and control technology of borehole collapse in soft and fractured coal seams is targeted. However, there is little research on the prevention and control of water injection borehole collapse in the “special coal seam” with complex coal seam structure, many faults and gangue layers, and the gangue lithology is mostly clay rock, mudstone, or carbonaceous mudstone. Therefore, given the problem of hole collapse in water injection drilling of “special coal seam” in the Qi Panjing coal mine, the author first analyses the occurrence conditions of coal seam and the causes of hole collapse and then puts forward a complete set of process method of drilling layout, drilling technology combined with gangue material consolidation, forming a systematic water injection dust removal drilling hole collapse prevention technology, which has been applied to engineering practice with remarkable effect.

2. Cause Analysis of Hole Collapse in Water Injection Dust Removal Drilling

2.1. FMCF of Water Injection Dedusting. The natural thickness of the coal seam of I020902 FMCF for coal seam water injection in Qi Panjing coal mine is 2.18-8.68 m, with an average of 4.19 m. The reserve utilisation thickness is 1.70-5.31 m, with an average of 2.91 m. The coal seam is thin in the East and thick in the West. There are 1-8 layers of gangue in the whole coal seam, most of which are 4-5 layers. The main lithology of gangue is a clay rock, mudstone, or carbonaceous mudstone. The coal seam of I020902 FMCF is difficult to clean coal with medium ash content, low sulfur

content, low medium phosphorus coal, high volatile matter, medium-high calorific value, and medium clean coal recovery rate. The coal quality grade is 1/3 JM, which belongs to soft coal with more fractures. I020902 FMCF elevation +800-913 m, FMCF length of 230 m, coal seam affusion drilling design length of 170 m, and ZYWL-3200 crawler type drilling rig are selected. The drilling rig is matched with the drill pipe and head. The pulverised coal particles in the drilling hole are discharged by water flushing. After drilling for some time, the drilling team drilled seven boreholes. Generally, the hole collapse occurs at the length of 70-80 m, as shown in Figure 1, which is far from the designed, so it is impossible to inject water into the long hole coal seam.

2.2. Stress Analysis of Water Injection Dedusting Borehole. The stress state around the water injection dust removal borehole in “special coal seam” is the decisive factor for whether the borehole collapses. With the drilling of the borehole, the stress balance is destroyed due to the application of redistribution around the borehole. According to the stress direction, there are radial stress, tangential stress, and drilling direction stress [8, 9]. The stress size is affected by coal seam buried depth, geological structure, mechanical properties of coal, and drilling characteristics. According to the different distances between the stress-strain of coal and the borehole, it can be divided into an elastic zone, plastic zone, and fracture zone. When it is in the elastic zone, the coal body around the borehole is far away from the borehole and fails to reach the plastic deformation condition; when it is in the plastic zone, the coal body around the borehole is close to the borehole to reach the plastic deformation condition, but it does not cause fracture deformation and is in the plastic state; When it is in the fracture zone, the coal body around the borehole reaches the plastic deformation condition and causes fracture deformation.

It is assumed that there is ideal elastic-plastic material around the borehole of the coal body [10], and it is incompressible. Because the length of the borehole is far larger than the diameter of the borehole, it can be regarded as a plane stress problem for analysis. The effective stress in

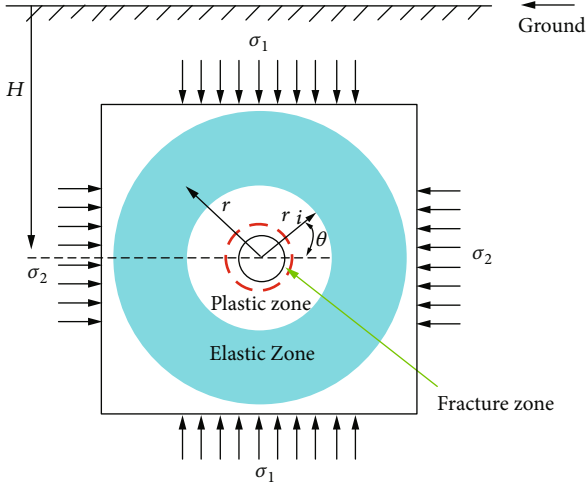


FIGURE 2: Stress state of water injection dust removal borehole in coal body.

“special coal seam” is the difference between coal stress and coal pore pressure, and its expression is

$$\delta_e = \delta - \alpha p, \quad (1)$$

where δ is the stress of coal mass (MPa), α is the effective stress coefficient of special coal, $\alpha = C_0/C$, which is generally 0.4-0.7 as soft coal, and p is pore pressure (MPa).

(1) Stress in the elastic zone of coal seam water injection dust removal borehole

The stress state of water injection dust removal borehole in the coal body is shown in Figure 2. Without considering the seepage of the hole wall, under the combined action of radial stress, tangential stress, drilling direction stress, and pore pressure [11-13], the effective stress expression of the elastic zone around the hole wall is as follows:

$$\delta_r = \frac{\delta_1 + \delta_2}{2} \left(1 - \frac{r_i^2}{r^2} \right) + \frac{\delta_1 - \delta_2}{2} \left(1 - 4 \frac{r_i^2}{r^2} + 3 \frac{r_i^4}{r^4} \right) \cos 2\theta + \frac{r_i^2}{r^2} p_1 - \alpha p, \quad (2)$$

$$\delta_\theta = \frac{\delta_1 + \delta_2}{2} \left(1 + \frac{r_i^2}{r^2} \right) - \frac{\delta_1 - \delta_2}{2} \left(1 + 3 \frac{r_i^4}{r^4} \right) \cos 2\theta - \frac{r_i^2}{r^2} p_1 - \alpha p, \quad (3)$$

$$\delta_z = \delta_a - 2\mu(\delta_1 - \delta_2) \frac{r_i^2}{r^2} \cos 2\theta - \alpha p, \quad (4)$$

$$\tau_{r\theta} = \frac{\delta_1 - \delta_2}{2} \left(1 - 3 \frac{r_i^2}{r^2} + 2 \frac{r_i^4}{r^4} \right) \sin 2\theta, \quad (5)$$

where C_0 is the skeleton compressibility of coal, C is volume compressibility of coal, δ_r is radial effective normal stress

(MPa), δ_θ is circumferential effective normal stress (MPa), δ_z is drilling direction effective normal stress (MPa), $\tau_{r\theta}$ is shear stress (MPa), δ_1 is vertical maximum principal in-situ stress (MPa), δ_2 is horizontal maximum principal in-situ stress (MPa), δ_a is upper pressure of original rock (MPa), θ is the angle between the vector diameter of the point on the hole wall and the maximum horizontal principal geostress ($^\circ$), r_i is drilling radius (m), and r is the distance from drilling centre line (m).

(2) Stress in the plastic zone of coal seam water injection dust removal borehole

According to the division of the stress area around the borehole, assuming that the coal mass is incompressible and $r = r_i$, the stress distribution in the plastic zone is as follows:

$$\delta_r = p_1 - \alpha p, \quad (6)$$

$$\delta_\theta = \delta_1(1 - 2 \cos 2\theta) + \delta_2(1 + 2 \cos 2\theta) - p_1 - \alpha p, \quad (7)$$

$$\delta_z = \delta_a - 2\mu(\delta_1 - \delta_2) \cos 2\theta - \alpha p, \quad (8)$$

$$\tau_{r\theta} = 0, \quad (9)$$

where p_1 is the minimum wall support pressure (gas pressure in the hole for soft special coal seam and slag removal by wind) (MPa).

(3) Failure pressure of coal seam water injection dust removal borehole

As long as the strength of the borehole itself is lower than the stress of the coal around the borehole, the shear failure will occur, and the hole collapse will occur [14]. According to the mechanical analysis of borehole wall stability, combined with the Mohr-Coulomb criterion, the effective stress can be expressed as follows:

$$\delta_{\max} = \delta_{\min} \frac{1 + \sin \phi}{1 - \sin \phi} + 2C \frac{\cos \phi}{1 - \sin \phi}, \quad (10)$$

where δ_{\max} is the maximum principal stress of the hole wall (MPa), δ_{\min} is the minimum principal stress of the hole wall (MPa), ϕ is the internal friction angle of the coal body ($^\circ$), and C is the cohesion of the coal body (MPa).

From the above formula, it can be seen that the internal friction angle and cohesion of the coal body are related to the mechanical properties of coal, which are fixed constant values; the shear failure of the coal body is mainly controlled by the maximum and minimum principal stress of hole wall, and the greater the difference between δ_{\max} and δ_{\min} , the easier the hole wall collapses. According to the analysis of the principal stress of coal drilling, the horizontal stress distribution around the borehole is not uniform, and the stress (δ_θ) around the borehole changes with the change of θ angle. The maximum principal stress of the coal body can be approximately δ_θ , and the minimum principal stress can be approximately δ_r . When $\theta = 90^\circ$ or 270° , the effective stress

difference $\delta_\theta - \delta_r$ is the largest, which is most likely to cause borehole collapse. At this time, the effective stress formula of borehole collapse is as follows:

$$\delta_{r|r=r_i} = p_1 - \alpha p_1, \quad (11)$$

$$\delta_{\theta|r=r_i} = \eta(3\delta_1 - \delta_2 - p_1) - \alpha p_1, \quad (12)$$

$$\tau_{r\theta}|_{r=r_i} = 0, \quad (13)$$

where η is the nonlinear correction coefficient.

Substituting (11) and (12) into equation (10) and making $k = \cot(45^\circ - \phi/2)$, the collapse pressure of the hole wall is obtained as follows:

$$p_1 = \frac{\eta(3\delta_1 - \delta_2) - 2Ck + \alpha p_1(k_2 - 1)}{k^2 + \eta}. \quad (14)$$

2.3. Concrete Analysis of Hole Collapse. According to the occurrence and geological conditions of the coal seam in Qi Panjing coal mine, the water injection feasibility of the coal seam sampling in Qi Panjing coal mine is analysed. The original moisture value of the coal seam is 2.38%. The average total porosity of the coal seam is 6.42% calculated from the dry block density and true density of the test coal body. The natural water absorption rate of the coal is 1.305%, the firmness coefficient of the coal seam is 0.6848, which is compared with the standard value of the water injection injectability of the coal seam, it can be concluded that the coal seam is water injectable [15–17]. Combined with the complexity of water injection technology, roadway layout, and water injection effect, long borehole water injection is finally adopted.

From the beginning of drilling to the depth of 70 m, it is normal. After 70–80 m, the backwater in the hole decreases, the hole collapse occurs, and the load of the drilling rig increases. After slowing down and punching, the drilling continues, and the drilling is difficult. Under the circumstances of taking measures such as stopping drilling, punching, and reverse reciprocating hole cleaning, there is still no practical effect. After analysis, the specific reasons are as follows:

- (1) This coal seam is soft, with faults, many fractures, and many gangue layers. To avoid the position of faults and fractures, the middle and upper part of the coal seam in the air return roadway of the working face shall be drilled for water injection from a certain angle to the advancing direction of the FMCF, or the middle and upper part of the FMCF shall be transported by the belt of the FMCF to the advancing direction of the FMCF at a certain angle. Considering that the pipeline and equipment are arranged in the belt conveyor roadway of the FMCF, the drilling water injection is carried out in the middle and upper part of the coal seam of the return air roadway of the FMCF perpendicular to the advancing direction of the FMCF. Due to the influence of driving on both sides of the roadway, the stress concentration area is

formed, and the coal body cracks are relatively developed. During the long hole drilling, affected by the pressure, the coal seam will give out a “click” sound during the drilling process. Then, the hole collapse phenomenon will occur, blocking the normal borehole backwater

- (2) There is an SF12 normal fault in the scope of I020902 FMCF, which is located in the centre of 1200 m of FMCF. It is an East-West strike; the dip angle is 65° , and the drop is 5 m. The strike extension length is about 400 m. The fault position is accurately controlled, but hole collapse will occur when the fault is encountered during drilling
- (3) During drilling, the gangue in the coal seam will be encountered when drilling to 70 m. The gangue is mainly claystone, mudstone, or carbonaceous mudstone, with argillaceous cementation, low hardness, and loose sand grain when meeting water. After analysis and research, the hole wall cannot form an effective whole, but loose, and hole collapse occurs

3. Technical Measures for Hole Collapse Prevention

3.1. Drilling Site Selection

- (1) The drilling location is the place with poor development of coal seam fissures. The drilling angle is arranged according to the coal seam strike and dips angle. The water injection hole is arranged at 1.8 m away from the coal seam floor to avoid the sinking of the drill pipe and penetrating the floor when the long hole drill pipe is long
- (2) Accurately judge the fault within the scope of I020902 working face, select the position that can avoid the fault, and ensure that the drilling does not pass through the fault affected area
- (3) When passing through the stress concentration area on one side of the roadway, the drilling speed should be appropriately slowed down, and the “feed pressure” of drilling should be reduced to maintain the normal drilling backwater state. After passing through the stress concentration area, the normal drilling speed should be restored. When drilling down from the middle and upper part of the coal seam perpendicular to the advancing direction of the FMCF, the drill pipe will speed up the drilling speed due to its weight, so the drilling speed should be controlled properly

3.2. Drilling Arrangement. In deep hole drilling, drilling design plays a fundamental role. In the coal seam, the specific drilling position and drilling angle play an important role [18–22]. According to the coal seam thickness of I020902 FMCF, combined with roadway height, borehole inclination angle, and water movement along joint fissure after water injection, it cannot be close to the lower part of the coal seam,

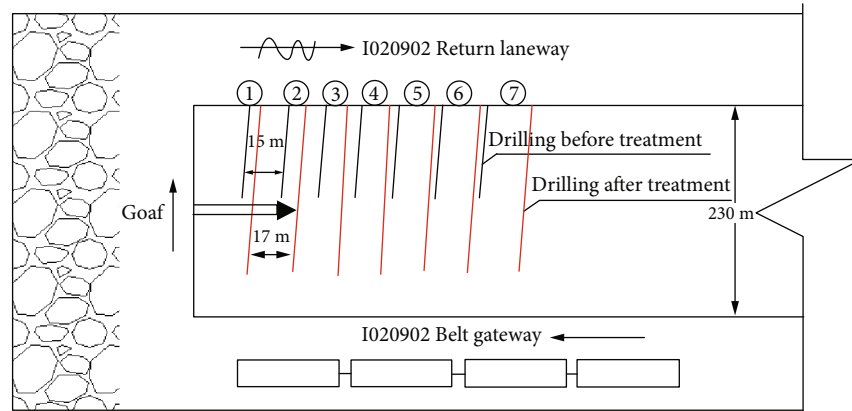


FIGURE 3: Comparison of the layout before and after dedusting drilling treatment.

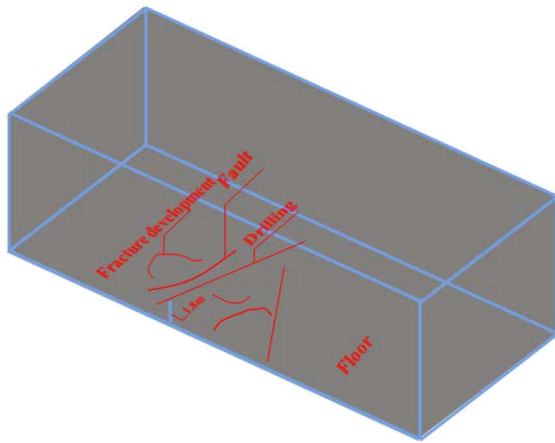


FIGURE 4: Details of dedusting drilling.

to avoid side slope phenomenon of lower FMCF after water injection. The above factors are considered comprehensively. Finally, it is determined that the drilling direction is nearly perpendicular to the main body of the coal seam, and the height from the coal seam floor is 1.8 m, the drilling angle is divided into the upward hole and downward hole [23]. After analysing the specific conditions of the FMCF, the drilling angle of the upward hole should be less than 2° to 3° of the coal seam inclination angle. The down hole drilling angle should be 1° to 2° greater than the coal seam dip angle, to ensure the drilling track trace basically goes along the coal seam [24–26], which can increase the drilling depth.

3.3. Drilling Tool Selection. To reduce the occurrence of hole collapse during drilling, the long conical bit should be considered. Compared with the ordinary drill bit, the long conical bit has the following characteristics: the head is sharp and can eat into the coal seam well. First, form a small area of drilling, and then through the middle and bottom of the long cone drill bit to expand the hole diameter required for coal seam water injection. Because this kind of drill bit is easy to drill holes, with good hole shape and fine coal powder, it can be discharged well with the drilling machine, so as not to block the drilling hole. On the premise of meeting the

requirements of water injection drilling hole diameter, properly reducing the drilling hole diameter can reduce the hole collapse phenomenon caused by the pressure on the deep coal seam due to the large drilling area.

When drilling, we usually use high-pressure water to flush out the pulverised coal in the drilling hole. Sometimes, some pulverised coal and particles in the hole cannot be discharged. In this case, if we continue to use high-pressure water to wash the coal powder, the water pressure in the borehole will increase suddenly, resulting in the stress concentration of the newly drilled wall, which will damage the newly drilled hole, in the case of larger area collapse. The drill pipe with pulse water flushing and hollow screw is designed, that is, there are large alternate threads on the drill pipe. During normal drilling, the long conical bit reduces the occurrence of hole collapse. Even if the hole collapse occurs, the amount of hole collapse is greatly reduced. The back end spiral drill pipe can effectively discharge the coal powder and particles produced.

3.4. Drilling Technology and Method. During drilling, the drilling rig must be stable. It is to connect the drilling rig and the ground as a stable whole. Solid wood can be padded on the bottom of the drilling rig, and the position of the drilling rig can be firmly controlled with columns to avoid vibration during drilling. Once the vibration occurs, the drilling eccentricity will be formed, and the hole wall will be uneven, the drilling resistance will be increased, and the drilling capacity of the drilling rig will be virtually weakened, which will affect the drilling effect. The probability of drilling hole plugging is largely promoted.

During drilling, the relationship between pressure and speed should be grasped. The limit drilling pressure is fixed in the drilling process of each drilling rig, but the pressure given by layers with different hardness is different. It is necessary to analyse the specific layers and pay attention to the changes of pressure during layer change, withdrawal, and pull out the drilling. When changing the layer, it is easy to block the hole and damage the drilling tool, resulting in the pressure change of the whole drilling device. It needs to be observed at any time. Once the pressure rises, the drilling should be stopped in time for mucking. The drilling speed

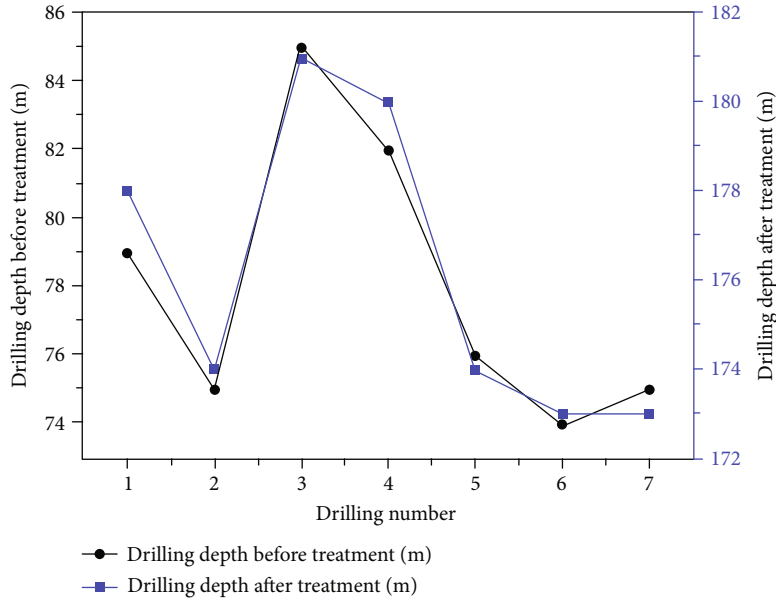


FIGURE 5: Comparison of dedusting drilling depth.

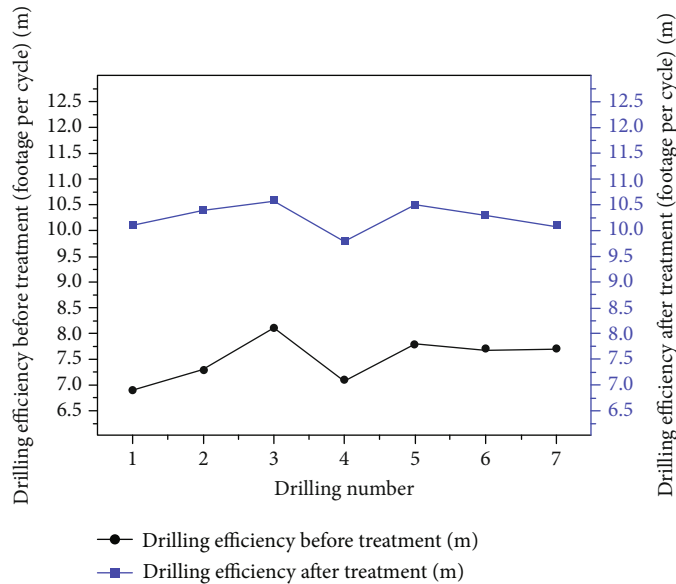


FIGURE 6: Comparison of dedusting drilling efficiency.

should not be too fast when withdrawal and pulling out the drilling. To maintain the appropriate speed and grasp the strength, experienced drilling operators are required to make a reasonable judgment on the slag discharge conditions and drilling speed according to the summary.

Ensure that drilling operators have high drilling skills. People have an important impact on the quality of drilling rig drilling, especially the technological level of drilling personnel is the decisive factor of whether the drilling can achieve the expected quality, which requires the professional level training of drilling operators and the implementation of the system so that they all have professional technical knowl-

edge. The operators can not only drill but also repair the drilling rig, know how to operate the rig efficiently and normally, and can deal with emergencies.

3.5. Material Consolidation Method. In the process of drilling, encountered in the coal seam gangue [27, 28], the measures taken are water glass chemical grouting material grouting consolidation, the original collapse hole filled with water glass chemical grouting material, so that the sediment in the hole and sodium silicate chemical grouting material mixed, can be better cemented into a whole. It can effectively fill the collapse hole space and solidify the collapse hole wall.

According to the actual situation and repeated discussion and analysis, although this method is not used in coal seam water injection drilling hole collapse treatment, it has been used in other temporary or semipermanent engineering projects, and the effect is good. Considering its good profitability, low cost, and high safety coefficient, this method is adopted. In this method, water glass, ethylene glycol adipate, Ma additive, and water are mixed in the proportion of 50:2:6:42 to form grouting raw materials. The mud pump is used to pour the bottom of the drill pipe to the collapsed hole. Starting from the lowest end of the hole collapse, the drill pipe is moved back and forth during grouting, so that the loose sediment at the collapsed hole floats with the sodium silicate chemical grouting material under the impact of water glass chemical grouting material, forming the whole structure. After the water in the hole is discharged and the water glass chemical grouting material flows out of the hole, stop the grouting and trip out, clean the drilling tool. After 48 hours, the hole can be swept after the grouting material, and the sediment in the hole are solidified.

4. Results and Discussion

This paper analyses the reasons for the hole collapse of water injection dust removal borehole in I020902 FMCF, and after taking relevant technical measures, the ZYWL-3200 crawler drilling rig is used for drilling. The comparison layout position before and after drilling treatment is shown in Figure 3, and the detailed hole drawing after hole collapse prevention technology is shown in Figure 4. The comparison data before and after the drilling depth is shown in Figure 5. Through the analysis of Figure 5, the drilling depth of the seven boreholes after treatment is increased by 85-100 m, the average depth is increased by 98 m, and the drilling depth of water injection in coal seam can reach 170-185 m, which indicates that the treatment measures are appropriate. The treatment effect has reached the expectation. Also, when the coal seam water injection drilling operation was started, the drilling team made a footage of 7 meters per cycle, and then the borehole collapse occurred. Corresponding measures were taken to control the drilling efficiency, and the drilling efficiency was also greatly improved. The detailed data and trends are shown in Figure 6. Through the analysis of Figure 6, it can be seen that after treatment, the footage per cycle has been greatly improved, with a minimum increase of 30.86%, a maximum increase of 46.38%, and an average increase of 36.77%, thus saving valuable time and bringing greater economic benefits. Also, there is no hole collapse phenomenon in water injection dust removal drilling, which ensures the safety of production.

5. Conclusion

- (1) Based on the analysis of the causes of hole collapse in water injection dust removal drilling, the paper puts forward the new technology of systematic prevention and control of hole collapse in water injection dust removal drilling hole: from the selection of drilling site, drilling layout, drilling tool selection, determina-

tion of drilling technology, and other aspects, the treatment measures are put forward. Especially in case of hole collapse caused by gangue in the coal seam, water glass grouting material is adopted for grouting consolidation. After reaching a certain strength, the hole shall be drilled again. This has great reference significance and popularisation value for the prevention and control of hole collapse of water injection dust removal drilling hole in another coal mine FMCF

- (2) For the coal seam with complex coal seam structure, many gangue layers, and complicated gangue lithology, seven water injection dust removal boreholes were drilled. The borehole collapse occurred, and the prevention measures were taken. The drilling depth was 85-100 m higher than the original, with an average increase of 98 m, and the water injection drilling depth of the coal seam could reach 170-185 m
- (3) The drilling team's footage per cycle was 7 meters, and then the borehole collapse occurred. After treatment, the footage per cycle increased greatly, at least by 30.86%, the maximum increase of 46.38%, and the average increase of 36.77%. The drilling time was saved, and the economic benefit was good. Moreover, there was no hole collapse in the drilling, which ensured the production safety

Data Availability

All data included in this study are available upon request by contact with the corresponding author.

Conflicts of Interest

The authors declare no conflict of interest.

Acknowledgments

This work was conducted with support from the 2017 Hunan Provincial Graduate Research Innovation Project of China (No. CX2017B649), the Excellent youth project of Hunan Provincial Department of Education (No. 19B223), National Natural Science Foundation of China (No. 51774134), and General scientific research projects of Hunan University of Science and Engineering (No. 19XKY056).

References

- [1] D. W. Li, J. Ma, and H. Q. Liu, *Prevention and Control of Dust and Occupational Diseases in Coal Mines*, China University of Mining and Technology Press, Xuzhou, 2007.
- [2] Y. Peng, Z. A. Jiang, E. Q. Fu, S. Han, and G. Lan, "Study on-seam water injection and dust control optimisation and effect of fully-mechanized coal mining face," *Coal Science and Technology*, vol. 46, no. 1, pp. 224-230, 2018.
- [3] T. Liu, S. Y. Lan, C. M. Wang, and E. Z. Lv, "Comparative study on application of high-pressure spray and foam dust removal technology in fully mechanized heading face," *Mining*

- Safety & Environmental Protection*, vol. 43, no. 1, pp. 50–53, 2016.
- [4] D. Q. Li, G. T. Deng, H. G. Li, and M. Z. Wang, “Technology of preventing drilling hole collapse in soft coal seam by inserting casing in drill pipe,” *Journal of Safety Science and Technology*, vol. 11, no. 2, pp. 95–98, 2015.
 - [5] J. F. Chen, J. Z. Wei, G. J. Zhang, and L. Wang, “Study on permeability improvement technology of the large-diameter drilling combined with hole protection,” *Coal Science and Technology*, vol. 46, no. 10, pp. 73–77, 2018.
 - [6] C. Zhai, Q. G. Li, and C. Su, “Analysis on borehole instability and control method of pore-forming of hydraulic fracturing in soft coal seam,” *Journal of China Coal Society*, vol. 37, no. 9, pp. 1431–1433, 2012.
 - [7] D. Hahn, F. Makohl, and L. Watkins, “Casing-while-drilling system reduces hole collapse risks,” *Offshore*, vol. 58, no. 2, p. 54, 1998.
 - [8] L. G. Zhang, X. P. Sun, S. B. Li, and Y. X. Li, *Fundamentals and applications of rock mechanics*, Harbin Institute of Technology Press, Harbin, 2016.
 - [9] Z. Wang, Y. P. Liang, and H. W. Jin, “Analysis of mechanics conditions for instability of outburst-preventing borehole,” *Journal of Mining & Safety Engineering*, vol. 25, no. 4, pp. 444–448, 2008.
 - [10] E. Papamichos, “Analysis of borehole failure modes and pore pressure effects,” *Computers and Geotechnics*, vol. 37, no. 1-2, pp. 141–152, 2010.
 - [11] T. Meier, E. Rybacki, A. Reinicke, and G. Dresen, “Influence of borehole diameter on the formation of borehole breakouts in black shale,” *International Journal of Rock Mechanics and Mining Sciences*, vol. 62, pp. 74–85, 2013.
 - [12] A. Patutin and S. Serdyukov, “Transverse hydraulic fracture initiation by indentation in an uncased borehole,” *Procedia Engineering*, vol. 191, pp. 287–290, 2017.
 - [13] J. Ptáček, P. Konicek, L. Staš, P. Waclawik, and R. Kukutsch, “Rotation of principal axes and changes of stress due to mine-induced stresses,” *Canadian Geotechnical Journal*, vol. 52, no. 10, pp. 1440–1447, 2015.
 - [14] L. G. Zhang, “Borehole stability analysis accounting for anisotropies in drilling to weak bedding planes,” *International Journal of Rock Mechanics and Mining Sciences*, vol. 60, pp. 160–170, 2013.
 - [15] H. Guo, *Study on Technological Method of Water Injection in Coal Seam*, Kunming University of Science and Technology, Kunming, 2014.
 - [16] S. Hu, B. Si, H. Shu, and X. Song, “Fisher information of mine collapse hole detection based on sensor nodes connectivity,” *International Journal of Advancements in Computing Technology*, vol. 5, no. 9, pp. 1245–1254, 2013.
 - [17] L. Huang, Y. Y. Lu, B. W. Xia, Y. J. Jia, and F. Huang, “Elasto-plastic analysis of surrounding rock of drilling with strain softening model in deep soft rock,” *Rock and Soil Mechanics*, vol. 34, Supplement 1, pp. 179–186, 2013.
 - [18] X. R. Yao, G. L. Chen, and B. M. Shi, “Analysis on gas extraction drilling instability and control method of pore-forming in deep surrounding-rock with a weak structure,” *Journal of China Coal Society*, vol. 35, no. 12, pp. 2073–2081, 2010.
 - [19] S. X. Chen, F. Yang, and J. J. Zhang, “Key technology of offshore drilling for gold mine in the northern sea area of Sanshandao,” *Gold Science and Technology*, vol. 24, no. 1, pp. 17–22, 2016.
 - [20] Q. H. Ji, “Research and application of auger-air drilling and sieve tube borehole protection in soft outburst-prone coal seams,” *Procedia Engineering*, vol. 73, pp. 283–288, 2014.
 - [21] Z. Zhang, Y. X. Sun, Y. K. Fu, and T. Wang, “Study and application of pre-reinforcement of soft and breaking coal mass in gas drainage drilling field,” *Coal Engineering*, vol. 51, no. 8, pp. 44–47, 2019.
 - [22] T. Li, Y. Gao, D. C. Ai, J. W. Yang, H. Feng, and G. J. Zhao, “Floor precise grouting for prevention and control of water-based on confined water single-hole drainage experiment,” *Journal of China Coal Society*, vol. 44, no. 8, pp. 2494–2501, 2019.
 - [23] Z. Q. Wu, “Treatment of drilling collapse by water injection in deep hole coal seam,” *Shandong Coal Science and Technology*, no. 1, pp. 15–16, 2007.
 - [24] Z. X. Dai, H. Q. Chen, and S. C. Zheng, “Innovation and application of deep hole drilling technology in outburst soft coal seam,” *Safety in Coal Mines*, vol. 38, no. 8, pp. 20–21, 2007.
 - [25] W. He, X. W. Zhou, and R. Xu, “Experimental research on the new type of sodium silicate chemical grouting material,” *Journal of China Coal Society*, vol. 36, no. 11, pp. 1812–1815, 2007.
 - [26] H. Z. Zhang and X. C. Wang, “The treatment process of ZK0702 drilling accident in Baoxinggou gold mine, Heilongjiang province,” *Gold Science and Technology*, vol. 19, no. 5, pp. 53–55, 2011.
 - [27] T. Li, Y. Gao, P. Zhang et al., “Study on modification of grouting material with clay-based plate in deep mining under pressure,” *Metal Mine*, vol. 522, no. 12, pp. 173–177, 2019.
 - [28] H. Guo, H. Q. Wang, and J. Zhou, “Study on coal seam water infusion technology in fully mechanized coal face of Qipanjiang mine,” *Mining Safety & Environmental Protection*, vol. 44, no. 5, pp. 14–17, 2017.

Research Article

A New Method for the Measurement of Gas Pressure in Water-Bearing Coal Seams and Its Application

Xiao Cui ^{1,2} Jiayong Zhang ^{1,2} Liwen Guo,^{1,2} and Xuemin Gong ³

¹College of Mining Engineering, North China University of Science and Technology, Tangshan, Hebei 063210, China

²Mining Development and Safety Technology Key Lab of Hebei Province, Tangshan, Hebei 063210, China

³College of Chemical Engineering, North China University of Science and Technology, Tangshan, Hebei 063210, China

Correspondence should be addressed to Jiayong Zhang; zjy815@ncst.edu.cn and Xuemin Gong; gongxm1212@163.com

Received 2 August 2020; Revised 11 September 2020; Accepted 1 October 2020; Published 19 October 2020

Academic Editor: Bin-Wei Xia

Copyright © 2020 Xiao Cui et al. This is an open access article distributed under the Creative Commons Attribution License, which permits unrestricted use, distribution, and reproduction in any medium, provided the original work is properly cited.

Coal seam gas pressure is one of the fundamental parameters used to assess coal seam gas occurrence and is an important index in assessing the risk of gas disaster. However, the geological characteristics of coal seams become increasingly complex with increasing mining degree, thus decreasing the accuracy and success rate of direct methods for measuring gas pressure. To address such issues, we have developed a new method for direct measurement of gas pressure in water-bearing coal seams. In particular, we developed a pressure measurement device based on theoretical analysis and quantified the basic parameters of the device based on well testing. Then, we verified the applicability of our method based on comparative analysis of the results of field experiments and indirect measurements. Our results demonstrate that this new method can resolve the effects of water pressure, coal slime, and other factors on the estimation of gas pressure. The performance of this new method is considerably better than that of traditional methods. In particular, field test results demonstrate that our method can accurately and efficiently measure gas pressure in water-bearing coal seams. These results will be of great significance in the prevention and control of coal seam gas disaster.

1. Introduction

Coal is the most important primary energy source and an important raw material in China [1, 2]. Nevertheless, coal output in China has decreased in recent years and more coal mines have progressed to deep mining [3, 4]. With increasing mining depth, both geological characteristics and mining conditions become increasingly complex, increasing the risk of gas disaster [5, 6].

Coal seam gas pressure is a fundamental parameter in the study of coal seam gas occurrence [7, 8]. This gas pressure is an important index describing the risk of gas outburst from coal seams; accordingly, accurate determination and control of coal seam gas pressure is critical for coal mine safety [9–11].

Previously, gas pressure has been determined based primarily on predictive models and field tests [12]. In particular, many studies have considered the relationship

between gas pressure and surface depth, typically adopting one-dimensional linear or polynomial regression methods. Such studies have derived empirical relationships based on measured gas pressure data and the specific geological characteristics of mining areas [13]. However, there are shortcomings associated with regression methods, because many factors cause estimated gas pressure to deviate considerably from measured values; accordingly, regression methods are often inaccurate and can introduce additional risk [14–17]. Furthermore, geological conditions, the construction environment, and space restrictions can make it difficult to validate these methods on site. Thus, the distribution of coal seam gas pressure has yet to be constrained accurately.

To date, measurement of coal seam gas pressure has relied heavily on certain geological criteria being met. Geological characteristics become increasingly complex with increasing mining depth and concomitant increases in gas pressure and temperature; heat damage and the risk of water

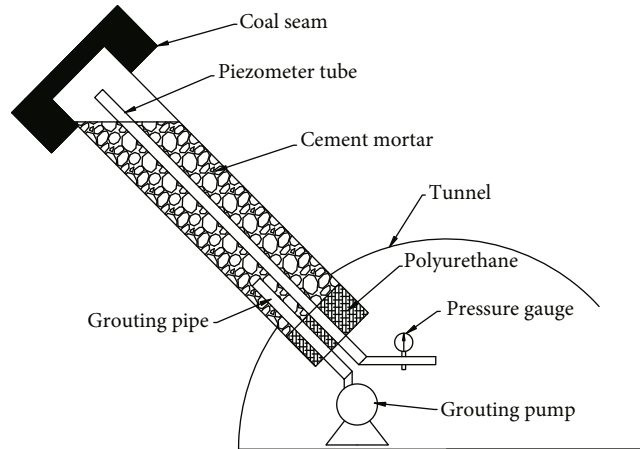


FIGURE 1: Schematic diagram illustrating direct determination of gas pressure.

inrush also increase with mining depth [18, 19]. Therefore, the measurement of gas pressure in water-bearing coal seams becomes increasingly difficult with depth [20]. In particular, achieving accuracy in the measurement of gas parameters in coal seams is extremely difficult under the coupled gas-liquid flow field, thus restricting the accuracy of prediction and on-site measurement of gas risk. Such inaccuracy has serious implications for the safety of coal mine production. Traditional methods for measuring gas pressure in water-bearing coal seams have a number of disadvantages. For example, water and coal cinder can flood into the pressure measuring borehole; this can block the borehole or produce a potential energy gradient (due to water pressure) that can affect the accuracy of the measured pressure. Devices developed in recent years are more suited to measuring pressure in water-bearing coal seams. These more recent devices typically measure pressure using a double pipe in the upper hole: a high-level pipe is used to tighten the connection between the pressure measuring gas chamber and the pressure gauge, whereas a low-level pipe is used to connect the external water discharging device to the pressure release. Although this type of device is of some practical use, it remains difficult to prevent water and coal cinder from entering the upper hole; this makes it impossible to monitor changes in water flow in real time and can result in gas leakage in the borehole. Development of an accurate means of measuring the gas pressure of water-bearing coal seams will help constrain the laws governing gas occurrence in deep coal seams. This constitutes important theoretical research that will have considerable practical significance.

The present study discusses the limitations of existing methods for the direct determination of gas pressure in water-bearing coal seams and proposes a new method for the determination of gas pressure in such coal seams. Here, the accuracy of this new method is demonstrated based on an indirect measurement method and field comparison tests. The results show that this method is sufficiently robust for application in real coal mine settings. Moreover, the proposed method provides an important theoretical basis for the determination of coal seam gas parameters and will help inform gas control measures.

2. Traditional Methods of Gas Pressure Measurement

2.1. Direct Measurement Method. Coal seam gas pressure is pressure generated by gas within coal seams, expressed in MPa. In the absence of any other constraining factors, coal seam gas pressure will reflect absolute pressure. Direct measurements of coal seam gas pressure can be obtained using boreholes and other methods that allow measurement at depth. When gas pressure is measured using a borehole, the borehole is first sealed to allow gas pressure to equilibrate in response to the natural permeability of the coal seam; then, the gas pressure is measured within a measuring chamber [21]. In practice, this is achieved as shown in Figure 1. First, the piezometer tube is installed to a predetermined depth; the length of the pipe is determined by underground roadway and transportation conditions. Then, the pipe is sealed at the orifice with polyurethane and the grouting pipe is installed. The borehole is filled with expandable/nonshrinking material comprising clean water and cement; this cement slurry is injected into the borehole in one continuous process using the cement pump. The grout is left to dry for 24 h before the pressure gauge is installed at the orifice [22, 23].

If gas pressure changes considerably within one week of installation of this apparatus, the observation time interval should be shortened appropriately. Observation results are typically plotted with time (in days) on the abscissa and gas pressure (MPa) on the ordinate. When the pressure measurement process is complete and the pressure gauge is removed (adhering to relevant safety measures), the quantity of water released from the borehole can be measured. If the borehole is connected to an aquifer or karst cave, any water flow measurements obtained from the borehole will be invalid; accordingly, the borehole should be sealed. Otherwise, measurement of water flow from the borehole can proceed. Flow rates can be obtained by measuring the volume of water released from the borehole and various borehole and sealing parameters. When there is no water flow from the borehole, for upward drilling, the results of gas pressure measurement can be expressed as shown in equation (1).

$$P^* = P_1, \quad (1)$$

where P_1 is the measured value, read from the pressure gauge, and P^* is the gas pressure (both in MPa).

When the borehole contains water, correction should be undertaken as follows. When $V > V_1$ and $V - V_1 < V_2$, the correction described by equation (2) should be applied.

$$P^* = P_1 - 0.01L \sin \theta - 0.01 \frac{4(V - V_1)}{\pi D^2} \sin \theta. \quad (2)$$

Conversely, when $0 < V \leq V_1$, correction should be undertaken according to equation (3).

$$P^* = P_1 - 0.01 \frac{4V}{\pi d^2} \sin \theta, \quad (3)$$

where V is water flow out of the borehole (cm^3), V_1 is the volume of air inside the measuring pressure tube (cm^3), V_2 is the volume of air remaining in the borehole (cm^3), L is the length of the pressure measuring tube (m), D is the diameter of the borehole (m), and d is the diameter of the piezometer tube (m).

When $V > V_1$ and $V \geq V_2 + V_1$, the volume of water flowing out of the borehole exceeds the combined volume of the air remaining in both the pressure measuring tube and the borehole. However, the potential energy of water present in the borehole means that the measured pressure is not an accurate reflection of the actual coal seam gas pressure P^* . To address this, the present study proposes a new method for measuring coal seam gas pressure that is suitable for seams with high water content.

2.2. Indirect Measurement Method. The indirect method described here is based on the coal seam gas adsorption theory. Coal seam gas pressure can be calculated according to equation (4), based on gas content and some basic parameters [24].

$$Q = \frac{abP}{1 + bP} \cdot \frac{1}{1 + 0.31M_t} \cdot \frac{100 - A_d - M_t}{100} + \frac{10\pi P}{\gamma}, \quad (4)$$

where Q is the adsorption gas content of coal (cm^3/g), P is the coal seam gas pressure (MPa), a is an adsorption constant (when P tends to infinity, this represents the saturation adsorption capacity) in cm^3/g , and b is a second adsorption constant (MPa^{-1}). Here, A_d and M_t represent the ash and water content (%) of coal, respectively; π is coal porosity (cm^3/cm^3), and γ is the bulk density of coal (g/cm^3).

This method of determining coal seam gas content was first investigated based on an exploration drilling desorption method that considers geological characteristics. The determination of gas content is a recognized industrial standard, and a desorption method for coal seam gas content has been established previously [25]. Smith and Williams proposed a method of calculating air leakage during coring [26]; the Smith–Williams desorption method was established based on this method [27]. Subsequently, a direct method of determining gas content based on dynamic equilibrium and gas

desorption characteristics was developed, building upon the geological exploration desorption method. This direct method originated in the United States and has been used widely, including as the Chinese national standard (GBT 23250-2009) [24, 28].

Determination of coal seam gas content can be achieved by considering the volumes of desorption gas (X_2), gas lost during sample collection (i.e., lost gas, X_1), and gas emitted during degassing before crushing (X_3) and after crushing (X_4), all measured in cm^3 . Calculation in this manner is described by equation (5) [29, 30]

$$Q_i = \frac{\sum_{j=1}^3 X_i^j}{m}, \quad (5)$$

where Q_i is the coal gas content of a sample at each stage ($i = 1, 2, 3, 4$) in $\text{cm}^3 \cdot \text{g}^{-1}$, m is the coal sample quality (g), and X_i^j is the volume of gas at each stage ($i = 1, 2, 3, 4, j = 1, 2, 3$) in cm^3 .

A degassing method can be adopted to determine the adsorption gas content of coal seams, as described by equation (6).

$$Q = Q_1 + Q_2 + Q_3 + Q_4, \quad (6)$$

where Q is the adsorbed gas content, Q_1 is the lost gas content, Q_2 is the desorption gas content, and Q_3 and Q_4 are the gas contents degassed before and after crushing, all measured in $\text{cm}^3 \cdot \text{g}^{-1}$.

3. The New Method of Gas Pressure Measurement

Water pressure and water inflow are the primary factors affecting determination of gas pressure in water-bearing coal seams. In particular, water pressure in the seam can make it difficult to obtain a pressure estimate that reflects gas pressure in the coal seam accurately. Similarly, the influx of water and coal slime induces error in the pressure measuring device, further reducing the accuracy of the pressure estimate obtained.

To account for the influence of water on the piezometer, a new method has been developed that can separate water and gas and prevent coal slime obstruction. This device was designed based on the principle of automatic compensation and balancing of the water level (Figure 2) and is ideal for use in water-bearing coal seams. The primary components of the device include a piezometric tube, gas pressure gauge, water level sensor, solenoid valve, drain valve, power supply, and control devices. When the device is connected to a pressure measuring borehole, the gas and water in the coal seam enter the gas inlet and the water inlet device, respectively. Gas also enters the gas pressure gauge via the piezometric tube to allow measurement of the true coal seam gas pressure. Water and coal cinder are collected at the bottom of the device to promote gas-liquid separation, and the liquid level is controlled by the water level sensor to ensure a stable pressure measuring space. Thus, the application of this device can

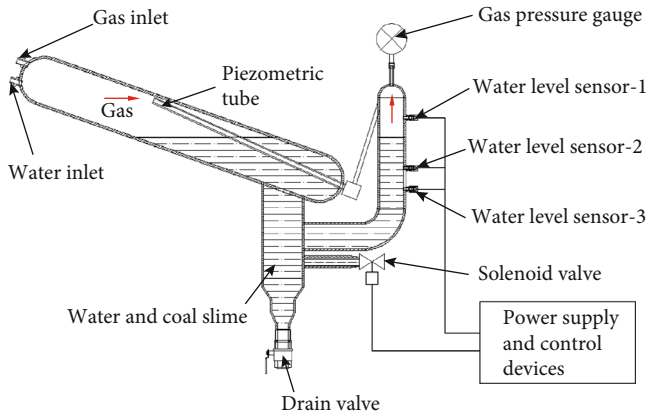


FIGURE 2: Schematic diagram of gas pressure measuring device for water-bearing coal seams.

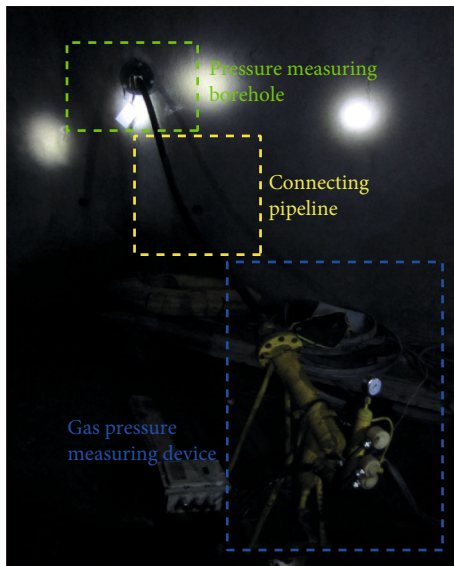


FIGURE 3: Schematic diagram showing underground connection of gas pressure measuring device.

eliminate the influence of water pressure and coal cinder on gas pressure, allowing measurement of the true gas pressure of water-bearing coal seams.

Our method for field testing can be summarized as follows.

- (1) Measurement sites were selected carefully, focusing on those in tunnels, in areas of massive lithology with no faults, cracks, or other geological structures. Drilling was undertaken to a depth of at least 15 m and proceeded through the rock surrounding the roadway until the edge of the coal seam was reached. The drilling diameter and dip angle were 146 mm and $>0^\circ$, respectively. Then, the coal dust was cleaned up and the drilling parameters were recorded
- (2) A pressure measuring pipe with a diameter of 108 mm was placed into the borehole, and the grouting pump was used to fill the borehole with expanding/nonshrinking cement slurry in one continuous

process, as shown in Figure 3. Then, water discharge (per minute) from the borehole was recorded

- (3) The pressure measuring borehole was connected to the pressure measuring device through the flange and the high-pressure hose. Then, the drain valve of the pressure measuring device was closed and the power supply was started; the value exhibited by the gas pressure gauge was recorded after it had stabilized
- (4) Figure 3 illustrates the discharge of water by the pressure measuring device during the pressure measuring process. After measuring the pressure, the power was turned off and the drain valve was opened slowly to discharge the pressure. When the pressure gauge reached 0, the flange and high-pressure hose were removed. The steps above were then repeated at the next measurement location. In this manner, it was possible to determine the distribution of gas in the coal seam at different locations

4. Results and Discussion

4.1. Parameter Measurement. The experimental setup shown in Figure 4 was designed to simulate real conditions in water-bearing coal strata and allow both the determination of pressure parameters and the measurement of error for the gas pressure measuring device.

The following procedure was adopted. First, 20 L of water was measured and injected into the tank; then, the high-pressure gas valve was opened and the pressure reducing valve was adjusted to achieve the desired gas pressure. The gas and water inlet valves were opened simultaneously to observe the action of the solenoid valve, and the inlet and outlet speeds and any changes in the pressure gauge were recorded.

The gas pressure was varied, and the start and end times of water flowing from the solenoid valve were recorded. Simultaneously, a measuring cylinder was used to determine the volume of water flowing out of the electromagnetic valve and thus calculate its water flow. The inlet and outlet flow rate and velocity at various gas pressures are illustrated in Figure 5.

The results demonstrate that water discharge increases linearly with increasing pressure (Figure 5(a)). Broadly, the inlet flow rate remains unchanged with increasing pressure (fitting equation: $Q_i = 1.87P + 30.25$). The average water outlet velocity increases with increasing pressure (Figure 5(b), fitting equation: $V_o = 1.973P + 2.443$), whereas the inlet velocity remains relatively unchanged with increasing pressure (fitting equation: $V_i = 0.04P + 0.6$). In this experimental setup, the inlet of the pressure measuring device is connected to the tank of the device simulating coal seam conditions. According to the Bernoulli equation, the inlet flow rate and velocity are affected only by the weight of the water under gravity and so remain constant.

Our field experiments have shown that, when the gas pressure has a stable output, the pressure measured by the pressure gauge changes with the gas pressure (Figure 6). In particular, when the air source pressure is less than 1 MPa, $P = P^*$ and pressure has little effect on drainage. Thus, under

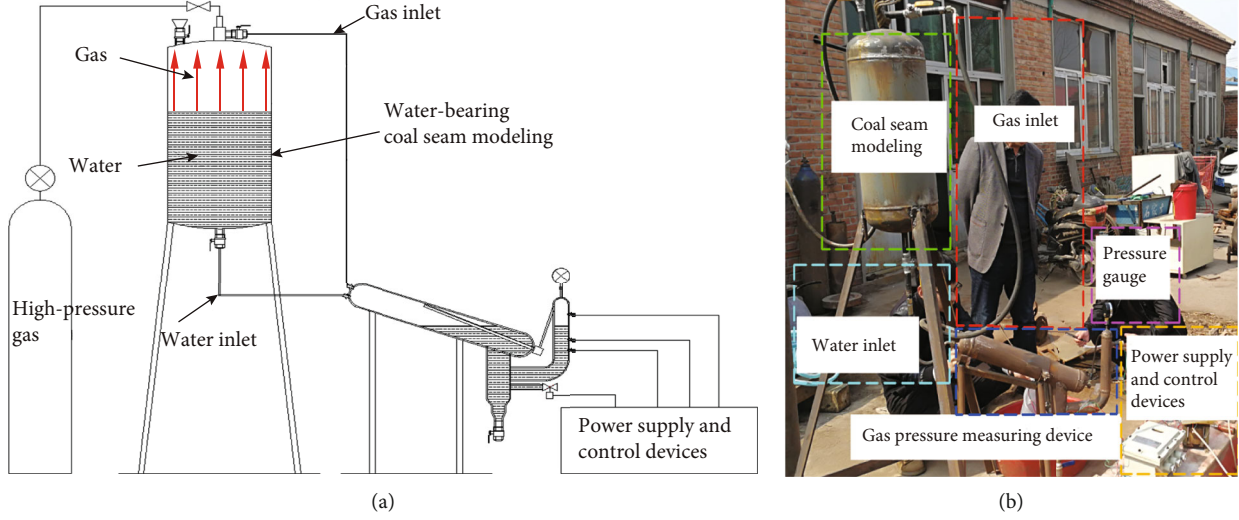


FIGURE 4: Gas pressure simulation testing in water-bearing coal seams: (a) experimental schematic diagram and (b) field test.

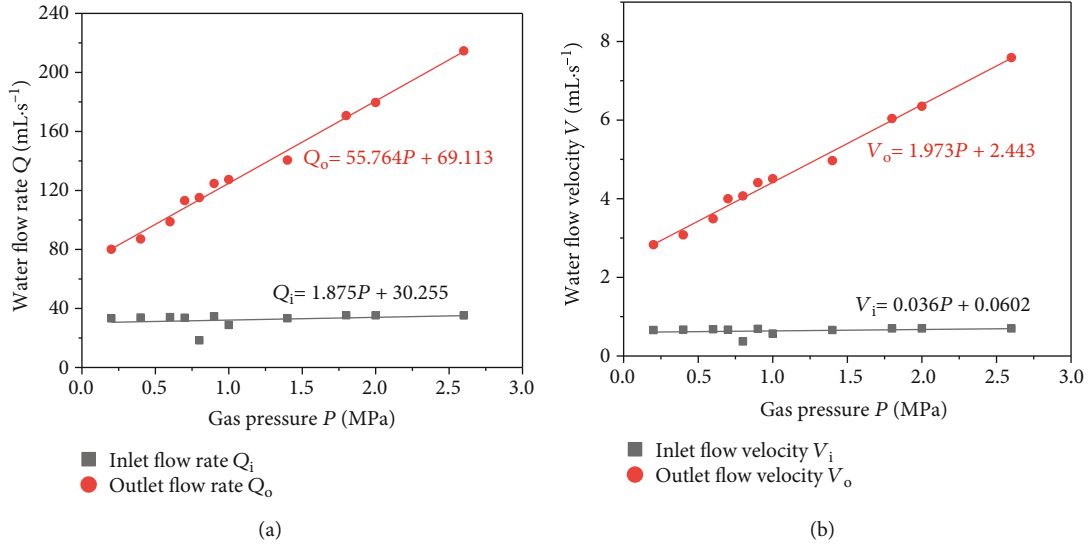


FIGURE 5: Inlet and outlet (a) flow rate and (b) flow velocity for the pressure measuring device at different gas pressures.

such conditions, drainage can be considered to be effectively zero and the pressure measured by the gauge is equal to the gas pressure. When the air source pressure exceeds 1 MPa, the pressure measured by the gauge is affected by the high gas pressure and the release of pressure during drainage; this relationship can be described by the equation $P^* = 0.977 P^{0.937}$. Conversely, when the solenoid valve remains closed for a certain time, $P = P^*$ and the pressure measured by the gauge equilibrates to the air source pressure. Under these conditions, the measured pressure reflects the real gas pressure in the water-bearing coal seam accurately.

4.2. Indirect Method of Measuring Gas Pressure

4.2.1. Coal Samples. Coal samples from three coal seams in the Kailuan mining area, China, were analyzed in the present study. Proximate analysis of these coal samples was undertaken, and the density of each sample was measured

(Table 1). All samples were ground before analysis, and the following fractions were selected to meet testing requirements: <0.05 mm, 0.20–0.25 mm, and >5 mm.

4.2.2. Determination of Methane Adsorption Parameters. Gas in coal typically exists in two states: free gas and adsorbed gas. Free gas content can be calculated based on the porosity and gas pressure of coal, whereas adsorbed gas content can be calculated based on the adsorption constants a and b . In the present study, we derived gas adsorption curves for the obtained coal samples using the HAC-1 high-pressure capacity method (Figure 7). The Langmuir function was used to fit the methane adsorption curve in the range 0–5 MPa. We determined adsorption constants based on equation (7).

$$Q_c = \frac{abP}{(1 + bP)}, \quad (7)$$

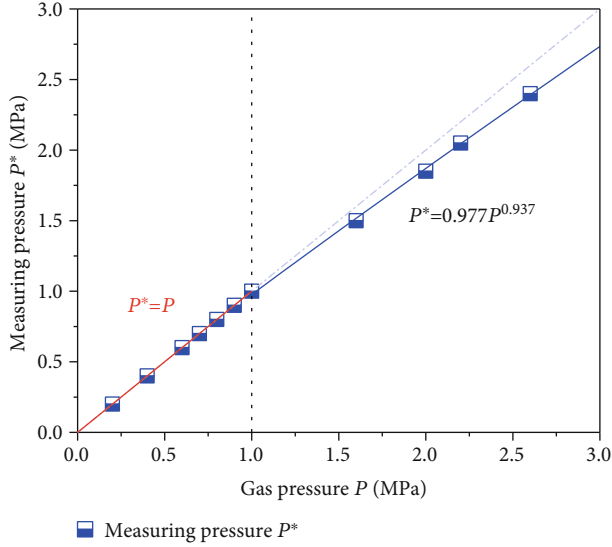


FIGURE 6: Relationship between simulated gas pressure P and measured gas pressure P^* .

TABLE 1: Density and proximate analysis results for coal samples.

Parameters	1 [#] coal	2 [#] coal	3 [#] coal
Proximate analysis			
Total moisture (M_t , %)	0.9	2.7	2.7
External moisture (M_f , %)	0.3	0.9	0.8
Inherent moisture (M_{inh} , %)	0.6	1.8	1.9
Ash content (A_d , %)	27.73	11.80	6.80
Volatile (V_d , %)	18.41	34.54	36.86
Total sulfur ($S_{t,d}$, %)	0.51	0.48	0.90
Density			
True relative density (g/cm^3)	1.62	1.42	1.37
Apparent relative density (g/cm^3)	1.58	1.39	1.32

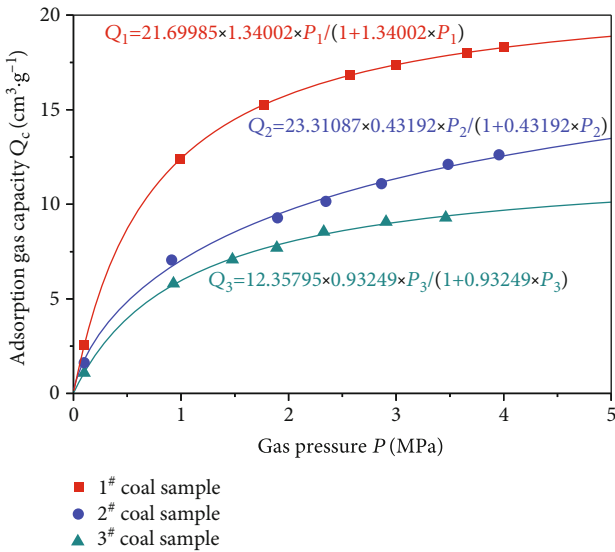


FIGURE 7: Gas adsorption curves for three coal samples under various pressures.

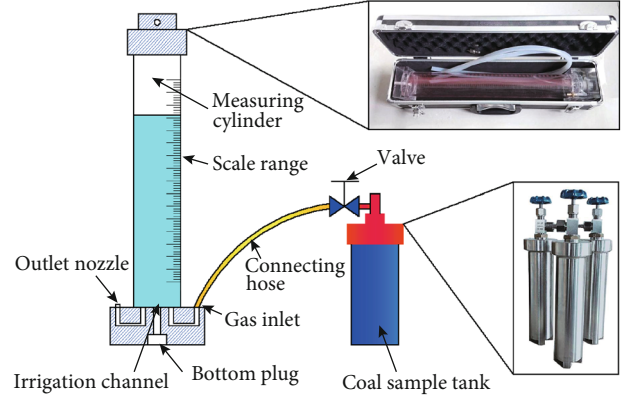


FIGURE 8: Schematic illustrating connection of DGC device.

where Q_c is gas adsorption capacity ($\text{cm}^3 \cdot \text{g}^{-1}$) and P is gas pressure (MPa). We obtained the following values for the adsorption constants (in MPa^{-1}): $a = 21.70, 23.31,$ and 12.36 and $b = 1.34, 0.43,$ and 0.93 for samples 1[#], 2[#], and 3[#], respectively.

4.2.3. Indirect Method of Gas Pressure Measurement

(1) *Lost Gas, X_1 , and Desorption Gas, X_2 .* The DGC device (Figure 8) is used widely to measure gas desorption. Here, we used this device for both downhole sampling and the measurement of gas desorption velocity.

After drilling to the required depth, we used a core tube to obtain fresh coal samples from the bottom of the hole and transferred the samples quickly to a sealed tank. To determine gas desorption X_2 , we measured the calibrated liquid level every 1 min for 30 min and recorded the total exposure time (t_1) during the sampling period, ambient temperature, and atmospheric pressure. Then, we calculated the volume of lost gas X_1 based on the curve shown in Figure 9, which illustrates both gas desorption and gas lost.

(2) *Gas Released during Degassing before Crushing, X_3 .* The coal sample tank was connected to the degasser using a puncture needle and vacuum hose. Each coal sample was degassed at room temperature until gas leakage was less than 10 cm^3 over a period of 30 min. Then, each sample was heated to 95°C at a constant rate. This degassing process was repeated until degassing was deemed to be complete; the total gas released during this stage was recorded as X_3 .

(3) *Gas Released during Degassing after Crushing, X_4 .* The coal sample tank was removed. Then, the coal samples were removed rapidly and placed into a kibble; the tank was sealed by tightening its cover. The coal samples were crushed in the tank, and pulverized samples with particle size $< 0.25 \text{ mm}$ (typically $> 80\%$ of each sample) were retained.

Degassing after crushing was measured in the same way as that before crushing, and X_4 was recorded after the measuring device had stabilized. After obtaining the

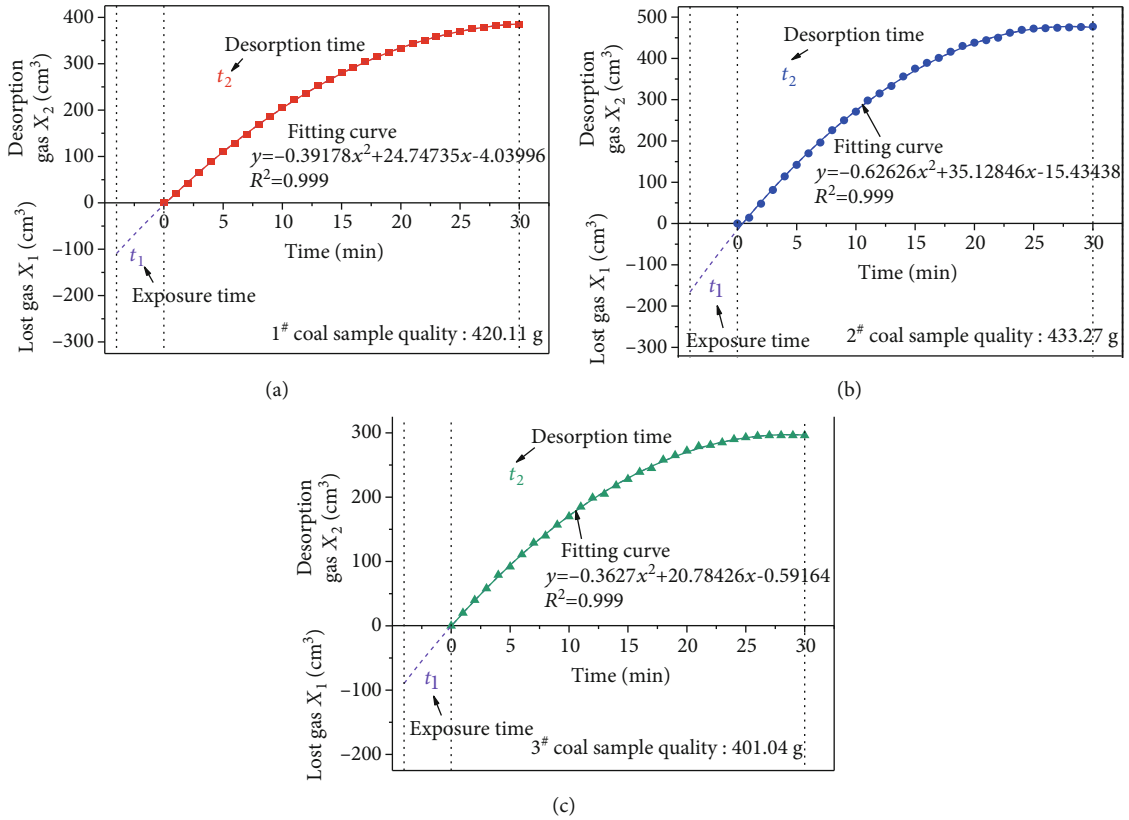


FIGURE 9: Fitting curve for lost gas X_1 and desorption gas X_2 .

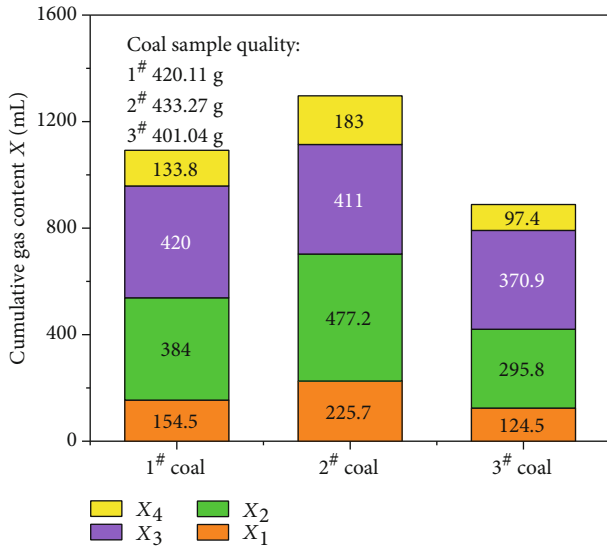


FIGURE 10: Gas content and coal quality for three coal samples.

measurements, the ball grinding tank was removed and the tank was cooled to ambient temperature before the coal sample was removed from the tank and weighed.

Gas volume and coal quality for each stage are shown in Figure 10 for the coal samples considered. Based on equation (6), the gas contents Q of the 1[#], 2[#], and 3[#] coal seams were calculated to be 2.60, 2.89, and 2.22 cm³ · g⁻¹, respectively. The gas pressure for each coal seam was calculated based

on several parameters (i.e., gas content, adsorption constant, density, and proximate analysis parameters) according to equation (4) (Table 2).

4.3. Application and Validation of the New Method

4.3.1. Gas Pressure Measurement in the Field. Field experiments were conducted on three working faces in different coal mines to determine coal seam gas pressure empirically. During testing, we drilled pressure measuring holes directly into water-bearing coal seams and grouted the holes to seal them. Then, we used both a traditional method and our new method to measure coal seam gas pressure. To allow comparison between the two methods, three pressure measuring holes were arranged at the same level for each working face, maintaining a spacing of 2 m between holes, and the pressure was measured over a period of 15 days. The drilling parameters for each working face are summarized in Table 3. Theoretically, gas is discharged slowly while the hole is being sealed; accordingly, pressure loss during sealing can be ignored. Measurements were obtained using the traditional method first, to avoid any influence of the changing of equipment on the test results.

The new method was validated by drilling three boreholes into each of the working surfaces considered. The results are presented in Figure 11. Using this novel method, maximum gas pressures of 0.25, 0.26, and 0.22 MPa were recorded for three of the boreholes considered; these values can be considered to exhibit low variability. In contrast,

TABLE 2: Gas pressure in three coal seams.

No.	Gas content ($\text{cm}^3 \cdot \text{g}^{-1}$)	Moisture (%)	Ash content (%)	Adsorption constant		Porosity (cm^3/cm^3)	Apparent relative density ($\text{g} \cdot \text{cm}^{-3}$)	Gas pressure (MPa)
				a ($\text{cm}^3 \cdot \text{g}^{-1}$)	b (MPa^{-1})			
1 [#]	2.60	0.9	27.73	21.70	1.34	0.0253	1.58	0.2
2 [#]	2.89	2.7	11.80	23.31	0.43	0.0216	1.39	0.79
3 [#]	2.22	2.7	6.80	12.36	0.93	0.0388	1.32	0.54

TABLE 3: Drilling parameters for pressure boreholes in coal seams.

Borehole parameters	1 [#] coal seam			2 [#] coal seam			3 [#] coal seam		
	B_1	B_2	B_3	B_4	B_5	B_6	B_7	B_8	B_9
Drilling depth (m)	24	25	28	32	31	34	28	29	31
Hole sealing length (m)	8	8	8	10	10	10	8	8	8
Drilling diameter (mm)	$\Phi 146/108$								
Seam inclination ($^\circ$)	20	20	20	12	12	12	30	30	30
Water flow rate ($\text{mL} \cdot \text{s}^{-1}$)	5	30	22	44	62	58	55	51	90

Note: drilling diameter $\Phi 146/108$ (coal seam drilling diameter was 146 mm and diameter of pressure measuring hole after sealing was 108 mm).

results of 0.06, 0, and 0.2 MPa were obtained for different boreholes using the traditional method. When the testing equipment was disassembled after completing the pressure measurement process, large amounts of water and coal were found to have accumulated in the B_1 and B_2 boreholes for the traditional method. Accordingly, it can be inferred that the results for the B_1 and B_2 boreholes may have been affected by water pressure and/or by coal slime blocking the pressure measurement boreholes. In contrast, only small quantities of water were found in the B_3 borehole, which yielded pressure measurements similar to those obtained for the new method described in the present study (Figure 11(b)). Gas pressure measurements of 0.8 and 0.84 MPa were obtained for the B_4 and B_5 holes, respectively, using the new method; however, the result obtained for the B_6 hole using this method is considered to be invalid. The detection of higher gas pressures for the B_4 and B_5 holes using the traditional method (relative to the novel method) can be explained with reference to the Bernoulli equation (8).

$$P^* + \rho gh = P_1, \quad (8)$$

where P^* is gas pressure (MPa), ρ is the density of the coal slime water (which exceeds $1000 \text{ kg} \cdot \text{cm}^{-3}$), g is the acceleration due to gravity ($\text{m} \cdot \text{s}^{-2}$), h is the vertical height of the hole (m), and P_1 is the measured pressure (MPa). This explains why the measured pressure exceeds the real gas pressure. The result obtained for the B_6 hole using the traditional method is also considered to be invalid, although this method yielded gas pressures of 1.1 and 1.0 MPa for the B_4 and B_5 holes, respectively. Based on these results, it can be concluded that the B_4 and B_5 holes were both well sealed. The higher pressures obtained using the traditional method can be attributed to the joint action of water pressure and gas pressure. Additionally, the failure of the B_6 hole can be attributed

to poor sealing of the hole due to the appearance of numerous primary cracks around the hole entrance.

For the three boreholes in the 3[#] coal seam (Figure 11(c)), gas pressure was found to be 0.55, 0.54, and 0.58 MPa according to our new method and 0, 0.1, and 0.14 MPa according to the traditional method; as for the B_7 and B_8 boreholes, this discrepancy can be attributed to differences in water and gas pressure. Based on this analysis, it can be concluded that the novel method is more accurate and reliable than the traditional method and offers a higher success rate. In particular, it can effectively resolve the effects of water, slime, and other factors relevant to water-bearing coal seams on the obtained gas pressure values.

4.3.2. Comparison of New Method with Indirect Method. To verify the accuracy of the novel method, gas pressures obtained using this method were compared with those obtained using the indirect method (Figure 12). The results were broadly consistent between methods, thus demonstrating the accuracy and feasibility of the new method. However, the gas pressures obtained using the new method are higher than those obtained using the indirect method; this is likely because the new method is not subject to the errors in gas desorption testing and gas content calculation that typically affect the indirect method. Moreover, the novel method reduces both the number of experimental steps and the engineering input required. In summary, the present study demonstrates that the novel method is both feasible and reliable for the determination of gas pressure in water-bearing coal seams. Therefore, the results presented here will have practical significance in addressing common engineering problems in settings involving water-bearing coal seams and will help ensure coal mine production safety.

5. Conclusions

We have established a new method for measuring gas pressure in water-bearing coal seams to address the shortcomings of existing methods. Our main conclusions are as follows.

- (1) We have developed a new method to determine gas pressure in water-bearing coal seams based on the principle of automatic water level compensation and balance. Our novel device can effectively resolve the effects of water pressure, slime water, and other factors on measurement results and can determine gas pressure in water-bearing coal seams accurately. In particular, our device includes a solenoid valve controlled by a water level sensor that can eliminate

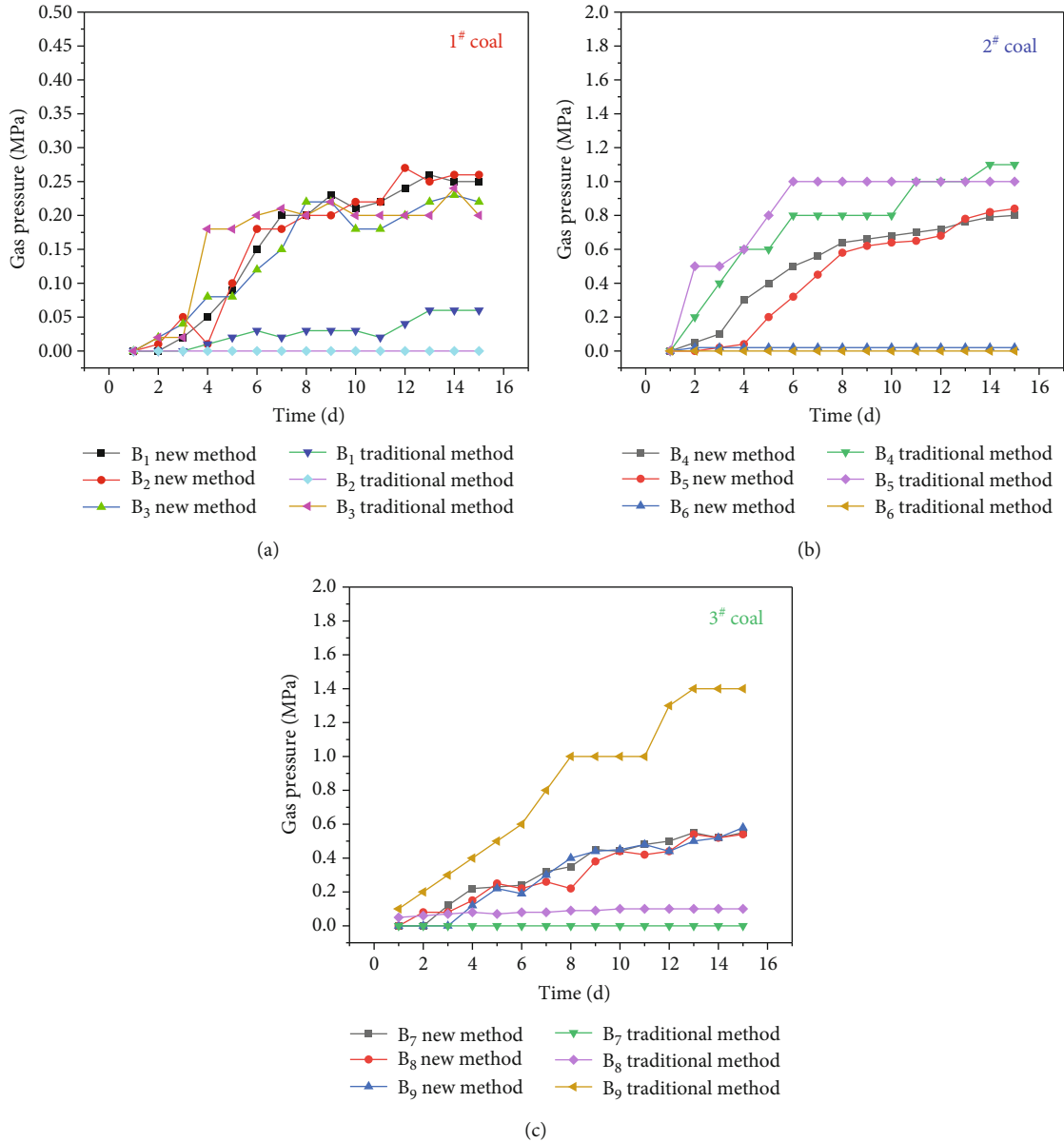


FIGURE 11: Gas pressure measurements obtained using new method and traditional method.

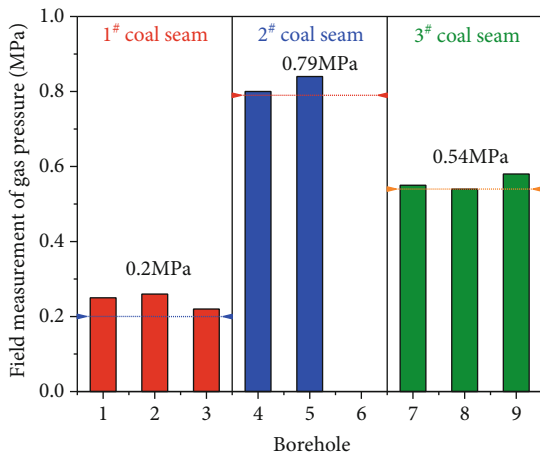


FIGURE 12: Comparison between new method and indirect method.

the effects of water over time and a drain valve that excludes the influence of coal slime

- Based on experiments considering well parameters, both water inflow and rate increase with increasing coal seam gas pressure; similarly, drainage rate increases with increasing pressure. Gas pressure has a minor effect on drainage when gas pressure < 1 MPa. Broadly, the measured gas pressure is consistent with gas pressure in the coal seam under such conditions, such that $P^* = P$. In contrast, when the gas pressure is >1 MPa, the pressure relationship can be separated into drainage and nondrainage stages. The measured pressure decreases with increasing gas pressure, and the drainage flow rate and velocity are both rapid. This relationship can be described by the following composite fitting curve:

$P^* = 0.977P^{0.937}$. When drainage has occurred continuously for a specific time period, the pressure indicated by the gauge is the same as the air source pressure value. Thus, when the gas pressure exceeds 1 MPa, the pressure measured when the solenoid valve is closed can be considered an accurate reflection of the true coal seam gas pressure

- (3) Based on field tests measuring gas pressure in water-bearing coal seams, the new method exhibits both a higher success rate and lower error than the traditional method. Moreover, there is only a small difference between the gas pressure calculated using the indirect method and that measured in the field tests of the present study, further demonstrating the accuracy of the new method. These results demonstrate that this novel method is both feasible and reliable for the determination of gas pressure in water-bearing coal seams

Data Availability

The data used to support the findings of this study are available from the corresponding author upon request.

Conflicts of Interest

The authors declare that there is no conflict of interest regarding the publication of this paper.

Acknowledgments

This research work was supported by the National Natural Science Foundation Fund (51874012), the National Key Research and Development Plan (2018YFC0808100), the Hebei Natural Science Foundation Fund (E2016209249), and the Graduate Student Innovation Fund of North China University of Science and Technology (2018B26).

References

- [1] L. Wang, S. Liu, Y. Cheng, G. Yin, D. Zhang, and P. Guo, "Reservoir reconstruction technologies for coalbed methane recovery in deep and multiple seams," *International Journal of Mining Science and Technology*, vol. 27, no. 2, pp. 277–284, 2017.
- [2] H. C. Lau, H. Li, and S. Huang, "Challenges and opportunities of coalbed methane development in China," *Energy & Fuels*, vol. 31, no. 5, pp. 4588–4602, 2017.
- [3] H. Xu, S. Sang, J. Yang et al., "Selection of suitable engineering modes for CBM development in zones with multiple coalbeds: a case study in western Guizhou Province, Southwest China," *Journal of Natural Gas Science and Engineering*, vol. 36, 2016.
- [4] S. Xue, L. Yuan, Y. Wang, and J. Xie, "Numerical analyses of the major parameters affecting the initiation of outbursts of coal and gas," *Rock Mechanics & Rock Engineering*, vol. 47, no. 4, pp. 1505–1510, 2014.
- [5] State Administration of Work Safety, *Safety regulations for coal mine in China*, 2016.
- [6] W. Yang, H. Wang, Q. Zhuo et al., "Mechanism of water inhibiting gas outburst and the field experiment of coal seam infusion promoted by blasting," *Fuel*, vol. 251, pp. 383–393, 2019.
- [7] Y. P. Cheng, L. Wang, and X. Zhang, "Environmental impact of coal mine methane emissions and responding strategies in China," *International Journal of Greenhouse Gas Control*, vol. 5, no. 1, pp. 157–166, 2011.
- [8] S. Lu, C. Wang, Q. Liu et al., "Numerical assessment of the energy instability of gas outburst of deformed and normal coal combinations during mining," *Process Safety and Environmental Protection*, vol. 132, pp. 351–366, 2019.
- [9] W. Xiong, Q. Gong, X. Duan et al., "Pressure building-up methodology to measure gas content of shale samples," *Journal of Petroleum Science and Engineering*, vol. 186, article 106678, 2019.
- [10] H. Wang, E. Wang, Z. Li et al., "Study and application of dynamic inversion model of coal seam gas pressure with drilling," *Fuel*, vol. 280, p. 118653, 2020.
- [11] A. Zhou, M. Zhang, K. Wang, D. Elsworth, J. Wang, and L. Fan, "Airflow disturbance induced by coal mine outburst shock waves: a case study of a gas outburst disaster in China," *International Journal of Rock Mechanics and Mining Sciences*, vol. 128, p. 104262, 2020.
- [12] F. An, Y. Cheng, L. Wang, and W. Li, "A numerical model for outburst including the effect of adsorbed gas on coal deformation and mechanical properties," *Computers & Geotechnics*, vol. 54, pp. 222–231, 2013.
- [13] Z. Pan and L. D. Connell, "A theoretical model for gas adsorption-induced coal swelling," *International Journal of Coal Geology*, vol. 69, no. 4, pp. 243–252, 2007.
- [14] D. M. Hu and B. Q. Lin, *Coal Seam Gas Occurrence Regulation and Control Technology*, China University of Mining and Technology Press, Xuzhou, 2006.
- [15] Y. P. Cheng, H. F. Wang, and W. A. Liang, "Principle and engineering application of pressure relief gas drainage in low permeability outburst coal seam," *Mining Science and Technology (China)*, vol. 19, no. 3, pp. 342–345, 2009.
- [16] R. D. Lama and J. Bodziony, "Management of outburst in underground coal mines," *International Journal of Coal Geology*, vol. 35, no. 1–4, pp. 83–115, 1998.
- [17] C. B. Lian and W. Li, "Exploration on the enhance of gas pressure prediction accuracies in coal seam," *Journal of Henan Polytechnic University(Natural Science)*, vol. 27, no. 2, pp. 131–139, 2008.
- [18] W. Nie, Y. Liu, C. J. Li, and J. Xu, "A gas monitoring and control system in a coal and gas outburst laboratory," *Journal of Sensors*, vol. 2014, 11 pages, 2014.
- [19] E. T. Chen, L. Wang, Y. P. Cheng et al., "Pulverization characteristics of coal affected by magmatic intrusion and analysis of the abnormal gas desorption index on drill cuttings," *Adsorption Science and Technology*, vol. 36, pp. 805–829, 2017.
- [20] J. I. Joubert, C. T. Grein, and D. Bienstock, "Effect of moisture on the methane capacity of American coals," *Fuel*, vol. 53, no. 3, pp. 186–191, 1974.
- [21] L. Wang, Y. P. Cheng, L. Wang, P. K. Guo, and W. Li, "Safety line method for the prediction of deep coal-seam gas pressure and its application in coal mines," *Safety Science*, vol. 50, no. 3, pp. 523–529, 2012.
- [22] State Administration of Work Safety, *The Direct Measuring Method of the Coal Seam Gas Pressure in Mine*, Beijing, 2007.
- [23] S. Y. Wu, Y. Y. Guo, Y. X. Li, G. L. Yang, and Y. Niu, "Research on the mechanism of coal and gas outburst and the screening

- of prediction indices,” *Procedia Earth and Planetary Science*, vol. 1, no. 1, pp. 173–179, 2019.
- [24] L. Wang, L. B. Cheng, Y. P. Cheng et al., “A new method for accurate and rapid measurement of underground coal seam gas content,” *Journal of Natural Gas Science and Engineering*, vol. 26, pp. 1388–1398, 2015.
- [25] F. N. Kissell, C. M. McCulloch, and C. H. Elder, *The Direct Method of Determining Methane Content of Coalbeds for Ventilation Design*, U.S. Bureau of Mines Report of Investigations, 1973.
- [26] D. M. Smith and F. L. Williams, “A new technique for determining the methanecontent of coal,” in *Proceedings of the intersociety energy conversion engineering conference*, pp. 1272–1277, Atlanta, GA, USA, 1981.
- [27] D. M. Smith and F. L. Williams, “Diffusion models for gas production from coals,” *Fuel*, vol. 63, no. 2, pp. 251–255, 1984.
- [28] State Administration of Work Safety of China, *Prevention and control of coal and gas outburst*, 2009.
- [29] W. P. Diamond, S. J. Schatzel, F. Garcia, and J. P. Ulery, *The modified direct method: a solution for obtaining accurate coal desorption measurements*, pp. 331–342, 2001.
- [30] Q. Wei, X. Li, B. Hu et al., “Reservoir characteristics and coalbed methane resource evaluation of deep-buried coals: a case study of the No.13-1 coal seam from the Panji Deep Area in Huainan Coalfield, Southern North China,” *Journal of Petroleum Science and Engineering*, vol. 179, pp. 867–884, 2019.

Research Article

Study on Statistical Damage Theory Model of Tailings in a Metal Ore under the Action of Moisture Absorption and Dehumidification Circulation

Bing Cao,¹ Hua Wei,² Mei-Qi Dou,³ Lin Hu,³ and Yao-hui Guo³ 

¹Department of Agriculture and Forestry Engineering, Tangshan Vocational and Technical College, Tangshan, 063000 Hebei, China

²School of Geography and Tourism, Baoding University, Baoding 071000, China

³School of Resource & Environment and Safety Engineering, University of South China, 421001 Hengyang, China

Correspondence should be addressed to Yao-hui Guo; 2698068623@qq.com

Received 23 August 2020; Revised 13 September 2020; Accepted 25 September 2020; Published 15 October 2020

Academic Editor: Zhengyang Song

Copyright © 2020 Bing Cao et al. This is an open access article distributed under the Creative Commons Attribution License, which permits unrestricted use, distribution, and reproduction in any medium, provided the original work is properly cited.

In order to explore the variation law of mechanical properties of tailing sand of a metal ore in Hunan Province under the action of moisture absorption and dehumidification circulation, based on the indoor triaxial test results of tailing sand, this paper introduces the statistical damage theory, combined with the physical and mechanical properties of tailing sand, and studies the elastic-plastic mechanical properties of tailing sand on the basis of the Lemaitre strain equivalent theory. Giving full consideration of the change of tailing sand's pore and volume in the deformation process, an improved statistical damage constitutive model is proposed; it can reflect that the residual strength of tailings after the peak value still has bearing capacity under the action of dry wet circulation. Compared with the results of indoor triaxial consolidation undrained test, this constitutive model is more reliable.

1. Introduction

Mineral resources are the material basis for human survival. Many scholars at home and abroad have done a lot of research on mining methods of mineral resources [1, 2]. According to the important premise of China's economic development, the development of mineral resources is gradually increasing, which will produce a large number of tailing waste. Most of the treatment methods of tailing waste are to store them in the open-air tailing pond. In the open-air environment, tailings are often exposed to wind, sunlight, rain, and snow and are in repeated moisture absorption and dehumidification state. When tailings are in this environment for a long time, its internal structure and mechanical properties will change irreversibly, and the degree of mechanical characteristic change gradually increases with the increase of the number of moisture absorption and dehumidification circulations [3].

In 1958, the Soviet plastic mechanics expert Kachanov [4, 5] proposed the concept of "effective stress factor." On this basis, in 1963, the Soviet expert Rabotnov [6, 7] pro-

posed the concept of "damage factor." Later, after unremitting efforts of more and more scholars, in 1977, Lemaitre [8], Chaboche [9], and others used the continuous medium method, according to the irreversible thermodynamic principles, and established the subject of damage mechanics. Based on that, foreign scholars Frantziskonis and Desai [10] proposed that the damaged material can be abstracted into two parts: damaged and undamaged. Xia et al. [11] proposed the expression of microunit strength of soil structure contact surface based on the Mohr-Coulomb yield criterion under plane strain condition and established a statistical damage softening constitutive model of soil structure contact surface on the basis of assuming that the microunit strength obeys Weibull distribution. Based on the Mohr criterion and combined with the theory of damage mechanics, Jiang et al. [12] established a damage constitutive model of rock under triaxial compression; compared with the experimental results, it was found that the simulation of stress-strain relationship curve achieved good effect. Yin et al. [13] adopted the Lade-Duncan and Drucker-Prager criteria to measure

TABLE 1: Tailing particle group.

Effective diameter d_{10}/mm	Median size d_{30}/mm	Particle composition parameters		
		Constrained size d_{60}/mm	Coefficient of nonuniformity C_u	Coefficient of curvature C_c
0.0780	0.1620	0.2000	2.5320	1.6610

the microunit strength of rock and established a statistical damage constitutive model of rock and modified the model. Cao and Zhang [14] discussed the influence of Weibull distribution parameters on the statistical constitutive model of rock damage based on the Mohr-Coulomb criterion and modified the model in combination with the characteristics of triaxial stress-strain curve. Shen [15, 16] optimized the original elastic-plastic damage model, proposed a nonlinear mechanical damage model, and conducted research and analysis for structural clay, which proved that by the new nonlinear damage model the turning point of compression curve and the peak point of shear curve can be automatically calculated; thus, it will be more simple and have more application prospects. Cheng et al. [17] studied the damage problem of rock caused by internal water migration in freeze-thaw environment, and finally, the stress distribution and migration path of pores were concluded. Yuan et al. [18] established a damage constitutive model of rock with correction coefficient by introducing the correction coefficient.

Based on the indoor triaxial test results, fully considering the changes of porosity and volume of tailing sand in the deformation process, according to the physical properties of tailings, the damage mechanics principle and Lemaitre strain equivalent theory are introduced, the microunit strength measurement method is established, and the damage model of tailing sample considering the dry wet circulation is proposed. It provides a new idea to explore the mechanical properties of tailing sand under the action of dry wet circulation.

2. Test Overview

The tailings used in this test were taken from a lead-zinc tailing pond in Hunan Province. After several surveys, the sampling point and sampling location are finally determined. The tailings taken from the site are dried. The particle size distribution obtained by screening method is shown in Table 1. It shows that the tailings are poorly graded in Table 1. The specimen used in the triaxial test is a cylinder with a diameter of 39.1 mm and a height of 80 mm. The sample preparation is carried out with the triaxial sample preparation device self-made from acrylic tube. The sample is compacted in four layers, and the intact sample is shown in Figure 1. The moisture absorption process is simulated by adding water manually, and the dehumidification process is realized by drying in an oven. The moisture content changes in the range of 1%-23% [3].

The fully automatic strain controlled triaxial apparatus developed and designed by Nanjing TKA Technology Co. Ltd. is used in the test, as shown in Figure 2. The equipment loading system is controlled by Windows computer. There



FIGURE 1: Complete preparation sample.



FIGURE 2: Fully automatic strain controlled triaxial apparatus.

are many test types, and the operator can choose according to the test content and then input the corresponding test parameters, such as test rate and confining pressure. The equipment is mainly composed of main engine loading frame, advanced pressure volume controller, and data acquisition instrument. All the data in the test are collected by the computer and stored automatically after the test.

3. Indoor Test Results and Analysis

It can be seen from Figure 3 that the peak strength of tailing sand decreases gradually with the increase of the number of moisture absorption and dehumidification circulations. From the downward trend in the figure, the peak strength decreases greatly from the zero cycle to the third cycle. The peak strength of the sample is 389 kPa when the sample does not undergo the moisture absorption and dehumidification cycle; the peak strength decreases to 340 kPa after three cycles and 322 kPa after six cycles. This may be due to the fact that when the number of moisture absorption and dehumidification cycles is small, some channels are formed in the process of moisture absorption and dehumidification, and the peak strength decreases greatly. When the number of cycles is large, the change of these channels tends to be stable. Therefore, the decrease of peak strength is gentle after three to six cycles.

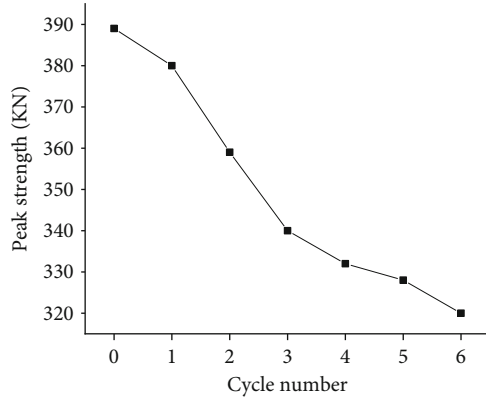


FIGURE 3: Peak strength of tailing sand under different numbers of moisture absorption and dehumidification cycles.

4. Preliminary Establishment of Tailing Sand Damage Model

According to the principle of damage mechanics, the stress-strain curve of tailings can be divided into five stages, as shown in Figure 4. The first stage is O-A compaction stage. In this stage, fine particles in tailings are gradually pressed into the pores between coarse particles due to external load. The second stage is A-B elastic deformation stage. In this stage, with the increase of axial strain, the stress of tailing sample presents a linear growth trend. The third stage is B-C plastic deformation stage. In this stage, the B-point tailing sample reaches the yield condition, and the stress increment gradually decreases with the increase of strain. The original arrangement and structure of particles in the tailing sample will change, and the pores will gradually derive. The fourth stage is the initial stage of C-D damage. The connection between internal particles of the sample weakens, even gradually breaks, and the particles begin to slide. It can be thought that the tailing sample has been completely damaged at this time. The fifth stage is the D-G post damage stage. In this stage, the tailing pattern has been completely damaged. With the increase of axial strain, some tailing particles are broken and the sliding increases. The stress of the sample gradually decreases with the increase of axial strain, showing the phenomenon of strain softening, finally tending to stable and reaching its residual strength.

In order to reflect the whole process of stress-strain deformation of tailings, based on the above five stages of stress-strain deformation of tailings, the constitutive model of stress-strain deformation process of tailings is studied and discussed.

Tailing is different from natural soil. As the broken geotechnical material after beneficiation, its particle shape is irregular and its particle hardness is relatively higher than other soil mass. After the circulation action of moisture absorption and dehumidification, the mechanical properties of tailings will change greatly. Therefore, referring to many research results, a damage model more suitable for tailings is established. Finally, the following assumptions are put forward:

- (1) A large number of pores and microcracks will be generated in the tailings after the circulation action of moisture absorption and dehumidification
- (2) It is assumed that the tailing sample after the circulation action of moisture absorption and dehumidification is composed of three parts: the damaged part, the undamaged part, and the pore. The total area is A , and the corresponding areas of each part are A_1 , A_2 , and A_3
- (3) Because the damage location in the tailing sample is random, there is no damage crack in an isolated area, so the strain in each part of tailings can be regarded as equal
- (4) Assuming that the stress of the tailings sample is σ_i , the stress of the damaged part is σ_i^s , then the undamaged part is σ_i^r , and the pore is unable to bear the function, so its stress is zero

According to the above, the model was established as

$$\sigma_i A = \sigma_i^s A_1 + \sigma_i^r A_2, \quad (1)$$

$$A = A_1 + A_2 + A_3, \quad (2)$$

$$A_3 = nA, \quad (3)$$

where n represents porosity.

For the selection of damage variable, according to the definition, $D = A_2 / (A_1 + A_2)$, and then, according to equations (1), (2) and (3), the following results can be obtained:

$$\sigma_i = (1 - n)[\sigma_i^r (1 - D) + \sigma_i^s D]. \quad (4)$$

Equation (4) is the tailing damage model established in this paper. A large number of research results show that the plastic deformation of geotechnical materials is accompanied by damage, and the greater the damage variable D , the greater the plastic deformation of geotechnical materials. The analysis shows that when the tailings are completely damaged, i.e., $D = 1$, equation (4) can be written as $\sigma = \sigma_i^s (1 - n)$, and the residual strength after complete damage of tailings is σ_i^s . According to the stress-strain curve of tailing samples, the value will not change when the tailing stress reaches the residual stress.

5. Establishment of Damage Constitutive Relation of Tailing Sand

Hereby, σ_i^r and σ_i^s are the stress values on the micro level, and n is the physical quantity gradually changing with the deformation of tailing sample, which cannot be directly measured by test. Therefore, it needs to be expressed by the quantity that can be measured under macro conditions.

A large number of studies have proved that the stress-strain relationship obeys the generalized Hooke's law when there is no damage and failure of geotechnical materials. So there are

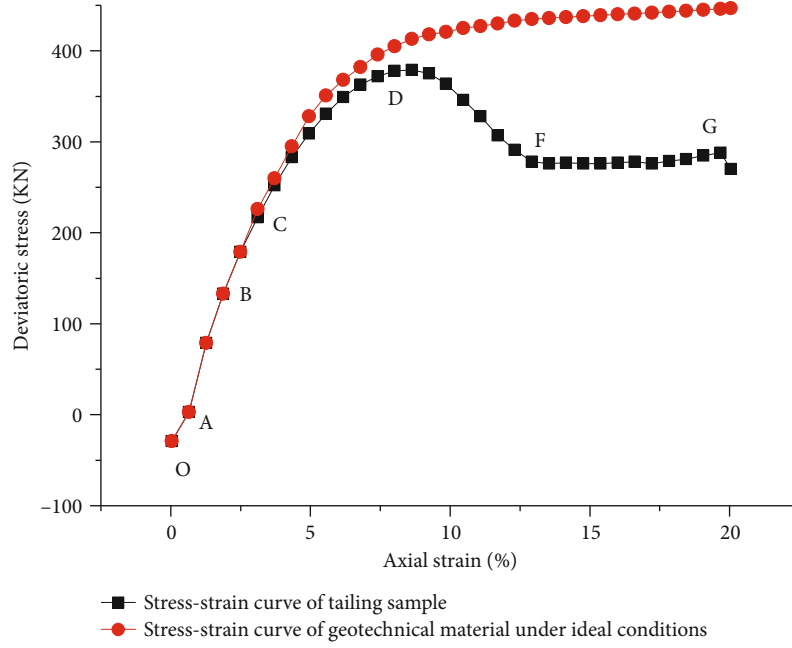


FIGURE 4: Stress-strain curve of tailings under confining pressure of 100 kPa.

$$\sigma'_1 = E' \varepsilon'_1 + \mu' (\sigma'_2 + \sigma'_3) \sigma'_1 = E' \varepsilon'_1 + \mu' (\sigma'_2 + \sigma'_3), \quad (5)$$

where E' is the elastic modulus when there is no damage and μ' is Poisson's ratio when there is no damage.

For the tailing sand, the relationship between the elastic modulus, Poisson's ratio, and the value of tailing samples without damage is as follows:

$$\begin{aligned} E &= (1-n)E' \\ \mu &= \mu'. \end{aligned} \quad (6)$$

According to reference [19], the following results can be obtained:

$$n = 1 - \frac{(1-n_0)(1-D) + P_{23}\sigma_3}{P_{24}\varepsilon_1 + 1 + (-P_{24}\varepsilon_1 + (P_{21}/\varepsilon_1) - P_{22} - 1)D}, \quad (7)$$

where

$$P_{21} = P_{23}P_{25}, \quad (8)$$

$$P_{22} = P_{23}P_{26}, \quad (9)$$

$$P_{23} = \frac{2(1-\mu-2\mu^2)}{E'}, \quad (10)$$

$$P_{24} = 2\mu - 1, \quad (11)$$

$$P_{25} = \frac{(1+\mu)\sigma_c^2 \cot \varphi}{[3(1+\tan \alpha)E']}, \quad (12)$$

$$P_{26} = \frac{c(\cot \varphi + 2 \sin \alpha)}{[\sin \alpha(1 + \tan \alpha)]}. \quad (13)$$

The values of c and φ here are the cohesion and internal friction angle of tailing samples at yield.

Considering that the damaged part and the undamaged part are a whole and the damaged part is completely random, so

$$\varepsilon_i = \varepsilon'_i = \varepsilon'_i, \quad (14)$$

where ε_i , ε'_i , ε''_i ($i=1, 2, 3$) refer to the macroscopic strain of tailing sample and the undamaged part, as well as the micro strain value of the damaged part.

The purpose of this paper is to investigate the damage process of tailings under triaxial loading, so $\sigma_2 = \sigma_3$. Substituting equation (13) into (5), the following results can be obtained:

$$\sigma'_1 = E' \varepsilon_1 + 2\mu' \sigma'_3, \quad (15)$$

$$\sigma'_3 = E' \varepsilon_3 + \mu' (\sigma'_1 + \sigma'_2). \quad (16)$$

For the volume strain of tailings after loading, there is

$$V_1 = (1 + \varepsilon_1)(1 + \varepsilon_2)(1 + \varepsilon_3) dx dy dz. \quad (17)$$

By simplifying the above formula, the following results can be obtained:

$$\varepsilon_V = \varepsilon_1 + \varepsilon_2 + \varepsilon_3. \quad (18)$$

According to the relation equation of porosity in reference [15], the following results can be obtained:

$$n = \frac{(n_0 - \varepsilon_V)}{(1 - \varepsilon_V)}. \quad (19)$$

Substituting equation (17) into (18), together with $\varepsilon_2 = \varepsilon_3$, the relational expression of ε_1 and ε_3 can be obtained:

$$\frac{n - n_0}{n - 1} = \varepsilon_1 + 2\varepsilon_3. \quad (20)$$

By simplifying the above formula, the following results can be obtained:

$$\varepsilon_1 = \frac{n - n_0}{n - 1} - 2\varepsilon_3. \quad (21)$$

By equations (14) and (15), there is

$$\sigma'_3 = \frac{E'}{1 - 2\mu'^2 - \mu'} \varepsilon_3 + \frac{E\mu'}{1 - 2\mu'^2 - \mu'} \varepsilon_1, \quad (22)$$

$$\sigma'_1 = \frac{E'(1 - \mu')}{1 - 2\mu'^2 - \mu'} \varepsilon_1 + \frac{2\mu'E'}{1 - 2\mu'^2 - \mu'} \varepsilon_3. \quad (23)$$

For the determination of the yield surface of tailings, firstly, the yield condition reaches the stress condition when the tailing sample initially reaches the plastic state. According to a large number of experiments, this paper selects M-C strength criterion as the yield criterion of tailings.

$$\sigma_1^s = \frac{(1 + \sin \varphi_s)\sigma_3^s + 2c_s \cos \varphi_s}{1 - \sin \varphi_s}. \quad (24)$$

The values of c_s and φ_s here are the cohesion and internal friction angle of residual stress after tailing samples are damaged.

Substituting equation (23) into (4), the following results can be obtained:

$$\sigma_3 = (1 - n) \left[\sigma'_3(1 - D) + \sigma_3^s D \right]. \quad (25)$$

By simplifying the above formula, the following results can be obtained:

$$\sigma_3^s = \frac{1}{(1 - n)D} \sigma_3 - \frac{1 - D}{D} \sigma'_3. \quad (26)$$

Substituting equation (21) into (25) and then into (23), the following results can be obtained:

$$\sigma_1^s = \frac{M}{(1 - n)D} \sigma_3 - MNP\varepsilon_3 - \mu' MNP\varepsilon_1 + Q, \quad (27)$$

where

$$M = \frac{1 + \sin \varphi_s}{1 - \sin \varphi_s}, \quad (28)$$

$$N = \frac{E'}{1 - 2\mu'^2 - \mu'}, \quad (29)$$

$$P = \frac{1 - D}{D}, \quad (30)$$

$$Q = \frac{2c_s \cos \varphi_s}{1 - \sin \varphi_s}. \quad (31)$$

Substituting equations (22) and (26) into (4), the following results can be obtained:

$$\sigma_1 = (1 - n)(1 - D)N \left[\left(1 - \frac{2\mu'}{1 - \sin \varphi_s} \right) \varepsilon_1 + (2\mu' - M) \varepsilon_3 \right] + M\sigma_3 + (1 - n)QD. \quad (32)$$

Equation (32) is the damage model of tailings established in this paper.

The key to establish the evolution model of tailings by using statistical damage theory is to determine the microunit strength of tailings. Cao et al. [20] established a measurement method of rock microunit strength on the basis of the Drucker-Prager material yield criterion. This method can comprehensively reflect the influence of stress state on microunit strength, but the disadvantage is that it cannot reflect the influence of damage threshold on damage measurement. Therefore, this paper uses the relevant methods proposed in reference [21]; thus, the measurement method of microunit strength of tailings can be obtained:

$$F = \sigma'_1 - \frac{1 + \sin \varphi}{1 - \sin \varphi} \sigma'_3 - \frac{2c_s \cos \varphi}{1 - \sin \varphi}. \quad (33)$$

By simplifying the above formula, the following results can be obtained:

$$F = \sigma'_1 - M\sigma'_3 - Q. \quad (34)$$

Substituting equations (21) and (22) into (34), the following results can be obtained:

$$F = N \left[(1 - \mu' - M\mu') \varepsilon_1 + (2\mu' - M) \varepsilon_3 \right] - Q. \quad (35)$$

Equation (35) is the microunit strength measurement method established in this chapter. Based on the idea of references [12, 21], assuming that the microunit strength of tailings conforms to Weibull distribution, the statistical evolution model of tailing damage can be obtained as

$$D = \begin{cases} 1 - \exp \left[- \left(\frac{F}{F_0} \right)^m \right], & F \geq 0, \\ 0, & F < 0, \end{cases} \quad (36)$$

where m and F_0 are Weibull distribution parameters of tailing microunit strength. The model also reflects the influence of damage threshold on the evolution of the model. Only when the threshold is exceeded, the tailings will be damaged.

Substituting equation (35) into (32), the damage constitutive model of tailings in triaxial test can be obtained.

For the two model parameters m and F_0 , the determination of their values is the key to the establishment of the tailing constitutive model. Therefore, in this chapter, the stress and strain values corresponding to the peak points of the stress-strain curve of tailings under different confining pressures are set as σ_{ss} and ε_{ss} ; then, equation (31) can be derived as

$$\left. \frac{d\sigma_1}{d\varepsilon_1} \right|_{\sigma_1=\sigma_{ss}, \varepsilon_1=\varepsilon_{ss}} = 0. \quad (37)$$

Equations (36) and (26) are combined and solved to get the following results:

$$m = -\frac{K_1^{ss} F_{ss}}{L_1 K_2^{ss} (1 - D_{ss}) \ln(1 - D_{ss})}, \quad (38)$$

$$F_0 = \frac{F_{ss}}{[-\ln(1 - D_{ss})]^{1/m}}, \quad (39)$$

where

$$\begin{aligned} K_1^{ss} &= -\mu' N (1 - D_{ss}), \\ F_{ss} &= L_1 \varepsilon_{ss} - k_0, \\ K_2^{ss} &= Q + 3 \left(\mu' - \frac{1}{2} \right) N \varepsilon_{ss}, \\ D_{ss} &= \frac{\sigma_{ss} - (1 - 2\mu' N) \varepsilon_{ss} - M \sigma_3}{Q + (1 - 2\mu' N) \varepsilon_{ss}}. \end{aligned} \quad (40)$$

The parameters m and F_0 of the statistical damage constitutive model of tailings can be determined by equations (37) and (38). However, σ_{ss} and ε_{ss} represent only the stress and strain values corresponding to the peak value under a certain confining pressure, so in order to establish the damage constitutive model of tailings under different confining pressures, it is necessary to determine the calculation method of σ_{ss} and ε_{ss} . Thus, the method of reference [20] is used hereby to calculate σ_{ss} and ε_{ss} by the following formula:

$$\begin{aligned} \sigma_{ss} &= \frac{2c_f \cos \varphi_f + (1 + \sin \varphi_f) \sigma_3}{1 - \sin \varphi_f}, \\ \varepsilon_{ss} &= b + a \sigma_3, \end{aligned} \quad (41)$$

where a, b are constants and φ_f and c_f are the internal friction angle and cohesion corresponding to the peak stress of tailings.

6. Model Validation

After the indoor consolidated undrained triaxial test of tailing samples was done, according to the stress-strain curve, the relevant mechanical parameters are $E = 78.46$ and $\mu = 0.258$ and the internal friction angle and cohesion at the peak

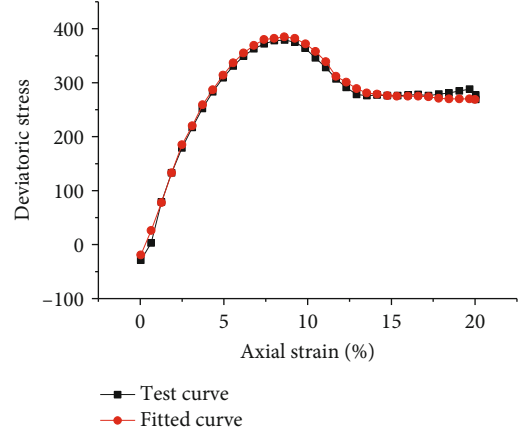


FIGURE 5: Comparison of theoretical and experimental curves.

point are 39.1° and 25.5 kPa. The internal friction angle and cohesion at yield are 24.72° and 25.5 kPa. The cohesion and internal friction angle of residual stress are 36.67 kPa and 15.95° , respectively. By substituting these parameters into the damage constitutive model of tailings established before, the stress-strain theoretical curve under this condition can be obtained, which is compared with the previous test curve, as shown in Figure 5. The fitting curve of damage constitutive model is in good agreement with the stress-strain curve of indoor tailing samples.

7. Conclusion

Based on the indoor triaxial consolidation undrained test results of tailing sand, the internal structure changes of tailing sand after repeated moisture absorption and dehumidification cycles are studied, and the statistical damage model is established in accordance with the statistical damage theory.

On the basis of the Lemaitre strain equivalent theory and considering the influence of pore and volume change on tailings in shear test, a statistical damage constitutive model which can reflect the stress-strain process of tailings is established. The model can reflect the characteristics of bearing capacity of tailings after damage.

In this paper, the principle of damage mechanics is introduced. According to the stress-strain curve obtained from the triaxial shear test of tailings, the loading deformation process of tailings can be divided into (1) elastic deformation stage, (2) plastic deformation stage, (3) gradual damage stage, and (4) post damage stage.

The model established in this paper can reflect the volume deformation process of tailings after triaxial test, with good fit. Fewer parameters are required, which is conducive to engineering application.

Data Availability

The data that support the findings of this study are available from the corresponding author upon reasonable request.

Conflicts of Interest

The authors declare no conflicts of interest.

Acknowledgments

This study was supported by the Graduate Scientific Research Innovation Project (CX20200919). Thanks are due to Hengyang City Province Engineering Technology Research Center for Disaster Prediction and Control on Mining Geotechnical Engineering for providing experimental platform support.

References

- [1] Z. Song and H. Konietzky, "A particle-based numerical investigation on longwall top coal caving mining," *Arabian Journal of Geosciences*, vol. 12, no. 18, p. 556, 2019.
- [2] Z. Song, H. Konietzky, and M. Herbst, "Drawing mechanism of fractured top coal in longwall top coal caving," *International Journal of Rock Mechanics and Mining Sciences*, vol. 130, article 104329, 2020.
- [3] Y. H. Guo, Y. K. Tian, L. L. Wu et al., "Mechanical properties of tailings under different confining pressures under dry and wet cycling," *Nonferrous Metal Engineering*, vol. 10, no. 4, pp. 87–93, 2020.
- [4] L. M. Kachanov, "Rupture time under creep conditions," *International Journal of Fracture*, vol. 97, no. 1/4, pp. 11–18, 1999.
- [5] L. M. Kachanov and D. Krajcinovic, "Introduction to continuum damage mechanics," *Journal of Applied Mechanics*, vol. 54, no. 2, p. 481, 1987.
- [6] Y. N. Rabotnov, "On the equation of state of creep," *Various Titles labelled Volumes A to S*, vol. 178, no. 31, pp. 117–122, 1963.
- [7] Y. N. Rabotnov, "Progress in applied mechanics," *Mechanics of Surface Structures*, vol. 6, 1987.
- [8] J. Lemaitre, "How to use damage mechanics," *Nuclear Engineering & Design*, vol. 80, no. 2, pp. 233–245, 1984.
- [9] J. L. Chaboche, "Continuous damage mechanics — a tool to describe phenomena before crack initiation," *Nuclear Engineering and Design*, vol. 64, no. 2, pp. 233–247, 1981.
- [10] G. N. Frantziskonis and C. S. Desai, "Analysis of a strain softening constitutive model," *Mathematical & Computer Modelling*, vol. 10, no. 10, p. 795, 1987.
- [11] C. H. Xia, G. Q. Zhou, and X. Y. Shang, "Softening constitutive model of soil-structure contact surface based on Weibull distribution," *Journal of China University of Mining and Technology*, vol. 36, no. 6, pp. 734–747, 2007.
- [12] W. Jiang, J. Deng, and Q. C. Si, "Constitutive model of rock damage and its modification based on Mohr criterion," *Journal of Hebei University of Engineering (Natural Science Edition)*, vol. 27, no. 2, pp. 30–37, 2010.
- [13] J. Yin, G. C. Jiang, and N. L. Hu, "Comparison and correction of constitutive models of rock statistical damage based on different criteria," *Mining Research and Development*, vol. 35, no. 12, pp. 101–105, 2015.
- [14] W. G. Cao and S. Zhang, "Study on statistical analysis method of rock damage based on Mohr-Coulomb criterion," *Journal of Hunan University (Natural Science Edition)*, vol. 32, no. 1, pp. 43–47, 2005.
- [15] Z. J. Shen, "Nonlinear damage mechanics model of structural clay," *Water Conservancy and Water Transport Science Research*, no. 3, pp. 247–255, 1993.
- [16] Z. J. Shen, "Elastic-plastic damage model of structural clay," *Journal of Geotechnical Engineering*, vol. 15, no. 3, pp. 21–28, 1993.
- [17] H. Cheng, H. Q. Chen, G. Y. Cao, C. X. Rong, Z. S. Yao, and H. B. Cai, "Damage mechanism and experimental verification of freezing-thawing water transfer in porous rocks," *Journal of Rock Mechanics and Engineering*, vol. 39, pp. 1–11, 2020.
- [18] C. Yuan, H. M. Zhang, X. Z. Meng, G. S. Yang, and L. Y. Wu, "Study on constitutive relation of rock based on correction coefficient," *Coal Science and Technology*, vol. 47, no. 9, pp. 177–182, 2019.
- [19] W. G. Cao, H. Zhao, Y. J. Zhang, and L. Zhang, "Constitutive model and parameter determination method of rock strain soft hardening damage considering volume change," *Rock and Soil Mechanics*, vol. 32, no. 3, pp. 647–654, 2011.
- [20] W. G. Cao, X. Li, and F. Liu, "Study on constitutive model of strain softening damage in fractured rock mass," *Journal of Rock Mechanics and Engineering*, vol. 12, pp. 2488–2494, 2007.
- [21] W. G. Cao, H. Zhao, L. Zhang, and Y. J. Zhang, "Statistical softening constitutive model of rock damage considering the influence of damage threshold and its parameter determination method," *Journal of Rock Mechanics and Engineering*, vol. 27, no. 6, pp. 1148–1154, 2008.

Research Article

Prediction and Analysis of Abnormal Gas Emission Law in Low-Gas Tunnel Based on K-Line Diagram

Haiyang Wang ^{1,2}, Shulei Zhao,² Jialiang Liu,^{1,2} Yanmin Zhou,² Xiang Chen,² Jie Wang,² and Liang Cheng ^{3,4}

¹State Key Laboratory Breeding Base of Mountain Bridge and Tunnel Engineering, Chongqing Jiaotong University, Chongqing 400074, China

²School of Civil Engineering, Chongqing Jiaotong University, Chongqing 400074, China

³China Merchants Chongqing Communications Technology Research & Design Institute Co., Ltd., Chongqing 400067, China

⁴State Key Laboratory of Coal Mine Disaster Dynamics and Control, Chongqing University, Chongqing 400044, China

Correspondence should be addressed to Liang Cheng; chengliang@cqu.edu.cn

Received 28 August 2020; Accepted 21 September 2020; Published 10 October 2020

Academic Editor: Bin-Wei Xia

Copyright © 2020 Haiyang Wang et al. This is an open access article distributed under the Creative Commons Attribution License, which permits unrestricted use, distribution, and reproduction in any medium, provided the original work is properly cited.

The risk of gas disaster in the low-gas tunnel is easy to be ignored. By tracking and analyzing the gas monitoring data of the low-gas tunnel, it is found that the cyclic abnormal gas emission occurred many times during the construction period, leading to local gas accumulation, which greatly increases the risk of gas explosion accidents. To scientifically predict the abnormal gas emission in low-gas tunnels, the idea of K-line diagram-based prediction of abnormal gas emission in low-gas tunnels is put forward, and in combination with the field monitoring data of low-gas tunnel (Huanguashan Tunnel), the prediction results with different prediction indexes of K-line diagram are compared and analyzed. The results show that the K-line diagram can reflect the changing trend of gas concentration in real time accurately and show the change law of gas concentration during different construction processes; the moving average (MA) of the K-line diagram can accurately reflect the time of abnormal gas emission, the moving average convergence divergence (MACD) index can reflect the upward or downward power and trend of gas, and the Bollinger Band (BOLL) index can reflect the fluctuation range of gas concentration. The research results can provide a reference for the prediction and prevention of abnormal gas emission in low-gas tunnels.

1. Introduction

Gas is one of the important disaster factors of gas tunnels. The gas emission quantity and gas content of exposed coal seam in low-gas tunnels are low, which leads to the risk of gas disaster easily underestimated during the construction period. In case of abnormal gas emission during low-gas tunnel construction, local gas overrun and accumulation will easily occur, which will greatly increase the risk of gas explosions and other disasters, and seriously threaten the safety of tunnel construction [1–3]. There are frequent reports of gas accidents in low-gas tunnels. On February 24, 2015, gas explosions occurred in No.1 low-gas tunnel in Luodai Ancient Town, Chengdu, China, due to abnormal gas emission, resulting in 2 deaths and 22 injuries [4]. Scientific pre-

dition of abnormal gas emission in low-gas tunnels can provide important early-warning information for gas disaster prevention and control and then help to take targeted measures to intervene and reduce the probability of gas explosion and other disaster accidents. However, the changes in the occurrence characteristics, gas content, gas pressure, geological structure, and other factors of the tunnel-exposed coal seam have a complex nonlinear effect on gas emission, which brings great difficulties to the prediction of abnormal gas emission [5–8]. In the 1980s, Russian scholars proposed for the first time that gas emission should be predicted during coal mining; Greedy [9], a British scholar, initiated the Airey method to predict the gas emission in coal mines based on time and mining technology; Dong [10] proposed gas emission time series method and used it as the regression function

to establish the Gaussian process regression model, the prediction results of which are accurate and reliable; Liang et al. [11] proposed that, under the condition of considering gas emission source and fluid-solid coupling process, it would be more accurate to predict coal mine gas emission by establishing a dynamic gas prediction model; Booth et al. [12] believe that the limitations of existing gas emission prediction can be solved by the prediction results obtained from improved spatial data sets and the technology including basic physics and energy-related principles. The above research methods are often used to predict the gas emission in coal mines, but there are little research on abnormal gas emission in gas tunnels.

The change in tunnel gas concentration is characterized by fluctuation variability, continuity, and real time [13]. The K-line diagram based on time series can not only weaken the influence of objective factors such as geological conditions and external disturbances but also scientifically and reasonably analyze the gas monitoring information and identify the hidden gas disaster characteristics. More and more researchers have recognized the advantages of the K-line diagram in massive data processing, derivation of related indexes, clear and intuitive trend laws, etc. The introduction of the K-line diagram analysis method into tunnel gas data analysis allows us to analyze and study the changing trend of gas concentration from different angles, which is helpful to the study of gas emission law. Therefore, this paper puts forward the idea of the K-line diagram-based prediction of abnormal gas emission in low-gas tunnels and forecasts and analyzes the gas emission in low-gas tunnels, to reduce the possibility of gas disasters.

2. Introduction and Characteristic Analysis of K-Line Diagram

2.1. Introduction of K-Line Diagram. K-line diagram, also known as the candlestick chart, can be traced back to the era of the Tokugawa Shogunate in the 18th century in Japan [14, 15]. It is three dimensional and intuitive with a unique method covering comprehensive records and containing large information content, which is widely used in stock, futures, foreign exchange, options, and other securities markets. Like the stock market, the change of tunnel gas concentration is also affected by many factors under the internal and external complex environments. Therefore, it is a promising means to introduce the K-line diagram method into the cause diagnosis and early-warning analysis of tunnel gas anomaly and to make use of its advantages in processing and analyzing data. By analyzing the theoretical basis of K-line and the meaning of K-line shapes for tunnel gas monitoring and extending them to the characterization method of gas anomaly patterns [16], it can provide a new research idea for the field of gas data monitoring and early warning.

The traditional K-line diagram usually revolves around four data of the K-line—the opening, the highest, the lowest, and the cut-off prices—thus reflecting the trend and price of stocks. When it is applied to gas early warning, a single K-line diagram can reflect the changing trend of gas emission concentration in a unit time. When combined with other techni-

cal indexes, it can also predict the change direction and trend of gas emission intensity in the future. The K-line diagram has different unit times, such as minute K-line, hour K-line, and day K-line. In this paper, the initial gas concentration O , the highest concentration H , the lowest concentration L , and the cut-off concentration C are taken as the four data of the K-line diagram. In the traditional K-line diagram, the red line represents the upward trend of gas concentration in one cycle, and the green line represents the downward trend of gas concentration in one cycle. The specific parameters are shown in Figure 1.

The K-line diagram contains four elements: color, entity size, shadow length, and unit time. Therefore, when it is applied to the time series of tunnel gas concentration, the trend of gas concentration contained in it can be found out; thus, the time point at which the abnormal gas concentration occurs can be captured more accurately. The main function of the K-line diagram is to make a reasonable judgment according to its K-line shape. The process of understanding the K-line diagram is mainly to observe the red line, green line, entity size, and shadow length, taking the red line as an example, as shown in Table 1.

2.2. Common Characteristics of K-Line Diagram and Gas Concentration Change Curve. The change of tunnel gas concentration shares the following common characteristics with the stock market, so the use of the K-line diagram to describe gas concentration change has a theoretical basis.

(1) Fluctuation variability

The essence of K-line is to reflect the fluctuation of commodity value caused by the natural law of market supply and demand and manmade speculation, while the assessment of gas disaster risk is mainly to record and analyze the gas concentration and to properly display the geological conditions and artificial disturbance in the tunnel site area through the change of gas concentration, so the change of gas concentration state also has two influencing factors: objective natural-ity and external factors.

(2) Continuity

Both the market price changes recorded by K-line and the monitoring results by existing gas concentration monitoring equipment are continuous records. Through the existing instruments and equipment, long-time, continuous and uninterrupted data collection can be achieved to provide necessary conditions for judging the change of gas concentration.

(3) Real time

Real-time acquisition of stock market data enables investors to obtain market dynamic changes more quickly. Similarly, the real-time change of gas concentration is very important for assessing the current gas disaster risk and adjusting the construction ventilation scheme. With the development of science and technology, the indicators for assessing the risk of gas disasters have developed from

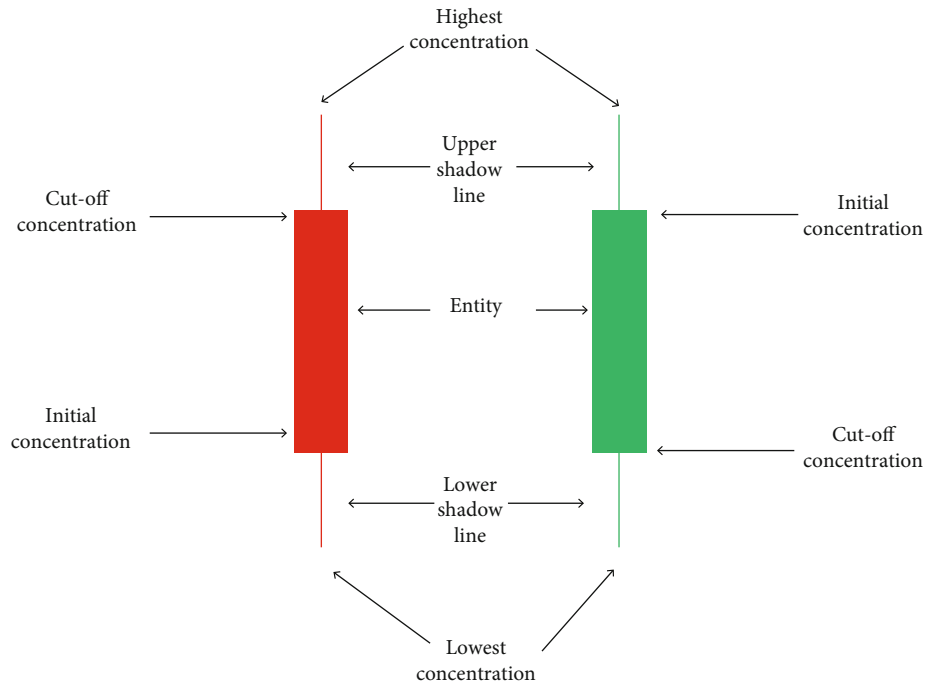


FIGURE 1: Sketch diagram of K-line.

TABLE 1: Graphics of the K-line diagram and their meanings.

Graph					
Name	Short red line	A red entity with long lower shadow	A red entity with upper and lower shadows	A red entity with lower shadow	A red entity with an upper shadow
Meaning	Indicating that the growth trend in the cycle is not obvious, which needs further observation	Indicating that the gas concentration increases in the cycle	Indicating that it will jump, open high, and go low in the next period of the cycle	Indicating that the gas concentration may increase in the cycle	Indicating that the gas concentration in the cycle has a strong growth momentum
Graph					
Name	A red entity without a shadow	Inverted T-line	T-line	Cross	
Meaning	Indicating a strong growth in the next period of the cycle	Indicating that the cycle may be shortened	Indicating that the cycle may expand	Indicating a peak signal or a bottom signal, which indicates that, in the cycle, the trend of the gas concentration interval will change or it will enter a plateau	

subjective judgment and manual acquisition to objective quantitative evaluation of equipment detected physiological indexes, and from the index parameter acquisition in a cer-

tain period to current real-time recording of continuous parameters, which also provides conditions for complete and instant monitoring of gas concentration changes.

3. K-Line Diagram of Low-Gas Tunnel Abnormal Gas Emission

3.1. *Overview of Huangguashan Tunnel.* Huangguashan Tunnel is located in Yongchuan District, Chongqing, which is constructed by the drilling-and-blasting method. It is an extralong tunnel, with a total length of 3268 m. The coal measure stratum that the tunnel passes through is the 5th member of Xujiuhe Formation, which only contains coal locally, and belongs to the extremely thin coal seam. The thickness of the coal seam is unstable, and even pinch out occurs. It is a typical low-gas tunnel. The construction can be divided into the construction processes of drilling and blasting, mucking, frame erecting, and shotcreting. Through long-term tracking of the gas concentration change data of Huangguashan Tunnel, it was found that there was gas continuously emitting into the tunnel in each construction process during the construction. The difference was that the gas concentration emitting into the tunnel is different in different processes. Through the study of the relationship between gas concentration and construction processes, the gas concentration emitting into the tunnel during each construction process can be distinguished. The changes in gas concentration based on the data of gas concentration at the tunnel face in one construction cycle are shown in Table 2 and Figure 2.

From the comparative analysis of Figures 2 and 3, it can be seen that (1) there is an abnormal point of gas concentration higher than the highest point of the box diagram, which indicates that the gas concentration fluctuates greatly and there is abnormal gas emission, and (2) the gas concentration during the construction period is generally maintained between 0.00% and 0.1%, but during the blasting operation, the gas concentration will increase to 5%. So, it can be seen that the blasting operation is the main cause of abnormal gas emission in tunnels.

3.2. *K-Line Diagram of Gas Concentration.* The tunnel gas monitoring system will record the change of gas concentration in real time. If the selection period is too small, the data will be disordered and not intuitive; if the selection period is too large, it cannot timely describe the abnormal gas emission. After a large number of experiments, the period of 10 min is most appropriate. So, in this paper, taking 10 min as a cycle, a K-line of gas concentration in one construction cycle is drawn by using Origin and Excel software jointly and improved, as shown in Figure 4. The traditional K-line diagram has only two colors to express the change in stock price. When it is applied to the change of tunnel gas concentration, it can only express the increase or decrease of gas concentration in different cycles, but it is not accurate enough. For this purpose, this paper innovatively introduces a three-color K-line diagram. The yellow line is the new red line, representing an increase in gas concentration; the green line represents the decrease of gas concentration; when the gas concentration is greater than 0.5%, the K-line diagram of the gas concentration becomes eye-catching red to remind the construction personnel of the gas overrun. At the same time, when the gas concentration of the adjacent K-line dia-

gram changes greatly, the K-line diagram is transformed into the corresponding gradient color. The improved three-color K-line diagram has the following advantages over the traditional K-line diagram:

- (1) The color-gradient line represents abnormal gas emission and is named as “sharply-increasing line.” The moment of abnormal gas emission can be accurately determined by the position of “sharply-increasing line”
- (2) The gas concentration at 0.5% is set as a warning line. When the gas concentration is greater than 0.5%, both the “yellow line” and “green line” turn red, which can express the situation of gas concentration overrun more intuitively

In Figure 4, except for the small fluctuation of gas concentration in the blasting stage, the gas concentration in other stages is consistent with the actual situation in the previous section, indicating that it is feasible to express the change of gas concentration with the K-line diagram.

To express the change of gas concentration more accurately, the concept of “K-line coordinates” is introduced, and the position matching issue between K-lines is solved by defining the coordinates of K-lines in the sequence. The order of K-lines in the K-line sequence is called the K-line abscissa, the increasing degree of the gas cut-off concentration in each cycle relative to that in the previous cycle is called the K-line ordinate, with the ordinate of the first K-line in the K-line sequence set to 1, as shown in Figure 5. By analyzing the increasing degree, the moment that the abnormal gas concentration occurs can be obtained intuitively and clearly, which is consistent with the actual situation.

4. Application of K-Line Diagram Basic Indexes in Prediction of Low-Gas Tunnel Gas Emission Law

It is too one sided to judge the gas emission trend by using the K-line diagram only. The K-line combinatory analysis of gas emission trends by MA, MACD, and BOLL indexes is more reasonable.

4.1. *Moving Average (MA).* Using MA to calculate the arithmetic moving average of the monitored gas concentration value in a cycle and draw it into a line can directly reflect the trend of gas emission. The calculation formula of MA is as follows:

$$MA(X, N) = \frac{X_1 + X_2 + \dots + X_N}{N}, \quad (1)$$

where MA is the moving average, X_i is the end value in the unit time, and N is the calculation cycle.

There is no fixed rule for the choice of long-cycle and short-cycle MAs. The intersection of the long-cycle average and short-cycle average represents the development trend of gas concentration. The short-term average can closely follow the development trend of gas concentration and can

TABLE 2: Gas concentration in different construction processes at the tunnel face.

Construction process	Time (h)	Gas concentration (%)	Construction process	Time (h)	Gas concentration (%)
Drilling and blasting	0	0.02	Frame erecting	8	0.06
	1	0.02		9	0.05
	2	0.47		10	0.04
	3	0.35		11	0.04
	4	0.26		12	0.06
Mucking	5	0.04	Shotcreting	13	0.02
	6	0.02		14	0.01
	7	0.03		15	0.04

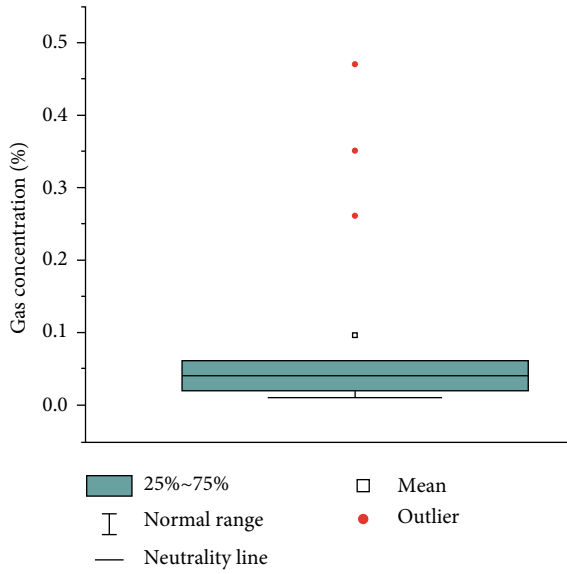


FIGURE 2: Box plot of gas concentration in different construction processes.

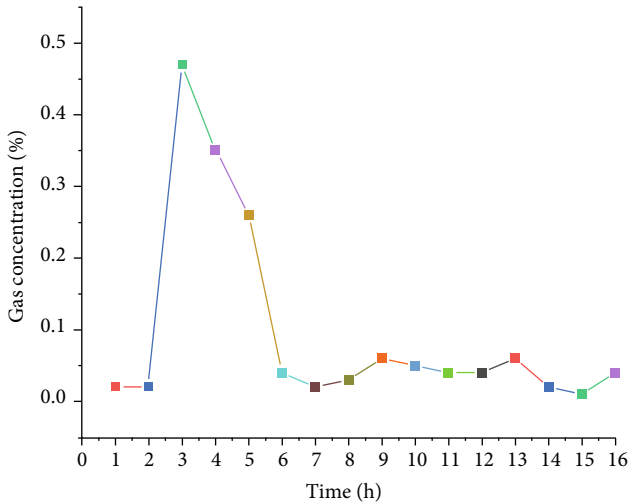


FIGURE 3: Gas concentration over time series.

better represent the gas change in the short term; while the long-term average is less affected by short-term gas concentration fluctuation, which is more stable and can well reflect

the long-term trend. Set the black line and red line in Figure 6 as MAs with the calculation cycles of 0.5 h and 1 h, respectively.

It can be seen from Figure 6 that, when the short-term average (0.5 h) crosses the long-term average (1 h) upwards, this breakthrough point is called “golden cross.” When the “golden cross” appears, the gas concentration shows an upward trend in the short term. When the short-term average falls below the long-term average, the breakthrough point is called “death crossing,” and the gas concentration shows a downward trend in the short term. The MA shows strong regularity during the normal gas fluctuation stage, and MA starts to rise in the blasting stage, then reaches the peak value, and then falls back immediately after the end, which is in line with the actual situation.

There is a lag phenomenon in the MA signal, but the trend can often last for a while. Therefore, when MA sends a signal that the gas emission increases or decreases, although the current gas emission may still be in a stable trend, it still indicates that the next gas emission may change significantly. Therefore, timely gas prevention measures can be taken according to the signal at this time. Moving average is used in the calculation of the next two types of indexes.

4.2. Moving Average Convergence Divergence (MACD) Index. Moving average convergence divergence index is referred to as the MACD index for short, which is aimed at revealing the changes in the intensity, direction, momentum, and duration of the gas trend, and has a certain guiding role in preventing gas concentration overrun. MACD index is a collection of three time series calculated from historical data, which are MACD series itself, “average” series, and “divergence” series. MACD series is the DIF of the fast MA (EMA1) and slow MA (EMA2) and the difference (DIF) between EMA1 and EMA2. The average series is composed of N -cycle moving average convergence divergence (DEA) of DIF. Divergence is the difference between the MACD series and the “average” series, which is usually displayed as a bar graph, and its length is twice that of DIF-DEA. Therefore, the MACD index includes two lines and one stick; the fast line is DIF, and the slow line is DEA, as shown in Figure 7.

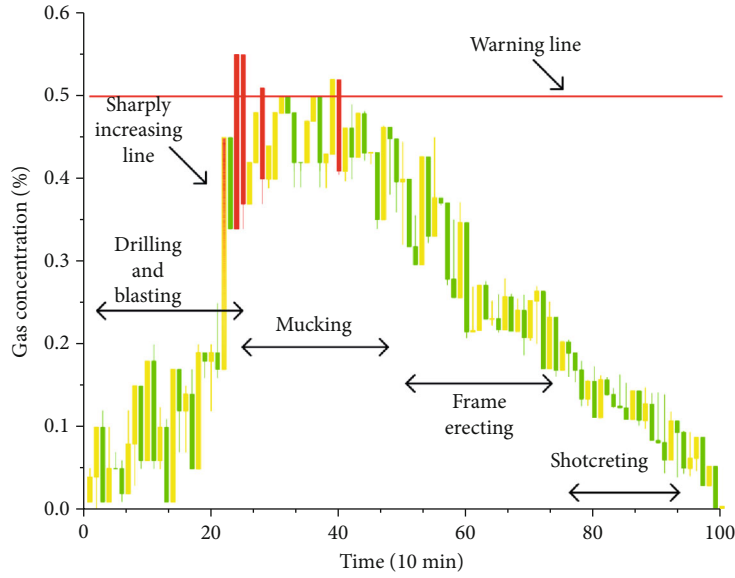


FIGURE 4: K-line diagram of gas concentration.

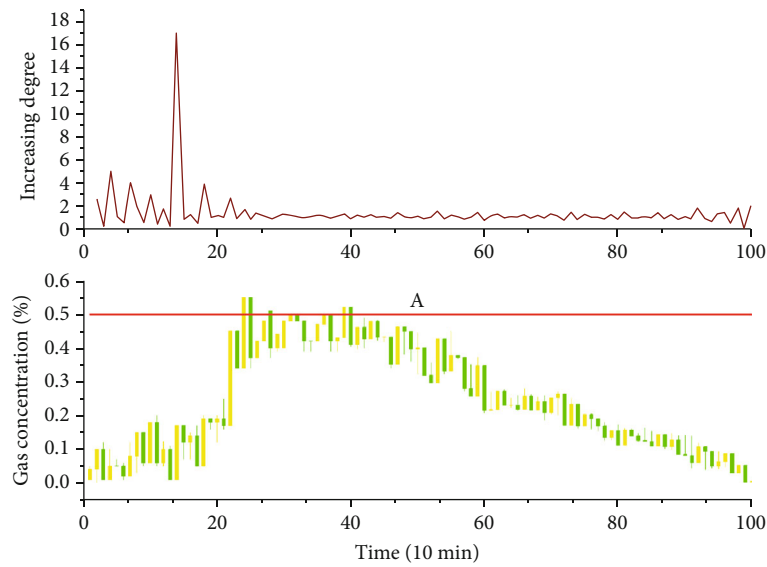


FIGURE 5: Increase degree of gas concentration.

The calculation formula is as follows:

$$EMA_T(12) = \frac{2}{12+1} \times C(T) + \frac{11}{12+1} \times EMA_{T-1}, \quad (2)$$

where $EMA_T(12)$ is today's fast-moving MA, $C(T)$ is today's gas cut-off concentration, and EMA_{T-1} is yesterday's fast-moving MA.

$$EMA_T(26) = \frac{2}{26+1} \times C(T) + \frac{25}{26+1} \times EMA_{T-1}, \quad (3)$$

where $EMA_T(12)$ is today's slow-moving MA, $C(T)$ is today's gas cut-off concentration, and EMA_{T-1} is yesterday's

slow-moving MA.

$$DIF = EMA(12) - EMA(26),$$

$$DEA(MACD) = \frac{2}{10} \times DIF_T + \frac{8}{10} \times DEA_{T-1}, \quad (4)$$

where DEA_{T-1} is yesterday's DEA.

In Figure 7, the blue bar graph represents twice DIF-DEA, the black line is slow line DEA, and the red line is fast line DIF. When applying the MACD index, it is mainly to analyze the relationship between DIF and 0 axis, DIF and DEA, and the sticks and 0 axis. When the bar graph is above the 0 axis, it means that the gas concentration is rising, and the higher the bar graph, the greater the upward amplitude

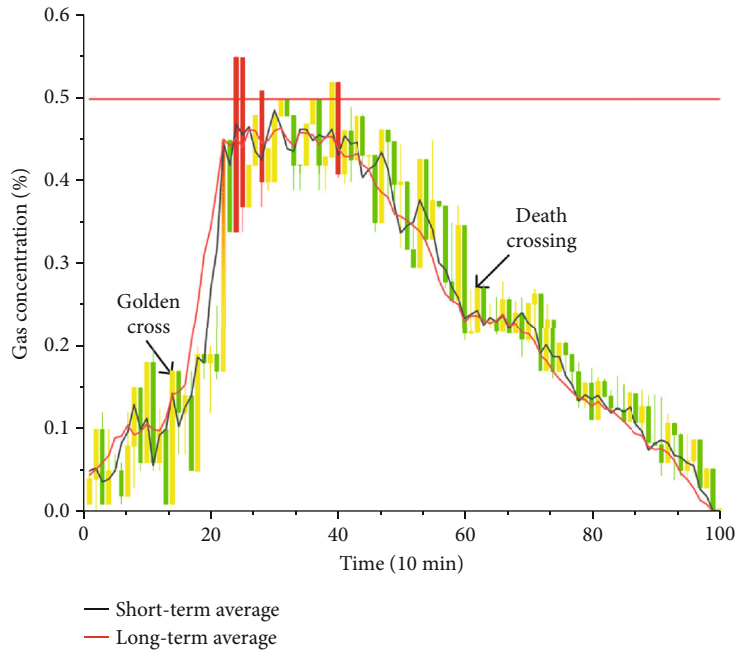


FIGURE 6: MA diagram of gas concentration.

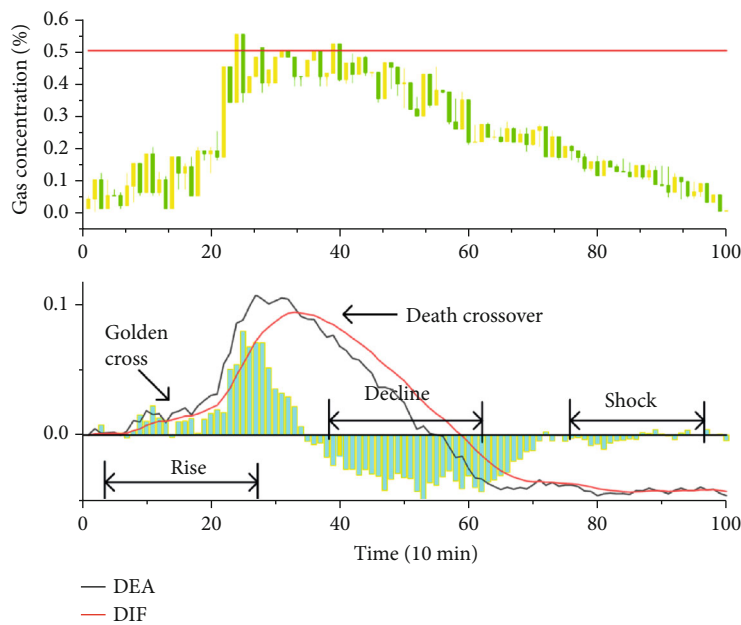


FIGURE 7: MACD index of gas concentration.

and the stronger the upward power. If the bar graph is below the 0 axis, it means that the gas concentration is in a downward trend. This index can intuitively indicate the degree of gas concentration increase in the blasting stage and the degree of gas concentration decrease when the blasting stage ends and enters the supporting stage, and the corresponding sticks have increased or decreased, thus quantifying the magnitude of the change. When the black line (slow line DEA) crosses the red line (fast line DIF) upwards, a “golden cross” appears. At this time, the bar graph is above the 0 line and its

height represents the increased amplitude. When the gray line crosses the red line downward, a “death crossing” appears. At this time, the bar graph is below the 0 line and the height of the bar graph represents the decline amplitude. Compared with the “golden cross” of MA, the golden cross signal of the MA index indicates that the short-term gas concentration exceeds the long-term gas concentration, which is a signal that the whole gas concentration is about to increase. The “golden cross” signal of the MACD index indicates that the decreased speed of the gas concentration is slowing down,

or the increased speed is accelerated, which also proves that the gas concentration will increase in the future. If the golden cross signals of the two indexes appear at the same time, or almost at the same time, they play a role of mutual verification. It shows that the gas concentration not only shows an increasing trend but also will increase faster and faster in the future. When such signals appear, it can be determined that the gas concentration will increase in a period in the future, so we should pay close attention to its increased amplitude and changing trend.

According to these characteristics of MACD, it can be determined that in tunnel gas monitoring, when DIF crosses DEA and breaks through DEA from bottom to top in MACD index, it indicates that the monitoring value will rise; when DIF breaks through from bottom to top, it means that the monitoring value will rise; if DIF line continues to rise, it means that the monitoring value will be in danger of exceeding the limit in a period in the future, and corresponding preventive measures should be taken at this time. MACD index can also express the convergence and divergence of the exponential moving average (EMA), which uses the speed difference between short cycle and long cycle to express the comparison trend between the gas concentration compared to the current cycle and the average value of the last cycle. When the gas concentration is in a state of fluctuation, the difference between the short cycle and the long cycle will be small. If the MACD value continues to increase at this time, the divergence will continue to expand.

4.3. Bollinger Band (BOLL) Index. The technical index of BOLL in the K-line diagram can be automatically adjusted with the change of gas concentration, and it is more flexible and intuitive than other methods. Bollinger Band is a technical index designed according to the standard deviation principle in statistics. The index consists of three track lines. In the field of gas early warning, the upper and lower lines in this index can be regarded as the pressure line and support line of the gas index, respectively. Between the two lines, there is an average line of a gas index. Generally, the gas index will wander within the band-shaped interval composed of the upper and lower tracks, which can be called the reasonable range of gas concentration, and the position of the track can be automatically adjusted with the change of numerical value. When the band narrows, the gas index may fluctuate violently, as shown in Figure 8. BOLL index includes three curves, namely, the upper track, the middle track, and the lower track, where the middle trajectory is the moving average, denoted as u_n .

The calculation method of the upper track is

$$\overline{Bn} = u_n + \alpha \times \sigma_n. \quad (5)$$

The calculation method of the lower track is

$$\overline{Bn} = u_n - \alpha \times \sigma_n, \quad (6)$$

$$\sigma_n = \sqrt{\frac{1}{n} \sum_{i=1}^n (X_i - u_n)^2},$$

where α is a multiple of standard deviation, which is generally 2 by default.

The moving range of the channel formed by the upper, middle, and lower tracks in the BOLL index is uncertain, and the upper and lower limits of the channel change with the fluctuation of gas concentration. Under normal circumstances, the gas concentration K-line should always run on the channel. If the gas concentration exceeds the channel range, it means that the gas concentration in the working face is in an overrun state, and the construction should be stopped immediately. In the BOLL index, the upper and lower tracks of the channel indicate the highest and lowest positions of gas concentration in a certain period. Generally speaking, when the gas concentration runs above the middle track of BOLL, it indicates that the gas concentration is in a strong upward trend; when the gas concentration runs below the middle track of BOLL, it indicates that the gas concentration is in a strong downward trend. Under normal conditions, the gas index usually runs within a band a certain width, and its characteristic is that the index value does not appear to suddenly increase or decrease, in a relatively balanced state. When the gas index crosses the upper limit pressure line, it is an upward signal; when the index crosses the lower limit support line, it is a downward signal; when the index crosses the middle boundary line from bottom to top, it means that it may rise continuously for some time; when the gas concentration crosses the middle boundary line from top to bottom, it means that it may decline continuously for a while.

BOLL has three functions in gas early warning: (1) BOLL can indicate the allowable maximum and minimum values of gas index, (2) BOLL can show the trend of gas concentration, and (3) Bollinger Bands are usually used as an auxiliary index to judge the trend, that is, to evaluate the strength of the gas index trend by the position of the gas index in the Bollinger Bands.

4.4. Technical Indexes of K-Line Diagram and Verification. To avoid contingency, the original abnormal fluctuation data of gas concentration is increased from 100 groups to 200 groups for trend analysis and prediction. The time series diagram is shown in Figure 9, and the K-line and technical indexes of gas concentration are shown in Figure 10.

From the comparative analysis of Figures 9 and 10, it can be seen that the overall trend of the K-line diagram is the same as that of the time series diagram, and the abnormal emission of gas concentration can be accurately expressed in combination with the increasing degree. As for the moving average, according to Figure 10, when the overall gas concentration reaches the peak, the corresponding short-term moving average is higher than the long-term moving average, so the gas concentration shows an upward trend in this period. After reaching the peak, the long line and short line immediately fell back, and the falling speed of the short-line was faster than that of the long-line, which proved that the gas concentration shows a downward trend.

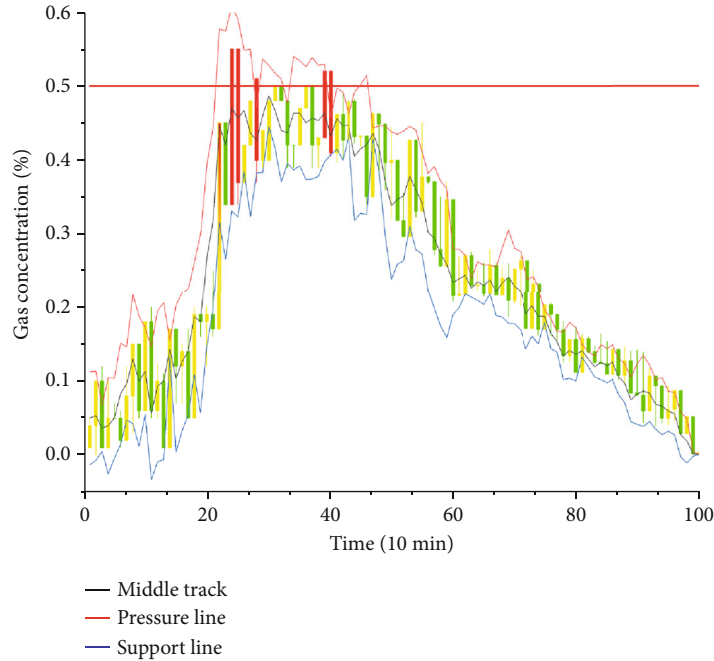


FIGURE 8: BOLL of gas concentration.

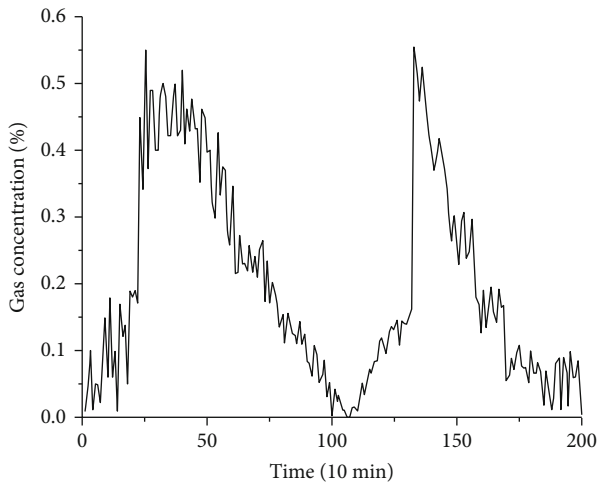


FIGURE 9: Time series diagram.

For the MACD index, when the gas concentration rises to the peak, the corresponding bar graph is above the 0 axis and reaches the highest value. When the gas concentration falls back, the bar graph is below the 0 axis and changes from high to low, which proves that the gas concentration drops. This shows that the corresponding sticks have changed obviously, thus quantifying the amplitude of variation. As shown in Figure 10, DIF crosses DEA and breaks through DEA from bottom to top in the MACD index, which indicates that the monitoring value is rising, and DIF is gradually increasing and continuously rising upwards, indicating that the gas monitoring value is in danger of exceeding the limit at this time. At this time, the moving average and MACD index has a “golden cross,” so it can be determined that the gas con-

centration is in a strong upward stage at this time, which is consistent with the actual gas trend.

For the BOLL index, when an abnormal gas concentration emission occurring, the difference between the middle track and the upper track is small, and when the middle track breaks through the upper track, it means gas concentration overrun in the working face, so the construction should be stopped immediately.

Based on the above, using the increasing degree, the MA, MACD, and BOLL indexes of gas, the changing trend of gas concentration can be displayed intuitively, and the gas emission state, gas concentration change trend, and whether the gas concentration fluctuates abnormally can be judged according to various technical diagrams and lines.

5. Conclusions

- (1) The amplitude and fluctuation of gas emission concentration in the tunnel construction operation cycle can be described by the K-line diagram. The improved K-line diagram is easy to read, practical, and effective, and the actual change of gas concentration can be observed more comprehensively and thoroughly. A series of other indexes are derived based on this diagram to describe the law of gas emission, which can better predict the trend of abnormal gas emission in low-gas tunnels
- (2) MA index is used to reflect the long-term change trend or cycle of gas emission concentration; the MACD index is used to reflect the intensity, direction, energy, and trend cycle of gas emission concentration change; BOLL is used to reflect the possible

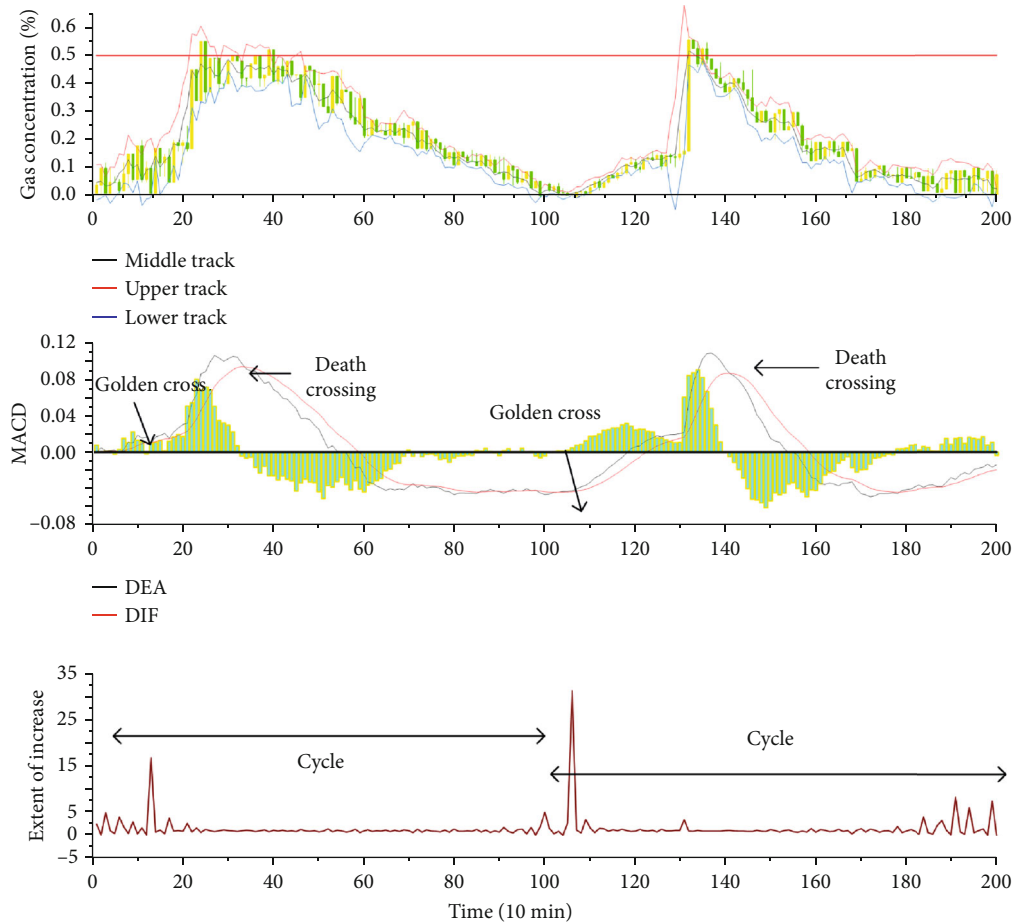


FIGURE 10: K-line and technical indexes of gas concentration.

upper and lower limits of gas emission. The abnormal gas emission law judged in combination with the K-line diagram and its indexes is consistent with the actual situation

- (3) The K-line diagram and its indexes can not only be used to describe the change law of gas concentration in low-gas tunnels but also provide ideas for describing the change of gas concentration in high-gas tunnels and mines

Data Availability

The data used to support the findings of this study are included within the article.

Conflicts of Interest

The authors declare that they have no conflicts of interest.

Acknowledgments

This paper is jointly funded by the National Natural Science Foundation of China (No. 51804058 and No. 51804055), the science and technology research plan of Chongqing Education Commission (Grant No. KJQN201800729), and the sci-

ence and technology innovation project (2020S0022) of Chongqing Jiaotong University.

References

- [1] M. Deng, G. S. Zhang, and Q. H. Chen, "Forecast of coal and gas outburst based on time series of gas concentration," *Journal of China Coal Society*, vol. 35, no. 6, pp. 260–263, 2010.
- [2] J. H. Fu and Y. P. Cheng, "Situation of coal and gas outburst in China and control counter measures," *Journal of Mining & Safety Engineering*, vol. 24, no. 3, pp. 253–259, 2007.
- [3] W. Liang, *Research on mine gas anomaly diagnosis and early warning based on K-line principle*, China University of Mining and Technology, 2017.
- [4] J. Zhou, *Research on disaster early warning method based on gas emission law of working face*, Xi'an University of science and technology, 2019.
- [5] T. Liu, B. Q. Lin, W. Yang, T. Liu, and C. Zhai, "An integrated technology for gas control and green mining in deep mines based on ultra-thin seam mining," *Environmental Earth Sciences*, vol. 76, no. 6, pp. 243–259, 2017.
- [6] K. Wang, J. Zang, G. Wang, and A. Zhou, "Anisotropic permeability evolution of coal with effective stress variation and gas sorption: model development and analysis," *International Journal of Coal Geology*, vol. 130, pp. 53–65, 2014.

- [7] Z. Pan, Y. Ma, L. D. Connell, D. I. Down, and M. Camilleri, "Measuring anisotropic permeability using a cubic shale sample in a triaxial cell," *Journal of Natural Gas Science and Engineering*, vol. 26, pp. 336–344, 2015.
- [8] W. Li and Z. H. Han, "Application of improved grey prediction model for power load forecasting," in *International Conference on Computer Supported Cooperative Work in Design*, Xi'an, China, April 2008.
- [9] D. P. Greedya, "Geological controls on the formation and distribution of gas in British coal measure strata," *International Journal of Coal Geology*, vol. 10, no. 1, pp. 1–31, 1988.
- [10] D. W. Dong, "Mine gas emission prediction based on Gaussian process model," *Procedia Engineering*, vol. 45, no. 2, pp. 334–338, 2012.
- [11] L. Chen, E. Wang, J. Feng, X. Kong, X. Li, and Z. Zhang, "A dynamic gas emission prediction model at the heading face and its engineering application," *Journal of Natural Gas Science and Engineering*, vol. 30, pp. 228–236, 2016.
- [12] P. Booth, H. Brown, J. Nemcik, and R. Ting, "Spatial context in the calculation of gas emissions for underground coal mines," *International Journal of Mining Science and Technology*, vol. 27, no. 5, pp. 787–794, 2017.
- [13] T. H. Lu and Y. M. Shiu, "Tests for two-day candlestick patterns in the emerging equity market of Taiwan," *Emerging Markets Finance & Trade*, vol. 48, no. sup1, pp. 41–57, 2014.
- [14] Y.-J. Goo, D.-H. Chen, and Y.-W. Chang, "The application of Japanese candlestick trading strategies in Taiwan," *Investment Management and Financial Innovations*, vol. 4, no. 4, pp. 49–79, 2007.
- [15] Y. Izumi, T. Yamaguchi, S. Mabu, K. Hirasawa, and J. Hu, "Trading rules on the stock markets using genetic network programming with candlestick chart," in *2006 IEEE International Conference on Evolutionary Computation*, Vancouver, BC, Canada, July 2006.
- [16] W. W. Y. Ng, X.-L. Liang, P. P. K. Chan, and D. S. Yeung, "Stock investment decision support for Hong Kong market using RBFNN based candlestick models," in *International Conference on Machine Learning & Cybernetics*, pp. 538–543, Guilin, China, July 2011.

Research Article

Macroscopic and Mesoscopic Mechanical Properties of Mine Tailings with Different Dry Densities under Different Confining Pressures

Zhi-jun Zhang ^{1,2,3}, Yao-hui Guo,^{1,2,3} Ya-kun Tian ^{1,2,3}, Lin Hu,^{1,2,3} Xi-xian Wang,^{1,2,3} Huai-miao Zheng,^{1,2,3} and Ling-ling Wu ^{1,2,3}

¹School of Resource & Environment and Safety Engineering, University of South China, 421001 Hengyang, China

²Hunan Province & Hengyang City Engineering Technology Research Center for Disaster Prediction and Control on Mining Geotechnical Engineering, China

³Key Discipline Laboratory for National Defense for Biotechnology in Uranium Mining and Hydrometallurgy, University of South China, 421001 Hengyang, China

Correspondence should be addressed to Ling-ling Wu; wllshmily@foxmail.com

Received 27 June 2020; Revised 10 August 2020; Accepted 24 August 2020; Published 30 September 2020

Academic Editor: Zhengyang Song

Copyright © 2020 Zhi-jun Zhang et al. This is an open access article distributed under the Creative Commons Attribution License, which permits unrestricted use, distribution, and reproduction in any medium, provided the original work is properly cited.

Particle flow numerical simulation software (PFC^{3D}) was utilized to establish the consolidated-undrained triaxial compression test numerical models of mine tailings with different dry densities to deeply investigate the macroscopic and microscopic characteristics of mine tailings in a tailing pond in Hunan Province. Comparing the results of the simulation and the laboratory experiment, the mesoscopic parameters of the particle flow numerical simulation were obtained through continuously adjusting the mesoscopic parameter with the higher degree of agreement between the stress-strain curve, the peak strength, and the elastic modulus as the determining standard. The macroscopic and microscopic characteristics of mine tailings were studied from the perspectives of stress-strain, axial strain-volume strain, coordination number, particle velocity vector, and contact force between particles. After numerous numerical tests, it was found that the PFC^{3D} simulation results are consistent with experiment results of the dry density tailing samples under different confining pressures; compared with the high confining pressure, the simulation test results at lower confining pressures were more with that of the laboratory tests; low density and high confining pressure both have inhibitory effect on the dilatancy characteristics of triaxial samples; with the same confining pressure, the dilatancy tendency of low dry density samples is suppressed comparing with the high dry density samples. The initial coordination number of the numerical model is large, which proves that the contact degree of the model is good to some extent.

1. Introduction

Tailings are complex geotechnical materials whose mechanical properties are greatly affected by various factors. As the main material of the tailing dam, the mechanical properties of the tailings exhibit great relevance with the safe operation of the tailing dam. Therefore, it is of great practical significance of studying the tailing mechanical properties. Under the load, the deformation of the tailing structure is mainly determined by its structural strength and modulus, while the structural strength and modulus are mainly determined by

the size, shape, and arrangement of its particles, that is, the macroscopic deformation and failure of the tailing structure resulted from its fine and microstructure changes. In geotechnical and rock materials studies, many scholars at home and abroad have paid great attention on researching it from the perspective of discrete element particle flow [1–4]. The relationship between mesoparameters and macroparameters in discrete-element particle flow simulation has always been a difficult point. Cui et al. [5] embedded the mode search method in the least square method to automatically calibrate the mesoparameters of the discrete element numerical test

of the biaxial compression of sand materials. Iterative calibration method was utilized by Xu and Sun [6] to calibrate the mesoparameters of the sand, and compared with the laboratory test results, it was found that it can reduce many unnecessary and repeated test parameter work. In rock materials, discrete element method was utilized by some scholars to perform PFC numerical simulation [3, 4]. Liu et al. [7] established a parallel bonding model for uniaxial and biaxial numerical simulations of rock materials through PFC^{2D} and studied the effect of the change of mesoparameters on the strength of the specimen under the parallel bonding model. A series of PFC numerical experiments were conducted by Yang and Han [8] to explore the effects of particle friction coefficient, normal stiffness, tangential stiffness, and the bonding strength between particles in particle clusters on the macroscopic mechanical properties of rockfill materials. The particle flow discrete element has also been widely used in geotechnical materials, and Xu [9] had performed the secondary development of PFC^{2D} software. He bundled the basic particles belonging to the same particle to obtain a sample that can be crushed and carried out many direct shear simulation tests. It was found that the degree of particle crushing exhibited influence on the shear expansion characteristics of coarse-grained soil and the internal friction angle. Luo et al. [10] used Chengde medium-density sand as the basic research object to simulate the sliding condition between particles with the contact friction sliding model and studied how the porosity and the internal friction angle between the particles influence on the mechanical properties of sand. By comparing the numerical simulation results of particle flow between transparent sand and standard sand, Li [11] supposed that transparent sand that can replace natural sand for indoor testing is reasonable under certain conditions. Zhou and Chi [12] explained the assumptions and basic principles of particle flow using PFC^{2D} to numerically simulate the sand biaxial test, and their results showed that the particle flow numerical simulation test can effectively simulate the formation and development of sand shear bands mechanism. Shen et al. [13] conducted particle flow biaxial compression tests on loose sand and dense sand to explore the macroscopic parameter response corresponding to the changes in mesoscopic parameters by adjusting the size of mesoscopic parameters such as particle contact stiffness and internal friction coefficient. Yin et al. [14] conducted a PFC uniaxial compression test on geotechnical materials under different particle size conditions, showing that the numerical simulation of geotechnical materials has certain stability when the internal scale ratio is less than 0.01. Yang and Li [15] used the PFC^{3D} particle flow program to numerically simulate the direct shear test of sand under different vertical pressures and explain the phenomenon of sand dilatation at a mesoscopic point of view. Based on the spherical particles in PFC, Yang and Li [16] introduced a rigid clump unit composed of pebble to establish dumbbell-shaped and elliptical cluster particles and found that the elliptical particles exhibited higher relevance with the simulation results. Based on the results of the laboratory triaxial test, Geng et al. [17] utilized PFC software to carry out the numerical simulation of the particle flow of coarse-grained soil and

found that the shape of the particle has a significant effect on the shear strength of the material. Wang et al. [18] used PFC^{2D} to study the size effect of the large triaxial sample, suggesting that scaling the sample by the equal mass substitution method was finite but could not be infinitely reduced. Yin et al. [19] conducted particle flow simulation tests on sand through PFC^{2D} and found that the friction angle between the sand and that between the particles could be approximated as an inclined line, and the cohesive force and the contact strength of the particles obeyed the linear law as well approximately.

There are relatively numerous researches about sandy soil, coarse grained soil, and rock materials, but few studies on tailings. In addition, the nonbonded linear contact model is used in most of above studies, and some are exploring through the direct shear test. Compared with the triaxial test, the direct shear test artificially defines the location of the shear failure surface, while that of triaxial test shear is along the weakest surface of the specimen. Based on the laboratory triaxial test results of tailings specimen, this paper compares the simulation results with the laboratory test results, and by continuously adjusting the parameters with the higher degree of agreement between the stress-strain curve, the peak strength, and the elastic modulus as the determining standard. The microstructure characteristics of tailings were analyzed from the perspective of coordination number, particle velocity vector, and particle displacement field. The method obtains parameters that are not easily obtained in laboratory tests.

2. Materials and Method

The tailings used in this test were taken from a tailing pond in Hengyang, Hunan Province, and the grading parameters of the samples obtained by sieving are shown in Table 1. Coefficient of nonuniformity C_u is 2.5320; coefficient of curvature C_c is 1.6610. As $C_u \geq 5$ and $C_c = 1 \sim 3$ cannot be satisfied at the same time, the tailing grading is not good. These samples were dried to a constant weight and then cooled down to room temperature to make compact samples with a diameter of 39.1 mm and a height of 80 mm. All samples were prepared using self-made triaxial device of acrylic tube. The device is composed of two semicircular cylinders of specified size. The correspondence between the number of compactions and the dry density was determined by a large amount of tests. The specific dry density sample was obtained by controlling the number of compactions with compacting in four layers. The samples before and during the triaxial test are shown in Figure 1.

LH-TTS series automatic triaxial apparatus were employed with the maximum axial loading force of 10 kN at the loading rate ranging between 0.0001 and 4.8 mm/min. The process of triaxial loading is controlled by a computer, and the axial strain of the sample reaches 15% as the termination condition of loading. The consolidated-undrained triaxial compression test was carried out for each specific dry density sample with the loading rate of 0.6 mm/min at a confining pressure of 100 kPa, 200 kPa, and 300 kPa, respectively. The test data was automatically collected and collated by the computer, and Figure 2 is the picture of the automatic triaxial apparatus.

TABLE 1: Particle composition parameters of tailings.

Effective diameter (d_{10} /mm)	Median size (d_{30} /mm)	Particle composition parameters		
		Constrained size (d_{60} /mm)	Coefficient of nonuniformity (C_u)	Coefficient of curvature (C_c)
0.0780	0.1620	0.2000	2.5320	1.6610



FIGURE 1: Samples before and during loading.

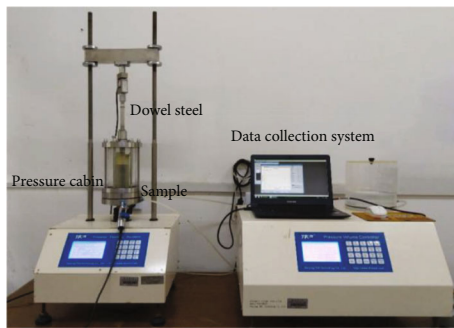


FIGURE 2: Automatic triaxial apparatus

3. Experimental Results and Analysis

Excess pore water pressure has been the main cause of many engineering accidents. The increase of excess pore water pressure would lead to the decrease of the equivalent axial and radial effective principal stresses as well as the diameter of the Mohr circle to be unchanged and shifting to the left, causing soil instability and destruction [20]. The value of the excess pore water pressure corresponding to each axial strain can be obtained directly from the triaxial consolidated-undrained test. Figure 3 shows the relationship between pore water pressure and axial strain under different confining pressures (only the excess pore water pressure is involved in this paper).

From Figures 3(a) to 3(c), the pore water pressure of each dry density tailing sample under different confining pressures exhibited the trend of increasing and then decreasing as the axial strain increased. The pore water pressure can reflect the shear expansion and contraction characteristics of the specimen during triaxial compression [21]. When the confining pressure is the same, the larger dry density, the larger peak pore water pressure; and the larger dry density sample is more likely to be negative, causing the development

of sample dilatancy characteristic. When the dry density is the same, the larger confining pressure is, the larger pore water pressure corresponds to each axial strain, suppressing the negative value of the pore water pressure. Hence, the occurrence of sample dilatancy was limited by the high confining pressure. When the density is 1.61 g/cm^3 and 1.66 g/cm^3 , dilatancy happened on all the samples with confining pressure of 100 kPa (limited to space, the relationship between stress and strain in the laboratory test was not discussed separately).

4. Particle Flow Model

4.1. Particle Size and Model Size. If the model is generated according to the original gradation of the sample, millions of spherical particles will be required. In order to avoid generating more particles when generating the numerical model of the triaxial test, resulting in longer calculation time, the original gradation of the sample cannot be used directly. Ning [22] found in the triaxial particle flow test of cohesive soil that the effect of particle size on the macroscopic strength characteristics of the soil is much smaller than the friction coefficient and bond strength between the particles, and when $D/R \geq 20$, the effect on the strength parameters of the soil is almost negligible (D is the model diameter; R is the maximum particle size). Combined with the size of the laboratory triaxial test sample and the distribution of the particle gradation of the tailings itself, the size of the triaxial particle flow model is the same as the laboratory test size, and the particle size is uniformly distributed between 0.85 mm and 1.41 mm.

4.2. Contact Model. In the simulation test of the particle flow of sandy soil, the contact method chosen by most researchers is the nonbonded contact [10–12]. Considering that the tailing material itself has bonding characteristics, it is more reasonable to select a linear contact bond model. Linear contact bond model is generally composed of linear group, damping group, and bonding group. Within the range of the target gap, the bonding force between the particles can be generated but the moment cannot be resisted. Between the particles, there can be no coexistence between bonding and sliding. It is assumed that there are two springs at the bond between the particles to provide a constant normal, tangential stiffness and specific tensile and shear strength [23]. If the normal tensile force is greater than the tensile strength, the bond will break, and the normal and tangential bonding will disappear; if the tangential shear force is greater than the tangential bond strength, the bond will fail, but the contact is subjected to normal pressure and the tangential shear force. The force at the contact will not change if it is less than the product of normal pressure and particle friction coefficient. Figure 4 shows a linear contact bond model.

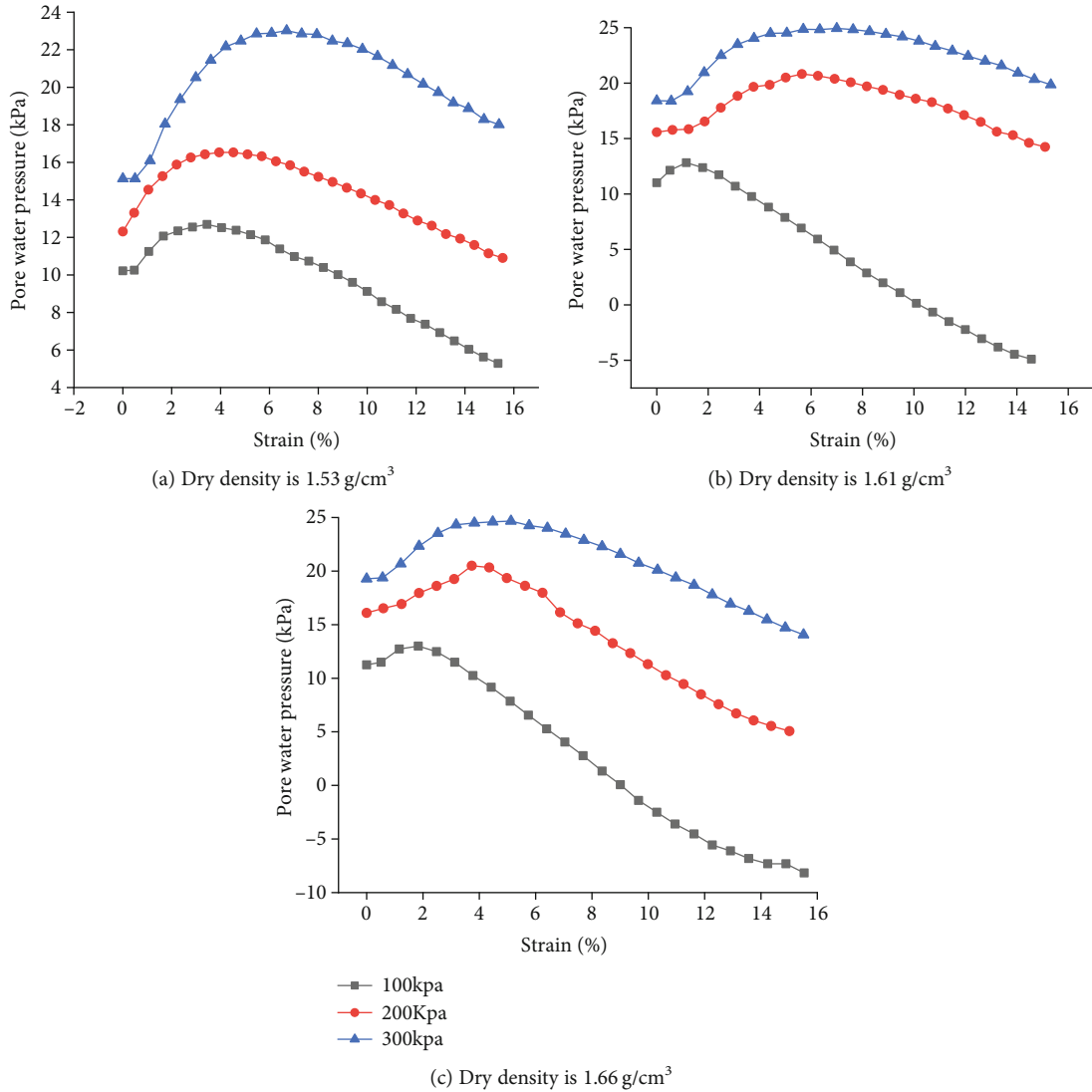


FIGURE 3: Relationship between pore water pressure and axial strain.

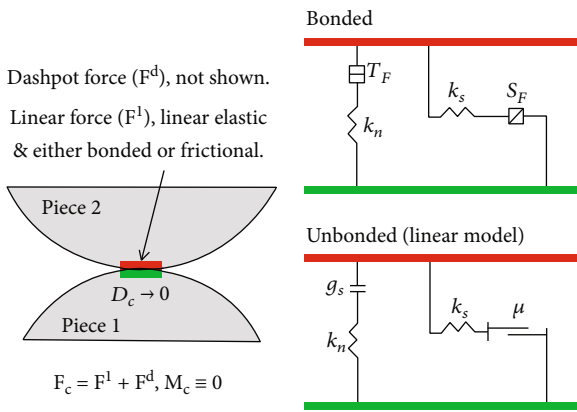


FIGURE 4: Linear contact bond model (from PFC5.0). F_c is contact force. D_c is distance between of particles. M_c is contact moment. T_F is tensile force. S_F is shear force. g_s is specific gap. k_n is normal stiffness. k_s is shear stiffness. μ is friction coefficient.

4.3. *Model Establishment.* According to the determined model size and particle size, linear bonding contact was set between the spherical particles, and the cylinder command was utilized to generate the uncovered cylindrical side wall of the particle flow triaxial test model. To reduce the calculation time of wall generation, the plane command was utilized to create a plane rigid wall at the top and bottom of the specimen. To ensure the uniformity of the generated model, the friction coefficient of the wall is 0 [24]. In the laboratory test, the flexible restraint was provided by the rubber jacket on the side wall of the sample, hence setting the wall of the uncovered cylindrical side wall as a flexible wall. Due to the lateral deformation of the sample under the force during the loading phase, the length of each side of the plane rigid wall is set to twice the diameter of the model to prevent some particles from exceeding the wall. The PFC particle flow numerical simulation is shown in Figure 5.

4.4. *Confining Pressure Servo and Loading System.* During the PFC simulation process, the confining pressure is provided

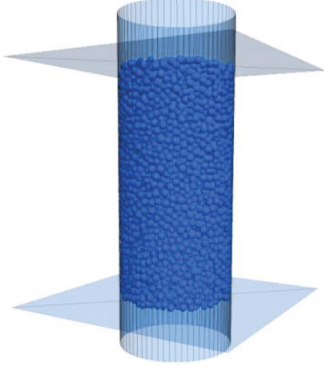


FIGURE 5: Model of the particle flow numerical simulation.

by the top and bottom plane rigid walls and the flexible wall with uncover cylindrical side wall in the initial consolidation stage before loading; the confining pressure is only provided by the flexible uncovered cylindrical side wall during the loading stage. The confining pressure and the axial pressure were adjusted by controlling the movement speed of the cylindrical side flexible wall and the plane rigid wall, respectively. The magnitude of the force is obtained by formula (1). Setting the target strain value to reach the target strain value as the loading stop condition, the top and bottom rigid planes move slowly at the same time to load the sample [25].

$$\Delta F^W = K_n^w N_c u^w \Delta t, \quad (1)$$

where ΔF^W is confining or axial pressure. K_n^w is the average normal stiffness of particles in contact with the wall. u^w is the wall velocity. N_c is the number of particles in contact with the wall. Δt is time step.

4.5. Calibration of Mesomechanical Parameters. Calibration of mesomechanical parameters has always been an important issue in PFC simulation because there is no specific relationship between the mesoscopic parameters and the macroscopic parameters. Based on the calibration of mesoscopic parameters in recent studies, the parameters are continuously adjusted by trial and error until the stress-strain curve, elastic modulus, peak strength, and laboratory test results are approximately the same [26]. The detailed simulation parameters are shown in Table 2.

5. PFC Numerical Simulation Results and Analysis

5.1. The Relationship Curve of Stress-Strain. From Figures 6(a) to 6(c), the stress-strain curve, peak strength, and elastic modulus of the numerical simulation of each dry density tailing sample and laboratory tests under different confining pressures were basically consistent. With the increase of the dry density, the peak strength of the samples with the same confining pressure increased significantly. With the increase of confining pressure, the simulation curves at each dry density showed that the degree of strain softening to strain softening was suppressed and finally strain hardening occurred. That could be explained that as the confining pres-

sure increased, the sliding and turning of the particles in the simulation were restricted to enhance the load-bearing capacity, and the sample strain hardening phenomenon occurred macroscopically. At the same time, as the confining pressure increased, the axial strain corresponding to the peak stress in the simulation curve also tended to increase. In the simulation curve, the peak stress of each dry density tailings increased with the increase of confining pressure and showed a nearly linear relationship consistent with the conclusion that the peak strength and the confining pressure exhibited linear relationship [18]. Figure 7 showed the relationship between peak strength and confining pressure. When the confining pressure was 100 kPa and 200 kPa, the stress-strain curve of PFC simulation and laboratory test were in excellent relevance; but when the confining pressure was 300 kPa, the curve matched poorly. This was mainly because the larger particles in the tailings sample were more likely to be crushed when compressed under high confining pressure, but the PFC numerical simulation model assumes that the ball particles are rigid, so the matching degree between laboratory tests and PFC numerical results under high confining pressures is poor. It can be seen from Figure 6 that the initial elastic modulus of the simulation curve was slightly smaller than the laboratory test due to the large crushed particles in the real sample, but the particles in the numerical simulation cannot be crushed. In the numerical experiment, different dry densities were achieved by controlling the change of porosity while keeping other simulation parameters unchanged. The peak strength decreases by 46.7 kPa when the porosity increases from 0.32 to 0.45 at the confining pressure of 100 kPa; the peak strength decreases by 213.3 kPa and 317.7 kPa when the porosity increases from 0.32 to 0.45 kPa at the confining pressure of 200 kPa and 300 kPa. The stress-strain curves of the numerical test showed strain hardening before the deviatoric stress reached the peak value, and the volume change showed a shear shrinkage characteristic. The stress-strain curve of the numerical test before the deviatoric stress reached the peak shows strain hardening, and the volume change became the shrinkage characteristic. After the peak stress was reached, the volume change showed the tendency of shear expansion, which was consistent with the laboratory test results in Figure 3. From a mesoscopic point of view, as the loading progresses gradually, the pores in the sample are continuously compressed, the particle spacing decreases, the number of contact points increases, and the body shrinkage characteristics appear macroscopically before the peak stress is reached; after the deviatoric stress reaching the peak stress, the bite force between the particles reached the peak due to the maximum restriction and restraint effect between the particles at the peak stress; therefore, as further loading destroyed the bite between the particles, the particles began to slip and rotate, with the tendency to expand radially. The mutual restriction between particles and the deviatoric stress decreased, and the volume of the sample began to expand, and the macroscopic performance is the dilatancy characteristic.

5.2. Volumetric Strain-Axial Strain Relationship. The volume strain of the tailing sample is the amount of change per unit volume of the sample. Based on the initial volume, volume

TABLE 2: Particle flow simulation parameters.

Radius (R/mm)	Radius ratio ($R_{\text{Max}}/R_{\text{Min}}$)	Friction coefficient (μ)	Normal stiffness ($k_n/(\text{kN}/\text{m})$)	Normal-to-shear stiffness ratio (k_n/k_s)	Tensile strength (T_F/KN)
85-141	1.66	0.5	60	1.33	5

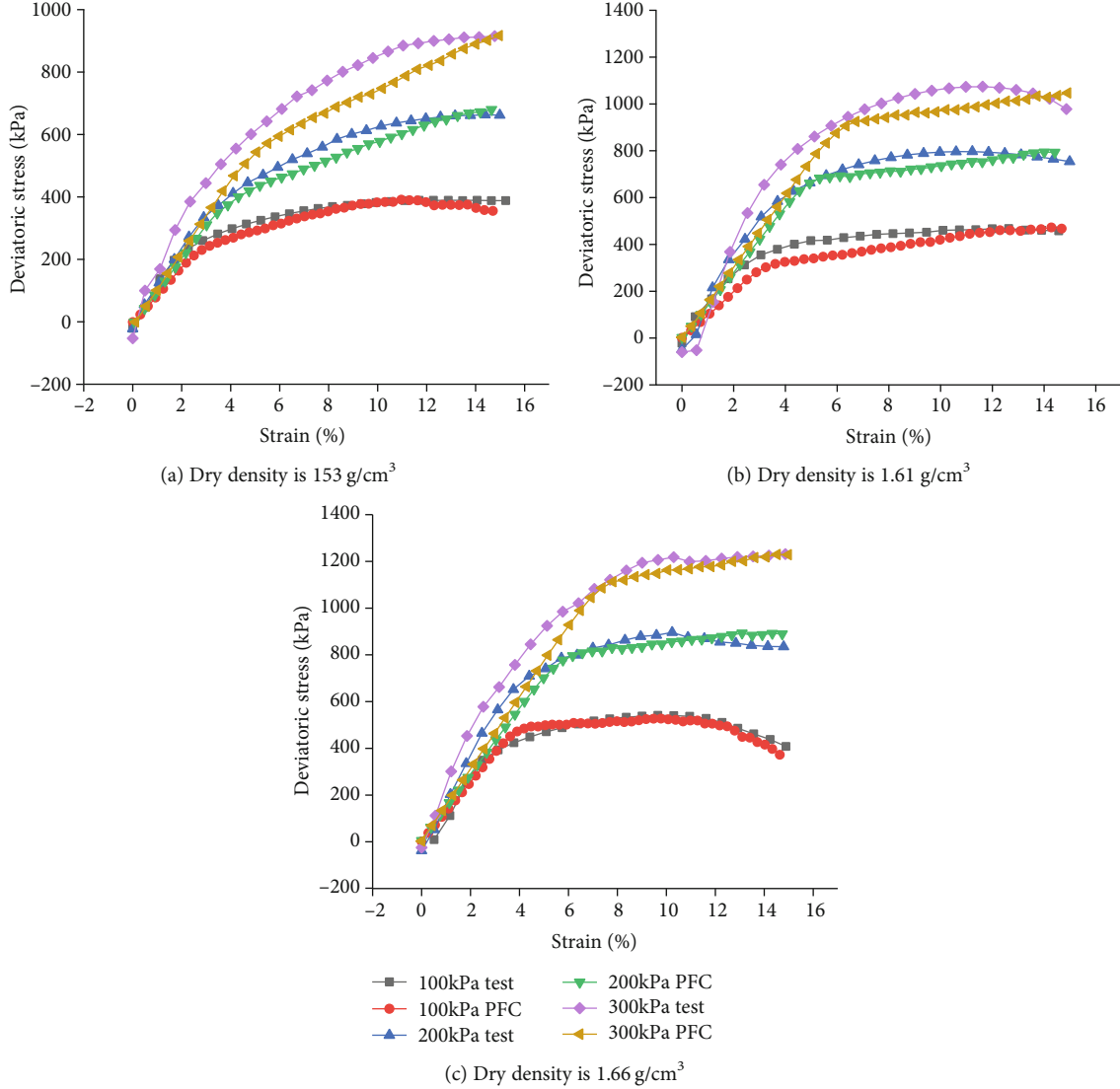


FIGURE 6: Stress-strain curves of laboratory tests and PFC simulation.

compression serves as positive volume strain, volume expansion serves as negative volume strain, and the point where the slope of the axial strain and volume strain curve of is 0 is defined as the critical point of the shear expansion trend. The relationship between axial strain and volume strain under PFC numerical simulation is shown in Figure 8.

In the PFC simulation, there is no dilatancy phenomenon on the sample with a confining pressure of 100 kPa and a dry density of $1.61 \text{ g}/\text{cm}^3$, which is not consistent with the result of a slight dilatation phenomenon in Figure 3. This is that the particle flow simulation assumed that the particles are rigid bodies, and the particles in the laboratory test can be crushed and deformed. The crushed and deformed particles are

recombined and replaced into the large pores in the sample, resulting in the number of large pores reduced, and the degree of crushing and deformation is greater under high confining pressure. Unlike laboratory tests, the dominant factor in the change of sample volume in PFC numerical simulation is the rearrangement between particles due to the sliding and squeezing between particles. It can be clearly seen from Figures 8(a) to 8(c) that there is a big difference in the relationship between the volume strain-axial strain curves of different confining pressure simulations at the same dry density. The sample at the confining pressure of 100 kPa with lower dry density has a more obvious dilatancy trend, but no dilatation occurs compared with the initial sample volume; as the

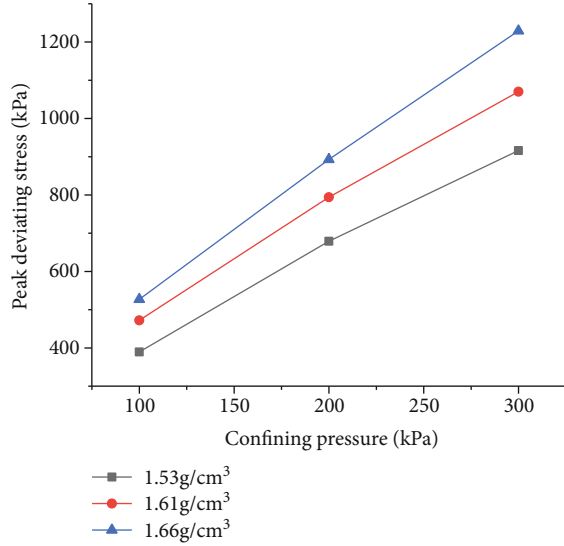


FIGURE 7: The relation curve between peak strength and confining pressure in PFC test

confining pressure increases, the critical point of the dilatation trend that corresponds to the axial strain becomes larger; there is no obvious tendency of shear expansion when the axial strain reaches 15% at the confining pressure of 300 kPa. This is because, for samples with a low dry density at small confining pressure, the lateral restraint force is small, and when loaded to a certain degree, the sample expanded radially due to the slippage and rotation between the particles. When the confining pressure is larger, the larger lateral binding force enables to compress to a greater degree due to the larger porosity of the sample itself, showing the axial strain corresponding to the critical point of the shear dilatancy trend increases. Compared with the low dry density sample, the larger dry density has a certain promoting effect on the sample's dilatancy trend at the same confining pressure. This can be explained as, when the density is higher, the porosity is lower, and the gap between the particles is smaller. After the load increases to a certain degree, the particles in the sample slide and renew arrangement under the combined action of axial pressure and confining pressure, resulting in particles from a tightly arranged state to a relatively loose degree, which is more prone to more obvious radial expansion; the particles with a small dry density are loosely arranged, and the particles squeeze, slide, and rotate against each other under load by filling some large pores; the sample had a higher degree of compression, and the macroscopically showed that the dilatancy characteristic was suppressed. High confining pressure and low density exhibited inhibitory effect on the dilatancy characteristics of the sample. The volume strain shows a negative value, which shows the phenomenon of shear dilatation macroscopically with the confining pressure of 100 kPa at dry density of 1.66 g/cm³.

5.3. Coordination Number Changes during Loading. Coordination number is an extremely important index in particle flow simulation, which is used to evaluate the degree of good contact between particles and compactness of a particle

system. In this paper, the coordination number in the loading process is monitored by setting a measuring ball with a radius of 17 mm at the center of the model, as shown in Figure 9. The coordination number C_n is obtained by formula (2), and the coordination number changes of different dry density models in the loading process are shown in Figure 10 (coordination number, particle velocity vector, and contact force between particles were all obtained at a confining pressure of 100 kPa).

$$C_n = \frac{2N_c}{N_b} \quad (2)$$

where C_n is coordination number. N_c is actual number of contacts. N_b is total particles number.

When the confining pressure was 100 kPa, the change of coordination number of different dry density models during loading showed that the initial coordination number of each dry density model was large, indicating good contact between particles in each model. With the loading process continued, the coordination numbers of different dry density models showed a trend of first increasing and then decreasing, and in the whole loading process, the coordination numbers of models with higher dry density were larger than those with lower dry density. When the dry density was 1.66 g/cm³, the coordination number of the models decreased greatly at the later stage of loading, which may be because the samples with high dry density and low confining pressure were more prone to dilatation. The radial expansion of the model reduced the numbers of contact between particles, and the coordination number decreased significantly.

5.4. Velocity Vector Diagram between Particles. When the confining pressure is 100 kPa, the velocity vector diagram corresponding to different axial strains in the loading process is shown in Figure 11. By observing the particle velocity vector field corresponding to each axial strain of the model under different densities, it was found that when the axial strain was 5%, the particle velocity directions in the model with different dry densities were more orderly. Due to the loading mode of upper and lower loading plates moving slowly at the same time is adopted in the model, when the axial strain is small, the particles in the upper part of the model show a downward movement trend as a whole, while the particles in the lower part of the model show an upward movement trend. Therefore, the particle movement direction is more orderly. With the increase of axial strain, the movement tendency of particles becomes disordered. When the axial strain is 10% or 15%, the particles near the side wall of the model with different dry densities show a trend of radial horizontal outward motion, which indicates that the model has shown a trend of dilatancy at this time, which is consistent with the phenomenon in Figure 8. Compared with the low dry density model, when the axial strain is the same, the particle velocity field of the high dry density model has a higher degree of disorder and the radial horizontal movement of the particles near the side wall is more obvious. It is proved from the microscopic point of view that the high dry density has a certain promotion effect on the dilatancy

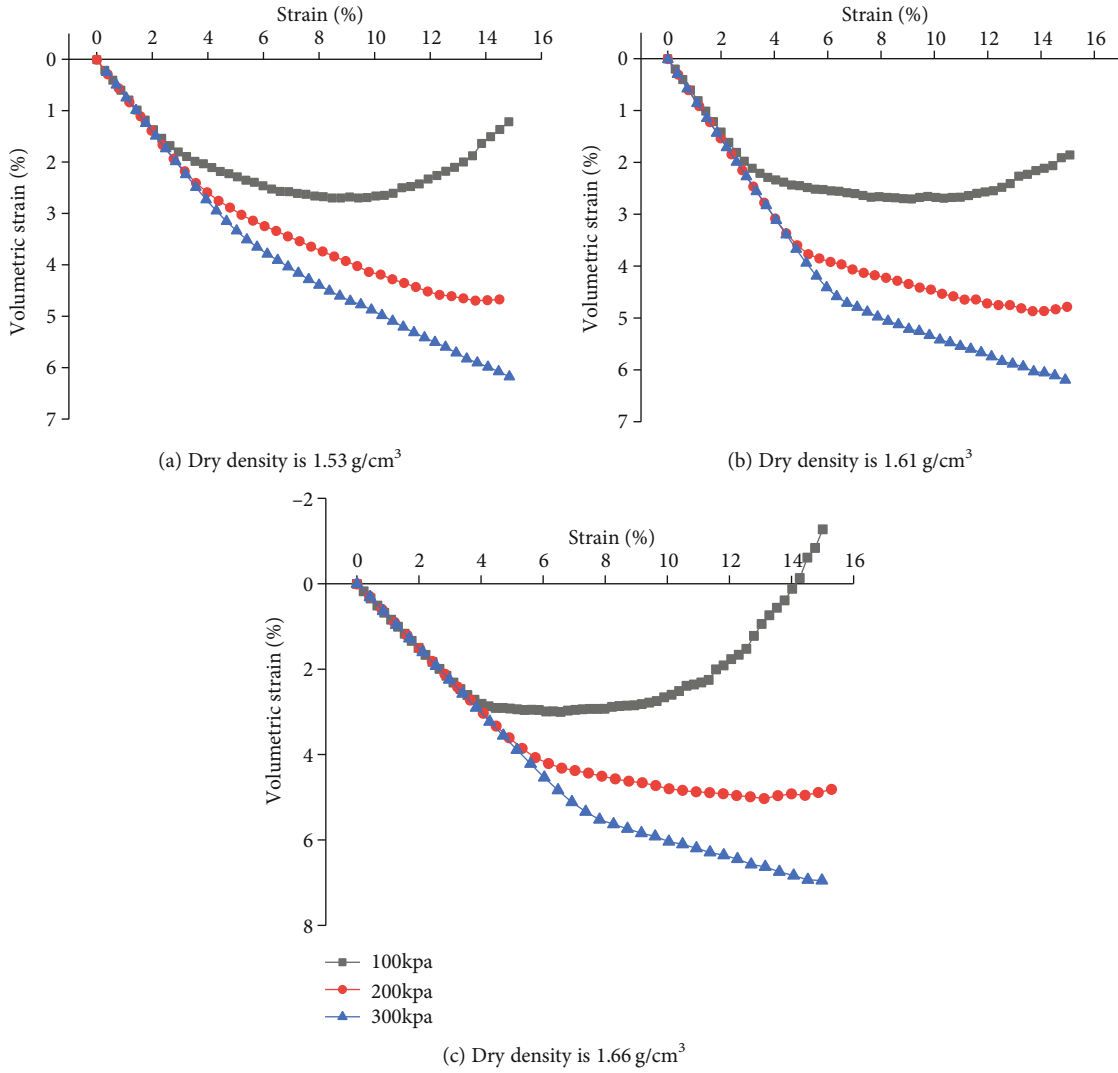


FIGURE 8: The relation curve of axial strain and volume strain in PFC numerical simulation.

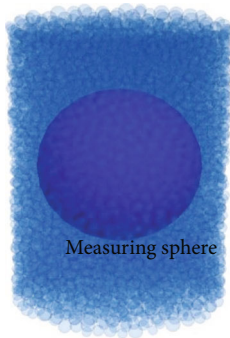


FIGURE 9: Measuring ball diagram.

of the sample. It is corresponding to the conclusion in Section 5.2 that the sample shows dilatancy with 100 kPa confining pressure and 1.66 g/cm³ dry density.

5.5. *Contact Force between Particles.* When the confining pressure is 100 kPa, the contact force between particles corresponding to different axial strains in the loading process is

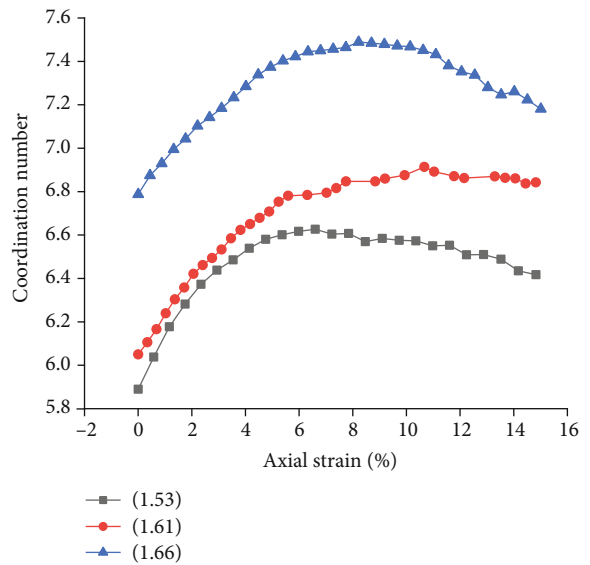


FIGURE 10: Coordination number changes of different dry density models during loading.

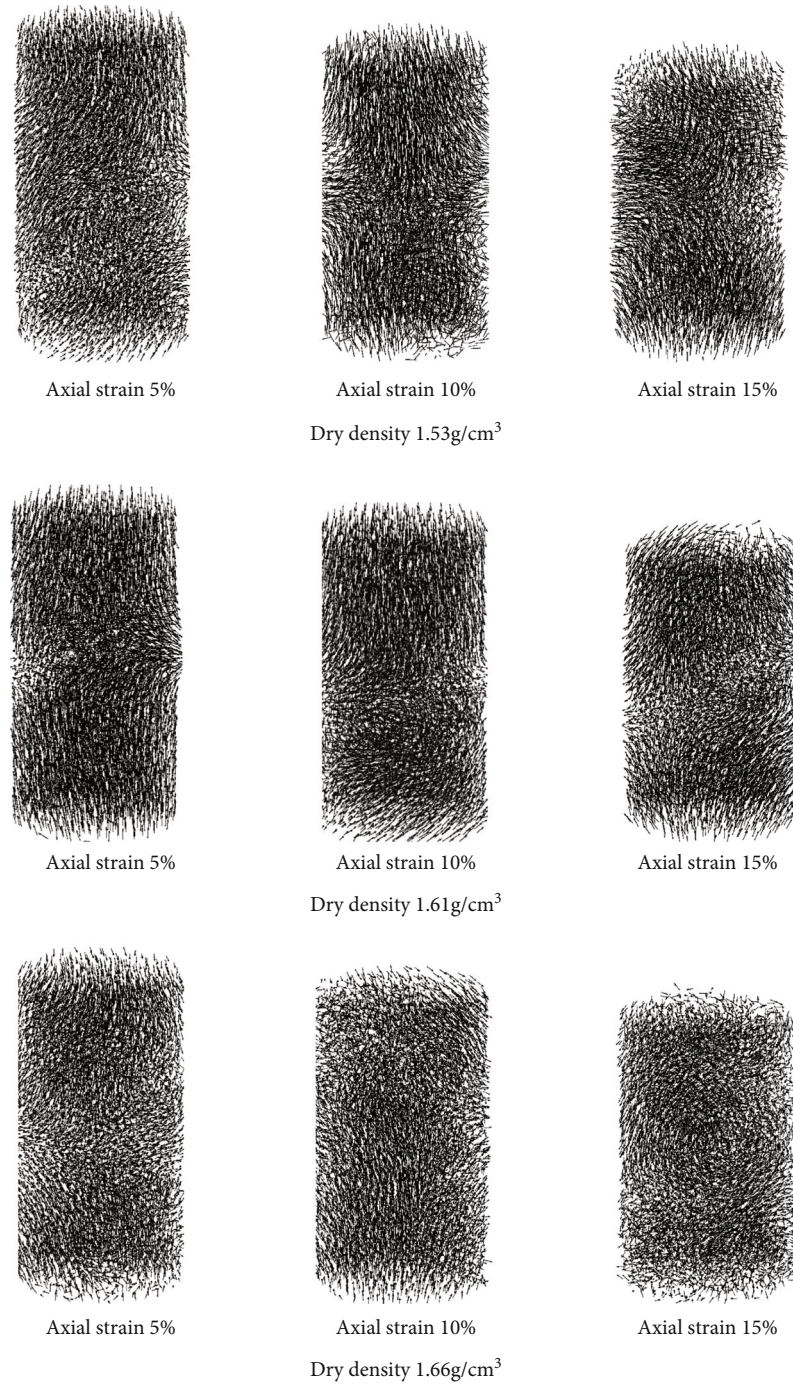


FIGURE 11: Velocity vector diagram of various axial strain sample under different dry density.

shown in Figure 12. The thicker the black line, the greater the contact force. By observing the contact force corresponding to each axial strain of the models under different dry densities, it is found that the magnitude of contact force between particles is smaller and more homogeneous in the consolidation stage when the axial strain is 0. With the continuation of the loading procedure, the homogenization of the magnitude of contact force between particles with different dry density models presented a trend of first decreasing and then increasing. When the axial strain was large, the magnitude of contact force

between particles also developed toward homogenization. With the increase of axial strain, the contact force between the particles and the upper and lower loading plates increased significantly, and the contact force of the core area connecting the upper and lower loading plates in the middle of the model also increases obviously. When the axial strain is 10% or 15%, the core area of the models bears most of the axial pressure. When the dry density was 1.66 g/cm³ and the axial strain was 15%, the particle contact force within a certain range near the side wall of the model decreased significantly, which may

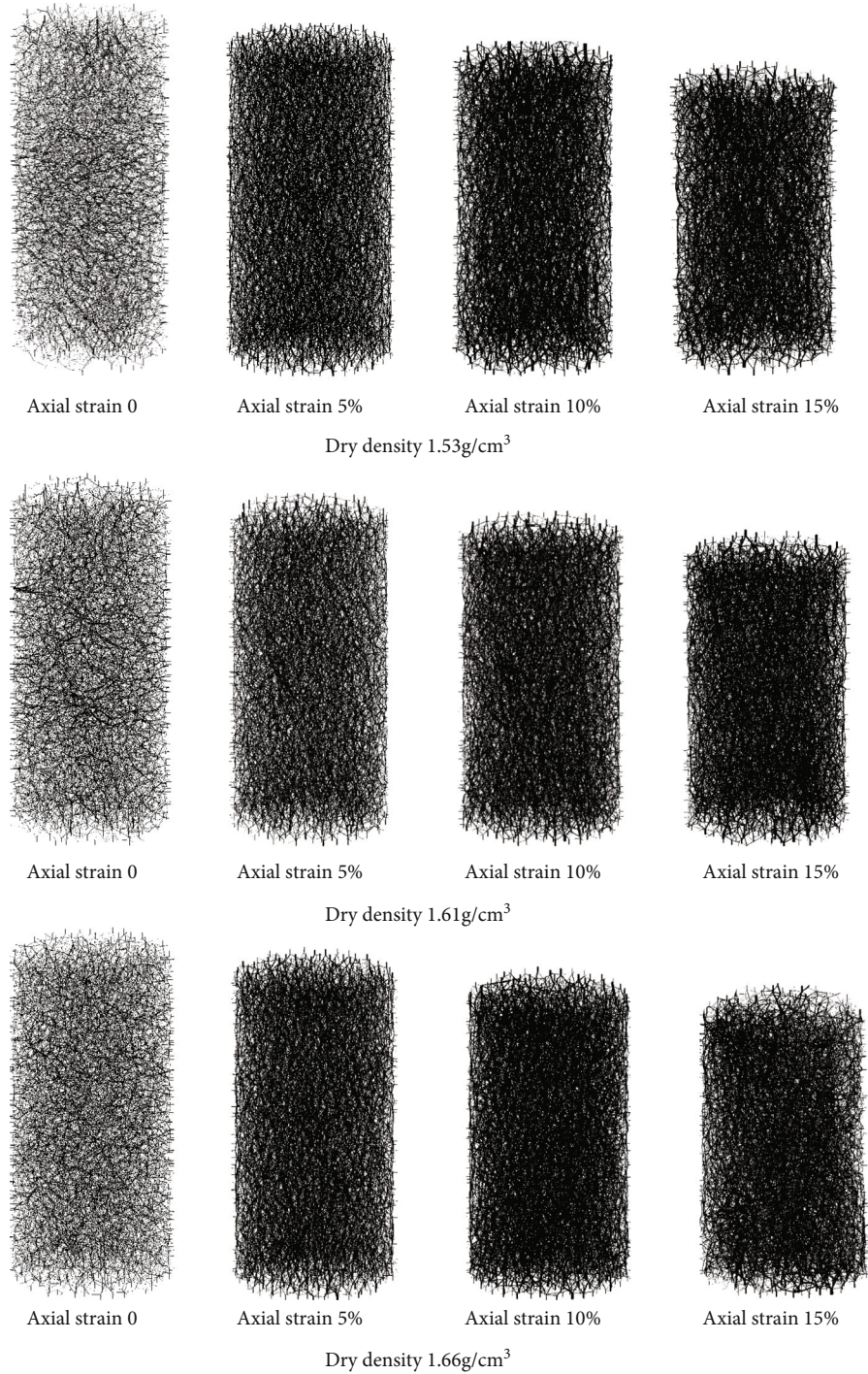


FIGURE 12: Contact forces between particles of axial strain samples under different dry densities.

also be due to the phenomenon of dilatancy in the high-density model under low confining pressure.

6. Conclusions

Based on the laboratory consolidated-undrained triaxial compression experiment, PFC is used to conduct numerical tests on tailings with different dry densities, and the fish language is used to monitor the stress, strain, peak strength and coordi-

nation number, particles velocity, and contact force between particles of the sample. Following conclusions are drawn:

- (1) By comparing the laboratory test with the PFC triaxial compression simulation test, the stress-strain curve, peak strength, and elastic modulus of the numerical simulation of each dry density tailing sample under different confining pressures and the laboratory test are in good agreement

- (2) Compared with the case of high confining pressure, the numerical test at low confining pressure has a higher degree of coincidence with the laboratory triaxial compression test. This is due to the assumption that particles are rigid and incompressible in PFC. However, the greater the confining pressure, the greater the degree of particle crushing and deformation in laboratory test
- (3) Under large confining pressure, the sliding and rotation of the particles inside the sample are restricted, suppressing the dilatancy of the sample
- (4) The initial coordination number of the numerical model is large, which proves that the contact degree of the model is good to some extent
- (5) In the triaxial numerical test, with the strain increases to a certain extent, the core area of the models bears most of the axial pressure
- (6) Both macroscopic and mesoscopic studies have proved that due to the close arrangement of high-density particles, the restraint force is small and the sample will tend to expand radially as loaded to a certain degree due to the slip and rotation between particles

Data Availability

The data that support the findings of this study are available from the corresponding author upon reasonable request.

Conflicts of Interest

The authors declare no conflicts of interest.

Acknowledgments

This work is supported by the National Natural Science Foundation of China (51774187 and 51804164); the Research Foundation of Education Bureau of Hunan Province (17A184); and the Natural Science Foundation of Hunan Province (2019JJ50498). Thanks to Hunan Province Engineering Technology Research Center for Disaster Prediction and Control on Mining Geotechnical Engineering (2019TP2070) for providing experimental platform support and thanks to the Central South University.

References

- [1] Z. Song, H. Konietzky, and M. Herbst, "Bonded-particle model-based simulation of artificial rock subjected to cyclic loading," *Acta Geotechnica*, vol. 14, no. 4, pp. 955–971, 2019.
- [2] Z. Song and H. Konietzky, "A particle-based numerical investigation on longwall top coal caving mining," *Arabian Journal of Geosciences*, vol. 12, no. 18, 2019.
- [3] B. Dai, Y. Chen, G. Zhao, W. Liang, and H. Wu, "A numerical study on the crack development behavior of rocklike material containing two intersecting flaws," *Mathematics*, vol. 7, no. 12, p. 1223, 2019.
- [4] Z. Song, H. Konietzky, and M. Herbst, "Three-dimensional particle model based numerical simulation on multi-level compressive cyclic loading of concrete," *Construction and Building Materials*, vol. 225, pp. 661–677, 2019.
- [5] Y. Y. Cui, J. H. Zhang, A. Tong, and N. Wu, "Automatic identification of discrete element meso parameters of sand materials," *Mechanics and practice*, vol. 41, no. 3, pp. 300–307, 2019.
- [6] G. Y. Xu and Y. P. Sun, "Macro-microscopic parameter calibration for triaxial test of sand soil using iterative thought," *Journal of Harbin Institute of Technology*, vol. 49, no. 9, pp. 65–69, 2017.
- [7] C. Liu, X. X. Cheng, W. Zhang, and B. Wang, "Research on the calibration process of parallel bonding mesoscopic parameters in PFC numerical simulation," *Value engineering*, vol. 36, no. 26, pp. 204–207, 2017.
- [8] J. Yang and X. F. Han, "Correlation analysis of macro-microscopic parameters of rockfill material based on PFC," *People's Yangtze River*, vol. 49, no. 16, pp. 106–111, 2016.
- [9] Y. F. Xu, "Simulation analysis of shear strength of coarse-grained soils based on particle breakage," *Journal of Engineering Geology*, vol. 26, no. 6, pp. 1409–1414, 2012.
- [10] Y. Luo, X. N. Gong, and F. Liang, "Engineering mechanical properties of cohesionless soil simulated by three-dimensional discrete particle unit," *Journal of Geotechnical Engineering*, vol. 30, no. 2, pp. 292–297, 2008.
- [11] N. Li, "Transparent sand particle flow simulation of triaxial test," Geological society of China engineering geology professional committee, China geological survey, the hall of Qing Hai province, 2011 national engineering geological academic essays, Geological society of China engineering geology professional committee, the China geological survey, the hall of Qing Hai province: journal of engineering geology editorial office, vol. Supplement, no. 19, pp. 320–326, 2011.
- [12] J. Zhou and Y. Chi, "Microscopic simulation of mechanical properties of sandy soil," *Rock and Soil Mechanics*, vol. 24, no. 6, pp. 901–906, 2003.
- [13] Z. F. Shen, M. J. Jiang, F. Y. Zhu, and H. J. Hu, "Effects of discrete element microscopic parameters on macroscopic parameters of sand," *Journal of northwest seismology*, vol. 33, no. S1, pp. 160–165, 2011.
- [14] X. T. Yin, Y. N. Zheng, and S. K. Ma, "Study on the internal scale ratio of geotechnical materials based on particle flow numerical test," *Rock and Soil Mechanics*, vol. 32, no. 4, pp. 1211–1215, 2011.
- [15] S. Yang and X. Q. Li, "Direct shear simulation and macro microanalysis of sand based on PFC~(3D)," *Chinese journal of computational mechanics*, vol. 36, no. 6, pp. 777–783, 2019.
- [16] S. Yang and X. Q. Li, "Simulation of PFC~(3D) sand soil with different particle shapes," *Water conservancy and hydropower technology*, vol. 50, no. 3, pp. 139–144, 2019.
- [17] L. Geng, Z. Q. Huang, and Y. Miao, "Microsimulation of triaxial test of coarse grained soil," *Journal of Civil Engineering and Management*, vol. 28, no. 4, pp. 24–29, 2011.
- [18] F. Wang, P. H. Xu, J. W. Gao, and B. Q. Lu, "Study on size effect of triaxial test of coarse grained soil based on PFC method," *Highway engineering*, vol. 39, no. 2, pp. 80–83–80162, 2014.
- [19] C. W. Yin, B. Ling, and L. G. Jiang, "Macroscopic and microscopic parameter analysis of sand based on particle flow method," *Journal of coal*, vol. 36, no. S2, pp. 264–267, 2011.

- [20] Y. H. Guo, Y. K. Tian, L. L. Wu et al., “Mechanical properties of tailings under different confining pressures under dry and wet cycling,” *Nonferrous metal engineering*, vol. 10, no. 4, pp. 87–93, 2020.
- [21] W. H. Liu, Q. Yang, X. W. Tang, and W. G. Li, “Mechanical properties of soils with different initial dry densities under dry-wet cycling conditions,” *Chinese journal of water resources*, vol. 45, no. 3, pp. 261–268, 2014.
- [22] X. L. Ning, *Mesoscopic Triaxial Simulation and Microstructure Study of Clay Soils (Doctor’s Degree Thesis)*, Zhejiang University, 2017.
- [23] D. D. Shi, J. Zhou, M. C. Jia, and D. X. Yan, “Particle flow simulation of high stress one-dimensional compression characteristics of granular sand,” *Journal of Geotechnical Engineering*, vol. 29, no. 5, pp. 736–742, 2007.
- [24] M. J. Jiang, J. M. Konrad, and S. Leroueil, “An efficient technique for generating homogeneous specimens for DEM studies,” *Computers and Geotechnics*, vol. 30, no. 7, pp. 579–597, 2003.
- [25] C. Shi, Q. Zhang, and S. N. Wang, “Numerical simulation technology and application of particle flow (PFC5.0),” *Rock and Soil Mechanics*, vol. 39, no. S2, p. 36, 2018.
- [26] T. Liu, B. Q. Lin, Q. L. Zhou, C. J. Zhu, and F. Z. Yan, “Mechanical behaviors and failure processes of precracked specimens under uniaxial compression: a perspective from microscopic displacement patterns,” *Tectonophysics International Journal of Geotectonics & the Geology & Physics of the Interior of the Earth*, vol. 672, pp. 104–120, 2016.

Research Article

Rib Spalling 3D Model for Soft Coal Seam Faces with Large Mining Height in Protective Seam Mining: Theoretical and Numerical Analyses

Shuai Liu,^{1,2,3} Ke Yang^{1,2,3}, Tong Zhang^{1,2,3}, and Chunan Tang^{1,4}

¹School of Resources and Civil Engineering, Northeastern University, Shenyang 110819, China

²Institute of Energy, Hefei Comprehensive National Science Center, Hefei 230031, China

³State Key Laboratory of Mining Response and Disaster Prevention and Control in Deep Coal Mines, Anhui University of Science and Technology, Huainan 232001, China

⁴School of Civil and Hydraulic Engineering, Dalian University of Technology, Dalian 116024, China

Correspondence should be addressed to Ke Yang; keyang2003@163.com and Tong Zhang; 1099731996@qq.com

Received 16 July 2020; Revised 18 August 2020; Accepted 23 August 2020; Published 24 September 2020

Academic Editor: Qiqing Wang

Copyright © 2020 Shuai Liu et al. This is an open access article distributed under the Creative Commons Attribution License, which permits unrestricted use, distribution, and reproduction in any medium, provided the original work is properly cited.

Fully-mechanized mining of coal face with a large cutting height is generally jeopardized by rib spalling disaster in the working face. Preventive measures based on undisturbed coal seam conditions fail to provide safe predictions, as large-scale fractures in soft coal face frequently appear before excavation due to mining-induced stresses. This paper investigates a case study of the Paner Mine 11224 working face in the Huainan mine area, China, which features an overlying protected layer in the protective seam mining. To simulate the failure process in such a mine, we elaborated a simplified physical-mechanical model of a coal wall that underwent shear failure and sliding instability, in compliance with the triangular prism unit criterion. Similar simulation experiments, theoretical calculations, and borehole monitoring were used to comprehensively analyze the overburden fracture and movement after mining the lower protective seam. The development height of three overburden zones was determined, and the characteristics of the protected layer affected by mining were obtained. The results show that the failure is mainly related to the roof load, coal cohesion, internal friction angle, coal seam inclination, and sidewall protecting force. The key to limiting the frictional sliding of a slip body is to reduce the roof load and increase the sliding coefficient and cohesion of the main control weak surface (MCWS). Besides, a self-developed three-dimensional numerical calculation software RFPA3D (Realistic Fracture Process 3D Analysis), which considered the rock heterogeneity, was used to reproduce a weak triangular prism's progressive failure process. The numerical simulation results agreed with the fracture pattern predicted by the theoretical model, which accurately described the rib spalling mechanisms in a soft coal face with a large cutting height and a protective layer.

1. Introduction

Sustainable development of the coal mining industry is quite topical, especially in China, where coal remains the main energy resource [1–3]. This problem comprehensive solution requires the account of such subtopics as the development of efficient mining technology [4–6], protection of the ecological environment and groundwater [7–9], clean use of methane [10, 11], and prevention and control of disasters caused by coal production [12, 13]. The primary sources of coal in China are thick continuous coal seams that account for about

45% of the total coal resource reserve and production [14]. Longwall fully-mechanized mining and top coal caving methods are mainly used for the most efficient mining of thick coal seams [15, 16]. When the thickness of a coal seam exceeds 3.5 m, longwall mining with top coal caving is generally adopted, but the problems of low recovery rate and complicated technology have not been adequately resolved [17–19]. With the improvement of mining equipment and management level of working face in recent years, a stope's cutting height was gradually increased. For coal seams with a thickness of 3.5–7.5 m, coal cutting of the full height can

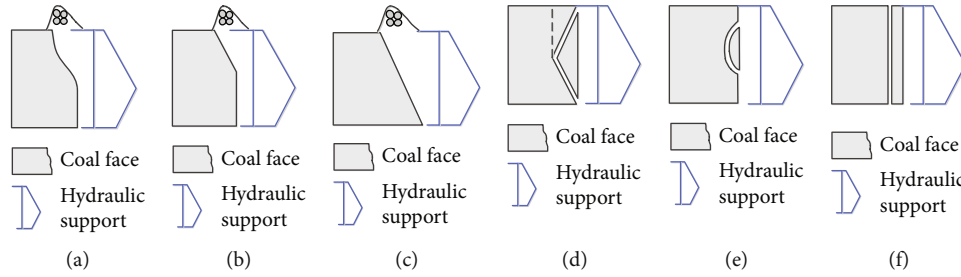


FIGURE 1: The common form of rib spalling in a working face with a large cutting height: (a–c) soft coal seam rib spalling; (d–f) hard coal seam rib spalling.

effectively overcome the above problems. However, an increase in cutting height can produce such problems as intense ground pressure, rib spalling, roof failure, support dumping, and sliding, which are hardly avoidable in the stope [20, 21]. In particular, rib spalling is the most common disaster when the working face coal seam is thick, yet becomes soft, which is a severe safety infringement. Simultaneously, the start-up rate of mining equipment is dramatically decreased, creating a less efficient system for fully mechanized mining with large cutting height. The instability caused by rib spalling of the surrounding rock supporting the stope has become a bottleneck restricting the technology's sustainable development. It is an urgent issue that needs to be resolved for safe and efficient extraction of soft, thick coal seams.

Coal wall fractures and slips during mining are known to cause the rib spalling of the working face, but the latter's mechanism is not well understood. Several physical-mechanical models based on the fracture characteristics and rib spalling location in thick coal seams with a large cutting height have been developed [22–24]. The influence of several parameters on the coal wall's stability and further preventive and control measures has also been proposed [25]. Field observations have shown that soft coal seams are prone to arcing or linear rib spalling on the upper part of the coal wall or the working face's overall shear slip. The immediate roof fall is usually synchronized with these three forms as well (Figures 1(a)–1(c)). The instability of hard coal seams is sudden and brittle. Depending on the occurrence location, the rib spall forms grooves or horizontal overall tensile fractures throughout the wall (Figures 1(d)–1(f)).

Several theoretical models have been proposed to describe these forms of rib spalling in a coal wall. Zhang et al. [26] proposed layered plate structure models using fracture damage and elastoplastic theories. Yin et al. [27] and Ning [28] improved the coal wall's deflection characteristics by using the proposed pressure bar structure model. Yuan et al. [25] established a mechanical model of the wedge-shaped sliding body of the coal wall and analyzed vital factors affecting a wedge-shaped body's stability. Hao et al. [29] applied the stochastic analysis method for slope engineering to establish a mechanical model of coal-face slippage for sections with a large mining height. Wang [30] proposed a shear failure model for soft, thick coal seams, which found wide practical and theoretical applications. Fu et al. [31] used the unloading rock mass mechanics theory and fracture mechanics theory to establish an unloading effect model of coal wall

excavation. They introduced a new instability criterion for a wedge-shaped structure. Yang et al. [32] studied the development of coal seam cracks formed during mining and analyzed coal wall instability's mechanical process using the slip line theory. Based on the unique geological background of coal mines, Wang et al. [33] proposed a coal wall rock beam model to analyze the influence of mining thickness on steep seam stability. Wu et al. [34] used the shear-slip failure criterion to establish a space stress model of the coal wall block elements in a working face. Pang et al. [35] elaborated on a tensile cracking-sliding model, which implied that it was problematic to prevent the coal wall from tensile cracking only by the force of the hydraulic support guard plate. Still, the latter could suppress the damaged body's sliding. Liu et al. [36] monitored the damage process in coal walls with a large mining height using the smart control system, which was found very effective. Chang et al. [37] used the Mohr-Coulomb criterion to derive the analytical expressions of coal wall horizontal displacement, fracture zone, and plastic zone radius. They also reported that the abutment pressure concentration factor, cutting height, and support resistance of support were the key factors controlling the rib spalling. Song et al. [38] used the Ritz method based on the displacement variation principle to analyze the coal wall failure mechanism and used a three-dimensional similarity simulation platform to study the coordinated deformation law of the "roof-support-coal wall" system.

The above research results have significantly improved the understanding of coal wall fracture and slip. However, most researchers reduced the coal wall instability problem to a plane strain problem when establishing the mechanical model of rib spalling. This approach is not suitable for some cases with complex three-dimensional failure characteristics. Moreover, the obtained failure mechanical models were mostly based on coal seam mining in its original state. Rib spalling in coal seams that have been disturbed by mining stress and have large-scale mining fractures before extracting are rarely studied. For gas outburst coal seams with low permeability, the protective-layer mining is the most effective method for regional elimination of gas outbursts hazards in protected coal seams [11]. The coal seams within a specific range of the top and bottom layers of the protective layer are depressurized to form mining cracks through the mining operation. This allows for increased permeability and degassing of the protected coal seam by pumping the methane out of the coal seam in advance [10]. Yet, this damages the

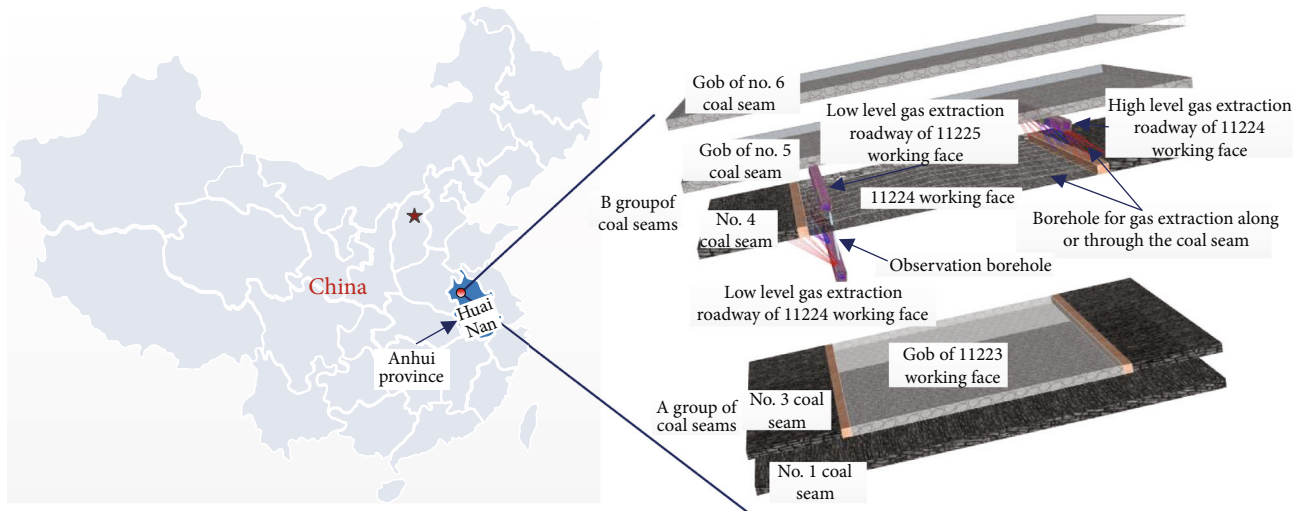


FIGURE 2: Distribution of the protective layer #3 coal seam and protected layer #4 coal seam.

integrity of coal rock mass before normal mining occurs. Further research is needed to determine failure, slip, and rib spalling in a large-height cutting face of protected coal seam. This would allow for the adoption of engineering measures to prevent and control rib spalling and improve the efficiency of fully mechanized mining face.

In this study, a simplified physical-mechanical model of a remote lower protective layer mining is established to determine the range of influence and coal wall instability during the protective-layer mining. This model includes overburden fracturing and movement based on simulation, theoretical analysis, and field measurements to improve model accuracy. The range of three vertical zones (caving zone, fracture zone, and bending-and-sinking zone) affected during protective mining was determined to model the range of influence of the protective mining under various conditions. Self-developed RFPA3D numerical calculation software was then used to simulate a large-height mining soft coal face's load instability to verify the proposed physical-mechanical model. The research results can guide the development of prevention and control measures, as well as ensure safe and efficient mining of a fully mechanized working face of a large-height, soft coal wall.

2. Project Overview

The case study mine is the Paner Coal Mine, located in the Huainan mine area, China, an important coal and electricity production base in eastern China. There are two coal seam strata groups in the mining area, A and B, with an inclination (dip angle) from 15 to 30°. Group A coal stratum is located in the lower part of group B coal strata with a thickness of 75–90 m. Seams #1 and #3 are mainly mined from the group A coal, while coal seams #4, #5, and #6 are mainly mined from group B coal. The test working face for this research is the first working face of coal seam #4, also called working face 11224. Working face 11224 has a burial depth of about 700 m and an average thickness of 3.5 m. Longwall fully mechanized mining with a large cutting height is currently

used to extract the working face. There is a high risk of coal and gas outburst of the coal seam #4, as it has a gas content of 12.5 m³/t and a gas pressure of 2.9 MPa. The recovery of #5 and #6 coal seams has been completed. #5 coal goaf is about 25 m away from #4 coal seam. Numerical analysis and on-site observations have shown that mining of #6 and #5 coal seams has not affected #4 coal seam. The research results have been published [39].

About 80 m of the #4 coal floor is the #3 coal, and the gas pressure and content are relatively low in the seam. A lower protective layer is also implemented during mining to eliminate the #4 coal seams outburst danger. The working face 11223 of the #3 coal is first mined, and pregas extraction is performed after the #4 coal pressure relief. The position of the two working faces is shown in Figure 2.

The stratigraphy and coal rock mass mechanical parameters of #3 and 4 coal seams were obtained through field coring and laboratory mechanical tests, as shown in Figure 3.

During the lower protective layer's mining process, the pregas extraction of the 11224 working face of the protected coal seam is exceedingly successful. The pressure and content of gas outburst coal seam were significantly reduced. During normal mining of the 11224 working face, the stope's surrounding rock integrity was poor, and rib spalling frequently occurred at varying degrees. Concurrently, the immediate roof fall of working face severely restricted the safe and efficient mining of the stope. Field observations found that rib spalling on the 11224 working face had complicated spatial rupture patterns. The rib spall traces are shown in Figure 4.

It can be seen from Figure 4 that rib spalling occurs in the upper part of the coal wall, area ① in Figure 1, and the exfoliated coal body is an irregular triangular prism. A top surface of this triangular prism is the coal seams top surface, and the side surface is almost parallel to the coal seam normal. At the same time, macrocracks penetrating the coal seam were observed in the traces. After rib spalling occurred in area ①, the coal body in areas ② and ③ was fractured and slipped. The exfoliated coal is also an irregular triangular prism, but its shape and volume are significantly different. Generally,

Lithology	Columnar	Strata thickness (m)	Density (kg.m ⁻³)	Elastic modulus (GPa)	Compressive strength (MPa)	Tensile strength (MPa)	Poisson's ratio	Remarks
4-2# Coal seam		1.00	1460	2.43	4.20	0.35	0.31	Rock group 3
Mudstone		1.00	2533	10.45	21.00	1.40	0.30	
4-1# Coal seam		3.50	1460	2.43	4.20	0.35	0.31	
Mudstone		6.80	2533	10.45	21.00	1.40	0.30	
Fine sandstone		1.30	2684	24.03	55.30	3.90	0.19	
Sandy mudstone		3.65	2605	16.90	43.50	2.00	0.23	
Mudstone		3.25	2567	11.37	21.00	1.40	0.32	
Flower-porphyrific mudstone		3.80	2433	6.39	22.50	1.50	0.23	
Oolitic mudstone		1.01	2433	6.39	22.50	1.50	0.23	
Aluminum mudstone		3.43	2433	6.39	22.50	1.50	0.23	
Coarse sandstone		12.01	2704	15.15	61.40	5.60	0.13	
Sandy mudstone		5.00	2565	21.64	43.50	2.00	0.27	Rock group 2
Mudstone		4.80	2567	11.37	21.00	1.40	0.32	
Fine sandstone		6.50	2720	18.01	55.30	3.90	0.21	SKS2
Silty mudstone		5.65	2565	21.64	43.50	2.00	0.27	Rock group 1
Siltstone		2.00	2705	9.86	55.30	3.90	0.18	
Mudstone		5.60	2689	10.45	21.00	1.40	0.30	
Fine sandstone		3.60	2720	18.01	55.30	3.90	0.21	
Siltstone		3.20	2705	9.86	55.30	3.90	0.18	
Medium-coarse sandstone		4.60	2741	27.46	61.40	5.60	0.15	
Silty mudstone		2.05	2565	21.64	40.00	2.00	0.27	
3# Coal seam		5.00	1460	2.43	4.08	0.34	0.31	
Sandy mudstone		1.50	2605	16.90	43.50	2.00	0.23	
1# Coal seam		3.50	1460	2.43	4.08	0.34	0.31	
Sandy mudstone		2.20	2494	16.90	43.50	2.00	0.23	

FIGURE 3: Stratigraphic column mechanical parameters of the strata between #3 and #4 coal seams.

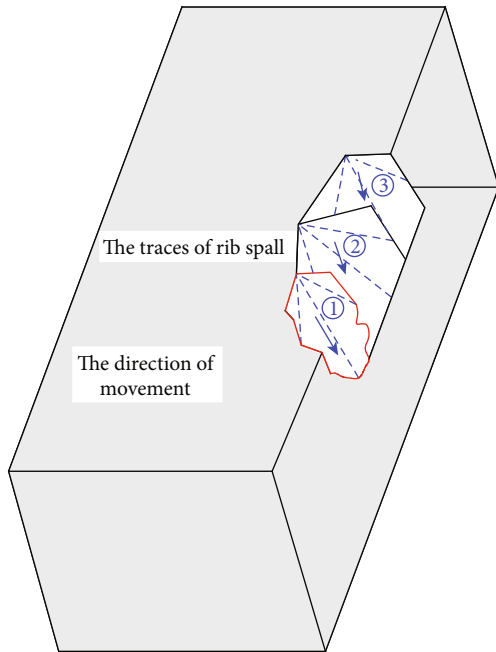


FIGURE 4: Rib spalling traces of the coal wall.

the rib spalling shape is relatively uniform in the same working face (Figure 1). The coal wall instability with a complex spatial rupture shape, such as 11224 working face, cannot

be reduced to the plane strain problem when establishing a mechanical model.

3. Mining Effects on the Protected Coal Seam

Pregas extraction of the protected layer was successful, indicating that the lower protective layer's exploitation changed the stress environment and the fracture distribution characteristics from the initial state of the 11224 working face. Therefore, it is necessary to study the disturbance effect of mining the 11223 working face on the #4 coal seam. The principal analysis distinguishes three vertical zones in the overburden of the protective layer's mined-out area after mining, because the overlying protected layer is located in a different spatial zone and has different degrees of disturbance and damage.

The key strata theory proposed by Qian et al. [40] implied that the structures of the region and key strata are the main factors determining the overlying strata's spatial structure above the goaf and the development height of these three zones of mining fractures. The key strata judgment theory proposed by Qian et al. [40] and Qu et al. [41] was used in this study to verify the presence of three subkey strata (SKS) between the #3 and #4 coal seams (Figure 3). Relatively weak rock layers controlled by each SKS belong to the same rock group, which moves synchronously with the corresponding SKS breaking.

TABLE 1: The proportions of materials to simulate various lithologies available between the two working faces.

Lithology	Weight proportion			
	Fine river sand	Lime	Gypsum	Water
Coal	10	0.5	0.5	1.1
Mudstone	10	0.7	0.3	1.1
Fine sandstone	6	0.6	0.4	0.7
Sandy mudstone	7	0.7	0.3	0.8
Coarse sandstone	8	0.6	0.4	0.9
Siltstone	9	0.5	0.5	1.0

3.1. Similar Simulation Test

3.1.1. The Simulation Scheme. Based on strata structural characteristics between #3 and #4 coal seams, a self-developed test device capable of bidirectional unequal pressure loading was used to simulate the inclined mining process of the 11223 working face. The size of the simulation platform was $2.4\text{ m} \times 0.2\text{ m} \times 2.0\text{ m}$ (length \times width \times height). In the test, fine river sand was used as aggregate and mixed with gypsum and lime as cement. Water was used as a binder, and mica was sprayed to simulate native layering. The preparation of similar materials and the establishment of physical models are not the focus of this article. Due to space limitations, the details can be found elsewhere, e.g., Ghabraie et al. [42]. The proportions of materials to simulate various lithologies are shown in Table 1, and the curing time of each material in the simulating test is about 15 days. The similar stress ratio was 1:160, and the simulated geometric and strength ratio was 1:100. The model's bottom surface was fixed, while the top surface and side surface were subjected to constant normal stress, respectively. A load of 0.096 MPa was applied to the physical model top to simulate the overburden weight. The lateral pressure coefficient was 1.442, so 0.138 MPa was applied in the horizontal direction. The artificial excavation was used to simulate the 11223 working face mining.

3.1.2. Similar Simulation Results. Figure 5 shows the characteristics of overburden mining-induced fractures after the extraction of the 11223 working face. After mining the 11223 working face, SKS1 and its controlling rock group 1 collapsed together and slipped towards the lower part of the mined-out area. Mining layer separation developed along the bottom of SKS2, and the caving zone stopped here. Subsequently, stratum fractures developed in the upper and middle sections of SKS2. With the rupture of SKS2, the fracture and movement occurred continuously in the controlling rock group 2. However, due to the limited collapse space, no new separation between layers appeared at the bottom of SKS3, and the development of the fracture zone stopped at the bottom of SKS3. The #4 coal seam is a synchronous moving layer controlled by SKS3. After mining, rock group 3 was located in the gob bending-and-sinking zone. Rock movement in the bending-and-sinking zone still maintained continuity and integrity. The amount of subsidence and

deformation of each section of this zone was small in the vertical section.

The physical simulation also found that many macrocracks in the normal direction appeared in the #4 coal seam and the surrounding area. The cracks' spatial location and scale were disordered, as shown in areas (a) and (b) in Figure 5. After mining the lower protective layer, the initial state of the #4 coal seam was broken. Normal direction fractures violated the integrity of the #4 coal with random distribution.

3.2. The Theoretical Basis of Height Calculation of Fracture Zones. Previous research results on the three zones of overburden's development height are mostly reduced to empirical formulas derived via statistical processing. Still, the calculation results do not typically embody actual measurements. Xu et al. [43] assumed that the primary key stratum's spatial position could be based on similar simulation results and field measurements to determine the fracture zone's height. However, this model failed to consider multiple SKS in the overburden during deep mining. For deep mining, Yang et al. [44] used the key stratum theory to treat each subkey stratum as a thin sloping plate fixed around a central position. A calculation model of the three-overburden zones' development height was elaborated by analyzing the breaking conditions of subkey strata. According to this model, the three zones' development status in the overlying strata above the stope was determined by key strata structure, mining height, and rock expansion coefficient. Assuming the stope mining thickness of m (i.e., full thickness of the coal seam), n rock layers under a certain SKS, the thickness of each rock layer of H_i , and the corresponding fracture expansion coefficient of r_i , the SKS breaking conditions would be as follows:

$$m - H_1(r_1 - 1) - \sum_i^n H_i(r_i - 1) > 0. \quad (1)$$

If rock stratum below SKS1 satisfies formula (1) when SKS1 reaches its limit span, it breaks, and the fracture zone develops to the bottom of SKS2. Then, if the rock stratum below SKS2 satisfies formula (1) when SKS2 reaches its limit span, it breaks, and the fracture zone continues to develop to the bottom of SKS3. Until the rock strata below the SKS fails to satisfy formula (1), the fracture zone height ends at the bottom of the first unbroken SKS.

3.3. Borehole Monitoring

3.3.1. The Monitoring Scheme. On-site monitoring is the most intuitive and reliable method to study layer fractures and movement. The low-level gas extraction roadway of the 11224 working face is located in SKS3, 25 m away from the #4 coal seam. The low-level gas extraction roadway of the 11225 working face is located 21 m above the #4 coal roof and is a predraining roadway for the #5 coal seam. The horizontal distance between the two roadways is 13 m. A monitoring borehole was placed at an inclined slope of 75° in the 11224 low-level gas extraction roadway roof. The observation

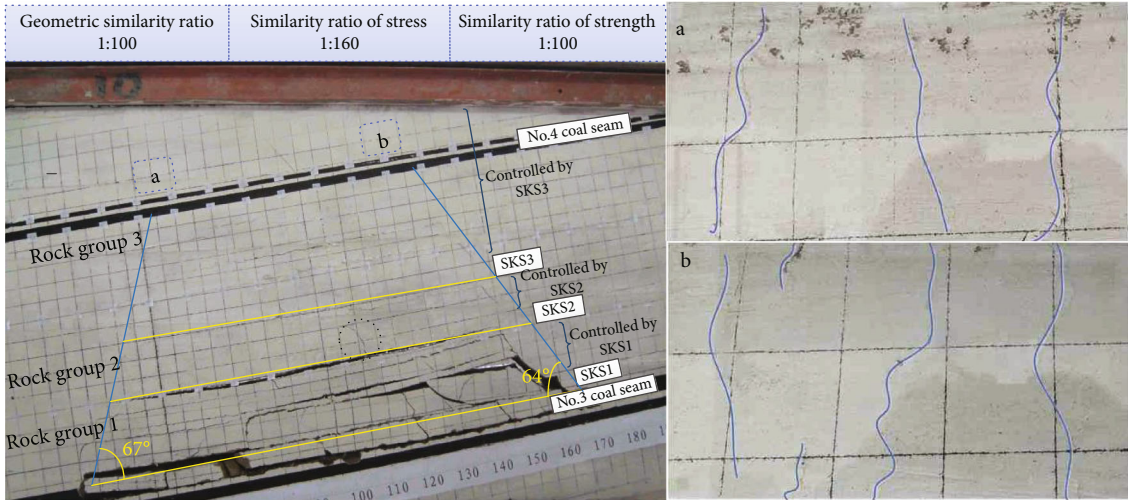


FIGURE 5: Development characteristics of fractures in the overlying strata during mining of the lower protective #3 coal seam.

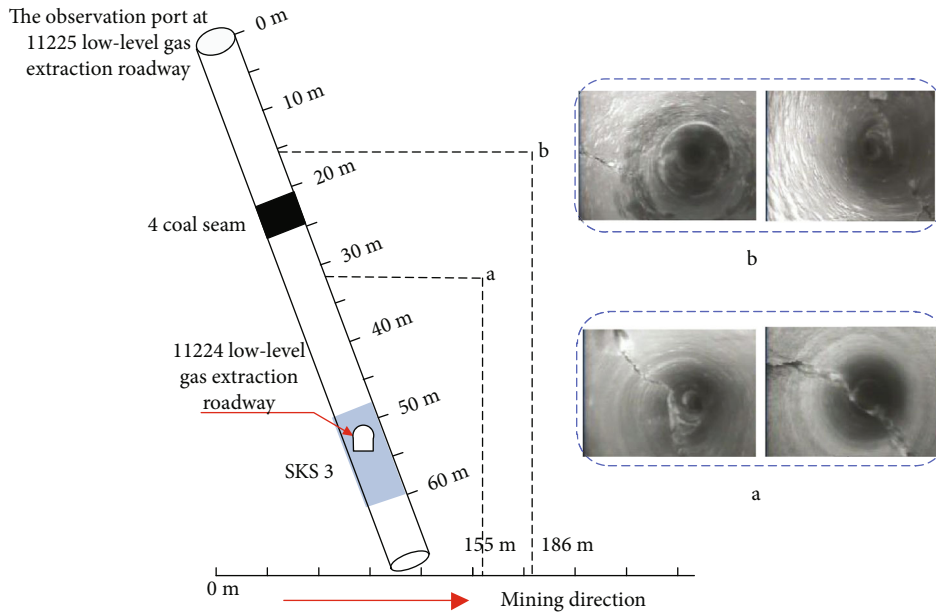


FIGURE 6: Observation results of borehole monitoring during the mining of 11223 working face. (a) Vertical cracks penetrating the layer at a depth of 32 m; (b) Vertical cracks formed at a depth of 16 m.

port is located at the bottom of the 11225 low-level gas extraction roadway. The borehole spatial position is shown in Figure 2. To monitor the protected seams disturbing characteristics after mining the 11223 working face, a rock drilling detector was used to observe the borehole wall's deformation.

3.3.2. *The Monitoring Results.* The observation results are shown in Figure 6. When 11223 working face passed the observation port 155 m, vertical cracks penetrating the rock layers were observed at a depth of 32 m, as shown in Figure 6(a). When working face passed observation port 186 m, #4 coal seam collapsed and blocked the borehole. Vertical cracks were also observed at a depth of 16 m, as shown in Figure 6(b). During the mining of 11223 working face, no

layer separation was monitored in the borehole, indicating that SKS3 did not break. However, vertical fractures were widely observed. Therefore, the disturbed rock layers around #4 coal seam were located in the overburden bending-and-sinking zone. Fractures paralleled to the borehole appeared in the protected coal seams vicinity, which was consistent with physical simulation results. Simultaneously, macronormal penetrating fractures were more intuitively observed during the mining of 11224 working face, as shown in Figure 7.

3.4. *Comprehensive Analysis.* Similar simulations show that after mining the 11223 working face, the fracture zone that transmits water ceases at the bottom of SKS3. Also, the #4 coal protected layer was located in a bending-and-sinking

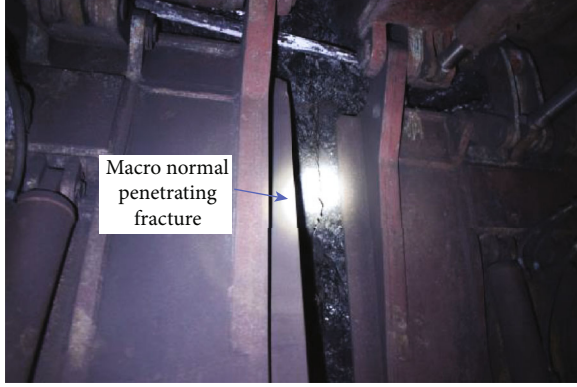


FIGURE 7: Macronormal penetrating fracture in the 11224 working face.

overburden zone. However, due to the test rig's limited size in the indoor physical simulation experiment, limit spans of key stratum may not be reached. Therefore, it is not possible to accurately determine the development status of the three overburden zones simply based on the experimental results.

Equation (1) is the SKS breaking criterion obtained based on the thin plate theory [45]. Given the lack of measured data on the layer expansion coefficient in the overburden of the 11223 goaf, Hao [46] results on the Yangquan Coal Mine with similar geological conditions were used in this study.

$$r = 1.083 - 0.017 \cdot \ln(h) \quad h < 100m, \quad (2)$$

where r is the rock expansion coefficient, and h represents the vertical distance from the coal seam.

Based on the measured expansion coefficient of rock layers and values from the Yangquan Coal Mine, it was calculated that only SK1 and SKS2 fractures occurred in the overburden of the 11223 working face, and the fracture zone stopped at the base of SKS3. The weak rock penetration controlled by SKS3 was located in the bending-and-sinking zone, including the #4 coal seam. Borehole monitoring observed mining fractures near the #4 coal, but no layer separation occurred. It was inferred that SKS3 did not fracture after extracting the 11223 stope. Similar simulations, theoretical analysis, and borehole monitoring conclusions are consistent. All results reflect that the #4 coal protected layer is located in the bending-and-sinking overburden zone. Coal and rock layers in the bending-and-sinking zone are typically less affected by mining the lower protective layer, and no large-scale severe mining damage occurs.

Macrocracks along the normal direction of rock layers appeared in the area near the #4 coal seam, and they were also all observed in similar simulation and borehole monitoring. This phenomenon was also seen during normal mining of the 11224 working face. It shows that the protective layer #3 coal mining affected the original rock state of the protected layer #4 coal located in the bending-and-sinking zone; the #4 coal was not seriously fractured. The coal rock mass, which had good integrity before mining, was intersected by randomly distributed fractures.

4. A Mechanical Model for Rib Spalling of Protected Coal Seam

4.1. Physical Mechanics Model. The previous analysis shows that the 11224 working face is affected by the mining of the lower protective layer even though it is located in the continuous bending overburden zone. Even in this zone, there were already several randomly distributed normal-direction fractures before mining began. Affected by the advanced abutment pressure, the coal wall properties gradually deteriorated during the mining process. The normal direction fractures in the coal body in front of the working face continued to develop and penetrate due to the increasing abutment pressure, thus forming weak joint faces of different sizes [47]. The existence of joint cracks and a weak surface dramatically reduces the coal body's integrity and increases the difficulty in controlling the coal wall's stability [48].

The study here suggests that the weak surface that is the largest and has a main mechanical control role is the main control weak surface (MCWS) among the joint cracks. The MCWS divides a coal body adjacent to the working face into units and has weak mechanical bonds with the surrounding coal bodies. Due to the coal body's roof pressure and weight, the soft coal unit undergoes shear failure to a certain height and direction to form a slip body. When the surrounding unit fails to restrict the slipping body's sliding along the weak surface, rib spalling forms. Due to the randomness of the MCWS distribution, the morphology of the unit body is different. The unit on the side of the coal wall facing the air can be reduced to a triangular prism by determining the MCWS, as shown in Figure 8.

Based on the above simplification, a three-dimensional mechanical model of coal wall instability in the protected large-cutting height soft coal working face, as shown in Figure 8, is established. The intersection of MCWS $abcd$ and MCWS $bfec$ formed by mining operation creates the triangular prism $abfdec$ with a weak mechanical bond with the surrounding coal bodies. The shear failure criterion of a triangular prismatic unit with an arbitrary shape and the sliding criterion of the slip body are proposed based on the Mohr-Coulomb criterion. Most of the actual shear slips are curved surfaces. Due to the limited height of the coal wall and rib spalling, the fracture surface is treated as a plane for strength analysis convenience.

4.2. Shear Failure Criterion of Unit. Triangular prism $abfdec$ undergoes shear failure along MCWS $abcd$ and MCWS $bfec$ due to the roof pressure, gravity, sidewall protecting force, and the surrounding unit confining pressure. The shear fracture traces ba' and bf' are formed, respectively, and the surface $ba'f'$ formed by the intersection of the two traces is the unit fracture surface. The sidewall protecting force provided by hydraulic support is P_h , and the confining pressure of the surrounding unit on MCWS $abcd$ and MCWS $bfec$ can be derived as:

$$P_w = P_v \cdot \nu / (1 - \nu). \quad (3)$$

Where P_w is the normal stress on MCWS, P_v is the combined force of the roof load and vertical component of gravity along MCWS, and ν is Poisson's ratio of a coal body. It is

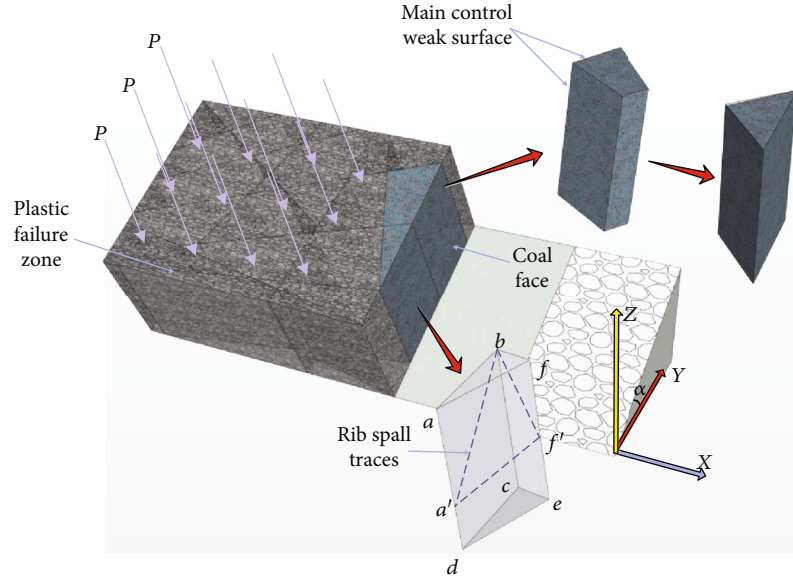


FIGURE 8: Physical-mechanical model of coal wall failure in a protected soft coal seam with large cutting height. P is the normal load on the coal wall, and α is the inclination of the coal seam (dip angle).

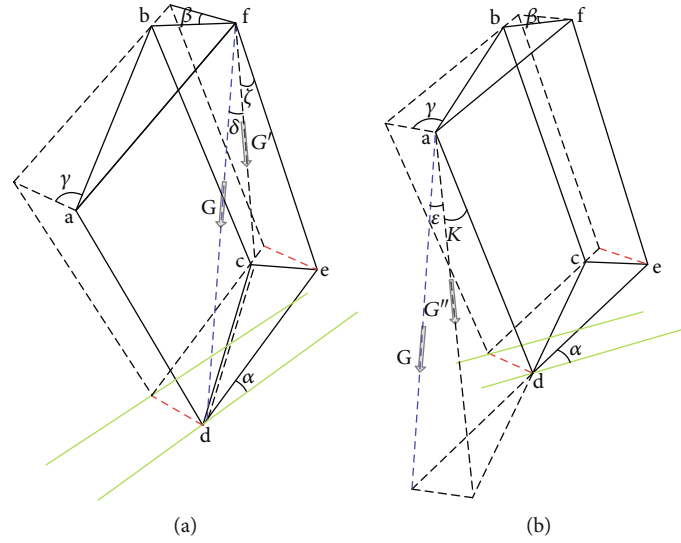


FIGURE 9: The component of gravity on MCWS. (a) The component of gravity on MCWS $bfec$. (b) The component of gravity on MCWS $abcd$.

assumed that $P_h < P_w < P_v$. When applying the Mohr-Coulomb criterion to the strength analysis of a triangular prism, the intermediate principal stress P_w is not considered, and its fracture surface is parallel to P_w .

Figure 9 depicts the spatial components of gravity of the coal body on the two MCWS of the triangular prism. From the spatial geometric relationship in Figure 9, we can obtain:

$$\cos \delta = \sqrt{1 - \sin^2 \alpha \cos \beta^2} \quad G' = G \cos \delta \quad \sin \zeta = \frac{\sin \beta \tan \alpha}{\sqrt{1 + \sin^2 \beta \tan^2 \alpha}} \quad \cos \zeta = \frac{1}{\sqrt{1 + \sin^2 \beta \tan^2 \alpha}}, \quad (4)$$

$$\cos \varepsilon = \sqrt{1 - \sin^2 \alpha \cos \gamma^2} \quad G'' = G \cos \varepsilon \quad \sin \kappa = \frac{\sin \gamma \tan \alpha}{\sqrt{1 + \sin^2 \gamma \tan^2 \alpha}} \quad \cos \kappa = \frac{1}{\sqrt{1 + \sin^2 \gamma \tan^2 \alpha}}. \quad (5)$$

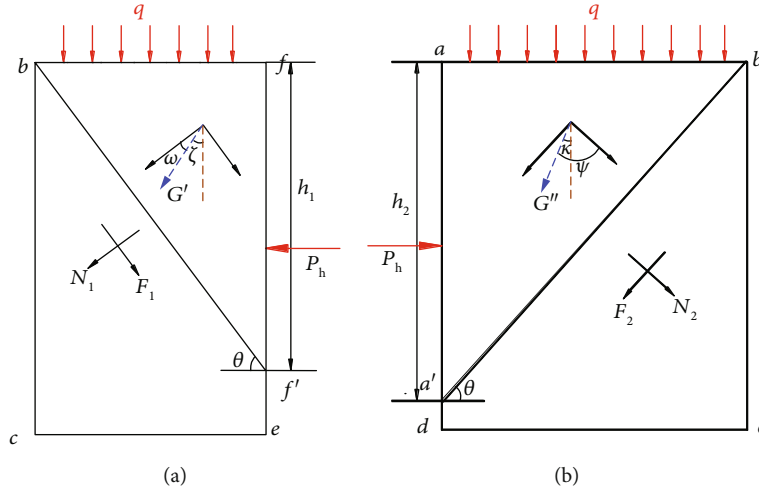


FIGURE 10: Analysis of shear failure of MCWS. (a) MCWS $bfec$. (b) MCWS $abcd$.

Here, G is the gravity of the coal wall slip body, G' is the component of G on MCWS $bfec$, and G'' is the component of G on MCWS $abcd$; β and γ are the angles between MCWS $bfec$, MCWS $abcd$, and the coal seam strike, respectively, and are random; δ and ε are the angles between the direction of G , MCWS $bfec$, and MCWS $abcd$, respectively; ζ and κ are the angles between the component of G on the MCWS $bfec$, MCWS $abcd$, and the coal wall.

According to the Mohr-Coulomb strength theory, the failure criterion of MCWS $bfec$ and MCWS $abcd$ can be expressed as the difference between the sliding force F along the shear plane and the shear resistance force D . If the difference is greater than 0, shear failure occurs in the triangular prism unit:

$$W = F - D \geq 0. \quad (6)$$

Figure 10 depicts a schematic diagram of the shear fracture of MCWS, where θ is the angle between the shear plane and the coal wall; q is the load concentration of the roof, and N is the normal stress on the shear plane. h_1 is the shear failure height of MCWS $bfec$; N_1 is the normal stress on the MCWS $bfec$ shear surface; F_1 is the sliding force on the shear plane of MCWS $bfec$; h_2 is the shear failure height of MCWS $abcd$; N_2 is the normal stress on the MCWS $abcd$ shear surface; F_2 is the sliding force on the shear plane of MCWS $abcd$.

From the geometric relationship of the components in Figure 10(a), we can obtain:

$$P_1 = qh_1 \cot \theta, \quad (7)$$

$$\omega = \theta - \zeta, \quad (8)$$

$$N_1 = P_1 \cos \theta + G' \cos \omega + P_h h_1 \sin \theta. \quad (9)$$

Assuming that the width of the sliding surface is 1 m, the sliding force and shear resistance force are the following, respectively:

$$F_1 = P_1 \sin \theta + G' \sin \omega + P_h h_1 \cos \theta, \quad (10)$$

$$D_1 = Ch_1 \csc \theta + N_1 \tan \varphi, \quad (11)$$

where C is the cohesion of coal, and φ is the internal friction angle.

The substitution of Eq. (9) into Eq. (11) gives:

$$D_1 = Ch_1 \csc \theta + \left(P_1 \cos \theta + G' \cos \omega + P_h h_1 \sin \theta \right) \tan \varphi. \quad (12)$$

After substituting Eq. (10) and (12) into Eq. (6), W_1 can be defined as:

$$W_1 = P_1 \sin \theta + G' \sin \omega - P_h \cos \theta - Ch_1 \csc \theta - \left(P_1 \cos \theta + G' \cos \omega + P_h h_1 \sin \theta \right) \tan \varphi. \quad (13)$$

Substituting Eq. (4), (7), and (8) into Eq. (13) gives:

$$\begin{aligned} W_1 = & qh_1 \cot \theta (\sin \theta - \cos \theta \tan \varphi) \\ & - Ch_1 \csc \theta + G \sqrt{1 - \sin^2 \alpha \cos^2 \beta} \\ & \times \left((\sin \theta - \cos \theta \sin \beta \tan \alpha) / \left(\sqrt{1 + \sin^2 \beta \tan^2 \alpha} \right) \right. \\ & \left. - (\cos \theta + \sin \theta \sin \beta \tan \alpha) \tan \varphi / \left(\sqrt{1 + \sin^2 \beta \tan^2 \alpha} \right) \right) \\ & - P_h (\cos \theta + \sin \theta \tan \varphi). \end{aligned} \quad (14)$$

Similarly, from Figure 10(b):

$$P_2 = qh_2 \cot \theta, \quad (15)$$

$$\psi = \theta + \kappa, \quad (16)$$

$$N_2 = P_2 \cos \theta + G'' \cos \psi + P_h h_2 \sin \theta, \quad (17)$$

$$D_2 = Ch_2 \csc \theta + \left(P_2 \cos \theta + G'' \cos \psi + P_h h_2 \sin \theta \right) \tan \varphi, \quad (18)$$

$$F_2 = P_2 \sin \theta + G'' \sin \psi + P_h h_2 \cos \theta. \quad (19)$$

By substituting Eq. (18) and (19) into Eq. (6), W_2 is expressed as:

$$W_2 = P_2 \sin \theta + G' \sin \psi - P_h \cos \theta - Ch_2 \csc \theta - \left(P_2 \cos \theta + G' \cos \psi + P_h \sin \theta \right) \tan \varphi. \quad (20)$$

Substituting Eq. (5), (15) and (16) into Eq. (20) gives:

$$\begin{aligned} W_2 = & qh_2 \cot \theta (\sin \theta - \cos \theta \tan \varphi) \\ & - Ch_2 \csc \theta + G\sqrt{1 - \sin^2 \alpha \cos^2 \gamma^2} \\ & \times ((\sin \theta + \cos \theta \sin \gamma \tan \alpha) / (\sqrt{1 + \sin^2 \gamma \tan^2 \alpha})) \\ & - (\cos \theta - \sin \theta \sin \gamma \tan \alpha) \tan \psi / (\sqrt{1 + \sin^2 \gamma \tan^2 \alpha}) \\ & - P_h (\cos \theta + \sin \theta \tan \varphi). \end{aligned} \quad (21)$$

When both W_1 and W_2 exceed zero, the triangular prism $abfdce$ undergoes shear failure along the surface $ba'f'$ to form a slip body. Equation (22) is the shear failure criterion of the coal wall unit considering the confining pressure:

$$\left\{ \begin{array}{l} qh_1 \cot \theta (\sin \theta - \cos \theta \tan \varphi) - Ch_1 \csc \theta + G\sqrt{1 - \sin^2 \alpha \cos^2 \beta^2} \\ \times \left(\frac{\sin \theta - \cos \theta \sin \beta \tan \alpha}{\sqrt{1 + \sin^2 \beta \tan^2 \alpha}} - \frac{\cos \theta + \sin \theta \sin \beta \tan \alpha}{\sqrt{1 + \sin^2 \beta \tan^2 \alpha}} \tan \varphi \right) \\ - P_h (\cos \theta + \sin \theta \tan \varphi) \geq 0 \\ qh_2 \cot \theta (\sin \theta - \cos \theta \tan \varphi) - Ch_2 \csc \theta + G\sqrt{1 - \sin^2 \alpha \cos^2 \gamma^2} \\ \times \left(\frac{\sin \theta - \cos \theta \sin \gamma \tan \alpha}{\sqrt{1 + \sin^2 \gamma \tan^2 \alpha}} - \frac{\cos \theta + \sin \theta \sin \gamma \tan \alpha}{\sqrt{1 + \sin^2 \gamma \tan^2 \alpha}} \tan \varphi \right) \\ - P_h (\cos \theta + \sin \theta \tan \varphi) \geq 0 \end{array} \right. \quad (22)$$

In Eq. (22), which determines the unit spatial shape, G , h_1 , h_2 , β , γ , and θ are constant values. Therefore, shear failure in the unit is mainly related to the roof load q , coal cohesion C , internal friction angle φ , coal seam inclination α , and sidewall protecting force P_h . Prevention and control of rib spalling should start by reducing the roof load and increasing coal cohesion, the internal friction angle, and the sidewall protecting force. Increasing the inclination of the coal seam can reduce the influence of gravity and roof pressure in the coal seam normal direction, but increases the difficulty of antifall and antislip control of the hydraulic support.

4.3. The Sliding Criterion of the Slip Body. A slip body forms after triangular prism shear failure. When the MCWS and protection measures are not sufficient to restrict the sliding of a slip body, it will slip along the fracture surface $ba'f'$ to form a rib spall. Rib spalling often occurs during coal cutting and support removal, so the effect of sidewall protecting force on the slip body is not considered.

According to Eq. (3), the normal pressure of the two MCWS are

$$\begin{aligned} P_{w1} &= (P_1 + G' \cos \zeta) \nu / (1 - \nu), \\ P_{w2} &= (P_2 + G'' \cos \kappa) \nu / (1 - \nu). \end{aligned} \quad (23)$$

The sliding force τ parallel to MCWS is

$$\begin{aligned} \tau_1 &= P_1 \sin \theta + G' \sin \omega, \\ \tau_2 &= P_2 \sin \theta + G'' \sin \psi. \end{aligned} \quad (24)$$

The stability coefficient K of the slip body can be expressed as:

$$\begin{aligned} K = & (P_1 \sin \theta + G' \sin \omega + P_2 \sin \theta + G'' \sin \psi) \\ & / \left(\mu_1 (P_1 + G' \cos \zeta) \nu / (1 - \nu) + \frac{1}{2} C_1 h_1^2 \cot \theta \right. \\ & \left. + \mu_2 (P_2 + G'' \cos \kappa) \nu / (1 - \nu) + \frac{1}{2} C_2 h_2^2 \cot \theta \right), \end{aligned} \quad (25)$$

where μ_1 and μ_2 are the sliding coefficients of MCWS $b'fec$ and MCWS $abcd$, respectively, while C_1 and C_2 are MCWS's cohesion coefficients.

At $K > 1$, the slip body will cause frictional sliding. At $K \leq 1$, even if the unit has been broken, there will be no sliding instability, and no rib spalling would occur in the coal wall. Therefore, the key to limiting the frictional sliding of a slip body is to reduce the roof load and increase the sliding coefficient and cohesion of the MCWS.

5. Numerical Simulation

5.1. Brief Description of RFPA3D. The difference in the mechanical properties of various mineral components and defects, such as pores and fissures, determines that natural rock is a complex heterogeneous material. Tang et al. [49–51] developed an analysis system for simulating the failure process of heterogeneous rock materials-RFPA2D. This software is based on the mesoelement elastic damage constitutive relationship and combines the statistical distribution assumptions of material properties with finite element calculation methods. The maximum tensile stress criterion and the Mohr-Coulomb criterion are used to determine when these elements reach their damage thresholds. In contrast to conditional finite element numerical calculation software programs, RFPA can simulate the initial cracking, deformation localization, and fracture in the rock failure process, so that the application of finite element technology can be developed to simulate the whole process of rock failure. RFPA3D is based on the development of RFPA2D software. In this study, a numerical analysis was performed with RFPA3D to simulate the damage and fracture process of a triangular prism under the roof load and confining pressure.

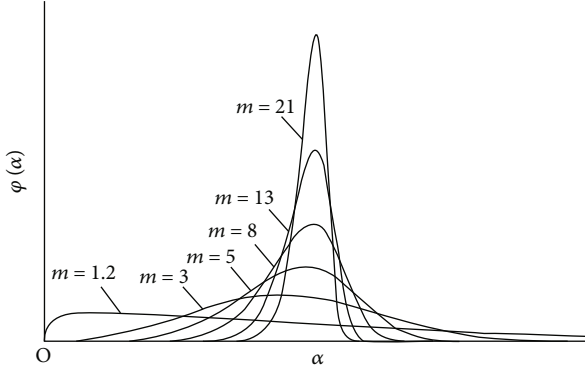


FIGURE 11: Weibull distribution for material parameters with different indices m .

5.2. *Material Heterogeneity Description.* Weibull first proposed a method to describe the heterogeneity of materials using statistical mathematics. The Weibull theory states that it is impossible to accurately measure the strength of the mesoscopic element at the time of failure, but rather, the probability of failure at a given stress level can be defined. RFPA3D assumes that the distribution of the mesoscopic elements' mechanical properties is statistical and introduces the Weibull distribution function to describe the statistical distribution density of the mechanical properties of the mesoscopic element:

$$\varphi(\partial) = \frac{m}{\partial_0} \cdot \left(\frac{\partial}{\partial_0}\right)^{m-1} \cdot e^{-\left(\frac{\partial}{\partial_0}\right)^m}, \quad (26)$$

where ∂ is the mechanical parameter (strength, elastic modulus, etc.) of the rock mesoscopic elements, ∂_0 is its average value, and m is the uniformity coefficient, which reflects the uniformity of the rock medium. Figure 11 shows the statistical distribution of the mechanical properties of the mesoscopic elements with different uniformity coefficients. Tang et al. [50, 52] have a detailed introduction on the effect of homogeneity on the macroscopic response of a sample.

5.3. *The Constitutive Relationship of the Mesoscopic Element.* It is widely recognized that stress in a rock body induces microcracks that propagate throughout the internal rock structure. These microcracks are caused by nonplastic deformation and contribute to the nonlinearity of the stress-strain curve. This also illustrates the rock fracture mechanism from the mesostructural standpoint. Therefore, it is reasonable to use elastic damage mechanics' constitutive relationship to describe the mechanical properties of mesoscopic elements of the rock body. Furthermore, according to the strain equivalent hypothesis, the strain caused by the stress σ acting on the damaged material is equivalent to the strain caused by the effective stress $\tilde{\sigma}$ acting on the intact material:

$$\begin{cases} \varepsilon = \frac{\sigma}{E} = \frac{\tilde{\sigma}}{E_0} = \frac{\sigma}{E_0(1-D)}, \\ \sigma = E_0(1-D)\varepsilon \end{cases} \quad (27)$$

where E_0 and E are the elastic moduli before and after damage, respectively, and D is the damage variable. $D = 0$ repre-

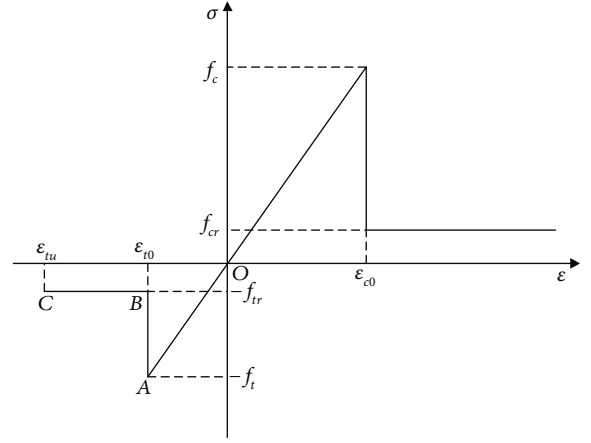


FIGURE 12: Mechanical behavior model of a mesoscopic element under uniaxial loading.

sents a nondamaged state, $D = 1$ represents a complete loss of bearing capacity, and $0 < D < 1$ corresponds to various degrees of damage. In the initial state, the mesoscopic elements are all elastic, and their mechanical properties are expressed by their elastic moduli and breaking ratios. With a change in external conditions, the stress or strain state of the mesoscopic elements changes and is calculated by the elastic finite element program. Each element has a damage threshold where the coal body will be damaged beyond this point. Figure 12 shows the constitutive relationship of elastic damage of an element under the uniaxial stress state. Based on this, the constitutive relationship is extended to the three-dimensional stress state.

In the uniaxial tension state, the constitutive relationship of the mesoscopic element's elastic damage is shown in the left section of the coordinate axis in Figure 12. The expression of the damage variable is

$$D = \begin{cases} 0 & \varepsilon_{t0} \leq \varepsilon \leq 0 \\ 1 - \frac{f_{tr}}{E_0\varepsilon} & \varepsilon_{tu} \leq \varepsilon \leq \varepsilon_{t0}, \\ 1 & \varepsilon \leq \varepsilon_{tu} \end{cases} \quad (28)$$

where f_{tr} is the residual tensile strength of the element, ε_{t0} is the tensile strain corresponding to the elastic limit, which is the tensile damage strain threshold, and ε_{tu} is the ultimate tensile strain of the element when the uniaxial tensile strain reaches the limit. When the tensile strain is reached, the element is completely damaged and reaches a fractured state, i.e., $D = 1$. When the element is in a three-dimensional stress state and assuming that the damage is still isotropic, the equivalent strain $\tilde{\varepsilon}$ is used to replace the tensile strain ε in Eq. (28). The equivalent strain is derived from the following relationship: $\tilde{\varepsilon} = \sqrt{\langle -\varepsilon_1 \rangle^2 + \langle -\varepsilon_2 \rangle^2 + \langle -\varepsilon_3 \rangle^2}$, where $\langle \rangle$ is a function defined as follows:

$$\langle x \rangle = \begin{cases} x & x \geq 0 \\ 0 & x < 0 \end{cases} \quad (29)$$

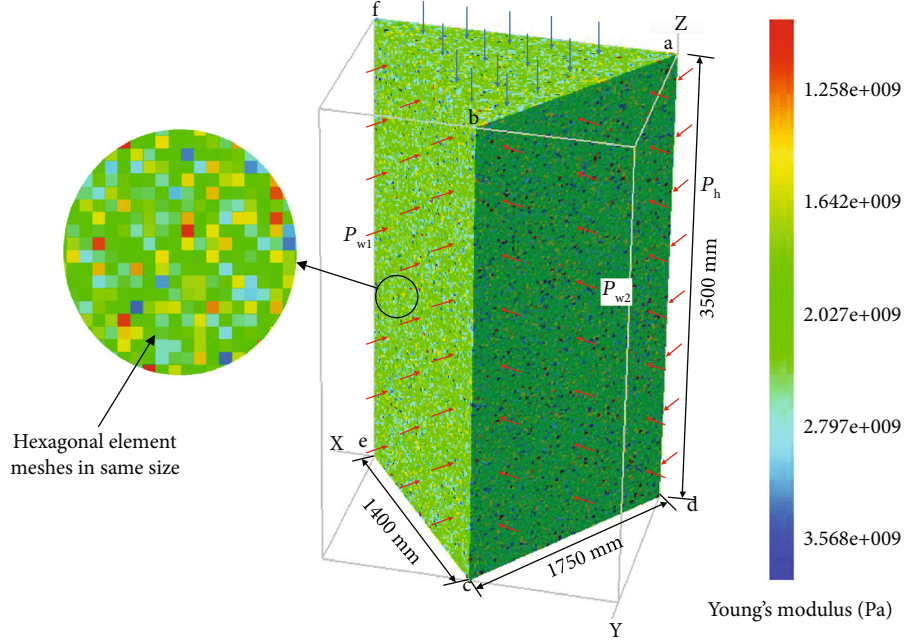


FIGURE 13: Triangular prism numerical model using the RFPA3D code.

The Mohr-Coulomb criterion is used as the damage threshold criterion when the shear damage of a mesoscopic element is caused by uniaxial compression or shear stress:

$$F = \sigma_1 - \frac{1 + \sin \phi}{1 - \sin \phi} \sigma_3 \geq f_c, \quad (30)$$

where ϕ is the internal friction angle of the mesoscopic element, f_c is the uniaxial compressive strength of the mesoscopic element, while σ_1 and σ_3 are the maximum and minimum principal stresses, respectively. In compliance with the constitutive relationship of the element's uniaxial tensile stress, its elastic damage constitutive relationship under the uniaxial compression stress of the element is shown on the right side of the coordinate axis in Figure 12. The damage variables are

$$D = \begin{cases} 0 & \varepsilon \leq \varepsilon_{c0} \\ 1 - \frac{f_{cr}}{E_0 \varepsilon} & \varepsilon_{c0} \leq \varepsilon \end{cases}, \quad (31)$$

where f_{cr} is the compressive residual strength of the element, and ε_{c0} is the maximum compressive strain.

$$\varepsilon_{c0} = \frac{1}{E_0} \left[f_c + \frac{1 + \sin \phi}{1 - \sin \phi} \sigma_3 - \mu(\sigma_1 + \sigma_2) \right], \quad (32)$$

where σ_2 is the intermediate principal stress and μ is Poisson's ratio. The constitutive relationship in the state of one-dimensional compressive stress is extended to a three-dimensional one. When the element has the triaxial stress state and satisfies the Mohr-Coulomb criterion, the maximum compressive principal strain ε_1 is used to replace the

uniaxial compressive strain in Eq. (31), and ε_{c0} is derived via Eq. (32). The expression of the damage variable takes the following form:

$$D = \begin{cases} 0 & \varepsilon_1 \leq \varepsilon_{c0} \\ 1 - \frac{f_{cr}}{E_0 \varepsilon} & \varepsilon_{c0} \leq \varepsilon_1 \end{cases}. \quad (33)$$

The RFPA3D analysis system adopts the assumption that the damaged element still has a specific stiffness and bearing capacity. Only the maximum principal tensile strain of the element reaches the ultimate tensile strain, and at $D = 1$, the element is considered to be completely fractured. Notably, the treatment of cracks in the RFPA3D system is not to remove the primitive from the model but to replace the original solid primitive with a very low elastic modulus. Moreover, due to the extremely low elastic modulus of the new primitives, solid media's behavior can be approximated as nonexistent. In this way, without changing the mathematical structure, the model can reflect the change in physical characteristics caused by the primitives' rupture in terms of the overall characteristics.

5.4. Mechanical Model and Parameters. Based on the physical model of the triangular prism unit of a coal wall, the corresponding numerical model is constructed using the RFPA3D. The dimensions of the triangular prism $abfdce$ model are shown in Figure 13. As the triangular prism has an arbitrary shape in the theoretical model, there is no special requirement for the model size. In this simulation, the model's height of 3500 mm is consistent with the site cutting height. The lengths of cd and ce sides are set as 1750 and 1400 mm, respectively. The model contains 392,000 hexahedrons of

TABLE 2: Material properties of a triangular prism for the numerical model.

Parameter	Value
Homogeneity index m	5
Average elastic modulus/GPa	2.43
Poisson's ratio	0.31
Mean of uniaxial compressive strength/MPa	4.2
Compressive-to-tensile strength ratio	12
Residual coefficient	0.2

the same size. The elastic modulus and uniaxial compressive strength of the mesoscopic element are set via the Weibull distribution based on Eq. (26). The bottom surface dec is fixed, while the top surface afb is subjected to a displacement load (an 8 mm increment per step). Surfaces $bfec$ and $abcd$ are subjected to constant normal stress to simulate the confining pressure applied by the surrounding elements on the triangular prism. The initial vertical stress of 11224 working face is about 17.5 MPa. The peak abutment stress measured by five coal stress detectors ahead of the working face is about 22.2~26.8 MPa, and the distance from the coal wall is 9.6~12 m. Monitoring data show that the vertical pressure at 6 m from the coal wall is 7.6 MPa. As the coal body, Poisson's ratio is 0.31, from Eq. (3), the confining pressure applied to $bfec$ and $abcd$ surfaces is 3.4 MPa. Surface $afed$ is subjected to a constant normal stress of 0.2 MPa, which simulates the confining pressure on the coal wall applied by the hydraulic support guard plate. The material parameters of the triangular prism model are listed in Table 2.

5.5. Numerical Results. In calculations, the finite element degradation was simulated according to the statistical damage constitutive model described in subsection 5.1. The stress in each element was iteratively calculated at a certain loading step via the current boundary conditions, and the shift to the next loading step occurred only after the damage saturation (when no more damage was generated). During the top displacement application, the model lost its bearing capacity at step 49.

Figures 14 and 15 illustrate the failure process of the model on both $abcd$ and $bfec$ surfaces, respectively. For brevity sake, only a few typical details of the mesoscopic failure process in the triangular prism are shown for several selected loading stages. Here, the elastic modulus, position, acoustic emission energy level, and the maximum shear stress evolution are shown separately. The maximum shear stress and elastic modulus colors indicate their relative magnitude at a certain loading step. In acoustic emission, the center position of the sphere represents the location of elastic strain energy release, and the diameter represents the relative magnitude of energy. The blue spheres represent the acoustic emission generated during a certain loading step, and the red ones represent the accumulation at all previous steps. Both at step 8 and step 22, the triangular prism was at the stage of elastic deformation. At calculation step 8, the distribution of the elastic modulus was almost the same as before loading,

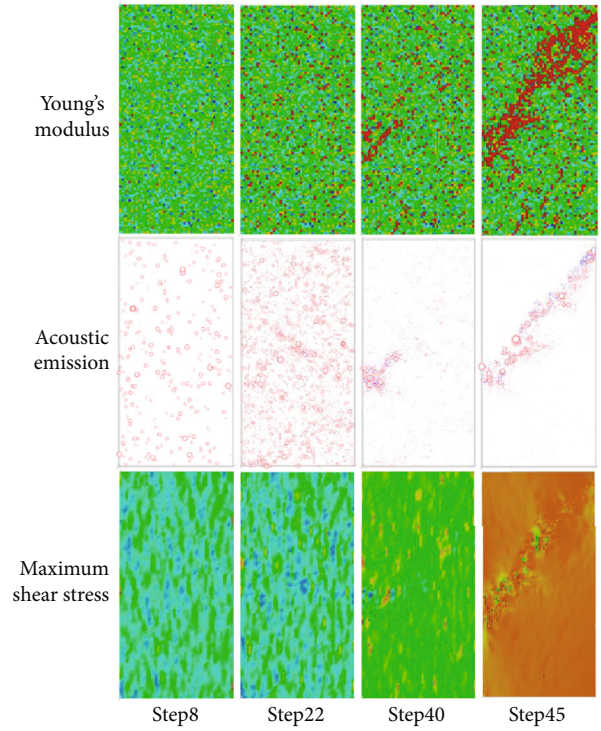


FIGURE 14: The continuous shear fracture process of $abcd$ surface.

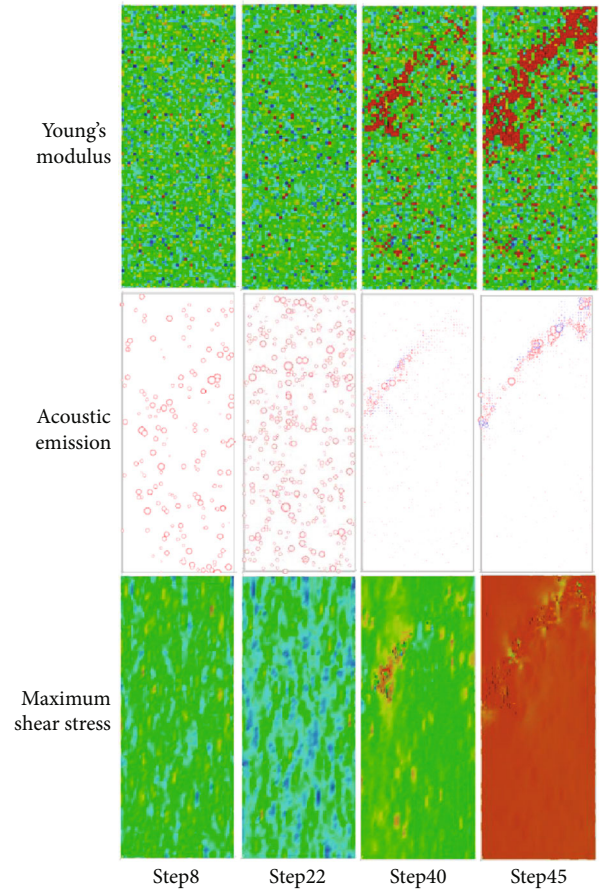


FIGURE 15: The continuous shear fracture process of $bfec$ surface.

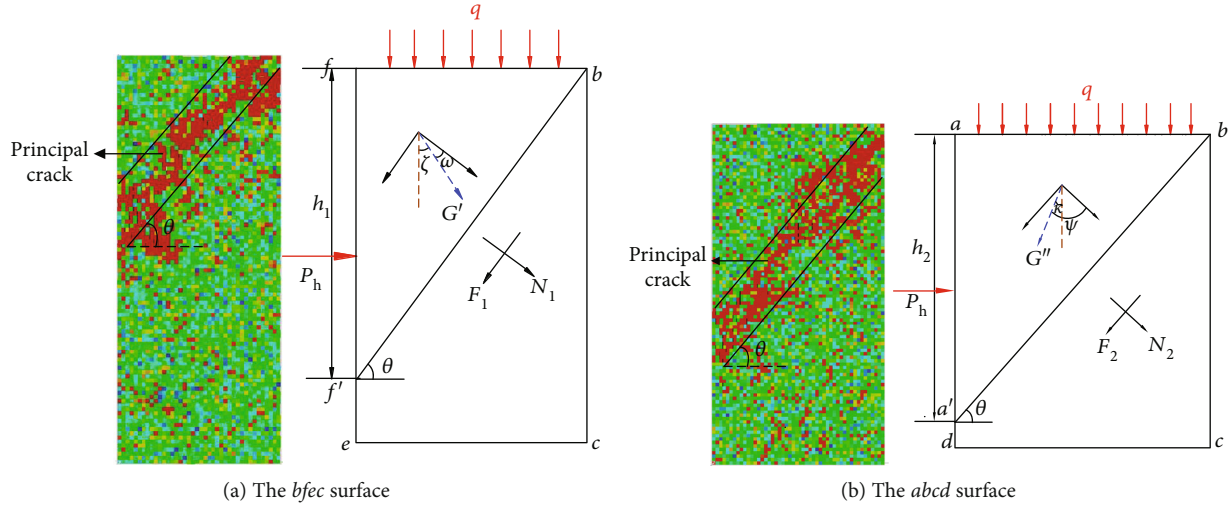


FIGURE 16: Comparison of fracture patterns predicted by the numerical and physical models.

indicating a zero dielectric unit damage. Therefore, only a few smaller acoustic emission sources with even energy levels were uniformly distributed in the model. The maximum shear stress distribution at this step was also relatively evenly distributed. With the axial displacement increased to step 22, numerous acoustic emission events caused by the release of elastic strain energy appeared in the two surfaces, indicating that many elements were close to being damaged. However, at this step, the distribution of maximum shear stresses was still uniform, and there was no indication of nucleation sites for the initiation and propagation of large cracks. At loading step 40, the two surfaces began to show a preliminary shear nucleation zone, which was caused by the unevenness of the unit. Macrocracks (depicted by red areas) appeared in the elastic modulus graph. A large number of acoustic emission events clustered around the shear nucleation zone, and macrofracture began to occur. At this time, the accumulated acoustic emissions in other areas of the surfaces were no longer displayed due to the relatively small magnitude of energy. Meanwhile, the maximum shear stress of the mesoscopic elements around the shear nucleation zone on the surfaces was higher than that of other areas. When the axial displacement continued to rise until step 45, the scattered cracks in the shear nucleation zone gradually expanded, coalesced, and penetrated, leading to a distinct shear band. At the same time, continuous macroscopic cracks were formed across the shear band both on $abcd$ and $bfec$ surfaces. The acoustic emission resource locations were more concentrated along the shear band and associated crack. At loading step 45, the triangular prism lost its bearing capacity, and only a small residual strength remained.

5.6. Comparative Analysis of Fracture Patterns. It can be seen from the numerical results that when the soft triangular prism is loaded axially by variable confining pressure, the model will undergo shear fracture. The ultimate failure location is in the middle-upper part of the triangular prism. On both side surfaces loaded with a larger confining pressure, there is a separation through shear band, and both shear

bands have the same fracture angle θ and intersection point b . The sliding body formed by the failure will slip across the surface, which has the minimum confining pressure. It can be seen from Figure 16 that the fracture mode of the numerical model is in good agreement with the instability mode of the physical model using the Mohr-Coulomb criterion to analyze the failure process of the coal wall unit. Therefore, the physical model proposed in this paper is suitable for the study of rib spalling of large cutting height soft coal face in protected seam mining.

6. Conclusions

The results obtained make it possible to draw the following conclusions:

- (1) In coal mines with a large cutting height of soft coal, after the lower protective layer is mined, the upper portion of the working face forms an intricate spatial fracture pattern, which significantly differs from that of a traditional coal wall. Structural planes across the coal seam are observed in the remnants of rib spalling
- (2) The physical simulation of the case study (the Paner Coal Mine, located in the Huainan mine area, China) shows that after mining of the 1223 working face, the fractured zone extended throughout SKS1 and 2 and ceased at the base of SKS3. Also, the remote protected layer was in the bending-and-sinking zone, and a large number of randomly distributed normal joint fractures appeared. Based on the analysis of the ultimate deflection of the thin plate model, a theoretical calculation model for the three overlying zones of influence was proposed, and the fracture expansion coefficient of the measured rock strata was used to calculate the fracture zone height. These measurements were consistent with the physical simulation results. Furthermore, through borehole monitoring, forward fractures of boreholes were observed in the

vicinity of the protected layer, and no separation was revealed, indicating that SKS3 did not break and the disturbed rock strata in the boreholes were located entirely in the bending zone

- (3) Based on the characteristics affected by the disturbance and the form of rib spalling, a spatial physical-mechanical model of the protected coal wall was established, and the shear failure criterion of the triangular prism formed by the division of the MCWS was proposed. The stress state analysis revealed that damage to a coal wall was related to the roof load, coal cohesion, coal internal friction angle, protection force, and coal seam inclination. The coal wall unit broke down to form a sliding body. The MCWS determined whether it could frictionally slip off along the fracture surface. The friction and sliding instability criterion of the sliding body featuring the slip body stability coefficient K were also proposed. At $K > 1$, the sliding body frictionally slides and forms a rib spalling
- (4) The results obtained are considered quite instrumental in the analysis of rib spalling mechanisms in soft coal faces with a large cutting height and a protective layer

Data Availability

The data used to support the findings of this study are available from the corresponding author upon request.

Conflicts of Interest

The authors declare that there is no conflict of interest regarding the publication of this paper.

Acknowledgments

This work is supported by the National Natural Science Foundation of China (No. 51634007), the Institute of Energy, Hefei Comprehensive National Science Center under Grant No. 19KZS203, the National Youth Science Foundation (No. 51904011), the Anhui Provincial Natural Science Foundation (No. 1908085QE183), the Anhui University Scientific Research Foundation (No. QN2018108), and the Open Fund of State Key Laboratory of Water Resource Protection and Utilization in Coal Mining (No. GJNY-18-73.7).

References

- [1] S. Yang, J. Zhang, Y. Chen, and Z. Song, "Effect of upward angle on the drawing mechanism in longwall top-coal caving mining," *International Journal of Rock Mechanics & Mining Sciences*, vol. 85, pp. 92–101, 2016.
- [2] Y. J. Zhang, G. R. Feng, M. Zhang, H. R. Ren, and J. W. Bai, "Residual coal exploitation and its impact on sustainable development of the coal industry in China," *Energy Policy*, vol. 96, pp. 534–541, 2016.
- [3] Y. Z. Shang, P. F. Hei, S. B. Lu, L. Shang, and X. F. Li, "China's energy-water nexus: assessing water conservation synergies of the total coal consumption cap strategy until 2050," *Applied Energy*, vol. 210, pp. 643–660, 2018.
- [4] G. F. Wang, Y. X. Xu, and H. W. Ren, "Intelligent and ecological coal mining as well as clean utilization technology in China: review and prospects," *International Journal of Mining Science and Technology*, vol. 29, no. 2, pp. 161–169, 2019.
- [5] X. Y. Li, N. Zhang, Z. Z. Xie, D. X. Liang, and Y. M. Zhao, "Study on efficient utilization technology of coal pillar based on gob-side entry driving in a coal mine with great depth and high production," *Sustainability*, vol. 11, no. 6, 2019.
- [6] S. J. Chen, D. W. Yin, X. Y. Liu, H. L. Wang, and F. W. Cao, "Collaborative mining using different equipment for a coal seam varying in thickness in a long wall working face," *International Journal of Oil, Gas and Coal Technology*, vol. 13, no. 1, pp. 73–86, 2016.
- [7] Y. Zhang, S. G. Cao, T. Wan, and J. J. Wang, "Field Measurement and Mechanical Analysis of Height of the Water Flowing Fracture Zone in Short-Wall Block Backfill Mining beneath the Aquifer: A case study in China," *Geofluids*, vol. 2018, Article ID 7873682, 12 pages, 2018.
- [8] L. M. Fan, T. Li, M. X. Xiang, W. Z. He, and B. Y. Wu, "Effect of Coal Mining on Springs in the Yushenfu Mining Area of China," *Geofluids*, vol. 2018, 16 pages, 2018.
- [9] F. P. Cui, Q. Wu, Y. H. Lin, Y. F. Zeng, and K. L. Zhang, "Damage features and formation mechanism of the strong water inrush disaster at the Daxing co mine, Guangdong Province, China," *Mine Water and Environment*, vol. 37, no. 2, pp. 346–350, 2018.
- [10] T. Liu, B. Q. Lin, W. Yang, T. Liu, and C. Zhai, "An integrated technology for gas control and green mining in deep mines based on ultra-thin seam mining," *Environmental Earth Sciences*, vol. 76, no. 6, pp. 1–17, 2017.
- [11] C. Zhang, S. H. Tu, M. Chen, and L. Zhang, "Pressure-relief and methane production performance of pressure relief gas extraction technology in the longwall mining," *Journal of Geophysics and Engineering*, vol. 14, no. 1, pp. 77–89, 2017.
- [12] D. P. Edwards and W. F. Laurance, "Preventing tropical mining disasters," *Science*, vol. 350, no. 6267, p. 1482, 2015.
- [13] X. J. Chen, L. Y. Li, L. Wang, and L. L. Qi, "The current situation and prevention and control countermeasures for typical dynamic disasters in kilometer-deep mines in China," *Safety Science*, vol. 115, pp. 229–236, 2019.
- [14] Z. J. Wen, E. R. Xing, S. S. Shi, and Y. J. Jiang, "Overlying strata structural modeling and support applicability analysis for large mining-height stopes," *Journal of Loss Prevention in the Process Industries*, vol. 57, pp. 94–100, 2019.
- [15] Z. Y. Song and H. Konietzky, "A particle-based numerical investigation on longwall top coal caving mining," *Arabian Journal of Geosciences*, vol. 12, no. 18, p. 556, 2019.
- [16] Z. Y. Song, H. Konietzky, and M. Herbst, "Drawing mechanism of fractured top coal in longwall top coal caving," *International Journal of Rock Mechanics & Mining Sciences*, vol. 130, p. 104329, 2020.
- [17] B. X. Huang, Y. Z. Wang, and S. G. Cao, "Cavability control by hydraulic fracturing for top coal caving in hard thick coal seams," *International Journal of Rock Mechanics and Mining Sciences*, vol. 74, pp. 45–57, 2015.
- [18] Q. S. Bai, S. H. Tu, F. T. Wang, and C. Zhang, "Field and numerical investigations of gateroad system failure induced by hard roofs in a longwall top coal caving face," *International Journal of Coal Geology*, vol. 173, pp. 176–199, 2017.

- [19] Z. H. Wang, J. C. Wang, and S. L. Yang, "An ultrasonic-based method for longwall top-coal cavability assessment," *International Journal of Rock Mechanics & Mining Sciences*, vol. 112, pp. 209–225, 2018.
- [20] Z. S. Meng, Q. L. Zeng, K. D. Gao, S. Kong, and P. Liu, "Failure analysis of super-large mining height powered support," *Engineering Failure Analysis*, vol. 92, pp. 378–391, 2018.
- [21] T. D. Le, J. Oh, B. Hebblewhite, C. G. Zhang, and R. Mitra, "A discontinuum modelling approach for investigation of longwall top coal caving mechanisms," *International Journal of Rock Mechanics & Mining Sciences*, vol. 106, pp. 84–95, 2018.
- [22] L. Si, Z. B. Wang, X. H. Liu, C. Tan, and R. X. Xu, "Assessment of rib spalling hazard degree in mining face based on background subtraction algorithm and support vector machine," *Current Science*, vol. 116, no. 12, pp. 2001–2012, 2019.
- [23] W. B. Guo, C. Y. Liu, G. W. Dong, and W. Y. Lv, "Analytical study to estimate rib spalling extent and support requirements in thick seam mining," *Arabian Journal of Geosciences*, vol. 12, no. 8, p. 276, 2019.
- [24] Y. Yuan, S. H. Tu, X. G. Zhang, and A. X. Liu, "Mechanism and control technique of rib spalling disaster in fully-mechanized mining with large mining height in soft coal seam face," *Disaster Advances*, vol. 6, no. 3, pp. 92–98, 2013.
- [25] Y. Yuan, S. H. Tu, X. T. Ma, L. L. Sun, and Q. S. Bai, "Coal wall stability of fully mechanized working face with great mining height in 'three soft' coal seam and its control technology," *Journal of Mining & Safety Engineering*, vol. 29, no. 1, pp. 21–25, 2012.
- [26] H. L. Zhang, L. G. Wang, and H. Qin, "Study of spalling mechanism and control techniques of mining roadway," *Rock and Soil Mechanics*, vol. 33, no. 5, pp. 1462–1466, 2012.
- [27] X. W. Yin, S. H. Yan, and Y. An, "Characters of the rib spalling in fully mechanized caving face with great mining height," *Journal of Mining & Safety Engineering*, vol. 25, no. 2, pp. 2–5, 2008.
- [28] Y. Ning, "Mechanism and control technique of the rib spalling in fully mechanized mining face with great mining height," *Journal of China Coal Society*, vol. 34, no. 1, pp. 50–52, 2009.
- [29] H. J. Hao and Y. Zhang, "Stability analysis of coal wall in full-seam cutting workface with fully-mechanized in thick seam," *Journal of Liaoning Technical University*, vol. 24, no. 4, pp. 489–491, 2005.
- [30] J. C. Wang, "Mechanism of the rib spalling and controlling in the very soft coal seam," *Journal of China Coal Society*, vol. 32, no. 8, pp. 785–788, 2007.
- [31] B. J. Fu, M. Tu, and M. Z. Gao, "Study on unloading instability model of working face with large mining height," *Journal of Mining & Safety Engineering*, vol. 34, no. 6, pp. 1128–1133, 2017.
- [32] P. J. Yang, C. Y. Liu, and F. F. Wu, "Breakage and falling of a high coal wall in a thick mined seam," *Journal of China University of Mining & Technology*, vol. 41, no. 3, pp. 371–377, 2012.
- [33] H. W. Wang, Y. P. Wu, P. S. Xie, S. H. Luo, and K. Z. Liu, "Coal rib stability effect of mining-thickness with large mining height of working face in steeply inclined seams," *Journal of Mining & Safety Engineering*, vol. 35, no. 1, pp. 64–70, 2018.
- [34] Y. P. Wu, D. Lang, and P. S. Xie, "Mechanism of disaster due to rib spalling at fully-mechanized top coal caving face in soft steeply dipping seam," *Journal of China Coal Society*, vol. 41, no. 8, pp. 1878–1884, 2016.
- [35] Y. H. Pang and G. F. Wang, "Hydraulic support protecting board analysis based on rib spalling 'tensile-sliding' mechanical model," *Journal of China Coal Society*, vol. 42, no. 8, pp. 1941–1950, 2017.
- [36] J. F. Liu, E. X. Tang, Y. X. Xu, and Y. L. Zhang, "Study on full process precision control technology of coal wall under large mining height intelligent mining condition," *Coal Science and Technology*, vol. 47, no. 10, pp. 131–135, 2019.
- [37] J. C. Chang, G. X. Xie, and X. H. Zhang, "Analysis of rib spalling mechanism of fully-mechanized top-coal caving face with great mining height in extra-thick coal seam," *Rock and Soil Mechanics*, vol. 36, no. 3, pp. 803–808, 2015.
- [38] G. F. Song, S. L. Yang, and Z. H. Wang, "Longwall face stability analysis using Ritz method and its 3D physical modelling study," *Journal of China Coal Society*, vol. 43, no. 8, pp. 2162–2172, 2018.
- [39] K. Yang, X. Y. Kong, W. Lu, and S. Liu, "Study of strata pressure behaviors with longwall mining in large inclination and thick coal seam under closed distance mined gob," *Chinese Journal of Rock Mechanics and Engineering*, vol. 34, no. S2, pp. 4278–4285, 2015.
- [40] M. G. Qian, X. X. Miao, and J. L. Xu, "Theoretical study of key stratum in ground control," *Journal of China Coal Society*, vol. 21, no. 3, pp. 2–7, 1996.
- [41] Q. D. Qu, J. L. Xu, R. L. Wu, W. Qin, and G. Z. Hu, "Three-zone characterisation of coupled strata and gas behaviour in multi-seam mining," *International Journal of Rock Mechanics & Mining Sciences*, vol. 78, pp. 91–98, 2015.
- [42] B. Ghabraie, G. Ren, and J. V. Smith, "Characterising the multi-seam subsidence due to varying mining configuration, insights from physical modelling," *International Journal of Rock Mechanics & Mining Sciences*, vol. 93, pp. 269–279, 2017.
- [43] J. L. Xu, W. B. Zhu, and X. Z. Wang, "New method to predict the height of fractured water-conducting zone by location of key strata," *Journal of China Coal Society*, vol. 37, no. 5, pp. 762–769, 2012.
- [44] K. Yang, S. Liu, C. A. Tang, Z. Wei, and X. L. Chi, "Mechanism and prevention of coal seam rib spalling in remote protected layer across coal group," *Journal of China Coal Society*, vol. 44, no. 9, pp. 2611–2621, 2019.
- [45] D. G. Zhang and Y. H. Zhou, "A theoretical analysis of FGM thin plates based on physical neutral surface," *Computational Materials Science*, vol. 44, no. 2, pp. 716–720, 2008.
- [46] H. Shao, S. G. Jiang, L. Y. Wang, and Z. Y. Wu, "Bulking factor of the strata overlying the gob and a three-dimensional numerical simulation of the air leakage flow field," *Mining Science and Technology (China)*, vol. 21, no. 2, pp. 261–266, 2011.
- [47] H. Alehossein and B. A. Poulsen, "Stress analysis of longwall top coal caving," *International Journal of Rock Mechanics & Mining Sciences*, vol. 47, no. 1, pp. 30–41, 2010.
- [48] N. Bilim and I. Özkan, "Determination of the effect of roof pressure on coal hardness and excavation productivity: an example from a Çayırhan lignite mine, Ankara, Central Turkey," *International Journal of Coal Geology*, vol. 75, no. 2, pp. 113–118, 2008.
- [49] C. A. Tang, H. Liu, P. K. K. Lee, Y. Tsui, and L. Tham, "Numerical studies of the influence of microstructure on rock failure in uniaxial compression—part I: effect of heterogeneity," *International Journal of Rock Mechanics & Mining Sciences*, vol. 37, no. 4, pp. 555–569, 2000.

- [50] C. A. Tang, W. T. Yang, Y. F. Fu, and X. H. Xu, "A new approach to numerical method of modelling geological processes and rock engineering problems—continuum to discontinuum and linearity to nonlinearity," *Engineering Geology*, vol. 49, no. 3–4, pp. 207–214, 1998.
- [51] C. A. Tang, L. G. Tham, S. H. Wang, H. Liu, and W. H. Li, "A numerical study of the influence of heterogeneity on the strength characterization of rock under uniaxial tension," *Mechanics of Materials*, vol. 39, no. 4, pp. 326–339, 2007.
- [52] C. A. Tang, L. G. Tham, P. K. K. Lee, Y. Tsui, and H. Liu, "Numerical studies of the influence of microstructure on rock failure in uniaxial compression—part II: constraint, slenderness and size effect," *International Journal of Rock Mechanics & Mining Sciences*, vol. 37, no. 4, pp. 571–583, 2000.

Research Article

Experimental Study on MICP Aqueous Solution under the Action of Different Organic Substrates

Huai-miao Zheng,^{1,2} Ling-ling Wu^{1,2}, Kai-wen Tong,³ Lin Hu,^{1,2} Qing Yu,^{1,2} Gui-cheng He,^{1,2} and Zhi-jun Zhang^{1,2}

¹School of Resource & Environment and Safety Engineering, University of South China, 421001 Hengyang, China

²Hunan Province & Hengyang City Engineering Technology Research Center for Disaster Prediction and Control on Mining Geotechnical Engineering, 421001 Hengyang, China

³University of Chinese Academy of Sciences, 100049 Beijing, China

Correspondence should be addressed to Zhi-jun Zhang; zzj181@163.com

Received 27 June 2020; Revised 15 August 2020; Accepted 27 August 2020; Published 22 September 2020

Academic Editor: Bo Li

Copyright © 2020 Huai-miao Zheng et al. This is an open access article distributed under the Creative Commons Attribution License, which permits unrestricted use, distribution, and reproduction in any medium, provided the original work is properly cited.

The precipitation rate and cementation strength of calcium carbonate crystals during the process of microorganism-induced calcium carbonate precipitation (MICP) are key factors that affect the application effect of this technology. In order to improve the quality of calcium carbonate formation in the MICP process, egg white protein with a volume fraction of 20%, bovine serum albumin with a mass fraction of 0.3%, sucrose with a mass fraction of 5%, bamboo leaves with a mass concentration of 25 g/L, and bamboo leaf-magnesium chloride ($Mg^{2+}/Ca^{2+} = 4 : 1$) were added during the experiment of different groups of MICP solutions. The results of the solution test study showed that there was no obvious lag period for bacterial growth under the action of organic matrix. The concentration of bacteria in the reaction solution was higher under the action of sucrose and egg white. The conversion rate of Ca^{2+} under the action of egg white was the fastest, which was about 2.5 times higher than that of the control group. After 14 days of grouting reaction, it was found that the proportion of calcite-type calcium carbonate produced under the action of egg white was the highest, and the Ca element accounted for 66.24% in the solidified material. Sucrose was second; bovine serum albumin was the lowest. The calcium carbonate crystals generated by the control of each organic matrix had a high degree of pore size matching with the tailings under a dry-wet cycle. The structural characteristics of the calcium carbonate crystals, such as crystal form, morphology, and particle size, were mainly due to the interaction between the organic matrix and the calcium carbonate crystals. This study proves that the addition of the organic matrix can improve the formation rate and crystal structure of calcium carbonate during MICP, thus providing a new reference for the development of MICP technology.

1. Introduction

With the enrichment of scientific theories and research methods in geotechnical engineering and the increase of cross-disciplinary interaction, the research on microbial-induced calcium carbonate precipitation (MICP) has attracted wide attention in China and abroad. In recent years, this biochemical reaction has achieved certain results in strengthening soft soil such as loose silt and silty clay, but the cementation effect of calcium carbonate precipitation obtained is not ideal, mainly manifested in a low calcium car-

bonate crystallization conversion rate, insufficient strength of induced calcium carbonate crystals, and low matching degree between crystal size and interparticle pores [1]. Therefore, based on the principle of the soft template method, this study carried out comparative experiments of MICP aqueous solution under the control of different organic substrates, trying to find an organic matrix that can effectively promote the formation of calcium carbonate in the MICP process. The principle of this method is to use the interaction between the organic matrix and the calcium carbonate cement in geometric lattice matching, stereochemical complementation,

and molecular recognition at specific interfaces to regulate the formation of carbonate composites with specific structures and functions. By improving the crystal form, crystal morphology, and particle size characteristics of the original induced calcium carbonate crystals, it can better exert its material properties in the field of sand reinforcement [2–5].

In the past ten years, domestic and foreign research institutions and scholars had carried out some laboratory studies, mainly using microemulsion, natural biological macromolecules, small molecules, polymers, etc., as soft templates to synthesize calcium carbonate. Mann et al. applied the microemulsion method to the synthesis of calcium carbonate for the first time and synthesized an interesting polycrystalline spongy aragonite structure [6]; Xie and others initially studied the interaction between bovine serum albumin (BSA) and calcium carbonate and found that BSA can promote the nucleation of calcium carbonate crystals, increase the water solubility of calcium carbonate, control the crystallization rate, prevent the generation of amorphous calcium carbonate, and form a highly ordered structure of calcium carbonate, thus inducing and regulating calcium carbonate crystals [7]; Sugawara et al. copolymerized chiral phosphoserine-aspartic acid into polypeptide, inducing the formation of specular spiral calcite [8]. Subsequently, Nishino et al. conducted biomimetic mineralization of CaCO_3 at different Mg^{2+} concentrations. The results show that different Mg^{2+} concentrations can significantly change the crystal morphology [9]; Adamiano et al. studied the change of calcium carbonate crystal morphology and kinetics formation process by fluorescence microscopy after alkali treatment of abalone shell green sheet protein fragment (GP) [10]; Wittaya et al. further added different long-chain amino acids such as glycine, 4-aminobutyric acid, and 6-aminocaproic acid to calcium hydroxide suspension, and calcium carbonate prepared by a gas phase diffusion method was transformed from spherical to acicular with the increase of carbon chain length [11]. Under high temperature and high pressure hydrothermal conditions, calcium carbonate crystals were prepared by the urea hydrolysis method with organic carboxylate sodium citrate as an additive. The effects of sodium citrate concentration, ethanol volume fraction, Ca^{2+} concentration, and ionic liquid concentration on the crystal form and morphology of calcium carbonate were investigated [12]. In recent years, Qiao has used egg white protein foam and egg white protein as organic templates to prepare calcium carbonate in different forms by traditional chemical methods [13]; Li used CaCl_2 and $(\text{NH}_4)_2\text{CO}_3$ as raw materials to study the effect of SDBS with different concentrations in solution on the crystallization behavior and morphology of CaCO_3 by a gas diffusion method [14].

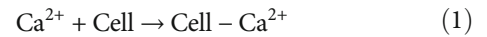
The above research results show that an organic matrix has the potential to improve MICP technology for strengthening soft soil. As there is few related research on the application of an organic matrix to soft soil at home and abroad at present, in view of this, this paper will initially select the organic matrix with biomineralization and cementation functions as the control template of calcium carbonate crystals. By discussing the influence of different organic matrices on various indexes of calcium carbonate finally induced

under the control of different organic matrices and combining with the pore distribution law between tailing sand bodies, it will lay a good foundation for the subsequent solidification research of tailing sand.

2. Test Materials and Devices

2.1. Bacteria and Culture Medium. The bacterium used in this test was *Bacillus pasteurianus* ii, purchased from the American strain collection center, No. ATCC11859. The bacterium is a facultative anaerobic bacterium. The liquid culture medium used in the test process was CASO+ urea culture medium. Each liter of bacterial culture liquid contains 15 g casein peptone, 5 g soybean peptone, 5 g sodium chloride, 20 g urea, and 1000 mL deionized water, and the pH value is adjusted to 7.3 with 1 M NaOH. Since urea is easy to decompose under high temperature conditions (121°C), urea and other solutions need to be separately sterilized when preparing the medium. The urea solution is subjected to filtration sterilization treatment; other mixed solutions are subjected to high temperature sterilization. After completion, the two are mixed in a septic operation table.

2.2. Preparation of Cementing Fluid. The cementing solution used in this test is a mixture of urea and CaCl_2 , which mainly provides carbonate ions and calcium sources for the microbial grouting reinforcement process (see formulas (1)–(3)). Based on the previous research of the research group [15, 16], the concentration ratio of urea and CaCl_2 in this solution test is 1:1, and the specific concentration of both is 0.05 mol/L:



2.3. Organic Matrix. In order to explore the regulation of different organic substrates on microorganism-induced calcium carbonate crystals, five organic templates, including egg white protein 20%, bovine serum albumin 0.3%, sucrose 5%, bamboo leaves 25 g/L, and bamboo leaves-magnesium chloride ($\text{Mg}^{2+}/\text{Ca}^{2+} = 4 : 1$), were preliminarily selected by referring to previous accumulated results [17–21].

Among the five selected organic matrices, bovine serum albumin (BSA) is a globulin in bovine serum, which is generally used as a stabilizer in reaction solution. It often plays the role of protection and carrier, can greatly improve the activity of biological cells, and can combine with a variety of cations, anions, and small molecular substances to guide the formation of inorganic substances through biomimetic methods. Egg white mainly contains water and colloidal protein, which is similar to the organic components in pearls, and has low price and good water solubility. It can effectively be used as a carrier to guide the bionic synthesis of calcium carbonate crystals, and the colloidal substance in egg white can enhance the cohesion between sand particles and calcium carbonate cement. The reason why sucrose is used to guide the synthesis of calcium carbonate is that, on the one hand, it can

TABLE 1: Specific parameters of organic substrates.

Name	Specifications	Content	Manufacturer
Bovine serum albumin (25 g)	Analytic pure AR	BR, 98%	Shanghai Budding Technology Co., Ltd.
Egg white protein (970 g)	Pasteurized egg white	98%	Suzhou Orfu Egg Co., Ltd.
Sucrose (500 g)	Analytic pure AR	99.9%	Tianjin Heyday Xin Chemical Co., Ltd.
Bamboo leaf	Fresh and alive	25 g/L	Picking on campus

decompose and enhance the viscosity between soil particles under high temperature conditions and, on the other hand, it can effectively prepare calcium carbonate crystals with specific structures. Bamboo leaves are gramineous plants and are rich in manganese, iron, copper, nickel, selenium, silicon, and other trace elements and other organic matters. Relevant studies [22] show that the organic components extracted from natural bamboo leaves can control the crystal form and morphology of synthesized calcium carbonate crystals. At the same time, amorphous calcium carbonate (ACC) can be kept in a stable state for a long time under the coordinated control of magnesium ions. The method of using natural plants to control bionic calcium carbonate is convenient to operate, and also, the product is environment-friendly and pollution-free. The egg white used in the experiment can be directly separated from fresh eggs, but because the separated egg white is very inconvenient to sterilize, this experiment uses the commercially available bottled pasteurized egg white liquid. The specific specifications and parameters of each organic matrix are shown in Table 1.

2.4. Test Physical Devices. In order to meet the test conditions of convenient sampling, waterproof device, aseptic reaction, oxygen supply, and ventilation, a new MICP technology solution test reaction device was designed in this study. The main body of the device is made of high borosilicate glass. The overall height of the device is 22.5 cm, and the inner diameter is 10 cm. The main structure consists of upper and lower reaction vessels. A circular rubber water stop ring is arranged between the two parts. The upper and lower structures are firmly connected by steel rings. The reaction vessel at the upper part of the device comprises a plurality of basic structures such as an oxygen supply port, a grouting port, a liquid discharge port, and the like. In order to avoid serious blockage of the liquid discharge port caused by generated tiny calcium carbonate crystals, a permeable gauze with tiny pore diameter is arranged at the inner side of the liquid discharge port at the upper part of the device. In the lower reaction vessel, the bottom is a solid member, and the bottom is covered with eggshells ($10 \text{ g} \pm 0.1 \text{ g}$) with uniform size, so that calcium carbonate crystals generated in the reaction are organically connected into a whole, which is convenient for final cutting and sampling. The physical model device used in the test is shown in Figure 1.

3. Test Methods

3.1. Preparation and Extraction of Organic Matter Such as Chlorophyll from Bamboo Leaves. Fresh and tender green bamboo leaves are picked in the campus, stems from the

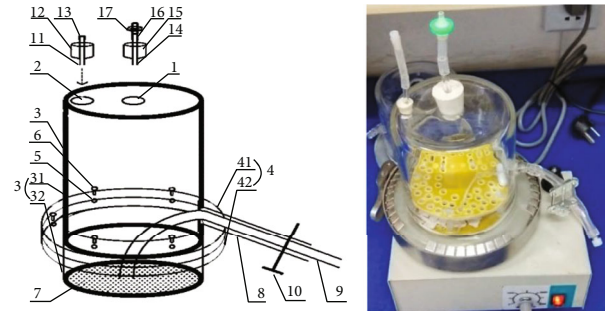


FIGURE 1: Structure of the reaction device in the solution test.

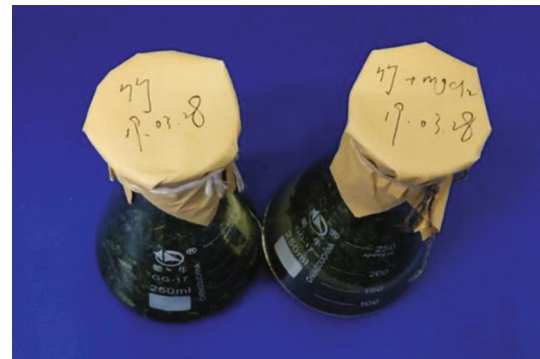


FIGURE 2: Extraction of chlorophyll from bamboo leaves.

bamboo leaves are removed, the bamboo leaves are cleaned with ultrapure water for 2-3 times, the bamboo leaves are dried in a drying oven at 30°C for 20 minutes, the bamboo leaves are soaked in 0.07% CuSO_4 solution for 5 hours, the bamboo leaves are washed with ultrapure water for 3-4 times, and the bamboo leaves are dried to constant weight. Then, the dried bamboo leaves are cut and poured into ultrapure water just above the surface of the bamboo leaves for water bath treatment and filtered by a filter funnel; the filtrate is subjected to reduced pressure distillation operation to a semifluid state and finally is cooled to room temperature and stored in a conical flask [23–25], as shown in Figure 2.

3.2. Preparation and Sampling of Powdered Calcium Carbonate Cements. After the solution test reaction is finished, the calcium carbonate gel on the support body is scraped into a culture dish with a knife and tweezers, put into a drying box to dry at 50°C for 2-3 days after the sampling is finished, weighed to constant weight, poured into a grinder, and ground repeatedly and evenly, and then, fine powder samples were taken through a 300-target screen for SEM, XRD, TEM, and other tests.

3.3. MICP Solution Test under the Control of Organic Matrix

3.3.1. Test Methods. This study is a MICP aqueous solution test under the action of the organic matrix. Five organic matrices, including egg white protein, bovine serum albumin, bamboo leaves, sucrose, bamboo leaves-magnesium chloride, which have obvious regulatory effects on the crystal form and crystal habit of calcium carbonate crystals, are selected. Six experimental groups including the control group (without adding any organic matrix) are set up. Under the conditions of temperature of 30°C, initial pH of 7.3, initial OD₆₀₀ of 2.0, and stirring rate of 150 rpm, the grouting test was started. Considering the actual size of the device and the amount of sample liquid required for each detection item, the grouting volume of each reaction liquid in the test was the following: 15 mL of bacterial liquid, 200 mL of culture medium, 100 mL of calcium chloride solution, 100 mL of urea solution, and 100 mL of organic matrix solution (the control group was ultrapure water). After the solution in the device was drained out every 24 hours, a new round of reaction slurry was poured by a peristaltic pump. During the test reaction, the change rule of each index (bacterial concentration, pH, Zeta potential, dissolved oxygen, calcium ion concentration) in the reaction solution within 1 d was measured, and the monitoring time interval was 2 h. After the grouting period reaches 14 days, the reaction liquid is discharged, the fixed steel ring is opened, the upper and lower structures of the separation device are disassembled, and the sample is put into a drying box (60°C) for drying for 24 hours, and then, the solidified sample is taken out and tested by SEM, XRD, and other items, and the test results of the six experimental groups are compared qualitatively and quantitatively.

3.3.2. Determination of Bacterial Quantity. The measurement of the number of bacteria is realized by detecting the absorbance of the bacterial solution. The measuring equipment is a protein nucleic acid analyzer (Eppendorf Company of Germany, model number is BioPhotometer). In the experiment, 5 mL of reaction supernatant is taken from the device every 2 hours to measure the OD₆₀₀ value of the bacterial suspension. The obtained value is substituted into the following formula for conversion to obtain the actual number of bacteria in the reaction solution [26]:

$$Y = 8.59 \times 10^4 Z^{1.3627}. \quad (4)$$

In the formula, Z is OD₆₀₀ value and Y is bacterial concentration (units/ μL^{-1}). This formula can only be used when the value of OD₆₀₀ is within the range of 0.2~0.8. If it is beyond this range, it needs to be diluted before conversion.

3.3.3. pH Value. Every 2 hours, 100 mL of the reaction solution is taken into a conical flask, and the change of the pH value of the reaction solution within 1 day is observed by using a diamagnetic precision desktop pH meter (HACH Company of the United States, model HQ411D).

3.3.4. Monitoring of Dissolved Oxygen in Solution. Dissolved oxygen in the reaction solution is very important to the life activities of microorganisms. In this experiment, a 100 mL

centrifuge tube is used to contain 80 mL of reaction solution in different reaction periods. The dissolved oxygen in the solution in one day is monitored by a convenient dissolved oxygen meter (China Guangzhou Jinhe Technology Testing Co., Ltd., model 958787-1KTOK).

3.3.5. Zeta Potential. The stability of colloidal dispersion in the reaction liquid system before and after the addition of the organic matrix was judged by the variation of Zeta potential. The Zeta potential value in the solution was monitored every 2 hours during the experiment. Monitoring equipment was the Zeta potential measuring instrument (JS94HK, China Beijing Zhongyi Kexin Technology Co., Ltd.). The approximate relationship between Zeta potential and stability of the solution system is shown in Table 2 [27].

3.3.6. Determination of Ca²⁺ Concentration. Regularly, the discharged solution from the device was collected, made to pass through a 0.22 μm filter and dropped into a 20 mL centrifuge tube, and measured according to "EDTA Titration of Calcium in Water Quality" GB 7476-87.

3.3.7. Microstructure Test. In order to analyze the microstructure of the generated samples, the ground and dried calcium carbonate cemented samples were analyzed by scanning electron microscopy (FEI-F50 test field emission scanning electron microscopy) to observe the morphological characteristics of calcium carbonate samples generated under different organic substrates. Then, typical powdered samples were selected for XRD detection (X-ray diffractometer model SMARTLAB9) and FT-IR testing (FT-IR testing Fourier infrared spectrometer model Nicolet), respectively, and then, the crystal form and composition of calcium carbonate samples were obtained.

4. Results and Discussion

This solution test mainly detects and analyzes the change rule of bacterium quantity, pH value, Zeta potential, dissolved oxygen, and calcium ion concentration in the reaction solution of each experimental group within 24 hours, and the composition, crystal form, morphology, and particle size of the carbonate gel were compared and analyzed. Figure 3 shows the effect of dismantling the device after the test.

4.1. Changes in the Number of Bacteria in Reaction Solution. The change curve of bacterial number in Figure 4 shows that the bacterial number in the reaction solution under the control of the five organic substrates shows an obvious upward trend within one day. The bacterial growth basically conforms to the gong bozi-Richard model, and there is no obvious lag period. This may be due to the nutrient components such as the carbon source, nitrogen source, and the like required by microorganism's life activities in the culture medium of the reaction solution. The microorganism continuously absorbs the nutrient substances in the surrounding environment under the stirring action, so that the cells grow and multiply rapidly, thus increasing the bacterial concentration in the reaction solution.

TABLE 2: Relationship between Zeta potential and solution system stability.

Zeta potential	Colloidal stability
0~±5	Rapid condensation or condensation
±10~±5	Began to be unstable
±30~±40	General stability
±40~±60	Better stability
>±61	Excellent stability

Among them, the bacterial concentration of the reaction solution under the control of sucrose and egg white increased rapidly, reaching about 160,000/ μL at 24 hours. Compared with other organic substrates, it played a better role in promoting bacterial growth, which was related to the organic matter contained in egg white protein and sucrose itself and could be better absorbed by bacterial cells. However, no organic substrate was added in the blank control group, and its bacterial activity was slightly lower than that of the other four. Its cell concentration is only 101,000 cells/ μL , which indicates that egg white protein, sucrose, and other organic substrates are rich in nutrients required by the life activities of *Bacillus pasteurianus*, thus significantly enhancing its bacterial activity, promoting bacterial growth and division, enabling it to grow faster in one day, with higher urease activity, and always at the logarithmic growth stage of bacterial growth, providing a better reaction basis for urea hydrolysis.

4.2. pH Change. The change rule of pH in Figure 5 shows that the pH value of the reaction solution in each experimental group rises rapidly within 0-12 h, mainly due to the higher urease activity of bacteria in this stage, which can effectively hydrolyze urea in the solution and generate ammonium ions, thus continuously increasing the pH value in the reaction solution. However, when urea is completely hydrolyzed, the pH value in the reaction solution will gradually stabilize, and the change rule of pH value in each experimental group shown in the figure is basically the same. The pH value of the reaction solution in the other experimental groups was basically stable at 9.0 in the 20-24 h period except the pH value in the bamboo leaf+magnesium chloride control group. This is because magnesium chloride will ionize into Cl^- and Mg^{2+} after hydrolysis and combine with H^+ and OH^- in water to form HCl and $\text{Mg}(\text{OH})_2$, of which $\text{Mg}(\text{OH})_2$ is a weak base, so the overall pH value is slightly acidic, resulting in a lower pH value compared with the other five reaction liquid phases.

4.3. Change of Dissolved Oxygen in Reaction Solution. As can be seen from Figure 6, the dissolved oxygen of the reaction solution in the six groups of experiments decreased with the increase of time, which indicates that the growth and metabolism of microbial cells need to consume oxygen continuously. Except for egg white and bamboo leaf+magnesium chloride groups, the dissolved oxygen of the solution in the other four groups of experiments decreased slowly within 0~8 hours, at which time the bacterial growth was in the lag phase, so the bacterial growth was slower. Within

8~18 h, the dissolved oxygen decreased rapidly due to the logarithmic phase of bacterial growth. However, the microbial activity was still relatively high within 22~24 hours, but the oxygen content in the solution was seriously insufficient, so it gradually stabilized.

4.4. Zeta Potential. The curve change in Figure 7 shows that the Zeta potential of the reaction solution in each experimental group is always negative, so negative particles dominate the reaction process of the solution within 24 hours. Most of its potentials rose from -15 mV to -0.5 mV, which shows that the dispersed particles in the solution are unstable at the beginning of the reaction stage due to the continuous combination of Ca^{2+} and CO_3^{2-} . As time increases, the metabolism of microorganisms accelerates, which increases urease activity. Urease accelerates the hydrolysis of urea and continuously generates CO_3^{2-} . The dispersed particles in the solution tend to agglomerate, the attraction force is greater than the repulsive force, and the accumulated amount of calcium carbonate cementation increases due to the destruction of dispersion. The Zeta potential of the solution under the regulation of egg white and sucrose approaches zero at the 16th hour, which is related to the number of bacteria in the solution and the conversion rate of calcium ions. When it reaches 24 h, the potential values of all experimental groups approach zero, at which time the calcium ions in the solution are basically converted.

4.5. Ca^{2+} Concentration. From the change data in Figure 8, it can be seen that the calcium ion concentration in the sample solution in each experimental group shows a downward trend within 0~20 h, and the conversion basically ends at 20 h. The decrease gradient of calcium ion concentration in the egg white protein group is the largest. Compared with the blank control group, the conversion rate of calcium ion in the egg white protein group is increased by about 2.5 times at the same time, mainly due to the rapid increase of bacterium number and the increase of urea hydrolysis rate by urease, which greatly improves the binding rate of calcium ion with carbonate and bicarbonate ions and increases the precipitation rate of calcium carbonate.

4.6. Microstructure. Figure 9 is a scanning electron microscope view of calcium carbonate gel induced by microorganisms under the control of different organic substrates, wherein Figure 9(a) is an enlarged view of deposited calcium carbonate crystals under the condition of the blank control group, i.e., without adding any organic substrates. From the figure, it can be seen that the main form of calcium carbonate is a mixture of calcite and vaterite, and the induced particle size distribution is uneven, with the particle size ranging from 1.3 μm to 25.49 μm . Figure 9(b) is a microscopic particle diagram of calcium carbonate under the control of bovine serum albumin. The crystal particles are relatively uniform, mainly vaterite, and the particle size is basically about 5.30 μm . Figure 9(c) is an SEM image of the calcium carbonate crystal product under the control of sucrose, which is mainly composed of spherical and square crystal particles, showing a layered structure, and the particle size range of the

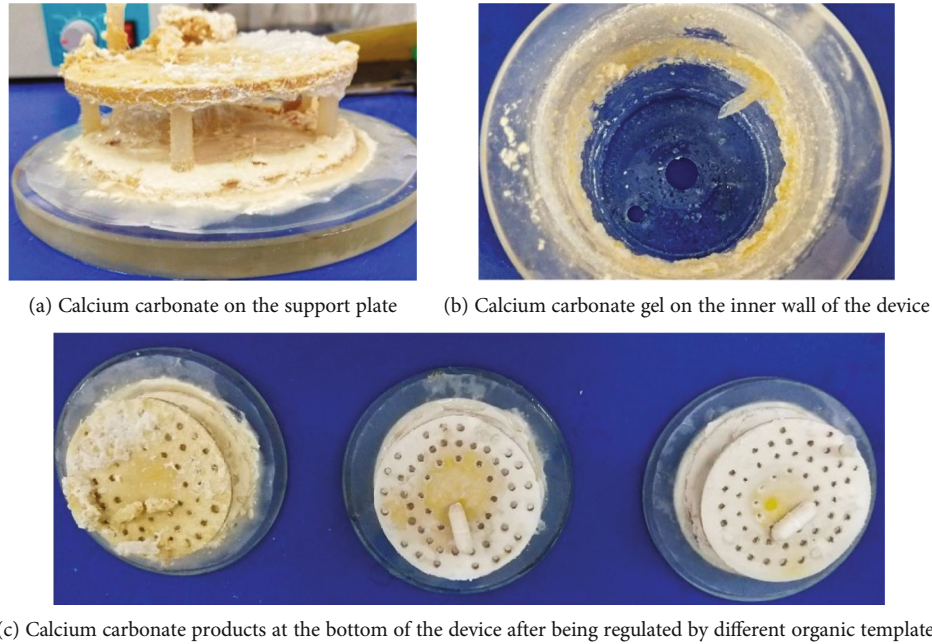


FIGURE 3: Calcium carbonate sample after device removal.

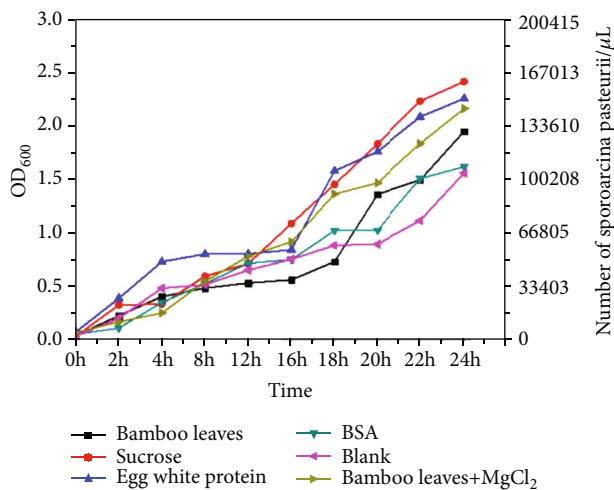


FIGURE 4: Variation chart of bacterium number.

particles can reach $1.8 \mu\text{m}$ to $4.67 \mu\text{m}$. Figure 9(d) shows the crystal morphology under the control of bamboo leaves. Most of them are regular and uniform rhombus crystal structures. When MgCl_2 with a concentration of 2 mol/L is added, the crystal structure changes to multiangular crystal and gradually evolves into an oval state (Figure 9(e)). Figure 9(f) is a microscopic view of calcium carbonate gel crystals under the control of egg white protein. Compared with induced crystals in other experimental groups, calcium carbonate crystals in this group are more closely linked. The main form of calcium carbonate shown in the figure is calcite crystals with a particle size of $2.0 \mu\text{m} \sim 10 \mu\text{m}$, which are mostly firmly bonded to each other through fiber substances of egg white. Since the pore sizes of tailings are mostly distributed between

0 and $40 \mu\text{m}$ under the dry-wet cycle state, the cementation form between tailing particles is mainly the accumulation connection between calcium carbonate crystals under the control state of the above experimental group.

Through further analysis of the elemental state of calcium carbonate gel in each experimental group (point-scanning energy spectrum, Figure 10), it is found that in the elemental analysis shown in Figure 10(a), Ca and O have larger peaks, while the peaks of Cl, N, C, and other elements are lower, which indicates that the main elements of calcium carbonate gel in the blank experimental group are Ca, O, Cl, N, and C, which are the basic constituent elements in the reaction liquid, and the specific proportions of each element are 35.06%, 42.35%, 7.95%, 8.64%, and 6.00%. Compared with Figure 10(b), Sr element is missing, which is related to the main components in BSA. The counting rate of other overlapping elements is obviously lower, which indicates that the detected Ca, O, and other signals in Figure 10(b) are stronger and more reliable, and the proportions of Ca, O, Cl, N, C, and Sr elements are 55.42%, 33.26%, 3.12%, 3.86%, 4.14%, and 0.21%, respectively. On the basis of Figure 10(a), Figure 10(c) contains trace elements such as Mg, Na, Al, Si, Cu, and Ni. Similarly, the counting rate of Ca, O, and other elements in the cements of this group is higher than that of the blank group, with the total proportion of Ca and O elements reaching 81.12%. The element distribution (Figure 10(d)) of calcium carbonate gel under the control of bamboo leaves shows that the elements P, Na, Cu, Zn, and the like contained in bamboo leaves are combined with calcium carbonate crystals, and the content of Ca in the cement is as high as 47.6%. In the synergistic regulation of MgCl_2 , the content of Mg element in gel is 6.90%, and the content of Ca element is increased by 8.66%. In Figure 10(f), the calcium carbonate cement under the action of egg white has the highest content of Ca, up to 66.24%.

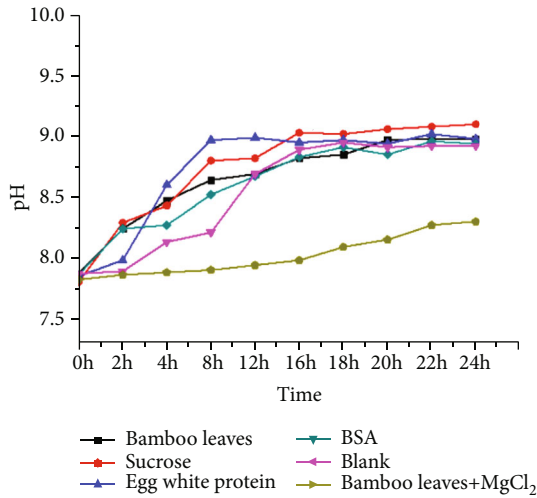


FIGURE 5: pH change diagram of reaction solution.

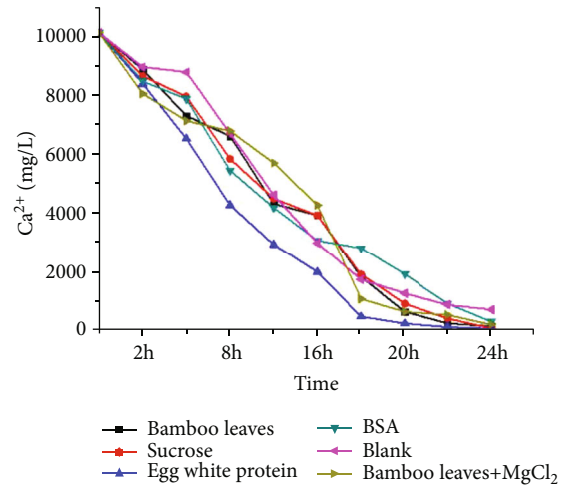


FIGURE 8: Change chart of calcium ion concentration.

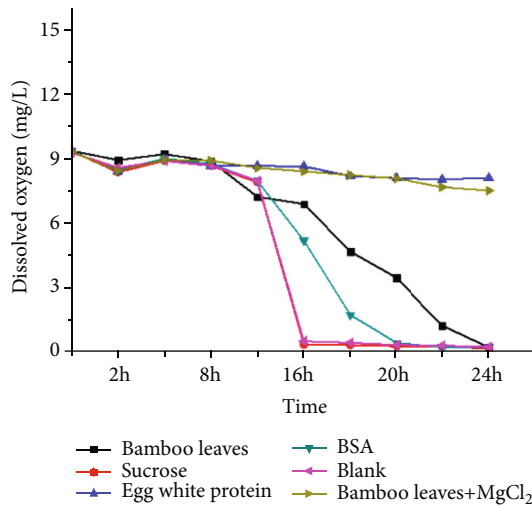


FIGURE 6: Change chart of dissolved oxygen.

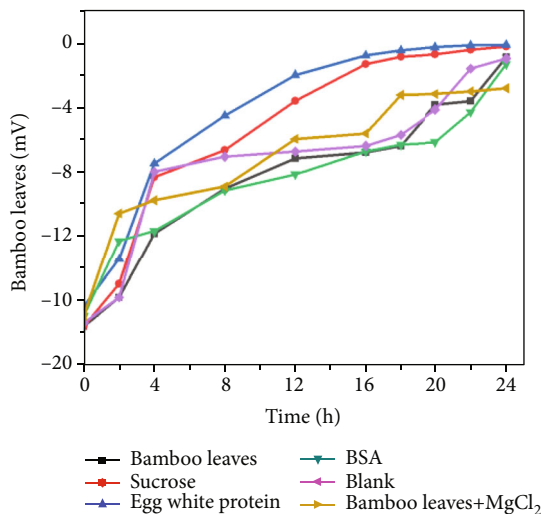


FIGURE 7: Zeta potential value change diagram.

Meanwhile, the S, Al, Mg, Ca, O, N, and other elements rich in egg white coordinate with each other to form calcium carbonate gel.

4.7. Crystal Form and Composition Analysis of Calcium Carbonate. XRD tests were carried out on calcium carbonate mineralized samples under the control of different organic substrates, and the results are shown in Figure 11. By comparing the relevant data of the PDF standard card, it can be found that the calcium carbonate sample in the control group is a mixture composed of calcite and vaterite. The diffraction angle positions of calcite crystal are $2\theta = 23.0, 29.4, 35.9, 39.5, 43.1, 47.5, 48.5, \text{ and } 57.4$, respectively, corresponding to (012), (104), (110), (113), (202), (018), (116), and (122) crystal planes. However, the diffraction angle of vaterite crystal is around $2\theta = 24.8, 26.9, 32.7, \text{ and } 43.8$, corresponding to (110), (112), (114), and (300) crystal planes, respectively. Most of the samples under BSA regulation are mainly vaterite crystal form ((110) crystal plane) but are still doped with a little calcite ((104) crystal plane). XRD patterns detected in three groups of experimental samples of sucrose, bamboo leaves, and egg white protein show that calcium carbonate induced is calcite type ((104) crystal plane). The calcium carbonate sample produced by adding MgCl_2 to bamboo leaves is still a mixture of calcite and vaterite.

In order to further quantify the molar ratio of calcite and vaterite contained in the product, the data of the above three groups of experimental samples were calculated according to the following formula:

$$\frac{I_c^{104}}{I_v^{110}} = 7.619 \times \frac{X_c}{X_v} \quad (5)$$

In the formula, the ratio of the diffraction peak integral intensity of calcite and vaterite in the mixture is expressed; 7.619 is the proportional constant; and X_c/X_v is the ratio of the amount of calcite to vaterite in the mixture.

Calculations show that the molar ratios of calcite to vaterite in the blank group, BSA group, and bamboo leaf+ MgCl_2 experimental group are 2.736, 0.894, and 0.615, respectively.

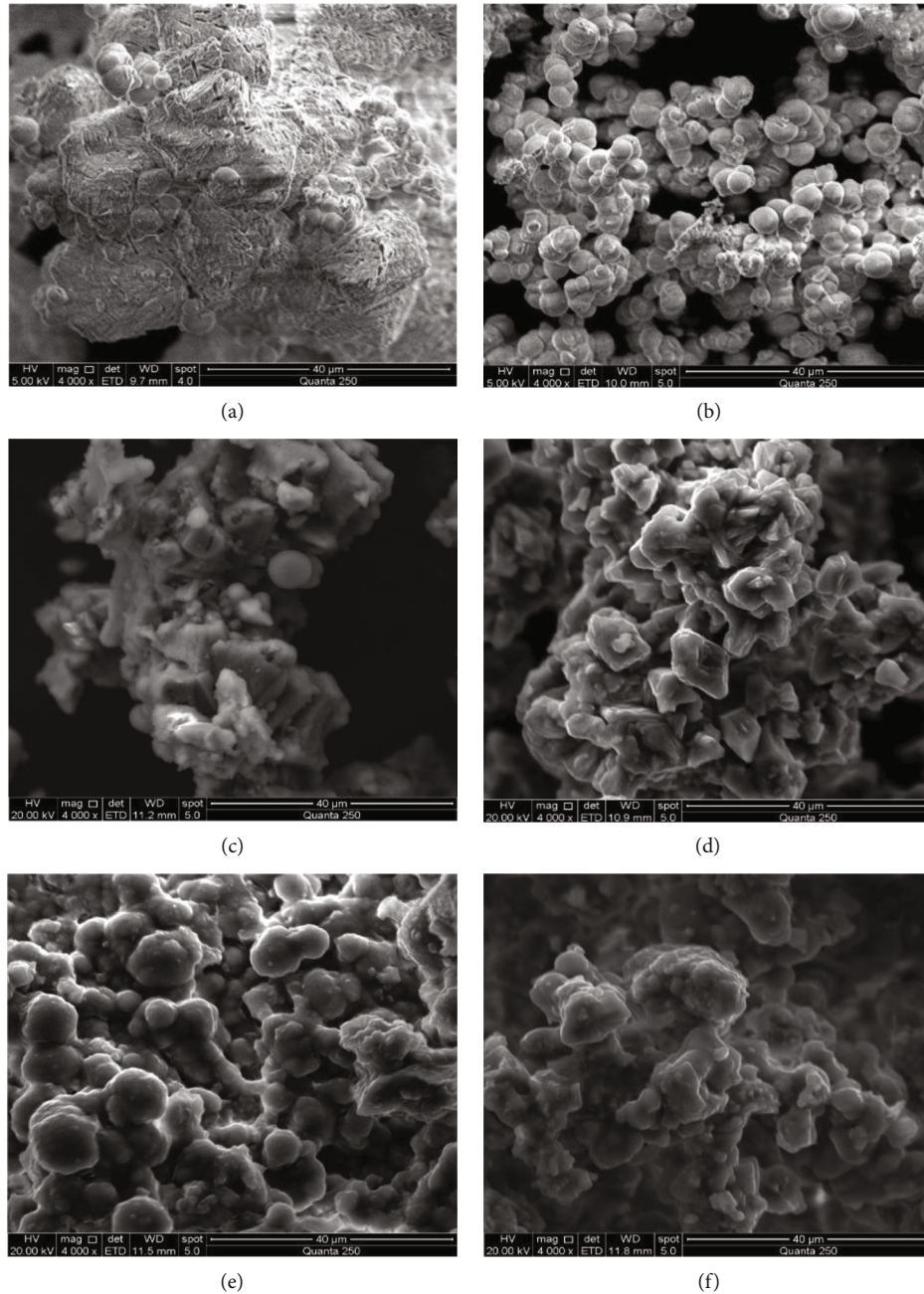


FIGURE 9: SEM images of cements of each experimental group (magnification: 4000), reaction concentration: blank group (a); (b) BSA with mass fraction of 0.3%; (c) sucrose with a mass fraction of 5%; (d) bamboo leaves with a mass concentration of 25 g/L; (e) the mass fraction of bamboo leaves is 25 g/L + 2 mol/L $MgCl_2$; (f) 20% egg white protein by volume.

Therefore, the above-mentioned preliminarily screened organic matrix has obvious regulation effect on the crystal form of induced calcium carbonate crystal.

According to the infrared spectrum shown in Figure 12, calcium carbonate samples in the blank group have characteristic absorption peaks at 3419.79 cm^{-1} , 2509.39 cm^{-1} , 1406.83 cm^{-1} , 1076.28 cm^{-1} , 878.68 cm^{-1} , and 711.73 cm^{-1} . Among them, the absorption peaks of 2509.39 cm^{-1} and 3419.79 cm^{-1} are mainly caused by symmetric stretching vibration and asymmetric stretching vibration of O-H bond, which are mainly due to the existence of hydroxyl groups and

adsorbed water of calcium carbonate particles, while 711.73 cm^{-1} and 878.68 cm^{-1} , respectively, correspond to the characteristic absorption peaks of calcite crystal at V_4 and V_2 ; the peak at V_2 is strong and sharp; and 1076.28 cm^{-1} corresponds to the absorption peak at V_4 of vaterite crystal, so the detection results are consistent with XRD, and the calcium carbonate crystals in the blank group are aragonite and calcite crystal. When BSA was added, the out-of-plane bending vibration peak (878.68 cm^{-1}) of calcium carbonate shifted to the low wave number direction (873.75 cm^{-1}), which indicated that the interaction between BSA and

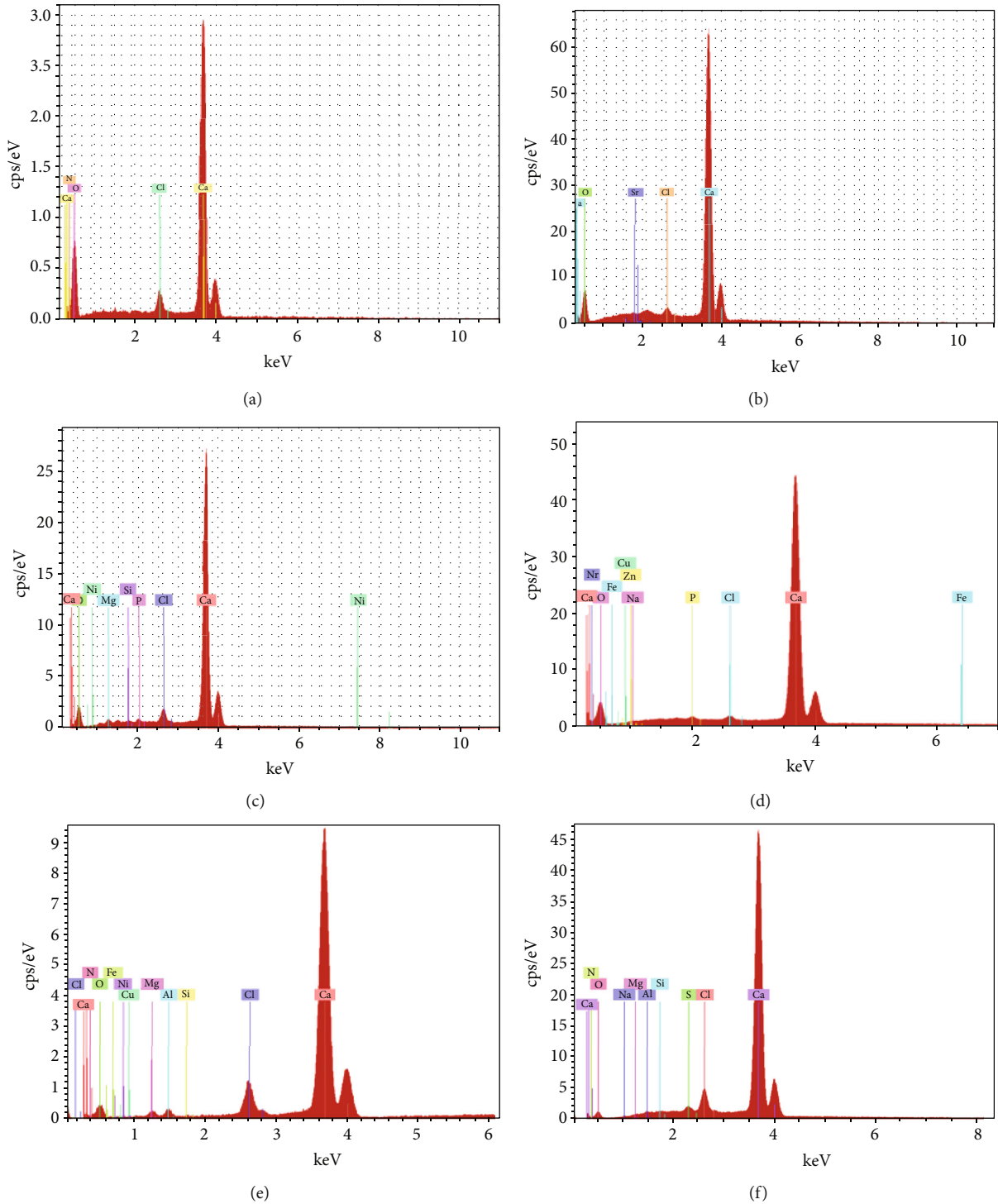


FIGURE 10: Energy spectrum analysis of cement. The energy spectrum analysis chart of the calcium carbonate cement deposited in each experimental group: (a) blank group; (b) BSA; (c) sucrose; (d) bamboo leaves; (e) bamboo leaves+MgCl₂; (f) egg white protein.

calcium carbonate changed the form of O-C-O. The absorption peaks at 873.75 cm⁻¹, 711.73 cm⁻¹, and 1076.28 cm⁻¹ still indicated that the calcium carbonate in the sample was calcite type and vaterite type. The infrared spectra of the samples in the bamboo leaf+magnesium chloride experimental group show absorption peaks at 874.19 cm⁻¹ and 712.15 cm⁻¹, so the calcium carbonate samples obtained are also the mixture of calcite and vaterite. From the infrared spectra of sucrose,

bamboo leaves, and egg white, it can be seen that there are absorption peaks at 878 cm⁻¹ and 710 cm⁻¹, which indicates that the experimental sample is calcite type, and the egg white group moves 20 cm⁻¹ and 10 cm⁻¹ towards high wave displacement at 3419.79 cm⁻¹ and 1406.83 cm⁻¹, respectively, on the basis of the blank group, indicating that there is a strong interaction between egg white protein and calcium carbonate.

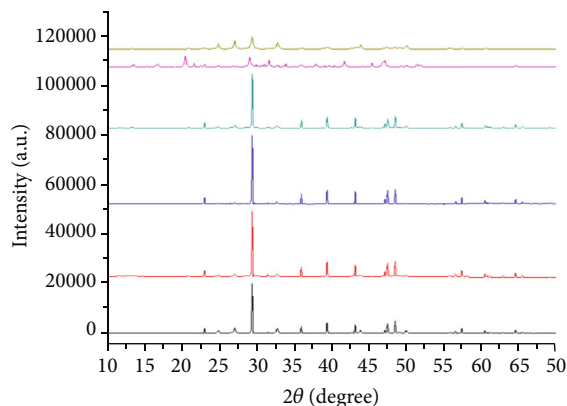


FIGURE 11: XRD test of cement samples.

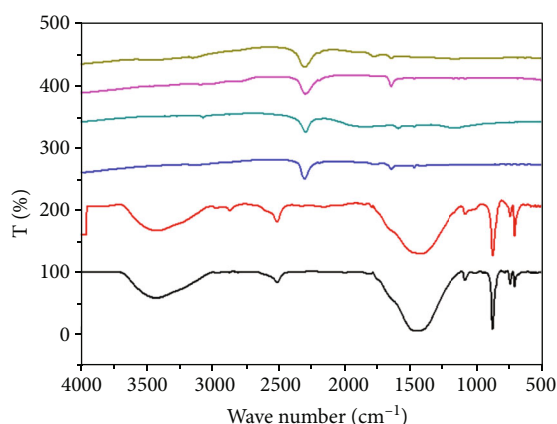


FIGURE 12: FT-IR test of cement samples.

5. Conclusion

In this paper, the number of bacteria, pH value, dissolved oxygen, Zeta potential value, and Ca^{2+} concentration in the reaction solution were detected and analyzed through MICP aqueous solution tests under the control of five different organic substrates. The microstructure characteristics of calcium carbonate cements generated by the control of various organic substrates were compared and studied, and the following main conclusions were obtained:

- (1) The five organic substrates, egg white, bamboo leaves, sucrose, and bovine serum albumin, can significantly enhance the urease activity of *Bacillus Pasteurella*. Among them, egg white and sucrose have the highest contribution to the growth and reproduction of *Bacillus Pasteurella* cells. The change of dissolved oxygen in the reaction solution is directly proportional to the concentration of bacteria. The dissolved oxygen decreases fastest in 8~18h and tends to be stable in 22~24h. With the continuous progress of the reaction, except for the effect of bamboo leaves and magnesium chloride, the pH value of the reaction solution in each experimental group will gradually stabilize at 9.0 in the period of 20~24 hours

- (2) Negative particles in the reaction solution in each experimental group are dominant. With the increase of time, Ca^{2+} and CO_3^{2-} in the solution tend to coagulate continuously, and the coagulation rate under the regulation of egg white and sucrose is the fastest. When reaching 24h, the potential value of each experimental group is close to 0. The calcium ion concentration showed the same change trend, and the calcium ion conversion rate of the egg white protein group was the highest, which was about 2.5 times higher than that of the control group
- (3) The above-mentioned five organic substrates have significant regulation effect on the crystal form, crystal appearance, and particle size characteristics of calcium carbonate crystals induced by MICP technology. Under the action of 5% sucrose, 25 g/L bamboo leaves, and 20% egg white protein, the above-mentioned five organic substrates are easy to be all calcite calcium carbonate, and the calcium carbonate cement under the action of egg white has the highest Ca content, which can reach 66.24%. In addition, the changes in the structural characteristics of calcium carbonate crystals are mainly due to the strong interaction between the organic matrix and calcium carbonate crystals

Data Availability

All data used in this study can be obtained by contacting the corresponding author (Zhang Zhi-jun), email address: zzj181@163.com.

Conflicts of Interest

The authors declare no conflicts of interest related to the publication of this paper.

Authors' Contributions

Wu Ling-ling and Zheng Huai-miao contributed equally to this work.

Acknowledgments

This study was supported by the National Natural Science Foundation of China (51804164, 51774187, and 51974163), the Natural Science Foundation of Hunan Province (2019JJ50498 and 2017JJ3274), and the Scientific Research Foundation of Hunan Provincial Education Department (18B276 and 17A184). Thanks to the Hunan Province & Hengyang City Engineering Technology Research Center for Disaster Prediction and Control on Mining Geotechnical Engineering (2019TP2070) for providing experimental platform support.

References

- [1] C. X. Qian, A. H. Wang, and X. Wang, "Advances of soil improvement with bio-grouting," *Rock and Soil Mechanics*, vol. 36, no. 6, pp. 1537–1548, 2015.
- [2] D. Walsh and S. Mann, "Fabrication of hollow porous shells of calcium carbonate from self-organizing media," *Nature*, vol. 377, no. 6547, pp. 320–323, 1995.
- [3] W. K. Zhu, X. G. Luo, X. Y. Lin, J. Zhou, and Y. Lu, "Effects of temperature on the crystallization of calcium carbonate in egg white protein solution system," *Materials Science Forum*, vol. 675–677, no. 1, pp. 349–352, 2011.
- [4] H. Tong, W. Ma, L. Wang, P. Wan, J. Hu, and L. Cao, "Control over the crystal phase, shape, size and aggregation of calcium carbonate via a L-aspartic acid inducing process," *Biomaterials*, vol. 25, no. 17, pp. 3923–3929, 2004.
- [5] Z. Wang, N. Zhang, J. Ding, C. Lu, and Y. Jin, "Experimental study on wind erosion resistance and strength of sands treated with microbial-induced calcium carbonate precipitation," *Advances in Materials Science and Engineering*, vol. 2018, 10 pages, 2018.
- [6] S. Mann, B. R. Heywood, S. Rajam, and J. D. Birchall, "Controlled crystallization of CaCO₃ under stearic acid monolayers," *Nature*, vol. 334, no. 6184, pp. 692–695, 1988.
- [7] A. J. Xie, Y. H. Shen, S. Y. Zhang, and F. X. Xie, "Study on the interaction between bovine serum albumin and calcium carbonate in physiological saline," *Journal of Inorganic Chemistry*, vol. 4, 607 pages, 2001.
- [8] T. Sugawara, Y. Suwa, K. Ohkawa, and H. Yamamoto, "Chiral biomineralization: mirror-imaged helical growth of calcite with chiral phosphoserine copolypeptides," *Macromolecular Rapid Communications*, vol. 24, no. 14, pp. 847–851, 2003.
- [9] Y. Nishino, Y. Oaki, and H. Imai, "Magnesium-mediated nanocrystalline mosaics of calcite," *Crystal Growth & Design*, vol. 9, no. 1, pp. 223–226, 2009.
- [10] A. Adamiano, S. Bonacchi, N. Calonghi et al., "Structural changes in a protein fragment from abalone shell during the precipitation of calcium carbonate," *Chemistry - A European Journal*, vol. 18, no. 45, pp. 14367–14374, 2012.
- [11] W. Chuajiw, K. Takatori, T. Igarashi, H. Hara, and Y. Fukushima, "The influence of aliphatic amines, diamines, and amino acids on the polymorph of calcium carbonate precipitated by the introduction of carbon dioxide gas into calcium hydroxide aqueous suspensions," *Journal of Crystal Growth*, vol. 386, pp. 119–127, 2014.
- [12] Y. F. Gao, *Study on the Crystal Form and Morphology of Calcium Carbonate Controlled by Sodium Citrate*, South China University of Technology, 2015.
- [13] Z. Qiao, *Preparation of Bionic Calcium Carbonate by Egg White Template Method and Its Adsorption Properties [D]*, Southwest University of Science and Technology, 2017.
- [14] M. W. Li, *Study on Crystallization Behavior of Calcium Carbonate Controlled by Sodium Dodecylbenzene Sulfonate Template [D]*, Jilin University, 2018.
- [15] L. L. Wu, Z. J. Zhang, Q. Yu, Y. X. Pan, and L. Hu, "Improvement of the tailings properties in a metal mine by microbiological grouting," *Journal of China University of Mining & Technology*, vol. 47, no. 6, pp. 1354–1359, 2018.
- [16] R. Gui, Y.-X. Pan, D.-X. Ding, Y. Liu, and Z.-J. Zhang, "Experimental study on the fine-grained uranium tailings reinforced by MICP," *Advances in civil engineering*, vol. 2018, 10 pages, 2018.
- [17] A. M. Ding, H. Luo, M. Cheng, J. M. Zhu, and J. C. Yao, "Biomimetic synthesis of calcium carbonate controlled by egg white protein and semipermeable membrane," *Journal of Analytical Testing*, vol. 31, no. 6, pp. 696–699, 2012.
- [18] Z. J. Zhang, K. W. Tong, H. Lin, Y. Qing, and L. L. Wu, "Experimental study on solidification of tailings by MICP under the regulation of organic matrix," *Construction and Building Materials*, vol. 265, p. 120303, 2020.
- [19] Y. P. Wu, *Preparation and Characterization of Calcium Carbonate by Plant Template Method*, Anhui University, 2009.
- [20] R. Lakshminarayanan, X. J. Loh, S. Gayathri et al., "Formation of transient amorphous calcium carbonate precursor in quail eggshell mineralization: an in vitro study," *Biomacromolecules*, vol. 7, no. 11, pp. 3202–3209, 2006.
- [21] Z. X. Chen, *Application of Histidine Modified Chitosan in Biomimetic Synthesis and Protein Isolation [D]*, overseas Chinese university, 2014.
- [22] Y. P. Wu and A. J. Xie, "Research progress on calcium carbonate biomineralization-soft template regulation," *Journal of Anqing Teachers (Natural Science Edition)*, vol. 15, no. 1, pp. 78–80, 2009.
- [23] Z. D. Zulkafli, H. Wang, F. Miyashita, N. Utsumi, and K. Tamura, "Cosolvent-modified supercritical carbon dioxide extraction of phenolic compounds from bamboo leaves (*Sasa palmata*)," *The Journal of Supercritical Fluids*, vol. 94, pp. 123–129, 2014.
- [24] J. Xie, Y. S. Lin, X. J. Shi, X. Y. Zhu, W. K. Su, and P. Wang, "Mechanochemical-assisted extraction of flavonoids from bamboo (*Phyllostachys edulis*) leaves," *Industrial Crops and Products*, vol. 43, pp. 276–282, 2013.
- [25] S. Shen, J. L. Duan, Y. Li, C. Wang, J. J. Fu, and H. B. Wang, "Study on extraction technology and functional application of chlorophyll from bamboo leaves," *New Chemical Materials*, vol. 46, no. 1, pp. 117–120, 2018.
- [26] X. Zhao, *Experimental study on microbial induced calcium carbonate precipitation (MICP) solidification of soil*, China University of Geosciences, 2014.
- [27] M. Yu, A. M. Lu, X. T. Li, G. Z. Li, and R. Peng, "Study on influencing factors of Zeta potential in carbonate rocks," *Science, Technology and Engineering*, vol. 16, no. 20, pp. 165–168, 2016.

Research Article

Experimental Study on the Mechanical Properties and Damage Evolution of Hollow Cylindrical Granite Specimens Subjected to Cyclic Coupled Static-Dynamic Loads

Yongming Xue,^{1,2} Bing Dai,^{1,2} Ying Chen ,^{1,2} Lei Zhang,^{1,2} Guicheng He,^{1,2} and Zhijun Zhang ^{1,2}

¹School of Resources Environment and Safety Engineering, University of South China, Hengyang, China

²Hunan Province Engineering Technology, Research Center for Disaster Prediction and Control on Mining Geotechnical Engineering, 421001 Hengyang, China

Correspondence should be addressed to Ying Chen; csu_chenyong@csu.edu.cn

Received 13 July 2020; Revised 19 August 2020; Accepted 26 August 2020; Published 22 September 2020

Academic Editor: Zhengyang Song

Copyright © 2020 Yongming Xue et al. This is an open access article distributed under the Creative Commons Attribution License, which permits unrestricted use, distribution, and reproduction in any medium, provided the original work is properly cited.

To study the characteristics of roadway surrounding rock damage caused by frequent disturbances under different static stress conditions, cyclic impact tests on granite with vertical holes under different axial prestress conditions were performed by a modified split Hopkinson pressure bar test, and the damage of the specimens was recorded with a high-speed camera process. The test results show that under the same air pressure cyclic impact, the rock specimens mainly undergo the compaction-fatigue-failure transition. As the axial prestress increases, the compaction-fatigue phase gradually weakens, and the dynamic compressive strength decreases. When the axial prestress is 42% of the UCS and 62% of the UCS, the rock specimen shows a certain “strengthening” effect during the initial cyclic impact stage. During the failure of the rock specimens, the axial prestressing effect limited the initiation of some transverse cracks, and a mixed tensile-shear failure mode appeared. The rock specimens with an axial prestress of 62% of the UCS showed energy release during cyclic impact. To some extent, the probability of “rock bursts” has been induced. Based on the one-dimensional stress wave theory, the damage variables of wave impedance during the cyclic impact loading of the rock with vertical holes are defined. It is found that when the rock specimen is in the stage of compaction and fatigue damage, the damage is small, and the damage is even reduced.

1. Introduction

As the main carrier of loads in underground engineering applications, the structure and structural stability of rock are closely related to engineering safety. In recent years, with the continuous lack of shallow resources and the need for economic development for various countries, an increasing number of underground spaces have been developed at greater depths, such as mining, highway tunnel construction, and roadway excavation engineering projects [1–3], which trigger the continuous change of the stress state of the deep surrounding rock. In the process of underground rock excavation, the surrounding rock structure will inevitably be subjected to ground stress and mechanical drilling and blasting. The common effect of frequent disturbance [4, 5] and various

factors lead to deformation, failure, and instability of the rock mass structure, which leads to a series of engineering disasters, such as intensified instability of the roadway [6–8] and rock burst [9, 10]. Therefore, one-dimensional dynamic static coupling can better reflect the actual stress state of roadway excavation. The study of the dynamic characteristics of the surrounding rock under dynamic and static coupling has important reference significance for the safe construction [11, 12], efficient operation [13], and long-term stability of underground rock engineering.

Therefore, domestic and foreign scholars have performed much research on the mechanical properties of rocks under coupled static-dynamic loads. Zhou et al. [14–18] used an improved Hopkinson pressure bar system to analyse the mechanical properties of rock under the combined action

of one-dimensional dynamic and static combinations and tested dried sandstone and water-saturated sandstone with different axial prestresses to study the influence of water saturation on the dynamic characteristics of rock under static prestress. Wang et al. [19] carried out experimental studies on different axial pressures and different impact loads on red sandstone and analysed the effects of axial pressure and impact loads on their mechanical properties and energy loss. Gong et al. [20–22] studied the dynamic characteristics of sandstone under coupled static-dynamic loads. The study found that when sandstone is loaded and destroyed within a certain range of axial pressure ratios, as the incident energy increases, the sandstone successively undergoes the three stages of “absorbed energy-release energy-absorbed energy”. The above studies are based on the experimental study of intact rock samples under impact loading and have obtained abundant research results. However, rock failure and instability usually begin with primitive defects such as rock cracks and holes [23, 24]. At present, there are few studies on defective rocks under impact loading. Li et al. [25–27] performed a one-dimensional dynamic and static combination test on samples containing circular and elliptical holes and found that the size, shape, and location of the holes have a certain effect on the dynamic strength of the rock, and the existence of holes induces shear failure of rocks. Wang et al. [28] used Hopkinson rods and combined digital image correlation technology to carry out impact experiments on rock-like samples with an angle of 0° to 90° between the prefabrication and loading directions and analysed samples under conditions of multiple loading rates, single cracks, and multiple angles. Li et al. [29] tested granite with square and circular holes to test the instability failure characteristics and obtained the relaxation time T2 spectrum curve, nuclear magnetic porosity, and nuclear magnetic resonance images under nuclear magnetic resonance (NMR) tests. In summary, most of the previous studies utilized impact tests based on prefabricated lateral cavity rock samples perpendicular to the loading direction, and few studies have been conducted on vertical holes. In the actual underground tunnel excavation process, frequent dynamic disturbances generated by mechanical drilling and blasting in the form of stress waves act on the surrounding rock of the excavated tunnel, which has a greater impact on its stability, and the surrounding rock of the tunnel when subjected to dynamic load disturbances. The rock is subjected to static loads such as in situ stress and tectonic stress [30], as shown in Figure 1. Therefore, understanding the failure mechanism of roadway surrounding rock under cyclic impact loading and certain static stress conditions is the essential basic information and basis for scientifically evaluating the stability of surrounding rock during the excavation of underground roadways.

Thick wall cylinders are the preferred model for simulating underground tunnels, tunnels, mine shafts, and other structures [31]. To correctly understand the mechanical properties, energy, and damage evolution of surrounding rock under the coupling action of static stress and dynamic disturbance in an actual project, this paper selects a granite cylinder with inner and outer diameters of 5 mm and 25 mm, respectively, and uses the modified Hopkinson bar

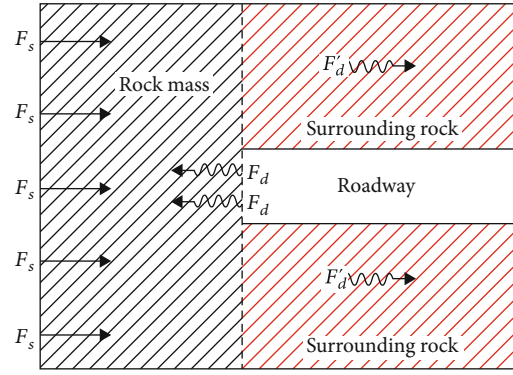


FIGURE 1: Schematic diagram of the surrounding rock forces during tunnel excavation (F_s : static stress, F_d : dynamic load, and F_d' : dynamic disturbance).

system of Central South University to carry out cyclic impact tests on the granite under the same air pressure and different axial prestresses and uses high-speed photography. The image machine records the failure process of the specimen and analyses the mechanical behaviour, failure mode, energy evolution, and damage characteristics of the specimen under dynamic static coupling action.

2. Test Methods and Specimen Preparation

2.1. Specimen Preparation and Test System. The test material is granite with relatively good integrity and uniformity, processed into a $50 \text{ mm} \times 100 \text{ mm}$ cylindrical rock sample. Then, a vertical hole with a diameter of 10 mm is prefabricated in the centre of the circular cross-section, and the two cross sections at both ends of the sample, which exhibit nonparallelism and nonverticality, are less than 0.02 mm, as shown in Figure 2. To reduce the discreteness of the rock samples, a rock acoustic wave parameter test system (HS-YS4A type) is used to test the P -wave velocity of the rock samples. The average density of the rock samples is $2.79 \times 10^3 \text{ kg/m}^3$, the average P -wave velocity is 5345 m/s, and the average compressive strength is 140 MPa.

2.2. Testing Equipment. The test equipment uses the dynamic and static combined loading test system based on the SHPB device modified by Central South University. It consists of a punch device, an incident rod, a transmission rod, a buffer rod, and an axial compression device, as shown in Figure 3. The rods of the test system are made of 40Cr alloy steel with a diameter of 50 mm. The longitudinal wave velocity is 5400 m/s, the density is 7810 kg/m^3 , and the elastic modulus is 240 GPa. The data acquisition instrument and display equipment are a CS-1D super dynamic strain gauge and DL-750 oscilloscope, respectively. A spindle-shaped bullet is used in the launch cavity to eliminate wave oscillations and achieve stable half-sine wave loading to achieve a constant strain rate loading effect. To facilitate the observation of the microdestruction process of the test piece, a FASTCAM SA1.1 high-speed camera is used to synchronously record the crack propagation process of the test piece. The frame number of the high-speed camera is set to 43,200 fps



FIGURE 2: Rock test samples.

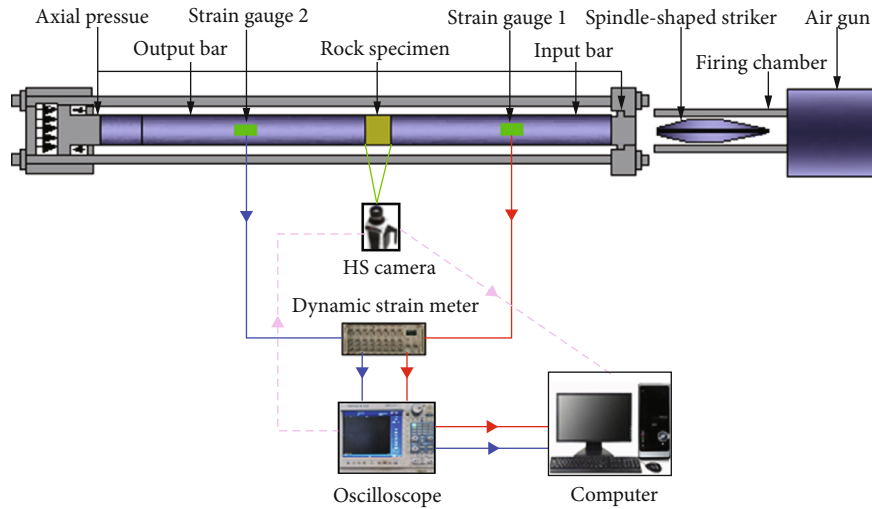


FIGURE 3: Rock dynamic and static combination based on the SHPB device.

and shot once at an interval of $23 \mu\text{s}$. Figure 4 shows the dynamic and static combination loading schematic of the test piece.

2.3. Test Plan

2.3.1. Test Method. To study the impact mechanical properties, energy, and damage evolution law of granite with vertical holes under different prestressing effects, the axial prestressing load was set to 0.55 MPa (42% of the UCS), 82 MPa (62% of the UCS), and 110 MPa in this experiment (83% of the UCS) to carry out cyclic impact loading. To ensure the reliability of the data, each group of data was tested for 3 samples. The test piece number was in the form of Z-0-1, where 0 and 1 represented the axial pressure of 0 and the test piece group number, and A, B, and C represented the prestress force of 55, 83, and 110 MPa, respectively. The test scheme is shown in Table 1.

2.3.2. Test Procedure. To test the effectiveness, before the start of the test, the incident rod and the transmission rod are closely pressed for empty punching, and the trend of the incident wave and the transmitted wave on the oscilloscope is observed to ensure whether the two rods are normally secured.

To achieve the purpose of cyclic impact of the rock sample under different prestressing effects and to avoid the rock sample being damaged, it is necessary to test the rock sample and finally set the impact pressure to 0.8 MPa.

During the test, lubricating oil should be applied between the incident rod and the transmission rod to reduce the end effect of the sample, the rock should be sandwiched between the incident rod and the transmission rod, and then the manual oil pump should be slowly prestressed to the set value. The strain gauge, oscilloscope, and high-speed camera are initiated to record data.

2.4. Test Principle. The SHPB system can simultaneously realize dynamic and static combined tests with an axial prestress of 0-200 MPa and an impact dynamic load of 0-500 MPa. The punch impacts the incident rod at a certain rate under the action of air pressure, and an incident stress wave is formed in the incident rod. When the incident stress wave is transmitted to the end face of the rock sample, transmission stress is formed on the end face of the rock sample due to the different wave impedances of the rock sample and the rod. The incident and transmitted waves can be measured from incident rod strain gauge 1 and transmitted rod strain gauge 2, respectively, as shown in Figure 2. Using the “three wave method” [32] to process the collected wave

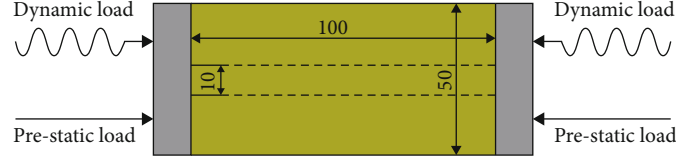


FIGURE 4: Schematic diagram of the combined dynamic and static loading of the test specimens.

TABLE 1: Basic physical parameters and test plan of the rock specimens.

Rock specimen number	Diameter (mm)	Height (mm)	Axial prestress (MPa)	Impact air pressure (MPa)
Z-0-1	50.2	99.81		
Z-0-2	49.98	100.21	0	
Z-0-3	50.03	100.10		
Z-A-1	49.81	99.89		
Z-A-2	49.98	100.02	55	
Z-A-3	50.12	99.89		0.8
Z-B-1	49.63	100.12		
Z-B-2	49.95	99.98	83	
Z-B-3	49.95	99.91		
Z-C-1	50.26	100.08		
Z-C-2	50.08	99.96	110	
Z-C-3	49.89	100.18		

forms, we can obtain the changes in the strain, stress, and strain rate with time as follows:

$$\begin{aligned}
 \varepsilon(t) &= \frac{C_e}{L_s} \int_0^t [\varepsilon_I(t) - \varepsilon_R(t) - \varepsilon_T(t)] dt, \\
 \sigma(t) &= \frac{E_e A_e}{2A_s} [\varepsilon_I(t) + \varepsilon_R(t) + \varepsilon_T(t)] dt, \\
 \dot{\varepsilon} &= \frac{C_e}{L_s} [\varepsilon_I(t) - \varepsilon_R(t) - \varepsilon_T(t)] dt.
 \end{aligned} \quad (1)$$

In the SHPB test, it is assumed that the energy loss generated by the end face of the specimen is negligible. The energy before the test is equal to the energy after the test. According to the law of the conservation of energy [32], the incident energy, reflection energy, transmitted energy, and formula for absorbed energy are as follows:

$$\begin{aligned}
 W_I &= \frac{A_e C_e}{E_e} \int_0^t \sigma_I^2(t) dt, \\
 W_R &= \frac{A_e C_e}{E_e} \int_0^t \sigma_R^2(t) dt, \\
 W_T &= \frac{A_e C_e}{E_e} \int_0^t \sigma_T^2(t) dt, \\
 W_s &= W_I - W_R - W_T,
 \end{aligned} \quad (2)$$

where A_e and A_s denote the cross-sectional area of the elastic

rod and the sample, respectively; E_e represents the elastic modulus of the elastic rod; C_e and L_s represent the longitudinal wave velocity of the elastic rod and the length of the sample; $\varepsilon_I(t)$, $\varepsilon_R(t)$, and $\varepsilon_T(t)$ represent incident, reflected, and transmitted strain wave signals, respectively; $\varepsilon(t)$ and $\sigma(t)$ are the strain and stress, respectively; W_I , W_R , W_T , and W_s are the incident energy, reflected energy, transmitted energy, and absorbed energy, respectively.

3. Test Results and Discussion

The posttest data are processed based on the three-wave method. Due to space limitations, some test specimens are selected for analysis in this article. The test results are shown in Table 2.

3.1. Mechanical Behaviour of Granite under Dynamic and Static Coupling

3.1.1. Dynamic Stress-Strain Curve. Figure 5 shows the stress-strain curve of a rock sample during cyclic impact under different axial prestressing forces. Figure 5 shows that the stress-strain curve can be roughly divided into a compaction stage, a crack propagation stage, and a postpeak unloading stage. In the crack growth stage, when a relatively smooth curve appears before the peak stress is approached, the stress growth is slow, and the strain growth rate is faster as the yield stage continues; when the strain increases to a certain level, the peak stress rapidly increases and is defined as the strengthening stage. As the axial prestress increases, the yield stage becomes less and less obvious. Before reaching the peak stress, the change trends of the stress-strain curves are similar, but there are obvious differences in the unloading phases after the peak. Before the failure of the rock sample, the maximum strain at the unloading stage after the peak increases first and then decreases with the decrease in the stress, showing a rebound phenomenon; when the rock sample is impacted and destroyed, the rebound phenomenon gradually disappears.

3.1.2. Effect of the Axial Prestress on the Peak Stress. In the process of cyclic impact loading under different axial prestresses, the peak stress and the number of cyclic impact changes are shown in Figure 6. As the number of cycles increases, the peak stresses of Z-0-1 and Z-C-1 continue to decrease, while the peak stresses of rock samples Z-A-3 and Z-B-2 have an increasing trend during the initial impact stage, and their peak stress performance thereafter gradually decreases. According to the analysis, in the initial impact stage of samples Z-A-3 and Z-B-2, internal microcracks are closed under the impact load, which means that the wave

TABLE 2: Test results of the rock specimens.

Rock specimen number	Impact sequence	Peak stress (MPa)	Peak strain (mm)	Maximum strain (mm)	Average strain rate (s^{-1})	Absorbed energy (J)
Z-0-1	1	148.84	0.0039	0.0040	34.74	2.77
	2	144.70	0.0034	0.0035	35.10	10.64
	3	118.62	0.0042	0.0043	38.78	14.43
Z-A-3	1	118.20	0.0034	0.0034	34.62	-25.03
	2	121.45	0.0035	0.0035	35.99	-12.27
	3	138.33	0.0027	0.0028	30.73	1.14
	4	132.89	0.0028	0.0028	29.31	2.42
	5	131.08	0.0029	0.0031	32.16	7.88
	6	97.97	0.0028	0.0044	41.67	28.48
Z-B-2	1	106.01	0.0032	0.0033	27.43	-39.23
	2	109.27	0.0028	0.0030	29.27	-30.46
	3	124.45	0.0027	0.0030	27.04	-42.09
	4	109.57	0.0028	0.0031	28.69	-44.10
	5	109.27	0.0035	0.0037	33.57	-37.96
	6	100.09	0.0033	0.0039	34.07	-16.52
	7	61.42	0.0026	0.0081	41.22	-7.95
Z-C-1	1	101.93	0.0026	0.0029	25.01	-18.92
	2	99.60	0.0031	0.0034	30.60	8.79

impedance of the rock sample increases and the peak stress increases [33]. In the subsequent impact process, the internal cracks of the rock samples gradually increase, the wave impedance of the samples gradually decreases, and the ability to resist external loads continues to weaken, which reflects the strength degradation characteristics of the rock sample during cyclic impact. However, due to the large axial prestress, Z-C-1 causes many internal microcracks, which greatly weakens the resistance of the rock sample to external loads. Under dynamic loading, the peak stress shows a decrease with an increase in the number of cycles.

Figure 6 can further illustrate the effect of the axial prestress on the peak stress of the rock samples under the same air pressure. It can be seen from Figure 6 that the dynamic peak strength of unstressed rock samples is higher than that of prestressed axial forces, and the dynamic peak strength decreases as the axial prestress increases. When the axial prestress is 42% of the UCS and 62% of the UCS, the number of impacts increases compared to the case without axial prestress, and when the axial prestress is 83% of the UCS, the number of impacts is reduced. From the above phenomenon, it can be determined that the axial prestress has a certain effect on the dynamic strength and stiffness of the material. These phenomena can be explained by different stress stages under uniaxial compression [14]. Generally, the behaviour of brittle rock can be divided into three stages during uniaxial compression: (I) elastic deformation stage: approximately 0-30% of the UCS; (II) crack steady propagation stage: approximately 30-70% of the UCS; and (III) unstable crack growth stage: approximately 70-100% of the UCS, as shown in Figure 7.

The axial prestress is in the stage of stable crack propagation, and activated cracks regenerated inside the rock sample.

When the peak strength of the dynamic load is lower than a certain value, during the initial cyclic impact of the rock sample, the damage caused by the dynamic load is generally lower than the crack closure amount, and the rock sample shows a compaction process [34]. When the axial prestress is 42% of the UCS and 62% of the UCS, the dynamic strength of the rock sample is lower than that without prestressing, indicating that the prestress has caused some damage to the rock sample, but due to the axial prestressing effect, the local damage has an impact on the specimen failure and has a strengthening effect on the rock material. Therefore, the stiffness is enhanced compared with the prestress. At an axial prestress of 83% of the UCS, the rock sample is in the stage of unstable crack propagation. The internal cracks greatly deteriorate the mechanical properties of the rock, showing its minimum dynamic strength and minimum number of impacts.

3.1.3. Variation in the Average Strain Rate and Maximum Strain. The average strain rate represents the amount of strain per unit time of the rock during a single impact [34]. Figures 8 and 9 show the relationship between the average strain rate and the maximum strain with the number of cycles when the rock samples are subjected to different axial prestresses. It can be seen that the average strain rate and the maximum strain increase as a whole. Z-0-1 shows a relatively large average strain rate and maximum strain during the first impact. According to the analysis, some initial cracks cannot be avoided inside the rock sample, and more stress may be generated around the hole wall during the impact due to the stress concentration. The crack shows a larger strain rate and maximum strain during the initial impact; the average strain rate and maximum strain of Z-A-3 during

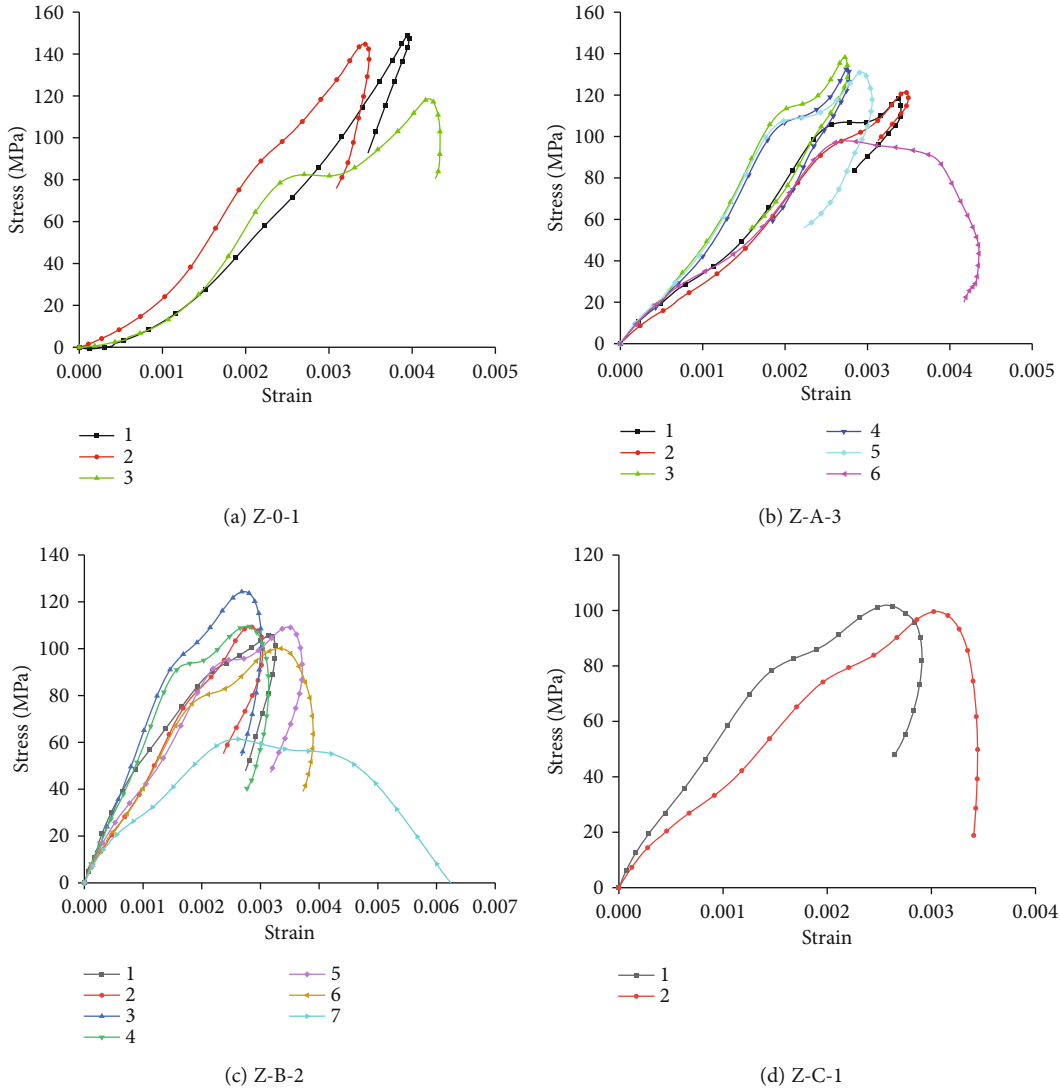


FIGURE 5: Dynamic stress-strain curve.

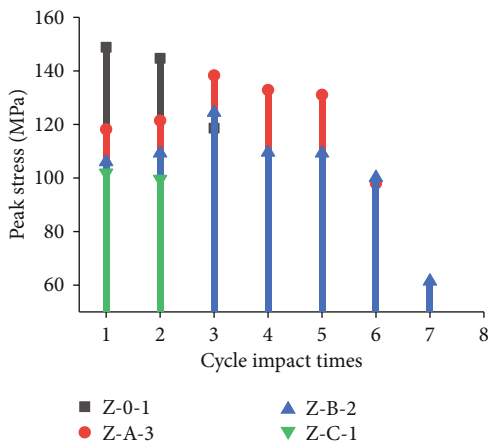


FIGURE 6: Relationship between the peak stress and cycle impact times.

the first impact are lower than those of Z-0-1, which is due to the axial prestress. Effected by the initial crack closure, the first time the impact is initiated with the same air pressure, the crack closure amount is relatively small. In the same way, with the increase in the axial prestress, the internal crack closure of the rock samples increases, and the average strain rate and maximum strain of Z-B-2 and Z-C-1 are substantially reduced compared with Z-A-3 at the first impact. As the number of impacts accumulates, Z-A-3 and Z-B-2 show an average strain rate and a maximum strain that first decrease and then increase, and the strain of Z-C-1 increases as a whole. The analysis shows that during the initial impact of Z-A-3, the crack closure amount of the rock sample is larger than the crack initiation amount, showing a decreasing trend of the average strain rate and that the maximum strain decreases; with the increase in the number of cycles, the rock sample is in the third stage. During the fifth impact process, the average strain rate and the maximum strain change range decrease, indicating that the microcracks at this stage of the rock specimens develop slowly. The analysis indicates that

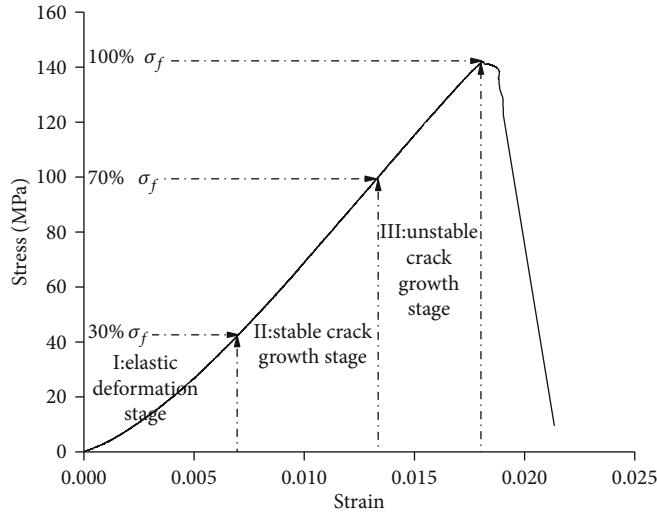


FIGURE 7: Uniaxial stress-strain curve.

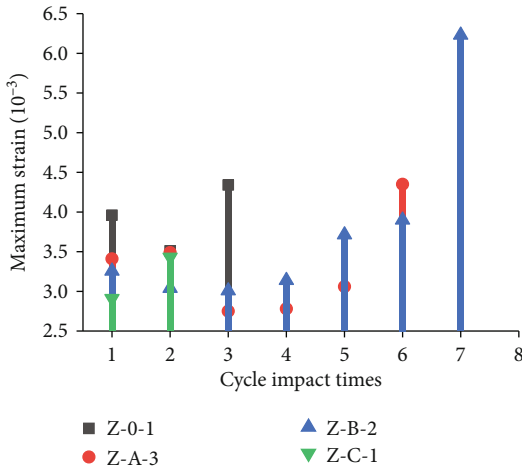


FIGURE 8: Relationship between the maximum strain and cycle impact times.

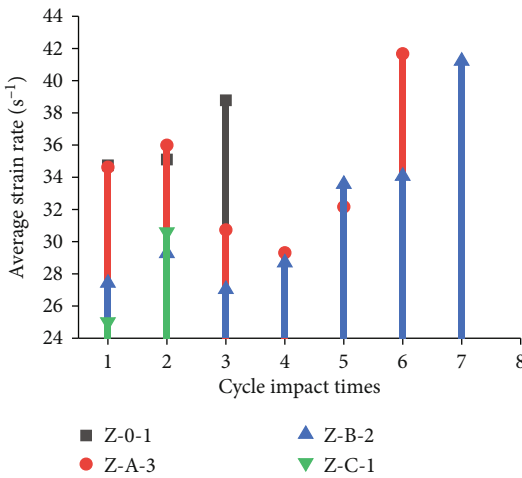


FIGURE 9: Relationship between the average strain rate and number of cycles.

the rock specimens transition from the initial compaction stage to the fatigue damage stage and finally collapse. At this time, cracks in the rock samples rapidly expand, and the average strain rate and maximum strain increase substantially. During the initial impact of Z-B-2, the average strain rate and the maximum strain change are small, and the crack growth rate of the rock sample is very slow or does not expand. The average strain rate and the maximum value during the third impact should reach a minimum, indicating that the rock sample is in the first three stages. The crack closure stage is at the initial stage of fatigue damage; when the rock sample is impacted for the fifth time, the average strain rate and maximum strain of the rock sample increase substantially, indicating that the crack growth speed of the rock sample accelerates, which represents the transition from the fatigue damage stage to the failure stage. The Z-C-1 strain rate and average strain rate increase with increasing number of cycles. According to the analysis, a large number of microcracks appear in the sample due to the prestressing effect. When the impact load is applied, the initiation cracks are promoted to develop into the macrocrack direction. No compaction stage or fatigue damage stage is shown. In summary, when the axial prestress is low, the rock sample undergoes three stages during the cyclic impact process: the compaction phase, fatigue damage phase, and failure phase; as the prestress increases, the rock sample compaction phase weakens. There are two phases: the fatigue damage phase and failure phase; when the prestress is greater than a certain value, the rock sample only shows the failure phase.

3.1.4. *Effect of Different Prestressing Effects on the Dynamic Deformation Modulus.* Figure 10 shows the relationship between the dynamic deformation modulus of the rock sample and the number of cycles during different axial prestressed cyclic impacts. The dynamic deformation modulus reflects the resistance of the rock to deformation. Because the dynamic stress-strain curve has no obvious straight line segment, to better reflect the rock's resistance to deformation during impact, reduce errors, and reduce test dispersion, this

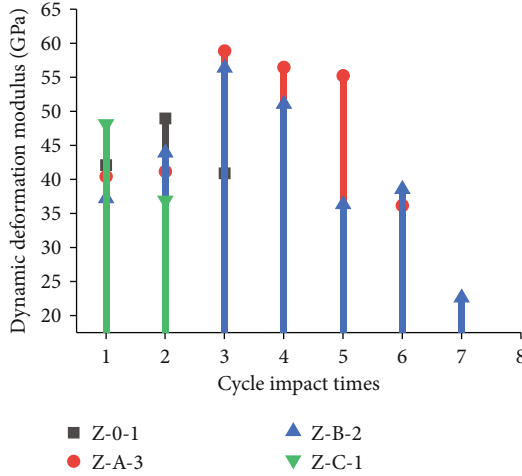


FIGURE 10: Relationship between the dynamic deformation modulus and the number of cycles.

paper adopts the following calculation method proposed by Tang et al. [35]:

$$\begin{aligned}
 E_1 &= \frac{\sigma_{d50}}{\varepsilon_{d50}}, \\
 E_2 &= \frac{\sigma_d - \sigma_{d50}}{\varepsilon_d - \varepsilon_{d50}}, \\
 E_3 &= \tan \alpha, \\
 E_d &= \frac{E_1 + E_2 + E_3}{3},
 \end{aligned} \tag{3}$$

where E_1 is the first secant modulus, E_2 is the second type of secant modulus, E_3 is the deformation modulus of the loading section, E_d is the dynamic deformation modulus, σ_{d50} is 50% of the peak stress, and ε_{d50} is 50% of the peak stress. The corresponding strain σ_d is the peak stress, ε_d is the peak strain, α is the angle between the tangent and the axis at 50% of the peak stress, and E_0 is the elastic modulus of the material without damage.

In combination with the stress-strain curve in Figure 3, it can be seen that when the axial prestress is low and when the dynamic load initially acts on the rock sample, the internal cracks are further closed, showing that the dynamic deformation modulus increases first and then decreases as the number of cycles increases. When the axial prestress is greater than a certain degree, there are more microcracks in the rock sample, but the overall structure is in a state of stress equilibrium due to axial compression. When the dynamic load is applied, the internal cracks expand rapidly, showing that the dynamic deformation modulus changes. The number of cycles increases at a smaller level. The overall trend of the Z-0-1, Z-A-3, and Z-B-2 dynamic deformation moduli first increases and then decreases, while Z-C-1 shows a decreasing trend. The increase in the dynamic deformation modulus means that its resistance to deformation is enhanced. The dynamic deformation modulus of the Z-A-3 and Z-B-2 rock samples increases during the first three impacts, indicating

that the rock samples are in the crack-closing stage under the impact load, showing a certain hardening effect. The dynamic deformation modulus followed by the cycle number decreases, and the resistance of the rock samples to deformation weakens.

It is further seen from Figure 8 that the maximum deformation modulus of the axial prestress of 42% of the UCS and 62% of the UCS is substantially higher than when the axial prestress is not applied. This is because the rock is enhanced when the axial prestress is low. The ability of the sample to resist deformation and the dynamic deformation modulus of the rock sample under impact failure are lower than when axial prestress is not applied. According to the analysis, the rock sample has sufficient internal crack expansion when subjected to multiple impact loads. The deformation modulus is low. When the axial prestress is 83% of the UCS, the maximum dynamic deformation modulus of the rock sample and the dynamic deformation modulus at failure are lower than those without axial prestress. This is because when the axial prestress is large, the prestress promotes the formation of microcracks in the rock sample, reducing its resistance to deformation.

3.2. Energy Evolution Characteristics of Granite under Dynamic and Static Coupling. Figure 11 shows the relationship between the absorbed energy of the rock sample and the number of cycles under different axial prestressing forces. It can be seen from Figure 11 that the variation law of the absorbed energy varies with different axial prestresses. When axial prestress is not applied, the absorption energy increases with the number of cycles, and the absorption energy is positive, which means that during the cyclic impact process, the rock sample continuously absorbs energy for the initiation and expansion of its internal cracks. In addition, when the axial prestress is 42% of the UCS, the rock sample increases with the number of cycles, and the energy is converted from the released energy to the absorbed energy. This is because the rock sample has a certain amount of energy stored during the axial prestress, and the first two impact loads, and during the action, the rock samples exhibit energy release, and the released energy decreases as the number of impacts increases. The analysis shows that during the initial impact process, the internal structure of the rock sample is fine-tuned, and the microcracks are continuously closed, resulting in a decrease in the released energy and energy as the number of cycles increases. During the third impact, the rock sample begins to absorb energy, and the absorbed energy is 1.14 J, indicating that the rock sample has a relatively stable internal structure during the third impact, and there is basically no energy dissipation; the rock sample is subjected to the fifth impact. When the load is applied, the energy absorption value is 7.88 J, which is substantially larger than that during the third and fourth impacts, indicating that the crack growth rate and degree of the rock sample increase. When the rock sample is impacted and damaged, the energy absorption value is 28.4 J, which increases sharply, indicating that the specimen has more absorbed energy when it is destroyed, and the degree of damage increases. The axial prestress is 62% of the UCS, the rock sample releases energy during cyclic impact, and

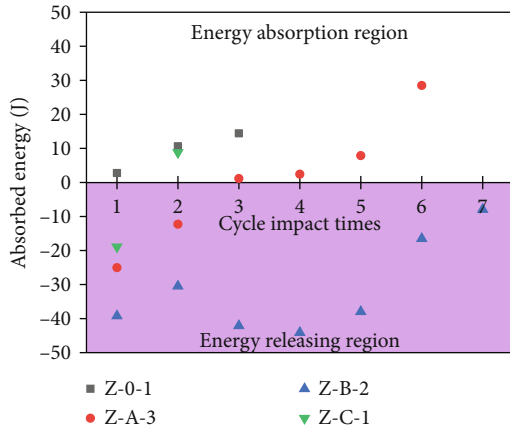


FIGURE 11: Relationship between axial the prestress and absorbed energy.

the overall trend is decreasing. The analysis shows that the rock sample stores substantial strain energy. As the number of cycles accumulates, the internally activated cracks will increase. Due to the release of energy, the internal cracks will continue to expand. During impact failure, the residual elastic energy inside the rock sample will be greater than the fracture. The surface requires energy, and under the action of dynamic loading, it triggers the release of its energy, which eventually leads to a “rock burst” in the rock sample. The axial prestress is 83% of the UCS, and more cracks have been induced inside the rock sample, resulting in less stored energy. During the first impact, the energy is released internally, causing more cracks to activate and propagate inside, and a certain macroscopic damage occurs on the surface. In this state, because the internal energy storage is low, the rock sample is under the impact of the impact load. “Rock bursts” are less likely to occur in this stage, so the specimens show absorbed energy when they finally fail.

3.3. Dynamic and Static Coupling Failure Modes of Granite. Understanding the rock failure mode is of practical engineering significance for underground mining processes and the prevention of hazards such as rock bursts. Figure 12 shows the fracture process of specimens under different axial prestressing forces under the same air pressure impact, and Figure 11 shows the corresponding failure mode.

When the axial prestress is not applied, under the impact of the dynamic load cycle of the sample, the reflected wave and the transmitted wave in the rock sample cannot be transmitted to the two ends of the sample in time, resulting in a superposition at a certain position inside the rock sample and a greater tensile wave. The existence of holes further weakens the tensile strength of the rock sample so that microcracks in other positions of the rock sample will not be able to propagate and penetrate in the future, and a through tensile crack perpendicular to the loading direction appears at a certain position, triggering the damage of the rock sample. The spalling damage leads to a larger size of the final damage and less damage. Figure 12(a) shows a diagram of the failure process of the rock sample without axial prestress failure. At 1104 μs , cracks perpendicular to the

loading direction begin to appear in the centre of the rock sample, and debris appears at the incident end of the rock sample, which eventually leads to spalling failure of the rock sample at 3335 μs .

When the rock sample is under axial prestress, a potential compression-shear surface is formed inside. During the initial cyclic impact process, because the impact strength is lower than the maximum compressive strength of the prestress, the rock sample does not undergo macroscopic damage. As the cyclic impact accumulates to a certain degree, the maximum strength of the prestress is continuously weakened. When the impact strength of the prestress is higher than the minimum strength to which the prestress is subjected, the rock sample will fail.

When the axial prestressing force is 42% of the UCS and 62% of the UCS, the axial prestress and dynamic load act simultaneously, resulting in mixed tensile-shear failure. When the axial prestress is 42% of the UCS, Figure 12(b) shows that when the transmitting end of the rock sample is at 276 μs , compression cracks begin to appear, and at 345 μs , tensile cracks appear at the ends while the end face of the rock sample is sheared and fragments began to peel off. At 598 μs , a tensile crack appears on the surface of the rock sample. When the axial prestress is 62% of the UCS, Figure 12(c) shows that the rock sample begins to undergo compression-shear failure when the rock sample is broken. At 161 μs , compression shear cracks appear from the entrance side of the specimen. At 368 μs , the fragments on the compression shear surface begin to eject from the side and make a loud noise. This phenomenon is similar to a “rock burst” in rock engineering.

When the axial prestressing force is 83% of the UCS, the axial prestress plays a major role, and shear tensile mixed failure occurs. It can be observed from Figure 12(d) that the rock sample cracks at 253 μs , and at 414 μs , chipping occurs on the side of the rock. The analysis shows that the prestress is 83% of the UCS, a more obvious compression zone is formed at the end of the sample, and the internal cracks parallel to the loading direction expand to the inside [21], forming a potential “shear failure surface”, resulting in more obvious compression on both sides. The shear rupture surface, when impact load is applied, further promotes this formation trend and triggers rock chipping on the side of the rock.

Sliding loads act on different axial prestress failure modes. Figure 13 shows that as the axial prestress increases, the failure block size of the rock samples does not decrease substantially. The main reason for this behaviour is that in this study, granite was not severely damaged. When the prestress is in the stage of stable crack growth, which is lower than the crack damage stress (70% of the UCS) [14], under cyclic impact loading, the rock sample will undergo certain fatigue damage, and its internal microcracks gradually change from the initial compaction stage. The crack propagation stage is transitional, and the crack propagation speed is slow. When the final impact is broken, the crack is full, and the fragmentation is small. When the prestress is higher than the crack damage stress, the number of cyclic impacts of the rock sample is lower, which indicates that the main crack is propagating faster, and the internal microcracks have time

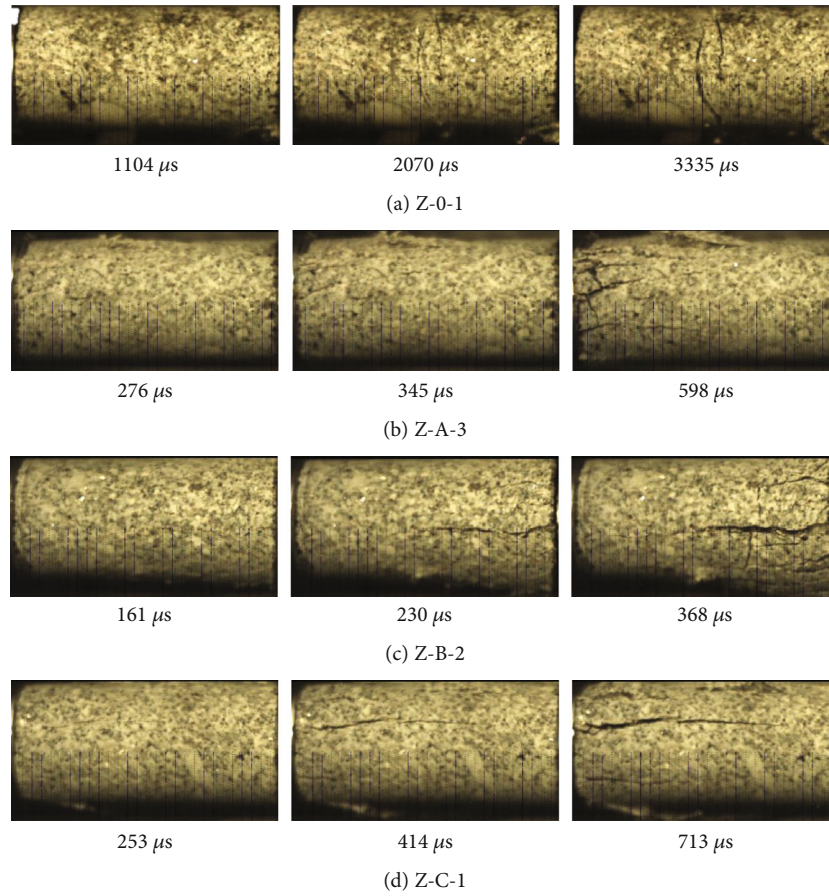


FIGURE 12: Failure process diagram of different axial prestress loads.

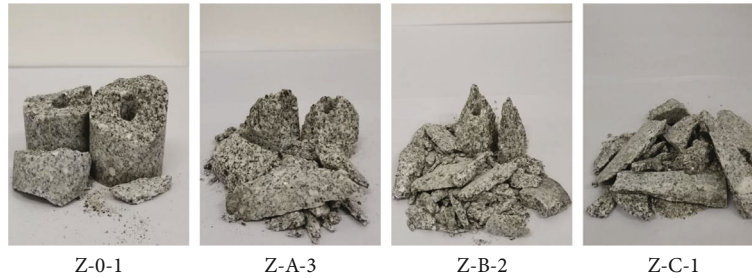


FIGURE 13: Different axial prestress failure modes.

to grow. The main crack expands and penetrates, resulting in larger fragments during failure.

3.4. Damage Characteristics Analysis

3.4.1. Selection and Establishment of the Dynamic Rock Damage Model. At present, the commonly used damage variables are defined as the elastic modulus, maximum strain, and ultrasonic wave speed. The ultrasonic wave speed is widely used because it is easy to operate and can effectively reflect the crack propagation trend in rock, but it has a cycle under a certain axial prestress. Impact tests limit the application of this method. For this reason, Jin Jiefang established a method

based on the one-dimensional stress wave theory. Under the same cross-sectional area of the test specimen and the elastic rod, the wave impedance is used to define the damage variable for the first time, as shown in Equation (4). The elastic modulus, energy dissipation, and maximum strain are not suitable for defining the damage variables of rock during cyclic impact [36]. In this paper, the vertical centre hole is prefabricated in the centre of the sample. Therefore, Equation (4) cannot be directly applied to this test. Assuming that the discontinuous contact surface between the rock sample and the elastic rod is regarded as the contact surface between two elastic half-spaces with displacement discontinuity, the propagation of the stress wave on the displacement discontinuity surface

can be transformed into a boundary value problem for solving the wave equation [32], as shown in Figure 14.

$$D = 1 - \left(\frac{\overline{\rho C}}{\rho C} \right)^{1.6}, \quad (4)$$

where D is the damage variable, $\overline{\rho C}$ is the wave impedance at a certain impact, and ρC is the initial wave impedance of the rock.

As shown in the figure, based on the one-dimensional wave theory, when the stress wave propagates from incident rod a to test piece b , its wave impedance changes from m_a to m_b . According to the one-dimensional stress wave theory, the interface has a continuous force and velocity on O_1O_2 with the following available conditions:

$$\sigma_R(t_i) = \lambda \sigma_I(t_i), \quad (5)$$

$$\sigma_T(t_i) = (1 + \lambda)(1 - \lambda), \quad (6)$$

$$m_a = \rho_a C_a A_a, \quad (7)$$

$$m_b = \rho_b C_b A_b, \quad (8)$$

$$\lambda = \frac{m_a - m_b}{m_a + m_b}. \quad (9)$$

In the same way, $\sigma'_T(t_i)$ inside the rock enters the transmission rod at interface O_3O_4 to generate a transmitted wave:

$$\sigma_T(t_i) = (1 + \lambda)(1 - \lambda)\sigma_I(t_i). \quad (10)$$

The relationship between the transmitted wave and the incident wave at any time can be written as follows:

$$\xi(t_i) = \frac{\sigma_T(t_i)}{\sigma_I(t_i)} = (1 + \lambda)(1 - \lambda). \quad (11)$$

If m_a and m_b are known, Equation (11) can be rearranged, and Equations (7), (8), and (9) can be simultaneously used to obtain the actual wave impedance of the rock specimen at a certain moment during the i time impact:

$$\rho_i C_i = \frac{A_b \left(2 - \xi(t_i) - 2\sqrt{1 - \xi(t_i)} \right)}{A_a \xi(t_i)} \rho_a C_a. \quad (12)$$

By taking Equation (12) into Equation (4), the expression of the damage degree of the rock is as follows:

$$D = 1 - \left(\frac{A_b \left(2 - \xi(t_i) - 2\sqrt{1 - \xi(t_i)} \right) \rho_a C_a}{A_a \xi(t_i) \rho C} \right)^{1.6}, \quad (13)$$

where σ_I , σ_R , σ_T , and σ'_T are the incident wave, reflected wave, transmitted wave, and transmitted wave in the specimen, respectively; A_a and A_b are the cross-sectional areas of the elastic rod and the rock sample, respectively; ρ_a and C_a , and ρ_b and C_b are the density and P-wave velocity of the elas-

tic rod and rock sample, respectively; λ is the reflection coefficient of the wave entering the specimen from the elastic rod; and i is the i th time impact order.

The above inference formula assumes that the stress wave in the rock specimen generates a transreflective reflection. After the incident wave propagates into the specimen for a period of time, multiple transmissive reflections occur in the specimen at each instant. From the research in [36], it is evident that when $t \leq (2L_b/C_b)$, the reflected and transmitted waves obtained in the test are not affected by multiple transmissions and reflections. Figure 15 shows a trend chart of the change in the wave impedance when a certain specimen is impacted. The impedance of section AB basically remains unchanged. To produce comparable results, a certain time in section AB is selected as the reference point for each cycle of the test specimen.

3.4.2. Influence of the Axial Prestress on the Damage. Figure 16 shows the change in the damage degree and impact number of the rock samples under different axial prestressing forces. It can be seen from the figure that the rock samples show different damage evolution trends with the increase in the number of cycles under different prestresses. The initial damage of Z-0-1 is lower than that of the other rock samples, and the initial damage of Z-A-3, Z-B-2, and Z-C-1 increases with the increase in the axial prestress. The rock samples have different degrees of damage when the prestress is 42% of the UCS, 62% of the UCS, and 83% of the UCS. Z-C-1 has a large number of microcracks because the axial prestress is higher than the crack damage stress, resulting in a substantial reduction in the number of cycles of rock samples subjected to cyclic impact. The cumulative growth rate of the damage of Z-0-1 continues to increase, with growth rates of 60% and 150%, respectively. During the initial cyclic impact process, Z-A-3 is dominated by compaction, resulting in the reduction in the first three damage levels, and then with the increase in the number of cycles, the cumulative damage growth rate of the rock sample increases with the acceleration of the internal crack growth. Z-B-2 increases the cumulative damage rate during the first four cycles of slow impact, with a range of 0.24-0.25. From the establishment of the dynamic damage model, it can be seen that the damage D is a function of the strain [37], which is consistent with the maximum strain in the previous analysis. Since the rock sample belongs to the fatigue damage stage at this stage, the amplitude of the strain change is small, which means that during this impact process, the damage to the rock sample is small and can almost be ignored. This shows that the cumulative damage growth of the rock sample during the first four impacts is slow, and the damage accumulation during the subsequent cyclic impact process increases with the increase in the maximum strain.

4. Surrounding Rock Engineering Applications of Roadways under Different Prestresses

The in situ stress and dynamic load affect the safety and stability of the roadway. Among them, the magnitude of the

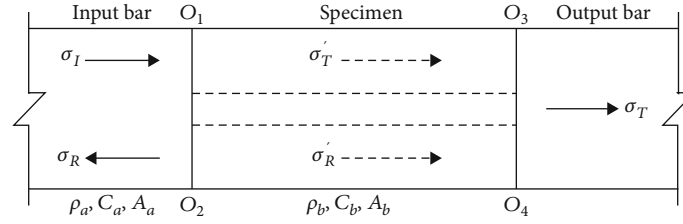


FIGURE 14: Transmission and reflection of a one-dimensional compressional wave in a rock sample.

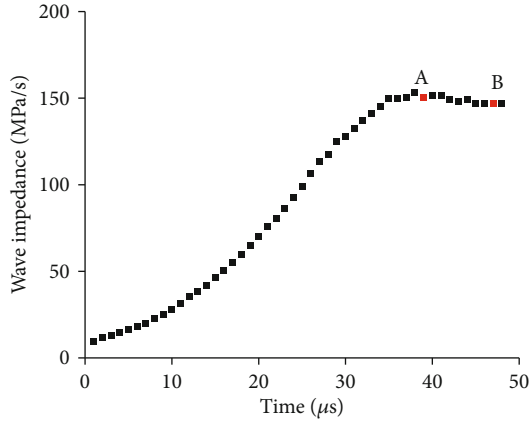


FIGURE 15: Trend chart of wave impedance over time.

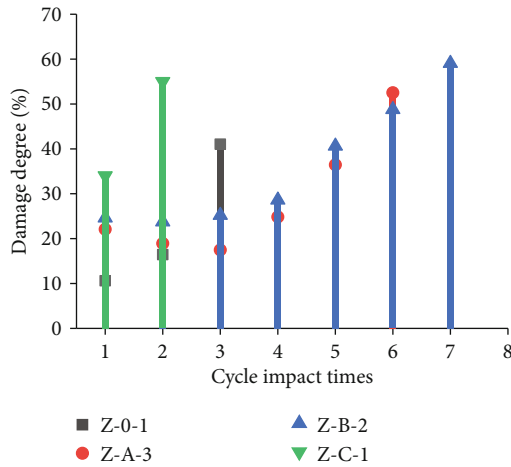


FIGURE 16: Relationship between different axial prestresses and damage levels.

ground stress (prestress) determines the strength and stiffness of the surrounding rock of the roadway. Figure 17 shows the maximum peak stress and dynamic deformation modulus, which indirectly reflect the rock mass stiffness. The test results show that when the prestress is higher than the crack initiation stress (30% of the UCS), the dynamic strength and stiffness are reduced and increased, respectively, compared with the absence of axial prestress, which indicates that the in situ stress improves the “toughness” of the surrounding rock. Under the same dynamic load disturbance action, the ability to resist the instability and damage of the surrounding rock of the roadway is enhanced. When the axial prestress is higher than the crack damage stress (70% of the UCS), the

strength and stiffness are reduced compared with the axial prestress. It can be concluded that under high prestress conditions, the dynamic load disturbance is extremely detrimental to the stability of the surrounding rock of the roadway, and it is more likely to cause instability.

The failure type and energy evolution law of the surrounding rock of the roadway are also important features that reveal the failure mechanism of the surrounding rock. For tunnels with shallow depths, it can be considered that there is no static stress. If the surrounding rock of the roadway is to be destabilized and destroyed, it is necessary to absorb the external energy, and the failure of the surrounding rock of the roadway is usually caused by the tensile spalling damage caused by the superposition of the stress waves due to the dynamic load at a certain position of the roadway surrounding rock. For the surrounding rock of the roadway where the prestress is in the stage of stable expansion of the crack, as the depth increases, a certain degree of shear surface is formed inside, and the stored energy increases; when the external load is disturbed, the surrounding rock of the roadway is transformed from absorbed energy to released energy when the surrounding rock is destroyed, which results in a greater probability of triggering a rock burst. For the prestressed roadway surrounding rock in the unstable stage of crack expansion, which is higher than the crack damage stress, the structure of the roadway surrounding rock is almost in an unstable state, there are many microcracks inside, the rock density is very low, and the stored energy is relatively small. When the load is disturbed, the internal absorbed energy is greater than the released energy. In this case, rock burst does not easily occur, and the roadway is easily induced to collapse and fall off.

5. Conclusion

- (1) The axial prestress has a certain effect on the dynamic strength and stiffness of granite: the axial prestress is in the stage of stable crack propagation, and its dynamic strength is lower than that of the pure dynamic compressive strength, but its stiffness increases. The axial prestress is in the unstable stage of crack propagation, showing its weakest dynamic strength and stiffness
- (2) During the cyclic impact failure process of granite, the granite mainly undergoes a transition from the compaction stage to the fatigue damage stage to the failure stage. With the increase in the prestressed axial pressure, the compaction stage and the fatigue

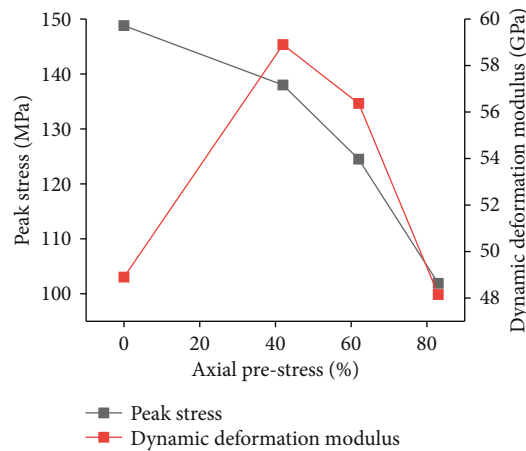


FIGURE 17: Relationship between the dynamic deformation modulus, peak stress, and axial prestress.

damage stage continue to weaken. When the axial prestress is 42% of the UCS, the rock sample shows the compaction stage-fatigue damage stage-failure stage trend; when the axial prestress is 62% of the UCS, the rock sample compaction stage weakens, showing the fatigue damage stage-failure stage trend; and when the axial prestress is 83% of the UCS, the rock sample only shows the failure stage

- (3) The existence of static stress is a necessary condition for “rock burst” to occur. Granite under different axial prestresses, the energy dissipation of rocks varies with the number of impacts. In general, when the axial prestress and impact load are at a certain value, the probability of “rock burst” is large
- (4) The failure mode of granite under different axial prestresses is different. When the axial prestress is 0, spalling tensile failure occurs. As the axial prestress increases, mixed tensile-shear failure occurs. This is due to the effect of axial prestressing, and different levels of shear planes are formed inside, which limits the initiation of transverse cracks
- (5) Based on the one-dimensional stress wave theory, the method of defining the rock damage degree by wave impedance is further studied. When the rock sample is in the compaction stage and the fatigue damage stage, the damage of the specimen is small, and the damage reduction phenomenon occurs

Data Availability

The data used to support the findings of this study are available from the corresponding author upon request.

Conflicts of Interest

The authors declare that they have no known competing financial interests or personal relationships that could have appeared to influence the work reported in this paper.

Authors' Contributions

Bing Dai is responsible for the methodology and conceptualization. Yongming Xue is responsible for the investigation and data curation. Lei Zhang is responsible for the writing of the original draft, validation, and visualization. Ying Chen is responsible for the resources and writing of the review and editing. Zhijun Zhang is responsible for the supervision.

Acknowledgments

This study is conducted under the joint grant of the National Natural Science Foundation of China (Nos. 51804163 and 51974163) and the China Postdoctoral Science Foundation (2018M642678), and it is supported by the Hunan Provincial Innovation Foundation for Postgraduate (CX20200920).

References

- [1] X. B. Li, F. Q. Gong, and S. F. Wang, “Coupled static-dynamic loading mechanical mechanism and dynamic criterion of rock burst in deep hard rock mines,” *Chinese Journal of Rock Mechanics and Engineering*, vol. 38, no. 4, pp. 708–723, 2019.
- [2] P. X. Li, X. T. Feng, G. L. Feng, Y. X. Xiao, and B. R. Chen, “Rockburst and microseismic characteristics around lithological interfaces under different excavation directions in deep tunnels,” *Engineering Geology*, vol. 260, p. 105209, 2019.
- [3] L. Hu, X. T. Feng, Y. X. Xiao et al., “Effects of structural planes on rockburst position with respect to tunnel cross-sections: a case study involving a railway tunnel in China,” *Bulletin of Engineering Geology and the Environment*, vol. 79, no. 2, pp. 1061–1081, 2020.
- [4] Z. Song, H. Konietzky, and M. Herbst, “Bonded-particle model-based simulation of artificial rock subjected to cyclic loading,” *Acta Geotechnica*, vol. 14, no. 4, pp. 955–971, 2019.
- [5] Z. Song, H. Konietzky, and M. Herbst, “Three-dimensional particle model based numerical simulation on multi-level compressive cyclic loading of concrete,” *Construction and Building Materials*, vol. 225, pp. 661–677, 2019.
- [6] F.-q. Gong, X.-f. Si, X.-b. Li, and S.-y. Wang, “Experimental investigation of strain Rockburst in circular caverns under deep three-dimensional high-stress conditions,” *Rock Mechanics and Rock Engineering*, vol. 52, no. 5, pp. 1459–1474, 2019.
- [7] X. B. Li, C. J. Li, W. Z. Cao, and M. Tao, “Dynamic stress concentration and energy evolution of deep-buried tunnels under blasting loads,” *International Journal of Rock Mechanics and Mining Sciences*, vol. 104, pp. 131–146, 2018.
- [8] Z. Song, W. Wei, and J. Zhang, “Numerical investigation of effect of particle shape on isolated extracted zone (IEZ) in block caving,” *Arabian Journal of Geosciences*, vol. 11, no. 12, 2018.
- [9] B. Y. Jiang, S. T. Gu, L. G. Wang, G. C. Zhang, and W. S. Li, “Strainburst process of marble in tunnel-excavation-induced stress path considering intermediate principal stress,” *Journal of Central South University*, vol. 26, no. 4, pp. 984–999, 2019.
- [10] Z. L. Li, X. Q. He, L. M. Dou, and G. F. Wang, “Rockburst occurrences and microseismicity in a longwall panel experiencing frequent rockbursts,” *Geosciences Journal*, vol. 22, no. 4, pp. 623–639, 2018.

- [11] B. Dai and Y. Chen, "A novel approach for predicting the height of the water-flow fracture zone in undersea safety mining," *Remote Sensing*, vol. 12, no. 3, p. 358, 2020.
- [12] K. Gao, S. N. Li, R. Han et al., "Study on the propagation law of gas explosion in the space based on the goaf characteristic of coal mine," *Safety Science*, vol. 127, article 104693, 2020.
- [13] Z. Song and H. Konietzky, "A particle-based numerical investigation on longwall top coal caving mining," *Arabian Journal of Geosciences*, vol. 12, no. 18, 2019.
- [14] Z. Zhou, X. Cai, X. Li, W. Cao, and X. du, "Dynamic response and energy evolution of sandstone under coupled static-dynamic compression: insights from experimental study into deep rock engineering applications," *Rock Mechanics and Rock Engineering*, vol. 53, no. 3, pp. 1305–1331, 2020.
- [15] X. Cai, Z. L. Zhou, and X. du, "Water-induced variations in dynamic behavior and failure characteristics of sandstone subjected to simulated geo-stress," *International Journal of Rock Mechanics and Mining Sciences*, vol. 130, article 104339, 2020.
- [16] X. Cai, Z. L. Zhou, H. Zang, and Z. Song, "Water saturation effects on dynamic behavior and microstructure damage of sandstone: phenomena and mechanisms," *Engineering Geology*, vol. 276, article 105760, 2020.
- [17] X. Cai, Z. L. Zhou, L. H. Tan, H. Zang, and Z. Song, "Fracture behavior and damage mechanisms of sandstone subjected to wetting-drying cycles," *Engineering Fracture Mechanics*, vol. 234, article 107109, 2020.
- [18] X. B. Li, Z. L. Zhou, and Z. Y. Ye, "Study of rock mechanical characteristics under coupled static and dynamic loads," *Chinese Journal of Rock Mechanics and Engineering*, vol. 7, pp. 1387–1395, 2008.
- [19] T. Wang, Z. P. Song, and J. Y. Yang, "Dynamic response characteristics of weathered red sandstone under cyclic impact," *Chinese Journal of Rock Mechanics and Engineering*, vol. 38, no. S1, pp. 2772–2778, 2019.
- [20] F. Q. Gong, X. B. Li, and X. L. Liu, "Experimental study on dynamic characteristics of sandstone under one-dimensional coupled static and dynamic loads," *Chinese Journal of Rock Mechanics and Engineering*, vol. 29, no. 10, pp. 2076–2085, 2010.
- [21] F. Q. Gong, *Experimental study of rock mechanical properties under l coupled static-dynamic loads and dynamic strength criterion*, Central South University, 2010.
- [22] X. B. Li, F. Q. Gong, and K. Gao, "Test study of impact failure of rock subjected to one-dimensional coupled static and dynamic loads," *Chinese Journal of Rock Mechanics and Engineering*, vol. 29, no. 2, pp. 251–260, 2010.
- [23] F. Wang, M. Wang, Z. M. Zhu, Q. Hao, Y. Peng, and W. Xuya, "Study on evolution law of rock crack dynamic propagation in complete process under impact loading," *Chinese Journal of Rock Mechanics and Engineering*, vol. 38, no. 6, pp. 1139–1148, 2019.
- [24] B. Dai, Y. Chen, G. Y. Zhao, W. Liang, and H. Wu, "A numerical study on the crack development behavior of rock-like material containing two intersecting flaws," *Mathematics*, vol. 7, no. 12, p. 1223, 2019.
- [25] D. Li, P. Xiao, Z. Han, and Q. Zhu, "Mechanical and failure properties of rocks with a cavity under coupled static and dynamic loads," *Engineering Fracture Mechanics*, vol. 225, article 106195, 2020.
- [26] D. Li, T. Cheng, T. Zhou, and X. Li, "Experimental study of the dynamic strength and fracturing characteristics of marble specimens with a single under impact loading," *Chinese Journal of Rock Mechanics and Engineering*, vol. 34, no. 2, pp. 249–260, 2015.
- [27] Y. Li, J. Peng, F. Zhang, and Z. Qiu, "Cracking behavior and mechanism of sandstone containing a pre-cut hole under combined static and dynamic loading," *Engineering Geology*, vol. 213, pp. 64–73, 2016.
- [28] Q. Z. Wang, B. B. Wu, F. Liu, K. W. Xia, and W. Wang, "Dynamic failure of manufactured similar rock plate containing a single fissure," *Chinese Journal of Rock Mechanics and Engineering*, vol. 37, no. 17, pp. 2489–2497, 2018.
- [29] X. B. Li, L. Weng, X. Xie, and Q. H. Wu, "Study on the degradation of hard rock with a pre-existing opening under static-dynamic loadings using nuclear magnetic resonance technique," *Chinese Journal of Rock Mechanics and Engineering*, vol. 34, no. 10, pp. 1985–1993, 2015.
- [30] J. Jin, X. Li, and Z. Yin, "Effects of axial pressure and number of cyclic impacts on dynamic mechanical characteristics of sandstone," *Journal of China Coal Society*, vol. 37, no. 6, pp. 923–930, 2012.
- [31] H. J. Su, H. W. Jing, C. Wang, and B. Meng, "Strength attenuation law of damaged rock samples and its structure effect," *Applied Mechanics and Materials*, vol. 353-356, pp. 602–607, 2013.
- [32] X. B. Li, *Rock Dynamics Foundation and Application*, Science Press, Beijing, 2014.
- [33] Z. L. Wang, H. Yang, and N. C. Tian, "Mechanical property and damage evolution mechanism of granite under uniaxial cyclic impact," *Journal of Harbin Institute of Technology*, vol. 52, no. 2, pp. 1–9, 2020.
- [34] J. F. Jin, *Study on Rock Mechanical Properties under Coupled Static-Cyclic Impact Loadings*, Central South University, 2012.
- [35] L. Z. Tang, T. Liu, C. Wang et al., "Study on dynamic deformation modulus of rock under confining pressure unloading and dynamic loading," *Explosion and Shock Waves*, vol. 38, no. 6, pp. 1353–1363, 2018.
- [36] J. F. Jin, X. B. Li, Z. Q. Yin, and Y. Zou, "A method for defining rock damage variable by wave impedance under cyclic impact loadings," *Rock and Soil Mechanics*, vol. 32, no. 5, pp. 1385–1393, 2011.
- [37] J. J. Zhu, X. B. Li, F. Q. Gong, and S. M. Wang, "Dynamic characteristics and damage model for rock under uniaxial cyclic impact compressive loads," *Chinese Journal of Geotechnical Engineering*, vol. 35, no. 3, pp. 531–539, 2013.

Research Article

Overburden Damage Degree-Based Optimization of High-Intensity Mining Parameters and Engineering Practices in China's Western Mining Area

Xiang He,^{1,2} Cun Zhang ,^{1,2,3} and Penghua Han^{1,2}

¹Beijing Key Laboratory for Precise Mining of Intergrown Energy and Resources, China University of Mining and Technology, Beijing 100083, China

²School of Energy & Mining Engineering, China University of Mining and Technology, Beijing 100083, China

³State Key Laboratory Cultivation Base for Gas Geology and Gas Control, Henan Polytechnic University, Jiaozuo, 454000 Henan, China

Correspondence should be addressed to Cun Zhang; cumt_zc@163.com

Received 16 June 2020; Revised 15 July 2020; Accepted 28 July 2020; Published 14 August 2020

Academic Editor: Zhengyang Song

Copyright © 2020 Xiang He et al. This is an open access article distributed under the Creative Commons Attribution License, which permits unrestricted use, distribution, and reproduction in any medium, provided the original work is properly cited.

China's western mining area is an arid and semiarid area with a fragile ecological environment, and the high-intensity mining activities aggravate ecological damage. Reasonable choice of the mining parameters (i.e., mining height, panel width, and advancing speed) can not only improve the mining efficiency but also weaken the mining-induced deformation and failures of the overburden and surface. The statistical analysis of the relationship between the mining parameters and periodic weighting interval (PWI) proves that mining parameters have significant influence on overburden failure. In this study, the damage constitutive equation was derived, and the overburden damage degree was defined to quantitatively characterize mining-induced stratum damage in a three-dimensional space. FLAC3D numerical models embedded with a damage constitutive equation were built to compare the panel width effect and advancing speed effect between the overburden damage degree and the water-conducted fracture zone (WCFZ). The reasonable range for mining parameters of the panel 12401 was provided based on the fitting function of the overburden damage degree versus mining parameters. The field measurements were carried out on panel 12401 of the Shangwan coal mine, including the advancing speed, PWI, and ground crack development. The results show that, under constant engineering and geological conditions, the damage degree of overburden will be weakened by increasing the advancing speed, reducing the mining height, or shortening the panel width. The overburden damage degree is more accurate than the height of the water-conducted fractured zone. The reasonable mining parameters of the panel 12401 are 8.8 m in mining height, 300 m in panel width, and 13.47 to 20.58 m/d in advancing speed, respectively. The field measurement results of the PWI and ground cracks have verified the validity using the overburden damage degree to determine high-intensity mining parameters.

1. Introduction

Coal is the dominant energy source in China. In 2018, the total consumption was 4.64 billion tons of standard coal, accounting for 59% of the nation's total energy consumption [1]. China's western mining area is an important energy base for the country, which is typically characterized by large reserves, shallow buried coal seams, simple geological structure, excellent coal quality, and fragile ecological environment [2]. Guo et al. [3] defined high-intensity mining as a

high-yield and high-efficiency coal mining method in thick coal seams (more than 3.5 m) with large panel width (more than 200 m), fast advancing speed (more than 5 m/d), high output (usually 5–10 million t/y), a small coal seam depth/thickness ratio (less than 100), and severe overburden and surface failures. For example, the mining height of panel 22307 in the Bulianta coal mine is 7.0 m with a panel width of 450 m and an advancing speed of 21.6 m/d. However, high-intensity longwall mining usually results in a drop of the groundwater table [4], death of vegetation [5], desertification

of land [6], and further deterioration of the fragile ecological environment in these arid and semiarid areas [7]. Therefore, it is one of the research hotspots for both ensuring the safety of high-intensity production and reducing surface ecological damage by optimizing mining parameters.

In general, based on the overburden movement and fracture development, an overburden can be divided into, from bottom to top, a caved zone, a fractured zone, and a continuous zone [8–11]. The water-conducted fracture zone (WCFZ) consists of the caved zone and fractured zone and can be considered plasticized [12]. Hence, its height is important for the safety of underground production and the surface ecological environment (Guo et al. 2018; [13–16]). The height of WCFZ depends on the mining method, mining height, advancing speed, panel width, overburden strength, stratum structure, and geological structure [2, 17–20]. The empirical formula method has been widely used to predict the height of WCFZ. Empirical formulas were usually established on a large number of field measurements with consideration of the rock mechanical strength and mining height; however, most of the field data from the eastern mining areas in China [21]. Guo et al. [3] presented a theoretical study to predict the height of the WCFZ based on the rock failure criteria to determine the maximum suspension length and maximum overhanging length during longwall mining. Liu et al. [22] and Hu et al. [23] obtained the empirical formulas of the height of WCFZ and the weights of variables using multivariate regression analysis. Majidi et al. [12] presented five mathematical approaches to estimate the height of a distressed zone and argued that the height of the distressed zone ranged from 6.5 to 24 times the mining height in the short term and from 11.5 to 46.5 times the mining height in the long term. Some scholars believe that the position and structure of the main key stratum are the determinants of the height of WCFZ. Therefore, key stratum theory is also a common method to predict the height of WCFZ [24–27].

The morphology of the WCFZ is also a main factor to characterize the damage of the overburden. The WCFZ is in a saddle shape after critical mining scale (i.e., length and width) which has been verified by numerous studies [21, 28–30]. Qian et al. [31] found O-shaped mining-induced fracture zone after the gob was compacted, which is the main storage place for gas. Lin et al. [32] established a mathematical model to depict the dynamic evolution of mining-induced fracture elliptic parabolic zone considering the mining height and distance from the first sub-key stratum to the coal seam roof. Wang et al. [33] described the spatial shape of mining-induced fracture as an arch shape through physical modeling. Using FLAC3D modeling, Zhang et al. [34] found that the spatial shape of the WCFZ was a “hat” in the conditions with thick alluvium and thin bedrock. Based on equivalent continuum methods, Zhou et al. [35] developed a new 3D numerical model to simulate the arch-shaped induced fractures in the roof.

Current studies on overburden damage mainly focused on the height and morphology of the WCFZ and provided an important reference for engineering design. However, due to severe surface subsidence and ground cracks are inevitably accompanied with high-intensity mining in the

western mining area, the height and shape of the WCFZ cannot quantitatively reflect the damage state of the overburden in three-dimensional space. In addition, when the WCFZ exceeds the surface during shallow coal seams mining and the WCFZ is incomplete in the overburden, the current predictive equations and shape models of the WCFZ become poor to describe the overburden damage. Therefore, this study reports a new method to describe overburden damage based on FLAC3D numerical simulations embedded with a damage constitutive equation. Reasonable mining parameters were determined through the method, and its reliability was verified by the field measurements.

2. Relationship between Mining Parameters and PWI

High-intensity mining usually results in enhanced deformation, overburden damage, and environmental impacts than those in general geological and mining conditions. Rock strata above the gob can be assumed to be the beam (or plates) structure. When the subsidence deformation of the rock stratum exceeds the threshold, it will fracture, leading to the upward development of fractures. Based on Equation (1); the subsidence deformation of the rock stratum is negatively correlated with the comprehensive expansion coefficient [31]. The more fragmented the roof is, the greater the comprehensive expansion coefficient is. Thus, as the caving interval of the basic roof decreases, the comprehensive expansion coefficient of the rock stratum will increase. Then, the upper rock stratum will be more difficult to fracture because of the decrease of its subsidence space, resulting in the height of the water-conducting fracture zone of the overburden to decrease.

$$\Delta S_i = M - H_i(k_{pi} - 1), \quad (1)$$

where ΔS_i is the subsidence deformation of the i th rock stratum, M is the mining height, H_i is the height difference between the i th rock stratum and the coal seam, and k_{pi} is the comprehensive expansion coefficient below the i th rock stratum.

Periodic weighting intervals (PWI) and the associated mining parameters were collected from 19 longwall faces in the western mining area (Table 1 and Figure 1).

The PWI is related to many factors, such as rock structure, mining parameters of the working face, coal mining methods, and in situ stress. However, the geological conditions of mines differ greatly from each other. Thus, the same mine adjacent working faces were selected as a case to ensure that the geological and coal seam occurrence conditions are as close as possible and that the influence law of mining parameters on rock fracture is analyzed accurately.

- (1) Four adjacent working faces of the Huojitu coal mine and Daliuta coal mine were selected as samples. As shown in Figure 1(a), the panel widths of one mine are same and the mining heights are very close. As shown in Figure 1(b), the PWI has a positive linear correlation with the advancing speed. However, due

TABLE 1: Mining parameters and PWI of the longwall faces in the western mining area.

No.	Coal mine	Panel name	Panel width (m)	Mining height (m)	Advancing speed (m/d)	PWI (m)
1	Huojiu	21305 (a)	257.2	4.3	5	8.5
2		21305 (b)	257.2	4.3	16	9.9
3		21306 (a)	257.2	4.3	5.2	9.1
4		21306 (b)	257.2	4.3	12.4	9.6
6	Daliuta	52304	301	6.8	13.8	18
7		52307	301	6.8	10.8	17.8
8		52303 (a)	301.5	6.8	4	16.9
9		52303 (b)	301.5	6.8	14	18.2
10		12211	210	5.6	15	13.1
11	Shangwan	12204	300	6.0	13	12.3
12		12205	308	6.0	11.7	12
13		12206	318	6.8	10.1	11.2
14		12201	240	5.3	15	20.6
15		44201	240	3.1	21.6	15
16		44202	301.1	3	18.7	12
17		44205	296.9	3.3	18.7	11.8
18	Yujialiang	44207	360	3.5	16.4	10.7
19		44208	400.5	3.6	15.6	9.9

to the different occurrence conditions of the coal seams, the PWI of the Daliuta coal mine is much longer than that of the Huojiu coal mine

- (2) Five adjacent working faces of the Shangwan coal mine were selected as samples, which have approximately equal panel widths and advancing speeds (Figure 1(a)). The influence law of the mining height on the PWI of the main roof was analyzed. As illustrated in Figure 1(c), with a negative exponential relationship between the mining height and PWI and the increase of the mining height, the basic roof is prone to fracture
- (3) Similarly, five adjacent working faces in the Yujialiang coal mine were selected as samples to analyze the effect of the panel width on the PWI. As illustrated in Figure 1(d), with the panel width increasing from 240 m to 400 m, the PWI of the basic roof is shortened from 15 m to 9.9 m

From the analysis above, under constant engineering geological conditions, the PWI of the basic roof increases as the advancing speed increases, the mining height reduces, or the panel width shortens. In other words, the degree of overburden damage degree will be weakened for one panel by increasing the advancing speed, reducing the mining height, or shortening the panel width.

3. The Study Site

The Bulianta coal mine and the Shangwan coal mine are located at southwest Ordos City, Inner Mongolia Autonomous Region, as shown in Figure 2(a). Coal 1-2 is the main

coal seam of the two coal mines, with a thickness of 7.56–10.79 m and a dip angle of 1–5°. The thickness of the overlying strata is 199–271 m, and thickness of the aeolian layer is 0–34 m in the study site. As demonstrated in Figure 2(b), panel 12511 is the second working face in the 5th district of the Bulianta coal mine, and panel 12401 is the first working face in the 4th district of the Shangwan mine. Panel 12511 was exploited with an average mining height of 7.4 m, a panel width of 319.1 m, and a panel length of 3139.3 m. The BLT-1 drillhole is located 75 m in front of the setup entry and 164 m away from the headgate, and the BLT-2 drillhole is located 909 m in front of the setup entry and 47 m away from the headgate. To maximize the recovery rate of coal resources, the panel 12401 was designed with a panel length of 3139.3 m and a full-seam mining height of 8.8 m which has been the largest mining height in China. Since there were no similar engineering geological conditions before, the mining parameters, especially the panel width and advancing speed, are required to be optimized to ensure the safety and efficiency of mine production and minimize the ecological damage caused by coal exploitation.

4. Damage Constitutive Model

4.1. Basic Hypotheses. Rock mass engineering practice and related experiments show that the deformation and strength characteristics of rock mass belong to the category of brittle failure [36, 37]. Thus, the following hypotheses were made: (a) rock mass is composed of two parts: matrix (noncrack part) and damaged body (microcrack part); (b) the matrix is isotropic elastic medium, and elastic deformation does not cause rock mass damage; (c) the damaged body is rigid perfectly plastic body without yield strength; (d) hydrostatic

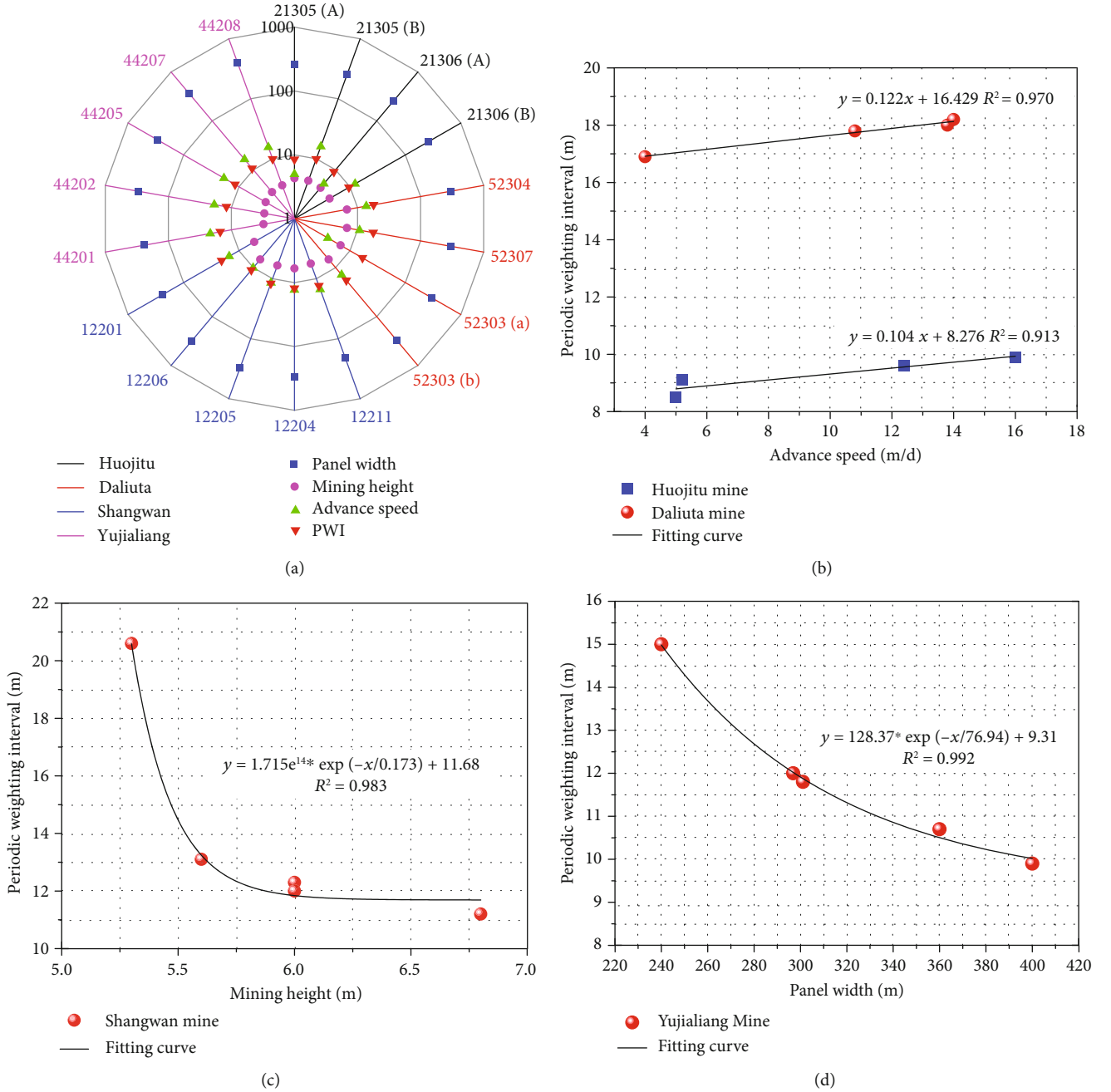


FIGURE 1: Analysis of the relationship between the mining parameters and PWI. (a) The statistics of the high-intensity mining parameters and the PWI; (b-d) the relationship between the advancing speed, mining height, and panel width, respectively.

pressure does not cause rock mass damage; and (e) the matrix and damaged body conform to the deformation compatibility, that is, the strain is equal. The damage variable of the unit body in the rock mass was defined as follows:

$$D = \frac{dV - dV_0}{dV} = \frac{dV_D}{dV}, \quad (2)$$

where D is the damage variable, dV is the volume of the unit body, dV_0 is the volume of the matrix, and dV_D is the volume of the damaged body, as shown in Figure 3.

4.2. *Derivation of Constitutive Equation.* The damaged body of rock mass is the stress release zone, and its deviatoric stress is zero. Under the condition of hydrostatic pressure, the cracks in the rock mass tend to close without any damage. Therefore, it can be considered that the damage of the rock mass is mainly caused by the deviatoric stress, and the rock mass stress σ_{ij} and the matrix stress σ_{ij}^0 lie in the identical plane of deviatoric stresses. Thus,

$$J_2 = (1 - D)J_2^0. \quad (3)$$

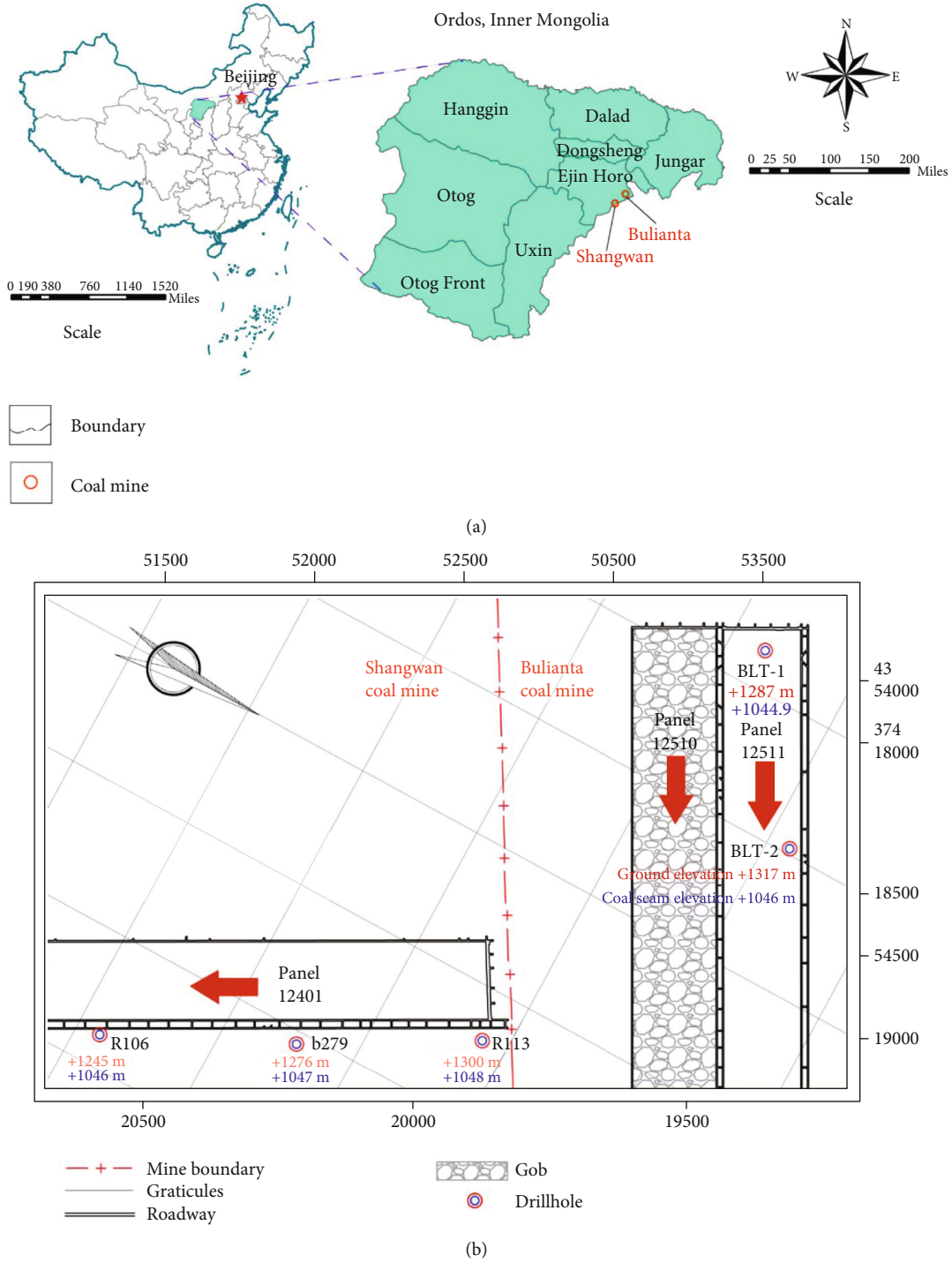


FIGURE 2: Location of the coal mines (a) and (b) layout of panel 12401 and panel 12511.

Thereinto,

$$J_2 = \frac{1}{2} S_{ij} S_{ji}, \quad (4)$$

$$S_{ij} = \sigma_{ij} - \frac{1}{3} \delta_{ij} \sigma_{mm}, \quad (5)$$

where J_2 and J_2^0 are the second invariants of the deviatoric

stress tensor of the rock mass and its matrix, respectively, S_{ij} is the deviatoric stress tensor of the rock mass, σ_{mm} is the hydrostatic pressure, and δ_{ij} is the Kronecker symbol.

Similarly,

$$J_2^0 = \frac{1}{2} S_{ij}^0 S_{ji}^0, \quad (6)$$

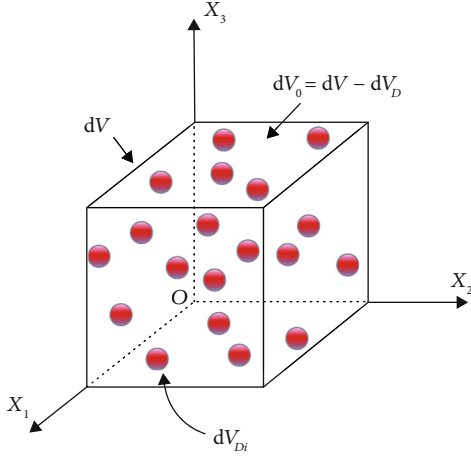


FIGURE 3: Distribution diagram of the matrix and damaged body in the unit body.

$$S_{ij}^0 = \sigma_{ij}^0 - \frac{1}{3} \delta_{ij} \sigma_{mm}^0. \quad (7)$$

Substituting Equations (4) to (7) into Equation (3),

$$\sigma_{ij} = (1 - D) \sigma_{ij}^0 + \frac{1}{3} \delta_{ij} \sigma_{mm}^0 - \frac{1}{3} \delta_{ij} \sigma_{mm}^0 + \frac{D}{3} \delta_{ij} \sigma_{mm}^0. \quad (8)$$

Based on the hypothesis that hydrostatic pressure does not cause damage to the rock mass, that is, $\sigma_{mm} = \sigma_{mm}^0$, Equation (8) can be rewritten as

$$\sigma_{ij} = (1 - D) \sigma_{ij}^0 + \frac{D}{3} \delta_{ij} \sigma_{mm}^0. \quad (9)$$

Based on the hypothesis that the matrix is isotropic elastic medium,

$$\sigma_{ij}^0 = E_{ijkl} \varepsilon_{kl}^0, \quad (10)$$

where E_{ijkl} is the elastic constant tensor of the matrix and ε_{kl}^0 is the strain tensor of the matrix.

Based on the hypothesis that the matrix and damaged body conform to the deformation compatibility,

$$\varepsilon_{kl} = \varepsilon_{kl}^0 = \varepsilon_{kl}^D, \quad (11)$$

where ε_{kl}^D is the strain tensor of the damaged body.

Substituting Equations (10) and (11) into Equation (9),

$$\sigma_{ij} = (1 - D) E_{ijkl} \varepsilon_{kl} + \frac{D}{3} \delta_{ij} E_{mmkl} \varepsilon_{kl} \quad (12)$$

Equation (12) is the damage constitutive equation of rock mass. However, the volume of the damaged body in rock mass is virtual, which cannot be measured, resulting in Equa-

tion (12) is unavailable to practical application. Based on Equations (3) and (11),

$$\begin{aligned} G &= (1 - D) G^0, \\ D &= 1 - \frac{G}{G^0}, \end{aligned} \quad (13)$$

where G is the shear modulus of the rock mass and varies with the degree of damage, variable, and G^0 is the shear modulus of the matrix, constant.

The relationship between equivalent stress and equivalent strain in elastoplastic mechanics is as follows:

$$\bar{\sigma} = 3G\bar{\varepsilon}. \quad (14)$$

Based on Equation (14), the change curve of shear modulus G of the rock mass can be obtained by mechanical tests. Substituting Equation (13) into Equation (12),

$$\sigma_{ij} = \frac{G}{G^0} E_{ijkl} \varepsilon_{kl} + \frac{1}{3} \left(1 - \frac{G}{G^0} \right) \delta_{ij} E_{mmkl} \varepsilon_{kl} \quad (15)$$

Equation (15) is the ultimate damage constitutive equation of the rock mass, which is more convenient for practical application than Equation (12).

4.3. Model Verification. During the mining process of panel 12511, the WCFZ was observed using the combination method of washing fluid leakage and drillhole color TV. At the drillhole depth of 24.80–130.71 m, the trend of washing fluid leakage is relatively gentle (Figure 4). Beyond the drilling depth of 130.71 m, the leakage of the washing fluid increased significantly. At 134.74 m, the washing fluid circulation was interrupted, indicating that all the liquid was lost. After the drilling was completed, a drillhole color TV was used for the borehole imaging of the wall. The images obtained showed that the integrity of the strata was good above the drilling depth of 130.2 m, with few original fractures. An inclined fracture with 2 to 3 cm aperture began to appear below the drillhole depth at 130.2 m that was considered to be the top of the WCFZ. The irregular cross fractures began to appear at the drillhole depth of 201.1 m, causing serious damage to the drillhole, which was considered to be the top of the caved zone.

Based on the measured results from the BLT-1, the top of the WCFZ is at a drillhole depth of 130.2 m. The ground elevation of the BLT-1 drillhole is +1287 m, the floor elevation of coal 1–2 is +1044.9 m, and the mining height is 7.1 m. The equation for calculating the height of WCFZ [38] is as follows:

$$H = D - h_f + W, \quad (16)$$

where H_f is the maximum height of WCFZ, H is the mining depth, h_f is the drillhole depth at the top of the WCFZ, and W is the compression value of rock strata in the fractured zone during drilling observation, generally set as $W = 0.2 M$. From the calculation, the measured height of the WCFZ is 106.22 m.

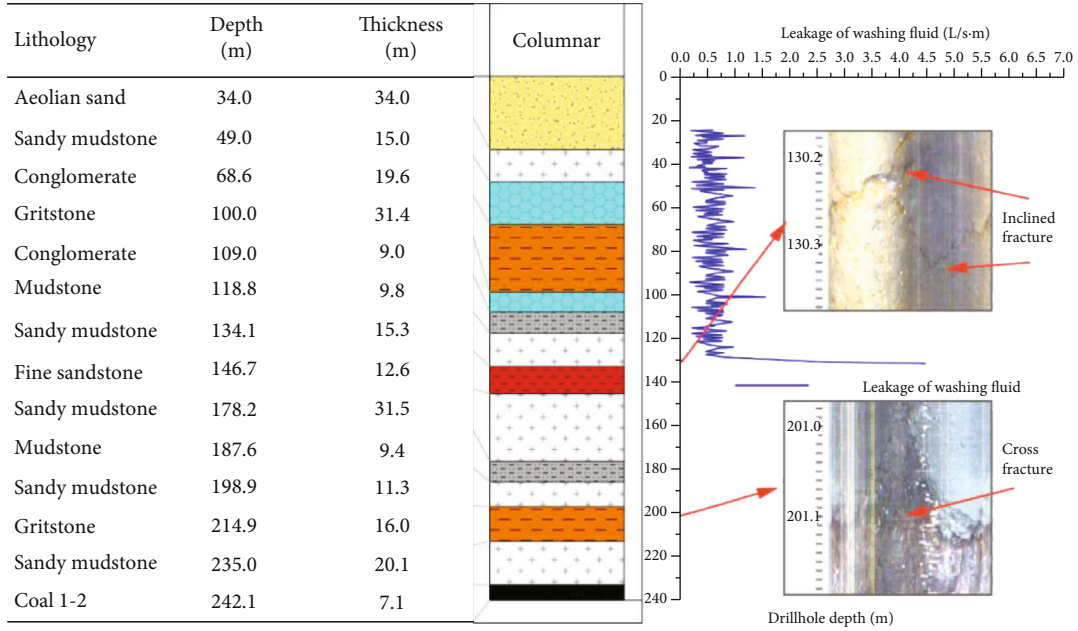


FIGURE 4: The histogram of the BLT-1 drillhole and the measurement results of WCFZ.

The damage constitutive equation of the rock mass was embedded into the FLAC3D model to simulate the overburden failure. FLAC3D allows operators to use C++ language for custom constitutive model secondary development. The custom constitutive model should be compiled into dynamic Link Library (DLL) and stored in the “exe64\plugins\cModel” folder under the FLAC3D installation directory. After configuration by the “Model Configure Plugin” command, the custom constitutive model can be called. The cycle of FLAC3D is mainly divided into five steps: (1) solving the equilibrium equation according to Newton’s second law to get the acceleration of grid node, (2) adopting time integration to calculate node velocity and displacement, (3) the strain rate of the element solved by spatial derivative, (4) updating element stress and state variables based on constitutive model, and (5) calculating the internal forces of grid nodes by element integration. The constitutive model of step (4) in the above steps is realized by secondary development in this paper, and the other steps are automatically calculated by FLAC3D.

The simulation model took the panel of the Bulianta coal mine as the prototype with dimensions of 420 m long × 420 m wide × 267 m high. A fixed boundary, roller boundary, and free boundary were set at the bottom, around, and at the top of the model, respectively. In the numerical simulation models, the excavation area was 50 m from the model boundary to eliminate the boundary effect. The Mohr-Coulomb criterion was adopted in the excavation simulation, and the double-yield constitutive model was applied in the gob elements [39–41]. Based on the lab tests and literature researches, the specific parameters are listed in Tables 2 and 3.

FLAC3D is a finite difference method software, which cannot simulate the height of water-conducting fracture zone. However, the height of plastic zone has been used to indirectly describe the height of water-conducting fracture zone for a long time [42, 43]. After the excavation of the model, the pro-

file of plastic zone was made in the middle of the model, as shown in Figure 5. The shape of WCFZ is similar to saddle shape, and the height of WCFZ is 108.6 m. There is merely a difference of 2.38 m from the measured value of 106.22 m, and the relative error is 2.24%. The simulation result is close to the measured value, indicating that the model embedded with a damage constitutive equation is highly reliable.

5. Optimization of Mining Parameters Based on Overburden Damage Degree

5.1. Definition of the Overburden Damage Degree. With the purpose of overcoming the shortcomings of existing methods for describing overburden damage, the concept of the overburden damage degree was proposed. As shown in Equation (17), the overburden damage degree is defined as the ratio of the total volume of plastic zones to the observation space volume vertically above the excavation range of the coal seam. The greater the overburden damage degree is, the more severe the strata damage is. The overburden damage degree is no longer confined to the spatial form and the three-zone distribution of the overburden and instead quantitatively describes the overburden failure. For numerical simulations, the calculation of the overburden damage degree is relatively convenient and practical.

$$D_d = \frac{\sum_{i=1}^n V_i}{V_o} \times 100\%, \tag{17}$$

where D_d is the overburden damage degree, V_i is the volume of a plastic zone, and V_o is the observed space volume.

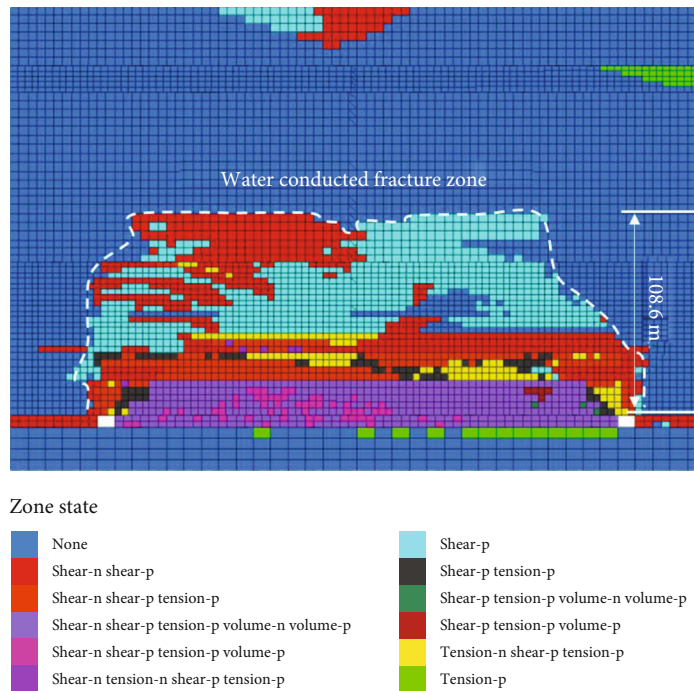
5.2. Numerical Modeling. In practice, in order to maximize the recovery rate of coal resource, the working face is usually

TABLE 2: Physical and mechanical parameters of coal and rock mass.

Lithology	Bulk modulus (GPa)	Shear modulus (GPa)	Internal friction angle (Deg.)	Tensile strength (MPa)	Cohesion (MPa)	Density (kg/m ³)
Aeolian sand	3.3	1.53	36.5	0	3.65e-3	1580
Gritstone	6.3	5.5	30	1.78	12.4	2372
Medium sandstone	8.1	6.37	28.1	1.73	18	2484
Fine sandstone	8.4	6.7	22.4	3.57	20.6	2615
Sandy mudstone	3.18	2.40	18	3.77	17.7	2330
Siltstone	3.0	2.47	24.7	2.56	23.1	2295
Mudstone	2.13	0.93	36.6	4.18	11.7	2311
Coal 1-2	1.51	5.7	23.6	1.69	17.9	1280

TABLE 3: Mechanical parameters of the double-yield gob elements.

Strain	0.0	0.02	0.05	0.07	0.1	0.12	0.15	0.17	0.20
Cap pressure (MPa)	0.0	0.1	0.3	0.6	1.25	2.25	5.0	10.0	20.0

FIGURE 5: Distribution characteristics of overburden plastic zone in the middle of the model ($Y = 200$ m plane).

designed with a full-seam mining technology. Thus, the influence of different panel widths and advancing speeds on overburden damage is more significant to production. The FLAC3D numerical models of different panel widths and advancing speeds were established by taking panel 12401 of the Shangwan coal mine as a prototype. As shown in Figure 6, the model height is $Z = 235.3$ m, and the length is $Y = 400$ m in the advancing direction, and the model width X is determined by the different panel widths. The settings of the boundary conditions and pillar width of the model

were the same as those in Section 4.3. The Mohr-Coulomb criterion was adopted in the excavation simulation, and the double-yield constitutive model was applied in the gob elements. Since panel 12401 is adjacent to the panel 12511 and has the same stratigraphic structure, the selection of physical and mechanical parameters is the same as in Tables 2 and 3.

5.3. Effect of the Panel Width on Overburden Damage. The number of working faces in a mining district will be reduced

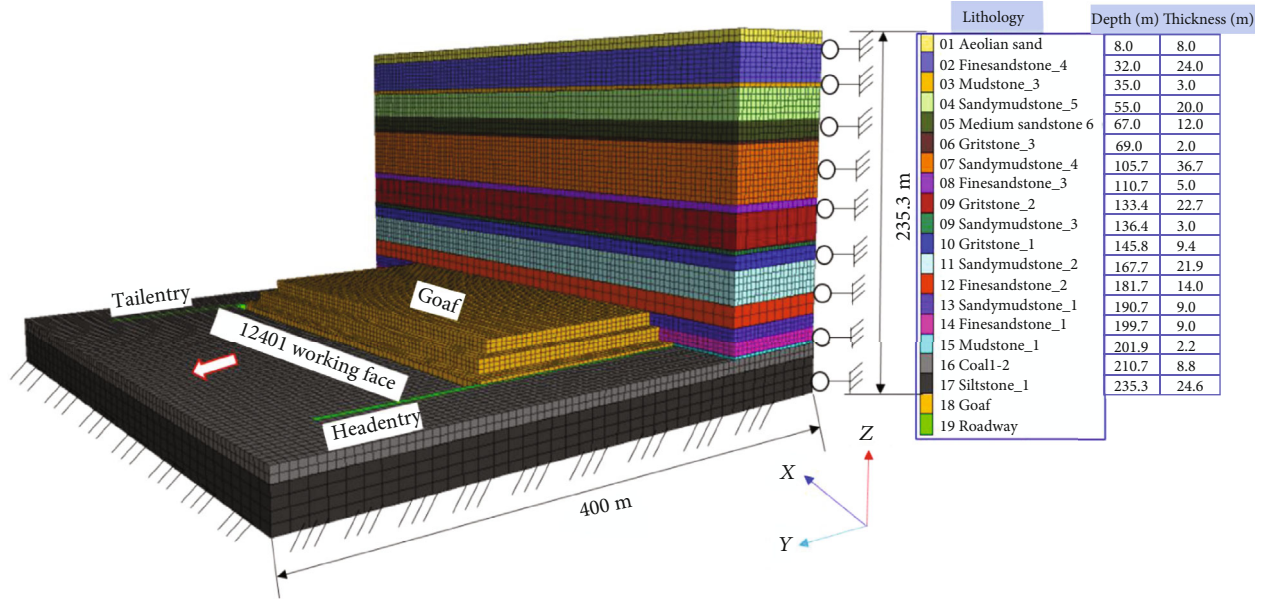


FIGURE 6: Numerical model of the overburden damage degree.

TABLE 4: Selection of different panel widths.

Panel width (m)	100	150	200	250	300	350	400	450	500
Model width (m)	200	250	300	350	400	450	500	550	600
Zone number	229478	284356	339100	397278	452156	510300	565178	623356	678100

by increasing the panel width; then, the number of coal pillars will be reduced correspondingly, which is conducive to improving the coal recovery. However, the increase of the panel width leads to a more intensive overburden movement, which is not conducive to the protection of aquifers and surface ecological environment. Nine numerical models with different panel widths (Table 4) were constructed to investigate the influence of the panel width on the overburden damage degree. Base on the current situation of high-intensity mining, the designed panel widths were ranging from 100 to 500 m with a gradient of 50 m. To improve the calculation efficiency, the model width X increased with the panel width on the premise of not affecting the calculation results. The headgate and tailgate were excavated with dimensions 5.0 m wide \times 4.5 m high when the initial stress balanced. After the roadways were excavated, the panel 12401 was mined with 8.8 m mining height. The advancing speed was selected as 10 m/d, considering the previous mining experience of the Shangwan coal mine in Section 2.

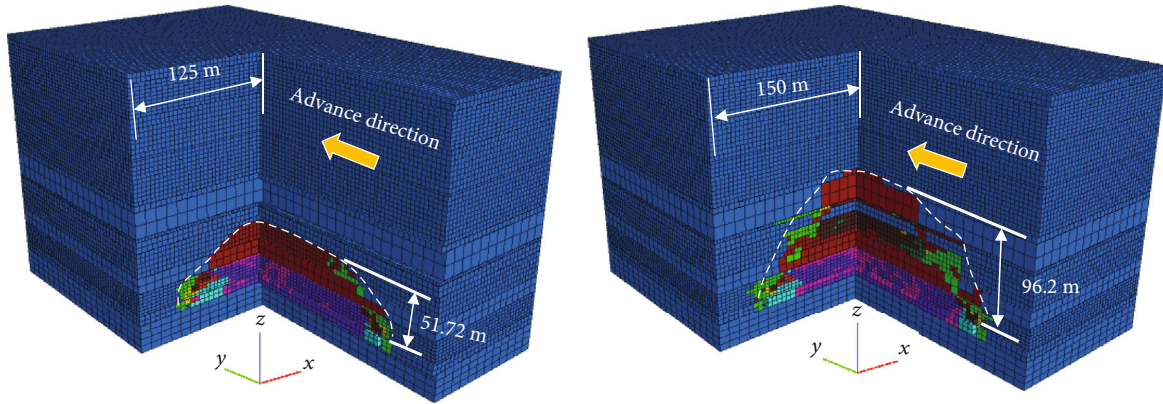
As shown in Figure 7, cross profiles were made through the center of the models, and the distribution characteristics of the plastic zone with different panel widths were obtained. The plastic zone of the overburden is arch-shaped, and the boundary of the plastic zone is mainly shear failure. As increases in the panel width, the width of the plastic zone increases synchronously and the height of plastic zone increases from 51.72 m to the surface. When the panel width

is 250 m, the aeolian sand appears to undergo shear failure, namely, when cracks occur on the surface. When the panel width is 300 m, the height of WCFZ and the depth of the surface failure further increase, but they are not connected. As depicted in Figure 7(e), the height of WCFZ reaches 162.9 m, but the burial depth of the panel 12401 ranges from 124 m to 244 m. Therefore, the coal exploitation of the panel 12401 has potential hazards such as air leakage, water, and sand inrush.

The overburden damage degree of the different panel widths was obtained by writing Fish language. As shown in Figure 8, as the panel width increases, the height of WCFZ and the overburden damage degree increase synchronously, verifying the reliability of the overburden damage degree to describe the overburden failure. The overburden damage degree versus the different panel widths was fitted as follows:

$$y_L = \frac{19.2755 + 72.2692}{1 + e^{-(x-319.8399)/58.0277}}, \quad R^2 = 0.9980. \quad (18)$$

The fitting curve is monotonically increasing, and the inflection point is (319.84, 55.85). Specifically, when the panel width is 319.84 m, the overburden damage degree increases fastest. As illustrated in Figure 6, the overburden of panel 12401 is mainly thick and hard sandstone stratum.



Zone state

- None
- Shear-n
- Shear-n shear-p
- Shear-n shear-p tension-p
- Shear-n shear-p tension-p volume-n volume-p
- Shear-n shear-p tension-p volume-p
- Shear-n tension-n shear-p tension-p
- Shear-n tension-n shear-p tension-p volume-n volume-p
- Shear-n tension-n shear-p tension-p volume-p
- Shear-p
- Shear-p tension-p
- Shear-p tension-p volume-n volume-p
- Shear-p tension-p volume-p
- Tension-n
- Tension-n shear-p
- Tension-n shear-p tension-p
- Tension-n shear-p tension-p volume-p
- Tension-n tension-p
- Tension-p

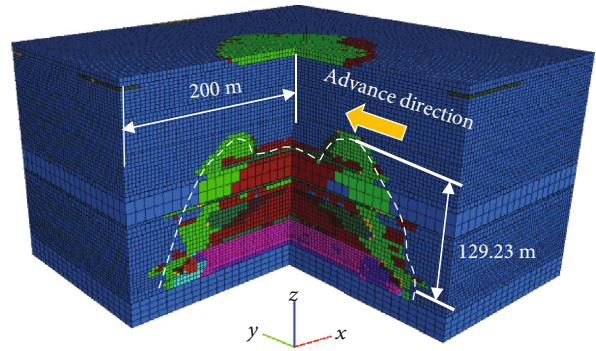
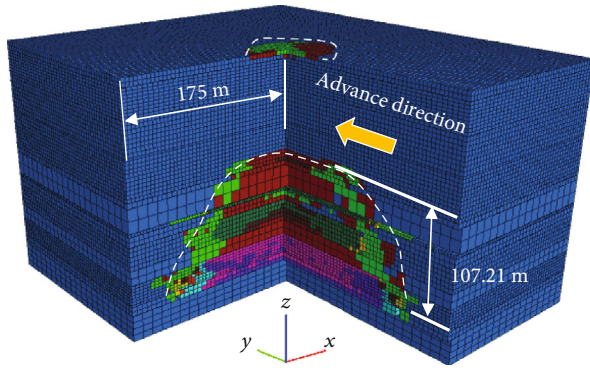
(a) 150 m

Zone state

- None
- Shear-n
- Shear-n shear-p
- Shear-n shear-p tension-p
- Shear-n shear-p tension-p volume-n volume-p
- Shear-n shear-p tension-p volume-p
- Shear-n tension-n shear-p tension-p
- Shear-n tension-n shear-p tension-p volume-n volume-p
- Shear-n tension-n shear-p tension-p volume-p
- Shear-p
- Shear-p tension-p
- Shear-p tension-p volume-n volume-p
- Shear-p tension-p volume-p
- Tension-n
- Tension-n shear-p
- Tension-n shear-p tension-p
- Tension-n shear-p tension-p volume-p
- Tension-n tension-p
- Tension-p

(b) 200 m

FIGURE 7: Continued.



Zone state

- None
- Shear-n
- Shear-n shear-p
- Shear-n shear-p tension-p
- Shear-n shear-p tension-p volume-n volume-p
- Shear-n shear-p tension-p volume-p
- Shear-n tension-n shear-p tension-p
- Shear-n tension-n shear-p tension-p volume-n volume-p
- Shear-n tension-n shear-p tension-p volume-p
- Shear-p
- Shear-p tension-p
- Shear-p tension-p volume-n volume-p
- Shear-p tension-p volume-p
- Tension-n
- Tension-n shear-p
- Tension-n shear-p tension-p
- Tension-n shear-p tension-p volume-p
- Tension-n tension-p
- Tension-p

(c) 250 m

Zone state

- None
- Shear-n
- Shear-n shear-p
- Shear-n shear-p tension-p
- Shear-n shear-p tension-p volume-n volume-p
- Shear-n shear-p tension-p volume-p
- Shear-n tension-n shear-p tension-p
- Shear-n tension-n shear-p tension-p volume-n volume-p
- Shear-n tension-n shear-p tension-p volume-p
- Shear-p
- Shear-p tension-p
- Shear-p tension-p volume-n volume-p
- Shear-p tension-p volume-p
- Tension-n
- Tension-n shear-p
- Tension-n shear-p tension-p
- Tension-n shear-p tension-p volume-p
- Tension-n tension-p
- Tension-p

(d) 300 m

FIGURE 7: Continued.

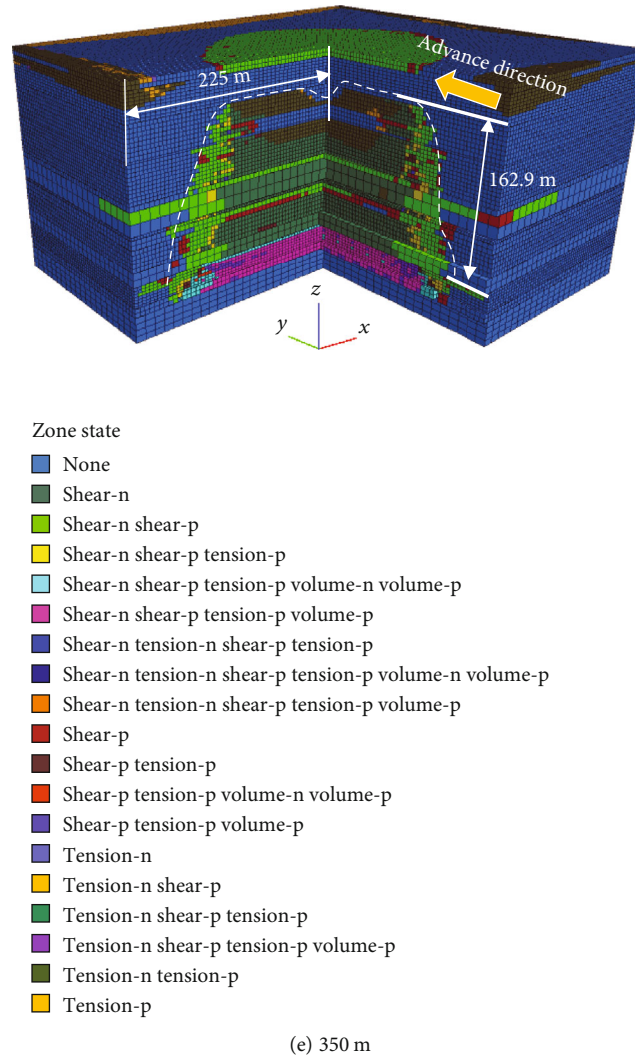


FIGURE 7: Distribution characteristics of plastic zone of the overburden with different panel widths.

The thick and hard strata not only bear the weight of the overlying strata, but also hinder the upward development of fractures below [27, 44]. As the panel width increases from 300 m to 350 m, the overburden damage degree and the height of WCFZ have relatively large increase. The result indicates that the thick and hard strata are broken, which hinder the upward development of fractures. Combined with Figures 6, 7(d) and 7(e), we concluded that the thick and hard stratum mentioned above were the medium sandstone, and the inflection point of the fitting curve was the critical point of the stratum break. Therefore, under the engineering geological conditions of panel 12401 of the Shangwan coal mine, the maximum panel width determined by the overburden damage degree should be less than 319.84 m, which promotes safe and efficient mining. Meanwhile, the panel width is restricted by the available coal mining technology and mechanical equipment. Yi [45] investigated that the reasonable panel width of the Shangwan coal mine determined by the working resistance of hydraulic support should not exceed 300 m.

5.4. Effect of Advancing Speed on Overburden Damage. The tensile strength of the overburden will be improved by speed-

ing up the panel advancing [46]. Nine Numerical models with different advancing speeds were constructed to investigate the influence law of advancing speed on the overburden damage degree. Based on the current situation of high-intensity mining, the designed advancing speed range was 5 to 21 m/d with a gradient of 2 m/d. The dimensions of the models were 400 m wide \times 400 m long \times 235.3 m high. The headgate and tailgate were excavated with dimensions 5.0 m wide \times 4.5 m high when the initial stress balanced. After the roadways were excavated, panel 12401 was mined with 8.8 m mining height and 300 m panel width. Different advancing speeds were simulated through stepwise excavation. The excavated step was equal to the advancing speed value, and the calculation time was 500 steps.

As shown in Figure 9, cross profiles were made through the center of models, and the distribution characteristics of the plastic zone with different advancing speeds were obtained. The plastic zone of the overburden is not connected with the surface, which indicates that the mining height and panel width are reasonably selected. As the advancing speed increases from 5 to 19 m/d, the height of WCFZ decreases from 132.7 to 114.35 m and the dimension of the surface

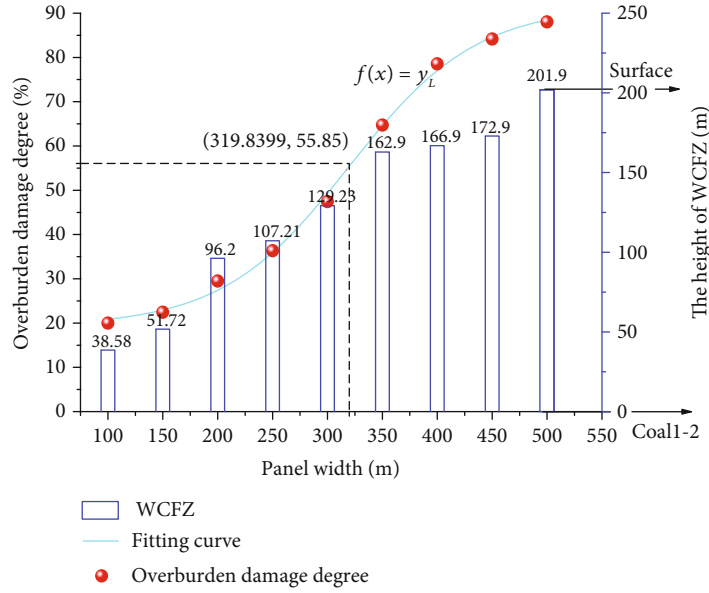


FIGURE 8: Overburden damage degree and the height of WCFZ versus panel width.

plastic zone decreases in the advancing direction of the working face. The results above indicate that the mining-induced failure on the overburden and surface is weakened as the advancing speed increases.

As shown in Figure 10, both the overburden damage degree and the height of WCFZ show a decreasing trend as the advancing speed increasing. When the advancing speed is 5 to 13 m/d, the height of WCFZ remains at 132.7 m, but different advancing speeds correspond to different overburden damage degree values, thereby indicating that the overburden damage degree is more accurate than the height of WCFZ in describing the overburden damage. The variation range of the overburden damage degree influenced by the advancing speed and panel width is 41% to 49.37% and 19.98% to 88.02%, respectively. Therefore, the damage degree is more sensitive to the variation in panel width. The damage degree with different advancing speeds was fitted as follows:

$$y_v = \frac{0.4105 + 0.0818}{1 + e^{-(x-13.4662)/-1.3243}}, \quad R^2 = 0.9677. \quad (19)$$

The fitting curve is monotonically decreasing, and the inflection point is (13.47, 45.08). Specifically, when the advancing speed is 13.47 m/d, the overburden damage degree decreases fastest. The overburden damage degree and the height of WCFZ change slightly after the inflection point; thus, the reasonable advancing speed of panel 12401 should not be less than 13.47 m/d.

Due to the limited speed of the shearer, the advancing speed of the working face has to simultaneously meet the following equation:

$$v \leq \frac{tv'd}{L}, \quad (20)$$

where v is the advancing speed of the working face, t is the

cutting time of the shearer, v' is the cutting speed of the shearer, d is the cutting depth, and L is the panel width.

Based on the operation regulations of panel 12401, the shearer cuts coal for 17 hours a day with a running speed of 7 m/min and a cutting depth of 0.865 m. The maximum advancing speed of the working face under ideal conditions is 20.58 m/d through Equation (20). Therefore, the reasonable advancing speed of the working face is 13.47 to 20.58 m/d.

6. Field Practice

Based on the analysis above in this study, the mining parameters of panel 12401 of the Shangwan coal mine were designed as 8.8 m in mining height, 300 m in panel width, and 13.47 to 20.58 m/d in advancing speed. There were no air leakages, water inrushes, surface river interruptions, or other hazards during the entire mining process, indicating that the mining parameters determined by the overburden damage degree were valid.

6.1. Effects of the Advancing Speed on the Periodic Weighting.

In the real-world production process, the advancing speed is easier to control than the mining height and panel width without affecting recovery rate of coal resources. During the new equipment debugging period from March 25, 2018, to May 27, 2018 (stage I), mining equipment failed frequently, and the continuity of the coal seam excavation was poor. As shown in Figure 11, the advancing distance of panel 12401 was 246.35 m in stage I, and the distribution of the advancing speed was discrete. The average advancing speed was merely 3.91 m/d, which was much less than the critical advancing speed of 13.47 m/d. During the normal mining period from May 28, 2018, to June 5, 2018 (stage II), the advancing distance reached 369.6 m, and the advancing speed was maintained at the critical value with an average advancing speed of 13.69 m/d.

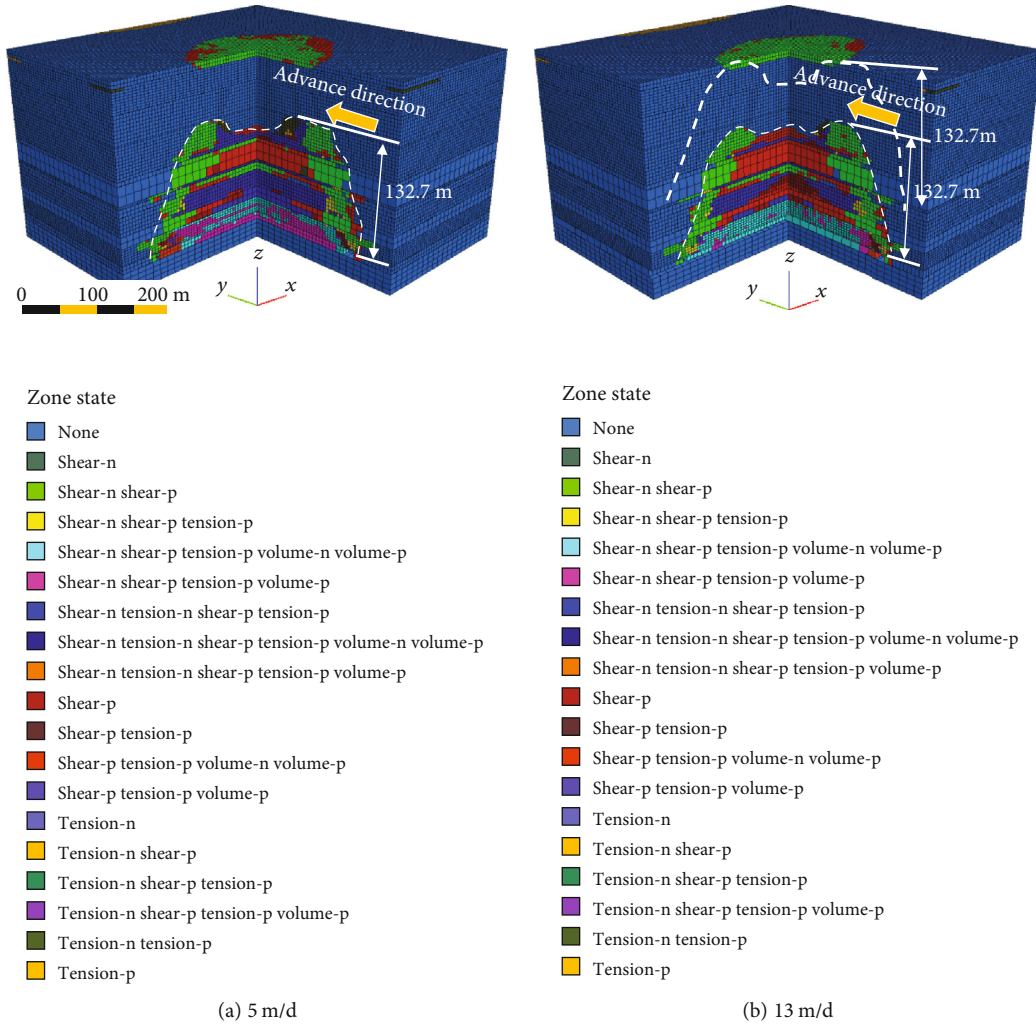


FIGURE 9: Continued.

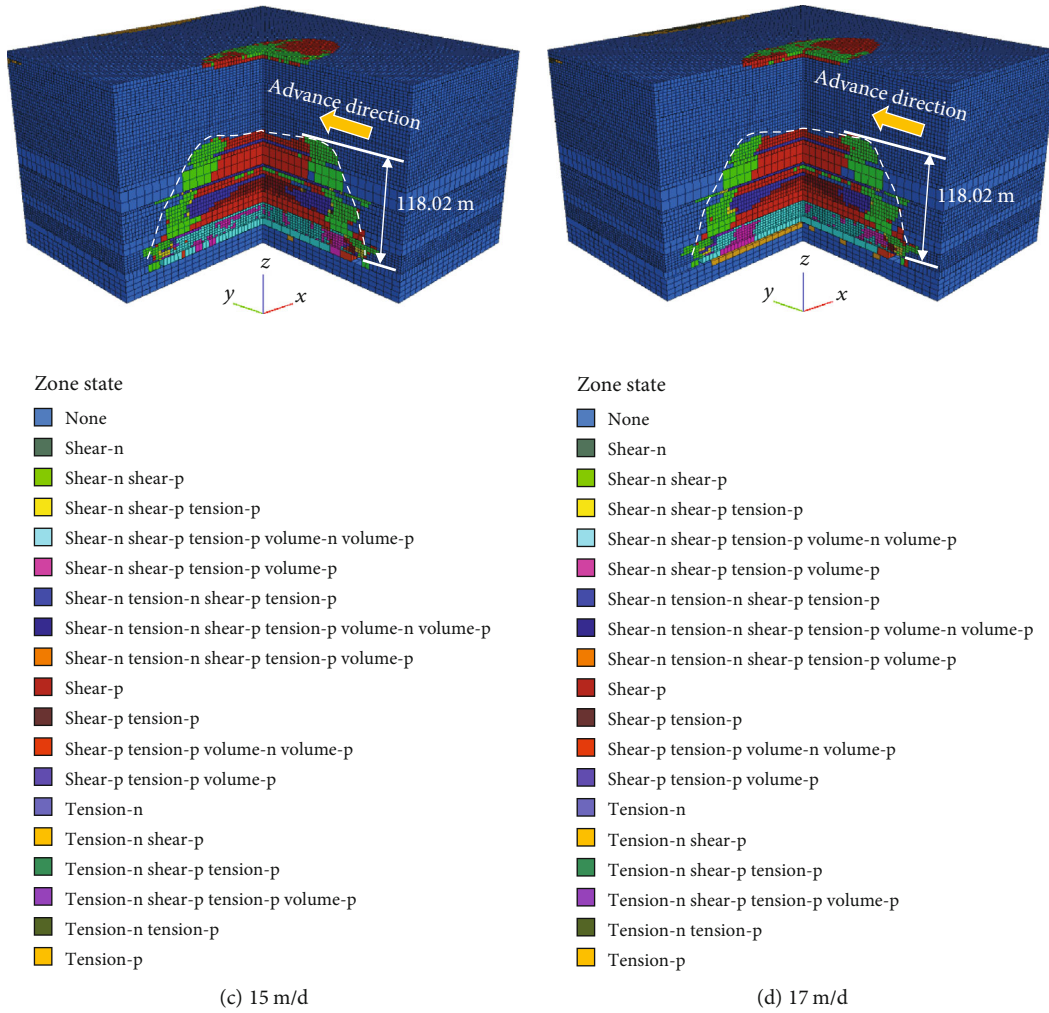


FIGURE 9: Continued.

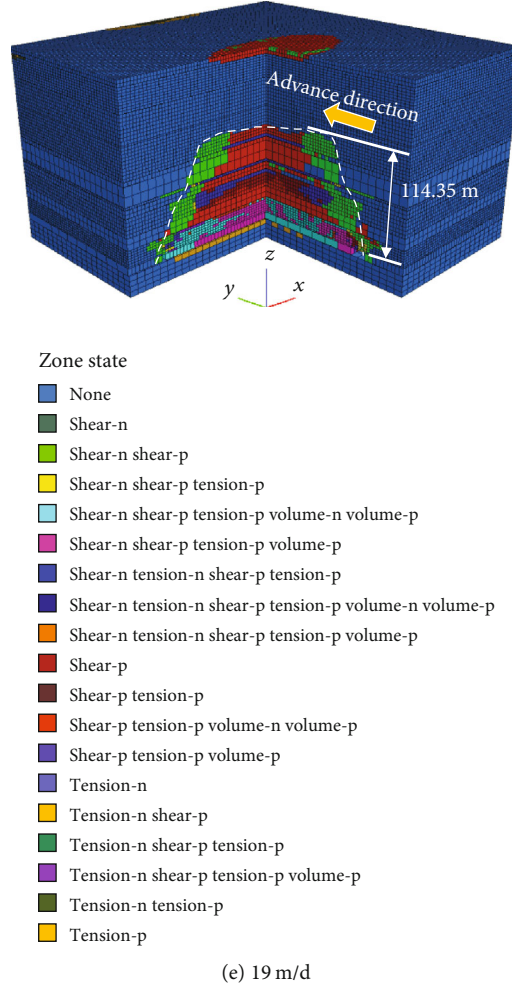


FIGURE 9: Distribution characteristics of plastic zones with different advancing speeds.

The sum of the mean value and standard deviation of the end-circulation resistance of supports was taken as the criterion to judge the first roof weighting (periodic roof weighting). The expressions are as follows:

$$\begin{cases} \bar{P}_i = \frac{1}{n} \sum_{i=1}^n P_{ti}, \\ \sigma_p = \sqrt{\frac{1}{n} \sum_{i=1}^n (P_{ti} - \bar{P}_i)^2}, \\ P_t = \bar{P}_i + \sigma_p, \end{cases} \quad (21)$$

where \bar{P}_i is the mean value of the end-circulation resistance of supports, n is the number of monitoring cycles, P_{ti} is the end-circulation resistance of the support, σ_p is the standard deviation of the end-circulation resistance of the supports, and P_t is the first roof weighting (periodic roof weighting) criterion. Statistics for the end-circulation resistance of the supports were within 360 m of the advancing distance, and the results show that $\bar{P}_i = 310.73$ bar, $\sigma_p = 56.11$ bar, and $P_t = 366.84$ bar.

The distribution characteristics of the support working resistance of the panel 12401 are shown in Figure 12. In stage I, the first weighting interval was 38 m, and the periodic weighting happened 14 times with an average periodic weighting interval of 15.12 m. In stage II, the periodic weighting happened 6 times with an average periodic weighting interval of 18.33 m. As the acceleration of the advancing speed, the periodic weighting interval increased, which was consistent with the statistical results in Section 2. Compared with stage II, stage I has an uneven distribution of the working resistance and a more durable weighting, which was resulting in frequent crushing accidents.

Due to the cumulative effect of overburden damage, accelerating the advancing speed shortens the accumulation time of overburden damage, and the periodic weighting interval of the basic roof increases accordingly. Meanwhile, accelerating the advancing speed shortens the duration of the periodic weighting, which promotes rapidly forming stable structure for the basic roof, and the overburden damage reduces accordingly. Therefore, the reliability of numerical simulation results for the overburden damage degree is verified by the distribution characteristics of the support working resistance in two stages.

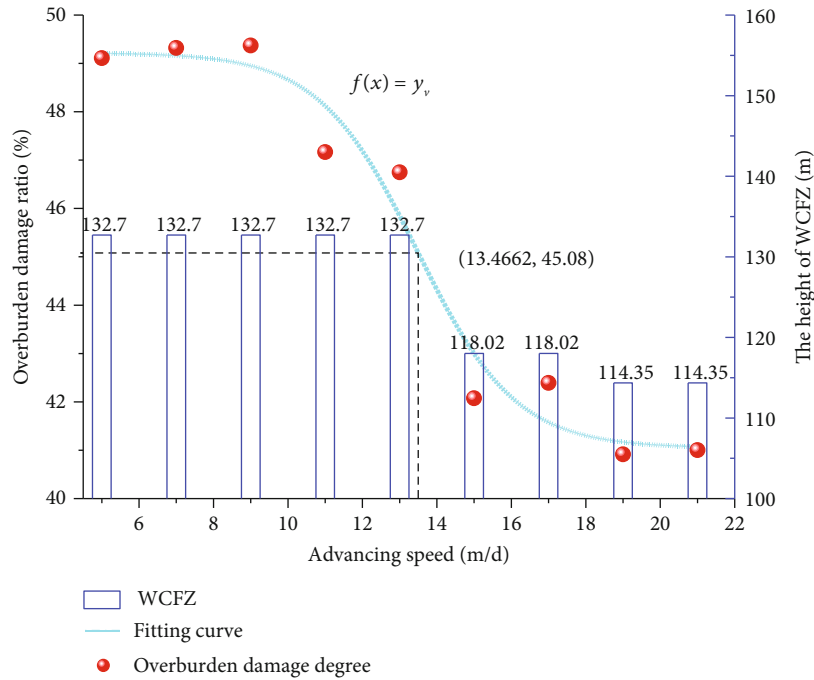


FIGURE 10: Overburden damage degree and the height of WCFZ versus advancing speed.

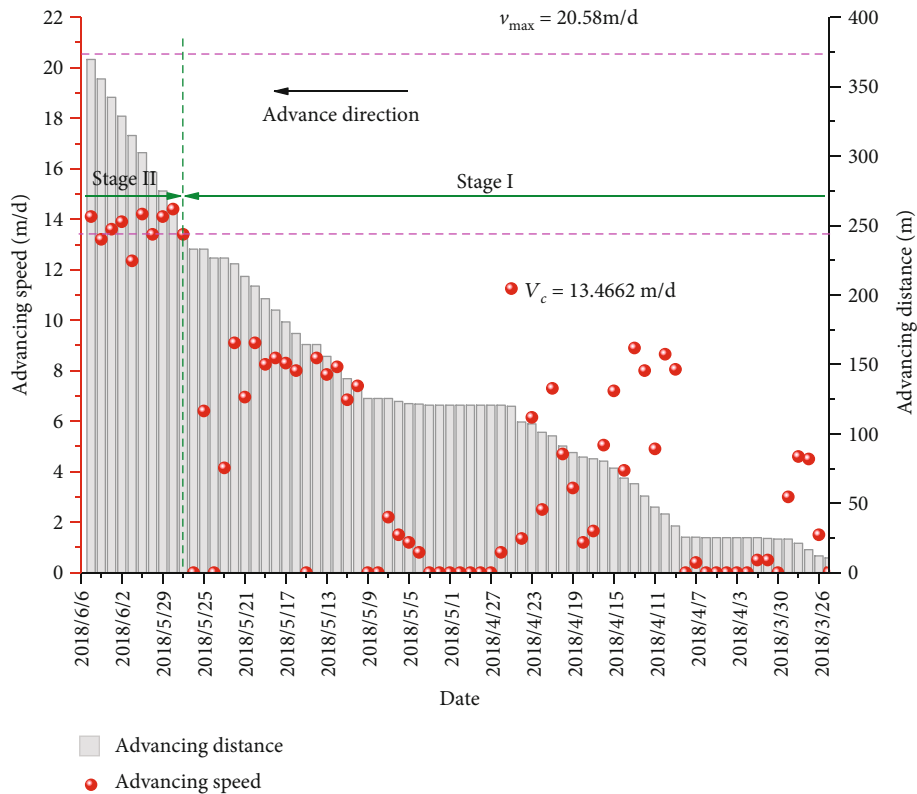


FIGURE 11: Statistics of the advancing speed and advancing distance of panel 12401.

6.2. *Effects of Advancing Speed on Ground Cracks.* Ground cracks are the external manifestation of the overburden damage caused by the high-intensity mining of the shallow coal seams. The surface of panel 12401 is a 0 to 27 m aeolian sand

with weak shear and tensile resistance, which is prone to forming ground cracks [16]. As shown in Figure 13, dynamic ground cracks of the two stages in the middle of the panel 12401 were selected for comparison. In stage I, due to the

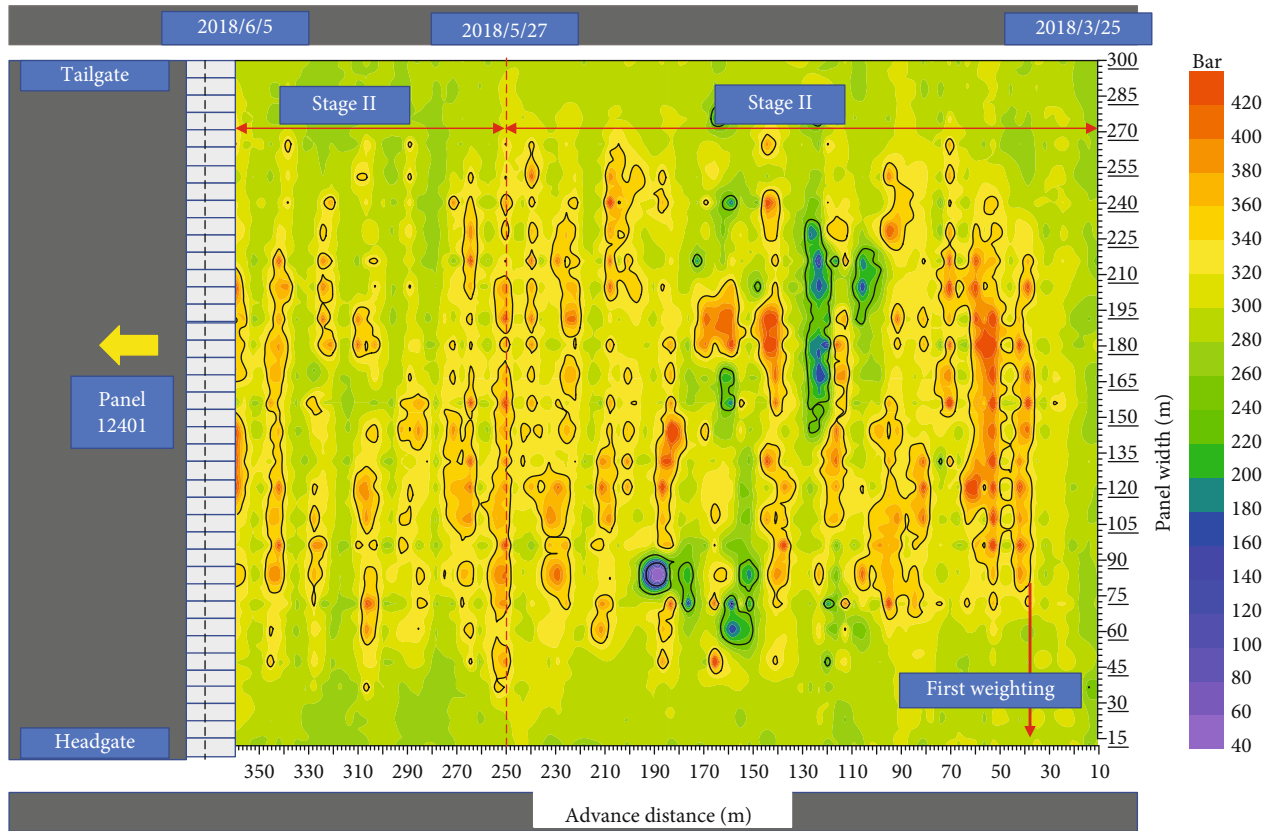
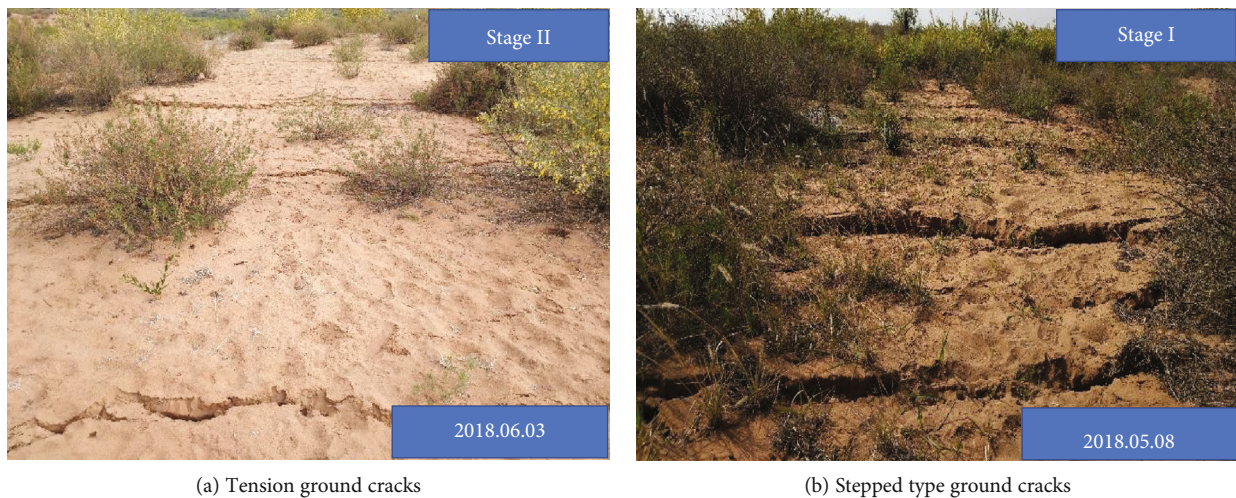


FIGURE 12: Distribution characteristics of the support working resistance of panel 12401.



(a) Tension ground cracks

(b) Stepped type ground cracks

FIGURE 13: Dynamic ground cracks in the middle of panel 12401.

low advancing speed, the overlying strata were in states of tension or shear for a long period, resulting in forming the stepped type ground cracks. In stage II, within a reasonable range of the advancing speed, the tension and shear time of the overlying strata is shortened. Thus, the surface failure is relatively weak, and only the tension cracks with small openings appear. The field engineering practice shows that the acceleration of the advancing speed weakens the damage degree of the overburden and surface. This conclusion is consistent with the

numerical simulation results, which verifies the reliability of the numerical simulation and the validity of the overburden damage degree in describing overburden failure.

7. Discussion

The statistical analysis of the relationship between the mining parameters and periodic weighting interval in the western mining area was carried out, which indicated that mining

parameters have significant influence on overburden failure. The overburden damage degree index was defined to quantitatively characterize the damage degree of the mining-disturbed overburden in a three-dimensional space. The reasonable mining parameters of panel 12401 are 8.8 m in mining height, 300 m in panel width, and 13.47 to 20.58 m/d in advancing speed, which were determined by the FLAC3D simulation of the overburden damage degree. The measured results of the PWI and the ground cracks of the two stages verified the validity of the determination of the high-intensity mining parameters through the overburden damage degree method.

Previous studies on overburden failure mainly focused on the height and morphology of the WCFZ considering the profile of the overburden ([10–12, 22, 47]), while the overburden damage degree, defined in this study, is a variable in a three-dimensional space to describe the damage volume ratio of the overburden. Based on the relationship between the overburden damage degree and the mining parameters, the reasonable mining parameters can be obtained. In addition, the mining parameters are closely related to the PWI and the crack development. Therefore, the overburden damage degree promotes ground pressure control and the surface crack management.

The concept of the overburden damage degree proposed in this study has been effectively applied in the production practices of the Shangwan coal mine in China's western mining area. The validity of the overburden damage degree method will be further verified with different panel conditions in the future. The extraction of the overburden damage degree can be easily realized in the numerical models. However, methods for extracting the overburden damage degree from physical simulations and field engineering practices require a further study.

8. Conclusions

Taking the high-intensity mining working faces in the western mining area as the background, the effects of mining parameters on the PWI, the height of WCFZ, the damage degree, and the ground cracks were investigated in this study by employing a combined method of statistical analysis, FLAC3D numerical simulation, and field measurement. The reasonable range for mining parameters of the panel 12401 was provided based on the fitting function of the overburden damage degree versus mining parameters. The main conclusions are as follows:

- (1) The PWI of the basic roof increases as the advancing speed increases, the mining height reduces, or the panel width shortens under constant engineering geological conditions. In other words, the degree of overburden damage degree will be weakened for one panel by increasing the advancing speed, reducing the mining height, or shortening the panel width
- (2) The overburden damage degree quantitatively describes the overburden failure in a three-dimensional space, but the height and morphology of the WCFZ merely consider the profile of the overburden. The numerical simulation results show that the overburden damage degree is more accurate than

the height of WCFZ in describing the overburden failure

- (3) The variation range of the overburden damage degree influenced by the advancing speed and panel width is 41% to 49.37% and 19.98% to 88.02%, respectively, which means the overburden damage degree is more sensitive to the variation in panel width
- (4) The reasonable mining parameters of the panel 12401 are 8.8 m in mining height, 300 m in panel width, and 13.47 to 20.58 m/d in advancing speed, respectively. The field measurement results of the PWI and ground cracks have verified the validity using the overburden damage degree to determine high-intensity mining parameters

Abbreviations

D :	Damage variable
dV :	Volume of the unit body
dV_0 :	Volume of the matrix
dV_D :	Volume of the damaged body
σ_{ij} :	Rock mass stress
σ_{ij}^0 :	Matrix stress
J_2 :	Second invariants of the deviatoric stress tensor of the rock mass
J_2^0 :	Second invariants of the deviatoric stress tensor of the matrix
S_{ij} :	Deviatoric stress tensor of the rock mass
σ_{mm} :	Hydrostatic pressure
σ_{mm}^0 :	Hydrostatic pressure of the matrix
δ_{ij} :	Kronecker symbol
E_{ijkl} :	Elastic constant tensor of the matrix
ε_{kl}^0 :	Strain tensor of the matrix
ε_{kl}^D :	Strain tensor of the damaged body
G :	Shear modulus of the rock mass
G^0 :	Shear modulus of the matrix
$\bar{\sigma}$:	Equivalent stress
$\bar{\varepsilon}$:	Equivalent strain
h_f :	Drillhole depth at the top of the WCFZ
W :	Compression value of rock strata
M :	Mining height
D_d :	Overburden damage degree
V_i :	Volume of a plastic zone
V_o :	Observed space volume
\bar{P}_i :	Mean value of the end-circulation resistance of supports
n :	Number of monitoring cycles
P_{ti} :	End-circulation resistance of the support
σ_p :	Standard deviation of the end-circulation resistance of the supports
P_t :	Threshold value of the roof weighting.

Data Availability

The data used to support the findings of this study are available from the corresponding author upon request.

Conflicts of Interest

The authors declared that they have no conflicts of interest to this work.

Acknowledgments

The financial support for this work was provided by the National Natural Science Foundation of China (Nos. 51874281, 51704274, and 51404272), the State Key Laboratory Cultivation Base for Gas Geology and Gas Control (Henan Polytechnic University) (WS2019A05), the Yue Qi Distinguished Scholar Project, China University of Mining & Technology, Beijing (2017JCB02), and the Fundamental Research Funds for the Central Universities (2020YQNY04).

References

- [1] National Bureau of Statistics of China, *2018 national economic and social development statistical bulletin [EB/OL]*, 2018, http://www.stats.gov.cn/tjsj/zxfb/201902/t20190228_1651265.html.
- [2] C. L. Wang, C. S. Zhang, X. D. Zhao, L. Liao, and S. L. Zhang, "Dynamic structural evolution of overlying strata during shallow coal seam longwall mining," *International Journal of Rock Mechanics and Mining Sciences*, vol. 103, pp. 20–32, 2018.
- [3] W. B. Guo, G. B. Zhao, G. Lou, and S. Wang, "A new method of predicting the height of the fractured water-conducting zone due to high-intensity longwall coal mining in China," *Rock Mechanics and Rock Engineering*, vol. 52, no. 8, pp. 2789–2802, 2019.
- [4] L. Sun, C. H. Li, Y. P. Cai, and X. Wang, "Interval optimization model considering terrestrial ecological impacts for water rights transfer from agriculture to industry in Ningxia, China," *Scientific Reports*, vol. 7, no. 1, p. 3465, 2017.
- [5] X. Y. Liu, W. Zhou, and Z. K. Bai, "Vegetation coverage change and stability in large open-pit coal mine dumps in China during 1990–2015," *Ecological Engineering*, vol. 95, pp. 447–451, 2016.
- [6] N. Li, C. Z. Yan, and J. L. Xie, "Remote sensing monitoring recent rapid increase of coal mining activity of an important energy base in northern China, a case study of Mu Us Sandy Land," *Resources, Conservation and Recycling*, vol. 94, pp. 129–135, 2015.
- [7] Y. L. Bi, L. L. Xie, J. Wang, Y. X. Zhang, and K. Wang, "Impact of host plants, slope position and subsidence on arbuscular mycorrhizal fungal communities in the coal mining area of north-central China," *Journal of Arid Environments*, vol. 163, pp. 68–76, 2019.
- [8] D. P. Adhikary and H. Guo, "Measurement of longwall mining induced strata permeability," *Geotechnical and Geological Engineering*, vol. 32, no. 3, pp. 617–626, 2014.
- [9] Q. S. Bai and S. H. Tu, "A General Review on Longwall Mining-Induced Fractures in Near-Face Regions," *Geofluids*, vol. 2019, 22 pages, 2019.
- [10] X. X. Miao, X. M. Cui, J. A. Wang, and J. L. Xu, "The height of fractured water-conducting zone in undermined rock strata," *Engineering Geology*, vol. 120, no. 1–4, pp. 32–39, 2011.
- [11] V. Palchik, "Formation of fractured zones in overburden due to longwall mining," *Environmental Geology*, vol. 44, no. 1, pp. 28–38, 2003.
- [12] A. Majdi, F. P. Hassani, and M. Y. Nasiri, "Prediction of the height of distressed zone above the mined panel roof in longwall coal mining," *International Journal of Coal Geology*, vol. 98, no. 1, pp. 62–72, 2012.
- [13] Z. Y. Song, H. Konietzky, and M. Herbst, "Drawing mechanism of fractured top coal in longwall top coal caving," *International journal of rock mechanics and mining sciences*, vol. 130, article 104329, p. 130, 2020.
- [14] J. X. Tang, Z. Y. Dai, Y. L. Wang, and L. Zhang, "Fracture Failure of Consequent Bedding Rock Slopes After Undergroundmining in Area," *Rock mechanics and rock engineering*, vol. 52, no. 8, pp. 2853–2870, 2019.
- [15] C. Xu, Q. Fu, X. Y. Cui, K. Wang, Y. X. Zhao, and Y. B. Cai, "Apparent-Depth Effects of the Dynamic Failure of Thick Hard Rock Strata on the Underlying Coal Mass During Underground Mining," *Rock mechanics and rock engineering*, vol. 52, no. 5, pp. 1565–1576, 2019.
- [16] X. L. Yang, G. C. Wen, L. C. Dai, H. T. Sun, and X. L. Li, "Ground Subsidence and Surface Cracks Evolution from Shallow-Buried Close-Distance Multi-seam Mining: A Case Study in Bulianta Coal Mine," *Rock mechanics and rock engineering*, vol. 52, no. 8, pp. 2835–2852, 2019.
- [17] L. Q. Ma, Z. Y. Jin, J. M. Liang, H. Sun, D. S. Zhang, and P. Li, "Simulation of water resource loss in short-distance coal seams disturbed by repeated mining," *Environmental earth sciences*, vol. 74, no. 7, pp. 5653–5662, 2015.
- [18] G. Wang, M. M. Wu, R. Wang, H. Xu, and X. Song, "Height of the mining-induced fractured zone above a coal face," *Engineering Geology*, vol. 216, pp. 140–152, 2017.
- [19] J. C. Zhang, "Investigations of water intrusions from aquifers under coal seams," *International Journal of Rock Mechanics and Mining Sciences*, vol. 42, no. 3, pp. 350–360, 2005.
- [20] C. Zhang, S. Tu, L. Zhang, Q. Bai, Y. Yuan, and F. Wang, "A methodology for determining the evolution law of gob permeability and its distributions in longwall coal mines," *Journal of Geophysics and Engineering*, vol. 13, no. 2, pp. 181–193, 2016.
- [21] B. N. Hu, H. X. Zhang, and B. H. Shen, *Regulations of Coal Mining and Protective Coal Pillar Design under Buildings, Water Bodies, Railways, Coal Mines and Roadways*, Coal Industry Press, Beijing, 2017.
- [22] Y. Liu, Q. M. Liu, W. P. Li, T. Li, and J. H. He, "Height of water-conducting fractured zone in coal mining in the soil-rock composite structure overburdens," *Environmental Earth Sciences*, vol. 78, no. 7, p. 242, 2019.
- [23] X. J. Hu, W. P. Li, D. T. Cao, and M. C. Liu, "Index of multiple factors and expected height of fully mechanized water flowing fractured zone," *Journal of China Coal Society*, vol. 37, no. 4, pp. 613–620, 2012.
- [24] E. Jiráňková, "Utilisation of surface subsidence measurements in assessing failures of rigid strata overlying extracted coal seams," *International Journal of Rock Mechanics and Mining Sciences*, vol. 53, pp. 111–119, 2012.
- [25] J. F. Ju and J. L. Xu, "Structural characteristics of key strata and strata behaviour of a fully mechanized longwall face with 7.0m height chocks," *International Journal of Rock Mechanics and Mining Sciences*, vol. 58, pp. 46–54, 2013.
- [26] Q. D. Qu, J. L. Xu, R. L. Wu, W. Qin, and G. Z. Hu, "Three-zone characterisation of coupled strata and gas behaviour in multi-seam mining," *International Journal of Rock Mechanics and Mining Sciences*, vol. 78, pp. 91–98, 2015.

- [27] J. L. Xu, W. B. Zhu, and X. Z. Wang, "(2012). New method to predict the height of fractured water-conducting zone by location of key strata," *Journal of China Coal Society*, vol. 37, no. 5, pp. 762–769, 2012.
- [28] Z. Y. Song, W. J. Wei, and J. W. Zhang, "Numerical investigation of effect of particle shape on isolated extracted zone (IEZ) in block caving," *Arabian Journal of Geosciences*, vol. 11, no. 12, p. 310, 2018.
- [29] Z. B. Yu, S. Y. Zhu, Y. Z. Guan, and D. X. Hu, "Feasibility of Modifying Coal Pillars to Prevent Sand Flow Under a Thick Loose Layer of Sediment and Thin Bedrock," *Mine water and the environment*, vol. 38, no. 4, pp. 817–826, 2019.
- [30] D. Y. Zhang, W. H. Sui, and J. W. Liu, "Overburden Failure Associated with Mining Coal Seams in Close Proximity in Ascending and Descending Sequences Under a Large Water Body," *Mine water and the environment*, vol. 37, no. 2, pp. 322–335, 2018.
- [31] M. G. Qian, P. W. Shi, and J. L. Xu, *Ground pressure and strata control*, China University of Mining and technology Press, Xuzhou, 2010.
- [32] H. F. Lin, R. F. Ma, S. G. Li, L. H. Cheng, H. Y. Pan, and L. Li, "Coupling model of evolution of mining fissure elliptic paraboloid zone and methane delivery," *Advanced Materials Research*, vol. 734–737, pp. 546–550, 2013.
- [33] F. Wang, J. L. Xu, and J. L. Xie, "Effects of arch structure in unconsolidated layers on fracture and failure of overlying strata," *International Journal of Rock Mechanics and Mining Sciences*, vol. 114, pp. 141–152, 2019.
- [34] C. Zhang, S. Tu, and Y. Zhao, "Compaction characteristics of the caving zone in a longwall goaf: a review," *Environmental Earth Sciences*, vol. 78, no. 1, pp. 27–46, 2019.
- [35] L. Zhou, X. P. Su, Y. Y. Lu, Z. L. Ge, Z. Y. Zhang, and Z. H. Shen, "A New Three-Dimensional Numerical Model Based on the Equivalent Continuum Method to Simulate Hydraulic Fracture Propagation in an Underground Coal Mine," *Rock mechanics and rock engineering*, vol. 52, no. 8, pp. 2871–2887, 2019.
- [36] M. Kachanov, "Effective properties of Solids: review of Concepts," *Applied Mechanics Reviews*, vol. 45, no. 8, pp. 304–335, 1992.
- [37] S. Murakami, "Mechanical representation of damage and damage variables," in *Continuum Damage Mechanics: A Continuum Mechanics Approach to the Analysis of Damage and Fracture*, pp. 15–55, Springer Netherlands, Dordrecht, 2012.
- [38] Z. Wang, L. Zhao, J. Kang, and L. Jia, "Technological study on height observation of water flowing fractured zone caused by repeated mining in multiple coal seam," *Coal engineering*, vol. 50, no. 12, pp. 82–85, 2018.
- [39] Q. S. Bai, S. H. Tu, F. T. Wang, and C. Zhang, "Field and numerical investigations of gateroad system failure induced by hard roofs in a longwall top coal caving face," *International Journal of Coal Geology*, vol. 173, pp. 176–199, 2017.
- [40] G. B. Zhang, W. Q. Zhang, C. H. Wang, G. L. Zhu, and B. Li, "Mining seams Bedrock–Deformation and failure of strata and Alluvium," *Geotechnical and Geological Engineering*, vol. 34, no. 5, pp. 1553–1563, 2016.
- [41] T. Zhang, Y. X. Zhao, Q. Gan, X. D. Nie, G. P. Zhu, and Y. Hu, "Investigations into Mining-Induced Stress–Fracture–Seepage Field Coupling in a Complex Hydrogeology Environment: A Case Study in the Bulianta Colliery," *Mine water and the environment*, vol. 38, no. 3, pp. 632–642, 2019.
- [42] C. Zhang and L. Zhang, "Permeability Characteristics of Broken Coal and Rock Under Cyclic Loading and Unloading," *Natural Resources Research*, vol. 28, no. 3, pp. 1055–1069, 2019.
- [43] Y. C. Luan, J. T. Li, X. H. Ban, C. Y. Sang, C. Q. Zhang, and D. P. Ma, "Observational research on the height of water flowing fractured zone in repeated mining of short-distance coal seams," *Journal of Mining and Safety Engineering*, vol. 27, no. 1, pp. 139–142, 2010.
- [44] Y. Y. Lu, T. Gong, B. W. Xia, B. Yu, and F. Huang, "Target Stratum Determination of Surface Hydraulic Fracturing for Far-Field Hard Roof Control in Underground Extra-Thick Coal Extraction: A Case Study," *Rock mechanics and rock engineering*, vol. 52, no. 8, pp. 2725–2740, 2019.
- [45] M. S. Yi, "Selection of echanized working face length by great height mining under shallow coal seam in Shendong coal district," *Journal of China Coal Society*, vol. 2007, no. 12, pp. 1253–1257, 2007.
- [46] J. H. Yang, S. L. Kong, and D. Z. Kong, "Effect of working face length and advancing speed on strata behaviors in high-intensity mining," *Rock and soil mechanics*, vol. S2, pp. 333–399+350, 2015.
- [47] J. A. Wang and H. D. Park, "Coal mining above a confined aquifer," *International Journal of Rock Mechanics and Mining Sciences*, vol. 40, no. 4, pp. 537–551, 2003.

Research Article

Study on Fracturing and Diffusion Mechanism of Non-slab Fracturing Grouting

Hua Cheng,^{1,2,3} Xiangyang Liu ,¹ Jian Lin,³ Liangliang Zhang,² Mingjing Li,² and Chuanxin Rong²

¹School of Civil and Hydraulic Engineering, Hefei University of Technology, Hefei 230000, China

²School of Civil Engineering and Architecture, Anhui University of Science and Technology, Huainan 232001, China

³School of Civil Engineering, Anhui Jianzhu University, Hefei 230000, China

Correspondence should be addressed to Xiangyang Liu; 2016010051@mail.hfut.edu.cn

Received 10 June 2020; Revised 1 July 2020; Accepted 11 July 2020; Published 12 August 2020

Academic Editor: Zhengyang Song

Copyright © 2020 Hua Cheng et al. This is an open access article distributed under the Creative Commons Attribution License, which permits unrestricted use, distribution, and reproduction in any medium, provided the original work is properly cited.

The coupling effect of a slurry and the fractured rock layer controls a spatial attenuation of the fracture channel width and grouting pressure from a grouting hole to the slurry top of fracture diffusion. This paper comprehensively considers the influencing factors such as the mechanical properties of the injected rock mass and the time-varying characteristics of the serous viscosity and introduces the control equation of the fracture channel width to establish a single-fracture non-slab fracturing grouting model. Combining the motion law of the slurry with the extension form of fracture, the equation of slurry diffusion motion, considering the fracture geometry and the time-varying characteristics of the serous viscosity, is derived. Comparing this equation with the existing theories and experiments, the validity and reliability of the theory are verified. In this paper, the effects of rock elastic modulus, slurry viscosity, and grouting rate on the fracturing grouting diffusion law of rock mass are analyzed. It is pointed out that when fracturing grouting in deep rock layers, a larger initial grouting rate and grouting pressure should be selected in the early stages of grouting to generate or penetrate fractures in the rock layer. Also, when the grouting pressure is stable, it is appropriate to increase the viscosity so that the slurry can quickly gel in the fractures thus sealing the fractures.

1. Introduction

Since the depth of coal mining in China has gradually increased into kilometers, the requirements of grouting for stopping up water during the construction of vertical shafts have also become higher [1, 2]. Deep well construction disturbed rock formations have characteristics such as high geostress, poor microfracture connectivity, and high pore water pressure [3–6]. According to the conventional grouting scheme in shallow formations, it is difficult to effectively block bored well water. Studying the fluid-solid coupling mechanism between the slurry and the microfracture in the rock formation and analyzing the law of fracturing grouting and diffusion in the deep microfractured rock mass are of great significance for guiding the design of deep well grouting and water blocking in coal mines.

The fracturing grouting process is the result of the coupling of the slurry flow field and rock mass stress field. During the migration of the slurry, resistance from the two sides of the fracture channel and its viscosity causes the grouting pressure to decay along the diffusion radius within the fracture channel. At the same time, the attenuation of the fracture channel width in the direction of the diffusion radius results in different resistances of the channel sidewall to the diffusion of the slurry at different positions, thereby affecting the flow of the slurry. Therefore, the mechanical characteristics of the injected rock mass, the fracture geometry, and the time-varying characteristics of the serous viscosity are all important criteria for evaluating the effect of fracturing grouting and designing related grouting parameters. Although domestic and foreign scholars have carried out a lot of research on the mechanism of fracture grouting

[7–12], these studies mostly focus on the theory of fracturing grouting in soil, and due to the lack of comprehensive understanding of the fracture mechanism and material parameters, it is not yet possible to correctly predict or explain the fracture pressure of deeply buried rock strata.

Presently, domestic and foreign scholars have conducted a series of studies in the field of fracturing grouting. In abroad, Murdoch [13] obtained qualitative conclusions about fracture geometry through laboratory experiments; Bezuijen et al. [14] analyzed the influence of fracture length and thickness on fracture propagation based on a single fracturing grouting model; Gustafson and Claesson [15] established the grout migration equation for a single fracture under constant pressure grouting based on the Bingham fluid constitutive model; Mohammed [16] studied the grouting of soil grouting through model tests and observed the law of slurry diffusion distribution by CT scanning; Kishida et al. [17] used a numerical software to simulate the grouting process of a single fracture and studied the change of grouting pressure during the grouting process. In China, Huang et al. [18] proposed a method of induced fracturing grouting based on the principle of elastic mechanics; Wang and Li [19] studied the diffusion law of slurry in rock fractures, obtained the equation between grouting pressure and fracturing diffusion radius, and carried out verification and analysis in combination with fracturing grouting laboratory simulation experiments; Sun et al. [20] derived the diffusion law of the Bingham fluid slurry fracturing grouting and discussed the influence of slurry time-varying on grouting diffusion; Zhang et al. [21] considered the effect of interface stress coupling between the slurry and soil and studied the law of fracturing grouting of the Newtonian fluid; Zhang et al. [22, 23] also established a single-fracture slurry migration equation based on the predecessors under the time-varying slurry viscosity. The above studies help to better understand the mechanism of fracturing grouting. However, the existing grouting fracture models only study the slurry diffusion from the motion of the slurry in the fracture channel, and few studies have taken into account the time-varying viscosity characteristics of the slurry and the fracture propagation geometry. In fact, the motion of the slurry and the expansion of the fracturing cracks are performed simultaneously. On the one hand, the motion of the slurry should be followed, and on the other hand, the diffusion of the slurry should also be followed as well as the spread of the fracturing cracks.

In order to solve the above problems, a nonslab fracturing diffusion model was built based on the fracture mechanics theory and fluid mechanics in this paper. Combining the motion of the slurry with the propagation of the fracturing crack, an equation about the slurry diffusion motion in the fracture channel was derived, and the impacts of the fracture geometry and the time-varying characteristics of the slurry viscosity have been taken into consideration. And compared with the existing theories and measured results, the validity and reliability of the theory were verified. Based on the established theoretical model, the fracturing diffusion mechanism of the slurry in the rock layer was also studied, and the influencing factors such as elastic modulus, viscosity, and grouting rate on the rule of fracturing and diffusion of the

slurry were analyzed, which provided a theoretical basis for the design and optimization of grouting in the future.

2. Diffusion Model of Single-Fracture Nonslab Fracturing Grouting

Studies have shown that during fracturing grouting, the slurry in the grouting holes does not diffuse spherically or in a column but splits vertically along the sides of the grouting holes. It is assumed that the maximum and minimum principal stresses in the rock formation are horizontal and vertical, respectively, and the grouting fracturing direction is horizontal, as shown in Figure 1(a). During the grouting process, due to the resistance of the slurry from the upper and lower sides of the fracture channel and its own viscosity, the grouting pressure attenuates and unevenly distributes in the fracture channel. At the same time, the width of the fracture channel decreases from the grouting hole to the slurry top of fracturing diffusion, and the width of the fracturing crack is 0 at the slurry top of fracturing diffusion, as shown in Figure 1(b). Therefore, a single-fracture nonslab fracturing diffusion model for vertical fracturing along the side wall of a grouting hole was established.

2.1. Basic Assumptions

- (1) The slurry is a generalized Bingham fluid, and the flow pattern does not change during the movement of the slurry, only the viscosity changes with time
- (2) The injected rock mass is an isotropic elastomer
- (3) There is no slip at the boundary of the fracture channel
- (4) The slurry exists only inside the fracture channel and flows laminarily in the fracture channel
- (5) The force on the upper and lower side walls of the fracture channel is perpendicular to the axis of symmetry of the fracture channel
- (6) The flow at different locations in the fracture is constant

2.2. Fracture Expansion Criterion

2.2.1. Fracturing Pressure. The stress in the grouting hole is shown in Figure 1(a). The direction of the maximum principal stress (σ_1) is horizontal and the direction of the minimum principal stress (σ_3) is vertical. When the grouting pressure in the grouting section reaches a certain critical value, the grouting hole will produce horizontal fracturing in a direction parallel to the maximum principal stress, the grouting pressure when forming horizontal fracture is [24]

$$P_0 = \frac{\sigma_3 + \sigma_t^*}{0.94}, \quad (1)$$

where σ_t^* is the tensile strength of the rock under confining pressure conditions, its value is generally 2-3 times the pure

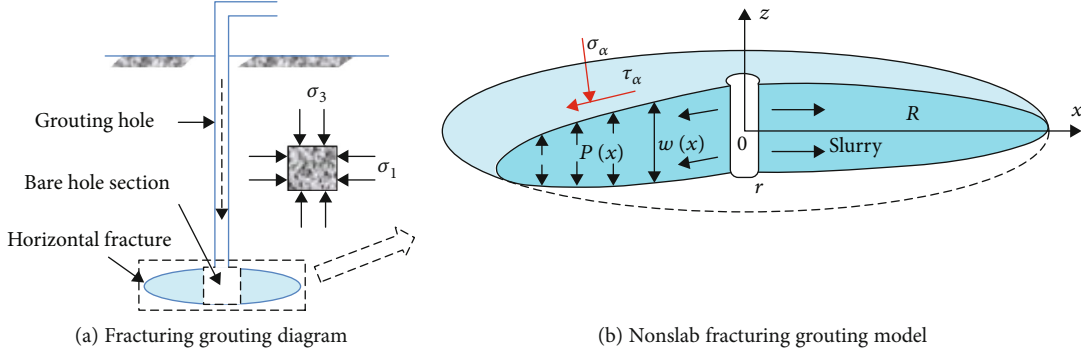


FIGURE 1: Analysis model of fracturing grouting process.

tensile strength value obtained by the uniaxial direct stretching method, and 0.94 is the correction factor.

2.2.2. *Channel Continues to Expand.* It can be known from geotechnical mechanics that under the stress conditions shown in Figure 1(a), the total normal stress σ_α (MPa) acting on the outer wall of the microcrack is

$$\sigma_\alpha = \frac{\sigma_1 + \sigma_3}{2} - \frac{\sigma_1 - \sigma_3}{2} \cos 2\alpha, \quad (2)$$

where $\sigma_3 = \sigma_{cz} + P_S$, $\sigma_1 = k\sigma_{cz} + P_S$; P_S is the hydrostatic pressure (MPa), $P_S = \gamma_w H_w$; σ_{cz} is the vertical effective stress; and k is the lateral pressure coefficient.

When the grouting pressure is nonuniformly distributed in the interior of the fracture channel, according to the hydraulic fracture expansion theory [25, 26], it can be derived that the stress intensity factor K_I is

$$K_I = \frac{2}{\sqrt{\pi R}} \int_r^R \frac{\Delta P(x)}{\sqrt{R^2 - x^2}} x dx, \quad (3)$$

where $\Delta P(x) = P(x) - \sigma_\alpha$, $P(x)$ is the grouting pressure distributed along the crack wall; r is the radius of the bare hole section, (because it is relatively small compared with the splitting radius, it is neglected in the calculation); and R is the disc-type crack radius.

According to the linear elastic fracture mechanics [25], the fracture extension standard is adopted as

$$K_I = K_{IC}, \quad (4)$$

where K_{IC} is the fracture toughness of the injected material.

2.3. *Spatiotemporal Distribution Equation of Slurry Viscosity.* Considering the slurry as the Bingham fluid, due to the existence of yield shear force, its viscosity changes directly affect the slurry diffusion range, and its viscosity increases with time [27]. As the slurry needs to overcome the shear force and the time-varying plastic viscosity, the slurry rheological equation is as follows:

$$\tau = \tau_0 + u(t) \dot{\gamma}, \quad (5)$$

where τ is the shear stress of the slurry, τ_0 is the yield shear force, $\dot{\gamma} = dv/dz$ is the shear rate, and t is the grouting time. Since the slurry viscosity time function is mostly obtained by fitting test data, its form is uncertain, so the general function form $u(t)$ is used to represent the viscosity-time relationship.

If the slurry only flows in the radial direction, the split and diffusion distance of the slurry at time t is x , and according to the conservation of mass, the corresponding time at x is

$$t = \frac{2\pi\omega x^2}{q}. \quad (6)$$

It should be noted that, in the derivation below, w is sometimes represented as $w(x)$.

When the grouting time is t , the space-time distribution equation of viscosity in the slurry diffusion zone corresponds to x :

$$u(t, x) = u\left(\frac{2\pi\omega x^2}{q}\right). \quad (7)$$

In equation (7), the grouting time t is eliminated. This is because under the condition of constant grouting rate, the spatiotemporal distribution of the slurry viscosity is determined by the spatial position, and the grouting time affects the slurry diffusion radius.

2.4. *Governing Equation of Fracture Channel Width.* During the grouting process, as the slurry is continuously injected and the fractures are continuously expanding, the width of the fractures along the fracture channel changes and gradually decreases. Therefore, the calculation of fracture morphology is a coupling problem of fluid mechanics and fracture mechanics. According to the literature [28], if the center of the crack root is 0 and the x -axis is established along the crack direction, the width of the crack at the distance x from the origin can be defined as

$$w(x) = \frac{4}{E} K_{IC} \sqrt{\frac{R^2 - x^2}{\pi R}}. \quad (8)$$

It can be seen that the morphological equation at any time during the fracture propagation is constant. The

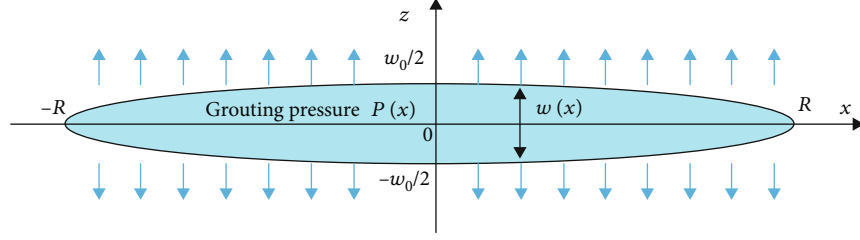


FIGURE 2: Fracture geometry model.

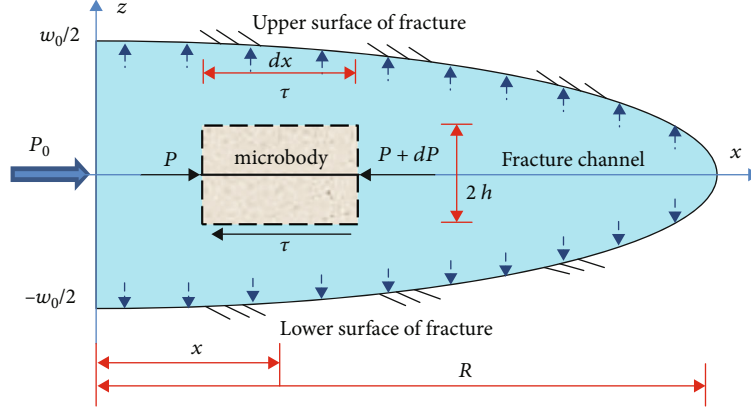


FIGURE 3: Microelement body balance analysis.

geometric model is shown in Figure 2. That is, there is a constant correspondence relationship between the fracture length and width, and the fracture width w_0 at the grouting hole can be expressed as $w_0 = 4K_{IC}/(E\sqrt{R/\pi})$.

2.5. Governing Equation of Slurry Fracturing and Diffusion.

According to the basic assumption (5), a rectangular coordinate system as shown in Figure 3 is established with the vertical axis passing through the grouting hole and the symmetry center of the fracture channel as the coordinate axis.

Taking the serous vein center as the axis of symmetry to take the slurry microbody for force analysis, ignoring the self-weight of the slurry, from the equilibrium conditions, the shear stress distribution can be obtained as [29]

$$\tau = -z \left(\frac{dP}{dx} \right), \quad (9)$$

where dx is the length of the microbody, τ is the shear stress, P is the slurry pressure, and dP is the slurry pressure volume.

The generalized Bingham body motion can be divided into two parts: the overall motion of the flow core area and the relative motion of the shear area. Through the force balance analysis of the unit body and substitution of the boundary conditions: $z = \pm w/2$ and $v = 0$, the velocity distribution of the slurry in the direction of the fracture thickness can be obtained as

$$v = \begin{cases} -\frac{1}{u(2\pi\omega x^2/q)} \left[\frac{(1/2)dP}{dx((w^2/4) - h^2) - \tau_0((w/2) - h)} \right], & (-h \leq z \leq h), \\ -\frac{1}{u(2\pi\omega x^2/q)} \left[\frac{(1/2)dP}{dx((w^2/4) - z^2) - \tau_0((w/2) - z)} \right], & (|h| \leq |z| \leq |w/2|), \end{cases} \quad (10)$$

According to integral formula $\bar{v} = \int_{-w/2}^{w/2} v dz$, ignoring the higher order minor terms, the average velocity of the slurry on the fracture surface can be simplified as

$$\bar{v} = \frac{-w^2}{12u(2\pi\omega x^2/q)} \left(\frac{dP}{dx - (3\tau_0/w)} \right). \quad (11)$$

It can be known from the law of conservation of mass that during the grouting process, the unit flow rate of the slurry on any diffusion section inside the fracture channel is equal to the grouting rate q at the grouting hole, then

$$q = 2\pi x \int_{-w/2}^{w/2} v dz. \quad (12)$$

Simultaneously implementing (11) and (12), the pressure gradient of the slurry in the fracture channel is obtained:

$$\frac{dP}{dx} = -\frac{6u(2\pi\omega x^2/q)q}{\pi x w^3} + \frac{3\tau_0}{w}. \quad (13)$$

From the literature [22], the viscosity change of the slurry material can be fitted as the following function law:

$$u(t) = mt^2, \quad (14)$$

where m is a time-varying parameter of viscosity.

Simultaneously implementing (13) and (14),

$$\frac{dP}{dx} = -\frac{3 \times 2^3 \times \pi x^3}{qw} + \frac{3\tau_0}{w}. \quad (15)$$

Substitute (8) into (15) and bring in the boundary conditions: $x \rightarrow 0, P = P_0$, the spatial distribution equation of the slurry pressure inside the fracture channel can be obtained as

$$P(x) = P_0 - \frac{6\pi^{3/2}mE\sqrt{R}}{qK_{IC}} \left(\frac{2}{3}R^3 + \frac{1}{3}(R^2 - x^2)^{3/2} - R^2\sqrt{R^2 - x^2} \right) + \frac{3\sqrt{\pi}RE\tau_0}{4K_{IC}} \arcsin\left(\frac{x}{R}\right). \quad (16)$$

Substituting (2) and (16) into (3), the diffusion equation of time-varying grout fracturing grouting based on crack fracturing discrimination condition ($K_I = K_{IC}$) is

$$P_0 = \frac{\sqrt{\pi}}{2\sqrt{R}}K_{IC} + \frac{3\pi^{3/2}mER^{7/2}}{2qK_{IC}} - \frac{3\sqrt{\pi}RE\tau_0}{4K_{IC}} + \sigma_\alpha. \quad (17)$$

3. Verify

Previously, when analyzing the mechanism of fracturing grouting, they often ignored the change in fracture width and assumed that the fracture width was a constant value, and when analyzing the influence of grouting pressure factors on the fracturing diffusion distance, the grouting pressure difference (the pressure at the grouting hole minus the rock fracture cracking pressure) was used as a variable. The relationship between the grouting pressure difference and the fracturing diffusion distance R is [29]:

$$\Delta P = P_0 - P_d = 3 \times 2^n \times \pi^{n-1} \frac{mw^{n-3}q^{1-n}}{n} (R^{2n} - r^{2n}) - \left(\frac{3\tau_0}{w} + \rho g \sin \alpha \cos \theta \right) (R - r). \quad (18)$$

However, during the field test, the grouting pressure is still the research object, so the determination of the fracturing pressure is particularly important. When Sun et al. [30] studied the fracturing grouting mechanism, they believed that the far-field stress could be eliminated and sustained development only when the grouting pressure inside the fracture channel was greater than the sum of the minimum principal stress σ_3 and tensile strength σ_t^* of the injected rock mass.

$$P_d = \sigma_3 + \sigma_t^*. \quad (19)$$

Substituting equations (13) of the slurry viscosity and (19) into equation (18), the slurry fracturing grouting diffusion equation, which ignores the radius r of the grouting hole

TABLE 1: Comparison of two theoretical values of grouting pressure with field measured values.

Fracture extension length	Field measured value	Equation (17) theoretical value	Equation (20) theoretical value
0.4 m	2.1 MPa	2.48 MPa	5.37 MPa
1.8 m	1.2 MPa	1.39 MPa	5.42 MPa
2.6 m	0.8 MPa	0.86 MPa	5.56 MPa

and the time-varying viscosity obtained by self-weight of slurry is as follows:

$$P_0 = \frac{6\pi m}{qw} R^4 - \frac{3\tau_0 R}{w} + \sigma_3 + \sigma_t^* \quad (20)$$

In order to compare and analyze the fracturing diffusion laws of the two theories, the field test of Peili [31] was used to verify the theory in this paper.

Peili [31] selected three representative test points for grouting and fracturing tests in the grouting project of Nantiao Tower Coal Mine, the modulus of elasticity E in the test area is 4 GPa, the tensile strength σ_t is 4.56 MPa, the yield shear force τ_0 is 3.19 Pa, the grouting rate $q = 500$ mL/s, the fracture toughness K_{IC} is $1.2 \text{ MPa}\cdot\text{m}^{0.5}$. The grouting slurry is a 1 : 1 cement slurry, the maximum principal stress in the grouting area is 1.8 MPa, and the minimum principal stress is 0.8 MPa. The fracture propagation lengths at each test point were 0.4 m, 1.8 m, and 2.6 m. The measured grouting pressures on site were 2.1 MPa, 1.2 MPa, and 0.8 MPa, respectively; equations (17) and (20) were used to calculate the grouting pressure in the three cases, as shown in Table 1.

As can be seen from Table 1,

- (1) The longer the fracture, the smaller the grouting pressure. Because the test uses a 1 : 1 cement slurry, the time-varying viscosity is not obvious, and the viscosity factor has not yet played a leading role. With reference to hydraulic fracturing theory, it can be known that the longer the fracture, the smaller the grouting pressure required
- (2) By comparison, the theoretical calculations in this paper show that the grouting pressure at the three test points is close to the actual measured value, but slightly higher than the measured value. This is because the theoretical derivation assumes that the slurry exists only inside the fracture channel and does not consider the influence of other factors such as the penetration of part of the slurry to both sides of the fracture on the fracturing diffusion, but the error is still within the allowable range of the project
- (3) Compared with the theoretical value of this paper, the theoretical value obtained from the traditional fracturing grouting theory has a large deviation from the measured value. This is because the strength of the rock is high. Judging whether the fractures are

TABLE 2: The relationship between the viscosity of different C-S slurries over time.

C/S	1 : 1	2 : 1	3 : 1
Relational	$u(t) = 0.00857t^2$	$u(t) = 0.01687t^2$	$u(t) = 0.02477t^2$
Fitting accuracy	0.996	0.972	0.999

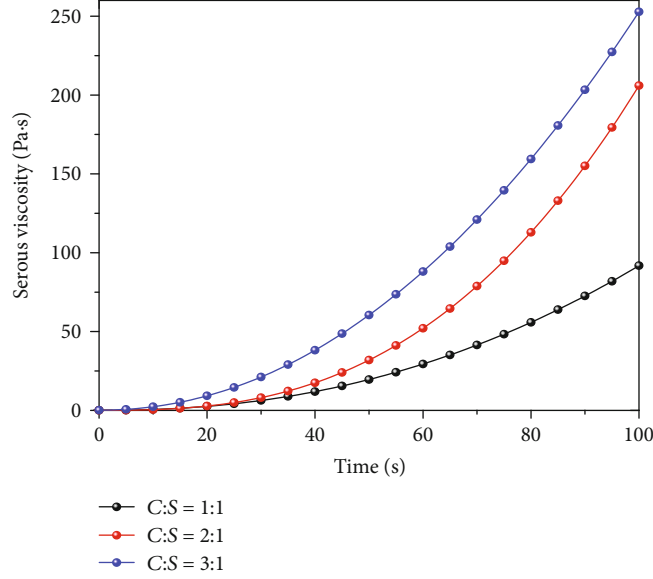


FIGURE 4: The curve of cement and sodium silicate slurry viscosity over time.

fracturing and expanding under the grouting pressure, the influence of the rock elastic modulus on the fracturing expansion and the uneven distribution of grouting pressure inside the fracture channel cannot be ignored, with the change of the fracture length, the fracturing pressure tend to be constantly changing instead of a fixed value. Therefore, the theory of fracturing grouting in this paper is more suitable for fracturing grouting in rock formations than the traditional fracturing grouting theory and can effectively guide the design and construction of fracturing grouting in the field

4. Fracturing Grouting Diffusion Law of Rock Formation and Its Influencing Factors

Based on the foregoing theoretical model, this section analyzes the law of fracturing grouting and diffusion and its influencing factors. The size of the grout fracturing expansion radius depends on the grouting pressure. By substituting related parameters into the fracturing grouting control equation (17), we can get the variation curve of grouting pressure P_0 with slurry diffusion radius R . The basic parameter values are as follows: effective stress $\sigma_3 = 10.73$ MPa, $\sigma_1 = 15.11$ MPa, side pressure coefficient $k = 1.5$, elastic modulus $E = 40$ GPa, fracture toughness $K_{IC} = 1.7$ MPa \cdot m^{0.5}, $\alpha = 30^\circ$, the slurry is cement and sodium silicate slurry (C : S = 1 : 1), grouting rate $q = 120$ L/min. According to the relationship between the viscosity of different cement slurry and sodium silicate slurry volume ratio slurry over time, the refitting relationship

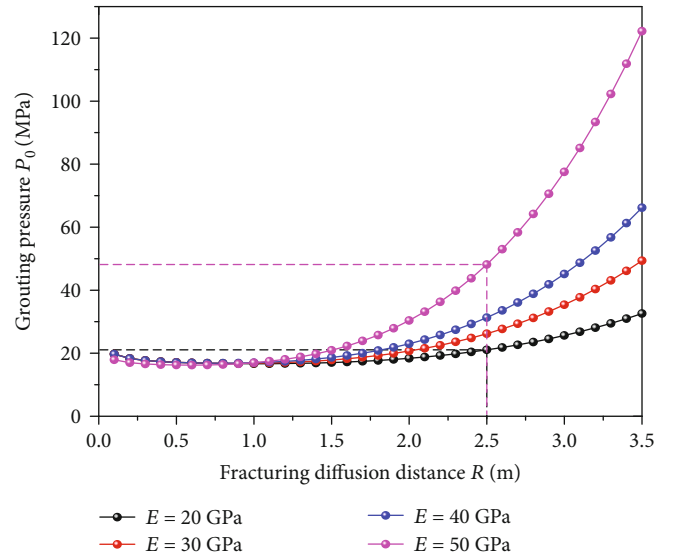


FIGURE 5: Effect of elastic modulus on slurry diffusion radius.

is shown in Table 2. The curve of cement and sodium silicate slurry viscosity over time was fitted, as shown in Figure 4.

The grouting pressure controls the size of the grout diffusion radius. When the relevant parameters are substituted into the time-varying slurry fracturing diffusion equation, the relationship curve $P_0 - R$ under the influence of formation factors (Figure 5) and the relationship curve $P_0 - R$

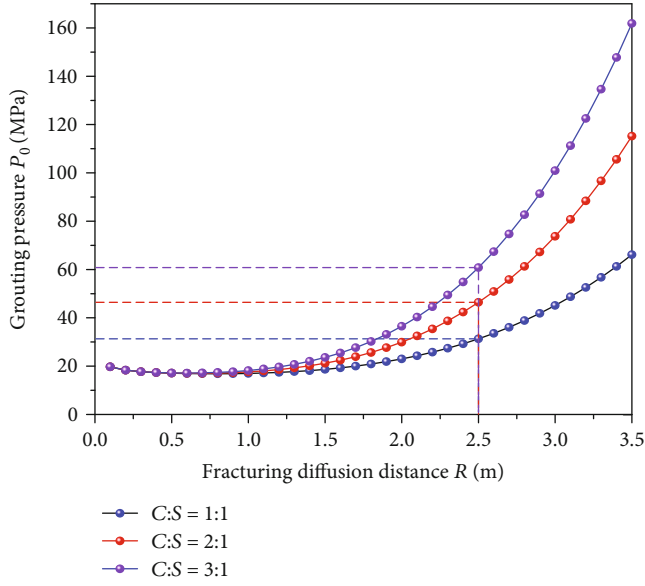


FIGURE 6: Effect of slurry viscosity on slurry diffusion radius.

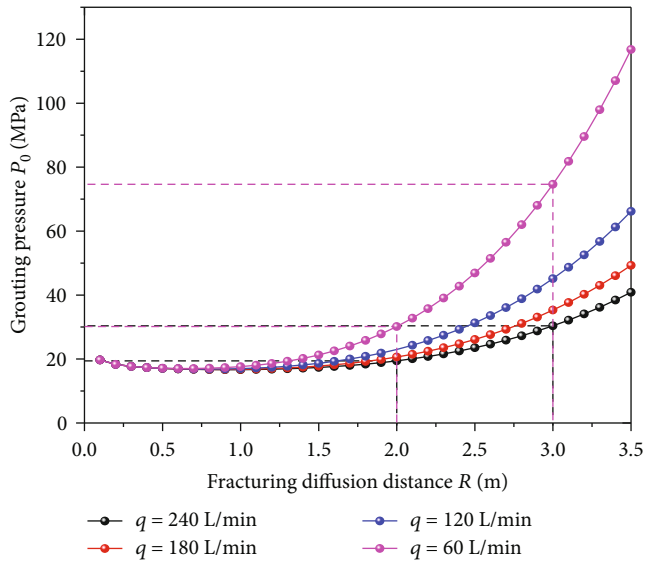


FIGURE 7: Effect of grouting rate on slurry diffusion radius.

under the influence of grouting parameter factors (Figures 6 and 7) can be obtained.

Analysis of Figures 5–7 shows the following:

- (1) Compared with the traditional infiltration grouting theory, the theoretical value of fracturing grouting pressure is very large. This is because split grouting must not only overcome the resistance caused by the viscosity of the slurry itself but also overcome the pressure required for rock initiation. However, in actual grouting projects, due to the large number of natural joints, fractures, bedding, and other structures distributed in the rock layer, the grouting pressure generally cannot reach the theoretical calculation value

- (2) In the initial stage of fracturing grouting, the plastic viscosity of the slurry with different proportions is small and the fracturing cracks are short. In order to continue the fracturing expansion, a larger grouting pressure must be accumulated. When the cleavage expands to 1 meter, the plastic viscosity of the slurry gradually increases with time, thus the required gradual pressure increases. It can also be seen from the theoretical formula that as the R increases, the $(\sqrt{\pi}/2\sqrt{R})K_{IC}$ term decreases rapidly, and then, the viscosity control term $3\pi^{3/2}mER^7/2qK_{IC}$ plays the main control role. Therefore, the required grouting pressure will decrease slightly and then increase as the fracture continues to expand

- (3) Under the same conditions of slurry diffusion radius R , the grouting pressure P_0 is proportional to the rock mass elastic modulus E and the slurry viscosity. For example, when the grouting diffusion radius $R = 2.5$ m, the elastic modulus of the injected rock mass increases from 20 GPa to 50 GPa and the corresponding grouting pressure P_0 increases from 21.08 MPa to 48.15 MPa; Corresponding C:S is 3:1, 2:1, and 1:1 are 60.79 MPa, 46.42 MPa, and 31.32 MPa, respectively. It can be seen that the greater the elastic modulus of the injected rock mass, the higher the resistance encountered during fracturing grouting, and the more difficult the fracture propagation. Moreover, the greater the viscosity of the slurry, the greater the viscosity resistance of the slurry encounters during the flow process, and the greater the grouting pressure required to reach the predetermined fracturing diffusion radius

- (4) Under the same conditions of slurry diffusion radius R , the grouting pressure P_0 is inversely proportional to the grouting rate q . When the fracturing diffusion radius is small, the required grouting pressure is not sensitive to changes in the grouting rate q . When the fracturing diffusion radius is larger, the grouting pressure required for the fracture continues to increase sharply, but the greater the grouting rate, the slower the grouting pressure increases

According to the above analysis, the elastic modulus of rock, time-varying characteristics of the serous viscosity, and grouting rate are the main influencing factors in controlling fracturing grouting. In the initial stage of grouting, the plastic viscosity of the slurry is relatively low. The grouting pressure and grouting rate are the main controlling factors of the grouting and spreading range of the slurry, increasing the grouting rate can significantly increase the grouting range. When the slurry viscosity exceeds a certain range, the viscosity becomes the main controlling factor of the slurry diffusion range. Therefore, in the design and selection of grouting parameters, stratum factors should be comprehensively considered, and a large initial grouting rate and grouting pressure should be selected in the early stage of

grouting, so that cracks can be generated or penetrated in the rock formation. When the grouting pressure is stable, while the slurry is sufficiently diffused in the fracture, the viscosity of the slurry is increased, the solidification reaction rate of the slurry is increased, and the slurry forms a blocking body in the fracture.

5. Conclusions

- (1) Combining the motion of the slurry with the expansion of the fracturing cracks, considering the various mechanical factors such as the mechanical properties of the rock formation and the time-varying characteristics of the serous viscosity, a theoretical model of fracturing grouting diffusion considering the spatial attenuation of the fracture channel width has been established. The fracturing grouting diffusion equation considering fluid-structure interaction was also derived and verified by experiments
- (2) Considering the time-varying characteristics of the serous viscosity, the main influencing factors on the effect of fracturing grouting and diffusion in rock formation are rock elastic modulus, slurry viscosity, and grouting rate. The larger the elastic modulus of the injected rock mass, the higher the resistance of the fracturing grouting and the more difficult the fracture extension. In the initial stage of grouting, the plastic viscosity of the slurry is low. The grouting pressure and grouting rate are the main controlling factors of the fracturing and spreading range of the slurry. When the viscosity of the grouting reaches a certain value, the viscosity becomes the main controlling factor of the slurry spreading range
- (3) Based on the fluid-solid coupling characteristics of grout and rock fractures, in order to meet the requirements of fracturing grouting in deep formations, a large initial grouting rate and grouting pressure should be selected in the early stage of grouting, so that fractures are generated or penetrated in the rock formation. When the grouting pressure is stable, while the slurry is sufficiently diffused in the fracture, the viscosity of the slurry increases, the solidification reaction rate of the slurry also increases, and the slurry forms a blocking body in the fracture

Data Availability

The data used to support the findings of this study are available from the corresponding author upon request.

Conflicts of Interest

The authors declare that there is no conflict of interest regarding the publication of this paper.

Acknowledgments

This study was supported by the National Key Research and Development program (2016YFC0600902).

References

- [1] H. Cheng, P. Shilong, R. Chuanxin, and S. Zehui, "Numerical simulation and engineering application of pre-grouting reinforcement of tunnel surrounding rock by L type drilling in a km deep well," *Rock and Soil Mechanics*, vol. 39, no. S2, pp. 281–291, 2018.
- [2] Z. Hua-lei, T. Min, H. Cheng, and T. Yongzhi, "Mechanism of overface rock fracture in thin bedrock stope and integrated grouting reinforcement technology for wind oxidation zone," *Acta Cae Sinica*, vol. 43, no. 8, pp. 40–46, 2018.
- [3] Z. Luo, Q. Hao, T. Wang, R. Li, F. Cheng, and J. Deng, "Experimental study on the deflagration characteristics of methane-ethane mixtures in a closed duct," *Fuel*, vol. 259, p. 116295, 2020.
- [4] Z. Luo, D. Li, B. Su, S. Zhang, and J. Deng, "On the time coupling analysis of explosion pressure and intermediate generation for multiple flammable gases," *Energy*, vol. 198, p. 117329, 2020.
- [5] T. Wang, Y. Zhou, Z. Luo et al., "Flammability limit behavior of methane with the addition of gaseous fuel at various relative humidities," *Process Safety and Environmental Protection*, vol. 140, pp. 178–189, 2020.
- [6] H. Cheng, J. Lin, Y. Zhishu, R. Chuanxin, and C. Guangyong, "Study on load outside shaft lining of single layer in porosity water-bearing bedrock in western China," *Journal of Rock Mechanics and Engineering*, vol. 38, no. 3, pp. 542–550, 2019.
- [7] M. Y. Fattah, M. M. Al-Ani, and M. T. A. Al-Lamy, "Studying collapse potential of gypseous soil treated by grouting," *Soils and Foundations*, vol. 54, no. 3, pp. 396–404, 2014.
- [8] M. Heidari and F. Tonon, "Ground reaction curve for tunnels with jet grouting umbrellas considering jet grouting hardening," *International Journal of Rock Mechanics and Mining Sciences*, vol. 76, pp. 200–208, 2015.
- [9] M. H. Salimian, A. Baghbanan, H. Hashemolhosseini, M. Dehghanipoodeh, and S. Norouzi, "Effect of grouting on shear behavior of rock joint," *International Journal of Rock Mechanics and Mining Sciences*, vol. 98, pp. 159–166, 2017.
- [10] Z. Luo, R. Li, T. Wang et al., "Explosion pressure and flame characteristics of CO/CH₄/air mixtures at elevated initial temperatures," *Fuel*, vol. 268, p. 117377, 2020.
- [11] P. Li, Q. S. Zhang, S. C. Li, and X. Zhang, "Time-dependent empirical model for fracture propagation in soil grouting," *Tunnelling and Underground Space Technology*, vol. 94, p. 103130, 2019.
- [12] H. Manchao, X. Heping, P. Suping, and J. Yaodong, "Research on deep mining rock mass mechanics," *Chinese Journal of Rock Mechanics and Engineering*, vol. 24, no. 16, pp. 2803–2813, 2005.
- [13] L. C. Murdoch, "Hydraulic fracturing of soil during laboratory experiments Part 3. Theoretical analysis," *Geotechnique*, vol. 43, no. 2, pp. 277–287, 1993.
- [14] A. Bezuijen, R. te Grotenhuis, A. F. van Tol, J. W. Bosch, and J. K. Haasnoot, "Analytical model for fracture grouting in sand," *Journal of Geotechnical and Geoenvironmental Engineering*, vol. 137, no. 6, pp. 611–620, 2011.
- [15] G. Gustafson, J. Claesson, and Å. Fransson, "Steering parameters for rock grouting," *Journal of Applied Mathematics*, vol. 2013, Article ID 269594, 9 pages, 2013.
- [16] K. O. G. Mohamed, *Compensation grouting in sand*, University of Cambridge, 2009.

- [17] K. Kishida, A. Sawada, H. Yasuhara, and T. Hosoda, "Estimation of fracture flow considering the inhomogeneous structure of single rock fractures," *Soils and Foundations*, vol. 53, no. 1, pp. 105–116, 2013.
- [18] H. Mingli, G. Xiaoming, and L. Qifeng, "Analysis of induced split grouting mechanism based on elastic mechanics," *Rock and Soil Mechanics*, vol. 7, pp. 241–246, 2013.
- [19] W. Zuocheng and L. Fenqiang, "Curtain grouting slurry and its water-blocking mechanism in complex coal mine areas," *Journal of Central South University*, vol. 2, pp. 335–341, 2013.
- [20] S. Feng, Z. Dingli, and C. Tielin, "Study on the mechanism of tunnel splitting grouting based on fluid time-varying," *Journal of Geotechnical Engineering*, vol. 33, no. 1, pp. 88–93, 2011.
- [21] Z. Qingsong, Z. Lianzhen, L. Rentai et al., "Theoretical study of split grouting based on the coupling effect of "slurry-soil" interface stress," *Chinese Journal of Geotechnical Engineering*, vol. 2, pp. 323–330, 2016.
- [22] W. Zhang, S. Li, J. Wei et al., "Grouting rock fractures with cement and sodium silicate grout," *Carbonates and Evaporites*, vol. 33, no. 2, pp. 211–222, 2018.
- [23] S.-c. Li, W. J. Zhang, Q. S. Zhang et al., "Research on advantage-fracture grouting mechanism and controlled grouting method in water-rich fault zone," *Rock and Soil Mechanics*, vol. 35, no. 3, pp. 745–751, 2014.
- [24] W. Hongxun, *Principles of hydraulic fracturing*, Petroleum Industry Press, 1987.
- [25] A. A. Savitski and E. Detournay, "Propagation of a penny-shaped fluid-driven fracture in an impermeable rock: asymptotic solutions," *International Journal of Solids and Structures*, vol. 39, no. 26, pp. 6311–6337, 2002.
- [26] J. R. Rice, "Mathematical analysis in the mechanics of fracture," in *Fracture, an Advanced Treatise*, H. Liebowitz, Ed., vol. II, pp. 191–311, Academic Press, New York, NY, USA, 1968.
- [27] S. Mohajerani, A. Baghbanan, R. Bagherpour, and H. Hashemolhosseini, "Grout penetration in fractured rock mass using a new developed explicit algorithm," *International Journal of Rock Mechanics and Mining Sciences*, vol. 80, pp. 412–417, 2015.
- [28] Y. Yang and X. Changfu, "Fracture morphology and pressure distribution in fractures during hydraulic fracturing," *Journal of Chongqing University: Natural Science Edition*, vol. 18, no. 3, pp. 20–26, 1995.
- [29] L. Shucai, Z. Weijie, Z. Qingsong et al., "Research on dominant split grouting mechanism and grouting control method in water-rich fault zone," *Rock and Soil Mechanics*, vol. 35, no. 3, pp. 745–751, 2014.
- [30] S. Feng, C. Lu, Y. Chunan, and L. Dayong, "Analysis of elastoplastic stress near split grouting boreholes," *Journal of Hydraulic Engineering*, vol. 4, no. 4, pp. 28–30, 2006.
- [31] S. Peili, *Research on grouting reinforcement and seepage mechanism of fractured coal and rock mass and its application*, Xi'an University of Science and Technology, 2010.

Research Article

Experimental and Numerical Study on Hydromechanical Coupled Deformation Behavior of Beishan Granite considering Permeability Evolution

Z. H. Wang ^{1,2}, W. G. Ren,³ Y. L. Tan,^{1,2} and Heinz Konietzky⁴

¹State Key Laboratory of Mining Disaster Prevention and Control Cofounded by Shandong Province and the Ministry of Science and Technology, Shandong University of Science and Technology, Qingdao Shandong 266590, China

²College of Energy and Mining Engineering, Shandong University of Science and Technology, Qingdao Shandong 266590, China

³School of Mechanics and Civil Engineering, China University of Mining and Technology, Beijing 100083, China

⁴Geotechnical Institute, TU Bergakademie Freiberg, Gustav-Zeuner-Str. 1, 09596 Freiberg, Germany

Correspondence should be addressed to Z. H. Wang; skd996340@sdust.edu.cn

Received 25 May 2020; Revised 12 July 2020; Accepted 21 July 2020; Published 5 August 2020

Academic Editor: Qiqing Wang

Copyright © 2020 Z. H. Wang et al. This is an open access article distributed under the Creative Commons Attribution License, which permits unrestricted use, distribution, and reproduction in any medium, provided the original work is properly cited.

Beishan granite is a potential host rock for a high-level radioactive waste (HLW) repository in China. Understanding the hydromechanical (HM) behavior and permeability evolution of Beishan granite is important for the HLW repository safety. Therefore, the granite of Beishan in Gansu province was studied. HM coupled tests are carried out on Beishan granite under different pore pressures. The results show that the initial pressure difference has little influence on permeability measurement before dilatancy starts. However, after onset of dilatancy, the permeability increases with the increasing initial pressure difference. The initial permeability of Beishan granite is about 10^{-18} m² under a confining pressure of 20 MPa. In the initial loading phase, the permeability shows a relatively large reduction. Then, the permeability almost keeps constant until dilatancy starts. From dilatancy point to peak stress, permeability increases linearly with volumetric strain. The proposed permeability evolution rule is implemented into a numerical code to perform HM coupled simulations. The simulation results show that the damaged zone first appears at the model boundary and then extends to the inside, forming high volumetric strain areas. And it provides seepage channels for fluid flow. The macroscopic fracture patterns indicate that pore pressure accelerates rock degradation during HM coupling. The obtained results help to understand the damage mechanisms of granite caused by pore pressures and are of great importance for the safety of a HLW repository.

1. Introduction

Disposal of high-level radioactive waste (HLW) deep underground is one of the most challenging research subjects in rock engineering. The biggest difficulty is the proof of safe and long-term isolation of the HLW from the biosphere. Granite, characterized by high strength and low permeability, is one of the preferred host rocks for geological disposal of HLW. China plans to build a HLW repository in the granite strata of Beishan, Gansu Province [1, 2]. Therefore, the understanding of the hydromechanical (HM) coupled behavior and permeability evolution of Beishan granite is of great significance to ensure the long-term safety of the HLW repository.

As a heterogeneous material, rock contains microcracks. The failure process of rock associated with crack propagation has been well studied [3–8]. On the other hand, cracks provide seepage channels for fluid flow. The fluid flow in the crack network will accelerate the rock failure process, which has influence on rock strength and deformation [9–12]. Therefore, after years of research, the permeability evolution during the rock failure process has gradually attracted the attention of researchers. Brace et al. [13] and Zoback et al. [14] studied the permeability of Westerly granite. Their results indicate that permeability has strong dependence on effective pressure and increases gradually after dilatancy threshold. Hydrostatic compression and triaxial compression tests were conducted on

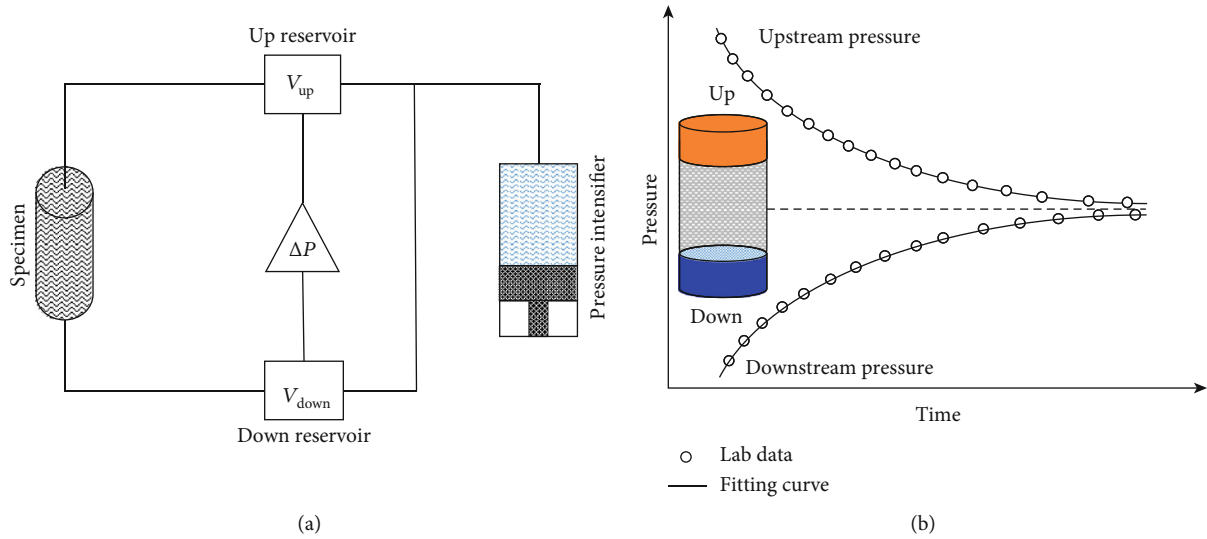


FIGURE 1: Simplified schematic of the transient pulse method: (a) testing system and (b) measuring pressure decay over time.

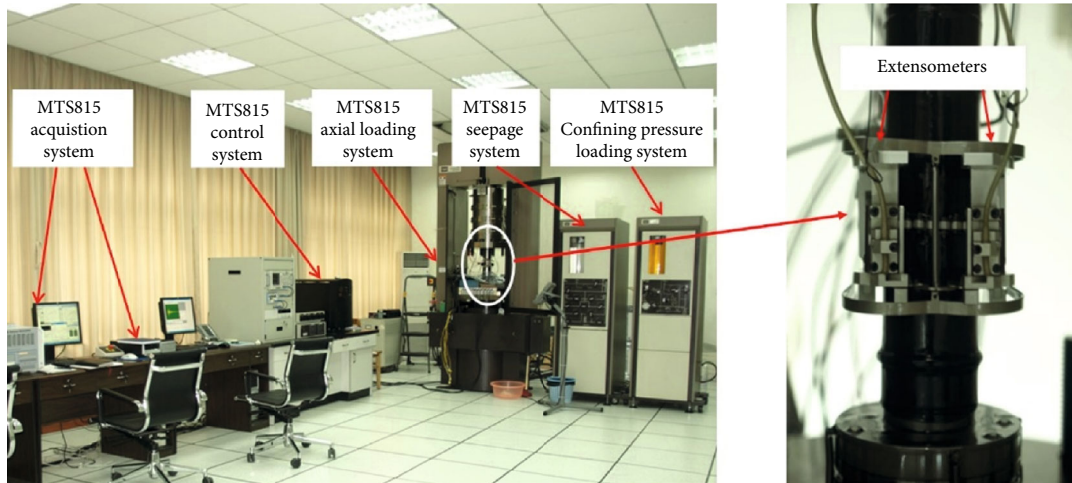


FIGURE 2: Rock mechanics experimental system of MTS815 and installation of sample.

Inada granite by Kiyama et al. [15]. The results show that permeability increases proportionally to the dilatation between the onset of dilatancy and the peak strength. Liu et al. [16] investigated the permeability evolution of granite gneiss during triaxial creep tests. They demonstrate that the permeability remains stable in the steady creep stage and increases rapidly in the accelerated creep stage. For granite, Chen [17] revealed that the permeability decreases when confining pressure is larger and increases when pore water pressure is larger under compressive stress conditions. Yi et al. [18], Heiland and Raab [19], Alam et al. [20], and Zhang et al. [21] studied permeability evolution of different rock types under compression. The results show similar permeability evolution trends, in which the permeability decreases at the stage of volumetric compaction and increases at the stage of volumetric dilation.

On the other hand, important progress has been made in numerical simulation of HM coupled processes in rocks, especially in the DECOVALEX project [22, 23]. A flow-stress-damage (FSD) coupling model considering permeabil-

ity evolution is proposed by Tang et al. [24]. And this FSD model is used to investigate the behavior of fluid flow and damage evolution under hydraulic conditions. Rutqvist et al. [25] linked two codes—TOUGH2 and FLAC^{3D}—for analysis of coupled THM processes, in which the coupling module containing nonlinear stress versus permeability functions is taken into account. Tan and Konietzky [26] proposed a micromechanical numerical model to simulate the HM coupled behavior of granite at the grain-sized level. It reveals the importance of tensile micro cracks for enhanced permeability, and linear correlations between volumetric strain and permeability are observed by numerical simulations. Lu et al. [27] presented a coupled continuum-based HM modeling approach using a two-scale conceptual model representing realistic rock material containing microfractures. This model is validated against failure under compression and replicates typical AE characteristics and permeability evolution.

This paper presents HM coupling tests carried out on Beishan granite under different pore pressures. The influence

TABLE 1: Permeability test results for specimen BSS-1 for three different initial pressure differences.

Axial strain (%)	Axial stress (MPa)	Permeability (10^{-18} m^2)		
		3.4 MPa	5.4 MPa	7.4 MPa
0	0	3.77	2.97	2.33
0.386	38.6	1.05	1.30	1.34
0.629	79.3	1.03	1.12	1.29
0.855	123.8	0.55	1.08	1.26
1.066	165.6	0.94	1.29	1.65
1.240	201.8	1.45	1.92	2.36
1.528	256.6	3.43	5.30	7.54
2.337	81.8	72.74	55.31	59.57

TABLE 2: Permeability test results for specimen BSS-2 for three different initial pressure differences.

Axial strain (%)	Axial stress (MPa)	Permeability (10^{-18} m^2)		
		3.4 MPa	5.4 MPa	7.4 MPa
0	0	1.32	1.24	0.64
0.414	48.7	0.71	0.66	0.66
0.716	106.1	0.78	0.50	0.47
0.940	150.1	0.48	0.56	0.48
1.163	200.0	0.75	0.61	0.70
1.425	252.5	1.33	1.12	1.54
1.855	315.6	5.81	9.86	15.36
2.011	79.5	13.56	16.07	17.74
2.599	75.9	13.25	14.08	14.69

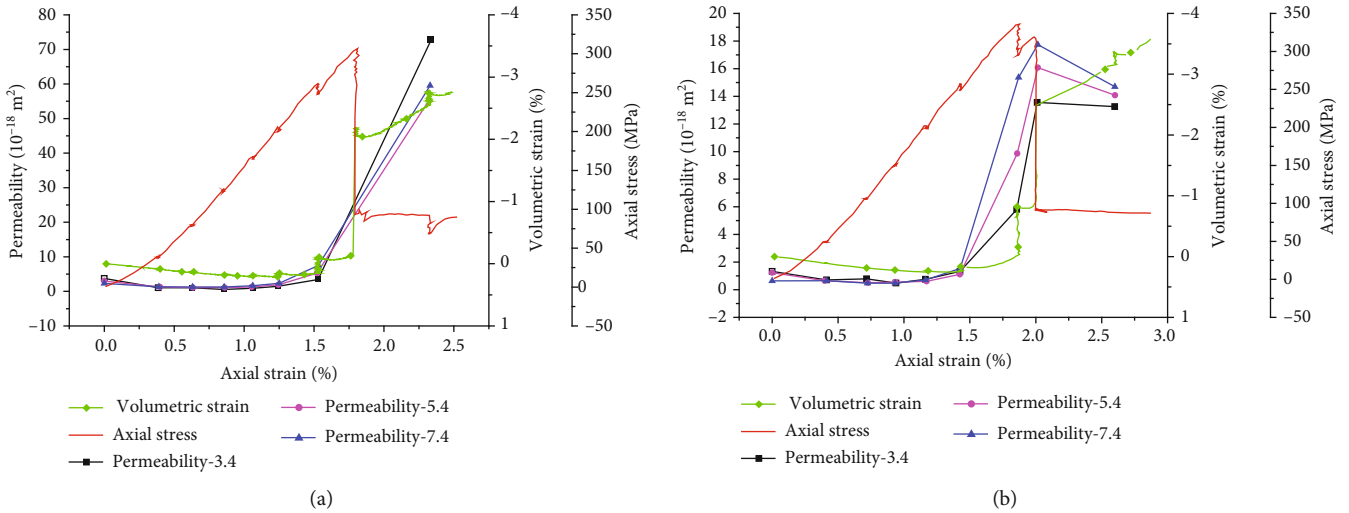


FIGURE 3: Permeability for different initial differential pressures (a) BSS-1 (b) BSS-2.

of initial pressure difference (ΔP_0) on permeability monitored by the transient pulse method is discussed. The permeability evolution of Beishan granite under compression is revealed. In addition, a heterogeneous numerical model is established to simulate the deformation and damage process under HM coupling considering volumetric strain and permeability evolution.

2. Permeability Measurements by the Transient Pulse Method

In most cases, permeability can be measured either by using the constant head method [28, 29] or the transient pulse method [30–33]. However, due to the low permeability of granite, it will take a long time for the fluid to reach a steady

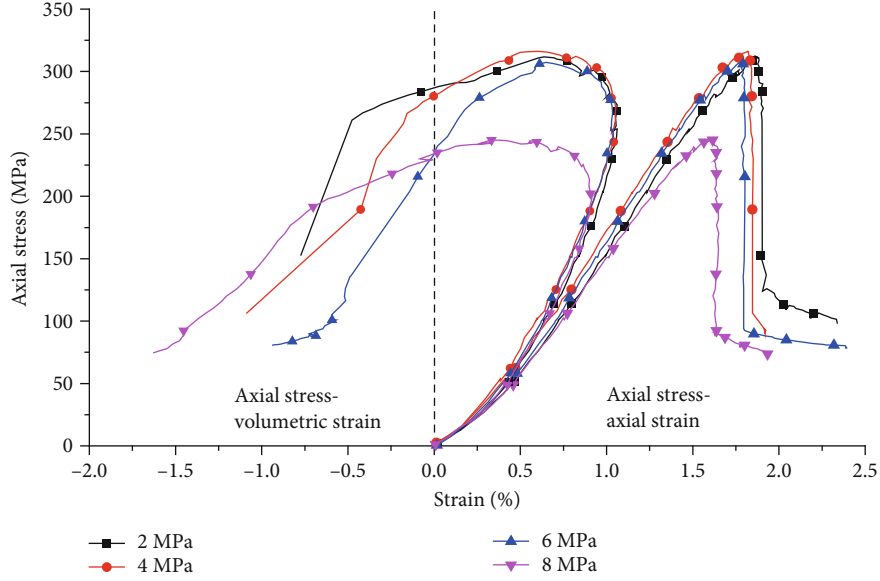


FIGURE 4: Stress strain curves of Beishan granite under different pore pressures [40].

TABLE 3: Permeability evolution under different pore pressures.

Sample	Pore pressure (MPa)	Permeability/ 10^{-18} m^2							
		1st ^a	2nd	3rd	4th	5th	6th	7th	8th
HM-1	2	5.8	2.78	4.91	6.5	20.29(p ^b)	22.71	22.89	25.49
HM-2	4	1.29	0.51	0.38	1.14(p)	3.04	3.74	5.38	—
HM-3	6	0.95	0.29	0.48	1.3	2.46	5.85	10.7(p)	32.78
HM-4	8	2.29	1.48	1.77	3.84	7.03	11.51	13.17(p)	26.16

^a"1st" represents the first time to measure permeability. ^b"p" represents the permeability measured around peak stress.

flow by using the constant head method. Compared with the constant head method, fluid does not need to achieve a steady flow by using the transient pulse method. Therefore, it will consume less time. And the transient method has higher accuracy for low permeability rocks. As a result, in this study, the transient pulse method is used.

The test principle of transient pulse method is shown in Figure 1. At the beginning, a constant pore pressure is maintained in the sample and adjacent upper and lower fluid reservoir. Then, the pressure in the upper reservoir is instantaneously increased and the pressure decay at both reservoirs is monitored. The pressure difference can be described by

$$\begin{cases} \frac{P_u(t) - P_d(t)}{\Delta P_0} = \exp(-\alpha t), \\ \alpha = \frac{kA}{\mu\beta L} \left(\frac{1}{V_u} + \frac{1}{V_d} \right), \end{cases} \quad (1)$$

with k as permeability (m^2), μ as viscosity of fluid (water at 20°C : $10^{-3} \text{ Pa}\cdot\text{s}$), β as the compression coefficient of fluid (water: $4.53 \times 10^{-10} \text{ Pa}^{-1}$), A as cross-sectional area of sample (m^2), L as the height of the sample (m), V_u as the volume of upper reservoir (m^3), V_d as the volume of the lower reservoir (m^3), t as the duration time (s), $P_u(t)$ as the pore pressure of the upper reservoir at time t (MPa), $P_d(t)$ as the pore pressure

of the lower reservoir at time t (MPa), and ΔP_0 as the initial differential pressure between upper and lower fluid reservoir (MPa). In general, V_u equals V_d ; thus, Equation (1) can be rewritten as

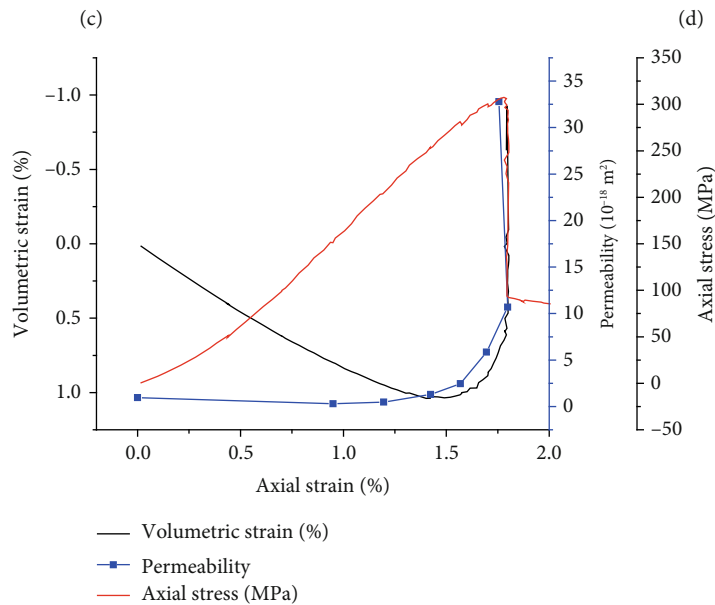
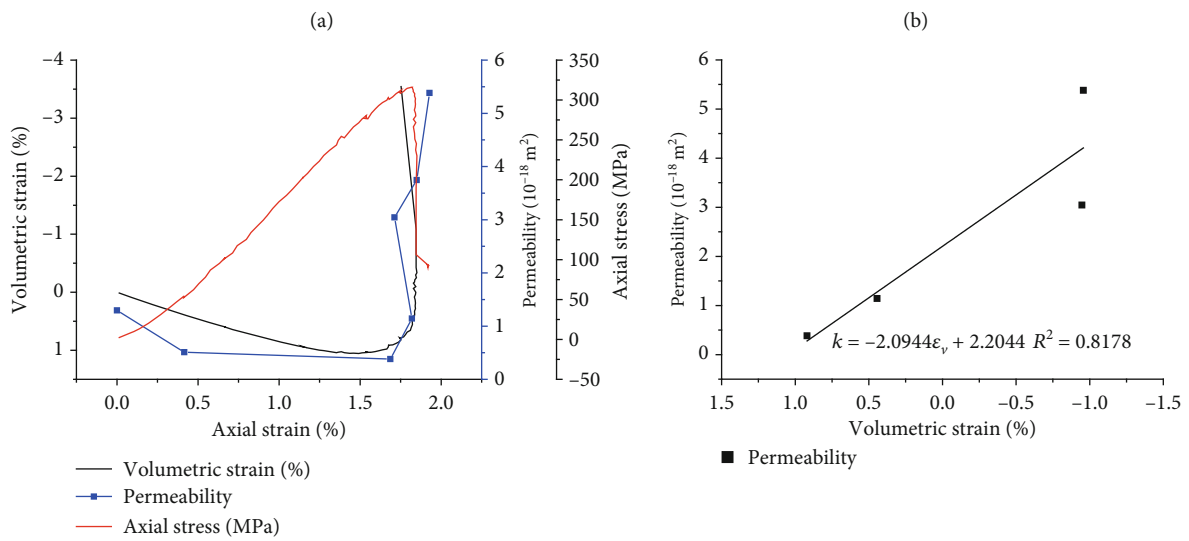
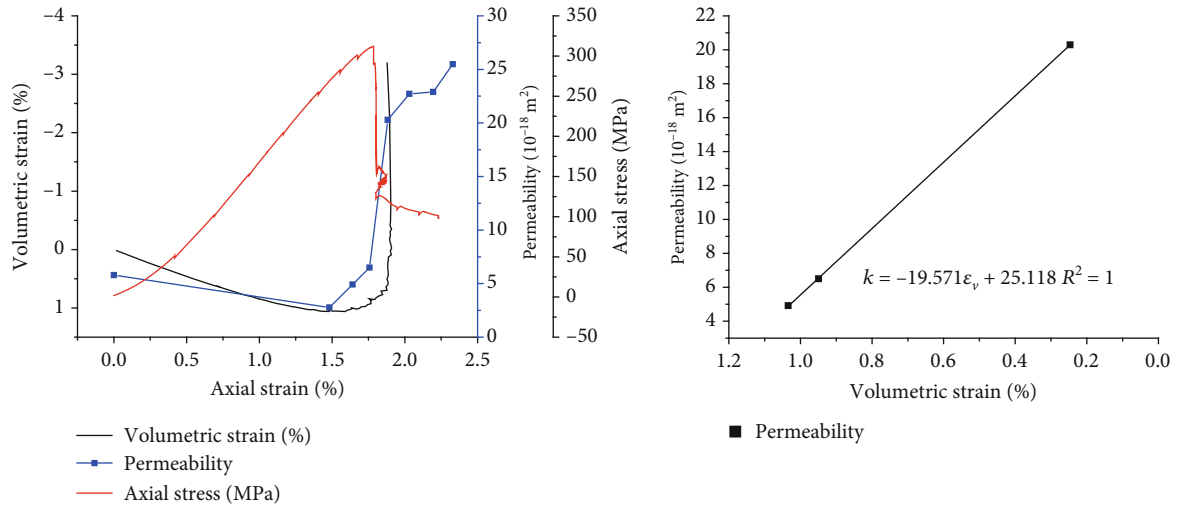
$$k = \mu\beta V \frac{\ln(\Delta P_0/P_f)}{2t(A/L)}, \quad (2)$$

with P_f as the final differential pressure between the upper and lower fluid reservoirs (MPa).

3. Laboratory Test Settings

3.1. Preparation of Rock Specimens. The granite samples were taken from the Beishan area, Gansu Province, China. The specimens, with a diameter of 50 mm and length of 100 mm, were prepared according to ISRM recommendations [34]. If readers want to know the basic properties and components of Beishan granite, please refer to literature [35, 36].

3.2. Test Facility. The HM coupled tests were carried out with a MTS815 Flex Test GT (see Figure 2) rock mechanical testing machine. This machine has a maximum loading capacity of 4,700 kN and can supply a maximum confining pressure of 140 MPa [37]. Axial and lateral strains are measured by extensometers.



(e)

FIGURE 5: Continued.

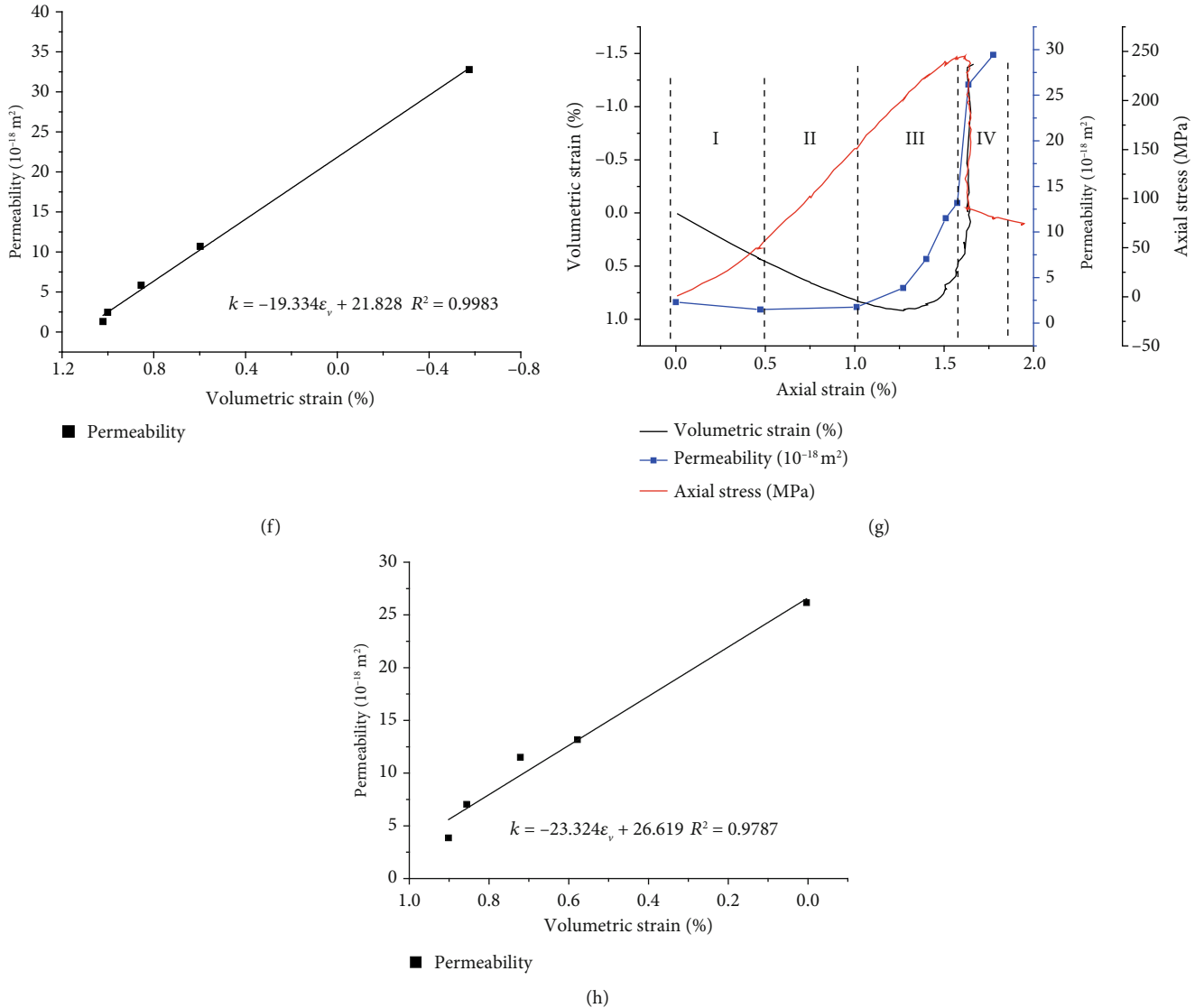


FIGURE 5: Permeability evolution of Beishan granite during HM coupling. (a, b) Pore pressure of 2 MPa, (c, d) pore pressure of 4 MPa, (e, f) pore pressure of 6 MPa, and (g, h) pore pressure of 8 MPa.

3.3. Testing Procedure. Four specimens were prepared for HM coupled testing. Before the tests, the specimens were immersed in water for 72 hours in the vacuum suction device to reach the saturated state [38]. For the HM coupled tests, first, a vertical load of about 2 kN was applied in order to fix the position of the specimen. Then, the desired confining pressure (20 MPa in all HM coupled tests) was reached with a constant loading rate of 0.05 MPa/s to ensure that the specimen was under uniform hydrostatic stresses [39]. Pore pressures were set to 2, 4, 6, and 8 MPa, which mirror the maximum potential water pressure at different buried depths in the Beishan region [38]. The desired pore pressure was reached with a constant rate of 1 MPa/min. Afterwards, the axial stress was increased with a constant loading rate of 30 kN/min. During the process of loading, the transient pulse method was used to measure the permeability of Beishan granite at different strain levels. Stress and strain were kept constant during the permeability testing.

In addition, in order to study the influence of initial pressure difference (ΔP_0) on the transient pulse method, three initial pressure differences were used to measure permeability under the same strain levels during loading. The initial pressure differences were set to 3.4, 5.4, and 7.4 MPa, which is close to the potential water pressure at different buried depths in the Beishan region. And if the initial pressure difference is small, it is not conducive to monitor the pressure decay for Beishan granite because of low permeability. Two specimens (BSS-1 and BSS-2) were used for this task.

4. Test Results

4.1. Influence of Initial Pressure Difference (ΔP_0) on Measurement Results of the Transient Pulse Method. The permeability measured by different initial pressure differences under the same strain levels is shown in Tables 1 and 2 and Figure 3. For a confining pressure of 20 MPa, the initial

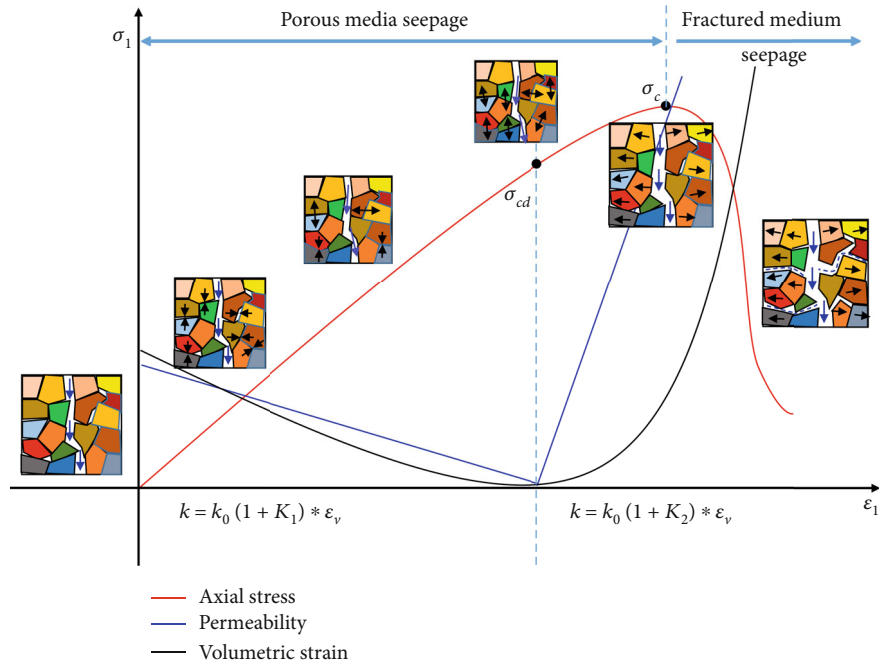


FIGURE 6: Simplified illustration of permeability evolution in HM coupling processes in Beishan granite.

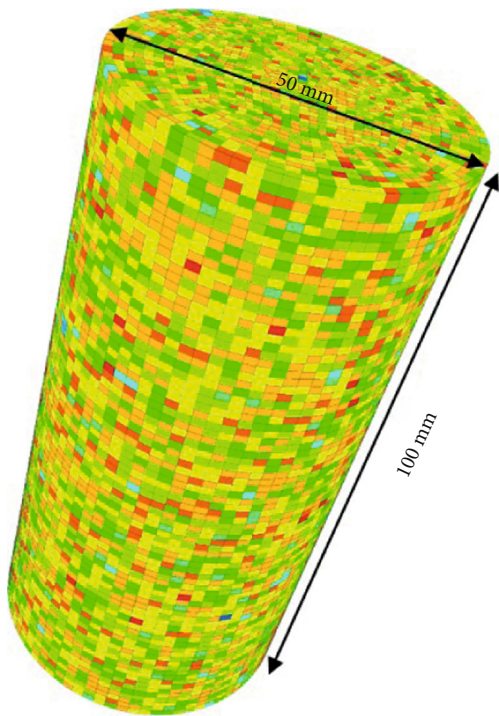


FIGURE 7: Schematic diagram of Beishan granite model.

permeability values measured by different initial pressure differences are quite similar. Because of the unique heterogeneity of each sample, the measured permeability will always show some minor differences.

At the initial stage of loading, due to the closure of micro cracks, permeability decreases. Before onset of dilatancy, the

permeability changes little. After onset of dilatancy, permeability is increasing. Also, the permeability increases with the increasing initial pressure. For instance, the permeability measured for sample BSS-2 under the initial pressure difference of 7.4 MPa ($15.36 \times 10^{-18} \text{ m}^2$) around the peak stress is 2.64 times of that measured under the initial pressure difference of 3.4 MPa ($5.81 \times 10^{-18} \text{ m}^2$). After the peak stress, permeability becomes unstable due to the thrived macro cracks in the sample. The permeability in the post failure region is not discussed in this study.

4.2. *Stress Strain Curves of HM Coupled Tests.* Figure 4 shows the stress-strain curves of Beishan granite under different pore pressures. With increasing pore pressure, maximum axial strain and peak stress decrease.

4.3. *Permeability Evolution of HM Coupled Tests.* The permeability measured during HM coupled testing is shown in Table 3 and Figure 5. It can be concluded that the initial permeability of Beishan granite is maintained at about 10^{-18} m^2 under the confining pressure 20 MPa. On the whole, the permeability first decreases slowly and then increases gradually during loading. The general trend of permeability evolution is the same for different pore pressures.

Taking the pore pressure of 8 MPa as an example, combined with the volumetric strain development, the permeability evolution of Beishan granite under loading can be roughly divided into the following stages. In the first stage (i.e., the initial stage of loading), micro cracks begin to close, which leads to a decrease of sample volume and loss of some seepage channels. Therefore, the decrease of permeability is relatively large compared to the initial permeability (for instance, reduction by 40% under pore pressure of 4 MPa). In the second stage, as the axial stress continues to increase,

TABLE 4: Mechanical parameters of Beishan granite.

Elastic modulus (GPa)	Poisson's ratio	Dilation ($^{\circ}$)	Density (kg/m^3)	Cohesion (MPa)		Friction ($^{\circ}$)		Tension (MPa)	
				Initial	Residual	Initial	Residual	Initial	Residual
28.6	0.122	17	2700	29.74	21.24	51	31.44	7.66	0

TABLE 5: Hydraulic parameters of Beishan granite.

Fluid modulus (GPa)	Fluid density (kg/m^3)	Initial permeability (m^2)	Porosity (%)	Saturation
2.2	1000	2.58×10^{-18}	0.02	1

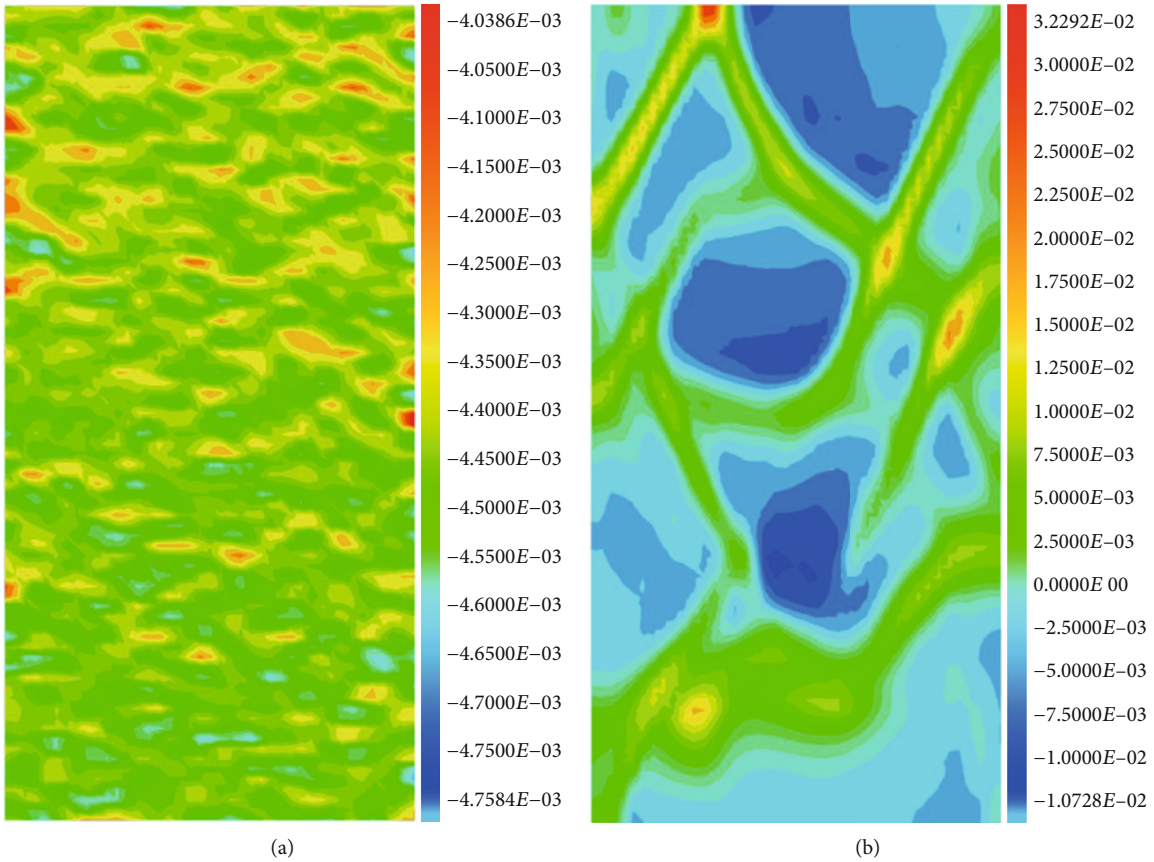


FIGURE 8: Volumetric strain for confining pressure of 20 MPa: (a) compressed stage and (b) damaged stage.

the volume of the specimen decreases. But there is possibility that new micro cracks are generated. Thus, the permeability almost keeps constant. After the dilatancy point, micro cracks are reactivated gradually and interact with each other, which leads to crack coalescence and provides new seepage channels. The permeability increases gradually with increasing volumetric strain. It can be concluded from Figures 5(b), 5(d), 5(f), and 5(h) that there is a linear relationship between permeability and volumetric strain from dilatancy point to peak stress. At peak stress, permeability can increase by an order of magnitude compared with the initial permeability (see sample HM-3). After the peak stress, the seepage behavior changes from porous medium seepage to fractured

medium seepage. In this stage, the permeability changes greatly, which is beyond the scope of this study.

According to tests results, the permeability evolution of Beishan granite in respect to volumetric strain can be roughly divided into two stages before reaching the peak stress, as shown in Figure 6. For the fractured medium seepage in the post peak stage, it is not possible to predict permeability just by volumetric strain. Before the dilatancy threshold σ_{cd} , permeability decreases with decreasing volumetric strain. It can be approximately expressed as linear relationship, and the linear coefficient is set to K_1 . From dilatancy threshold σ_{cd} to peak stress σ_c , permeability increases linearly with increasing volumetric strain. The correlation coefficients (see Figure 5)

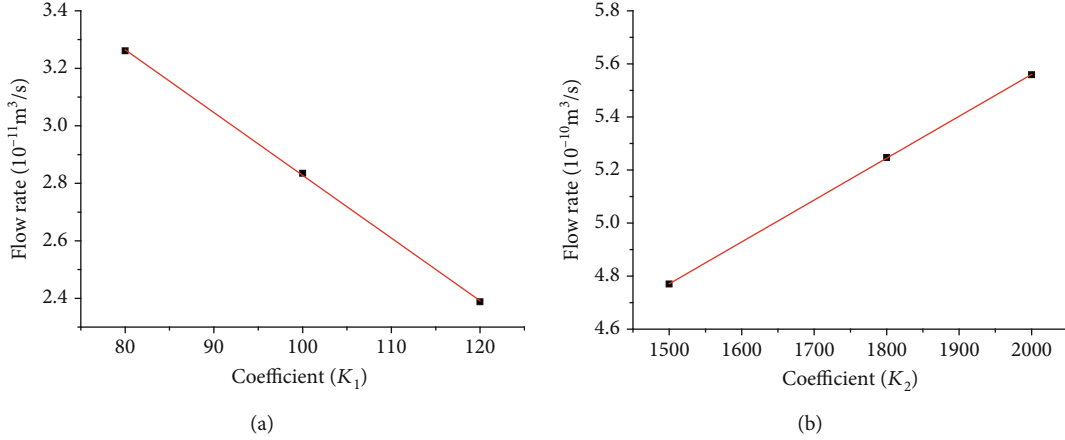


FIGURE 9: Flow rates and corresponding coefficients: (a) K_1 and (b) K_2 .

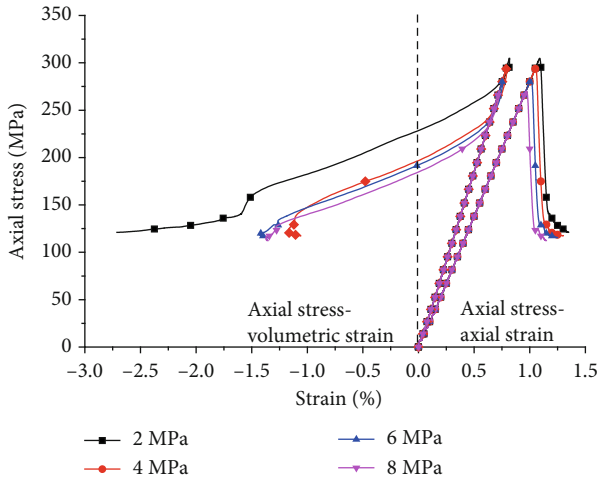


FIGURE 10: Simulated stress-strain curves for different pore pressures under 20 MPa confining pressure.

confirm the correctness of linear fitting, and the linear coefficient is set to K_2 . The relationships can be expressed by

$$\begin{cases} k = k_0(1 + K_1\varepsilon_v) & 0 < \sigma_1 < \sigma_{cd}, \\ k = k_0(1 + K_2\varepsilon_v)\sigma_{cd} & \sigma_{cd} < \sigma_1 < \sigma_c, \end{cases} \quad (3)$$

where k_0 initial permeability (m^2) and ε_v volumetric strain. It can be deduced from test data that K_2 is much greater than K_1 .

5. HM Coupled Simulations

5.1. Model Description and Setup. In order to study the stress strain state inside the specimen, a heterogeneous cylindrical model with 50 mm in diameter and 100 mm in length is established in the explicit Finite Difference code FLAC^{3D} as shown in Figure 7. The model has 96000 zones and 100521 gridpoints. For the HM coupled simulations, the confining pressure is set to 20 MPa. A compressive displacement rate of $5\text{e-}8\text{ m/step}$ is assigned on the top and bottom faces of the model. Permeable boundaries are applied at the top and bottom of the model. The pore pressure is fixed on the top

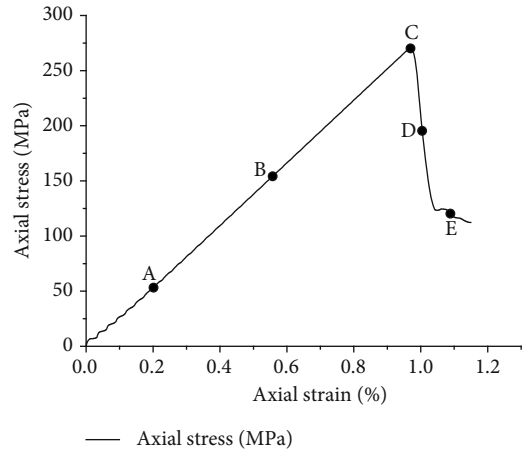


FIGURE 11: Simulated stress-strain curve for pore pressure of 8 MPa under confining pressure of 20 MPa.

and bottom of the model to simulate constant fluid pressure. A strain-softening model is used for mechanics, and an isotropic Darcy model is used for the fluid flow. All input parameters are listed in Tables 4 and 5. And the parameters in Tables 4 and 5 are consistent with the HM coupled test.

5.2. Determination of Linear Correlation Coefficients.

According to Section 4.3, the permeability has a linear relationship with volumetric strain. And volumetric strain of elements can be directly obtained in FLAC^{3D} . Therefore, the permeability is updated during the numerical simulation. However, the linear relationships cannot be applied to describe the permeability evolution of the elements directly. Therefore, the linear coefficients need to be calibrated by several numerical simulations [41].

First, simulation of the conventional triaxial compression (CTC) test under confining pressure of 20 MPa is conducted. A compressed numerical model (see Figure 8(a)) before the dilatancy threshold is chosen to determine the linear coefficient K_1 , and a damaged numerical model beyond the dilatancy threshold (see Figure 8(b)) is chosen to determine the linear coefficient K_2 . The initial permeability is set as 2.58

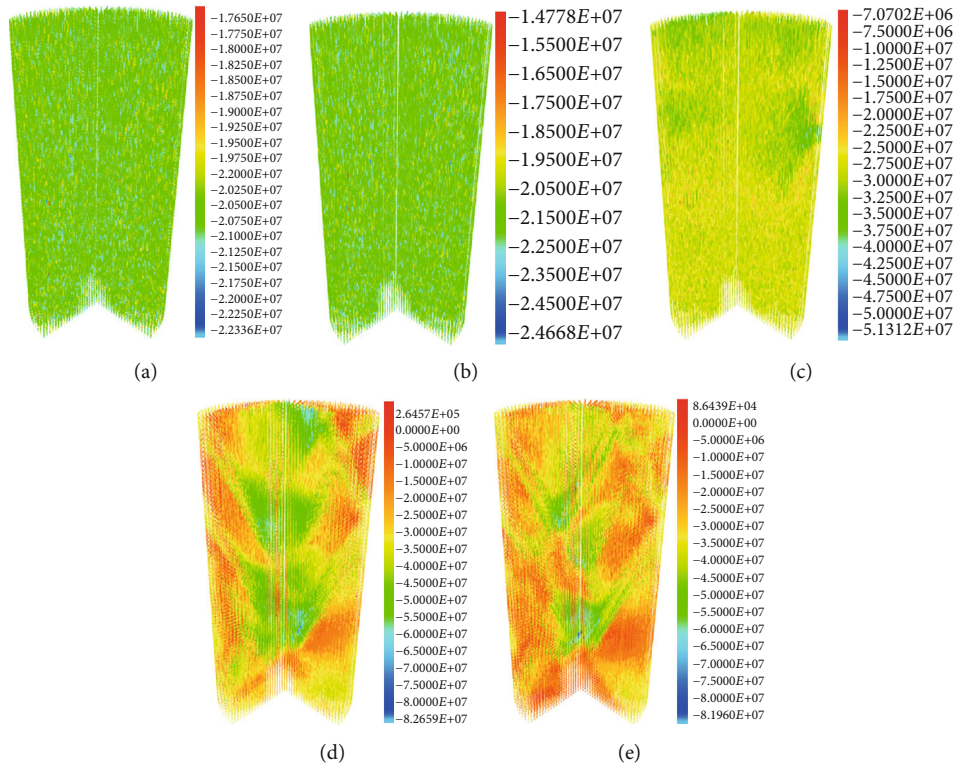


FIGURE 12: Evolution of maximum stress tensor (Pa) for simulated HM coupled test: (a) initial compressed stage, (b) elastic stage, (c) peak stress point, (d) stress drop stage, and (e) residual stage.

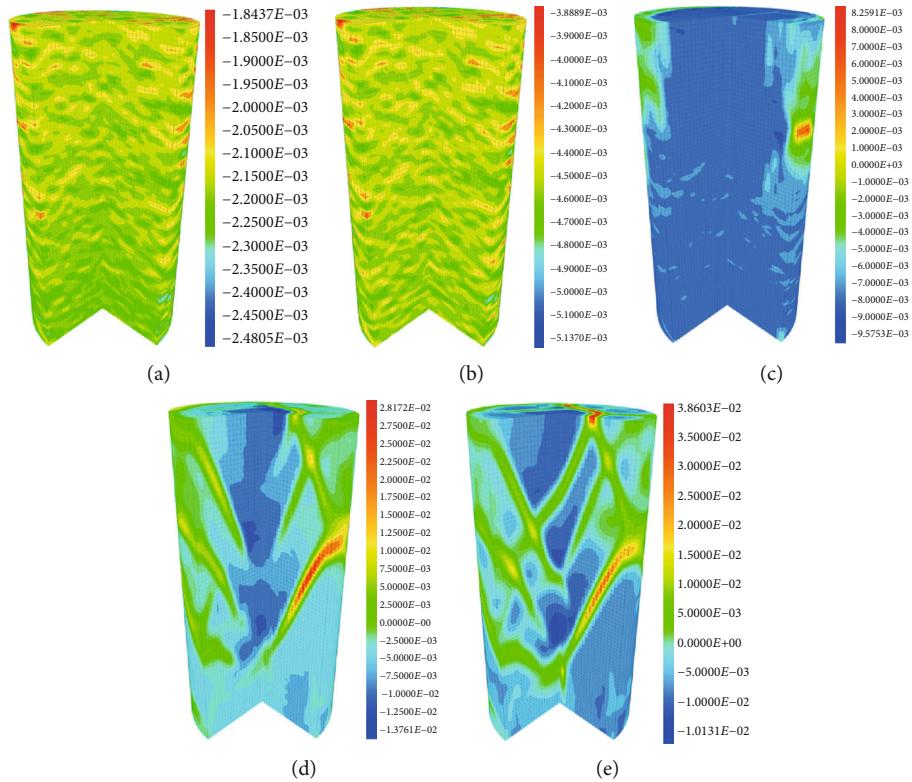


FIGURE 13: Evolution of volumetric strain for simulated HM coupled test: (a) initial compressed stage, (b) elastic stage, (c) peak stress point, (d) stress drop stage, and (e) residual stage.

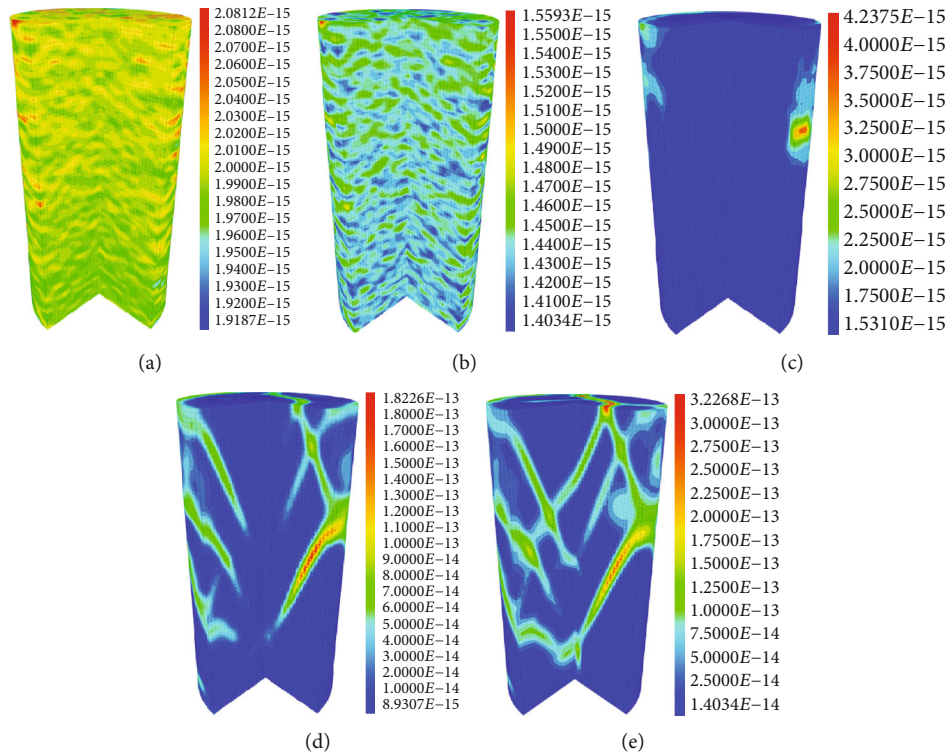


FIGURE 14: Evolution of permeability (10^{-3} m^2) for simulated HM coupled test: (a) initial compressed stage, (b) elastic stage, (c) peak stress point, (d) stress drop stage, and (e) residual stage.

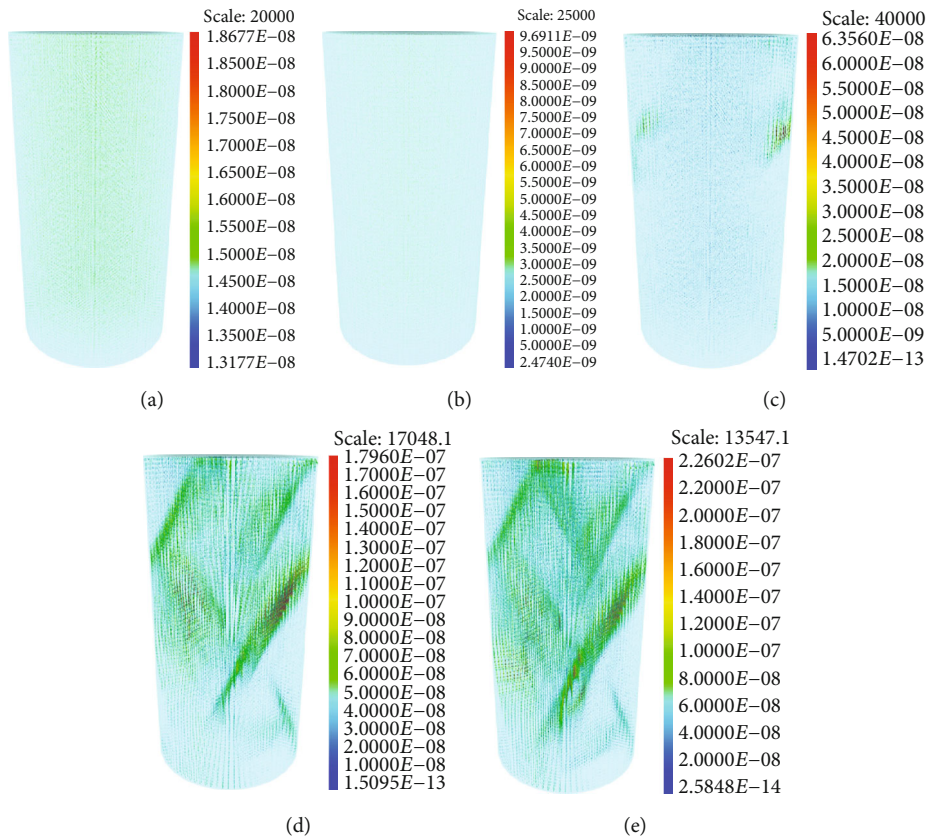


FIGURE 15: Evolution of discharge vectors (m/s) for simulated HM coupled test: (a) initial compressed stage, (b) elastic stage, (c) peak stress point, (d) stress drop stage, and (e) residual stage.

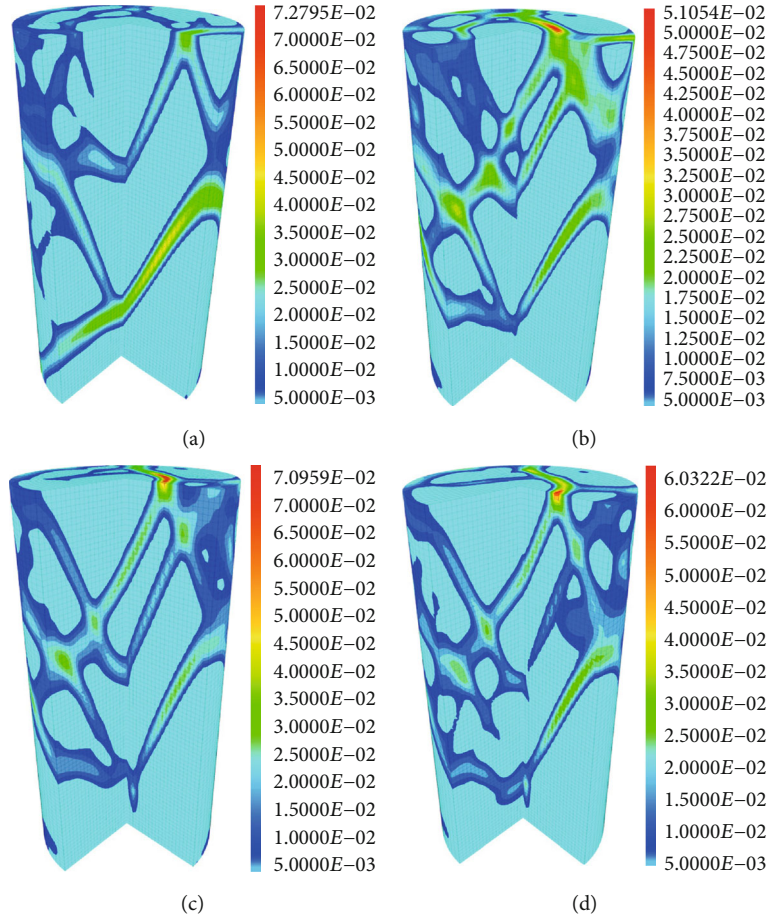


FIGURE 16: Volumetric strain ($\epsilon_v > 0.5\%$) at stage e under different fluid pressures: (a) pore pressure of 2 MPa, (b) pore pressure of 4 MPa, (c) pore pressure of 6 MPa, and (d) pore pressure of 8 MPa.

$\times 10^{-18} \text{ m}^2$. The two models are used to simulate steady flow with different linear coefficients, and the results are shown in Figure 9. According to the flow rate, $K_1 = 80$ and $K_2 = 1700$ fit the lab results.

5.3. HM Coupled Simulation Results. The proposed permeability evolution rule (Equation (3)) is implemented into FLAC^{3D} . The pore pressures correspond to the HM coupling tests. Figure 10 shows stress-strain curves obtained from simulations. Taking the pore pressure of 8 MPa as an example, the deformation and permeability evolution for different observation points (marked in Figure 11) are shown in Figures 12-15.

Some conclusions can be drawn from the numerical simulations. In the quasi elastic stage (points a and b), the stress state is nearly homogeneous; volumetric strain decreases with increasing axial stress, and all elements are compressed; permeability is decreasing and fluid flow is restricted. In brief, there is no damage at this stage. At the peak stress (point c), the stress distribution is no longer uniform; volumetric strain increases especially close to the model boundary; therefore, permeability and flow rate increase near the model boundary. During the stress drop (point e), local tensile stresses appear; volumetric strain increases rapidly and forms several shear bands, which develop from the model boundary to the inside.

And it provides several seepage channels with high permeability for fluid flow. In the residual stage (point e), the tensile stress area expands; the volumetric strain bands become wider and interact with each other.

The macroscopic fracture patterns for samples under different pore pressures are shown in Figure 16. With the increase of pore pressure, the volumetric strain band channels increase. In other words, macroscopic fractures become pronounced with increasing pore pressure. It indicates that the pore pressure accelerates rock degradation during HM coupling.

6. Conclusion

HM coupled tests are carried out on Beishan granite under different pore pressures. The permeability evolution is studied. And numerical simulations are conducted to study the stress state and deformation process. Based on the results, the following conclusions can be drawn.

Before dilatancy, the initial pressure difference (ΔP_0) has little influence on permeability measurement by using the transient pulse method. However, after dilatancy, the permeability increases with the increasing initial pressure difference. Overall, the permeability evolution trends are the same.

The initial permeability of Beishan granite maintains at the order 10^{-18} m^2 under the confining pressure 20 MPa. In the initial loading phase, the permeability shows a relatively large reduction. Then, the permeability almost keeps constant. From onset of dilatancy to peak stress, the permeability increases linearly with the volumetric strain. A rule of relating permeability evolution with volumetric strain is proposed.

The simulation results show that the damaged zone first appears close to the model boundary and then extends to the inside, forming local high volumetric strain areas. And it provides seepage channels for fluid flow. The macroscopic fracture patterns indicate that pore pressure accelerates rock degradation during HM coupling.

In the future, more tests are needed for further investigating permeability evolution and fracturing characteristics of Beishan granite subjected to different confining stresses and pore pressures.

Data Availability

The data used to support the findings of this study are available from the corresponding author upon request.

Conflicts of Interest

The authors declare that they have no competing financial interests or personal relationships that could have influenced the work reported in this paper.

Acknowledgments

This work was supported by the Major Program of Shandong Province Natural Science Foundation (ZR2018ZA0603) and the National Natural Science Foundation of China (51674266).

References

- [1] J. Wang, "High-level radioactive waste disposal in China: update 2010," *Journal of Rock Mechanics and Geotechnical Engineering*, vol. 2, no. 1, pp. 1–11, 2010.
- [2] J. Wang, "On area-specific underground research laboratory for geological disposal of high-level radioactive waste in China," *Journal of Rock Mechanics and Geotechnical Engineering*, vol. 6, no. 2, pp. 99–104, 2014.
- [3] S. Peng and A. M. Johnson, "Crack growth and faulting in cylindrical specimens of Chelmsford granite," *International Journal of Rock Mechanics and Mining Science and Geomechanics Abstracts*, vol. 9, no. 1, pp. 37–86, 1972.
- [4] P. Tapponnier and W. F. Brace, "Development of stress-induced microcracks in Westerly granite," *International Journal of Rock Mechanics and Mining Science and Geomechanics Abstracts*, vol. 13, no. 4, pp. 103–112, 1976.
- [5] M. Oda, T. Katsube, and T. Takemura, "Microcrack evolution and brittle failure of Inada granite in triaxial compression tests at 140 MPa," *Journal of Geophysical Research*, vol. 107, no. B10, pp. ECV 9-1–ECV 9-17, 2002.
- [6] L. Jian-po, L. Yuan-hui, X. Shi-da, X. Shuai, and J. Chang-yu, "Cracking mechanisms in granite rocks subjected to uniaxial compression by moment tensor analysis of acoustic emission," *Theoretical and Applied Fracture Mechanics*, vol. 75, pp. 151–159, 2015.
- [7] Y. H. Huang, S. Q. Yang, P. G. Ranjith, and J. Zhao, "Strength failure behavior and crack evolution mechanism of granite containing pre-existing non-coplanar holes: experimental study and particle flow modeling," *Computers and Geotechnics*, vol. 88, pp. 182–198, 2017.
- [8] X. Cai, Z. Zhou, L. Tan, H. Zang, and Z. Song, "Fracture behavior and damage mechanisms of sandstone subjected to wetting-drying cycles," *Engineering Fracture Mechanics*, vol. 234, p. 107109, 2020.
- [9] K. Suzuki, M. Oda, M. Yamazaki, and T. Kuwahara, "Permeability changes in granite with crack growth during immersion in hot water," *International Journal of Rock Mechanics and Mining Science*, vol. 35, no. 7, pp. 907–921, 1998.
- [10] S. C. Yuan and J. P. Harrison, "A review of the state of the art in modelling progressive mechanical breakdown and associated fluid flow in intact heterogeneous rocks," *International Journal of Rock Mechanics and Mining Science*, vol. 43, no. 7, pp. 1001–1022, 2006.
- [11] Y. Chitralla, C. Moreno, C. Sondergeld, and C. Rai, "An experimental investigation into hydraulic fracture propagation under different applied stresses in tight sands using acoustic emissions," *Journal of Petroleum Science and Engineering*, vol. 108, pp. 151–161, 2013.
- [12] G. Liu, J. Peng, Z. Zhang, Z. Wang, and Y. Yang, "Numerical investigation of fluid-driven crack propagation and coalescence in granite specimen with two pre-existing flaws," *Journal of Natural Gas Science and Engineering*, vol. 75, p. 103132, 2020.
- [13] W. F. Brace, J. B. Walsh, and W. T. Frangos, "Permeability of granite under high pressure," *Journal of Geophysical Research*, vol. 73, no. 6, pp. 2225–2236, 1968.
- [14] M. D. Zoback and J. D. Byerlee, "The effect of microcrack dilatancy on the permeability of westerly granite," *Journal of Geophysical Research*, vol. 80, no. 5, pp. 752–755, 1975.
- [15] T. Kiyama, H. Kita, Y. Ishijima, T. Yanagidani, K. Aoki, and T. Sato, "Permeability in anisotropic granite under hydrostatic compression and triaxial compression including post-failure region," in *2nd North American Rock Mechanics Symposium*, American Rock Mechanics Association, 1996.
- [16] L. Liu, W. Y. Xu, H. L. Wang, W. Wang, and R. B. Wang, "Permeability evolution of granite gneiss during triaxial creep tests," *Rock Mechanics and Rock Engineering*, vol. 49, no. 9, pp. 3455–3462, 2016.
- [17] Y. Chen, "Permeability evolution in granite under compressive stress condition," *Geotechnical and Geological Engineering*, vol. 36, no. 1, pp. 641–647, 2018.
- [18] H. Yi, H. Zhou, R. Wang, D. Liu, and J. Ding, "On the relationship between creep strain and permeability of granite: experiment and model investigation," *Energies*, vol. 11, no. 10, p. 2859, 2018.
- [19] J. Heiland and S. Raab, "Experimental investigation of the influence of differential stress on permeability of a lower permian (rotliegend) sandstone deformed in the brittle deformation field," *Physics and Chemistry of the Earth Part A*, vol. 26, no. 1–2, pp. 33–38, 2001.
- [20] A. K. M. B. Alam, M. Niioka, Y. Fujii, D. Fukuda, and J. I. Kodama, "Effects of confining pressure on the permeability of three rock types under compression," *International Journal of Rock Mechanics and Mining Sciences*, vol. 65, pp. 49–61, 2014.

- [21] Y. Zhang, Z. B. Liu, W. Y. Xu, and J. F. Shao, "Change in the permeability of clastic rock during multi-loading triaxial compressive creep tests," *Géotechnique Letters*, vol. 5, no. 3, pp. 167–172, 2015.
- [22] C. F. Tsang, L. Jing, O. Stephansson, and F. Kautsky, "The DECOVALEX III project: a summary of activities and lessons learned," *International Journal of Rock Mechanics and Mining Sciences*, vol. 42, no. 5-6, pp. 593–610, 2005.
- [23] C. F. Tsang, O. Stephansson, L. Jing, and F. Kautsky, "DECOVALEX Project: from 1992 to 2007," *Environmental Geology*, vol. 57, no. 6, pp. 1221–1237, 2009.
- [24] C. A. Tang, L. G. Tham, P. K. K. Lee, T. H. Yang, and L. C. Li, "Coupled analysis of flow, stress and damage (FSD) in rock failure," *International Journal of Rock Mechanics and Mining Sciences*, vol. 39, no. 4, pp. 477–489, 2002.
- [25] J. Rutqvist, Y. S. Wu, C. F. Tsang, and G. Bodvarsson, "A modeling approach for analysis of coupled multiphase fluid flow, heat transfer, and deformation in fractured porous rock," *International Journal of Rock Mechanics and Mining Sciences*, vol. 39, no. 4, pp. 429–442, 2002.
- [26] X. Tan and H. Konietzky, "Numerical simulation of permeability evolution during progressive failure of Aue granite at the grain scale level," *Computers and Geotechnics*, vol. 112, pp. 185–196, 2019.
- [27] Y. L. Lu, D. Elsworth, and L. G. Wang, "Microcrack-based coupled damage and flow modeling of fracturing evolution in permeable brittle rocks," *Computers and Geotechnics*, vol. 49, pp. 226–244, 2013.
- [28] J. Heiland, "Laboratory testing of coupled hydro-mechanical processes during rock deformation," *Hydrogeology Journal*, vol. 11, no. 1, pp. 122–141, 2003.
- [29] X. Tan, *Hydro-mechanical coupled behavior of brittle rocks, Dissertation*, Technische Universität Bergakademie Freiberg, Freiberg, Germany, 2013.
- [30] R. L. Kranz, A. D. Frankel, T. Engelder, and C. H. Scholz, "The permeability of whole and jointed Barre granite," *International Journal of Rock Mechanics and Mining Science and Geomechanics Abstracts*, vol. 16, no. 4, pp. 225–234, 1979.
- [31] R. L. Kranz, J. S. Saltzman, and J. D. Blacic, "Hydraulic diffusivity measurements on laboratory rock samples using an oscillating pore pressure method," *International Journal of Rock Mechanics and Mining Science and Geomechanics Abstracts*, vol. 27, no. 5, pp. 345–352, 1990.
- [32] J. B. Walsh and W. F. Brace, "The effect of pressure on porosity and the transport properties of rock," *Journal of Geophysical Research*, vol. 89, no. B11, pp. 9425–9431, 1984.
- [33] H.-D. Chen, C. Yuan-Ping, H.-X. Zhou, and W. Li, "Damage and permeability development in coal during unloading," *Rock Mechanics and Rock Engineering*, vol. 46, no. 6, pp. 1377–1390, 2013.
- [34] C. E. Fairhurst and J. A. Hudson, "Discussion," *International Journal of Rock Mechanics & Mining Science*, vol. 36, no. 3, pp. 279–289, 1999.
- [35] X. G. Zhao, M. Cai, J. Wang, and L. K. Ma, "Damage stress and acoustic emission characteristics of the Beishan granite," *International Journal of Rock Mechanics and Mining Science*, vol. 64, no. 12, pp. 258–269, 2013.
- [36] X. G. Zhao, J. Wang, F. Chen et al., "Experimental investigations on the thermal conductivity characteristics of Beishan granitic rocks for China's HLW disposal," *Tectonophysics*, vol. 683, pp. 124–137, 2016.
- [37] H. W. Zhou, Z. H. Wang, C. S. Wang, and J. F. Liu, "On acoustic emission and post-peak energy evolution in Beishan granite under cyclic loading," *Rock Mechanics and Rock Engineering*, vol. 52, no. 1, pp. 283–288, 2019.
- [38] L. Chen, J. Liu, C. P. Wang, J. Liu, R. Su, and J. Wang, "Characterization of damage evolution in granite under compressive stress condition and its effect on permeability," *International Journal of Rock Mechanics and Mining Science*, vol. 71, pp. 340–349, 2014.
- [39] S. Q. Yang, H. W. Jing, and S. Y. Wang, "Experimental investigation on the strength, deformability, failure behavior and acoustic emission locations of red sandstone under triaxial compression," *Rock Mechanics and Rock Engineering*, vol. 45, no. 4, pp. 583–606, 2012.
- [40] H. W. Zhou, Z. H. Wang, W. G. Ren, Z. L. Liu, and J. F. Liu, "Acoustic emission based mechanical behaviors of Beishan granite under conventional triaxial compression and hydro-mechanical coupling tests," *International Journal of Rock Mechanics and Mining Science*, vol. 123, p. 104125, 2019.
- [41] X. Tan, H. Konietzky, and T. Frühwirth, "Laboratory observation and numerical simulation of permeability evolution during progressive failure of brittle rocks," *International Journal of Rock Mechanics and Mining Sciences*, vol. 68, pp. 167–176, 2014.

Research Article

Effective Methane Extraction Radius after High-Pressure Water Jet Slotting

Hu Ke ¹, Xia Binwei,^{2,3} Liu Chengwei,⁴ and Lu Yiyu^{2,3}

¹Institute of Mining and Special Civil Engineering, TU Bergakademie Freiberg, 09599, Freiberg, Germany

²State Key Laboratory of Coal Mine Disaster Dynamics and Control, Chongqing University, Chongqing 400044, China

³School of Resources and Safety Engineering, Chongqing University, Chongqing 400044, China

⁴School of Mines and Civil Engineering, Liupanshui Normal University, Liupanshui 553004, China

Correspondence should be addressed to Hu Ke; ke.hu@student.tu-freiberg.de

Received 8 May 2020; Revised 31 May 2020; Accepted 4 June 2020; Published 1 August 2020

Academic Editor: Zhengyang Song

Copyright © 2020 Hu Ke et al. This is an open access article distributed under the Creative Commons Attribution License, which permits unrestricted use, distribution, and reproduction in any medium, provided the original work is properly cited.

The effective radius of methane extraction after high-pressure water jet slotting is the most important parameter for borehole optimization and extraction time planning. We applied a steady flow model and thermal-hydrological-mechanical (THM) coupling model to calculate the effective radius after high-pressure water jet slotting. Field measurements at the Zhongliangshan coal mine show that both the steady flow model and the THM coupling model can accurately represent the effective radius, and the THM coupling model provides further information regarding extraction time. After that, a variety of factors, including extraction time, coal burial depth, slot radius, initial permeability, and initial methane pressure, are discussed. The effective radius of a slotted borehole is 1.94 times larger than that of a conventional borehole.

1. Introduction

Coalbed methane (CBM) extraction is an intensive method for reducing the security risk of coal and methane outbursts during mine production [1] that can provide cleaner energy resources [2] and potentially reduce greenhouse gas emissions [3]. CBM is mainly composed of methane (CH₄), which has a greenhouse effect that is ~25 times stronger than that of carbon dioxide [4].

The CBM in China ranks third in the world with 3.68 × 10¹² m³ of reserves at depths < 2000 m [5]. The total potential CBM includes considerable amounts of onshore conventional natural gas resources and provided 7.26 billion m³ of energy in 2018 [6]. The target for underground CBM production in China is 14 billion m³ in 2020, according to the 13th five-year plan of the Development and Utilization of Coalbed Methane [7]. Preextraction of CBM can reduce the risk of methane explosion [8–11] as well as coal and gas outburst.

The permeability of most Chinese coal seams is < 1 mD, in which 35% have < 0.1 mD and 37% are tight with permeabilities ranging between 0.1 and 1 mD [1]. Drainage of coal seams with permeability < 1 mD is difficult according to the Coal Bed Methane Drainage Engineering Design Specification (GB50471-2008). For coal seams with extremely low permeability and low porosity, conventional extraction methods that involve drilling in coal seams from underground or at the surface are inefficient, costly, and time-consuming. Several methods have been proposed to improve the efficiency of CBM extraction.

High-pressure water jet slotting [12–16] has been widely applied to enhance CBM extraction from underground coal seams with extremely low permeability, as shown in Figure 1. The coal seams may undergo tensile, compressive, or shear failure under the dynamic loading of the high-pressure water jet [15, 17, 18], which can enhance intrinsic cracks and propagate new cracks. Discoid caves can reduce the effective stress in coal seams and exponentially increase

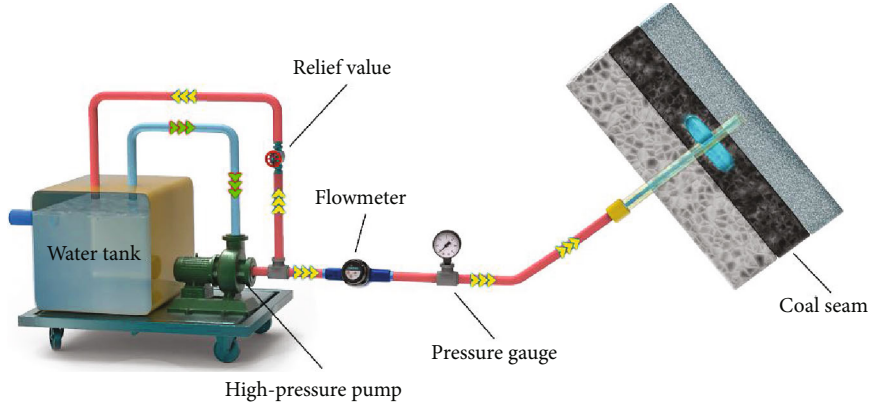


FIGURE 1: The schematic diagram of the high-pressure water jet system in the coal seam.

their permeability [19, 20]. A higher concentration of adsorbed methane can desorb from the enhanced coal seam surface after being slotted by a high-pressure water jet [21].

The most important parameter to consider during this process is the effective methane extraction radius after high-pressure water jet slotting, which has been determined empirically. A methane pressure of 0.74 MPa was set as the coal and gas outburst risk criterion according to the Specification of Coal and Gas Outburst Prevention [22]. This pressure eliminates hazards related to coal and gas outburst hazards and allows safe mining operations. The influence radius is generally considered that under which the range of methane pressure loss is 10% [23], whereas areas with pressure < 0.74 MPa are considered the effective methane extraction radius. The latter is clearly more advantageous for optimizing field applications and is therefore an important focus of the study.

An effective radius of methane excretion is a crucial parameter for the layout of drilling boreholes and the extracting plan. Exceedingly large spacing between boreholes tends to allow the emergence of blind spots in the coal seams with insufficient extraction and may lead to coal and gas outburst accidents during production. In contrast, if borehole spacing is too small, leakage can occur and more boreholes must be drilled, which is wasteful and inefficient.

With the increasing demand for coal, mining operations have descended to increasingly deeper depths at a rate of 20 m/yr [24]. The effects of temperature for methane adsorption/desorption, methane flow, and coal seam deformation are more prominent with increasing mining depth. Additionally, the distribution of stress and flow pattern of methane around discoid caves differs considerably from transitional cylinder boreholes. Most importantly, the techniques used to establish the effective radius of methane extraction from the traditional boreholes are invalid for deep boreholes.

To provide improved guidance for methane extraction, we propose an efficient and robust method within a thermal-hydrological-mechanical (THM) coupling model to calculate the effective radius of methane extraction after high-pressure water jet slotting. We applied theoretical analysis, numerical simulations, model validation, and sensitivity analysis to detect the methane distribution after slotting.

2. Methodology

2.1. Steady Methane Flow Model. When a discoid cave is slotted by a water jet, methane molecules desorb from the coal surface and flow through the borehole. The methane flow areas around the hole can be divided into three zones (Figure 2): a linear seepage zone, a low-speed nonlinear seepage zone, and a diffusion zone. The diffusion coefficient of methane in coal seams is extremely low, and the contribution of methane diffusion can be ignored for low-permeability coal seams [25].

According to Darcy's law, the velocity of methane flow in the linear seepage zone can be expressed as [26]

$$V = 10^{-3} \frac{k\Delta P}{\mu L_1}, \quad (1)$$

where V is the methane seepage velocity (m/s), k is the coal seam permeability (μm^2), μ is the dynamic viscosity of methane (mPa·s), ΔP is the pressure difference (MPa), and L_1 is the maximum methane migration distance in the linear seepage zone (m).

The Reynolds number (Re) has been recognized as the determining criterion for fluid flow patterns, and $Re = 10^{-4}$ represents the boundary between linear and nonlinear seepage [27]:

$$Re = 10^{-4} \frac{v\sqrt{k\rho}}{17.50\mu\phi^{3/2}}, \quad (2)$$

where ρ is the density of the methane (g/cm^3) and ϕ is the porosity. By substituting Equation (1) into Equation (2), L_1 can be expressed as

$$L_1 = \frac{10^{-15}\rho\Delta Pk^{3/2}}{17.5u^2\phi^{3/2}Re}. \quad (3)$$

When flowing in a low-permeability coal seam, methane molecules collide against coal pore walls because the pore diameters are smaller than the mean free path. On a macro-level, this collision is called a slippage effect and is conditional

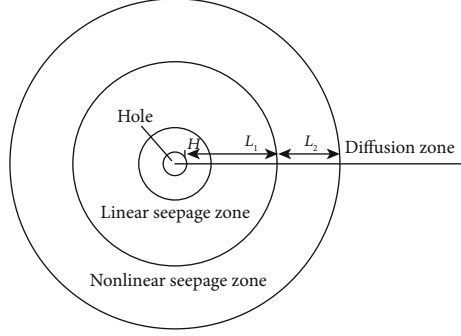


FIGURE 2: Steady methane flow field area around a discoid cave where H is the cave radius and L_1 and L_2 are the maximum distance for methane movement in the linear seepage zone and nonlinear seepage zone, respectively.

because of the starting pressure gradient (λ_B) when methane flows at a lower velocity. When the pressure gradient exceeds λ_B , the methane flow is predominantly low-speed nonlinear seepage; when the pressure gradient is less than λ_B , methane flow is only governed by diffusion. According to the low-speed nonlinear seepage law, it can be concluded that

$$V = \begin{cases} \frac{k}{\mu} \left(1 + \frac{2B}{P_1 + P_2} \right) \frac{\Delta P}{L}, & \frac{\Delta P}{L} > \lambda_B, \\ 0, & \frac{\Delta P}{L} \leq \lambda_B, \end{cases} \quad (4)$$

where P_1 and P_2 represent the methane pressure of the inflow and outflow sides, respectively, and B is the Klinkenberg coefficient.

The relationship between λ_B and coal seam permeability can be expressed as [28]

$$\lambda_B = 0.0113k^{-0.33034}, \quad (5)$$

when $V = 0$ in Equation (1) and L_2 represents the maximum distance of methane movement within the nonlinear seepage zone, thus

$$L_2 = \frac{\Delta P}{\lambda_B}. \quad (6)$$

The maximum radius of methane extraction can therefore be expressed as

$$R = H + L_1 + L_2 = H + \frac{10^{-15} \rho \Delta P k^{3/2}}{17.5 \mu^2 \phi^{3/2} \text{Re}} + \frac{\Delta P}{\lambda_B}, \quad (7)$$

where H represents the cave radius. In Equation (7), $H + L_1$ can be thought of as the effective radius and R as the influence radius. Equation (7) provides a time-independent solution of the effective radius and influence radius, but the extraction time remains unknown and the effect of temperature in methane extraction is ignored.

2.2. The THM Coupling Model for Methane Flow. The THM coupling model directly evaluates the effective radius of methane extraction as well as the extraction time [29]. To

establish the THM coupling model for methane extraction after high-pressure water jet slotting, we suggest the following basic assumptions [30–32]: (1) the coal seams are homogeneous and isotropic porous media; (2) the deformation of coal skeleton and porosity is minimal and can be described by the linear elasticity criterion; (3) thermodynamic parameters of coal seams and methane are temperature independent; (4) the coal seams are saturated by methane; (5) methane adsorption on coal can be represented by the Langmuir model, and the free methane is an ideal gas.

2.2.1. Governing Equations of Coal Deformation. During methane extraction after high-pressure water jet slotting, the coal seams will deform under the influence of temperature, methane pressure, and strata pressure. The coal seam strain is the sum of strains induced by effective stress, methane adsorption-induced strain, and thermal strain. The thermal strain can be expressed as

$$\varepsilon_T = \frac{1}{3} \alpha_s \Delta T \delta_{ij}, \quad (8)$$

where α_s is the coefficient of the thermal expansion ($\text{cm}^3/(\text{m}^3 \cdot \text{K})$), ΔT represents the change of absolute coal seam temperature (K), and δ_{ij} is the Kronecker symbol.

Considering the strain induced by methane adsorption, we assume that adsorption only induces volume strain and that the coal seam is isotropic. The constitutive equation of the coal seam can be drawn as follows and is negative during compression:

$$\varepsilon_{ij} = \frac{1}{2G} \sigma_{ij} - \left(\frac{1}{6G} - \frac{1}{9K} \right) \sigma_{kk} \delta_{ij} + \frac{\alpha}{3K} p \delta_{ij} + \frac{\varepsilon_s}{3} \delta_{ij}, \quad (9)$$

where G is the coal seam shear modulus (GPa), K is the coal seam volume modulus (GPa), α is the Biot effective stress coefficient, where $\alpha = 1 - K/K_s$ and K_s is the volume modulus of the skeleton of coal (GPa), σ_{kk} is the normal stress component ($\sigma_{kk} = \sigma_{11} + \sigma_{22} + \sigma_{33}$), ε_{ij} is the coal strain tensor component, and ε_s is the adsorption-induced strain.

Combining Equations (8) and (9), the constitutive equation that considers strata stress, methane pressure, adsorption-induced strain, and temperature can be expressed as [33]

$$\varepsilon_{ij} = \frac{1}{2G}\sigma_{ij} - \left(\frac{1}{6G} - \frac{1}{9K}\right)\sigma_{kk}\delta_{ij} + \frac{\alpha}{3K}p\delta_{ij} + \frac{\varepsilon_s}{3}\delta_{ij} + \frac{\alpha_s\Delta T}{3}\delta_{ij}. \quad (10)$$

The first term on the right side of Equation (10) represents the strain of the strata stress; the second term implies the strain of methane pressure. The third and fourth terms are the strain induced by adsorption and temperature, respectively.

The stress displacement equations of the coal seam are

$$\varepsilon_{ij} = \frac{1}{2}(u_{i,j} + u_{j,i}), \quad (11)$$

where u_{ij} is the coal seam displacement component. The equilibrium equation for the coal seam can be expressed as

$$\sigma_{ij,j} + f_i = 0, \quad (12)$$

where f_i is the volumetric component of the coal seam.

By combining Equations (10)–(12), the governing equation for coal seam displacement under the effects of stress, strain, methane pressure, and temperature is

$$Gu_{i,kk} + \frac{G}{1-2\nu}u_{k,ki} - \alpha_sKT_i - \alpha p_i - K\varepsilon_{s,i} + f_i = 0. \quad (13)$$

2.2.2. Governing Equations of Methane Flow. Assuming methane as an ideal gas, the density of methane can be described as

$$\rho_g = \beta P = \frac{MP}{R_0T}, \quad (14)$$

where β is the compressibility coefficient ($\text{kg}/(\text{m}^3\cdot\text{Pa})$), ρ_g is the methane density (kg/m^3), M is the molar mass of methane (16 g/mol), R_0 is the ideal gas constant ($8314 \text{ m}^2/(\text{s}^2\cdot\text{K})$), and T is the temperature (K).

According to the equations of state for an ideal gas, the free methane in coal cracks, fractures, and pores can be characterized as

$$C_f = \frac{\phi\rho_g P}{p_n}, \quad (15)$$

where C_f is the free methane per cubic meter of coal (kg/m^3) and p_n is the atmospheric pressure (0.1 MPa).

The Langmuir model is widely used for representing methane adsorption on coal and can be expressed as [34]

$$Q_x = \rho_c \rho_g \frac{abP}{1+bP}, \quad (16)$$

where Q_x is the mass of adsorbed methane per cubic meter of coal (kg/m^3), a is the maximum monolayer adsorption capacity (m^3/t), and b is the Langmuir pressure, which represents the pressure when the adsorbed methane equals 50% of its maximum quantity (MPa).

Methane adsorption is an exothermic process, and the relationship between temperature and the Langmuir parameter is described in the literature as [35]

$$\begin{cases} a = -0.0031T^2 + 0.2297T + 26.841, \\ b = -0.0157T + 1.6798. \end{cases} \quad (17)$$

Combining Equations (15), (16), and (17), the methane content is the sum of the free methane and adsorbed methane and can be described as

$$Q = C_f + Q_x = \frac{\phi\rho_g P}{p_n} + \rho_c \rho_g \frac{abP}{1+bP}, \quad (18)$$

where Q is the methane content for a unit volume of coal, kg/m^3 . According to Darcy's law and the conservation of mass,

$$\frac{\partial Q}{\partial t} + \nabla \cdot (\rho_g q) = I, \quad (19)$$

where I is the mass source term.

At an increased mining depth, the effect of temperature on the dynamic viscosity of methane can be ignored, and the dynamic viscosity of methane is set to $\mu = 1.08 \times 10^{-5} \text{ Pa}\cdot\text{s}$. We then obtain the governing equation for methane flow under nonisothermal conditions:

$$\begin{aligned} & \frac{(1-\phi)abM\rho_s}{R_0T} \left[\frac{4P^2 - bP^2}{(1+bP)^2} \right] \frac{\partial p}{\partial t} - \frac{abP^2M\rho_s}{(1+bP)R_0T} \frac{\partial \phi}{\partial t} \\ & - \frac{(1-\phi)abP^2M\rho_s}{(1+bP)R_0T^2} \frac{\partial T}{\partial t} - \nabla \cdot \left(\frac{k}{\mu} \nabla P^2 \right) = 0. \end{aligned} \quad (20)$$

2.2.3. Governing Equations of the Temperature Field. There are three types of thermal transmission in coal seams: heat exchange, thermal radiation, and thermal convection. Because the effect of thermal radiation is negligible and methane adsorption is an endothermic process, heat transfer in a coal seam can be simplified to unsteady thermal conduction in three dimensions with an internal heat source. According to the conservation of energy, we obtain [36]

$$\begin{aligned} & \frac{\partial (\rho_s c_s \Delta T + \phi \rho_g c_g \Delta T)}{\partial t} + T \alpha_s K \frac{\partial \varepsilon_v}{\partial t} + q_{st} Q_x \\ & + \nabla \cdot \rho_g h_g q_g + \nabla \cdot (k_t \nabla T) = Q_T, \end{aligned} \quad (21)$$

where c_s is the specific heat capacity of the coal seam ($\text{J}/(\text{K}\cdot\text{kg})$), c_g is the specific heat capacity of methane ($\text{J}/(\text{K}\cdot\text{kg})$), h_g is the specific enthalpy of methane (kJ/mol), q_{st} is the isosteric heat of methane ($33.4 \text{ kJ}/\text{mol}$) [37], and k_t is the weighted thermal conductivity for methane and coal.

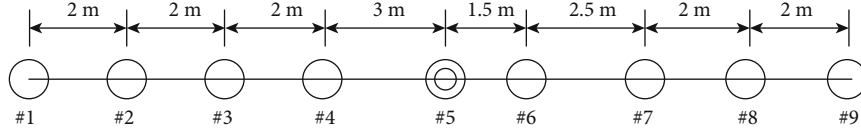


FIGURE 3: Schematic diagram of the boreholes.

2.2.4. *Coupled Governing Equations.* According to the definition of the porosity,

$$\phi = \frac{V_P}{V_B} = 1 - \frac{1 - \phi_0}{1 + \varepsilon_V} \left(1 + \frac{\Delta V_s}{V_{s0}} \right), \quad (22)$$

where V_{s0} is the initial volume of the coal seam skeleton (m^3), ΔV_s is the volume increment of the skeleton (m^3), V_P is the total pore volume (m^3), V_B is the total coal volume (m^3), ϕ_0 is the initial coal porosity of coal, and ε_V is the volume strain of the coal.

When the coal skeleton is affected by pore pressure, temperature, and adsorption-induced swelling, the volume change of the coal skeleton can be described as

$$\frac{\Delta V_s}{V_{s0}} = \alpha_s \Delta T - K_Y \Delta p + \frac{\varepsilon_s}{1 - \phi_0}, \quad (23)$$

where K_Y is the compression factor of coal, $K_Y = 1/K_S = 3(1 - 2\nu)/E$, where ν is Poisson's ratio.

The methane adsorption-induced swelling strain of coal can be expressed as [38]

$$\varepsilon_s = \frac{2\rho_s R_0 T a \ln(1 + bP)}{9V_m K}, \quad (24)$$

where K is the bulk modulus of the coal (GPa) and V_m is the molar volume of methane (22.4 L/mol). According to Equations (22)–(24), the dynamic evolution model of porosity can be achieved:

$$\phi = \frac{\varepsilon_v + \phi_0}{1 + \varepsilon_v} \left[1 + \alpha_s \Delta T - \frac{3\Delta P(1 - 2\nu)}{E} + \frac{2a\rho_s R_0 T \ln(1 + bP)}{9(1 - \phi_0)V_m K} \right]. \quad (25)$$

The Kozeny-Carman equation establishes the relationship between porosity and permeability:

TABLE 1: Parameters for the THM coupling model.

Parameter	Value
Overburden pressure	14.4 MPa
Elastic modulus, E	4.06×10^9 Pa [41]
Poisson's ratio, ν	0.28 [42]
Thermal expansion coefficient, α_s	$1.16 \times 10^{-5} \text{ m}^3/(\text{m}^3 \cdot \text{K})$ [43]
Methane viscosity, μ	1.08×10^{-5} Pa · s
Coal density, ρ_s	1400 kg/ m^3
Initial porosity, Φ_0	0.062
Initial permeability, k_0	0.025 mD
Initial methane pressure, P_0	2.0 MPa
Specific heat capacity of coal, c_s	4186 J/(kg·K) [44]
Specific heat capacity of methane, c_g	2227 J/(kg·K)

$$k = \frac{\phi V_p^2}{K_z A_s^2}, \quad (26)$$

where K_z is the Kozeny constant, V_p is the specific surface area of the unit volume (cm^2), and A_s is the specific surface area (cm^2).

Substituting Equation (25) into Equation (26), we obtain the dynamic evolution model of coal permeability using the THM coupling model:

$$k = \frac{k_0}{\exp(-K_Y \Delta \sigma')} \left[1 + \frac{\varepsilon_v}{\phi_0} - \frac{(\alpha_s \Delta T - K_Y \Delta P)(1 - \phi_0)}{\phi_0} - \frac{2\rho_s R_0 T a \ln(1 + bP)}{9\phi_0 V_m K} \right]^3, \quad (27)$$

where $\Delta \sigma'$ is the variation of the effective stress (MPa).

The THM coupling model for methane extraction after high-pressure water jet slotting can therefore be summarized as

$$\begin{cases} Gu_{i,kk} + Gu_{i,kk} + \frac{G}{1 - 2\nu} u_{k,ki} - \alpha_s K T_i - \alpha p_i - K \varepsilon_{s,i} + f_i = 0, \\ \frac{(1 - \phi)abM\rho_s}{R_0 T} \left[\frac{4P^2 - bP^2}{(1 + bP)^2} \right] \frac{\partial p}{\partial t} - \frac{abP^2 M \rho_s}{(1 + bP)R_0 T} \frac{\partial \phi}{\partial t} - \frac{(1 - \phi)abP^2 M \rho_s}{(1 + bP)R_0 T^2} \frac{\partial T}{\partial t} - \nabla \cdot \left(\frac{k}{\mu} \nabla P^2 \right) = 0, \\ \frac{\partial (\rho_s c_s \Delta T + \phi \rho_g c_g \Delta T)}{\partial t} + T \alpha_s K \frac{\partial \varepsilon_v}{\partial t} + q_{st} Q + \nabla \cdot \rho_g h_g q_g + \nabla \cdot (k_i \nabla T) = Q_T. \end{cases} \quad (28)$$

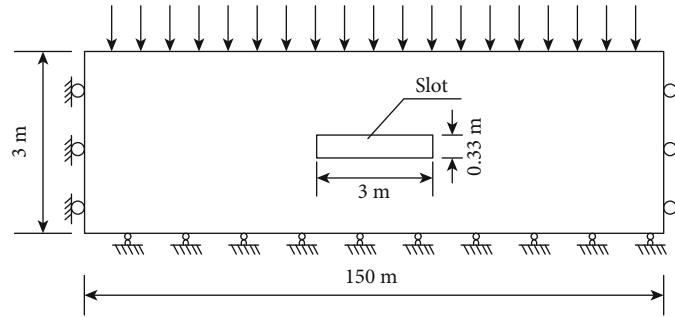


FIGURE 4: Schematic diagram of the calculation model.

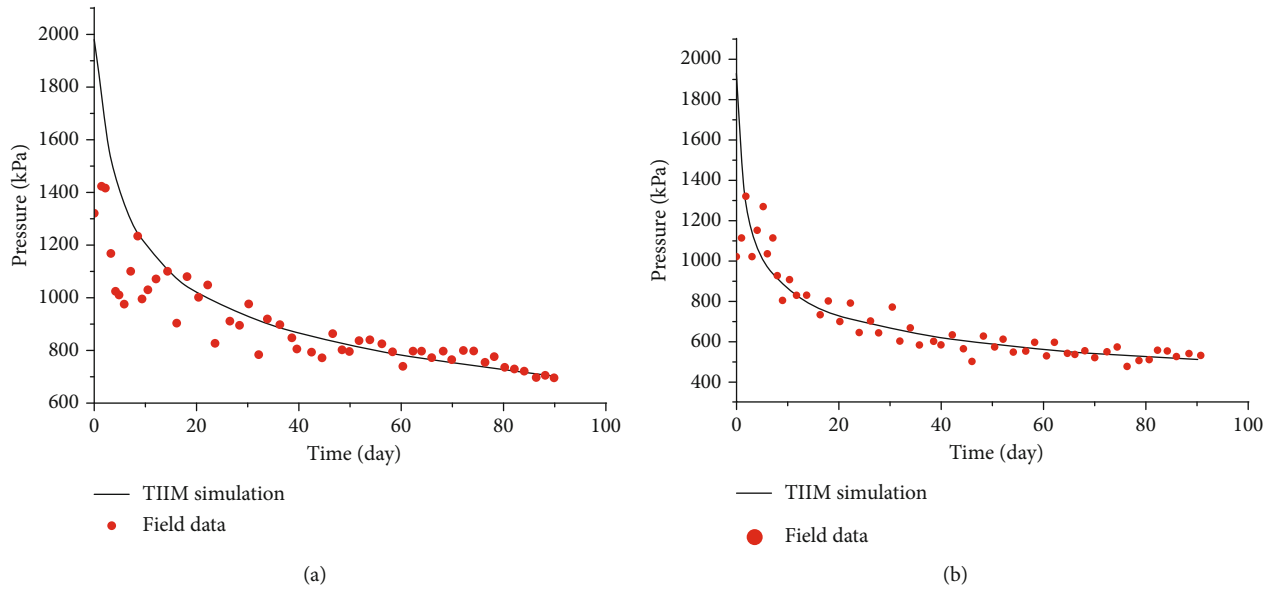


FIGURE 5: Field measurements and THM coupling model simulated methane pressures (a) for borehole #4 and (b) borehole #3. Red circles denote the field measured data, and solid lines represent the model simulation.

3. Model Validation

To validate the fully-coupled model, a field test was conducted in the K10 coal seam of the Zhongliangshan coal mine in Chongqing in southwestern China. The borehole layout for slotting and methane pressure determination is illustrated in Figure 3. Nine boreholes were drilled. Borehole #5 was used to perform high-pressure water jet slotting, borehole #6 was used to verify the slotting radius, and the other boreholes were used to detect the methane pressure. Slotting was stopped when water was observed in borehole #6. The depth of the K10 coal seam in the test is 575 m, the initial methane pressure was 1.9 MPa, the initial permeability was $1.7 \times 10^{-17} \text{ m}^2$, and the negative drainage pressure in the slotted borehole was 35 kPa. All parameters are listed in Table 1. The perfect symmetry of the coal seam and boreholes is shown as a two-dimensional model in Figure 4 and used to simulate methane extraction to simplify the calculation. The two-dimensional model is 150 m in length and 3 m in height. At the upper boundary of the model, we applied an evenly distributed normal stress according to depth. The left and right sides of the model are restrained from horizontal

displacement and insulated for methane and thermal transport purposes. The bottom boundary is restrained from normal displacement and insulated for methane and thermal transport. The above governing equations and complete set of coupled equations were solved by using the PDE module of COMSOL Multiphysics [39].

The comparative plot in Figure 5 represents that the THM coupling model can perfectly fit the data from the field measurement, and Figure 6 reveals that both the steady flow model and the THM coupling model can well represent the field data of methane extraction. For boreholes #3 and #4, the methane pressure decreases faster than the numerical results over a relatively short time. This is mainly because the stress distribution around the slot changes owing to the slotting process. Plastic deformation may have occurred, and the coal permeability is higher than the THM coupling model prediction [40]. After compaction and stress redistribution, the methane pressures were in good agreement with the numerical results. The results determined in the field also show good consistency with the effective radius and influence radius calculated by the steady flow model (Figure 6).

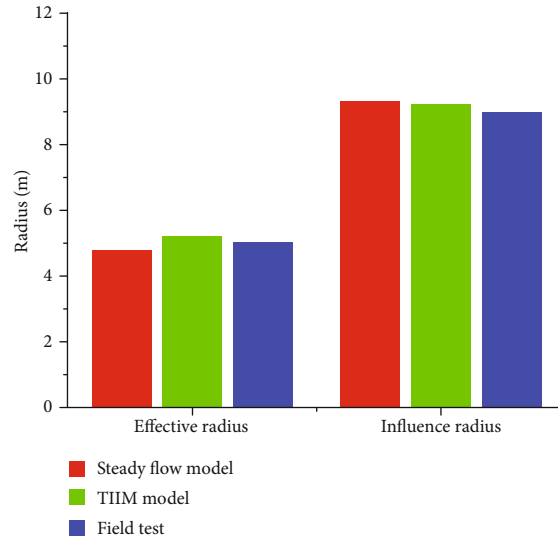


FIGURE 6: Effective radius and influence radius of methane extraction obtained from the steady flow model, THM coupling model, and field tests.

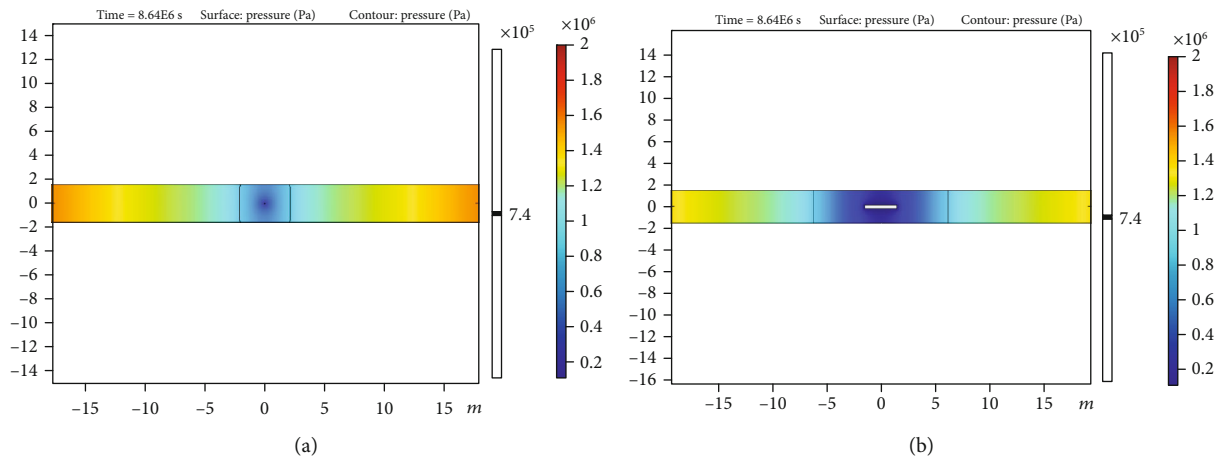


FIGURE 7: Comparison of a (a) traditional borehole and (b) slotted borehole after 100 days of extraction.

4. Analysis of Influencing factors

Methane flow in coal seams is controlled by a range of factors, including initial methane permeability, initial methane pressure, burial depth of coal seam, and extraction time. To better understand methane extraction after high-pressure water jet slotting, all of these factors should be analyzed based on the robust model. This provides information for optimizing borehole drilling and extraction time in practical operations in different coal seams with complicated parameters.

4.1. Comparison with a Traditional Borehole. Figure 7 shows the pressure distribution of methane for a traditional borehole with a diameter of 75 mm and a slotted borehole after 100 days of extraction. The black contour in Figure 7 represents 0.74 MPa. In the traditional borehole, the effective radius was 2.11 m, whereas the effective radius for the slotted borehole was 6.2 m. This indicates that the high-pressure

water jet slotting not only increases the exposed area but can substantially enhance the effective radius of methane extraction. The drilling of slotted boreholes in coal seams can be reduced by ~80% of that of traditional boreholes.

4.2. Influence of Extraction Time. Figure 8 shows the distribution of methane pressure in the coal seam after 1, 50, 300, 500, and 1000 days of extraction. The respective effective extraction radii are 1.77, 4.7, 9.78, 10.8, and 10.98 m, respectively. The fitting relationship between extraction time and effective radius (Figure 9) shows that the effective radius increases rapidly from the beginning until ~350 days and then increases slowly and remains nearly unchanged until 1000 days. In practical operations, the extraction time can be optimized to about 350 days.

4.3. Influence of Coal Burial Depth. To consider an actual situation of underground mining in China, we varied the coal

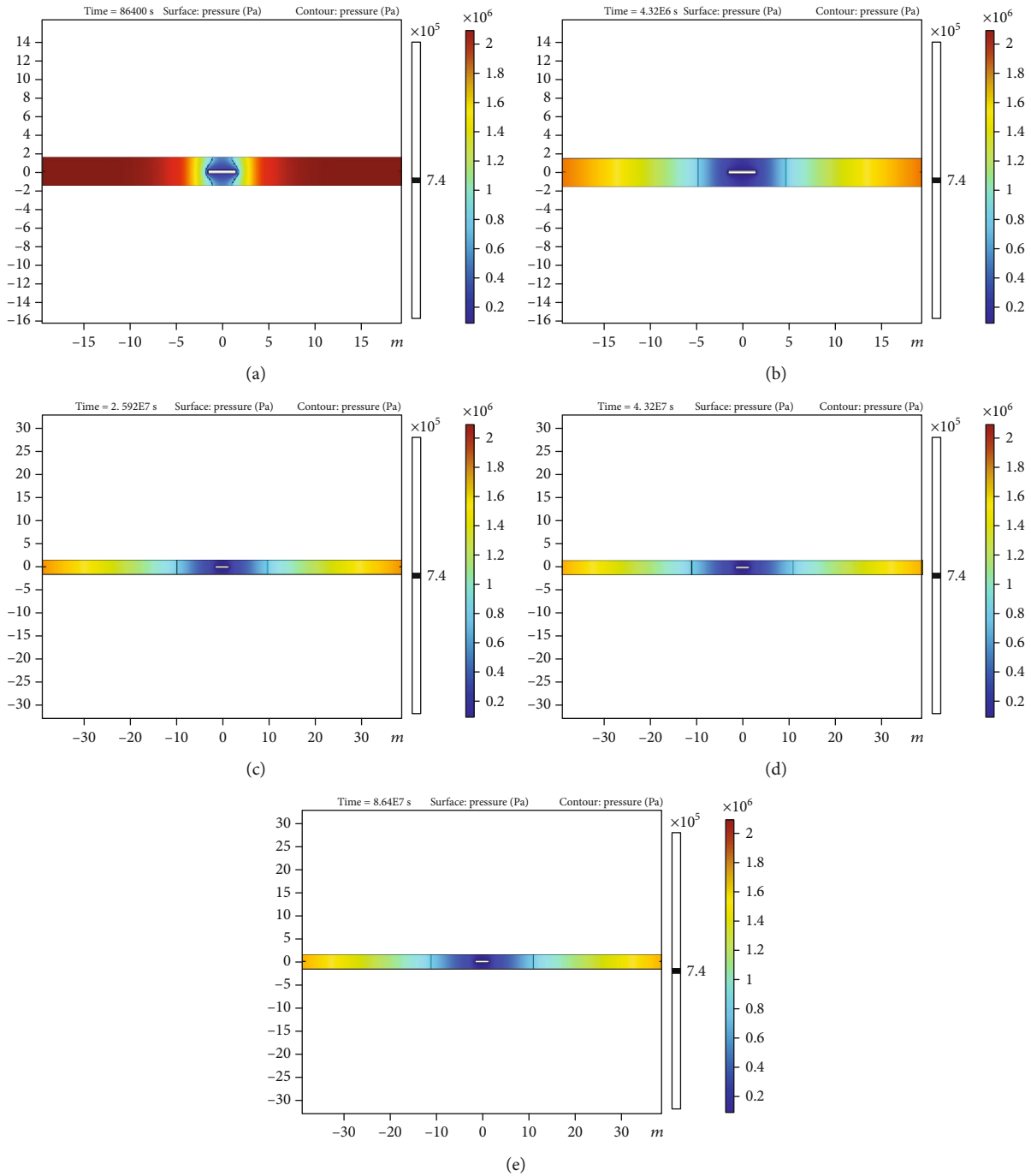


FIGURE 8: Methane pressure after different extraction times: (a) 1 day, (b) 50 days, (c) 300 days, (d) 500 days, and (e) 1000 days.

seam depth to 400, 600, 800, 1000, and 1200 m to determine the effective radius after high-pressure water jet slotting. Figure 10 shows that the effective radius of methane extraction decreases linearly with increasing coal seam depth. Increasing coal seam burial depth can increase the effective stress of the coal, which exponentially decreases the coal seam permeability. Deeper coal seams are also associated with higher temperatures, which further expand the coal matrix. Because the coal seam temperature is hard to change artificially, the investigation of burial depth is more appropri-

ate than temperature [45]. The restrained coal seam in the horizontal and vertical directions leads to a decrease of pores and fractures, which consequentially reduces the permeability.

4.4. Influence of Slot Radius. With regard to the high-pressure water jet slotting characteristics and coal mechanical parameters, we analyzed slot radii of 1, 1.5, 2.5, and 3 m. As illustrated in Figure 11, the effective radius of methane extraction increases linearly with increasing slot radius with

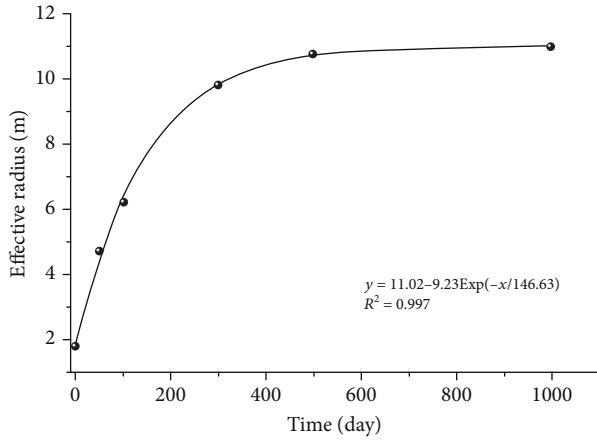


FIGURE 9: Relationship between extraction time and effective radius.

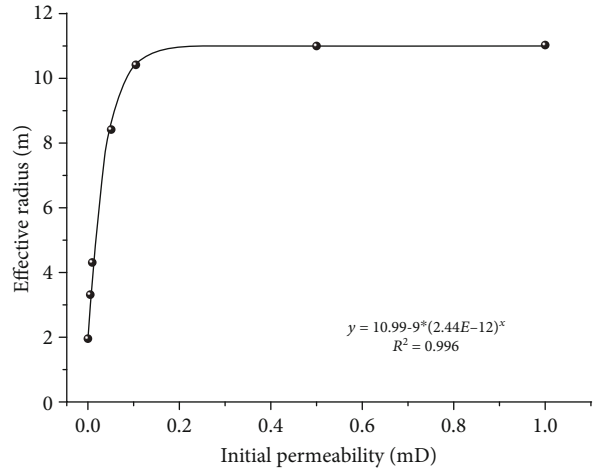


FIGURE 12: Relationship between initial permeability and effective radius (1 mD = 1×10^{-17} m²).

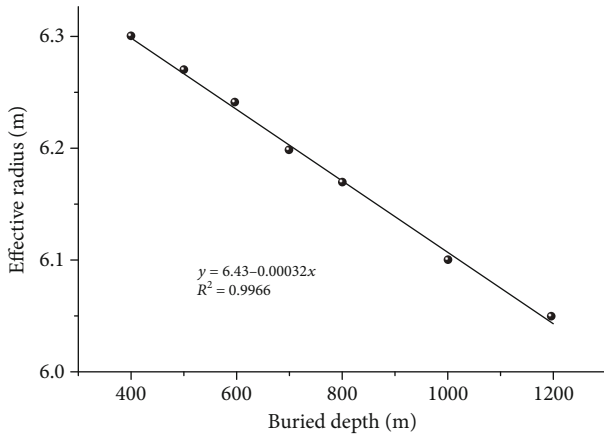


FIGURE 10: Relationship between coal burial depth and effective radius.

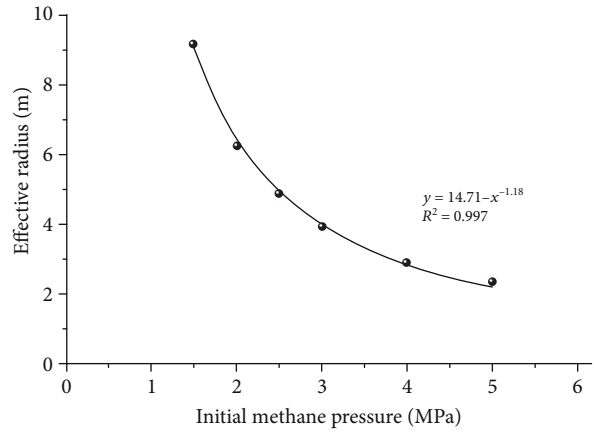


FIGURE 13: Relationship between methane pressure and effective radius.

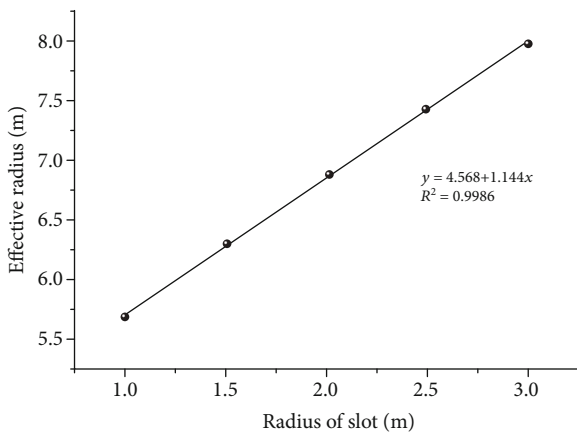


FIGURE 11: Relationship between slot radius and effective radius.

a slope of 1.144, which demonstrates that slotting not only enlarges the diameter of caves in coal seams but also varies the stress distribution and porosity [46, 47] around the caves and improves coal seam permeability. However, an improvement of slotted radius is challenging for pumps and pipelines.

4.5. Influence of Initial Permeability. Figure 12 shows an exponential relationship between the effective radius of methane extraction and initial coal seam permeability. The effective radius increases from 1.94 to 8.43 m after 100 days of extraction when the initial permeability of coal seam increases from 0.001 to 0.05 mD. Additionally, a slight increase of coal seam permeability can strongly enhance the effective radius of methane extraction when the initial permeability is <0.1 mD. During practical methane extraction in low-permeability coal seams, high-pressure water jet slotting, hydraulic fracturing, protective layer mining, and pre-splitting blasting can be applied to improve coal seam permeability and reduce extraction time.

4.6. Influence of the Initial Methane Pressure. Figure 13 shows the correlation between initial methane pressure and effective radius of methane extraction. The effective radius decreases following a power function with increasing initial methane pressure. Higher initial methane pressure can linearly improve the pressure gradient, which promotes methane flow by Darcy's law (Equation (1)). The elevated methane

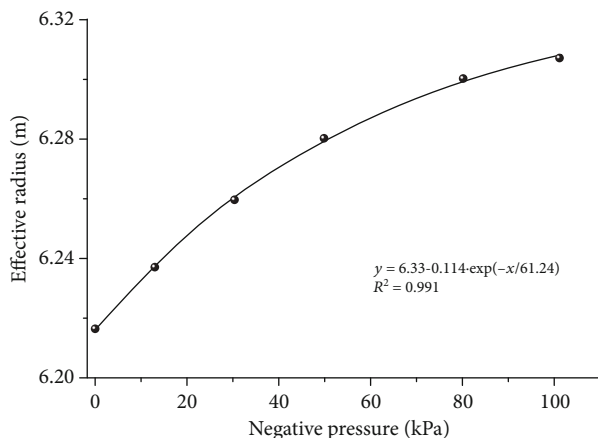


FIGURE 14: Correlation between negative pressure and effective radius.

pressure also enhances the amount of methane adsorbed via the Langmuir function, which leads to adsorption-induced swelling in the coal matrix and shrinks the tunnels for methane flow. During the methane extraction, the rapidly decreasing methane pressure increases the effective stress (ground stress minus the methane pressure) of the coal seams, which exponentially reduces the permeability. Hence, the predominant effect of effective stress variation largely retards methane extraction. Coal seams with higher initial methane pressure not only introduce a high risk of coal and methane outburst but also complicate methane drainage. Figure 14 shows that the effective radius of methane extraction slightly increases from 6.22 m for spontaneous flow to 6.31 m when the pipelines are under an absolute vacuum of 101 kPa (negative pressure).

5. Conclusions

We used a fully-coupled thermohydrromechanical model to simulate methane extraction after high-pressure water jet slotting and conducted field measurements to confirm the model reliability and validity. We compare our results with a traditional borehole and demonstrate the influence of extraction time, coal burial depth, slot dimensions, initial permeability, and initial coal seam pressure. The conclusions are summarized here.

- (1) The effective radius in the K10 coal seam in the Zhongliangshan coal mine reached 4 m after 16 days of methane extraction and 5 m after 80 days. The results are in good agreement with the steady flow model and THM coupling model simulation
- (2) Compared with a traditional borehole, a slotted borehole can increase the effective radius by a factor of 1.94 after 100 days of methane extraction
- (3) The extraction time largely enhances the effect radius up until ~350 days of methane production. Increasing coal seam burial depth is associated with a linear decrease of effective radius, and the effective radius increases linearly with slot radius

- (4) Permeability exponentially increases the effective radius of methane extraction, especially when the initial permeability of coal seam increases from 0.001 to 0.05 mD. The effective radius is reduced following a power function with increasing initial methane pressure. The influence of negative pressure on the effective radius is negligible

Data Availability

The data used to support the findings of this study are available from the corresponding author upon request.

Conflicts of Interest

The authors declare no competing financial interest.

Acknowledgments

This work is funded by the National Natural Science Foundation of China (grant no. 51974042) and the QianJiaoHe KY Zi [2019]073. The first author would like to thank the China Scholarship Council (no. 201406050029) for financial support.

References

- [1] L. Yuan, "Theories and techniques of coal bed methane control in China," *Journal of Rock Mechanics and Geotechnical Engineering*, vol. 3, no. 4, pp. 343–351, 2011.
- [2] S. Tao, S. Chen, and Z. Pan, "Current status, challenges, and policy suggestions for coalbed methane industry development in China: a review," *Energy Science & Engineering*, vol. 7, no. 4, pp. 1059–1074, 2019.
- [3] UNECE - United Nations Economic Commission for Europe (Methane to Markets Partnership), *Best Practice Guidance for Effective Methane Drainage and Use in Coal Mines. ECE Energy Ser. No. 31*, United Nations Publications, 2010.
- [4] L. Wang and Y. P. Cheng, "Drainage and utilization of Chinese coal mine methane with a coal-methane co- exploitation model: analysis and projections," *Resources Policy*, vol. 37, no. 3, pp. 315–321, 2012.
- [5] B. Li, J. Zhang, J. Wei, and Q. Zhang, "Preparation and sealing performance of a new coal dust polymer composite sealing material," *Advances in Materials Science and Engineering*, vol. 2018, Article ID 8480913, 10 pages, 2018.
- [6] Z. Zhang, D. Yan, X. Zhuang et al., "Hydrogeochemistry signatures of produced waters associated with coalbed methane production in the southern Junggar Basin, NW China," *Environmental Science and Pollution Research*, vol. 26, no. 31, pp. 31956–31980, 2019.
- [7] H. Wen, X. Cheng, J. Chen et al., "Micro-pilot test for optimized pre-extraction boreholes and enhanced coalbed methane recovery by injection of liquid carbon dioxide in the Sangshuping coal mine," *Process Safety and Environment Protection*, vol. 136, pp. 39–48, 2020.
- [8] Z. Luo, D. Li, B. Su, S. Zhang, and J. Deng, "On the time coupling analysis of explosion pressure and intermediate generation for multiple flammable gases," *Energy*, vol. 198, article 117329, 2020.

- [9] B. Su, Z. Luo, T. Wang, J. Zhang, and F. Cheng, "Experimental and principal component analysis studies on minimum oxygen concentration of methane explosion," *International Journal of Hydrogen Energy*, vol. 45, no. 21, pp. 12225–12235, 2020.
- [10] T. Wang, Z. Luo, H. Wen et al., "Flammability limit behavior of methane with the addition of gaseous fuel at various relative humidities," *Process Safety and Environment Protection*, vol. 140, pp. 178–189, 2020.
- [11] Z. Luo, R. Li, T. Wang et al., "Explosion pressure and flame characteristics of CO/CH₄/air mixtures at elevated initial temperatures," *Fuel*, vol. 268, article 117377, 2020.
- [12] Y. Lu, Y. Liu, X. Li, and Y. Kang, "A new method of drilling long boreholes in low permeability coal by improving its permeability," *International Journal of Coal Geology*, vol. 84, no. 2, pp. 94–102, 2010.
- [13] C. Liu, B. Xia, and Y. Lu, "Coalbed methane extraction using the self-oscillating water jet slotting method," *Energies*, vol. 11, no. 4, p. 897, 2018.
- [14] Y. Lu, S. Xiao, Z. Ge, Z. Zhou, Y. Ling, and L. Wang, "Experimental study on rock-breaking performance of water jets generated by self-rotatory bit and rock failure mechanism," *Powder Technology*, vol. 346, pp. 203–216, 2019.
- [15] B. Lin and C. Shen, "Coal permeability-improving mechanism of multilevel slotting by water jet and application in coal mine gas extraction," *Environment and Earth Science*, vol. 73, no. 10, pp. 5975–5986, 2015.
- [16] T. Lu, H. Yu, T. Zhou, J. Mao, and B. Guo, "Improvement of methane drainage in high gassy coal seam using waterjet technique," *International Journal of Coal Geology*, vol. 79, no. 1–2, pp. 40–48, 2009.
- [17] Y. Lu, J. Tang, Z. Ge, B. Xia, and Y. Liu, "Hard rock drilling technique with abrasive water jet assistance," *International Journal of Rock Mechanics and Mining Sciences*, vol. 60, pp. 47–56, 2013.
- [18] L. Bai-quan, L. Ting, Z. Quan-le, Z. Chuan-jie, Y. Fa-zhi, and Z. Zhen, "Crack propagation patterns and energy evolution rules of coal within slotting disturbed zone under various lateral pressure coefficients," *Arabian Journal of Geosciences*, vol. 8, no. 9, pp. 6643–6654, 2015.
- [19] Y. Li, D. Tang, H. Xu, Y. Meng, and J. Li, "Experimental research on coal permeability: the roles of effective stress and gas slippage," *Journal of Natural Gas Science and Engineering*, vol. 21, pp. 481–488, 2014.
- [20] X. Cui and R. M. Bustin, "Volumetric strain associated with methane desorption and its impact on coalbed gas production from deep coal seams," *American Association of Petroleum Geologists Bulletin*, vol. 89, no. 9, pp. 1181–1202, 2005.
- [21] H. Wang, B. Xia, Y. Lu, Z. Ge, and J. Tang, "Experimental study on sonic vibrating effects of cavitation water jets and its promotion effects on coalbed methane desorption," *Fuel*, vol. 185, pp. 468–477, 2016.
- [22] F. Hao, M. Liu, and W. Zuo, "Coal and gas outburst prevention technology and management system for Chinese coal mines: a review," in *Mine Planning and Equipment Selection*, pp. 581–600, Springer, 2014.
- [23] Z. Ge, X. Mei, Y. Jia, Y. Lu, and B. Xia, "Influence radius of slotted borehole drainage by high pressure water jet," *Cai-kuang yu Anquan Gongcheng Xuebao*, vol. 31, no. 4, p. 65, 2014.
- [24] X. Heping, W. Jinhua, S. Baohong et al., "New idea of coal mining: scientific mining and sustainable mining capacity," *Journal of China Coal Society*, vol. 37, no. 7, pp. 1069–1079, 2012.
- [25] M. Pillalamarry, S. Harpalani, and S. Liu, "Gas diffusion behavior of coal and its impact on production from coalbed methane reservoirs," *International Journal of Coal Geology*, vol. 86, no. 4, pp. 342–348, 2011.
- [26] M. B. Kirkham, *Principles of Soil and Plant Water Relations*, Academic Press, 2nd edition, 2014.
- [27] Ф. И. Котяхов, *Основы Физики Нефтяного Пласта*, Гос. научнотехн. Изд-во нефтяной и горно-топливной литературы, 1956.
- [28] G. Hong-yu and S. Xian-bo, "An experimental measurement of the threshold pressure gradient of coal reservoirs and its significance," *Natural Gas Industry*, vol. 30, no. 6, pp. 52–54, 2010.
- [29] L. Jing, C. F. Tsang, and O. Stephansson, "DECOVALEX—an international co-operative research project on mathematical models of coupled THM processes for safety analysis of radioactive waste repositories," *International Journal of Rock Mechanics and Mining Sciences*, vol. 32, no. 5, pp. 389–398, 1995.
- [30] Z. Chen, J. Liu, D. Elsworth, L. D. Connell, and Z. Pan, "Impact of CO₂ injection and differential deformation on CO₂ Injectivity under in-situ stress conditions," *International Journal of Coal Geology*, vol. 81, no. 2, pp. 97–108, 2010.
- [31] Y. Wu, J. Liu, D. Elsworth, H. Siriwardane, and X. Miao, "Evolution of coal permeability: contribution of heterogeneous swelling processes," *International Journal of Coal Geology*, vol. 88, no. 2–3, pp. 152–162, 2011.
- [32] N. Fan, J. Wang, C. Deng, Y. Fan, Y. Mu, and T. Wang, "Numerical study on enhancing coalbed methane recovery by injecting N₂/CO₂ mixtures and its geological significance," *Energy Science & Engineering*, vol. 8, no. 4, pp. 1104–1119, 2020.
- [33] H. Qu, J. Liu, Z. Chen et al., "Complex evolution of coal permeability during CO₂ injection under variable temperatures," *International Journal of Greenhouse Gas Control*, vol. 9, pp. 281–293, 2012.
- [34] I. Langmuir, "The adsorption of gases on plane surfaces of glass, mica and platinum," *Journal of the American Chemical Society*, vol. 40, no. 9, pp. 1361–1403, 1918.
- [35] T. Y. Zhang Xiang, "Experimental study on isotherms adsorption of coal on gas under different temperatures," *Coal Engineering*, vol. 1, no. 4, pp. 87–89, 2011.
- [36] W. Zhiyin and L. Yunpeng, *Rheological Theory of Rock and Numerical Simulation*, Science Press, 2008.
- [37] Z. Lai, *Experimental studies and simulations on coupled multiphysics of CO₂ sequestration in deep coal seam*, China University of Mining and Technology, 2009.
- [38] S.-Y. Wu and W. Zhao, "Analysis of effective stress in adsorbed methane-coal system," *Chinese Journal of Rock Mechanics and Engineering*, vol. 24, pp. 1674–1678, 2005.
- [39] COMSOL, *COMSOL Multiphysics 5.3 User Guide. Manual*, COMSOL AB, Stockholm, Sweden, 2014.
- [40] S. Xiao, Z. Ge, Y. Lu, Z. Zhou, Q. Li, and L. Wang, "Investigation on coal fragmentation by high-velocity water jet in drilling: size distributions and fractal characteristics," *Applied Sciences*, vol. 8, no. 10, p. 1988, 2018.
- [41] J. Pan, Z. Meng, Q. Hou, Y. Ju, and Y. Cao, "Coal strength and Young's modulus related to coal rank, compressional velocity

- and maceral composition,” *Journal of Structural Geology*, vol. 54, pp. 129–135, 2013.
- [42] Z. Xiong, C. Song, C. Su et al., “Uniaxial compression creep relaxation and grading of coal samples via tests on the progressive failure characteristics,” *Geofluids*, vol. 2019, Article ID 9069546, 13 pages, 2019.
- [43] Y. Q. Tao, J. Xu, M. J. Cheng, S. C. Li, and S. J. Peng, “Theoretical analysis and experimental study on permeability of gas-bearing coa,” *Chinese Journal of Rock Mechanics and Engineering*, vol. 28, pp. 3364–3370, 2009.
- [44] B. Leśniak, L. Slupik, and G. Jakubina, “The determination of the specific heat capacity of coal based on literature data,” *Chemik*, vol. 67, no. 6, pp. 560–571, 2013.
- [45] F. Gao, Y. Xue, Y. Gao, Z. Zhang, T. Teng, and X. Liang, “Fully coupled thermo-hydro-mechanical model for extraction of coal seam gas with slotted boreholes,” *Journal of Natural Gas Science and Engineering*, vol. 31, pp. 226–235, 2016.
- [46] Q. Zou, B. Lin, J. Liang et al., “Variation in the pore structure of coal after hydraulic slotting and gas drainage,” *Adsorption Science and Technology*, vol. 32, no. 8, pp. 647–666, 2014.
- [47] Q. ZouLe, B. Q. Lin, T. Liu, X. C. Hu, and C. S. Zheng, “Variations in coalbed gas content, initial gas desorption property and coal strength after drilling-slotting integration technique and gas drainage: insight into pore characteristics,” *International Journal of Oil, Gas and Coal Technology*, vol. 15, no. 3, p. 235, 2017.

Research Article

An Improved C-V Model and Application to the Coal Rock Mesocrack Images

Yulong Chen and Hongwei Zhang 

School of Energy and Mining Engineering, China University of Mining and Technology, Beijing, China

Correspondence should be addressed to Hongwei Zhang; hongwei@cumtb.edu.cn

Received 30 April 2020; Revised 10 May 2020; Accepted 16 May 2020; Published 17 July 2020

Academic Editor: Zhengyang Song

Copyright © 2020 Yulong Chen and Hongwei Zhang. This is an open access article distributed under the Creative Commons Attribution License, which permits unrestricted use, distribution, and reproduction in any medium, provided the original work is properly cited.

In order to accurately and comprehensively obtain information about coal rock mesocrack images, image processing technique based on partial differential equation (PDE) is introduced in order to expound on the active contour model without edges and overcome the deficiency of the C-V model. The improved C-V model is adopted in order to process mesoimages of coal rocks containing single and multiple cracks and obtain high-quality binary images of coal rock mesocracks and the effective characteristic parameters of coal rock mesostructures through quantitative processing, which will lay solid foundations for the follow-up research into coal rock seepage computation and damage calculation. Studies have shown that, compared to the original C-V model, the improved model achieves better image segmentation effects and more accurate quantitative information about coal rock mesostructures for coal rock mesoimages with low contrast ratios and nonuniform grayscale, a fact showing that it can be applied to the calculation of coal rock permeability and damage factors.

1. Introduction

Underground coal mining will inevitably trigger an inner stress response of coal rock and cause the concentration or release of local stress, thus resulting in the buckling failure of coal rock. In this process, different stress states and amplitudes will bring about different forms of destruction to the rock. The material composition within coal rock and its primary physical and mechanical structure determine its stress and strain status under the external load, which further controls the macromechanical response and failure mechanism. Cracks are generated under high stress in a certain area of underground mining, and the formed cracks of the unstable coal rock in turn affect its inner stress and strain state, thus causing the deflection of local principal stress and improving or worsening the stress state of local coal rock. Research on the damage to coal rock on the mesoscale mainly focuses on the crack initiation, expansion, connection, direction, scale, and properties. These important factors provide significant guidance and design basis for the prevention and control of coal rock instability and failure.

The digital image processing technique provides an effective means for the precise measurement and quantitative analysis of the materials on the mesoscale and opens up a new way for scientists and engineers to gain a comprehensive understanding of the heterogeneity, internal structure characteristics, and morphological characteristics of each component and the corresponding mesomechanic characteristics [1]. The image segmentation algorithms based on threshold segmentation, edge detection, and region growth have been widely applied to the processing of coal rock mesoimage processing. In order to extract the image characteristics of the different compositions of granite, Chen et al. [2, 3] proposed a multithreshold region partitioning method based on color space. Yue et al. [4, 5] combined digital image processing with numerical methods, such as FEM and FDM, in order to study the influence of the mesostructure of geotechnical engineering materials on inner stress distribution. Zhu et al. [6] also utilized the regional growth algorithm in order to extract the mesostructural information of marbles. Xu et al. [7] used digital image processing technique to study the internal mesostructure characteristics of soil-rock mixture, and by

using the geometry vectorization transformation technique, the vector concept model that can represent the actual internal mesostructures of soil-rock mixture is constructed. Liu et al. [8] expounded on the rock mesoimage analysis method based on LS-SVM. Yu et al. [9] introduced a digital image processing technique to the analysis system of rock failure processes and adopted a digital image processing technique in order to characterize the heterogeneity of rocks and establish a numerical model reflecting the mesostructure of materials.

Digital image processing includes the removal of noise, contrast enhancement, recovery, segmentation, and characteristic extraction of images through computers. The above-mentioned literature review is based on traditional image processing methods, which can inhibit noise but possess the deficiencies of obfuscation of detailed image information, susceptibility to interference, and low accuracy. It is worth noticing that it is inaccurate to process images obtained through coal rock mesomechanic experiments that are characterized by low contrast ratios, multiple details, and weak boundary information, which restricts the fundamental research on the calculation of coal permeability, coal rock damage, and multifield crack coupling. Compared to traditional image processing methods, image processing methods based on partial differential equations (PDE) have the distinctive advantages of conserving the marginal detailed information and realizing nonlinear noise removal while eliminating image noise. PDE-based methods also utilize numerical analysis theories and PDE, which are characterized by high speed, accuracy, and stability. These methods enable analysis from the perspective of the space geometry of the image on the basis of the natural connection between the geometric images and the equation in order to establish an image processing model that is close to reality. The C-V model is a widely applied PDE image processing method. This paper introduces and explains the principle of the C-V model and proposes an improved model based on image enhancement function. With respect to coal rock mesoimages with nonuniform grayscales and low contrast ratios, the improved C-V model obtains high-quality segmentation images through processing experiments on mesoimages with single and multiple cracks. This method also obtains coal rock mesostructural information through the binary image quantization process and studies the permeability coefficient and damage variables of coal rocks containing cracks, which provides a reliable support for the in-depth research on the mesomechanic characteristics of coal rocks.

2. The C-V Model Based on PDE

2.1. Image Processing Based on PDE. Currently, no universal segmentation theory can be applied to image segmentation technology. The proposed segmentation algorithms are mainly targeted at specific issues. When handling objectives with fuzzy boundaries or dispersed objectives in the image, the traditional segmentation technologies [10] are plagued by low efficiency and precision. If image segmentation is boiled down to an issue related to functional energy minimization, this issue can be converted into a PDE in order to exact solutions through gradient descent flows. The image processing method based on PDE is exercised in accordance with the

abovementioned concept. This method can effectively segment the objectives with fuzzy boundaries or dispersed objectives. With the segmentation effect reaching subpixel precision [11], it can automatically detect the inside and outside contours of the image and possess noise immunity. Because of these unique advantages, the image processing method based on PDE has been widely accepted, and it is one of the hot issues in the field of image segmentation. So far, it has been applied to every field of image processing.

The basic concept of the image processing method based on PDE is to evolve an image, a curve, or a curved face in the PDE model and to obtain the expected result by solving this equation [12]. The general type of a PDE of an unknown function $u(x_1, x_2, x_3, \dots, x_n)$ is as follows [13]:

$$\sum_{i,j=1}^n a_{ij} \frac{\partial u^2}{\partial x_i \partial x_j} + \sum_{i=1}^n b_i \frac{\partial u}{\partial x_i} + cu = f, \quad (1)$$

where a_{ij} , b_i , c , and f refer to coefficients and $a_{ij} = a_{ji}$; x_1 , x_2 , x_3 , and x_n are independent variables and contain a time variable.

2.2. Image Segmentation Based on the C-V Model. The C-V model proposed by Chan and Vese [14, 15] has taken into account the certain differences between the average grayscales within the region. If the curve is expressed by a parameter equation, then the segmentation issue can be boiled down to the minimization (the functional of the minimum Ω area: $\Omega = C + \Omega_0 + \Omega_b$) of the energy functional of a closed curve (boundary segmentation):

$$J(C, c_0, c_b) = \mu \oint_C ds + \lambda_0 \iint_{\Omega_0} (I - c_0)^2 dx dy + \lambda_b \iint_{\Omega_b} (I - c_0)^2 dx dy, \quad (2)$$

where I is the image grayscale matrix; C is the closed curve; Ω_0 is the internal area of the image divided by C ; Ω_b is the external area; c_0 and c_b refer to the arithmetic mean value of the grayscale of the input image, $I(x, y)$, at Ω_0 and Ω_b ; and μ , λ_0 , and λ_b are the weight coefficients of each energy item.

Variation level methods are adopted and embedded in function u and introduced in order to obtain the function of the embedded function u :

$$J(u, c_0, c_b) = \mu \iint_{\Omega} \delta(u) |\nabla u| dx dy + \lambda_0 \iint_{\Omega_0} H(u) (I - c_0)^2 dx dy + \lambda_b \iint_{\Omega_b} [1 - H(u)] (I - c_0)^2 dx dy, \quad (3)$$

where $H(u)$ is the function of Heaviside.

Under fixed function u , the following formula is obtained on the basis of the minimum Equation (3) of c_0 and c_b :

$$c_i = \frac{\iint_{\Omega_i} I dx dy}{\iint_{\Omega_i} dx dy} \quad (i = 0, b). \quad (4)$$

Under the fixed c_0 and c_b , the following formula is obtained under the minimum Equation (3) of u :

$$\frac{\partial u}{\partial t} = \delta_\varepsilon \left[\mu \operatorname{div} \left(\frac{\nabla u}{|\nabla u|} \right) - \lambda_0 (I - c_0)^2 + \lambda_b (I - c_b)^2 \right]. \quad (5)$$

In which,

$$\delta_\varepsilon(u) = \frac{dH_\varepsilon(u)}{du}, \quad (6)$$

where $H_\varepsilon(u)$ refers to the arbitrary function that meets the $\lim_{\varepsilon \rightarrow 0} H_\varepsilon(u) = H(u)$. Equations (4) and (5) are synthesized in order to obtain the steady-state solution as well as the segmentation results.

3. Improved C-V Model

3.1. Improved C-V Model. The C-V model can effectively detect the weak or fuzzy edge of images, which testifies to the high segmentation accuracy, simple calculation, and noise immunity. These advantages have substantially expanded its applied range. However, the evolutionary velocity $\partial u / \partial t$ of the level set function of the C-V model is intimately related to the mean difference ($c_0 - c_b$) between the internal and external grayscales of the evolving curve in image I . When $c_0 \approx c_b$, or the internal and external grayscales of the evolving curve are close to each other, the early iterations give rise to the slight changes in the level set function u ; under such circumstances, more iterations are required (sometimes more orders of magnitudes are needed) so as to displace the evolving curve. For the images with nonuniform grayscale and low contrast ratio, such as the coal rock images, the slight grayscale difference between the foreground and the background is prone to cause $c_0 \approx c_b$ in the C-V model, thus leading to the low segmentation efficiency. At the same time, the non-uniform grayscale is also prone to cause the segmentation of the background as false foreground, which will greatly reduce the image processing effect. Therefore, for the images, especially the coal rock images with nonuniform grayscale and low contrast ratio, the application of the C-V model has been enormously restricted.

In light of the aforesaid analysis, in order to enhance the utilization effect of the C-V model, it is necessary to improve the C-V model from the two perspectives of increasing the image contrast ratio and the equalization of image grayscale. By mapping the grayscale value, with a narrow grayscale distribution range, of images to be processed into a broadband output value, the contrast ratio of the target area can be effectively improved. The typical methods include logarithm transformation and power transformation. Gonzalez et al. [10] also point out that if the image pixel occupies all the gray levels and are evenly distributed, then the image possesses high contrast and varied gray tone. The image's grayscale is equalized using a histogram equalization method by effectively expanding the common grayscale. When the foreground and background grayscales are close to each other (nonuniform grayscale), the increase in the local con-

trast of images (without influencing the overall contrast ratio) will help with the better distribution of image grayscale on the histogram. In the meantime, in the aforesaid operation, the image grayscale value is prone to approach the two ends of the gray level, forming impulse noise. However, noise of this kind must be eliminated in order to maintain the efficiency of level set evolution. The median filtering function adopts the observation window consisting of odd sampling and checks the samples in the input signal in order to judge whether this sample can meet the signal requirements (eliminate the noise). The numerical values in the observation window are subjected to rank ordering with the median in the middle of the observation window as the output. Then, the earliest values are abandoned and new samples are obtained. In this way, the median filtering function can eliminate impulse noise while preserving edge characteristics.

This paper adopts an image enhancement function, $G(I)$, that combines power transformation, logarithm transformation, gray equalization, and a median filtering function to replace the image grayscale matrix, I , in the energy function of the original C-V model (Equation (2)). The results are listed below:

$$J(C, c'_0, c'_b) = \mu \oint_c ds + \lambda_0 \iint_{\Omega_0} [G(I) - c'_0]^2 dx dy + \lambda_b \iint_{\Omega_b} [G(I) - c'_b]^2 dx dy, \quad (7)$$

where c'_0 and c'_b represent the grayscale arithmetic mean values of the image at Ω_0 and Ω_b , respectively. In this way, the image enhancement function, $G(I)$, has increased the difference between the internal and external grayscale averages of the evolving curve ($c'_0 - c'_b$), thus greatly reducing the possibility that the internal and external grayscale averages of the evolving curve are close to each other and obtaining a higher level of set evolutionary velocity and better image processing effects.

The aforesaid image enhancement function, $G(I)$, can be specified as follows:

$$G(I) = \operatorname{med} \left\{ \left(\int_0^{F(I)} p_f(u) du \right)_k \mid k = 1, 2, 3, \dots, s \times r \right\}, \quad (8)$$

where $s \times r$ is the size of the median filter, with s and r as odd numbers; $p_f(u)$ is the grayscale distribution density function of image $F(I)$; and $G(I)$ is the grayscale matrix of the transformed images of the uniform random variable in $F(I)$ distribution interval, which is monotonic and nondecreasing. $F(I)$ can be expressed as follows:

$$F(I) = cI^\gamma, \quad (9)$$

or

$$F(I) = c \lg(1 + I), \quad (10)$$

where c is the constant of improving contrast. Equation (9) presents the stretching of contrast based on power

transformation, and Equation (10) introduces the improved contrast based on logarithm transformation.

By following the C-V derivation process, the minimum value of functional J against u is calculated as follows:

$$\frac{\partial u}{\partial t} = \delta_\varepsilon \left[\mu \operatorname{div} \left(\frac{\nabla u}{|\nabla u|} \right) - \lambda_0 [G(I) - c'_0]^2 + \lambda_b [G(I) - c'_b]^2 \right]. \quad (11)$$

In the original C-V model, the regularized Heaviside function must be conformed to the condition $\lim_{\varepsilon \rightarrow 0} H_\varepsilon(u) = H(u)$. The improved C-V model in this paper selects the following regularized Heaviside function:

$$H_\varepsilon(z) = \frac{1}{2} \left(1 + \frac{2}{\pi} \arctan \frac{z}{\varepsilon} \right). \quad (12)$$

Such regularized function is an odd symmetric function. Parameter ε is used in order to control the frequency of $H_\varepsilon(z)$ and change it from 0 to 1.

3.2. Numerical Implementation of the Improved C-V Model.

The numerical calculation scheme of PDE includes the explicit, implicit, and semi-implicit schemes. The explicit scheme refers to the direct calculation, which can be easily understood but is prone to the accumulation and propagation of error, which testifies to its low algorithm stability. The implicit scheme has the advantage of high stability but usually gives rise to the nonlinear simultaneous algebraic equation. It is usually accompanied by more complicated calculations compared to the explicit scheme. The semi-implicit scheme usually generates a linear difference equation. Different from the nonlinear simultaneous algebraic equation, it usually requires much easier numerical calculation; at the same time, the semi-implicit scheme is also characterized by high stability, and thus, it is widely applied to PDE numerical calculation. Therefore, the semi-implicit scheme is adopted in this paper.

Parameters λ_0 and λ_b refer to the weight coefficients of each energy item, representing the importance of the segmentation part. The foreground segmentation in image segmentation means the segmentation of the background and vice versa. Therefore, $\lambda_0 = \lambda_b = 1$. A discretization scheme combining forward difference and backward difference is adopted with the improved C-V model's semi-implicit numerical calculation scheme:

$$u_{ij}^{t+1} = u_{ij}^t + \tau \delta_\varepsilon u_{ij}^t \left\{ \mu P(u_{ij}^{t+1}) - [(G(I))_{ij} - c'_0]^2 + [(G(I))_{ij} - c'_b]^2 \right\}, \quad (13)$$

in which

$$P(u_{ij}^{t+1}) = D_x^{(-)} \left(\frac{D_x^{(+)}(u_{ij}^{t+1})}{\left[(D_x^{(+)}(u_{ij}^t))^2 + (D_y^{(0)}(u_{ij}^t))^2 \right]^{1/2}} \right) + D_y^{(-)} \left(\frac{D_y^{(+)}(u_{ij}^{t+1})}{\left[(D_y^{(+)}(u_{ij}^t))^2 + (D_x^{(0)}(u_{ij}^t))^2 \right]^{1/2}} \right). \quad (14)$$

Under the regularized Heaviside function, the following calculation is applied to the internal and external image grayscale averages of the current evolving curve (zero level set) in order to avoid the troubles of detecting zero level sets:

$$c'_0{}^t = \frac{\sum_{i,j} H_\varepsilon(u_{ij}^t) (G(I))_{ij}}{\sum_{i,j} H_\varepsilon(u_{ij}^t)}, \quad (15)$$

$$c'_b{}^t = \frac{\sum_{i,j} [1 - H_\varepsilon(u_{ij}^t)] (G(I))_{ij}}{\sum_{i,j} [1 - H_\varepsilon(u_{ij}^t)]},$$

where $c'_0{}^t$ and $c'_b{}^t$ represent the image grayscale averages after t iterations.

4. Experiment Results and Analysis

4.1. Experiment Process and Results. In order to verify the feasibility and superiority of the method proposed in this paper, both the C-V model and the improved C-V model were adopted to process images of coal samples with single and multiple cracks with the specific procedure that is listed below:

Step (i) *Image Acquisition.* The mesoimages of geotechnical materials are usually obtained by the following: (1) digital camera, (2) CCD vidicon with observation made by a stereoscopic microscope or polarizing microscope, and (3) electron microscope (TEM or SEM) [16]. In this study, SEM was used to obtain the mesoimages of coal rock. Figure 1 shows a typical example of a coal containing cracks

Step (ii) *Image Segmentation.* The C-V model and improved C-V model were adopted for the segmentation of the aforesaid images. In this experiment, the semi-implicit scheme was adopted with parameters $\lambda_0 = \lambda_b = 1$, $\varepsilon = 1$, $\mu = 250$, and time step $\tau = 0.1$. The image segmentation effect based on the C-V model is shown in Figure 2 and the image segmentation effect based on the improver C-V model in Figure 3. The left images in Figures 2 and 3 introduce the distribution of the evolving curve (zero level set) on the original

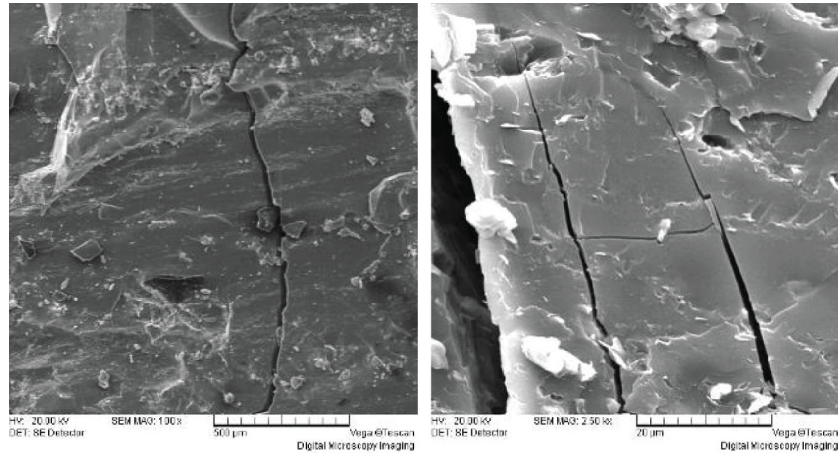
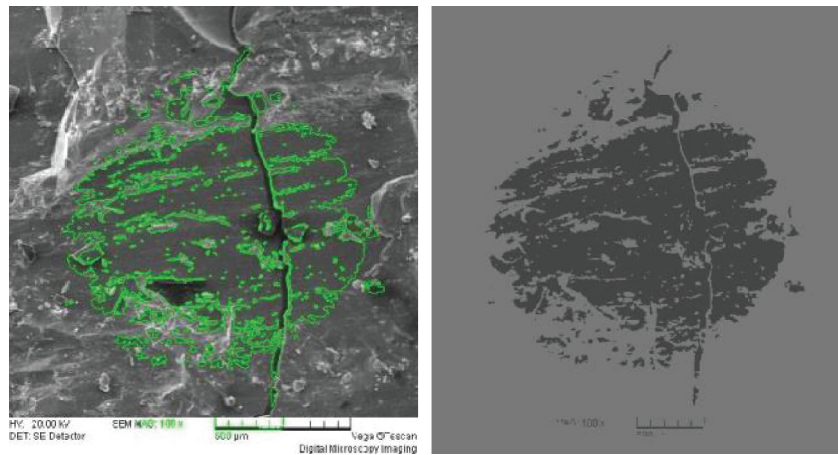
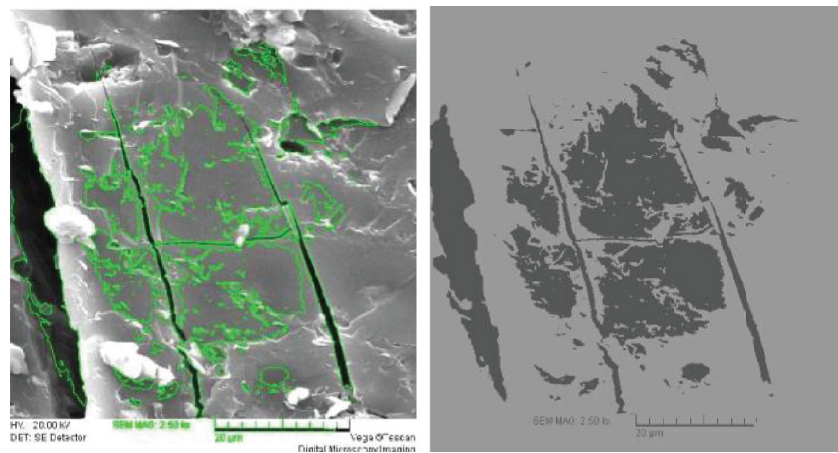


FIGURE 1: Original image of the coal sample containing cracks.



(a) Single crack



(b) Multicrack

FIGURE 2: Segmentation of the image by the C-V model (10000 times iteration).

image, and the right images present the image effect of this evolving curve (zero level set).

4.2. Analysis of the Experimental Results. Table 1 presents a comparison of the image segmentation effects and times based on the C-V model and the improved C-V model.

Table 1 shows that, for both single crack images and multiple crack images, the segmentation based on the C-V model does not have an ideal effect while the improved C-V model primarily reaches the segmentation effect and obtains a relatively clear crack profile. After 4000 times iterations, the method based on the C-V model still fails to reach the ideal

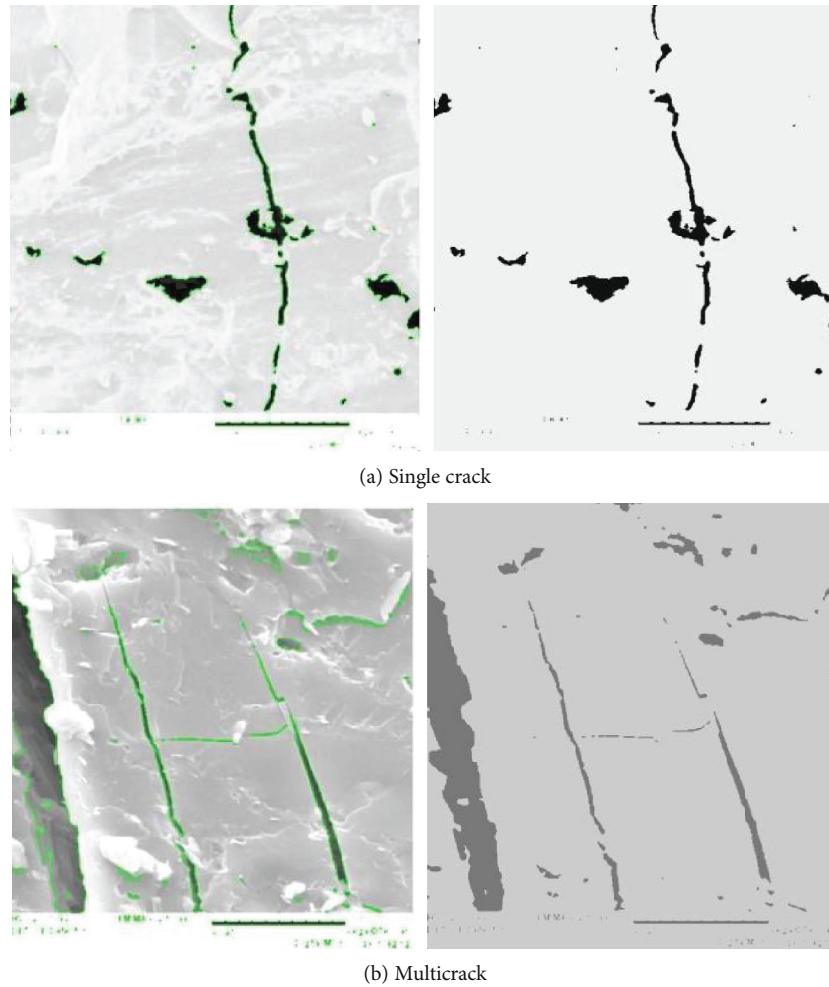


FIGURE 3: Segmentation of the image by the improved C-V model (4000 times iteration).

segmentation effect. Many background details are mixed with the foreground and segmented accompanied by the foreground. At the same time, many details of the foreground are not segmented because they are misunderstood as the background, which results in the failure of crack extraction; however, the improved C-V model results in better segmentation effects, as evidenced by the effective extraction of foreground objectives. Despite the fact that only a few background details, such as spots, are captured and distributed, they will be eliminated in the following processing in order to ensure the success of image segmentation. Besides, at the early stages of iteration (about 1000 times), the improved C-V model and original C-V model require similar amounts of time. Along with the increase in iteration times, especially at 4000 times iterations, the improved C-V model consumes 26 seconds less than the original C-V method when processing the single crack images and 7 seconds less when processing the multiple crack images. It can be seen that the improved C-V model can process the images with nonuniform grayscale and low contrast ratio better than the C-V model. Compared to the original C-V model, the improved C-V model can greatly enhance processing efficiency.

5. Application of Image Processing Results

5.1. Crack Information Obtainment. The aforesaid segmentation image based on the improved C-V model should be further processed in order to eliminate the interference of the background and obtain more effective crack information. The original image shows that the straight line portion that connects the top and bottom in Figure 3 is the crack and the other black spot-like part is a background detail, not a crack, which should be eliminated by the morphological method.

First, the improved C-V model is adopted in order to iterate image binarization for 4000 times and select the segmentation area in accordance with the original image by means of the use of the morphological function, *Bwselect*. A careful observation shows that the cracks in the original image have been segmented into several sections with the space between each section similar to the line connection. In this paper, the tangential direction growth method is utilized in order to reconnect the fractured cracks, as shown in Figure 4(b). At the same time, the morphological function, *Bwmorph*, is adopted in order to eliminate the burrs on edges and select the crack profile with the effect shown in

TABLE 1: Comparison between the effects of the C-V model and the improved C-V model.




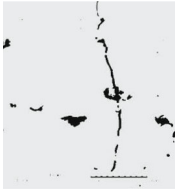

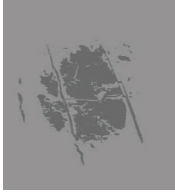


Conditions	1000 times iteration		4000 times iteration	
	Effect image	Time consumption	Effect image	Time consumption
Single crack				
C-V model		69 s		287 s
Improved C-V model		70 s		261 s
Multicrack				
C-V model		68 s		280 s
Improved C-V model		69 s		273 s

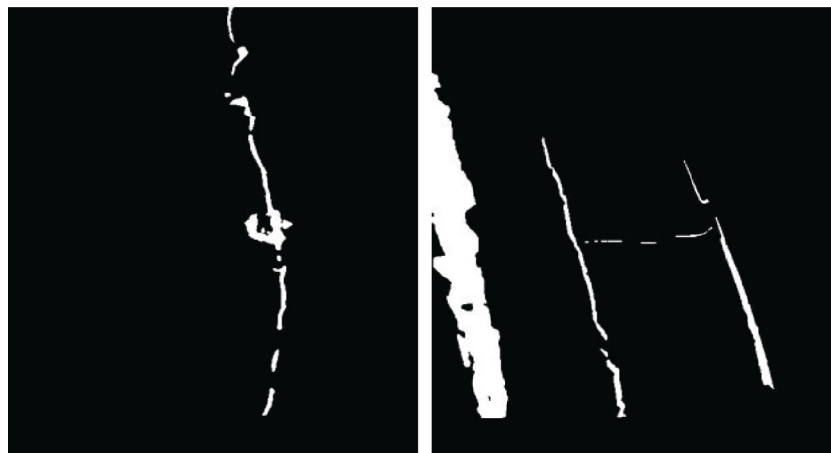
Figure 4(c). Then, the function, `Imfill`, is used to fill the crack profile with the effect shown in Figure 4(d). At last, Figure 4(e) is obtained by overlaying the aforesaid results on the original image. In comparison with the original image, the crack extracted can cover the original crack area, a fact showing the ideal processing results.

The function `Regionprops` is adopted to obtain the regional characteristic parameters in the image and crack information, as shown in Table 2. According to Table 2, it is convenient to obtain the area of each single-fracture or multiple-fracture crack (a), perimeter (p), long axis length (l), and short axis length (d) with the same standardized second central moment as the area, the radius (r) of the circle with the same area as the area, and the azimuth angle (α). For the multiple crack images, it is also possible to obtain the crack number, N , and group them according to the crack strike; it is worth noticing that further processing can obtain the space, m , between each group of cracks. Refer to the multiple crack images (Figure 5) for specific operation in this paper with a crack number of $N = 4$. In light of the different azimuth angle, these four cracks can be divided into two groups: crack 1, crack 2, and crack 4 in one group and crack 3 in another. Table 2 shows that the average azimuth of

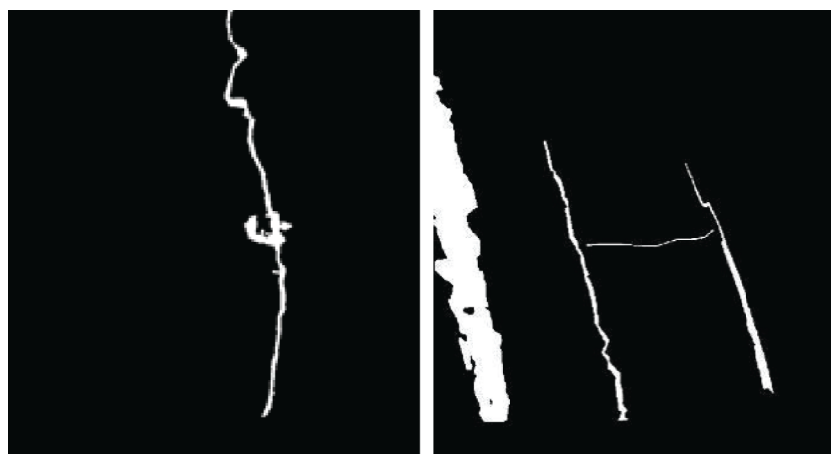
cracks 1, 2, and 4 is -74.4° . Therefore, a straight line is drawn on the binary image along the 15.6° direction (binary image with the crack) in order to intersect with the aforesaid three cracks. The distance between A and C is measured as 330 pixels; therefore, the space between these groups of cracks is 165 pixels.

5.2. Further Application of Crack Information Quantification. The mesocomposition and structure of coal rocks determine their stress-strain states under external force and control their macromechanical response and failure mechanisms. The existence and development of these mesocompositions and structures make the seepage-stress coupling of coal rock very complicated. Digital image processing technology provides an effective method of expressing the heterogeneity of coal rock from the perspective of mesophysical mechanic structure, which has made the mesoresearch on crack rock mass liquid-solid coupling more direct and efficient.

The method based on the improved C-V model is adopted in order to process the coal rock image containing cracks and obtain various two-dimensional data about cracks, such as the crack area (a), perimeter (p), azimuth (α), length (l), width (d), number (N), and crack space



(a) Crack image obtained at the initial stage



(b) Connection of crack image

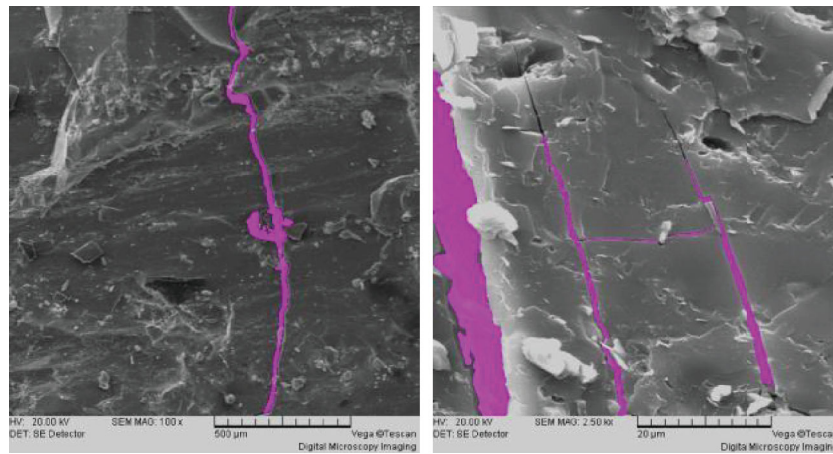


(c) Crack profile

FIGURE 4: Continued.



(d) Fill of crack profile



(e) Crack image overlaid on the original one

FIGURE 4: Extraction of crack information.

TABLE 2: Two-dimensional information of the crack (unit: pixel).

Characteristics	Crack 1	Crack 2	Crack 3	Crack 4
Single crack				
Crack area	4175			
Fitted long axis	499			
Fitted short axis	53			
Azimuth (°)	-81.9			
Crack perimeter	1385			
Equivalent radius	36.5			
Multicrack				
Crack area	16504	1888	277	1942
Fitted long axis	435	418	193	301
Fitted short axis	53	11	11	15
Azimuth (°)	-79.3	-73.6	4.4	-70.2
Crack perimeter	1096	816	338	679
Equivalent radius	72.5	24.5	9.5	25

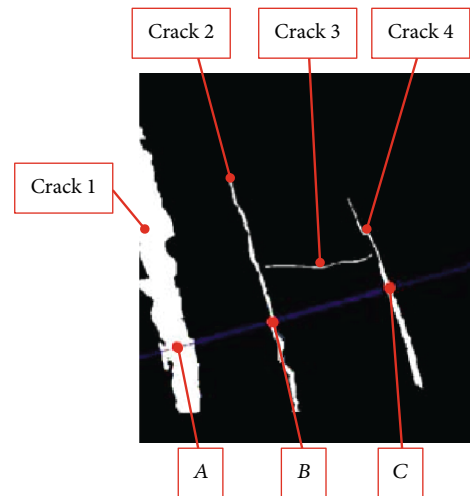


FIGURE 5: Measurement of the multicrack space.

(m). An analysis of this information can be used to realize a quantitative description of the mesostructure of coal rock; as a result, this information can also be further

applied to the theoretical study of the seepage mechanics and damage mechanics of coal rock.

5.2.1. Application of Coal Rock Crack Information to the Research on Seepage Mechanics. In coal rock containing

cracks, the cracks can be grouped according to their strike. In accordance with the model with equal-width crack, the coefficient of permeability for crack can be expressed as

$$K_f = gd^2/12\nu. \quad (16)$$

Romm [17] supposed that the cracked rock mass is a quasicontinuous medium and that the fluid flow conforms to the Darcy law:

$$q = -K_f \frac{d}{m} J'. \quad (17)$$

As the Darcy Law suggests,

$$q = -K_c J'. \quad (18)$$

Combining Equations (16)–(18) can obtain the coefficient of permeability of the crack group:

$$K_e = \frac{gd^3}{12\nu m}, \quad (19)$$

where g is the acceleration of gravity, ν is the viscosity coefficient of fluid motion, q is the permeation rate, and J' is the pressure gradient of fluid.

5.2.2. Application of Coal Rock Information to the Research on Damage Mechanics. The mesostructure of coal rock determines its damage state, which can be roughly obtained by evaluating the mesostructural characteristics of micro-cracks. The mesoimages obtained through the mesomechanic experiment can be used to quantitatively investigate the relationship among the initiation, expansion, and deformation response of cracks (mesostructure). In order to establish the correlation among the damage variables of mesostructures, macromechanical responses, and physical constitutive equations, variable γ should be introduced to express the surface damage degree of a sample and quantify it based on crack data with the expression listed as below:

$$\gamma(\varepsilon) = \frac{L_{cr}^f(\varepsilon)}{L_{cr}^f(\varepsilon)}, \quad (20)$$

where $L_{cr}^f(\varepsilon)$ is the effective length of the crack under the peak stress and $L_{cr}(\varepsilon)$ refers to the effective length of the crack under the corresponding strain.

The effective length of a crack is calculated according to the following equation [18]:

$$L_{cr}^{(1)} = \sum_{i=1}^n l_{cr}^{(i)} \cos^2 \beta^{(i)}, \quad (21)$$

where $L_{cr}^{(1)}$ is the effective length of the surface crack of the sample; $l_{cr}^{(i)}$ is the length of the i^{th} crack; n is the total number of cracks; and $\beta^{(i)}$ is the included angle between the i^{th} crack and the load orientation, i.e., $\beta^{(i)} = \pi/2 - \alpha^{(i)}$, where $\alpha^{(i)}$ is the

azimuth of the crack, in the unit of radian. The aforesaid quantitative method of measuring the degree of surface crack damage has effectively simplified data processing without taking into account the anisotropy of coal rock. However, in the practical project, the coal rock is characterized by significant heterogeneity and geometric discontinuity. For this reason, the evaluation of damage of coal rock should also take into consideration the anisotropy. In conformity with the theory of continuum damage mechanics [19–24], the damage tensor, \tilde{w} , of the rock mass is defined as follows:

$$\tilde{w} = \frac{m'}{V} \sum_{i=1}^N a^i (n^i \otimes n^i), \quad (22)$$

where m' is the minimum space of the crack surface, a is the area of the i^{th} crack, and n is the normal vector of the i^{th} crack.

6. Conclusions

In order to comprehensively and accurately obtain crack information from coal rock mesoimages, this paper introduces image processing technology based on PDE and expounds on the principle of active contour models without edges. In light of the uneven grayscale distribution of the C-V model and the limitations of coal rock images with low contrast ratios, an improved C-V model based on image enhancement functions is proposed with a discretization scheme that combines forward difference and backward difference and a semi-implicit scheme for numerical calculation is adopted.

The C-V model and improved C-V model were adopted for the image processing of coal rock mesoimages. The results show that the improved C-V model achieved a better image segmentation effect and provided more accurate quantitative information about coal rock mesostructure than the C-V method for images with both single cracks and multiple cracks. This fact demonstrates that the improved C-V model is superior when it comes to processing coal rock mesoimages with nonuniform grayscales and low contrast.

The extracted binary crack images were subjected to quantitative processing in order to extract the length, azimuth, area, perimeter, and space of cracks and crack sets. The quantitative information about crack images at different experimental stages of coal rock mesostructure is used in order to conduct more in-depth research into coal rock seepage and damage mechanics.

Data Availability

The data used to support the findings of this study are available from the corresponding author upon request.

Conflicts of Interest

The authors declare no conflict of interest.

Acknowledgments

This research was funded by the Beijing Natural Science Foundation (8204068).

References

- [1] C. Chen, X. M. Liu, and C. H. Liu, "Application of digital image processing to rock mesomechanics," *Rock and Soil Mechanics*, vol. 31, pp. 3468–3472, 2010.
- [2] S. Chen, Z. Q. Yue, and L. G. Tham, "Digital image based numerical modeling method for heterogeneous geomaterials," *Chinese Journal of Geotechnical Engineering-Chinese Edition*, vol. 27, pp. 956–964, 2005.
- [3] S. Chen, Z. Q. Yue, and L. G. Tham, "Digital image-based numerical modeling method for prediction of inhomogeneous rock failure," *International Journal of Rock Mechanics and Mining Sciences*, vol. 41, no. 6, pp. 939–957, 2004.
- [4] Z. Q. Yue, S. Chen, and L. G. Tham, "Finite element modeling of geomaterials using digital image processing," *Computers and Geotechnics*, vol. 30, no. 5, pp. 375–397, 2003.
- [5] Z. Q. Yue, S. Chen, H. Zheng, and L. G. Tham, "Digital image proceeding based on finite element method for geomaterials," *Chinese Journal of Rock Mechanics and Engineering*, vol. 23, pp. 889–897, 2004.
- [6] Z. D. Zhu, W. P. Qu, and Z. J. Jiang, "Quantitative test study on mesostructure of rock," *Chinese Journal of Rock Mechanics and Engineering*, vol. 26, pp. 1313–1325, 2007.
- [7] W. J. Xu, Z. Q. Yue, and R. L. Hu, "Study on the mesostructure and mesomechanical characteristics of the soil-rock mixture using digital image processing based finite element method," *International Journal of Rock Mechanics and Mining Sciences*, vol. 45, no. 5, pp. 749–762, 2008.
- [8] Y. B. Liu, S. G. Cao, and Y. C. Liu, "Discussion on analytical method for LS-SVM based mesoscopic rock images," *Chinese Journal of Rock Mechanics and Engineering*, vol. 27, pp. 1059–1065, 2008.
- [9] Q. L. Yu, T. H. Yang, C. Zheng, C. A. Tang, and P. T. Wang, "Numerical analysis of influence of rock mesostructure on its deformation and strength," *Rock and Soil Mechanics*, vol. 32, pp. 3468–3472, 2011.
- [10] R. C. Gonzalez, R. E. Woods, and S. L. Eddins, *Digital Image Processing Using MATLAB*, Gatesmark Publishing, USA, 2009.
- [11] M. Sonka, V. Hlavac, and R. Boyle, *Image Processing, Analysis, and Machine Vision*, Cengage Learning, USA, 2014.
- [12] Q. Q. Ruan and J. Y. Wu, "Partial differential equation(PDE) method on digital image processing," *Signal Process*, vol. 28, pp. 301–314, 2012.
- [13] D. Zhang and G. Chen, *Image Processing Based on Partial Differential Equations*, Higher Education Press, China, 2004.
- [14] T. Chan and L. Vese, "Active contours without edges," *IEEE Transactions on Image Processing*, vol. 10, no. 2, pp. 266–277, 2001.
- [15] T. Chan and L. Vese, "An efficient variational multiphase motion for the Mumford-Shah model," in *Proceedings of the 34th Asilomar Conference on Signals, Systems and Computers*, pp. 490–494, Pacific Grove, CA, USA, USA, November 2000.
- [16] Y. B. Liu, *Study on the deformation and damage rules of gas-filled coal base on mesomechanical experiments*, Chongqing University, China, 2009.
- [17] E. S. Romm, *Fluid Flow in Fractures*, Nedra Publishing House, Russia, 1966.
- [18] P. T. Qi, Z. X. Li, and Y. P. Hang, "Link between compressive deformation and crack propagation in cement mortar," *Chinese Journal of Rock Mechanics and Engineering*, vol. 22, pp. 425–428, 2003.
- [19] J. X. Yuan, "Problems of rock mass damage," *Rock and Soil Mechanics*, vol. 14, pp. 12–20, 1993.
- [20] Z. Y. Song and H. Konietzky, "A particle-based numerical investigation on longwall top coal caving mining," *Arabian Journal of Geosciences*, vol. 12, no. 18, p. 556, 2019.
- [21] Z. Y. Song, H. Konietzky, and M. Herbst, "Three-dimensional particle model based numerical simulation on multi-level compressive cyclic loading of concrete," *Construction and Building Materials*, vol. 225, pp. 661–677, 2019.
- [22] Z. Y. Song, H. Konietzky, and M. Herbst, "Bonded-particle model-based simulation of artificial rock subjected to cyclic loading," *Acta Geotechnica*, vol. 14, no. 4, pp. 955–971, 2019.
- [23] Z. Y. Song, H. Konietzky, and M. Herbst, "Drawing mechanism of fractured top coal in longwall top coal caving," *International Journal of Rock Mechanics and Mining Sciences*, vol. 130, article 104329, 2020.
- [24] Z. Y. Song, W. J. Wei, and J. W. Zhang, "Numerical investigation of effect of particle shape on isolated extracted zone (IEZ) in block caving," *Arabian Journal of Geosciences*, vol. 11, no. 12, p. 310, 2018.